

Electronic Thesis and Dissertation Repository

4-15-2020 9:30 AM

Impact-Generated Dykes and Shocked Carbonates from the Tunnunik and Houghton Impact Structures, Canadian High Arctic

Jennifer D. Newman, *The University of Western Ontario*

Supervisor: Osinski, Gordon R., *The University of Western Ontario*

A thesis submitted in partial fulfillment of the requirements for the Doctor of Philosophy degree in Geology

© Jennifer D. Newman 2020

Follow this and additional works at: <https://ir.lib.uwo.ca/etd>



Part of the [Geology Commons](#)

Recommended Citation

Newman, Jennifer D., "Impact-Generated Dykes and Shocked Carbonates from the Tunnunik and Houghton Impact Structures, Canadian High Arctic" (2020). *Electronic Thesis and Dissertation Repository*. 6950.

<https://ir.lib.uwo.ca/etd/6950>

This Dissertation/Thesis is brought to you for free and open access by Scholarship@Western. It has been accepted for inclusion in Electronic Thesis and Dissertation Repository by an authorized administrator of Scholarship@Western. For more information, please contact wlsadmin@uwo.ca.

Abstract

The Canadian High Arctic contains two impact structures created by hypervelocity impact events in carbonate-rich target rocks. The remote locations of the Tunnunik and Haughton impact structures means that there are aspects of these impact structures which have yet to be fully investigated. This study characterizes the range of impact-generated dykes exposed from both impact structures which include lithic breccias, impact melt-bearing breccias, and impact melt rocks. Breccias may include silicate impact glass fragments and evidence for carbonate melt. Impact melt rocks from the Haughton impact structure contain the rare terrestrial mineral moissanite. This is only the third reported occurrence of moissanite associated with an impact structure and the first to observe its presence in situ. Inclusions and variation of polytypes in moissanite provide information regarding high temperatures present during crater formation. The carbonate-rich rocks that form these impact structures contain well-developed shatter cones as evidence of shock metamorphism. As a shock classification system does not currently exist for carbonates, the effect of shock on the crystal structure of calcite and dolomite is examined using X-ray diffraction to better understand the extent of strain in both these minerals. Previous studies of shocked carbonates from terrestrial impact structures is limited and the goal here is to assign numerical values to indicate strain and thereby better quantify and compare shock in carbonates among impact structures.

The parallel studies of impact-generated dykes and shock at the Tunnunik and Haughton impact structures allow for the comparison of two impact structures with similar diameters, 28-km for Tunnunik and 23-km for Haughton, in different states of preservation. The deeply eroded Tunnunik impact structure and well-preserved Haughton impact structure provide insights into complex crater formation in carbonate rich rocks that would otherwise not be available by only studying one site. Results from this pair of impact sites has expanded the knowledge of carbonate-rich impact structures and will help future investigations of other known carbonate-rich impact sites and ones yet to be discovered.

Keywords

Tunnunik impact structure, Haughton impact structure, impact cratering, impact breccia, impact melt rock, dyke, carbonate, shocked carbonate, dolomite, calcite, lattice strain, Arctic, X-ray diffraction, moissanite.

Summary for Lay Audience

Impact craters form when a large projectile, typically a fragment from an asteroid or comet, survives its transit through Earth's atmosphere and strikes a solid rocky surface. The resulting crater may be tens of metres to several hundred kilometres in diameter, depending on the size and speed of the projectile. Examining the rocks affected and generated by impact events allow the impact process to be better understood.

This study focuses on two remote impact sites in the Canadian High Arctic, the Tunnunik impact structure and Haughton impact structure, that formed in carbonate rocks consisting mainly of limestone and dolostone. Rocks affected by the shock created during the impact often display shatter cones near the centre of the impact structures which appear as small fractures or striation to the unaided eye. A technique called X-ray diffraction uses X-rays to investigate the crystal structure of calcite and dolomite, the primary minerals in the carbonate rocks that form the impact structures. Shock effects increase strain within the crystal structure of these minerals and the strain values derived from the X-ray diffraction analyses are compared among samples collected from different locations in each impact structure.

The rocks generated by the impact event examined in this study include impact breccias and impact melt rocks found in impact-generated dykes. Breccias consist of fragments from one or more different types of carbonate rock and are held together by finer fragments that are too small to see without higher magnification. Breccias may also include small silicate glass fragments or melted carbonate clasts. Impact melt rocks consist of fine-grained recrystallized calcite, clasts from the limestone rocks adjacent to the dykes, and crystals of a rare mineral called moissanite. Moissanite is rare due to very specific conditions required for it to form and these conditions help identify temperatures reached in the impact melt rocks when they were generated.

Comparing the results from the Tunnunik and Haughton impact structures has provided insights into their formation and expanded the knowledge of carbonate-rich impact structures.

Co-Authorship Statement

Chapter 1. Literature review of information relevant to this work was completed and written by Jennifer Newman. Comments and editing were provided by Dr. Gordon Osinski.

Chapter 2. Sample analysis, data collection, and data processing were completed by Jennifer Newman. EPMA data collection was assisted by Marc Beauchamp. Chapter was written by Jennifer Newman. Comments and editing were provided by Dr. Gordon Osinski.

Chapter 3. Sample analysis, data collection, and data processing were completed by Jennifer Newman. EPMA data collection was assisted by Marc Beauchamp. Chapter was written by Jennifer Newman. Comments and editing of were provided by Dr. Gordon Osinski.

Chapter 4. Sample preparation, analysis, and data processing for all suite 1 samples were completed by Jennifer Newman. Powder X-ray diffraction data collection was assisted by Alexandra Rupert. Rietveld analyses for suite 2 samples began as a class project in Earth Sci 9516b: Advanced Mineralogy and Crystallography (2017). Dr. Roberta Flemming provided helpful and constructive discussions regarding sample processing and interpretation. I reprocessed all suite 2 samples, so that all samples were refined in a manner consistent with suite 1 samples. Ultimately all results presented in this chapter were processed and interpreted by Jennifer Newman. Chapter was written by Jennifer Newman. Comments and editing were provided by Dr. Gordon Osinski.

Chapter 5. Sample preparation, analysis, and data processing were completed by Jennifer Newman. Powder X-ray diffraction data collection was assisted by Alexandra Rupert. Chapter was written by Jennifer Newman. Comments and editing were provided by Dr. Gordon Osinski.

Chapter 6. Sample analysis and data processing were completed by Jennifer Newman. Data collection using the Raman spectrometer was assisted by Tianqi Xie. Chapter was written by Jennifer Newman. Comments and editing were provided by Dr. Gordon Osinski.

Chapter 7. Summary of thesis was written by Jennifer Newman. Comments and edits were provided by Dr. Gordon Osinski.

Acknowledgements

As I cast my leaving shadow on this five year mission, it could not have been achieved without the support and contribution of so many people. First, I would like to thank my supervisor Dr. Gordon 'Oz' Osinski for his guidance and the opportunity to work on an incredible project that included two amazing field seasons in the Arctic. I am grateful for field and research funding support from NSERC, the Canadian Space Agency, the Northern Scientific Training Program, and the OGS/QEII program from the Ontario government. The Polar Continental Shelf Program is thanked for logistical field support.

When I started this journey, I did not have a sense of scope regarding the numerous aspects this project would cover, let alone the unexpected mineral discovery from Haughton found as I was nearing completion! The opportunity to participate in two CanMars Mars sample return analogue missions through my NSERC CREATE/CSA fellowship and the CanMoon 2019 Lunar sample return analogue mission while at Western were great experiences and I hope to put these experiences into practice. I am also grateful to Dr. Livio Tornabene for the opportunity to participate in planning MRO/HiRISE cycle 301 with Sarah Simpson and Alyssa Werynski, this was a valuable and amazing experience. My thesis committee is thanked for their suggestions, collaborations, and guidance during this endeavour.

Racel Sopoco, Cassandra Marion, Taylor Haid, William Zylberman, Byung-Hun Choe, Gordon Osinski, Livio Tornabene, Jeremy Hansen, Rob Misener and the rest of the Tunnunik field team, thank you for your help collecting samples, fending off wildlife, and making camp life enjoyable. Even when the weather didn't cooperate with our field or flight plans, we persevered through!

Thank you to Alexandra Pontefract, Rebecca Greenberger, Elise Harrington, Anna Grau, Shamus Duff, Gordon Osinski, Livio Tornabene, Etienne Godin, Byung-Hun Choe, and the rest of the Haughton field team who assisted with sample collection and made life around camp fun despite the cold and all the rain. Whether we were getting stuck in the mud, sampling great outcrops, climbing gullies, or racing to pack up camp early because the plane was on its way, we made a great team.

My lab work at Western would not have been a success without the assistance of Racel Sopoco, Cassandra Marion, Marc Beauchamp, Dr. Roberta Flemming, Alexandra Rupert, Tianqi Xie, Joshua Laughton, Peter Christoffersen, and Stephen Wood. Mati Raudsepp (UBC) and Jacob Kabel (UBC) are thanked for their advice and insights regarding XRD sample mounting and Rietveld refinement.

Thank you to the Spacerocks Team, Western and CPSX/Western Space friends, office mates, and fellow planetary scientists I only see for a short time at conferences or field schools for encouraging me during this time and for discussions on impact cratering, meteorites, and all things space.

A special thanks and virtual high-fives to everyone who provided extra support and encouragement during the COVID-19 pandemic to see a successful end to this journey (on time!), albeit in a slightly modified and unexpected format.

Finally, I would like to thank my parents, Brad and Jayne, sister Melony, and the rest of my family for their messages, support, and listening to my adventures and rock talk over the years. I would also like to thank my extended family for fueling my DavidsTea obsession, my cupboard was never empty and always had the perfect cuppa for any occasion. This journey wasn't always easy from a distance, but it meant a lot and could not have done this without you.

Per conatus ad victoriam.

Victory through endeavour.

Dedication

To my grandparents Joan and John Allen and Marshall Newman for their interest and support when I began this journey but were not able to see its completion or join in the celebration. And to my little *Felis catus* buddy Amber with her endless snuggles, you will be missed but never forgotten.

Table of Contents

Abstract	ii
Keywords	iii
Summary for Lay Audience	iv
Co-Authorship Statement.....	v
Acknowledgements.....	vi
Dedication	viii
Table of Contents	ix
List of Tables	xiv
List of Figures	xvi
List of Appendices	xxviii
Chapter 1	1
1 Introduction	1
1.1 Impact cratering	1
1.1.1 Complex crater formation.....	3
1.1.2 Sedimentary targets.....	6
1.1.3 Impactites	7
1.1.4 Microscopic shock metamorphism	8
1.2 Arctic geology.....	9
1.2.1 Arctic Archipelago.....	9
1.2.2 Victoria Island (Kiilineq).....	11
1.2.3 Devon Island (Tallurutit)	14
1.3 X-ray diffraction	17
1.3.1 Powder X-ray diffraction theory.....	18
1.3.2 Rietveld refinement.....	21

1.4 Thesis objectives	22
1.5 References	22
Chapter 2	33
2 Impact-generated breccia dykes of the Tunnunik impact structure, Canada	33
2.1 Introduction.....	33
2.2 Geologic setting	34
2.3 Samples and methods.....	35
2.4 Results.....	36
2.4.1 Type 1	37
2.4.2 Type 2	50
2.4.3 Type 3	51
2.4.4 Type 4	58
2.5 Discussion.....	60
2.5.1 Silicate impact glass.....	60
2.5.2 Evidence for melting of carbonates	62
2.5.3 Origin and emplacement of the Tunnunik dykes	63
2.6 Conclusions.....	69
2.7 References.....	70
Chapter 3.....	75
3 Impact-generated carbonate-rich dykes from the Houghton impact structure, Canada	75
3.1 Introduction.....	75
3.2 Geologic setting	76
3.3 Samples and methods.....	76
3.4 Results.....	79
3.4.1 Lithic breccia dykes	80
3.4.2 Quartz-cemented carbonate breccia dyke	84

3.4.3	Sulfate-bearing polymict breccia	86
3.4.4	Impact melt rock dykes	88
3.4.5	Chert.....	95
3.5	Discussion.....	97
3.5.1	Impact-related features.....	97
3.5.2	Dyke formation	99
3.5.3	Clast-rich impact melt rocks	101
3.5.4	Comparison with other impact structures	103
3.6	Conclusions.....	105
3.7	References.....	106
Chapter 4.....		111
4	Shock effects in dolomite and calcite from the Haughton impact structure, Canada, using X-ray diffraction and Rietveld refinement.....	111
4.1	Introduction.....	111
4.2	Samples and methods.....	114
4.2.1	Suite 1: In situ carbonate target rocks.....	114
4.2.2	Suite 2: Shatter cone clasts from crater-fill and ballistic ejecta deposits...116	
4.2.3	Rietveld refinement.....	117
4.3	Results.....	118
4.3.1	Powder X-ray diffraction	118
4.3.2	Rietveld refinement.....	120
4.3.3	Williamson-Hall plots.....	123
4.4	Discussion.....	126
4.4.1	Shock effects in calcite versus dolomite.....	126
4.4.2	Comparison with other craters in carbonate target rocks.....	128
4.4.3	Carbonates as shock indicators	130

4.5	Conclusions.....	133
4.6	References.....	134
Chapter 5.....		140
5	An X-ray diffraction study of shocked carbonates from the deeply eroded Tunnunik impact structure, Canada.....	140
5.1	Introduction.....	140
5.2	Samples and methods.....	141
5.3	Results.....	144
5.3.1	Powder X-ray diffraction	144
5.3.2	Rietveld refinement.....	145
5.3.3	Strain estimation	146
5.4	Discussion.....	149
5.4.1	Peak broadening in X-ray diffraction patterns.....	149
5.4.2	Strain estimates and trends.....	150
5.4.3	Practicality of strain estimation	152
5.5	Conclusions.....	152
5.6	References.....	153
Chapter 6.....		156
6	Impact-generated moissanite (SiC) from the Houghton impact structure, Canada....	156
6.1	Introduction.....	156
6.2	Moissanite and polytypism background	157
6.3	Methods and results	159
6.3.1	Petrography	159
6.3.2	Electron probe microanalysis (EPMA).....	161
6.3.3	Raman Spectroscopy.....	164
6.4	Discussion.....	166

6.4.1	Natural versus synthetic SiC.....	166
6.4.2	Moissanite formation	167
6.4.3	Occurrence at terrestrial impact sites.....	169
6.5	Conclusions.....	170
6.6	References.....	170
Chapter 7.....		174
7	Summary of results from two terrestrial hypervelocity impacts into carbonate target sequences.....	174
7.1	Carbonate-rich target sequences	175
7.2	Deeply eroded versus well-preserved impact structures.....	177
7.3	Dyke emplacement in the Tunnunik and Haughton impact structures	178
7.4	Extent of shock	180
7.4.1	Strain versus distance from the centre of impact structures	180
7.4.2	Strain versus depth within impact structures	181
7.4.3	Future shock-related research opportunities	181
7.5	Conclusions.....	182
7.6	References.....	183
Appendices.....		188
Curriculum Vitae		339

List of Tables

Table 2-1. Electron microprobe WDS analyses of carbonates* for mineral grains and melt.	42
Table 2-2. Electron microprobe WDS analyses of silicate glass fragments in Type 1 breccia.	48
Table 2-3. Breccia dyke summary.	69
Table 3-1. Compositions from the quartz-cemented carbonate breccia dyke.....	86
Table 3-2. Electron probe microanalysis (WDS) of carbonate phases in impact melt rock dykes.	93
Table 3-3. Electron probe microanalysis (WDS) of silicate glass.	95
Table 4-1. Modal mineral proportions of samples in weight percent with crystal size and lattice strain values for carbonates determined by Rietveld refinement of bulk rock powders from the Haughton impact structure.	121
Table 4-2. Lattice strain values sorted by distance from the centre of the Haughton impact structure for suite 1 carbonates.	122
Table 4-3. Lattice strain values sorted by distance from the centre of the Haughton impact structure for suite 2 carbonates.	122
Table 4-4. Comparison of lattice strain measurements by Rietveld refinement from the Haughton impact structure and experimentally shocked carbonates.	131
Table 5-1. Comparison of lattice strain values determined by two methods for samples from the Haughton impact structure.	148
Table 5-2. Calculated lattice strain values for carbonate samples from the Tunnunik impact structure sorted by distance from centre.	148
Table 6-1. Distribution of moissanite crystals within impact melt rocks from the Haughton impact structure.	160

Table 6-2. Electron probe microanalysis of silicate glass and moissanite using wavelength dispersive spectrometry. 162

Table 7-1. Comparison of physical features and properties at the Tunnunik and Haughton impact structures. 174

List of Figures

Figure 1-1. Sequence of cross-sections highlighting the main components involved in the three stages of impact crater formation for complex craters; modified from Osinski and Pierazzo (2013).....	4
Figure 1-2. The Canadian Arctic Archipelago with study site locations indicated. Base map provided by d-maps.com.....	10
Figure 1-3. A) Google Earth (2018) image of Victoria Island; white square indicates the location of inset image B) showing the Tunnunik impact structure, outlined by white dashed circle. Coordinates for the centre of the Tunnunik impact structure are 72°27'16" N, 113°49'49" W (Impact Earth 2020).....	13
Figure 1-4. A) Google Earth (2018) image of Devon Island; white square indicates the location of inset image B) showing the Haughton impact structure. Coordinates for the centre of the Haughton impact structure are 75°22'39" N, 89°39'13" W (Impact Earth 2020).	15
Figure 1-5. Comparison of the unit cell for calcite and dolomite. View shown is looking through the <i>a</i> -axes which are perpendicular to the <i>c</i> -axis. Representative carbonate (CO ₃) and octahedral (CaO ₆ or MgO ₆) layers are indicated which include calcium (green), magnesium (yellow), carbon (grey), and oxygen (red) atoms. Structural model visualizations obtained from The Virtual Museum of Minerals and Molecules (Barak and Nater 2020).	18
Figure 1-6. Derivation and illustration of Bragg's Law. Incident X-rays (A, B, C) diffract at atoms within lattice planes (<i>hkl</i>), where <i>d</i> is the spacing between planes in the crystal structure, at an angle (θ) to generate diffracted X-rays (A', B', C').....	19
Figure 1-7. X-ray diffraction patterns for unshocked calcite and dolomite. Positions of Miller indices (<i>hkl</i>) for calcite are indicated by vertical green lines with diamond markers and dolomite by vertical blue lines with square markers.	20
Figure 1-8. Illustration of peak broadening observed in diffraction patterns associated with lattice strain (modified from Cullity 1978). The strained diffraction pattern can be thought of	

as a series of small peaks (dashed) caused by slight differences in d-spacing in crystal lattice that combine to generate one broad peak..... 21

Figure 2-1. Simplified geologic map of the Tunnunik impact structure indicating breccia dyke localities examined in this study; Shatter Cone Canyon (SCC), Shaler Supergroup (SS), Big Lake (BL), Big Lake south (BLs), Bouldering River (BR), West River (WR) and Rim Canyon (RC). B) Shatter cone distribution within the Tunnunik impact structure. UTM grid with Easting and Northing at 1000 m intervals for Zone 11 and Zone 12..... 35

Figure 2-2. Type 1 breccia dykes from Shatter Cone Canyon (A–C), Big Lake (D–E), and Bouldering River (N) with dyke boundaries indicated by white dashed lines. A) Nearly vertical dyke cuts through more horizontal bedding; breccia is fractured and fragments have fallen out of place. B) Dyke is parallel to bedding planes with a dip of 49°. C) Narrow dyke that follows the fold contour of the host rocks. D) Ground surface exposure of dyke has been strongly affected by freeze-thaw action and is highly fractured like surrounding rock. Inset image from top of dyke shows a location that was more resistant to freeze-thaw cycles. E) Similar to (D), breccia in dyke has been severely fractured by frost action. Samples (F–K) represent variations among T1 dykes. F) Breccia from Shatter Cone Canyon shows subtle banding in matrix with elongated clasts oriented parallel to bands. G) Sample from dyke in (C) shows small clasts oriented in horizontal direction. H) Bimodal clast size distribution in breccia from Big Lake. I) Minimal alignment of larger rounded clasts in this Big Lake breccia sample. J) The most diverse assemblage of clasts in any T1 breccia. K) Sample from dyke in (D) contains part of a large 10 cm grey dolostone clast. L) Breccia sample from dyke in (B) showing alignment of clasts parallel to green mudstone host rock along top of hand sample. M) Similar to (L) this breccia from Shatter Cone Canyon also shows clasts oriented in same direction as green mudstone host. N) Horizontal breccia dyke follows bedding planes of host dolostone. O) Close-up of breccia near right edge of dyke shown in (N). 38

Figure 2-3. Type 1 breccia optical microscopy. A) Coarse, clast-supported area of breccia. B) Small-scale clast orientation localized near host contact to right of image. C) Veins of coarse calcite cut across matrix and clasts. D) Euhedral grains of dolomite in small vug. E) Rounded, fine-grained calcite clast (pale grey) containing fine-grained dolomite (dark grey). F) Irregular-

shaped calcite clast (pale grey) with areas of dolomite (dark grey). (A–C) imaged in PPL and (D–F) imaged with BSE..... 40

Figure 2-4. Backscattered electron images of T1 breccia at 500x magnification. A) Well-defined grains of K-feldspar, pyrite (white), and quartz in dolomite-rich matrix along top of sample in Figure 2-4A. B) Dolomite and K-feldspar matrix from Figure 2-2F breccia has range of clast sizes with distinct edges. C) Dolomite-rich matrix from Figure 2-2J breccia is less defined than matrix in (A) and (B). D) Poorly defined dolomite matrix with feldspar grains and rare quartz. Minerals indicated include dolomite (Dol), quartz, (Qz), and K-feldspar (Kfs); black areas are pore spaces within the matrix..... 41

Figure 2-5. A) Fine-grained carbonate clast outlined by white dashed line partially in band of fine-grained calcite (pale grey) in BSE from grey T1 breccia in Figure 2-10A. B) Calcite band and lower left area of clast highlight localized occurrence of calcite within dolomite-rich matrix of T1 breccia from Shatter Cone Canyon. Minerals indicated include calcite (Cal), dolomite (Dol), K-feldspar (Kfs), quartz (Qz), and sulfides (S)..... 44

Figure 2-6. A–D) Area within a cm-sized clast in T1 breccia displaying fine-grained dolomite and calcite. A) Fine-grained dolomite is difficult to recognize from calcite as colours observed do not correspond to a specific composition. Dashed black line separates clast above line from matrix below. B) Fine-grained calcite (Cal) is readily distinguished from dolomite (Dol) in BSE. C) Calcium element map shows calcite in yellow and dolomite in pink. D) Silicon element map shows quartz (yellow) and K-feldspar (pink) grains within the clast and matrix. E–H) Carbonate clast with feathery texture. E) Clast is very fine-grained compared to matrix. Black dashed line separates clast below line from matrix above. F) Feathery clast is mainly dolomite, brighter edge along top of clast is calcite. G) Calcium map highlights the calcite band along top of clast. Dark areas are holes in sample. H) Silicon element map shows clast is silicate-free where quartz and K-feldspar grains are confined to the matrix. Colour scales on element maps range from zero counts (black) to highest counts (yellow). 45

Figure 2-7. A) Localized banding highlighting differences in matrix grain size and composition; dashed white lines outline silicate-rich band. B) Colourless grains in darker central matrix corresponds with silicate-rich band in (A). C) Contact between grey matrix and

dark grey-black K-feldspar-like band in (A) with a colourless crystalline K-feldspar and quartz clast at left edge of image. 46

Figure 2-8. Silicate impact glass. A) Large hypocrySTALLINE fragment displaying schlieren. B) Irregular contact between pale brown glass and colourless dolomite (PPL) with more contrast in XPL between isotropic glass (dark) and dolomite. C) HypocrySTALLINE fragment containing euhedral dolomite crystals visible as bright grains within the dark isotropic SiO₂-rich glass in XPL. D) A holohyaline fragment shows banding and mottling of silicate glass. E) Silicon element map highlights areas that are SiO₂-rich (yellow) and K₂O-rich (pink). F) Magnesium element map showing dolomite-rich matrix (yellow-orange). Colour scales ranges from zero counts (black) to highest counts (yellow) for the indicated element. 47

Figure 2-9. A Portion of a large 4400 µm impact glass fragment; dark area along top is dolomite-rich matrix. B) Same area as (A) in BSE. C) Enlarged area of (B) showing dolomite and K-feldspar inclusions in SiO₂-rich glass. D) Colour is a poor indicator of composition with partitioning of dolomite from dark isotropic SiO₂-rich glass apparent in XPL. E) Same clast as (D) in BSE. F) Enlarged area of (E) shows irregular shaped dolomite in K₂O-poor SiO₂-rich glass. Labels indicate dolomite (Dol), K-feldspar (Kfs), and SiO₂-rich glass (G). 49

Figure 2-10. A) The upper yellow coloured breccia is T2 with grey T1 breccia below, from dyke shown in Figure 2-2B. B) Breccia in (A) has a crackled appearance where clasts are separated by darker, fine-grained veins with little to no visible rotation. C) The yellow T2 breccia from Big Lake has a sharp contact with the grey T1 breccia. D) T2 breccia has thicker veins and a mosaic appearance with increased clast rotation compared to (B) while some adjacent clasts still fit together. 50

Figure 2-11. A) Contact between T3 dyke and host is sharp, however, the T3 breccia is not very distinctive from the grey limestone host; dyke outlined by dashed white lines. B–C) Examples of blue-grey T3 breccia that are clast-poor, compared to T1 samples. Large 1 cm clasts are outlined by black dashed lines. D) Contact between grey-toned West River T3 dyke and dolostone host; dyke is outlined by white dashed lines with black pen for scale; photo by G. Osinski. E) Dark mm-sized clasts are visible within the West River breccia dyke. 52

Figure 2-12. Type 3 breccia in BSE. A) mottled matrix of calcite (Cal) and dolomite (Dol). B) Matrix of T3 showing less mottling and a few calcite-rich clasts. C) Rounded polymict calcite-rich clast contains minor amounts of dolomite, quartz, and K-feldspar. Diagonal calcite vein cuts across clast and matrix. D) Calcite grain engulfed by quartz (Qz) with quartz veins extending into surrounding calcite. E) Enlarged area of (D). F) Quartz veins extend outward from quartz grains into surrounding calcite. G) Enlarged area of (F) to show intricate quartz veining..... 54

Figure 2-13. A) In PPL, a small feathery clast, outlined by dashed line, found within large clast indicated in Figure 2-11C. B) Band of fine-grained ferroan dolomite rich in sulfides. In PPL, areas of outlined band appear darker than surrounding calcite-rich matrix. C) Calcite and dolomite clast with an irregular radiating texture, clast above dashed outline; PPL. D) Compositional differences are evident in BSE in this enlargement of upper right limb of the outlined band in (B); calcite (Cal), dolomite (Dol), ferroan dolomite (Dol-Fe), sulfide (S).. 55

Figure 2-14. Type 3 breccia clast from Figure 2-12C with irregular radiating texture. A) Calcite (pale grey) and dolomite (darker grey) compositions are shown in BSE. B) Calcium element map shows clast is primarily calcite (yellow) as well as matrix in lower left corner. C) Iron element map shows ferroan dolomite (purple) and bright pyrite grains. D) Magnesium element map indicates the presence of dolomite (pink). Colour scales on element maps range from zero counts (black) to highest counts (yellow) for the indicated element. 56

Figure 2-15. A) PPL image of large dolomite clast with calcite veins shown in upper right with calcite matrix to lower left. B) In BSE the carbonate compositions become more apparent along with the dark grey devitrified glass, brown colour in (A); calcite is light grey and dolomite is darker grey. C-D) Pyrite-bearing dolomite clast shown in PPL and RL. E) Small group of dolomite clasts (dark grey) within a calcite (light grey) matrix. Small white spots within the dolomite are pyrite grains. F) Small toasted quartz grain. 57

Figure 2-16. Type 4 breccia from Rim Canyon. A) Wedge-shaped dyke with narrow branches extending into the host rock at the top of the dyke; dyke boundaries indicated by white dashed lines. B) Blocks of grey host dolostone with white chert are present within the dyke, surrounded by a very fine yellow matrix. C) Contact between dyke and host rock is sharp. D) Fine-grained yellow matrix contains dolomite and chert clasts. 58

Figure 2-17. A) Matrix and clasts in T4 breccia are composed of dolomite and chert; 2 chert (Cht) clasts are indicated, PPL. B) Large brecciated dolomite clast present within T4 breccia; PPL. C) BSE image shows dolomite matrix is poorly defined and individual clast boundaries are not visible..... 59

Figure 3-1. Simplified map of the Haughton impact structure with outlines of geological formations shown, see Osinski et al. (2005a) for detailed geologic map. A) Dyke locations in this study and the extent of crater-fill deposits are highlighted. First two numbers in each sample ID indicate the year the sample was collected. B) Dykes located along the Haughton River valley. UTM grid with Easting and Northing at 1000 m intervals for Zone 16..... 77

Figure 3-2. Classification of calcite twins in thin sections from the Haughton impact structure. Top row drawings are modified from Burkhard (1993) and bottom row photomicrographs, viewed in plane-polarized light, are calcite grains in lithic breccia samples 16-1035, 16-1006, 16-1012, and 16-1081 respectively..... 79

Figure 3-3. Monomict lithic breccia dykes. A) Dyke 16-1012 is outlined by white dashed lines and offset by two nearly parallel faults, indicated by solid black lines. Rock hammer at lower left corner for scale. B) Oblique view of dyke in (A) below the bottom fault showing the dyke protruding outward from the weathered host rock surface; black arrow indicates dyke width and white arrow shows depth of dyke. C) Dyke 00-059 protruding from weathered rock surface. Lens cap for scale; photo by G. Osinski. D) Weathering of dyke 16-1012, outlined by white dashed lines, gives it a more yellow hue compared to adjacent host rock; rock hammer for scale..... 81

Figure 3-4. Examples of lithic monomict breccias from various formations within the Haughton impact structure. A) Sample 16-1006 from the Eleanor River Formation. B) Sample 16-1063 from the Bay Fiord Formation Member C. C) Sample 00-088 and 01-028 (D) from the Allen Bay Formation Lower Member. E) Sample 02-010 from the Thumb Mountain Formation..... 82

Figure 3-5. Examples of the matrix in lithic breccias from the Haughton impact structure shown at 50x magnification in plane-polarized light. A) Sample 99-108. B) Sample 00-088. C) Sample 16-1006..... 83

Figure 3-6. Microfossils in lithic breccia samples originating from the Thumb Mountain Formation. (A–C) Microfossil assemblages in large clasts that include fragments of conodonts and trilobites; sample 16-1035. (D–E) Smaller sub-rounded lithic clasts surrounded by a fine-grained matrix from sample 02-010. Samples are shown at 50x magnification in plane-polarized light. 83

Figure 3-7. Crackle type fault breccia occurrences located adjacent to an impact melt rock dyke. Lithic fragments are separated by thin seams of fine-grained matrix. A) Sample 16-1026. B) Sample 16-1038. Samples are shown at 50x magnification in plane-polarized light. 84

Figure 3-8. Sample 00-011. A) Flat hand sample with angular dark dolomite and pale chert clasts visible. B) Image acquired using backscattered electrons (BSE) showing typical clast and cement association of quartz (Qz), calcite (Cal), and dolomite (Dol). Bottom series of images shows the same location in BSE and element maps to show the distribution of Ca (calcium), Mg (magnesium), and Si (silicon). 85

Figure 3-9. Sulfate-bearing polymict breccia. A) Vertically oriented dyke (outlined in white dashed lines) cuts through inclined gypsum and anhydrite beds within the Bay Fiord Formation Member A. B) Sample 16-1074 collected from top right area of dyke visible in (A). C) In situ photograph of sample 16-1023, with a light-toned, layered anhydrite clast near centre of image. 87

Figure 3-10. Impact melt rock dykes (A–C) show a range of morphologies. Dykes are outlined by white dashed lines for clarity as impact melt rock is very similar in colour to host rock; hammer for scale. A) A narrow H-shaped branching dyke. B) Wide dyke that has eroded in the centre to form a small cave. C) An intermediate width dyke that has irregular contact with host rock and large cavities and vesicles. D) Sample 16-1000 from the dyke shown in (A). E) Sample 16-1003 from the dyke in (B). F) Sample 16-1020 from the dyke in (C). 89

Figure 3-11. Examples of impact melt rock that vary in the proportion of vesicles they contain. A) Sample 16-1001. B) Sample 16-1003. C) Sample 16-1005. D) Sample 16-1020. 90

Figure 3-12. Backscattered electron images of impact melt rock groundmass. A) Groundmass consists entirely of microcrystalline calcite and black areas are holes or pore spaces; sample

16-1003. B) Groundmass is microcrystalline calcite with small rounded quartz grains. Small black spots are pore spaces; sample 16-1011. Magnification for both images is 500x. 91

Figure 3-13. Sample 16-1011. A) Flat cut surface of impact melt rock sample with a heavily weathered clast at its centre. B) Weathered clast showing analysis spots on the groundmass (C) and clast (D). C) Magnified (7x) image of impact melt rock groundmass indicated in (B). D) Magnified (7x) image of weathered clast indicated in (B). E) 2-D analysis of weathered clast at location D. F) 2-D analysis of aphanitic groundmass at location C. 92

Figure 3-14. A) MgO-rich glass from 16-1020B. B) MgO-rich glass from 16-1003. C) MgO-rich glass from 16-1020A. D) C4-like glass from 16-1020B. E) Cavity (white area) with silicate glass remnants along the interior edge from 16-1020A. Images shown in plane-polarized light with magnification of 200x (A, C, D), 100x (B), and 50x (E). 94

Figure 3-15. Occurrences of black chert in the Eleanor River Formation. A) Brecciated area within the Haughton River valley with abundant black chert. B) Large rounded black chert nodules are prominent within the middle layer. An impact melt rock dyke is directly below this layer, outlined by black dashed lines. 96

Figure 3-16. Toasted chert has a brown appearance when observed in thin section. A–D) Partially toasted chert clast viewed by different methods to highlight the differences between the colourless untoasted areas and brown toasted areas of the clast as shown in plane-polarized light (A); sample 16-1001. A) Plane-polarized light photomicrograph of chert surrounded by calcite-rich groundmass. B) Cross-polarized light. C) Backscattered electron imagery shows a slight texture change between the two areas of the clast. Box outlines view provided in (D). D) Area corresponding to the toasted area of the clast is more pitted than the untoasted area. E) Chert clast has a fully toasted appearance; sample 16-1038. F) Chert clast is toasted and fractured; sample 16-1026. 97

Figure 3-17. Comparison of vesicular impact melt rocks from terrestrial impact structures. A) Hand sample of vesicular melt rock from Coté Creek locality, Mistastin. B) Hand sample of vesicular melt rock from Babaudus locality, Rochechouart. C) Clast-rich impact melt rock from the Haughton impact structure; sample 16-1003, see Figure 3-11B. D) Clast-poor impact

melt rock from the Mistastin impact structure; sample MM 11-23A. E) Clast-poor impact melt rock from the Rochechouart impact structure; sample RO-01-043. 104

Figure 4-1. Location of samples from the Houghton impact structure with outlines of geological formations shown. Suite 1 consists of in situ samples collected from known outcrop locations while suite 2 consists of shatter cone clasts and fragments from crater-fill and ballistic ejecta deposits. Three suite 2 samples were collected from at the northernmost site. Three suite 1 samples are located beyond the visible extent of the map are indicated by an arrow for direction with approximate distance. UTM grid with Easting and Northing at 1000 m intervals for Zone 16. 115

Figure 4-2. Example shatter cones from the central uplift of the Houghton impact structure in suite 1. A) Sample 99-063B. B) Sample 02-139. C) Sample 06-093. Scale bars are 2 cm. . 115

Figure 4-3. Example shatter cone clasts from suite 2. A) Sample 00-019. B) Sample 02-061. C) Sample 02-127. D) Sample 02-128. Scale bars are 1 cm. 117

Figure 4-4. X-ray diffraction patterns of powdered samples divided by calcite (A) and dolomite (B) as the primary mineral phase from the Houghton impact structure. Stacked patterns arranged by relative peak broadening. Vertical numbers in brackets above stacks in (A) and (B) indicate Miller Indices (*hkl*) associated with peaks for calcite and dolomite, respectively. Unshocked samples are indicated by (*). A y-offset has been applied to sample patterns for clarity. Analyses were conducted with DIFFRAC.EVA software version 4.2 by Bruker AXS and phases were matched using the ICDD (International Centre for Diffraction Data) database PDF-4+ (2019). 119

Figure 4-5. Locations of A) calcite-bearing and B) dolomite-bearing samples from the Houghton impact structure. Four samples contain both calcite and dolomite and so appear on both maps (samples 00-019, 00-158, 02-127, and 05-023). UTM grid with Easting and Northing at 1000 m intervals for Zone 16. 120

Figure 4-6. Williamson-Hall plot for calculated line broadening due to strain by diffracted angle of shocked to unshocked calcite associated with the Houghton impact structure. Squares represent suite 1 in situ target rock samples and triangles represent suite 2 samples from crater-

fill and ballistic ejecta deposits. Numbers in brackets at bottom of chart indicate Miller indices (<i>hkl</i>).....	124
Figure 4-7. Williamson-Hall plot for calculated line broadening due to strain by diffracted angle of shocked to unshocked dolomite associated with the Houghton impact structure. Squares represent suite 1 in situ target rock samples and triangles represent suite 2 samples from crater-fill and ballistic ejecta deposits. Numbers in brackets at top of chart indicate Miller indices (<i>hkl</i>).....	125
Figure 5-1. Examples of shatter cones from the Tunnunik impact structure in limestone (A) and dolostone (B) target rock. Rock hammer for scale.	141
Figure 5-2. X-ray diffraction sample locations within the Tunnunik impact structure. Unshocked dolostone sample 40 (not shown) was collected ~37 km southeast from the centre of the impact structure. White ellipse indicates the extent of the shatter cone distribution. UTM grid with Easting and Northing at 1000 m intervals for Zone 11 and Zone 12.	142
Figure 5-3. X-ray diffraction patterns of powdered samples divided by dolomite (A) and calcite (B) as the primary mineral phase from the Tunnunik impact structure. Vertical numbers in brackets above stacks in (A) and (B) indicate Miller Indices (<i>hkl</i>) associated with peaks for dolomite and calcite, respectively. Unshocked samples are indicated by (*). A y-offset has been applied to sample patterns for clarity. Note: sample 16-1017 is from the Houghton impact structure.....	145
Figure 5-4. Williamson-Hall plot for dolomite sample 439 showing integral breadth values measured from peak area plotted for a given diffracted angle with (<i>hkl</i>) indicated. Linear trendline equation and R ² value are displayed on chart.....	147
Figure 5-5. Williamson-Hall plot for calcite sample 439 showing integral breadth values measured from peak area plotted for a given diffracted angle with (<i>hkl</i>) indicated. Linear trendline equation and R ² value are displayed on chart.....	147
Figure 6-1. A) Overview of the Houghton impact structure with 24 dyke locations containing lithic impact breccia or impact melt rock. Impact melt rock dykes containing moissanite (SiC) crystals are exposed along the Houghton River Valley, indicated with black rectangle. B)	

Enlargement of Haughton River Valley showing locations and proximity of moissanite-bearing impact melt rock dykes with sample names indicated. Sample 16-1000 and 16-1011 were collected from dykes only several meters apart at the same outcrop. UTM grid with Easting and Northing at 1000 m intervals for Zone 16..... 157

Figure 6-2. In situ colourless to blue moissanite (SiC) crystals in orange-brown silicate glass (GL). Cracks and holes (H) in glass appear white and surrounding fine-grained groundmass is composed of calcite (Cal). Distribution of SiC may be sparse A) or tightly packed B)..... 160

Figure 6-3. Colourless moissanite crystal with rounded orange metallic Si inclusion. Back-scattered electron (BSE) image and element maps of silicon (Si), iron (Fe), nickel (Ni), titanium (Ti), and vanadium (V) show distribution of metals within inclusion. Centre dark inclusion visible in plane-polarized light (PPL) is below the surface so it does not appear in element maps. Colour gradient on right edge indicates number of counts detected for each element from low (dark) to high (bright)..... 163

Figure 6-4. In plane-polarized light (PPL) the metallic inclusion in the dark blue moissanite crystal is difficult to identify but is more apparent in reflected light (RL) and with back-scattered electrons (BSE). The rounded metallic Si inclusion contains distinct silicide compositions of 1) aluminum (Al), iron (Fe), and nickel (Ni) and 2) barium (Ba), titanium (Ti), and vanadium (V). The hexagonal crystals are vanadium silicide (VSi₂) with minor Ti and Ba substitutions for V. Colour gradient on right edge indicates number of counts detected for each element from low (dark) to high (bright)..... 163

Figure 6-5. Metallic veins within moissanite crystals. A) Dark blue moissanite crystal shown in plane-polarized light (PPL) and back-scattered electron (BSE) image has a relatively even distribution of iron (Fe), manganese (Mn), and chromium (Cr) metal in the absence of silicon (Si). Trace amounts of nickel (Ni) and copper (Cu) were detected but are not shown. B) Pale blue moissanite crystal in PPL image has a more contrasting distribution of Ni and Cu metal within the moissanite crystal compared to the metals more evenly distributed within the crystal shown in (A). Colour gradient on right side of image indicates number of counts detected for each element from low (dark) to high (bright)..... 164

Figure 6-6. Micro-Raman spectra for the three moissanite polytypes identified (6H, 4H, and 15R) which are oriented parallel or close to parallel with respect to the *c*-axis. Major peak values for each polytype are indicated and a Y-offset was applied between spectra for clarity.

..... 165

Figure 7-1. Visual estimation of erosion levels at the Haughton (H) and Tunnunik (T) impact structures. Note the actual erosional surfaces of these impact structures are not flat horizontal planes, this is only a representation. Complex crater cross-section image is modified from Osinski and Pierazzo (2013); D = final rim-to-rim crater diameter, d_t = true depth, d_a = apparent depth, SU = structural uplift. 177

List of Appendices

Appendix A: List of samples	188
Appendix B: EDS electron probe microanalysis data.....	191
Appendix C: Powder X-ray diffraction (XRD) analysis data from the Tunnunik impact structure.....	193
Appendix D: Micro X-ray diffraction (μ XRD) analysis data.....	216
Appendix E: Detailed analytical methods and output values for Rietveld refinement of powder X-ray diffraction (pXRD) scans from the Haughton impact structure	231
Appendix F: Raman spectroscopy analysis data.....	316

Chapter 1

1 Introduction

1.1 Impact cratering

Impact cratering is a ubiquitous process to all solid surfaces in our Solar System. On Earth the terrestrial impact record is poorly preserved compared to the Moon or Mars due to active surface processes such as plate tectonics, erosion, and burial. Currently there are 198 confirmed terrestrial impact structures (Impact Earth 2020) Despite the identification of nearly 200 impact structures, there are still aspects that are not fully understood. This lack in understanding is attributed, in part, to the inaccessibility of a large portion of terrestrial impact structures as many are buried (63 are completely buried and 4 are partially buried) or found in very remote locations (Impact Earth 2020). The preservation level of impact structures can also affect what information can be acquired for a given impact site.

Impact cratering can occur on any solid surface, regardless of composition. The composition of the target material can affect the formation of an impact structure, the shock effects generated, and how well the structure and its components are preserved. Most terrestrial craters are classified as simple or complex based on their morphology, which is determined primarily by the size and speed of projectile that hits the surface during the impact event. Projectiles are asteroid or cometary fragments that when they enter Earth's atmosphere, have enough mass and a diameter usually $>20\text{--}50$ m, such that little to no deceleration occurs (French 1998). Without deceleration, the hypervelocity of the projectile remains >11 km/s when it impacts the surface and depending on the projectile diameter, a simple or complex crater will form (French 1998). Projectiles with a diameter of a few metres or less will lose much of their velocity and may strike the surface as a single projectile or disintegrate as it passes through the atmosphere, resulting in a low velocity impact or impacts with little penetration into the surface (French 1998).

Simple terrestrial craters are less than ~ 2 km in apparent diameter, are bowl-shaped with a raised rim, and have depth to diameter ratios between 1:3 and 1:5 (Melosh 1989). For simple craters, the dimensions of the transient cavity are similar to the final apparent crater

dimensions. Complex craters are larger in apparent diameter than simple craters, ranging from ~5 km to 300 km (Impact Earth 2020), contain a central uplift, wall terraces, and have a shallower depth to diameter ratio between approximately 1:10 and 1:20 (Melosh 1989). The transient cavity ratio is similar for complex and simple craters before the larger unstable transient cavity of the complex crater collapses. In consolidated sedimentary rocks the transition from simple to complex crater diameter is ~1.5–2 km and in crystalline rocks the diameter increases to ~4 km (Dence et al. 1977). Examples of transitional terrestrial craters include the 4 km Kärddla impact structure in Estonia (Puura and Suuroja 1992), the 4 km Mishina Gora impact structure in Russia (Shmayenok and Tikhomirov 1974), and the 3.2 km Zapadnaya impact structure in Ukraine (Gurov et al. 1985, 2002). On Earth, impact craters are subject to water and wind erosion, plate tectonics, and burial which degrade or destroy craters over time, and these factors are absent on other airless rocky planets and moons in the Solar System (Melosh 1989). The term *impact crater* refers to the well-formed circular feature resulting from a hypervelocity impact whereas *impact structure* is a more generalized term that includes all impact-derived terrestrial structures regardless of post-impact erosion or burial state (Baratoux and Reimold 2016; Stöffler and Grieve 2007).

Confirmation of a terrestrial impact structure requires the identification of one or more features that include shatter cones, shock metamorphism, or meteorite fragments if the projectile is small enough that it is not completely vapourized during the hypervelocity impact and large enough to survive transit through the atmosphere (French and Koeberl 2010). Impact-related shock features are generated at different shock pressures during impacts, so the resultant features are correlated, to a degree, with the apparent diameter of the impact structure, size of projectile, and target material. The target material is a major factor in determining what shock metamorphic effects can be generated. The ubiquity of quartz in terrestrial crystalline rocks and the response of quartz to varying shock pressure and subsequent ability to retain metamorphic effects to this pressure make it one of the most studied minerals associated with terrestrial impact structures (Grieve et al. 1996). It becomes a challenge, however, when hypervelocity impacts occur in targets where quartz-bearing rocks are absent such as basalts, carbonates, or unconsolidated sediments as these materials lack diagnostic shock effects or are indistinguishable from tectonic deformation unrelated to impacts (French and Koeberl 2010).

This research focuses on complex craters in sedimentary targets, specifically targets dominated by carbonates, to better understand the processes involved in generating craters and to identify signs of shock in non-crystalline rocks.

1.1.1 Complex crater formation

The three recognized stages of the impact cratering process are contact and compression, excavation, and modification (Fig. 1-1), which proceed as a continuum as there is no pause or exact moment when one stage ends and the next begins (Gault et al. 1968; Melosh 1989). The division of stages relates to the development of different physical processes that occur during the impact event. The contact and compression stage begins when the incoming projectile first contacts the solid target surface. The projectile penetrates up to twice its diameter into the target, depending on the target material and the density of the projectile (French 1998; Kieffer and Simonds 1980; O'Keefe and Ahrens 1982). The hypervelocity contact transfers kinetic energy from the projectile into the target in the form of shock waves that propagate through the projectile and the target material (Gault et al. 1968; Melosh 1989). The largest pressures generated during an impact event occur during the contact and compression stage where pressures at the point of impact can range from 100–1,000 GPa (Melosh 1989; Shoemaker 1960). As the projectile penetrates the target material, it becomes consumed by the shock wave. Once the shock wave reaches the upper free surface of the projectile, it then reflects back through as a rarefaction wave (Gault et al. 1968). Rarefaction is a means to decompress from the high impact pressure generated to return to ambient pressure, resulting in the melting or vapourization of the projectile (Gault et al. 1968). The rarefaction waves can also lead to melting, vapourization, and/or shock metamorphism of target material (Ahrens and O'Keefe 1972; Grieve et al. 1977). Shock waves also lose energy as they expand radially from the point of impact where energy is lost as heat into the target rocks (French 1998). For projectiles 10 m to 1 km in diameter, the contact and compression stage ranges from 10^{-3} to 10^{-1} seconds, the shortest of the three stages (Gault et al. 1968).

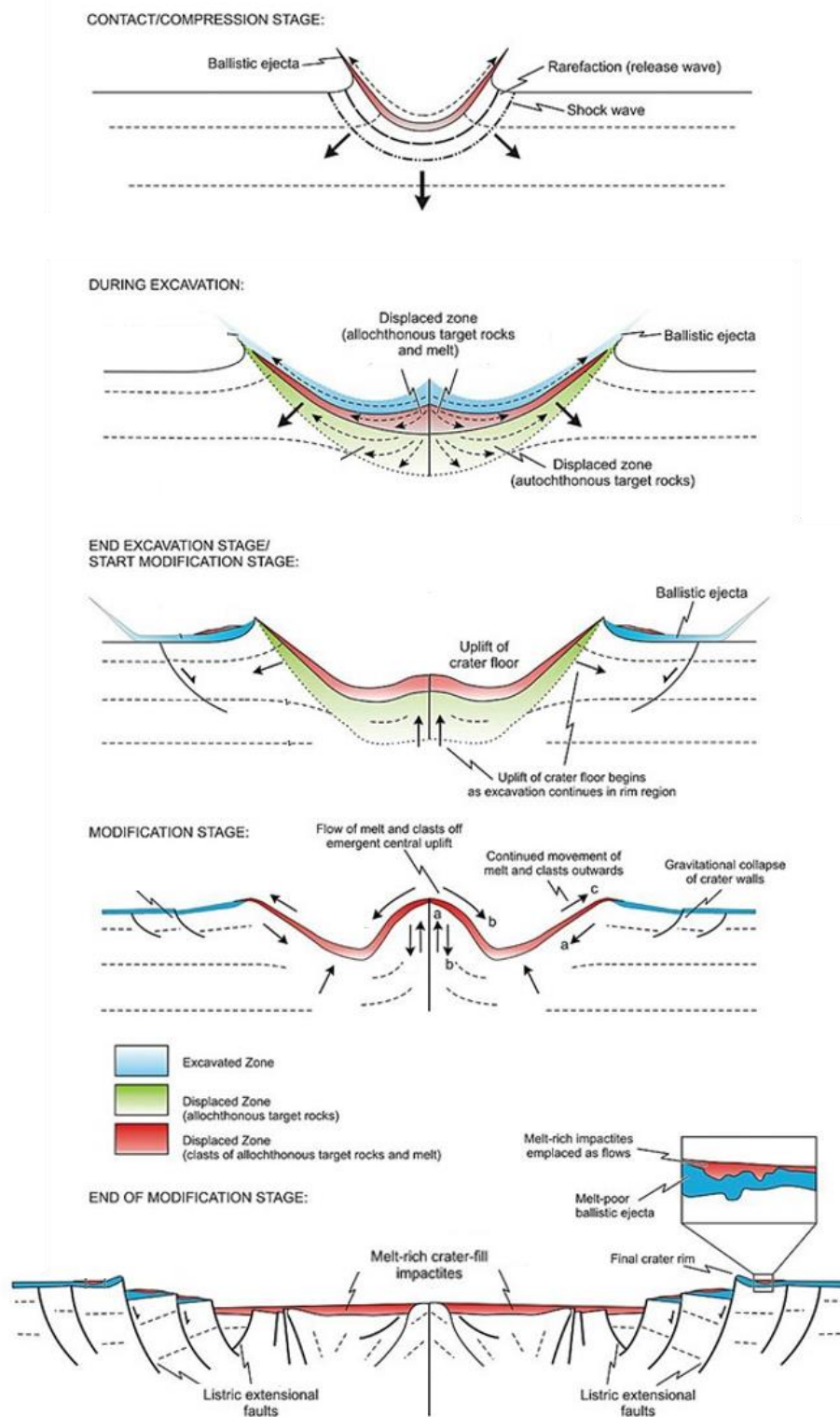


Figure 1-1. Sequence of cross-sections highlighting the main components involved in the three stages of impact crater formation for complex craters; modified from Osinski and Pierazzo (2013).

The excavation stage continues with the propagation of a hemispherical shock wave through the target material, outward from the penetration depth of the projectile. At this point, the projectile itself is no longer involved in the crater-forming process as it was melted and/or vapourized during the contact and compression stage (Melosh 1989). Additional shock waves are directed upward and reach the free surface where they reflect to produce rarefaction waves downward into the target material. Where the rarefaction waves interact with the hemispherical shock wave, an interference zone is generated and pressure here is reduced (Melosh 1989). Wave interaction in this zone produces an 'excavation flow-field' and generates a transient cavity of low to near ambient pressure (Dence 1968; Gault et al. 1968; Grieve and Cintala 1992). Some of the energy from the reflected rarefaction waves is converted back into kinetic energy, causing the transient cavity to open up and expand while fractured target material is accelerated and ejected out of the cavity (French 1998; Gault et al. 1968). The ejected material forms a continuous ejecta blanket extending to about one crater radius beyond the rim of the bowl-shaped transient cavity with ejecta becoming discontinuous to about 5 crater radii (French 1998; Melosh 1989; Oberbeck 1975). The release in pressure within the transient cavity and target material is also associated with fracturing and shattering within the target rock (French 1998).

Until this point in crater-formation, the process for developing a simple or complex crater has been essentially the same. The modification stage begins once the shock waves have decayed beyond the crater rim so that they no longer affect crater development and this is when different crater morphologies begin to develop based on the size of the excavated transient crater (French 1998; Melosh 1989). Modification of simple craters with a diameter less than a few kilometres is minor and they retain the stable and simple bowl-shape morphology of the transient cavity (French 1998). On Earth, when a transient crater reaches a diameter greater than ~2 km in sedimentary targets and ~4 km in crystalline targets, the cavity becomes unstable and is modified by gravitational force and centripetal movement (Dence 1968; French 1998). Gravity coupled with the strength and structure of the target material cause significant movement and shearing of target rocks outward, inward, and upward due to collapse, slumping, or faulting (French 1998). The resulting complex crater morphology includes a central uplift, a flat internal floor, and terraces

around the periphery of the crater (French 1998; Melosh 1989). Craters larger than 140 km in diameter develop an unstable central peak that collapses to form a peak ring, to resemble Schrödinger Crater on the Moon (Melosh 1989).

To put the rapid nature of crater-forming processes into perspective, detailed calculations project that the 1-km diameter simple crater Barringer (Meteor) Crater, Arizona formed in approximately 6 seconds while a 200-km diameter complex crater requires closer to 90 seconds to form (French 1998).

1.1.2 Sedimentary targets

Currently, there are 82 terrestrial impacts listed out of 198 confirmed impact structures that formed in completely sedimentary targets while another 54 formed in a mixed target of sedimentary and crystalline rocks (Impact Earth 2020). This maintains a similar value of ~70% of impacts occurring in target sequences that contain sedimentary rocks as reported over 10 years ago (Osinski et al. 2008). In 2007 there were 174 confirmed terrestrial impact structures with 68 occurring in sedimentary targets and mixed is the same as the 2019 total (Osinski et al. 2008). These numbers show the proportion of sedimentary rocks associated with terrestrial impacts remains relatively consistent as new impact structures are discovered and confirmed. The occurrence of sedimentary rocks is a significant portion within the terrestrial impact record yet have been largely overlooked when theoretical studies are carried out (Kieffer and Simonds 1980).

Sedimentary rocks add additional elements to the impact process as they often contain rocks which are more porous and contain volatiles, when compared with crystalline targets (Kieffer and Simonds 1980; Osinski et al. 2008). Porosity in sedimentary target rocks is complex and varies between sandstones and carbonates as well as within each group (Choquette and Pray 1970). The age of sedimentary rocks may also factor into porosity where sandstones have initial porosity around 25–40% and carbonates 40–70% is common, these decrease to 15–30% and none to <5%, respectively following diagenesis (Choquette and Pray 1970). Porous rocks are able to hold groundwater (up to 20% or more pore space filled by water) better than crystalline rocks, which tend to be non-porous leaving them to hold only several percent water (Kieffer and Simonds 1980). The presence of groundwater

increases the portion of volatiles available during an impact event, and increases more when the target sedimentary rocks contain carbonates (Kieffer and Simonds 1980). When carbonates are involved, the production of carbon dioxide (CO₂) during an impact could play a factor; calcite (CaCO₃) can decompose or devolatilize to produce CaO and CO₂ (e.g., O'Keefe and Ahrens 1989). The effect and volume of carbon dioxide produced from an impact event is not entirely understood. Estimates of carbon dioxide production from shock experiments have suggested substantial amounts of carbon dioxide is released from impacts into carbonate targets (e.g., Hörz et al. 2015; Kieffer and Simonds 1980; Lange and Ahrens 1986) and conversely, experiments have proposed the amount of carbon dioxide generated has been overestimated (e.g., Bell 2016; Jones et al. 2000; Martinez et al. 1995). Production of carbon dioxide during hypervelocity impacts is also related to research at terrestrial impact sites as well as experiments and models have investigated the extent to which carbonates melt (e.g., Graup 1999; Jones et al. 2000; Osinski et al. 2008, 2018) or decompose (e.g., Hörz et al. 2015, 2019; O'Keefe and Ahrens 1989; Stöffler et al. 2013) from the impact.

A consensus has yet to be reached regarding the fate of carbonates in hypervelocity impact events. More time and information are required to determine the causes which can lead to either or both outcomes while also reaching an agreement regarding these processes that involve carbonates.

1.1.3 Impactites

Impactites is a broad term that refers to rocks affected by a hypervelocity impact event and are categorized as proximal or distal based on where they are located with respect to the impact structure (Stöffler and Grieve 2007). Proximal impactites are located within the crater out to the farthest limit of the continuous ejecta blanket, or ~2.5 crater diameters, and include shocked rocks, impact melt rocks, and impact breccias (Glass and Simonson 2012; Stöffler and Grieve 2007). Distal impactites occur beyond the continuous ejecta blanket and include tektites, microtektites, and air fall beds (Stöffler and Grieve 2007). Only the proximal group of impactites is relevant to this research and will be discussed further as distal impactites are absent from both study sites.

Shocked rocks contain the effects of shock metamorphism and without any occurrence of melt. Some of the most common shock effects or features of shocked target rocks include quartz and feldspar with planar deformation features, diaplectic glass and other rock and mineral glasses, and high temperature polymorphs such as coesite and stishovite (Stöffler and Grieve 2007). These are discussed more in the following section as shock metamorphism is the primary evidence that high pressures were generated during a hypervelocity impact. Impact melt rocks are divided into three groups based on their clast content which are clast-free, clast-poor, and clast-rich melt rocks (Stöffler and Grieve 2007). Impact breccias consist of monomict, lithic, and impact melt-bearing breccias or suevites (Osinski et al. 2016; Stöffler and Grieve 2007). The term suevite originally referred to impact breccias from the Ries impact structure that contained impact glass clasts (Osinski et al. 2016 and references therein). Currently, a suevite is defined as an impact breccia that has a particulate matrix and contains clasts of lithic and mineral exhibiting shock metamorphism as well as impact glass fragments (Stöffler and Grieve 2007).

1.1.4 Microscopic shock metamorphism

Identification of shock metamorphism in rocks or mineral grains is a generally agreed upon as a requirement to confirming a new impact structure (French and Koeberl 2010). Target rocks and minerals associated with an impact event are subjected to short lived but intense shock pressures, that may exceed 100 GPa, that can generate microscopic effects such as planar fractures (PFs), planar deformation features (PDFs), or diaplectic glass in quartz or feldspars (e.g., French 1998; Stöffler et al. 2018). Specifically in plagioclase (feldspar) diaplectic glass is referred to as maskelynite (Stöffler et al. 2018). High-pressure polymorphs can also be generated through shock metamorphism including coesite or stishovite from quartz, ringwoodite from olivine, and diamond and lonsdaleite from graphite (Fron del and Marvin 1967; Stöffler et al. 2018). These products of shock are diagnostic of impact events and are used to confirm the origin of suspected impacts. When hypervelocity impacts occur in silicate-bearing target rocks, at least some of these shock metamorphic products should be generated, provided the scale of the impact is large enough. With over a third of impacts occurring in sedimentary targets (Osinski et al. 2008)

many of these contain carbonates which do not display the typical diagnostic shock products and effects listed above.

The ability to determine shock metamorphism in carbonates is not as straightforward as identifying shock in quartz and feldspars. Optical microscopy does not reveal diagnostic strain or shock effects in carbonates, however, studies using X-ray diffraction and Raman spectroscopy have shown varying ability to detect crystallographic or spectroscopic changes due to shock in carbonates. Shock effects in dolomite such as lower symmetry and broader peaks in the dolomite Raman spectra were detected while the Raman spectra for calcite remained unchanged making Raman spectroscopy a useful tool for identifying shock in dolomite (Lindgren et al. 2009). X-ray diffraction studies on shock effects in calcite (Skála and Jakeš 1999), calcite and dolomite (Huson et al. 2009), and dolomite (Seeley and Milam 2018) show potential for identifying shock in carbonates when FWHM values are derived using Rietveld refinements or peak broadening is examined. Rietveld derived values indicate shock is more easily distinguished in dolomite than calcite (Huson et al. 2009) so there may be additional differences to be uncovered for these two carbonate minerals.

1.2 Arctic geology

1.2.1 Arctic Archipelago

The Arctic Archipelago (Fig. 1-2) is a group of more than 36,000 islands, of which 94 are considered major islands having a land area greater than 130 km², off the northern Canada mainland (Hund 2014). The Arctic Archipelago is divided into seven geological provinces including the Arctic Platform and the Canadian Shield (Thorsteinsson and Tozer 1970). These geologic provinces consist largely of Phanerozoic-aged sedimentary rocks with isolated occurrences of Precambrian-aged rocks (Daae and Rutgers 1975; Douglas et al. 1963; Thorsteinsson and Tozer 1970).

There are correlations of sedimentary units between adjacent islands within the Arctic Archipelago and the extent of correlation can vary which is evident in geological maps (e.g., Okulitch 1991). The abundance of carbonates within the Arctic Platform geologic province indicates there was a vast continental shelf environment where local ocean

currents caused depositional changes to sediments, causing units to pinch in and out. Unconformities are common and vary in length of time across the archipelago. For example, an unconformity exists below the Allen Bay Formation on Devon Island and is restricted to a portion of the Upper Ordovician but ~300 km southwest on Somerset Island, the unconformity below Allen Bay is more extensive and ranges from Upper to Lower Ordovician (Stewart 1987). Variations in limestone dolomitization are also present, notably for the Ordovician-aged Thumb Mountain Formation where the formation consists of dolostone west of the Boothia Arch while the limestone east of the uplift avoided the dolomitization process (Dae and Rutgers 1975).

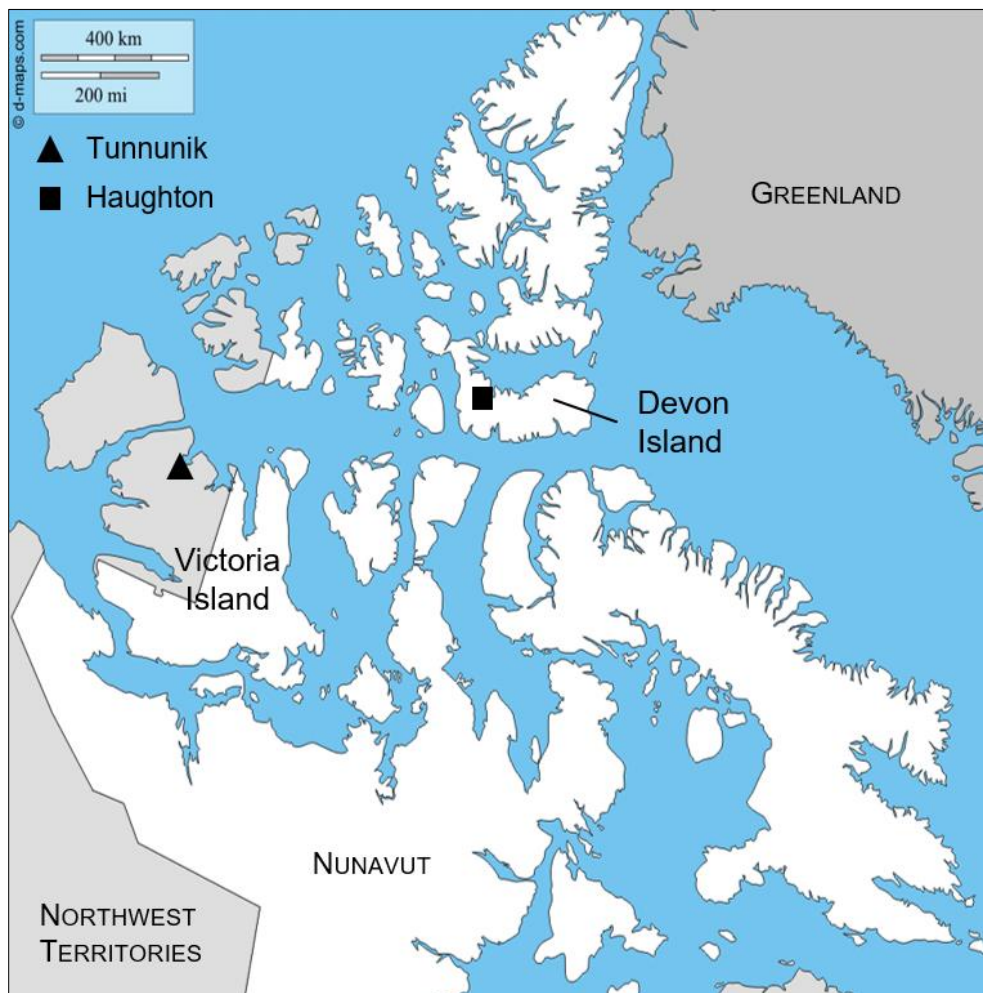


Figure 1-2. The Canadian Arctic Archipelago with study site locations indicated.
Base map provided by d-maps.com.

1.2.2 Victoria Island (Kiilineq¹)

Victoria Island, Canada's second largest island, lies north of mainland Northwest Territories and Nunavut and is found in the southwestern portion of the Arctic Archipelago (Fig. 1-2). Most of Victoria Island consists of lowlands of the Arctic Platform (Thorsteinsson and Tozer 1970) and a regional syncline that extends northeast across the island from the southwestern Minto Inlet (Okulitch 1991), exposing rugged Precambrian sedimentary and igneous rocks known by various names including the Minto Arch or Shaler Mountains (Thorsteinsson and Tozer 1962, 1970). The Arctic Platform on Victoria Island has been described as "a remarkably uniform and drab sequence consisting almost wholly of dolomite, dense to porous and vuggy, and fine to coarse grained" (Thorsteinsson and Tozer 1970). The perceived lack of interesting features within this area of the Arctic Platform coupled with the size and remoteness of the island contribute to why Victoria Island has been geologically under-studied.

The earliest map of Victoria Island was compiled by Thorsteinsson and Tozer (1962) but much of the island is unnamed in this map, including a 70 km wide band northwest of the Shaler Mountains up to Richard Collinson Inlet that is simply labeled as map unit 10. Areas of Victoria Island such as the central Shaler Mountains (Minto Arch) and coastal Minto Inlet have been well-documented based on extensive outcrop exposures of limestone, dolostone, sandstone, shale, basalt, and diabase (e.g., Dewing et al. 2015; Harrison et al. 2013; Mathieu et al. 2015; Okulitch 1991; Young and Long 1977). Palaeozoic units mapped as unit 10 in northwestern Victoria Island and east of the Shaler Mountains have a gentle dip or are essentially flat-lying (Thorsteinsson and Tozer 1962). The lack of significant outcrops throughout map unit 10 contributes to the absence of well-mapped units in these areas.

Regional mapping of northwestern Victoria Island was conducted from 2009 to 2011 by the Geological Survey of Canada (Dewing et al. 2013). This mapping program identified strata with anomalously steep dipping angles on an otherwise flat-lying expanse of

¹ Traditional Inuit names obtained from a map published by the Inuit Heritage Trust Place Names Program, Place Names in Nunavut at <http://iht.ca/eng/place-names/pn-index.html#>

carbonate rocks (Dewing et al. 2013). The only other indication of this remote anomaly in northwestern Victoria Island was on a 1962 geologic map. Thorsteinsson and Tozer's (1962) map shows a group of three inclined bedding measurements of 25 to 35° which are higher than nearby regional measurements with lower inclinations between 5 and 15°. As noted by Dewing et al. (2013), there was no further explanation provided by Thorsteinsson and Tozer (1962) to account for the anomalous measurements. The steeply dipping strata are now known to represent the centre of an eroded meteorite impact structure.

1.2.2.1 Tunnunik study area

The study area on Victoria Island is in the northwestern region near Richard Collinson Inlet (Fig. 1-3A) where the rocks consist of gently dipping 5 to 10° Cambrian to Silurian-aged sedimentary dolostone and limestone (Dewing et al. 2013). The topographic surface expression of the impact structure is poor due to glacial erosion and is weakly detectable through modern satellite imaging of the region (Fig. 1-3B). Victoria Island is currently unglaciated, but evidence of past glaciation is evident across the region. Glacially derived features and landforms present include polished and striated rocks, till, glacial erratics, kames, eskers and other gravel deposits. The persistence of glacial abrasions created during the retreat of the Laurentide ice sheet from Victoria Island ~13,000 years ago (Ullman et al. 2015), emphasizes the slow rate of weathering and erosion in this environment in the absence of glaciers. Quaternary glacial sediments blanket much of the area which further restricts the extent of exposed rock already limited by to erosion. Periglacial activity is observed throughout the impact structure as polygons, sorted and unsorted circles and stripes, and solifluction features. Polygons are the most common periglacial feature and range in diameter from about one metre up to several hundred metres and occur in vegetated and non-vegetated terrain. Within the context of the study area, vegetated refers to the presence of sparse grasses and plants that do not grow more than ~10 cm in height.

Stratigraphic units exposed in the study area from oldest to youngest are the Shaler Supergroup, Mount Phayre, Victoria Island, and Allen Bay formations (Newman and Osinski 2016). Sharp contacts between formations were not observed and are considered gradational, consistent with a shallow marine depositional environment.

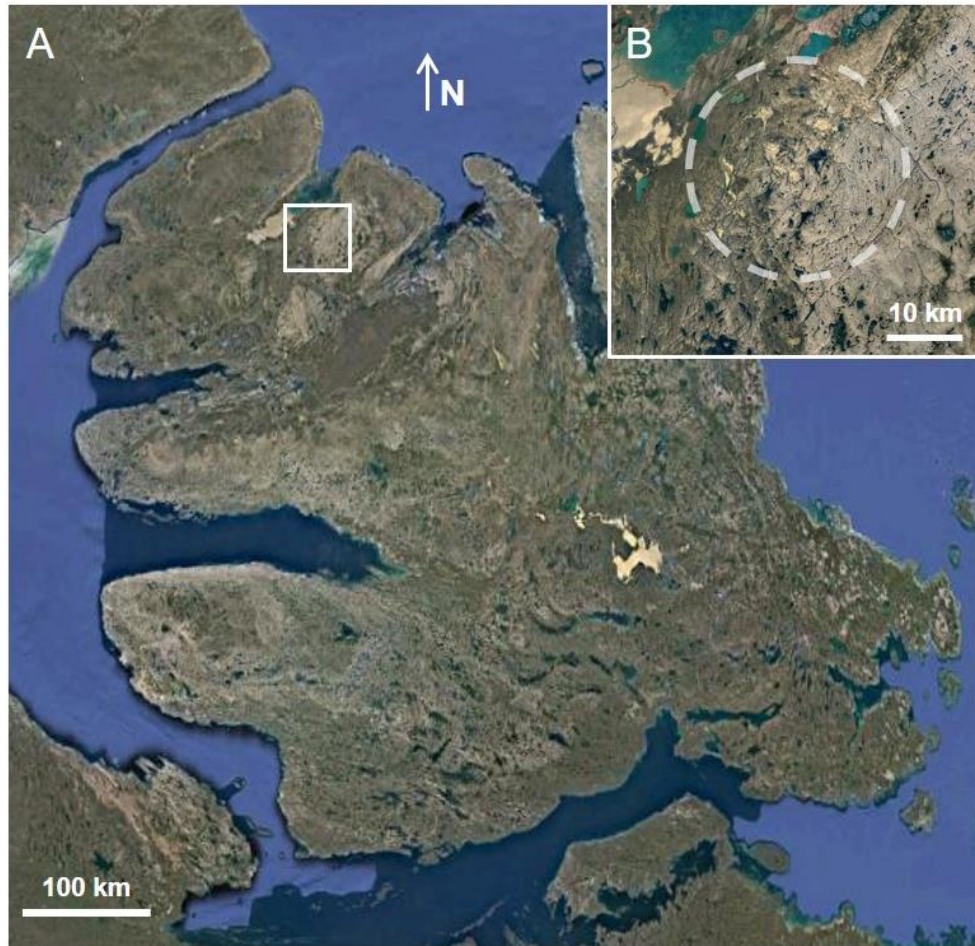


Figure 1-3. A) Google Earth (2018) image of Victoria Island; white square indicates the location of inset image B) showing the Tunnunik impact structure, outlined by white dashed circle. Coordinates for the centre of the Tunnunik impact structure are 72°27'16" N, 113°49'49" W (Impact Earth 2020).

The Victoria Island and Allen Bay Formations are primarily dolostone, the Mount Phayre Formation contains distinctive alternating beds of green and red dolomite-rich mudstones, and the members of the Shaler Supergroup exposed at the centre of the impact structure are limestone-rich. Field work conducted along the southwestern shores along the Minto Inlet has identified two additional units present between the Mount Phayre Formation and the Shaler Supergroup and have been provisionally named the Uvayualuk Formation and the Quyuuk Formation (Dewing et al. 2015; Durbano et al. 2015). The Uvayualuk and Quyuuk Formations were not identified in the Tunnunik study area, suggesting these units are intermittent within the shallow marine transgressional history for Victoria Island. The

Mount Phayre, Uvayualuk, and Quyuq Formations are the same units that were informally referred to respectively as the Stripy Unit, Tan Dolostone Unit, and Clastic Unit (Dewing et al. 2013; Osinski et al. 2013).

Observed and inferred faults are associated directly with the impact event or formed independently and follow more regional trends. Most faults are inferred from observing changes in topography while in the field and from digital elevation models (DEM) since the cover of Quaternary sediments make direct observations difficult. In addition to faults generated by the impact, there are larger regional faults that post-date the crater's formation which are nearly straight and more prominent features in digital elevation models (Osinski et al. 2013). The age of the Tunnunik impact structure is poorly constrained by stratigraphy as 450 to 130 Ma (Dewing et al. 2013) but recent palaeomagnetic dating has refined the age to 450 to 430 Ma (Lepaulard et al. 2019).

1.2.3 Devon Island (Tallurutit)

Devon Island is located north of Baffin Island and south of Ellesmere Island along the eastern edge of the Arctic Archipelago (Fig. 1-2). There are no permanent settlements on Devon Island, making Devon Island the largest uninhabited island on Earth. The main topographic regions of the island include coastal lowlands, plateaus, and an ice cap (Thorsteinsson and Mayr 1987). The eastern quarter of the island is glaciated and the main ice cap is roughly circular and domed (Thorsteinsson and Mayr 1987). The ice cap is a remnant of the Innuitian Ice Sheet that once covered the Queen Elizabeth Islands and likely connected the neighbouring Laurentide and Greenland Ice Sheets (Blake 1970). The lowlands on Devon Island are limited to swaths approximately 5–10 km wide and <100 in length along some of the coastal bay and channel areas. Most lowlands have a glacial origin while some appear to have a combination of glacial and fluvial processes (Thorsteinsson and Mayr 1987). The three quarters of Devon Island west of the ice cap make up the plateau, where its highest elevation of 1500 m in the east gradually slopes to the western coast, terminating with an elevation of 300 m above sea level (Thorsteinsson and Mayr 1987). Non-lowland coastal areas tend to have steep cliffs resulting from resistant rocks present within the plateau sequence.

Proterozoic to Cenozoic sedimentary units of the Arctic Platform comprise the plateau while the eastern quarter of the island underlying the ice cap is comprised mainly of Precambrian crystalline units of granulite-facies granitic and metamorphic rocks that outcrop along coastal exposures (Thorsteinsson and Mayr 1987). Sedimentary units are composed of dolostone, limestone, shale, sandstone, and gypsum with the oldest units located on the eastern side of Devon Island and sequentially become younger westward. The 2 to 5° west-dipping Cambrian to Devonian-aged rocks across the island makes exposures within the Arctic Platform succession accessible (Osinski et al. 2005a). In the western part of the island there is a prominent circular feature approximately 23 km in diameter that is easily recognized in satellite imagery (Fig. 1-4) known as the Houghton impact structure.

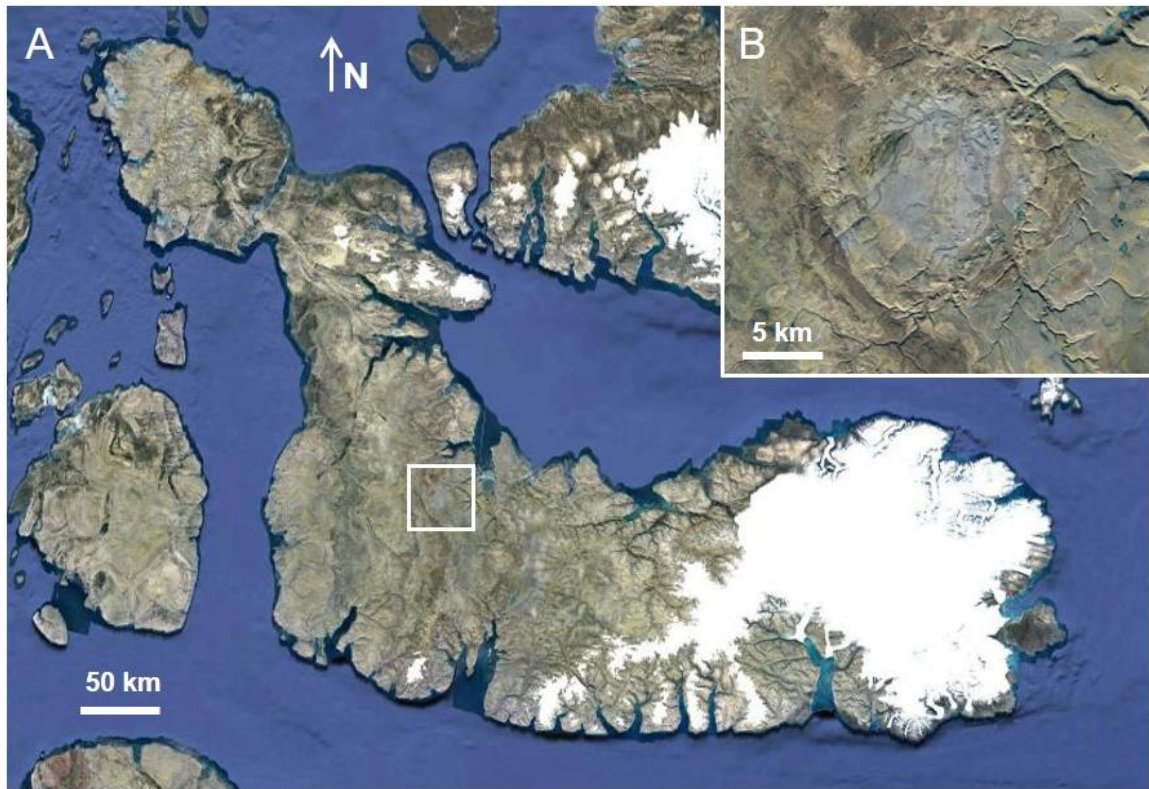


Figure 1-4. A) Google Earth (2018) image of Devon Island; white square indicates the location of inset image B) showing the Houghton impact structure. Coordinates for the centre of the Houghton impact structure are 75°22'39" N, 89°39'13" W (Impact Earth 2020).

The existence of this structure has been known since the 1950s and was confirmed to have an impact origin after shatter cones were identified by Robertson and Mason (1975). Over the past 30 years there have been numerous expeditions to the Haughton impact structure that have studied various aspects of the structure including geology, impactites, shatter cones, hydrothermal activity, geophysics, and geomicrobiology (e.g., Bischoff and Oskierski 1988; Osinski et al. 2001, 2005a, 2005b; Pontefract et al. 2014; Redeker and Stöffler 1988; Zylberman et al. 2017).

1.2.3.1 Haughton study area

The Haughton impact structure is approximately 80 km inland from the western coast of Devon Island (Fig. 1-4). The western side of Devon Island is unglaciated, and the study area consists of Ordovician to Silurian-aged sedimentary units of dolostones, limestones, evaporites, and sandstones. Stratigraphic units exposed within the Haughton impact structure from oldest to youngest are the Blanley Bay Formation, Eleanor River Formation, Bay Fiord Formation, Thumb Mountain Formation, and Allen Bay Formation (Osinski et al. 2005a). There are no outcrops of Precambrian crystalline rocks within the impact structure, however, crystalline clasts of various gneisses, amphibolite, and diabase have been identified within the impact melt rock crater-fill deposits and exhibit levels of shock from pressures ranging from 15 to 60 GPa (Metzler et al. 1988). Gneiss clasts that display higher shock metamorphism are poorly banded, paler in colour, and have a more vesicular texture compared to unshocked gneiss (Frisch and Thorsteinsson 1978). In addition to the crystalline clasts in the impact melt rock deposits, most of the lithic clasts present are dolostone, limestone, gypsum, and anhydrite which reflects the target lithology (Osinski et al. 2005b). The diverse assemblage of clasts within the crater-fill deposits show all lithologies within the target sequence were affected during the impact event, down to and including the crystalline basement.

Several areas within the impact structure the crater-fill deposits are overlain by the early Miocene Haughton Formation, a post-impact depositional unit. The geographically isolated Haughton Formation is the only source of Miocene biota and climate information within the northern Arctic (Hickey et al. 1988). Quaternary glacial deposits and fluvial deposits are also present within the impact structure and throughout the region. The

Haughton impact structure is relatively young geologically, and the Miocene-age deposits within the structure help constrain the age. Radiometric dating has been performed in separate experiments with the most recent age being 23.5 ± 2.0 Ma obtained through (U-Th)/He dating of zircon (Young et al. 2013). Previous experiments using Ar-Ar dating yielded 23.4 ± 1.0 Ma (Jessberger 1988) and 39.1 ± 1.7 Ma (Sherlock et al. 2005), respectively, for this well-preserved impact structure.

1.3 X-ray diffraction

X-ray diffraction is a means by which information about a mineral's crystal structure is examined. It was discovered in 1912 that crystals diffract X-rays by Max von Laue when he directed a beam of X-rays at a crystal of copper sulfate that was diffracted into spots on a photographic plate (Cullity 1978). In the same year as von Laue's discovery, the father and son team of W. H. Bragg and W. L. Bragg completed successful experiments on additional crystal structures while deriving a simpler mathematical form (Cullity 1978). The crystal structure of calcite was determined the following year (Bragg 1914; Bragg and Bragg 1913) and dolomite about ten years later (Wasastjerna 1924; Wyckoff and Merwin 1924).

The most common carbonate minerals, calcite (CaCO_3) and dolomite ($\text{CaMg}(\text{CO}_3)_2$), have a hexagonal crystal lattice but differ slightly in symmetry and their space groups; calcite is $R\bar{3}c$ and dolomite is $R\bar{3}$ (Reeder 1983). The unit cell for both minerals is similar with carbonate (CO_3) layers alternating with cation layers (Fig. 1-5). Dolomite preserves the structure of calcite but magnesium (Mg) substitutes in alternating octahedral cation layers for calcium (Ca). The substitution of Mg cations slightly modifies unit cell properties of dolomite including bond lengths and introduces less distortion into the CaO_6 octahedra with the addition of MgO_6 octahedra when compared to calcite since Mg and Ca cations are different sizes, Ca being the larger cation (Reeder 1983). The ionic radius of Ca cations is 1.00 \AA compared to an ionic radius of 0.72 \AA for Mg cations (Ross and Reeder 1992; Shannon 1976).

The unit cell for any mineral is the smallest unique three-dimensional unit that repeats along crystallographic axis directions to form larger crystals. The unit cell structure is

constant through a mineral which makes X-ray diffraction a useful analytical tool in examining a mineral at the crystal structure level.

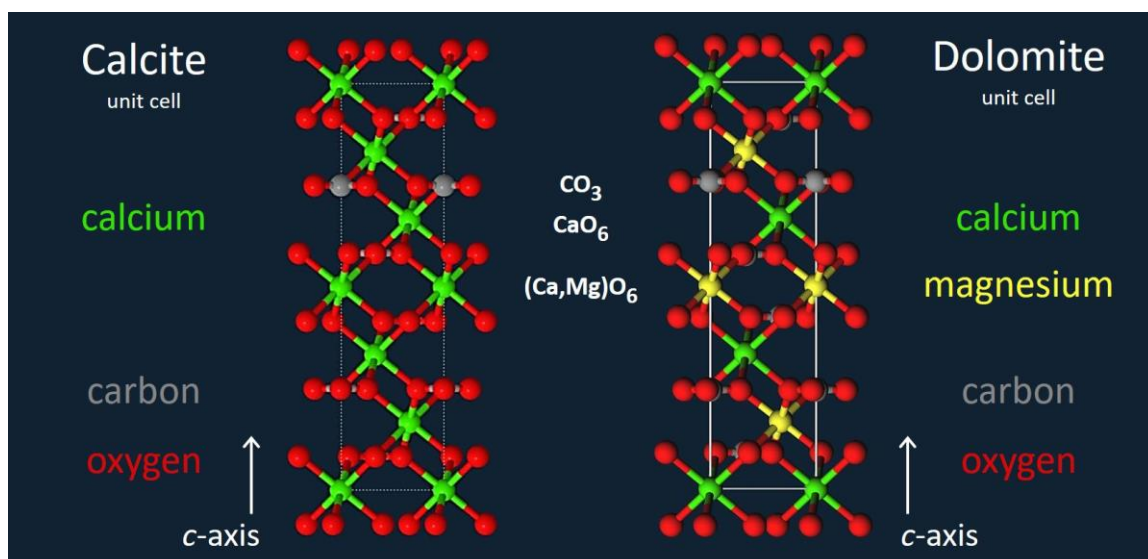


Figure 1-5. Comparison of the unit cell for calcite and dolomite. View shown is looking through the a -axes which are perpendicular to the c -axis. Representative carbonate (CO_3) and octahedral (CaO_6 or MgO_6) layers are indicated which include calcium (green), magnesium (yellow), carbon (grey), and oxygen (red) atoms. Structural model visualizations obtained from The Virtual Museum of Minerals and Molecules (Barak and Nater 2020).

1.3.1 Powder X-ray diffraction theory

X-ray diffraction uses an X-ray beam which interacts with lattice planes and atoms in a mineral and since every mineral has its own specific structure, the diffraction of X-rays provides a characteristic pattern for that mineral. A mineral's unit cell structure determines the line positions in the diffraction pattern and the atom positions within the unit cell determine the relative line intensities (Cullity 1978). X-ray diffraction can be conducted on single crystals or powders. Powders may consist of a single mineral phase or multiple mineral phases if working with whole rock powders. Powders consist of many tiny crystallites and when crystallites are small enough, less than $\sim 5 \mu\text{m}$, all crystallite orientations should be present and randomly oriented so that all crystal planes will intersect the incident X-ray beam (Cullity 1978; Jenkins and Snyder 1996).

To determine the angle the X-ray beam is diffracted the equation known as Bragg's Law (1.1) is used. In this equation n is the order of reflection, λ is the wavelength of incident X-rays, d (or d-spacing) is the perpendicular space between lattice planes, and θ is the angle of the diffracted X-rays (Bragg and Bragg 1913).

$$n\lambda = 2d\sin\theta \quad (1.1)$$

As illustrated in Figure 1-6, incident X-rays (A, B, C) interact with atoms in lattice planes associated with Miller indices (hkl) for a given mineral at an angle θ and if the orientation of the crystallites satisfies the Bragg's Law (1.1) the X-rays (A', B', C') are diffracted at an angle of 2θ . The angle that is measured experimentally is 2θ and is called the diffraction angle. When working with powders this is where the random orientation of crystallites is important as it ensures there are crystallites in the correct orientation for all possible d-spacings to satisfy Bragg's Law.

Figure 1-6 is a simplified view of X-ray diffraction to illustrate Bragg's Law that may suggest incident X-rays "reflect" off "lattice planes" in a manner similar to how visible light "reflects" off a mirror, however, X-rays are actually scattered in all directions by the atoms in a lattice plane and only where the X-ray reinforce each other through constructive interference does the diffracted X-ray (A', B', C') form (Cullity 1978).

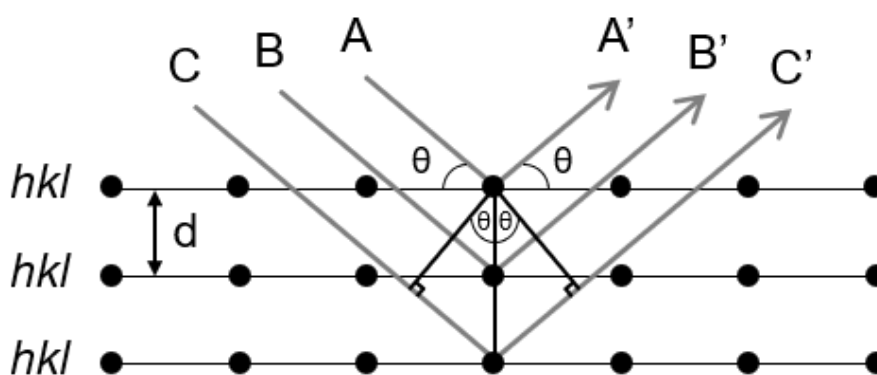


Figure 1-6. Derivation and illustration of Bragg's Law. Incident X-rays (A, B, C) diffract at atoms within lattice planes (hkl), where d is the spacing between planes in the crystal structure, at an angle (θ) to generate diffracted X-rays (A', B', C').

The measured diffraction angles (2θ) are converted to a one-dimensional diffraction pattern that is plotted against intensity or counts (Fig. 1-7). The diffraction pattern consists of Bragg reflections or peaks of varying intensities and the number of peaks depends on the symmetry and complexity of a mineral. The presence of the Mg atom layer in dolomite increases the number of lattice planes as more peaks occur in the diffraction pattern for dolomite versus calcite (Fig. 1-7). Peaks are typically sharp and narrow in shape. Diffraction patterns are unique and characteristic to a specific mineral that can be searched and indexed with a mineral database such as the International Centre for Diffraction Data (ICDD) Powder Diffraction File (PDF-4+) database.

Since X-ray diffraction provides information about the crystal structure of a mineral, it can also be used to detect strain within the crystal lattice. Lattice strain is caused by distortion within the crystal and the resulting strain can be observed in diffraction patterns by a broadening of diffraction peaks. The extent of broadening would depend on the amount and type of strain applied to the mineral, such as tectonic related strains or hypervelocity-induced shock. Strain would be applied to all lattice planes within a mineral but depending on crystal structure, specific planes may show a greater effect to strain. When a lattice plane is strained (Fig. 1-8) it bends causing one side to be under tension while the other side is compressed which affects the d-spacing and creates slight variances (Cullity 1978).

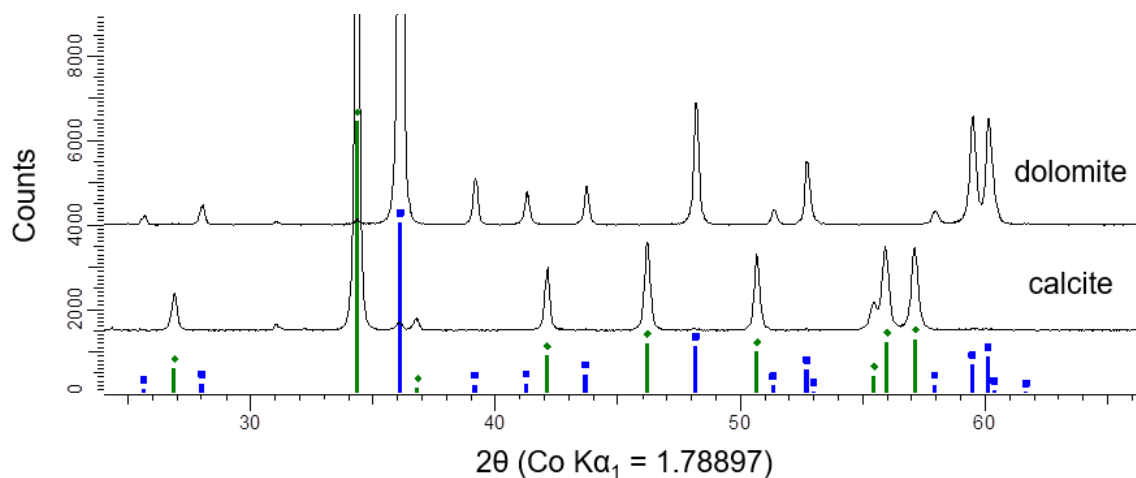


Figure 1-7. X-ray diffraction patterns for unshocked calcite and dolomite. Positions of Miller indices (hkl) for calcite are indicated by vertical green lines with diamond markers and dolomite by vertical blue lines with square markers.

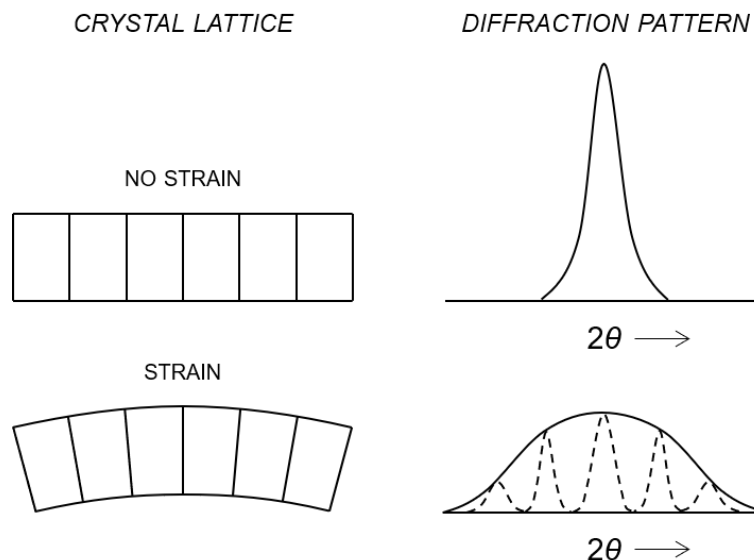


Figure 1-8. Illustration of peak broadening observed in diffraction patterns associated with lattice strain (modified from Cullity 1978). The strained diffraction pattern can be thought of as a series of small peaks (dashed) caused by slight differences in d-spacing in crystal lattice that combine to generate one broad peak.

When X-rays diffract at this point of strain, multiple Bragg reflections are very close together due to the variances in d-spacing which results in a single shorter and broader peak compared to a diffraction pattern that contains no strain (Cullity 1978).

1.3.2 Rietveld refinement

Rietveld refinement (Rietveld 1969) is a method of refining crystal structures based on data acquired from powder X-ray diffraction. This method refines the entire diffraction profile to estimate the modal proportion of mineral phases in whole rock samples and determine crystallite size and strain for the minerals present in the sample. The Rietveld method requires all mineral phases present to be identified prior to refinement as profile fitting takes into account the approximate positions of atoms for a given mineral phase (Young 1993). Knowing which mineral phases are present allows the crystal structure to be refined and can separate overlapping Bragg reflections (Young 1993). Various software programs are available for Rietveld refinement that refine parameters such as background, sample displacement, unit cell parameters, atomic positions, thermal parameters, preferred

orientation, occupancy, crystallite size, and crystal strain. Here, the software program TOPAS 5 by Bruker AXS was used.

1.4 Thesis objectives

The goals of this thesis are to understand the nature of impact-generated dykes in sedimentary targets, specifically in dolostone and limestone, and identify effects of shock in these carbonates as a product of hypervelocity impacts to help identify and verify impacts in sedimentary targets. The two impact sites studied here are located in remote Canadian Arctic locations and research from both sites include aspects that have not been previously explored or reported. Field work at the Tunnunik and Haughton impact structures involved documenting and collecting impact breccia and representative target rock samples. Breccia and melt rock samples from dykes were characterized through optical microscopy and electron probe microanalysis while shock effects in target rocks, crater-fill deposits, and ballistic ejecta were investigated using X-ray diffraction of powdered whole rock samples.

The similarity in diameter and target composition between the Tunnunik and Haughton impact structures provides an excellent opportunity to compare the products and processes of the events that generated these structures. The differing state of preservation between the study sites allows for the upper and lower sections of complex craters to be examined and compared, which could not be accomplished from studying only one of these impact sites. While characterizing impact melt rocks from Haughton, the rare terrestrial mineral moissanite was unexpectedly discovered. The presence of moissanite helps to better constrain temperatures and conditions present during the impact event. The insights gained from this research will improve the understanding of hypervelocity impacts into carbonate-rich targets which can be applied to other impact sites where carbonates are present in significant quantities.

1.5 References

Ahrens T. J., and O'Keefe J. D. 1972. Shock melting and vaporization of lunar rocks and minerals. *The Moon* 4:214–249.

- Barak P. and Nater E. A. The Virtual Museum of Minerals and Molecules. 2020. <http://virtual-museum.soils.wisc.edu> (Accessed April 18, 2020).
- Baratoux D., and Reimold W. U. 2016. The current state of knowledge about shatter cones: Introduction to the special issue. *Meteoritics & Planetary Science* 51:1389–1434.
- Bell M. S. 2016. CO₂ release due to impact devolatilization of carbonate: Results of shock experiments. *Meteoritics & Planetary Science* 51:619–646.
- Bischoff L., and Oskierski W. 1988. The surface structure of the Haughton impact crater, Devon Island, Canada. *Meteoritics* 23:209–220.
- Blake W. J. 1970. Studies of glacial history in Arctic Canada. I. Pumice, radiocarbon dates, and differential postglacial uplift in the eastern Queen Elizabeth Islands. *Canadian Journal of Earth Sciences* 7:634–664.
- Bragg W. H., and Bragg W. L. 1913. The reflection of X-rays by crystals. *Proceedings of the Royal Society of London. Series A, Containing Papers of a Mathematical and Physical Character* 88:428–438.
- Bragg W. L. 1914. The analysis of crystals by the X-ray spectrometer. *Proceedings of the Royal Society of London. Series A, Containing Papers of a Mathematical and Physical Character* 89:468–489.
- Choquette P. W., and Pray L. C. 1970. Geologic nomenclature and classification of porosity in sedimentary carbonates. *The American Association of Petroleum Geologists Bulletin* 54:207–250.
- Cullity B. D. 1978. *Elements of X-ray Diffraction*, Second Ed. Reading: Addison-Wesley Publishing Company, Inc.
- Daae H. D., and Rutgers A. T. C. 1975. Geologic history of the Northwest Passage. *Bulletin of Canadian Petroleum Geology* 23:84–108.
- Dence M. R. 1968. Shock zoning at Canadian craters: Petrography and structural

- implications. In *Shock Metamorphism of Natural Materials*, edited by French B. M., and Short N. M. Baltimore: Mono Book Corp. pp. 169–184.
- Dence M. R., Grieve R. A. F., and Robertson P. B. 1977. Terrestrial impact structures: Principal characteristics and energy considerations. In *Impact and Explosion Cratering*, edited by Roddy D. J., Pepin R. O., and Merrill R. B. New York: Pergamon Press. pp. 247–275.
- Dewing K., Pratt B. R., Hadlari T., Brent T., Bédard J., and Rainbird R. H. 2013. Newly identified “Tunnunik” impact structure, Prince Albert Peninsula, northwestern Victoria Island, Arctic Canada. *Meteoritics & Planetary Science* 48:211–223.
- Dewing K., Hadlari T., Rainbird R. H., and Bédard J. H. 2015. Phanerozoic geology, northwestern Victoria Island, Northwest Territories; Geological Survey of Canada, Canadian Geoscience Map 171 (preliminary). scale 1:500 000.
- Douglas R. J. W., Norris D. K., Thorsteinsson R., and Tozer E. T. 1963. *Geology and petroleum potentialities of northern Canada*, Paper 63-3. Geological Survey of Canada.
- Durbano A. M., Pratt B. R., Hadlari T., and Dewing K. 2015. Sedimentology of an early Cambrian tide-dominated embayment: Quyuq formation, Victoria Island, Arctic Canada. *Sedimentary Geology* 320:1–18.
- French B. M. 1998. *Traces of Catastrophe: A Handbook of Shock-Metamorphic Effects in Terrestrial Meteorite Impact Structures*, LPI Contribution No. 954, Lunar and Planetary Science Institute, Houston.
- French B. M., and Koeberl C. 2010. The convincing identification of terrestrial meteorite impact structures: What works, what doesn't, and why. *Earth-Science Reviews* 98:123–170.
- Frisch T., and Thorsteinsson R. 1978. Houghton astrobleme: A mid-Cenozoic impact crater Devon Island, Canadian Arctic Archipelago. *Arctic* 31:108–124.

- Frondel C., and Marvin U. B. 1967. Lonsdaleite, a hexagonal polymorph of diamond. *Nature* 214:587–589.
- Gault D. E., Quaide W. L., and Oberbeck V. R. 1968. Impact cratering mechanics and structures. In *Shock Metamorphism of Natural Materials*, edited by French B. M., and Short N. M. Baltimore: Mono Book Corp. pp. 87–99.
- Glass B. P., and Simonson B. M. 2012. Distal impact ejecta layers: Spherules and more. *Elements* 8:43–48.
- Graup G. 1999. Carbonate-silicate liquid immiscibility upon impact melting: Ries Crater, Germany. *Meteoritics & Planetary Science* 34:425–438.
- Grieve R. A. F., Dence M. R., and Robertson P. B. 1977. Cratering processes: As interpreted from the occurrence of impact melts. In *Impact and Explosion Cratering*, edited by Roddy D. J., Pepin R. O., and Merrill R. B. New York: Pergamon Press. pp. 791–814.
- Grieve R. A. F., and Cintala M. J. 1992. An analysis of differential impact melt-crater scaling and implications for the terrestrial impact record. *Meteoritics* 27:526–538.
- Grieve R. A. F., Langenhorst F., and Stöffler D. 1996. Shock metamorphism of quartz in nature and experiment: II. Significance in geoscience. *Meteoritics & Planetary Science* 31:6–35.
- Gurov E. P., Melnychuk E. V., Metalidi S. V., Ryabenko V. A., and Gurova E. P. 1985. The characteristics of the geological structure of the eroded astrobleme in the western part of the Ukrainian Shield. *Dopovidi Akademii Nauk Ukrain's'koi RSR* 8–11.
- Gurov E. P., Gurova E. P., and Sokur T. M. 2002. Geology and petrography of the Zapadnaya impact crater in the Ukrainian Shield. In *Impacts in Precambrian Shields*, edited by Plado J., and Pesonen L. J. Berlin: Springer. pp. 173–188.
- Harrison J. C., Ford A., Miall A. D., Rainbird R. H., Hulbert L. J., Christie R. L., and Campbell F. H. A. 2013. Geology, tectonic assemblage map of Aulavik, Banks Island

and northwestern Victoria Island, Northwest Territories; Geological Survey of Canada, Canadian Geosciences Map 35 (preliminary). scale 1:500 000.

Hickey L. J., Johnson K. R., and Dawson M. R. 1988. The stratigraphy, sedimentology, and fossils of the Haughton Formation: A post-impact crater-fill, Devon Island, N.W.T., Canada. *Meteoritics* 23:221–231.

Hörz F., Archer P. D., Niles P. B., Zolensky M. E., and Evans M. 2015. Devolatilization or melting of carbonates at Meteor Crater, AZ? *Meteoritics & Planetary Science* 50:1050–1070.

Hörz F., Cintala M. J., Thomas-Keprta K. L., Ross D. K., and Clemett S. J. 2019. Unconfined shock experiments: A pilot study into the shock-induced melting and devolatilization of calcite. *Meteoritics & Planetary Science* 28:1–28.

Hund A. J., ed. 2014. *Antarctica and the Arctic Circle: A Geographic Encyclopedia of the Earth's Polar Regions*, 2 volumes. ABC-CLIO.

Huson S. A., Foit F. F., Watkinson A. J., and Pope M. C. 2009. Rietveld analysis of X-ray powder diffraction patterns as a potential tool for the identification of impact-deformed carbonate rocks. *Meteoritics & Planetary Science* 44:1695–1706.

Impact Earth. Impact Earth Database. 2020. www.impactearth.com (Accessed February 18, 2020).

Jenkins R., and Snyder R. L. 1996. *Introduction to X-ray Powder Diffractometry*, New York: John Wiley & Sons, Inc.

Jessberger E. K. 1988. ^{40}Ar - ^{39}Ar dating of the Haughton impact structure. *Meteoritics* 23:233–234.

Jones A. P., Claeys P., and Heuschkel S. 2000. Impact melting of carbonates from the Chicxulub Crater. In *Impacts and the Early Earth, Lecture Notes in Earth Sciences*, edited by Gilmour I., and Koeberl C. Springer-Verlag, Berlin-Heidelberg-New York. pp. 343–361.

- Kieffer S. W., and Simonds C. H. 1980. The role of volatiles and lithology in the impact cratering process. *Reviews of Geophysics and Space Physics* 18:143–181.
- Lange M. A., and Ahrens T. J. 1986. Shock-induced CO₂ loss from CaCO₃; implications for early planetary atmospheres. *Earth and Planetary Science Letters* 77:409–418.
- Lepaulard C., Gattacceca J., Swanson-Hysell N., Quesnel Y., Demory F., and Osinski G. R. 2019. A Paleozoic age for the Tunnunik impact structure. *Meteoritics & Planetary Science* 1–12.
- Lindgren P., Broman C., Holm N. G., Parnell J., Bowden S., Osinski G. R., and Lee P. 2009. The Raman signature of shocked carbonates from the Haughton impact structure, Devon Island, Canada. *40th Lunar and Planetary Science Conference*. 1–2.
- Martinez I., Deutsch A., Scharer U., Ildefonse P., Guyot F., and Agrinier P. 1995. Shock recovery experiments on dolomite and thermodynamical calculation of impact induced decarbonation. *Journal of Geophysical Research* 100:15465–15476.
- Mathieu J., Kontak D. J., Turner E. C., Fayek M., and Layne G. 2015. Geochemistry of Phanerozoic diagenesis on Victoria Island, NWT, Canada. *Chemical Geology* 415:47–69.
- Melosh H. J. 1989. *Impact Cratering: A Geologic Process*, New York: Oxford University Press.
- Metzler A., Ostertag R., Redeker H. J., and Stoffler D. 1988. Composition of the crystalline basement and shock metamorphism of crystalline and sedimentary target rocks at the Haughton impact crater, Devon Island, Canada. *Meteoritics* 23:197–207.
- Newman J. D., and Osinski G. R. 2016. Geological mapping of the Tunnunik impact structure, Victoria Island, Canadian High Arctic. *47th Lunar and Planetary Science Conference* Abstract #1591.
- O’Keefe J. D., and Ahrens T. J. 1982. Cometary and meteorite swarm impact on planetary surfaces. *Journal of Geophysical Research* 87:6668–6680.

- O'Keefe J. D., and Ahrens T. J. 1989. Impact production of CO₂ by the Cretaceous/Tertiary extinction bolide and the resultant heating of the Earth. *Nature* 338:247–249.
- Oberbeck V. R. 1975. The role of ballistic erosion and sedimentation in lunar stratigraphy. *Reviews of Geophysics and Space Physics* 13:337–362.
- Okulitch A. V. 1991. Geology of the Canadian Archipelago and North Greenland; Figure 2; in Inuitian Orogen and Arctic Platform: Canada and Greenland H.P. Trettin (ed.), scale 1:2 000 000.
- Osinski G. R., Spray J. G., and Lee P. 2001. Impact-induced hydrothermal activity within the Haughton impact structure, Arctic Canada; generation of a transient, warm, wet oasis. *Meteoritics & Planetary Science* 36:731–745.
- Osinski G. R., Lee P., Spray J. G., Parnell J., Lim D. S. S., Bunch T. E., Cockell C. S., and Glass B. 2005a. Geological overview and cratering model for the Haughton impact structure, Devon Island, Canadian High Arctic. *Meteoritics & Planetary Science* 40:1759–1776.
- Osinski G. R., Spray J. G., and Lee P. 2005b. Impactites of the Haughton impact structure, Devon Island, Canadian High Arctic. *Meteoritics & Planetary Science* 40:1789–1812.
- Osinski G. R., Spray J. G., and Grieve R. A. F. 2008. Impact melting in sedimentary target rocks: An assessment. In *The Sedimentary Record of Meteorite Impacts, Special Paper 437*, edited by Evans K. R., Horton W., King Jr. D. K., and Morrow J. R. Geological Society of America, Boulder, CO. pp. 1–18.
- Osinski G. R., and Pierazzo E. 2013. Ch 01 Impact cratering: processes and products. In *Impact Cratering: Processes and Products*. pp. 1–20.
- Osinski G. R., Abou-Aly S., Francis R., Hansen J., Marion C. L., Pickersgill A. E., and Tornabene L. L. 2013. The Prince Albert structure, Northwest Territories, Canada: A new 28-km diameter complex impact structure. *44th Lunar and Planetary Science Conference* Abstract #2099.

- Osinski G. R., Grieve R. A. F., Chanou A., and Sapers H. M. 2016. The “suevite” conundrum, Part 1: The Ries suevite and Sudbury Onaping Formation compared. *Meteoritics & Planetary Science* 51:1–18.
- Osinski G. R., Grieve R. A. F., Bleacher J. E., Neish C. D., Pilles E. A., and Tornabene L. L. 2018. Igneous rocks formed by hypervelocity impact. *Journal of Volcanology and Geothermal Research* 353:25–54.
- Pontefract A., Osinski G. R., Cockell C. S., Moore C. A., Moores J. E., and Southam G. 2014. Impact-generated endolithic habitat within crystalline rocks of the Houghton impact structure, Devon Island, Canada. *Astrobiology* 14:522–33.
- Puura V., and Suuroja K. 1992. Ordovician impact crater at Kärđla, Hiiumaa Island, Estonia. *Tectonophysics* 216:143–156.
- Redeker H. J., and Stöffler D. 1988. The allochthonous polymict breccia layer of the Houghton impact crater, Devon Island, Canada. *Meteoritics* 23:185–196.
- Ross N. L., and Reeder R. J. 1992. High-pressure structural study of dolomite and ankerite. *American Mineralogist* 77:412–421.
- Reeder R. J. 1983. Crystal chemistry of the rhombohedral carbonates. In *Reviews in Mineralogy Volume 11 Carbonates: Mineralogy and Chemistry*, edited by Reeder R. J. Mineralogical Society of America. pp. 1–47.
- Rietveld H. M. 1969. A profile refinement method for nuclear and magnetic structures. *Journal of Applied Crystallography* 2:65–71.
- Robertson P. B., and Mason G. D. 1975. Shatter cones from Houghton Dome, Devon Island, Canada. *Nature* 255:393–394.
- Seeley J. R., and Milam K. A. 2018. Optical and X-ray diffraction analyses of shock metamorphosed dolostone at increasing depths within the central uplift of the Wells Creeks impact structure. *49th Lunar and Planetary Science Conference* Abstract #2755.

- Shannon R. D. 1976. Revised effective ionic radii and systematic studies of interatomic distances in halides and chalcogenides. *Acta Crystallographica* A32:751–767.
- Sherlock S. C., Kelley S. P., Parnell J., Green P., Lee P., Osinski G. R., and Cockell C. S. 2005. Re-evaluating the age of the Haughton impact event. *Meteoritics & Planetary Science* 40:1777–1787.
- Shmayenok A. I., and Tikhomirov S. N. 1974. The Mishina Gora explosive structure in the Lake Chud area. *Doklady Akademii Nauk SSSR* 219:701–703.
- Shoemaker E. M. 1960. Penetration Mechanics of High Velocity Meteorites, Illustrated by Meteor Crater, Arizona. In *International Geological Congress, Report of the Twenty-First Session, Norden. Part XVIII, Structure of the Earth's Crust and Deformation of Rocks*, edited by Kvale A., and Metzger A. Copenhagen: Det Berlingske Bogtrykkeri. pp. 418–434.
- Skála R., and Jakeš P. 1999. Shock-induced effects in natural calcite-rich targets as revealed by X-ray powder diffraction. In *Large Meteorite Impacts and Planetary Evolution II, Special Paper 339*, edited by Dressler B. O., and Sharpton V. L. Geological Society of America (GSA), Boulder, CO. pp. 205–214.
- Stewart W. D. 1987. *Late Proterozoic to Early Tertiary stratigraphy of Somerset Island and Northern Boothia Peninsula, District of Franklin, N.W.T.*, Paper 83-26, Geological Survey of Canada.
- Stöffler D., and Grieve R. A. F. 2007. Impactites. In *Metamorphic Rocks: A Classification and Glossary of Terms, Recommendations of the International Union of Geological Sciences*, edited by Fettes D., and Desmons J. Cambridge: Cambridge University Press. pp. 82–92.
- Stöffler D., Artemieva N. A., Wünnemann K., Reimold W. U., Jacob J., Hansen B. K., and Summerson I. A. T. 2013. Ries crater and suevite revisited—Observations and modeling Part I: Observations. *Meteoritics & Planetary Science* 48:515–589.
- Stöffler D., Hamann C., and Metzler K. 2018. Shock metamorphism of planetary silicate

- rocks and sediments: Proposal for an updated classification system. *Meteoritics & Planetary Science* 49:5–49.
- Thorsteinsson R., and Tozer E. T. 1962. *Banks, Victoria, and Stefansson Islands, Arctic Archipelago*, Memoir 330. Geological Survey of Canada.
- Thorsteinsson R., and Tozer E. T. 1970. Geology of the Arctic Archipelago. In *Geology and Economic Minerals of Canada*, edited by Douglas R. J. W. Geological Survey of Canada. pp. 547–590.
- Thorsteinsson R., and Mayr U. 1987. *The Sedimentary Rocks of Devon Island, Canadian Arctic Archipelago*, Memoir 411. Geological Survey of Canada.
- Ullman D. J., Carlson A. E., Anslow F. S., LeGrande A. N., and Licciardi J. M. 2015. Laurentide ice-sheet instability during the last deglaciation. *Nature Geoscience* 8:534–537.
- Wasastjerna J. A. 1924. The crystal structure of dolomite. *Societas Scientiarum Fennica* 2:1–14.
- Wyckoff R. W. G., and Merwin H. E. 1924. The crystal structure of dolomite. *The American Journal of Science* 48:447–461.
- Young G. M., and Long D. G. F. 1977. Carbonate sedimentation in a late Precambrian Shelf Sea, Victoria Island, Canadian Arctic Archipelago. *Journal of Sedimentary Petrology* 47:943–955.
- Young R. A. 1993. Introduction to the Rietveld method. In *The Rietveld Method*, edited by Young R. A. Oxford: Oxford University Press. pp. 1–38.
- Young K. E., Van Soest M. C., Hodges K. V., Watson E. B., Adams B. A., and Lee P. 2013. Impact thermochronology and the age of Haughton impact structure, Canada. *Geophysical Research Letters* 40:3836–3840.

Zylberman W., Quesnel Y., Rochette P., Osinski G. R., Marion C., and Gattacceca J. 2017. Hydrothermally enhanced magnetization at the center of the Haughton impact structure? *Meteoritics & Planetary Science* 52:2147–2165.

Chapter 2

2 Impact-generated breccia dykes of the Tunnunik impact structure, Canada

2.1 Introduction

The Tunnunik impact structure is a deeply eroded impact structure located on northwestern Victoria Island, Northwest Territories, Canada. It was discovered during regional mapping of northwestern Victoria Island in 2010 by the Geological Survey of Canada (Dewing et al. 2013). Dewing et al. (2013) identified tilted strata and an abundance of shatter cones within the central area of the impact structure, thus confirming its origin. It is notable that no impact breccias or impact melt rocks were documented by Dewing et al. (2013) during their reconnaissance. The erosion of all the ejecta, crater-fill impactites, and most of the topographic expression (i.e., rim and central uplift) of the original complex crater morphology is consistent with this being an old impact structure with an age between 430 and 450 Ma (Lepaulard et al. 2019). Recent expeditions to this remote Arctic impact site in 2012 and 2015 have studied the geology (Newman and Osinski 2016; Osinski et al. 2013), geophysics (Quesnel et al. 2020; Zylberman 2017), and palaeomagnetism (Lepaulard et al. 2019) of the Tunnunik impact structure.

Approximately one third of known impact structures have carbonates present in their target rock sequence (Osinski et al. 2008). Only a few of these structures are in completely sedimentary targets where carbonates dominate the entire target sequence. The products and processes of impacts into carbonates remains controversial, particularly with respect to the importance of melting versus decomposition. Observations and experiments on the response of carbonates to hypervelocity impact has been investigated for over 40 years and a consensus has yet to be achieved (Stöffler et al. 2018, and references therein). The most probable rocks in a given target sequence to preserve such clues are the rocks generated during an impact, or impactites, which can be found in crater-fill deposits, breccia dykes, and ejecta deposits.

For deeply eroded complex craters, such as Tunnunik, impact breccia dykes should be present (Dressler and Reimold 2004; Lambert 1981); however, their distribution in deeply

eroded craters is often underestimated in the field, attributed in part to poor exposure of the crater floor (Lambert 1981). Impact breccia dykes have been proposed to be emplaced to depths of several km during the early stages of crater formation (Dence 1971; Dressler and Sharpton 1997; Stöffler and Grieve 2007), thus potentially preserving crater-fill deposits and fragments of overlying target rocks that are no longer present. As noted above, allochthonous impactites were not documented at the Tunnunik impact structure in the discovery paper (Dewing et al. 2013). Osinski et al. (2013) reported on the findings from the 2012 Tunnunik expedition during which impact breccia dykes were discovered at four locations. This contribution focuses on the field and laboratory investigation of impact breccia dykes at the Tunnunik structure from the 2012 and 2015 field seasons. These dykes represent the only preserved allochthonous impactites at this impact structure and provide insight into the fate of carbonates during hypervelocity impact and how, and when, in the cratering process, breccia dykes are emplaced.

2.2 Geologic setting

Northwestern Victoria Island consists of Cambrian to Silurian-aged sedimentary rocks, dominated by carbonates, that dip gently from 5 to 10° and overlain by Quaternary sediments (Dewing et al. 2013). The Tunnunik impact structure has an apparent diameter of ~28 km and an age between 450 and 430 Ma (Lepaulard et al. 2019). Extensive erosion at Tunnunik has removed at least ~1 km of the original structure (Dewing et al. 2013; Quesnel et al. 2020; Zylberman 2017) such that no crater-fill deposits or ejecta are preserved and only the deeper layers of the crater floor remain. An abundance of well-preserved shatter cones helps define the limits of the central uplift in an elliptical area 10 by 12 km (Osinski and Ferrière 2016).

Four main stratigraphic units have been identified in the Tunnunik impact structure: from oldest to youngest these are the Shaler Supergroup, Mount Phayre Formation, Victoria Island Formation, and Allen Bay Formation (Fig. 2-1). Sharp contacts between formations were not observed and are considered gradational, consistent with a shallow marine depositional environment. The exposed section of the Shaler Supergroup is limestone that avoided the regional dolomitization activity that affected the three overlying formations which consist primarily of dolostone. An unconformity of ~200 Ma separates the

Precambrian Shaler Supergroup units from the Cambrian Mount Phayre Formation (Mathieu et al. 2013). The impact did not reach the crystalline basement.

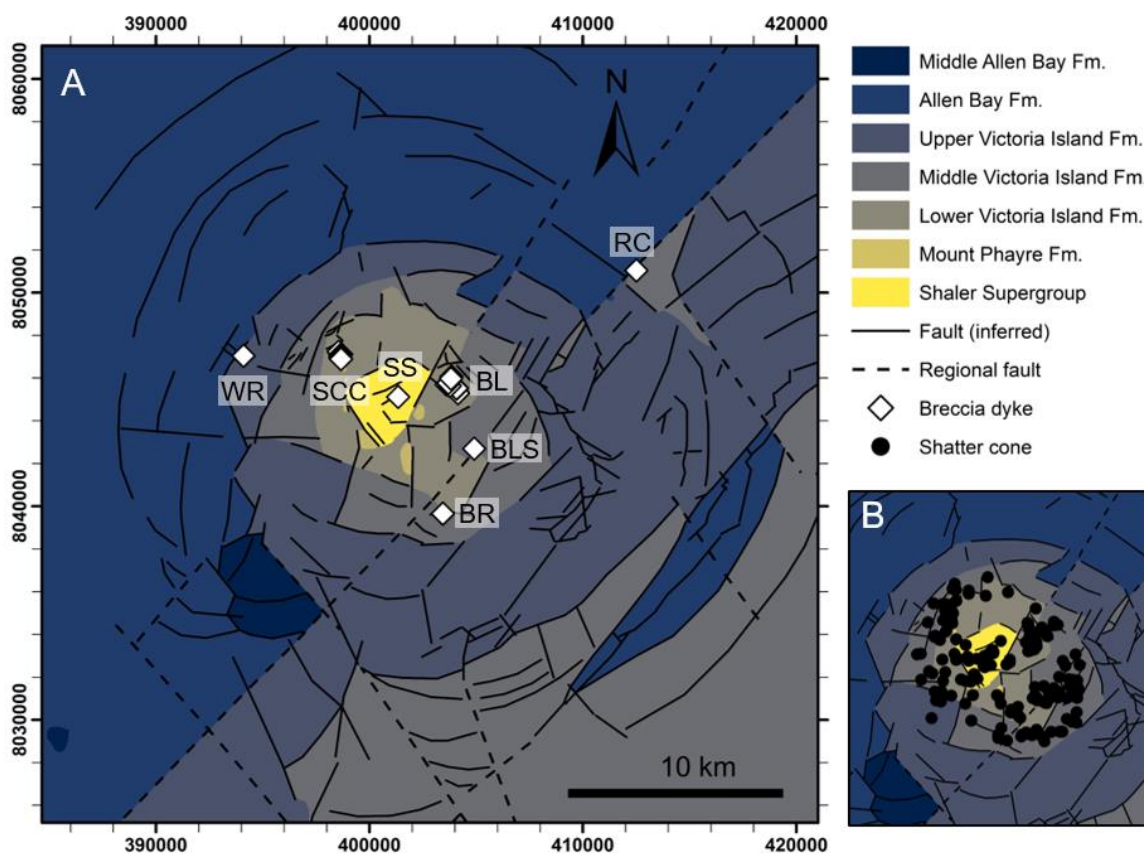


Figure 2-1. Simplified geologic map of the Tunnunik impact structure indicating breccia dyke localities examined in this study; Shatter Cone Canyon (SCC), Shaler Supergroup (SS), Big Lake (BL), Big Lake south (BLS), Bouldering River (BR), West River (WR) and Rim Canyon (RC). B) Shatter cone distribution within the Tunnunik impact structure. UTM grid with Easting and Northing at 2000 m intervals for Zone 11 and Zone 12.

2.3 Samples and methods

Fieldwork at the Tunnunik impact structure was carried out over two weeks in July 2012 and five weeks in July and August 2015. A systematic search of the impact structure identified and sampled twenty-five dykes (Fig. 2-1A) and determined the extent of shatter cones (Fig. 2-1B). Search extended beyond the 10 km by 12 km shatter cone extent (Fig. 2-1B) and additionally focused on canyons or bedrock exposures identified from satellite

imagery. From the twenty-five impact breccia dykes, a representative suite of thin sections was prepared for subsequent analysis. Polished thin sections were examined petrographically in transmitted light using Nikon Eclipse LV 100POL microscopes with a NIS-Elements D laboratory image analysis system. The nature, texture, and composition of clasts and matrix of each breccia were studied. Samples were carbon coated for electron probe microanalysis (EPMA) using a JEOL JXA-8530F field-emission electron microprobe in the Earth and Planetary Materials Analysis Laboratory at the University of Western Ontario. Energy dispersive spectrometry (EDS) was used to obtain semi-quantitative elemental data for mineral identification. Backscattered electron (BSE) images were captured and used to examine microtextures within the breccias using a 15 kV accelerating voltage and working distance of 11 mm. Wavelength dispersive spectrometry (WDS) provided quantitative compositions for silicate glass clasts and mineral inclusions within the glass. Analytical conditions for WDS analyses of elements Si, Al, Na, Mg, Ca, Ti, Fe, Mn, K, and S were an accelerating voltage of 15 kV, beam current of 20 nA, spot size of 5 μm , and working distance of 11 mm. Element maps of Al, K, Na, Si, Ti, Ca, Mg, Fe and Mn were acquired through EDS and WDS for specific targets with an accelerating voltage of 15 kV, beam current of 50 nA, and spot size of 1–2 μm using the same microprobe.

2.4 Results

Impact breccia dykes from the Tunnunik impact structure range from ~5 cm to ~1 m thick, and exposures of dykes extend up to ~5 m in length. There are seven localities within the impact structure where one or more breccia dykes were found (Fig 2-1A). Breccia samples from these localities were collected and examined in detail with most dykes concentrated at the Big Lake and Shatter Cone Canyon localities. All but two breccia localities in this study occur within the well-defined shatter cone distribution (Fig. 2-1B). We have divided the Tunnunik impact breccia into four general types based on whether the matrix and clasts are composed primarily of dolomite or calcite and if they are monomict or polymict. Features for a certain type may vary slightly among dykes but remain consistent within a given dyke.

2.4.1 Type 1

2.4.1.1 Field observations

Breccia samples designated as Type 1 (T1) were collected from four localities within the central uplift called Shatter Cone Canyon, Big Lake, Big Lake south, and Bouldering River (Fig. 2-1A). Shatter Cone Canyon is ~4 km northwest of the centre of the impact structure and is an exceptional feature within the impact crater. The walls of the canyon expose thrust faults, inclined strata and an abundance of well-developed and well-preserved shatter cones (Dewing et al. 2013; Osinski et al. 2013). Shatter Cone Canyon is one of the largest and longest continuous exposures within the impact structure providing excellent access to breccia dykes. The breccia dykes discovered in Shatter Cone Canyon occur in the Mount Phayre Formation which is located at the southern end of the canyon and gradually grades into the Victoria Island Formation northward about midway through the canyon. These dykes are found along fractures or bedding planes and have sharp contacts with the host rock (Figs. 2-2A–C). Larger clasts within several dykes have their long axes notably oriented parallel with the longitudinal axis of the dyke (Figs. 2-2L–M). Weathered outer surfaces of breccia are pale tan to yellow in colour for all dykes while fresh surfaces are grey to grey-green or yellow in colour. The dykes with yellow matrix also have yellow weathering but differences between shades of yellow are evident in hand samples.

The Big Lake breccia dykes are located ~3 km east from the centre of the impact structure and the Big Lake south dyke is located ~3 km south-southeast from the main Big Lake locality (Fig. 2-1B). The Big Lake breccia dykes are more difficult to identify than the dykes in Shatter Cone Canyon due to the highly fractured nature of the surface rocks and due to their occurrence on inclined slopes (Figs. 2-2D–E). The ground position of the dykes as opposed to a vertical outcrop means they are strongly affected by annual freeze-thaw cycles which has fractured not only the breccia dykes themselves but the surrounding host rock as well. Within the fragmented dykes at Big Lake, some larger blocks of breccia exist that are not completely broken apart while some large adjacent fragments fit together further showing minimal movement of rocks in this area.

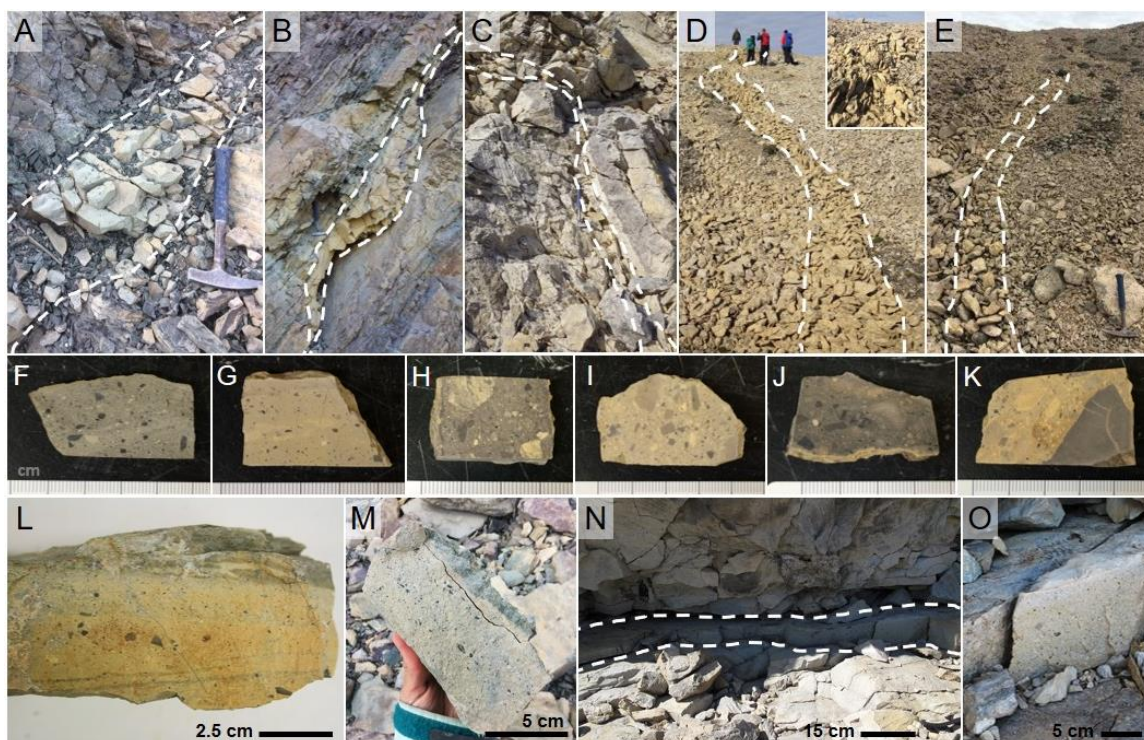


Figure 2-2. Type 1 breccia dykes from Shatter Cone Canyon (A–C), Big Lake (D–E), and Boulderling River (N) with dyke boundaries indicated by white dashed lines. A) Nearly vertical dyke cuts through more horizontal bedding; breccia is fractured and fragments have fallen out of place. B) Dyke is parallel to bedding planes with a dip of 49° . C) Narrow dyke that follows the fold contour of the host rocks. D) Ground surface exposure of dyke has been strongly affected by freeze-thaw action and is highly fractured like surrounding rock. Inset image from top of dyke shows a location that was more resistant to freeze-thaw cycles. E) Similar to (D), breccia in dyke has been severely fractured by frost action. Samples (F–K) represent variations among T1 dykes. F) Breccia from Shatter Cone Canyon shows subtle banding in matrix with elongated clasts oriented parallel to bands. G) Sample from dyke in (C) shows small clasts oriented in horizontal direction. H) Bimodal clast size distribution in breccia from Big Lake. I) Minimal alignment of larger rounded clasts in this Big Lake breccia sample. J) The most diverse assemblage of clasts in any T1 breccia. K) Sample from dyke in (D) contains part of a large 10 cm grey dolostone clast. L) Breccia sample from dyke in (B) showing alignment of clasts parallel to green mudstone host rock along top of hand sample. M) Similar to (L) this breccia from Shatter Cone Canyon also shows clasts oriented in same direction as green mudstone host. N) Horizontal breccia dyke follows bedding planes of host dolostone. O) Close-up of breccia near right edge of dyke shown in (N).

There are no indications that mass-wasting or movement of rocks has occurred, so the dykes and surrounding rocks are presumed to have broken and fractured in place and not been moved from elsewhere. Contacts between dyke and host rock are not observable due to the freeze-thaw fragmentation. The absence of soil or glacially deposited till means the dykes are identifiable by recognizing the yellow weathering of the breccia compared to the pale grey-yellow dolostone of the Victoria Island formation. Similar to the dykes from Shatter Cone Canyon, the breccia samples have an outer yellow weathered surface while the fresh surfaces vary from pale to dark grey or yellow. Diversity among the closely associated Big Lake dykes is shown in Figures 2-2H–K where these four samples were collected 150 to 600 m apart.

The breccia dyke exposed along Bouldering River is ~5 km from the centre of the structure near the southern extent of the shatter cone distribution in the Victoria Island Formation (Fig. 2-1). This horizontal dyke is parallel to bedding, exposed for several metres, has sharp contacts with the host rock, and larger clasts are oriented longitudinally within the dyke (Figs. 2-2N–O). The weathering of this breccia dyke is less extensive than previous sites and it does not display the same degree of yellow colouring as Shatter Cone Canyon and Big Lake dykes. Shatter cone fragments were observed in breccia samples found along the bank of Bouldering River. Due to the general cm-size or smaller breccia clasts, they were not commonly found and were only noticed in several clasts 3–4 cm in size. Shatter cones were likely present in smaller clasts as well, but larger clasts enabled the shatter cone striations to be more apparent and identifiable on recently broken surfaces and not older more smoothed surfaces resulting from fluvial erosion.

2.4.1.2 Petrography and geochemistry

Type 1 breccias are polymict with a carbonate-rich composition, poorly sorted, and are matrix-supported. A small portion of the Bouldering River breccia thin section is clast-supported (Fig. 2-3A); although this appears to be an isolated occurrence as the remainder of the sample is matrix-supported. The matrix is typically too fine-grained to resolve using transmitted light microscopy while clasts are resolvable and are angular to sub-rounded (Figs. 2-3A–C).

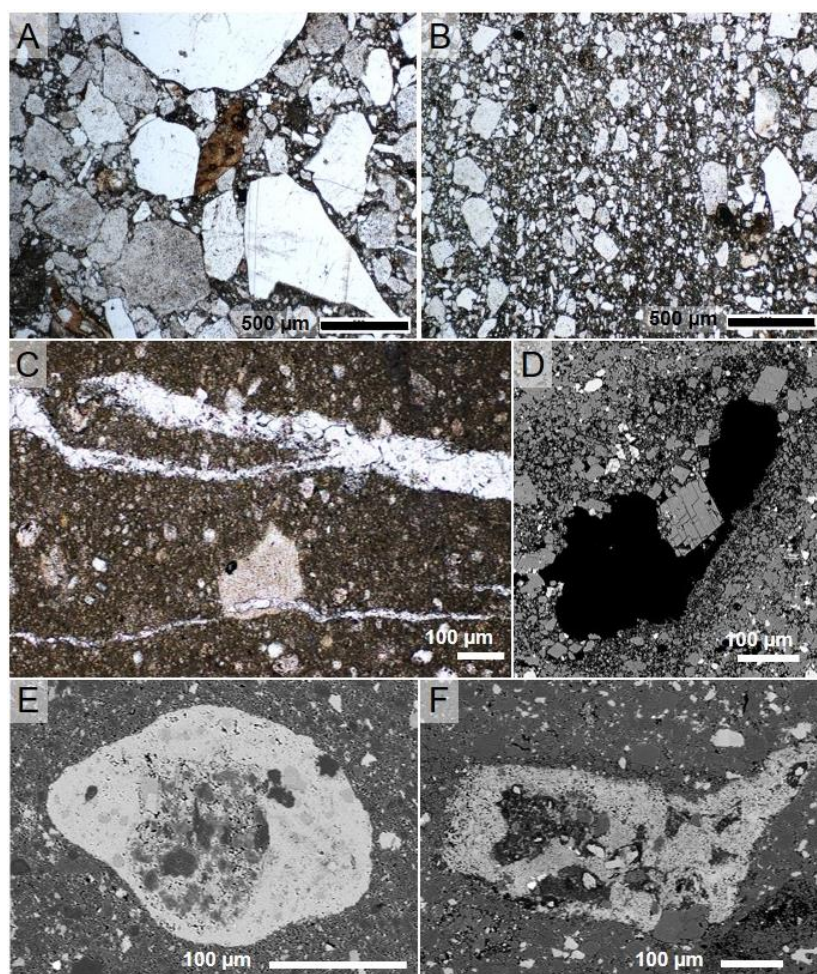


Figure 2-3. Type 1 breccia optical microscopy. A) Coarse, clast-supported area of breccia. B) Small-scale clast orientation localized near host contact to right of image. C) Veins of coarse calcite cut across matrix and clasts. D) Euhedral grains of dolomite in small vug. E) Rounded, fine-grained calcite clast (pale grey) containing fine-grained dolomite (dark grey). F) Irregular-shaped calcite clast (pale grey) with areas of dolomite (dark grey). (A–C) imaged in PPL and (D–F) imaged with BSE.

Dykes with T1 breccia have a bimodal clast size distribution of $\sim 500\ \mu\text{m}$ and smaller or greater than 1 cm, with rare large rounded clasts up to 10 cm found in one Big Lake dyke. The orientation of clasts is not always apparent at the thin section scale but alignment of elongated clasts (Fig. 2-3B) rather than a completely random orientation of clasts is typically observed. Clast orientation and distribution within a sample can be highly localized (e.g., compare Figures 2-3A and B which are from the same thin section). Breccias may contain crystalline veins of calcite up to $100\ \mu\text{m}$ wide that cut across matrix

and clasts (Fig. 2-3C) or small vugs up to several hundred μm in diameter with euhedral dolomite crystals (Fig. 2-3D). In addition to the small vugs, some samples contain holes of $\sim 100\ \mu\text{m}$ to over $1000\ \mu\text{m}$ in diameter which are rounded to sub-angular in shape.

Type 1 breccias have a dolomite-rich matrix that contains minor quartz, K-feldspar, and calcite grains; quartz and K-feldspar account for 1–10% of grains within the matrix. BSE imagery shows the grain size of matrix material is $<50\ \mu\text{m}$ (Fig. 2-4). Analyses of lithic clasts confirm the presence of dolostone, sandstone, chert, and mudstone. Minor mineral grains present in lithic clasts and the matrix include zircon, rutile, muscovite, biotite, apatite, sulfides, and iron oxides. Crystalline limestone clasts were not detected in the dolomite-rich T1 breccia samples; however, calcite was identified as highly localized fine-grained areas or rounded clasts (Figs. 2-3E, 2-3F). Backscattered electron imagery readily identifies areas of fine-grained dolomite from calcite which are difficult to distinguished in transmitted light (Figs. 2-3E, 2-3F, 2-5, 2-6). Fine-grained carbonate compositions do not differ from larger crystalline dolomite and calcite grains, therefore in Table 2-1, the dolomite and calcite analyses presented represent both the crystalline and fine-grained carbonate forms.

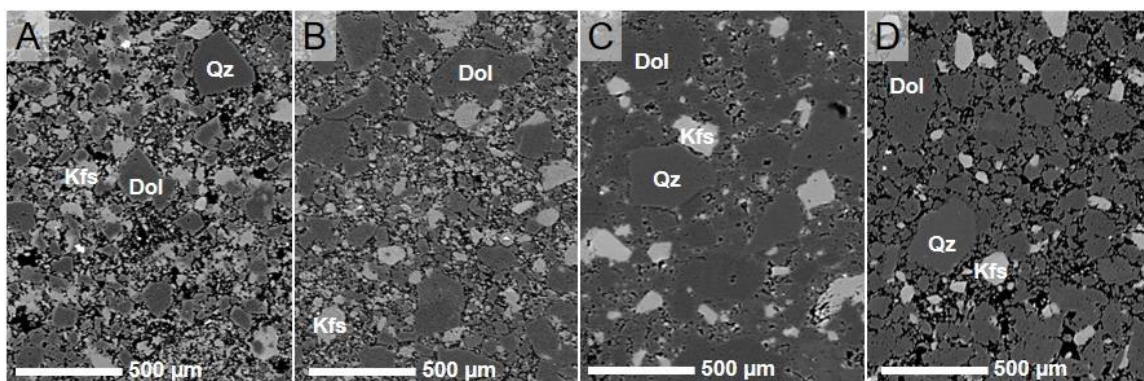


Figure 2-4. Backscattered electron images of T1 breccia at 500x magnification. A) Well-defined grains of K-feldspar, pyrite (white), and quartz in dolomite-rich matrix along top of sample in Figure 2-4A. B) Dolomite and K-feldspar matrix from Figure 2-2F breccia has range of clast sizes with distinct edges. C) Dolomite-rich matrix from Figure 2-2J breccia is less defined than matrix in (A) and (B). D) Poorly defined dolomite matrix with feldspar grains and rare quartz. Minerals indicated include dolomite (Dol), quartz, (Qz), and K-feldspar (Kfs); black areas are pore spaces within the matrix.

Table 2-1. Electron microprobe WDS analyses of carbonates* for mineral grains and melt.

Mineral phase	Dolomite		Porous dolomite		Low Mg ferroan dolomite		Porous low Mg ferroan dolomite		Calcite		Porous calcite		Carbonate-silicate ¹		Carbonate-silicate ²		Carbonate-silicate ³		Carbonate-silicate ⁴		
	wt% s.d.	n	wt% s.d.	n	wt% s.d.	n	wt% s.d.	n	wt% s.d.	n	wt% s.d.	n	wt% s.d.	n	wt% s.d.	n	wt% s.d.	n	wt% s.d.	n	
SiO ₂	0.2	48	0.2	20	0.2	2	0.4	11	0.2	20	0.1	9	5.3	24	1.9	5	3.1	31	24.4	4	
Al ₂ O ₃	0.1	0.1	0.1	0.1	0.1	0.1	0.1	0.1	0.1	0.1	b.d.	b.d.	0.5	0.6	0.7	0.4	1.0	0.7	8.0	1.5	
Na ₂ O	b.d.	b.d.	b.d.	b.d.	b.d.	b.d.	b.d.	b.d.	b.d.	b.d.	b.d.	b.d.	b.d.	b.d.	b.d.	b.d.	b.d.	b.d.	b.d.	0.1	0.1
MgO	21.0	0.6	20.3	0.7	10.5	4.1	10.2	1.9	1.0	0.9	0.4	0.2	19.5	1.4	15.1	2.9	1.9	1.1	3.3	1.1	
CaO	30.5	0.4	30.3	0.6	40.7	4.9	33.4	3.8	54.8	1.0	53.4	0.6	28.7	2.0	31.0	2.2	47.8	3.6	26.3	5.0	
TiO ₂	b.d.	b.d.	b.d.	b.d.	b.d.	b.d.	b.d.	b.d.	b.d.	b.d.	b.d.	b.d.	b.d.	b.d.	b.d.	b.d.	0.1	0.3	0.2	0.1	
FeO	0.3	0.6	0.3	0.2	2.1	0.2	1.5	0.9	0.1	0.1	0.1	0.1	0.3	0.2	2.2	1.4	0.3	0.4	1.6	1.1	
MnO	b.d.	b.d.	b.d.	b.d.	0.2	0.1	0.2	0.1	0.1	0.2	b.d.	b.d.	b.d.	b.d.	0.2	0.1	0.1	0.0	0.0	0.0	
SO ₃	b.d.	b.d.	b.d.	b.d.	b.d.	b.d.	0.1	0.1	0.1	0.0	b.d.	b.d.	0.1	0.1	b.d.	b.d.	b.d.	b.d.	0.7	1.1	
K ₂ O	b.d.	b.d.	b.d.	b.d.	b.d.	b.d.	0.1	0.2	b.d.	b.d.	b.d.	b.d.	0.2	0.3	b.d.	b.d.	0.2	0.4	2.0	0.7	
CO ₂ *	47.1	0.4	46.1	0.6	44.9	0.7	38.4	2.6	44.1	0.5	42.4	0.4	44.0	3.1	42.3	1.4	39.8	2.3	25.7	5.3	
Total	99.3	0.7	97.2	0.9	99.2	0.2	84.3	6.1	100.5	0.8	96.6	1.1	98.6	1.5	93.4	3.9	94.3	5.2	92.4	4.0	

* Back-calculated C-content, not measured by WDS.

n = number of points analyzed; wt% = average mineral composition in weight %.
s.d. = standard deviation; b.d. = below detection.

Carbonate-silicate¹ = dolomite with Si.

Carbonate-silicate² = ferroan dolomite with Si.

Carbonate-silicate³ = Mg-bearing calcite with Si.

Carbonate-silicate⁴ = Mg,Fe-bearing calcite with Si-Al.

The porous carbonate phases listed in Table 2-1 are associated with fine-grained carbonates and are characterized as porous due to their appearance. Textures associated with fine-grained areas become more apparent in backscattered electron images and element mapping (Figs. 2-5 and 2-6). Several clasts display a distinct feathery texture. These fine-grained feathery clasts are dolomite and one of these clasts is rimmed by a narrow band of fine-grained calcite (Figs. 2-6E–H).

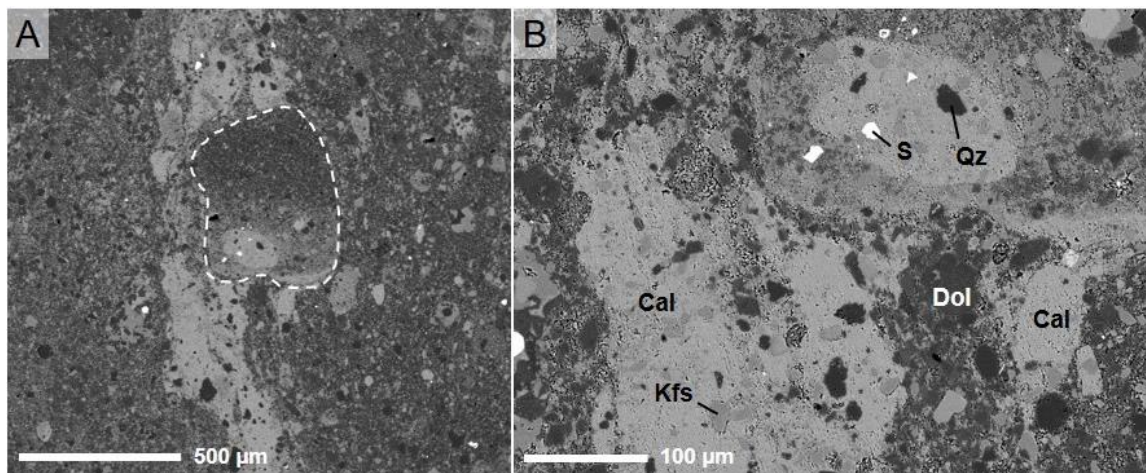


Figure 2-5. A) Fine-grained carbonate clast outlined by white dashed line partially in band of fine-grained calcite (pale grey) in BSE from grey T1 breccia in Figure 2-10A. B) Calcite band and lower left area of clast highlight localized occurrence of calcite within dolomite-rich matrix of T1 breccia from Shatter Cone Canyon. Minerals indicated include calcite (Cal), dolomite (Dol), K-feldspar (Kfs), quartz (Qz), and sulfides (S).

One sample from Shatter Cone Canyon has interesting textures and banding (Fig. 2-7). This banding is extremely localized and not widespread throughout the sample. A second thin section was prepared from the same sample and showed no evidence of the same banded feature and looked very similar to the rest of the T1 breccias. The incomplete mixing observed at the hand sample scale (Fig. 2-7A) is confirmed with microscopy. Adjacent bands have slight compositional variations and textures where some are finer grained or have more silicate grains present (Fig. 2-7B). Clasts and grains were found oriented with their long axes parallel to the band direction. The dark grey-black band in

Figure 2-7A has a K-feldspar-like composition with clasts of crystalline K-feldspar and quartz (Fig. 2-7C).

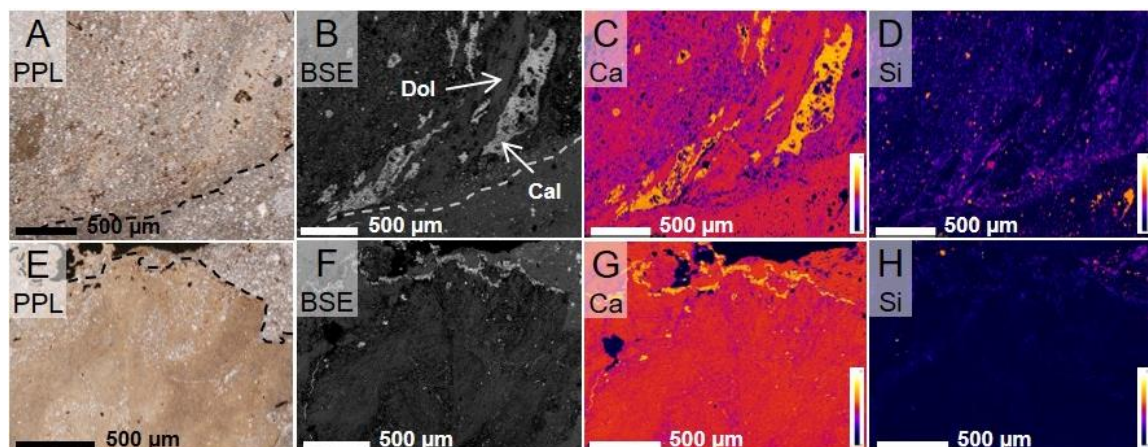


Figure 2-6. A–D) Area within a cm-sized clast in T1 breccia displaying fine-grained dolomite and calcite. A) Fine-grained dolomite is difficult to recognize from calcite as colours observed do not correspond to a specific composition. Dashed black line separates clast above line from matrix below. B) Fine-grained calcite (Cal) is readily distinguished from dolomite (Dol) in BSE. C) Calcium element map shows calcite in yellow and dolomite in pink. D) Silicon element map shows quartz (yellow) and K-feldspar (pink) grains within the clast and matrix. E–H) Carbonate clast with feathery texture. E) Clast is very fine-grained compared to matrix. Black dashed line separates clast below line from matrix above. F) Feathery clast is mainly dolomite, brighter edge along top of clast is calcite. G) Calcium map highlights the calcite band along top of clast. Dark areas are holes in sample. H) Silicon element map shows clast is silicate-free where quartz and K-feldspar grains are confined to the matrix. Colour scales on element maps range from zero counts (black) to highest counts (yellow).

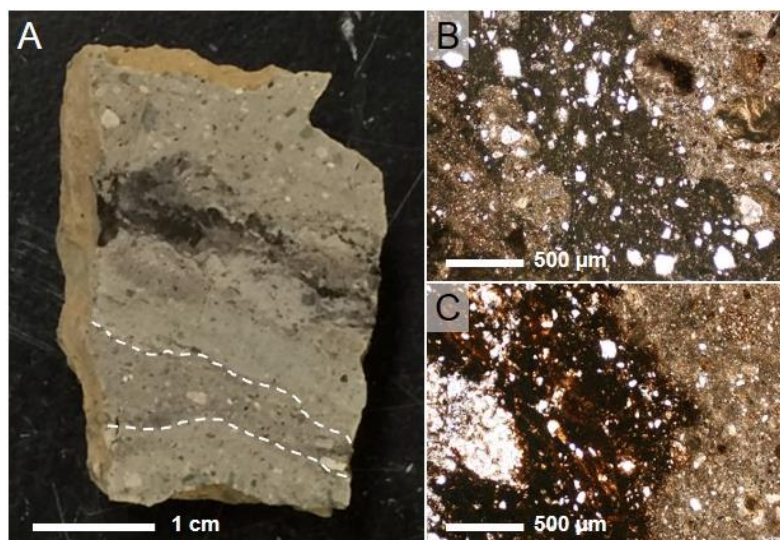


Figure 2-7. A) Localized banding highlighting differences in matrix grain size and composition; dashed white lines outline silicate-rich band. B) Colourless grains in darker central matrix corresponds with silicate-rich band in (A). C) Contact between grey matrix and dark grey-black K-feldspar-like band in (A) with a colourless crystalline K-feldspar and quartz clast at left edge of image.

2.4.1.3 Impact glass fragments

Devitrified impact glass fragments are present in T1 breccia samples but are relatively scarce (<10 glass fragments per thin section). The exception to this is the Big Lake south breccia where glass accounts for over 40% of silicate fraction with ~100 small glass fragments that are <100 μm with several up to 500 μm. Glass fragments range in size from ~50 to 4,400 μm. Transmitted light microscopy reveals glasses are colourless to pale orange-brown in plane polarized light, isotropic in cross polarized light, and fragments are sub-angular to sub-rounded in shape (Fig. 2-8). Samples containing large holes may have small glass remnants along part of the interior edge of these holes.

Colour variation observed in plane polarized light has some correlation with composition when compared to quantitative WDS or element mapping analyses. Colourless glass fragments tend to be SiO₂-rich whereas pale orange to brown coloured fragments are more K₂O-rich, but colour is not an absolute indicator of composition. It is common for an individual glass fragment to exhibit a range in composition. The heterogenous

compositional range extends to inter-fragment comparison as well, based on the high standard deviations of oxide totals (Table 2-2).

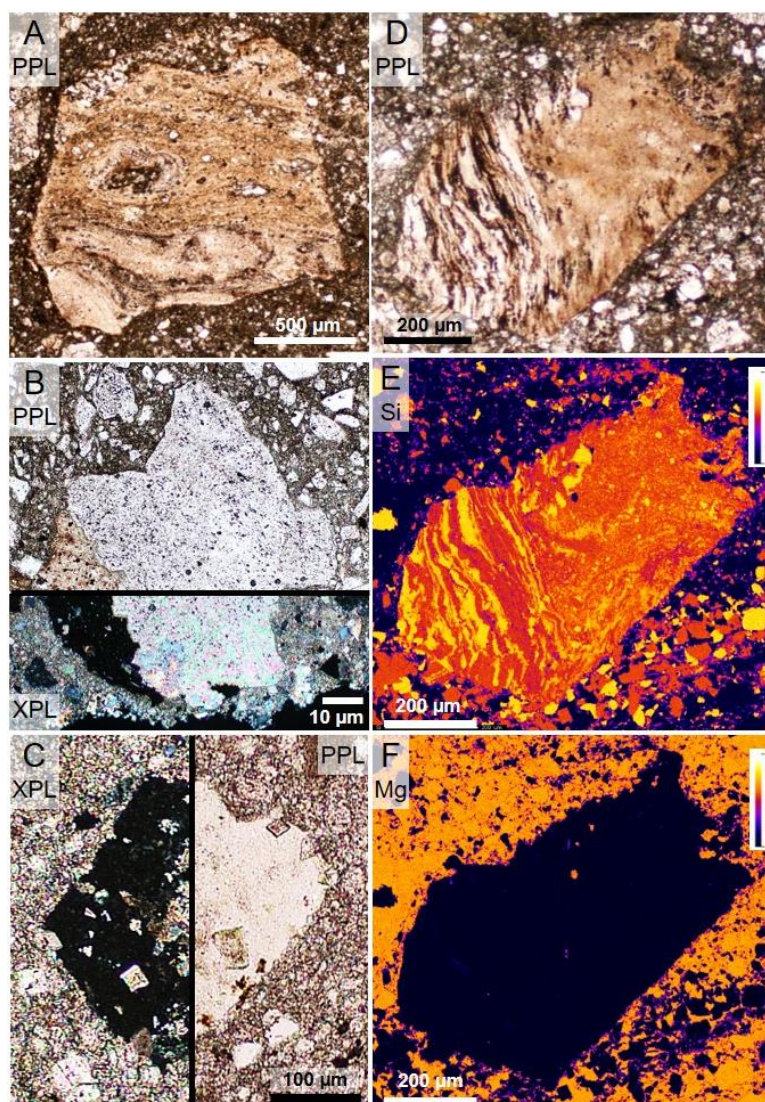


Figure 2-8. Silicate impact glass. A) Large hypocrySTALLINE fragment displaying schlieren. B) Irregular contact between pale brown glass and colourless dolomite (PPL) with more contrast in XPL between isotropic glass (dark) and dolomite. C) HypocrySTALLINE fragment containing euhedral dolomite crystals visible as bright grains within the dark isotropic SiO₂-rich glass in XPL. D) A holohyaline fragment shows banding and mottling of silicate glass. E) Silicon element map highlights areas that are SiO₂-rich (yellow) and K₂O-rich (pink). F) Magnesium element map showing dolomite-rich matrix (yellow-orange). Colour scales ranges from zero counts (black) to highest counts (yellow) for the indicated element.

Table 2-2. Electron microprobe WDS analyses of silicate glass fragments in Type 1 breccia.

Mineral phase	SiO ₂ -rich glass		K ₂ O-rich glass		Si-Al-K mixture ¹		Si-Al-K mixture ²		Si-Al-K mixture ³	
<i>n</i>	77		50		10		25		5	
	wt%	s.d.	wt%	s.d.	wt%	s.d.	wt%	s.d.	wt%	s.d.
SiO ₂	96.9	2.1	64.2	4.1	91.4	4.2	74.4	7.8	53.4	0.7
Al ₂ O ₃	0.6	0.5	15.8	1.8	2.5	1.2	10.4	2.3	19.8	0.9
Na ₂ O	b.d.	b.d.	0.2	0.2	b.d.	b.d.	0.1	0.1	0.1	0.0
MgO	b.d.	b.d.	0.1	0.3	0.4	0.3	0.8	0.8	4.6	0.4
CaO	0.1	0.0	0.3	0.4	0.1	0.0	0.3	0.4	0.3	0.0
TiO ₂	b.d.	b.d.	0.2	0.3	0.1	0.0	0.2	0.2	1.0	0.5
FeO	b.d.	b.d.	0.1	0.2	0.6	0.6	0.3	0.3	4.6	0.5
MnO	b.d.	b.d.	0.2	1.1	b.d.	b.d.	b.d.	b.d.	b.d.	b.d.
SO ₃	b.d.	b.d.	b.d.	b.d.	b.d.	b.d.	b.d.	b.d.	b.d.	b.d.
K ₂ O	0.3	0.3	14.2	1.4	1.1	0.4	7.7	2.8	9.2	0.4
Total	97.9	1.6	95.4	2.4	96.1	2.3	94.3	3.9	93.1	1.2

n = number of points analyzed; wt% = average oxide composition in weight %.
s.d. = standard deviation; b.d. = below detection.

Mixture¹ = composition from SiO₂-rich glass fragments.

Mixture² = composition from K₂O-rich glass fragments.

Mixture³ = K-feldspar-like composition from dark silicate melt band (Fig. 2-7).

Glasses are typically hypocrystalline and composed of varying amounts of K₂O-rich and SiO₂-rich glass with small nonmelted grains of quartz down to ~100 μm. Holohyaline fragments can be found but are rare. Element mapping helps distinguish grains of feldspar, dolomite, and calcite; mineral grains are typically 10s of μm in diameter or smaller but can be as large as 200 μm. WDS analyses give analytical totals within a range of 88–100 wt% with an average of 97 wt%. Fragments larger than 500 μm can display schlieren or flow textures (Figs. 2-8A, D) which have been characterized in clasts as an intricate mixture of SiO₂-rich and K₂O-rich glass (Fig. 2-8E). While most glass fragments are silicate-rich, the breccia from Boulderling River has some glass fragments that contain dolomite inclusions, up to ~50% of the fragment, where dolomite is partitioned in irregular or globular forms. (Figs. 2-8B and 2-9D). Textures of glass fragments are not uniform in their appearance within a given thin section (e.g., the two fragments in Figure 2-9 are from the same sample). Most glass fragments do not have a fresh appearance when imaged in BSE and appear devitrified. Glass areas that has not been devitrified appear amorphous and the SiO₂-rich

glass has varying quantities of K-feldspar grains (Figs. 2-9C, F). If dolomite is present in glass fragments, its morphology varies from small euhedral crystals (Fig. 2-8C) to irregular forms (Fig. 2-9F).

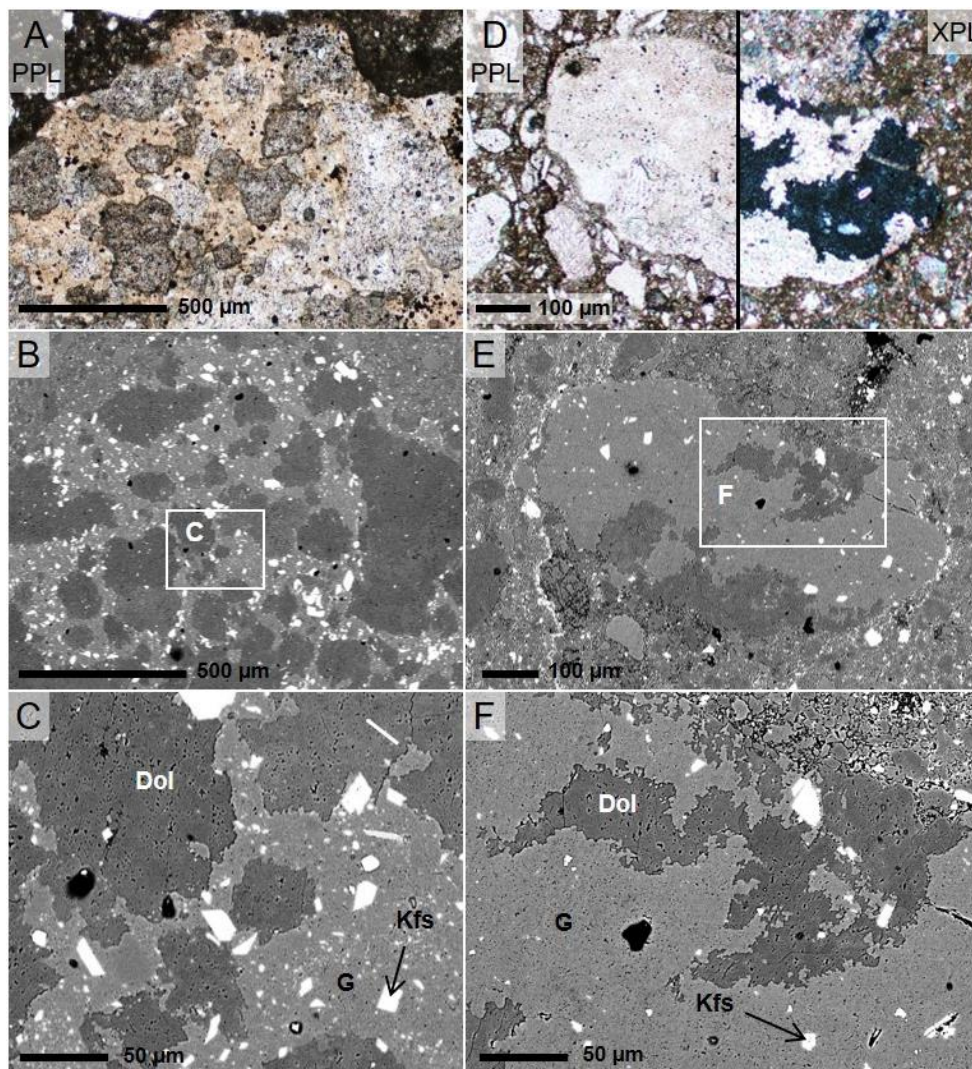


Figure 2-9. A Portion of a large 4400 μm impact glass fragment; dark area along top is dolomite-rich matrix. B) Same area as (A) in BSE. C) Enlarged area of (B) showing dolomite and K-feldspar inclusions in SiO_2 -rich glass. D) Colour is a poor indicator of composition with partitioning of dolomite from dark isotropic SiO_2 -rich glass apparent in XPL. E) Same clast as (D) in BSE. F) Enlarged area of (E) shows irregular shaped dolomite in K_2O -poor SiO_2 -rich glass. Labels indicate dolomite (Dol), K-feldspar (Kfs), and SiO_2 -rich glass (G).

2.4.2 Type 2

2.4.2.1 Field observations

One sample from Big Lake and one from Shatter Cone Canyon contain Type 2 (T2) breccia. In both cases T2 is a yellow coloured monomict breccia found adjacent to the main polymict T1 breccia (Fig. 2-10) and are primarily clast-supported. The extent of association between T2 and T1 breccias was not apparent at the outcrop scale due to limited dyke exposure and the similarity in colour of the T2 breccia and weathered host dolostone.

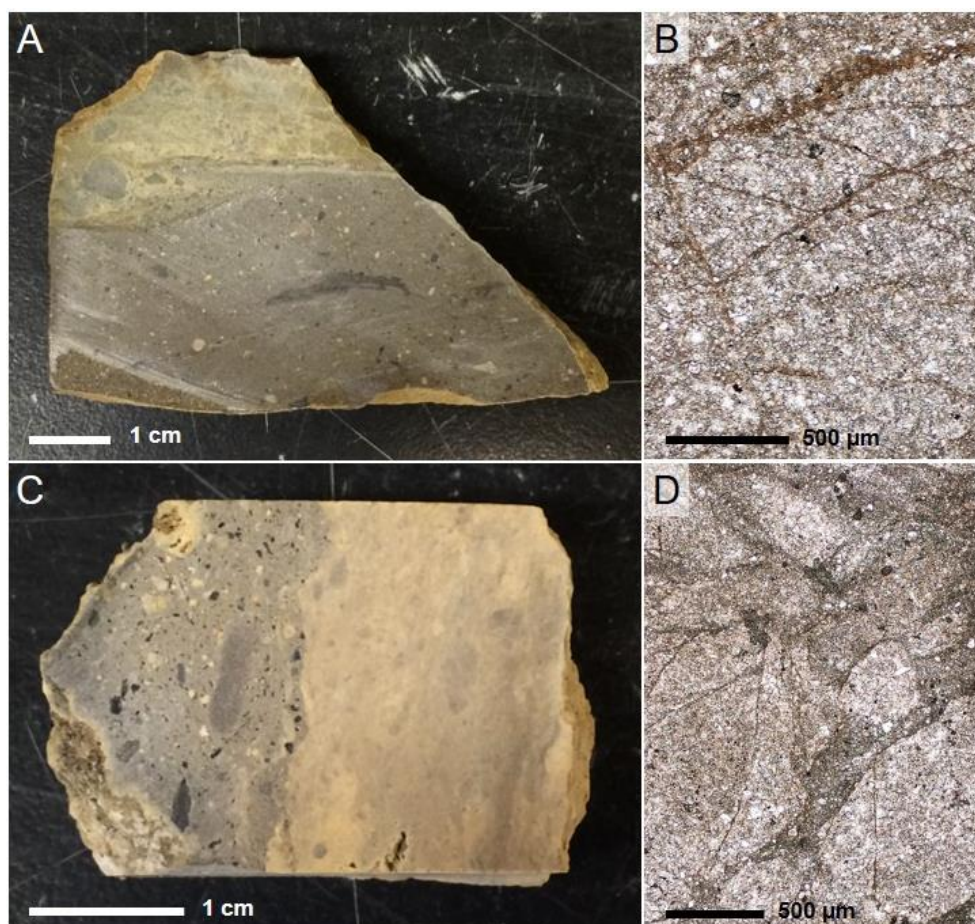


Figure 2-10. A) The upper yellow coloured breccia is T2 with grey T1 breccia below, from dyke shown in Figure 2-2B. B) Breccia in (A) has a crackled appearance where clasts are separated by darker, fine-grained veins with little to no visible rotation. C) The yellow T2 breccia from Big Lake has a sharp contact with the grey T1 breccia. D) T2 breccia has thicker veins and a mosaic appearance with increased clast rotation compared to (B) while some adjacent clasts still fit together.

2.4.2.2 Petrography and geochemistry

Cross-cutting relationships show some features of the monomict breccia are truncated by the polymict T1 breccia (Fig. 2-10). The interface along the two breccias may be wavy or straight and small T2 clasts are present along the contact but there is no indication of mixing between the breccias. No impact glass fragments were found in T2 breccias. The matrix and clasts in T2 breccia are dolomite which contain small grains of quartz, K-feldspar, sulfides, and Fe-oxides.

The T2 breccia from Shatter Cone Canyon shows fracturing and brecciation with thin veins of fine matrix (Fig. 2-10B). Many of the veins preferentially run parallel to the contact between the monomict and polymict breccia. This monomict breccia is clast-supported and most clasts do not display any significant rotation with respect to neighbouring clasts. A few clasts appear distinct from the rest of the monomict package near the T1 contact; closer inspection reveals they are unbrecciated T2 clasts and not clasts from the adjacent polymict breccia (Fig. 2-10A). The contact between breccia types is relatively sharp and straight with a slight offset and no mixing.

The Big Lake monomict breccia has regions with large sub-angular brecciated clasts that are clast-supported and other sections that have unbrecciated clasts that are supported by a fine-grained matrix (Fig. 2-10D). Smaller clasts display some rotation and alignment relative to nearby clasts and these clasts tend to be more sub-rounded. The contact between the monomict and polymict breccia is sharp but not straight (Fig. 2-10C) and do not appear to have undergone any mixing. The similarity in composition between the matrix and clasts make it difficult to readily discriminate them in BSE images.

2.4.3 Type 3

2.4.3.1 Field observations

Type 3 (T3) breccia is found within the Shaler Supergroup near the centre of the impact structure and in one dyke near the West River (Fig. 2-1). The Shaler T3 dyke is not very distinct from the surrounding blue-grey limestone and the bedding at this location differs by 22° on either side of the dyke (Fig. 2-11A). The narrow grey T3 dyke along the West

River is oriented perpendicular to the surrounding beds which are inclined by 18° (Fig. 2-11D).

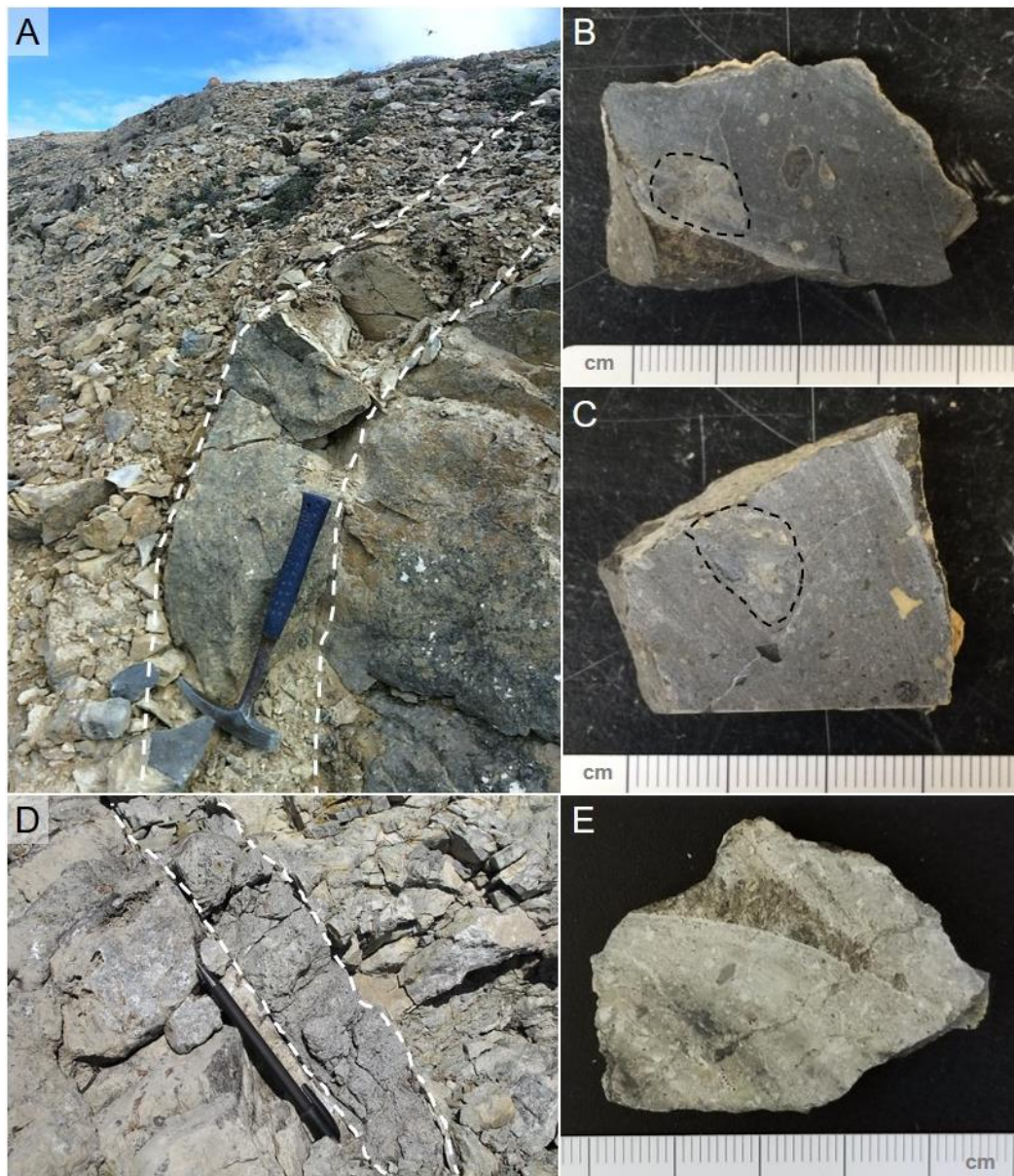


Figure 2-11. A) Contact between T3 dyke and host is sharp, however, the T3 breccia is not very distinctive from the grey limestone host; dyke outlined by dashed white lines. B–C) Examples of blue-grey T3 breccia that are clast-poor, compared to T1 samples. Large 1 cm clasts are outlined by black dashed lines. D) Contact between grey-toned West River T3 dyke and dolostone host; dyke is outlined by white dashed lines with black pen for scale; photo by G. Osinski. E) Dark mm-sized clasts are visible within the West River breccia dyke.

At the hand sample scale, the Shaler T3 breccia is relatively clast-poor (Figs. 2-11B, C) and its weathering and matrix colour closely resembles the limestone host rock. The area was searched for additional dykes but the limited exposure of the Shaler Supergroup within the impact structure hindered efforts to identify additional occurrences. The hand sample of the West River breccia contains more clasts than the Shaler breccia and differs slightly in colour due to its different location and source formations within the impact structure.

2.4.3.2 Petrography and geochemistry

The Type 3 Shaler breccia is polymict, matrix-supported, and dominated by carbonates with a calcite-rich matrix. Backscattered electron imagery reveals matrix grains are poorly defined and often displays a mottled appearance (Fig. 2-12A). Minor amounts of dolomite and ferroan dolomite are present in the matrix, which comprise the darker portions of the mottled matrix; ferroan dolomite contains up to 5 wt% Fe. Where mottling is absent in the matrix, it has a more clastic appearance with discrete grains visible (Fig. 2-12B). The Shaler breccia contains fewer clasts and has a different assemblage of clasts than T1 dykes. Clast textures and compositions indicate they originate from multiple Shaler units that include carbonate oolitic grainstone, sandstone, and mudstone in addition to the prevalent fine-grained crystalline carbonate clasts and are sub-angular to rounded. Grainstones displaying both concentric and non-concentric coarsely recrystallized grains were identified. Silicate clasts are less common than carbonate clasts and individual quartz and feldspar grains comprise ~5–10% of the matrix. Sulfides are more abundant in T3 than T1 breccias and are typically associated with clasts but can also be found within the matrix. No vugs were found in the T3 breccia.

A large clast ~1 cm in diameter has an irregular radiating texture and is very fine-grained compared to the surrounding matrix (Fig. 2-13C). The radiating texture is most apparent in the central areas of the clast and is less prevalent near the edges. The composition of the clast with the irregular radiating texture is better defined in BSE imagery (Fig. 2-14A) than optically (Fig. 2-13C) and element mapping clearly distinguishes the elemental components of this clast as being calcite-rich with some dolomite and ferroan dolomite (Fig. 2-14). This clast contains more sulfides and Fe-oxides than the surrounding matrix.

Silicates are present but are limited to small isolated dark spots <10 μm in Figure 2-14B that do not correspond to the bright Fe-rich areas in Figure 2-14C.

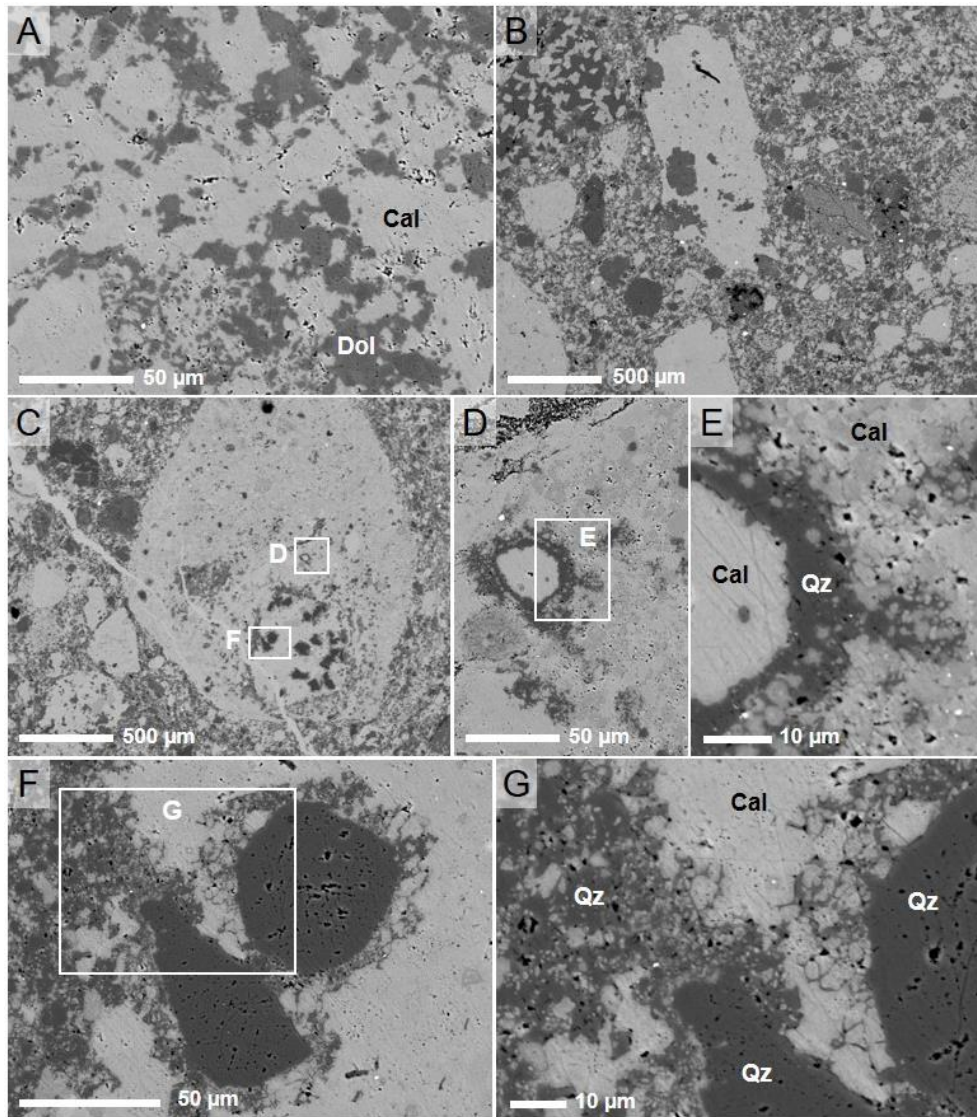


Figure 2-12. Type 3 breccia in BSE. A) mottled matrix of calcite (Cal) and dolomite (Dol). B) Matrix of T3 showing less mottling and a few calcite-rich clasts. C) Rounded polymict calcite-rich clast contains minor amounts of dolomite, quartz, and K-feldspar. Diagonal calcite vein cuts across clast and matrix. D) Calcite grain engulfed by quartz (Qz) with quartz veins extending into surrounding calcite. E) Enlarged area of (D). F) Quartz veins extend outward from quartz grains into surrounding calcite. G) Enlarged area of (F) to show intricate quartz veining.

Another fine-grained 1 cm clast has a similar appearance with portions resembling the radiating clast, but the pattern is less developed. Additionally, this clast contains a small rounded carbonate clast with a fine-grained feathery texture (Fig. 2-13A), small grainstone fragments, and wavy fine-grained carbonate bands rich in sulfide grains (Figs. 2-13B–D).

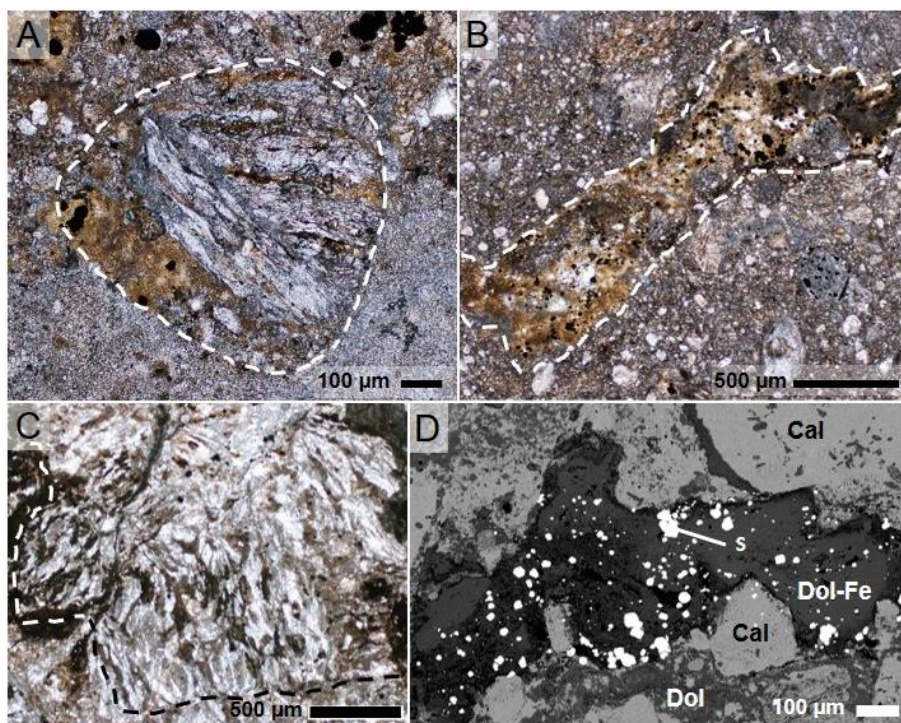


Figure 2-13. A) In PPL, a small feathery clast, outlined by dashed line, found within large clast indicated in Figure 2-11C. B) Band of fine-grained ferroan dolomite rich in sulfides. In PPL, areas of outlined band appear darker than surrounding calcite-rich matrix. C) Calcite and dolomite clast with an irregular radiating texture, clast above dashed outline; PPL. D) Compositional differences are evident in BSE in this enlargement of upper right limb of the outlined band in (B); calcite (Cal), dolomite (Dol), ferroan dolomite (Dol-Fe), sulfide (S).

Some clasts contain fine-grained, wavy or flow-like bands while others have fine veinlets extending from the clasts into the surrounding matrix (Figs. 2-12C–G). Figure 2-12C is a polymict breccia clast that contains small quartz grains that have thin veinlets of quartz extending outward into the calcite matrix (Figs. 2-12F–G). Similar quartz veinlets are also associated with quartz-rimmed calcite grains (Figs. 2-12D–E).

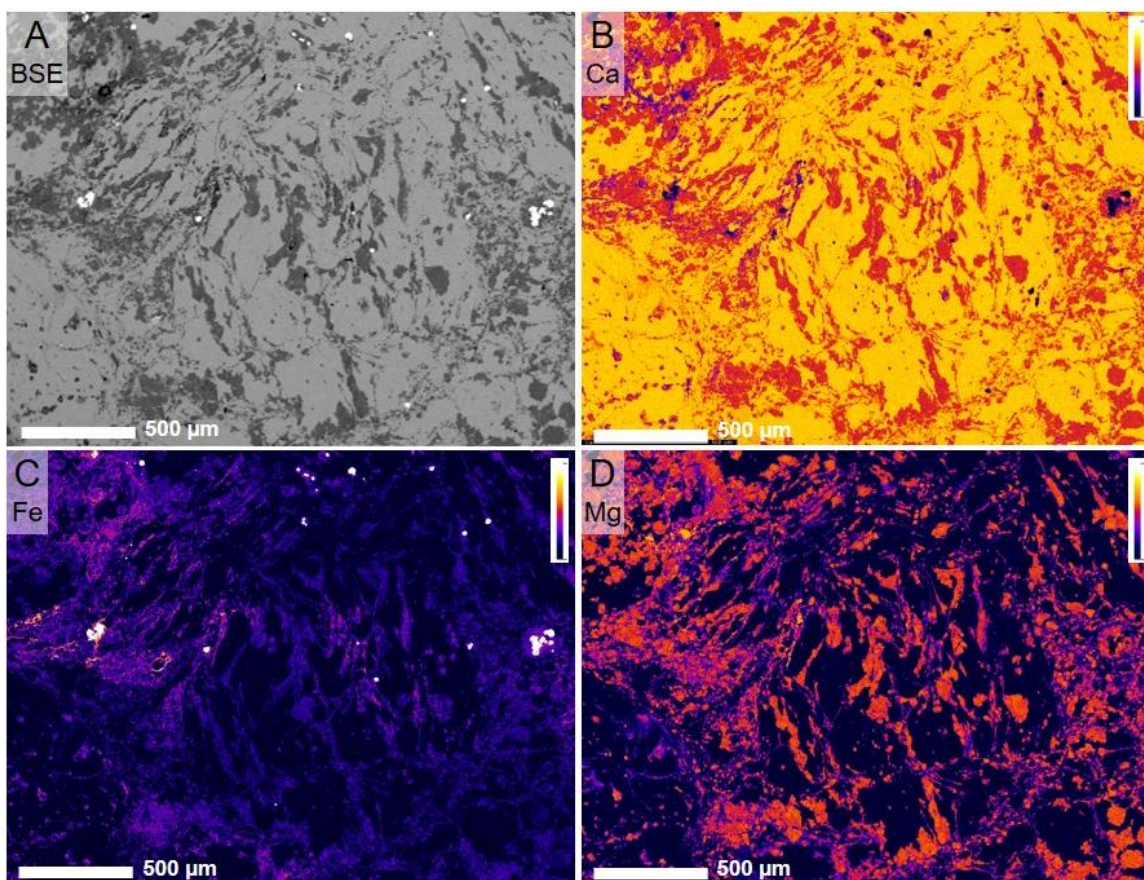


Figure 2-14. Type 3 breccia clast from Figure 2-12C with irregular radiating texture. A) Calcite (pale grey) and dolomite (darker grey) compositions are shown in BSE. B) Calcium element map shows clast is primarily calcite (yellow) as well as matrix in lower left corner. C) Iron element map shows ferroan dolomite (purple) and bright pyrite grains. D) Magnesium element map indicates the presence of dolomite (pink). Colour scales on element maps range from zero counts (black) to highest counts (yellow) for the indicated element.

The West River Type 3 breccia is also polymict, matrix-supported, and dominated by carbonates with a calcite-rich matrix and has a sharp contact with the host rock. Unlike the Shaler T3 breccia described above, there are no carbonate clasts with feathery or irregular radiating textures. Wavy carbonate bands were also not found in the West River breccia. Clasts are composed primarily of dolomite and calcite. Fine-grained chert, chert with ooids, and sandstone clasts along with quartz grains in the matrix comprise the bulk of the silicate fraction of the West River breccia. There are several locations within the sample that display somewhat wavy brown-orange bands of quartz, dolomite, and kaolinite (Figs. 2-

15A–B). Many of the dolomite clasts contain veins of coarse calcite (Figs. 2-15A–B) and pyrite (Figs. 2-15C–D), which were not observed in dolomite clasts or host rock from any other dyke within the impact structure.

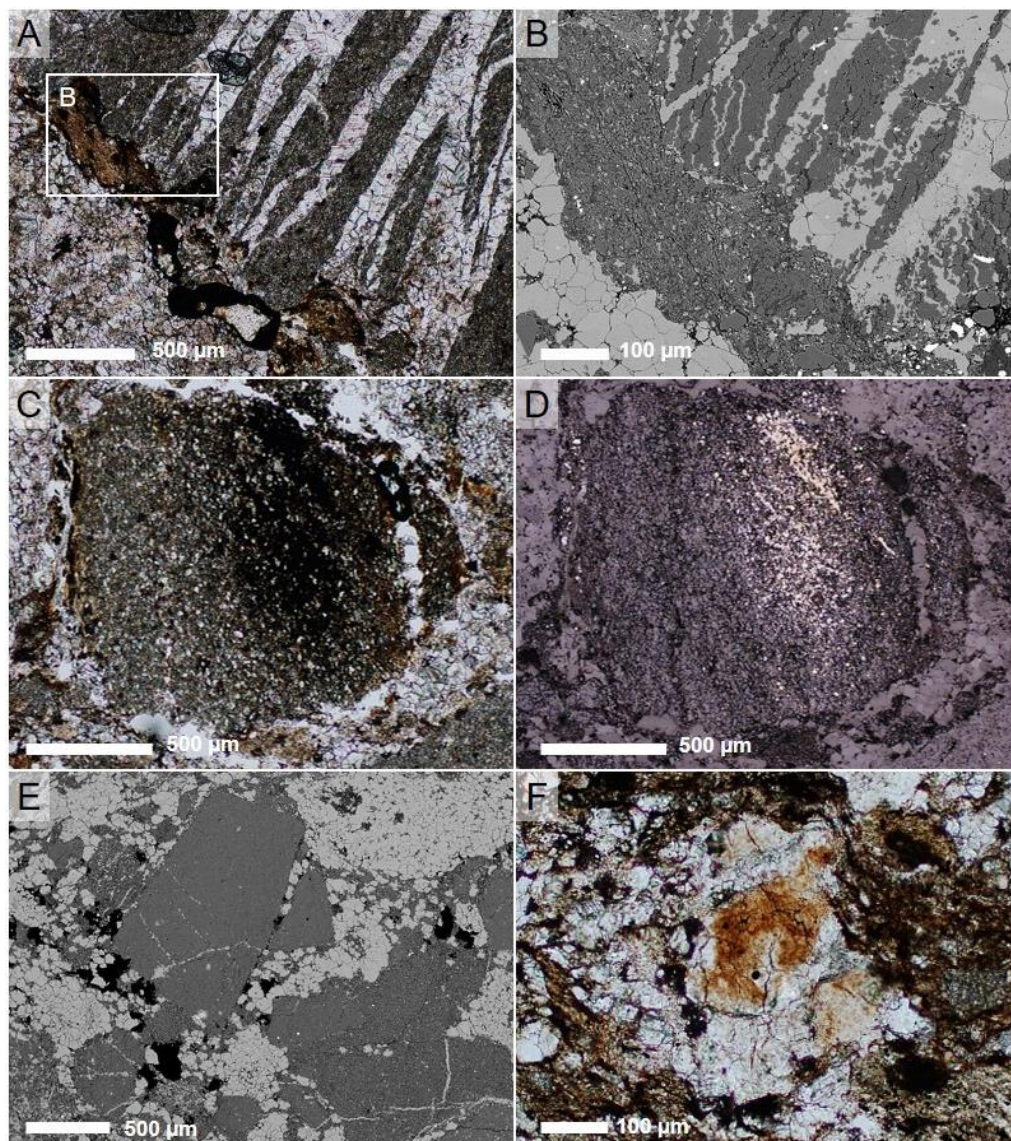


Figure 2-15. A) PPL image of large dolomite clast with calcite veins shown in upper right with calcite matrix to lower left. B) In BSE the carbonate compositions become more apparent along with the dark grey devitrified glass, brown colour in (A); calcite is light grey and dolomite is darker grey. C-D) Pyrite-bearing dolomite clast shown in PPL and RL. E) Small group of dolomite clasts (dark grey) within a calcite (light grey) matrix. Small white spots within the dolomite are pyrite grains. F) Small toasted quartz grain.

Clasts are not evenly distributed throughout the matrix, as shown in Figure 2-15E with a small group of dolomite clasts. These dolomite clasts also contain pyrite grains but are not as numerous as some clasts (i.e., Figs. 2-15C–D). There were a few quartz grains that were coloured orange-brown rather than colourless, giving them a toasted appearance (Fig. 2-15F).

2.4.4 Type 4

2.4.4.1 Field observations

The Rim Canyon breccia dyke is a wedge-shaped dyke in the eastern rim of the impact structure (Fig. 2-1) and is easily recognized due to its distinct yellow-orange colouring compared to the grey to beige host dolostone of the Victoria Island Formation.

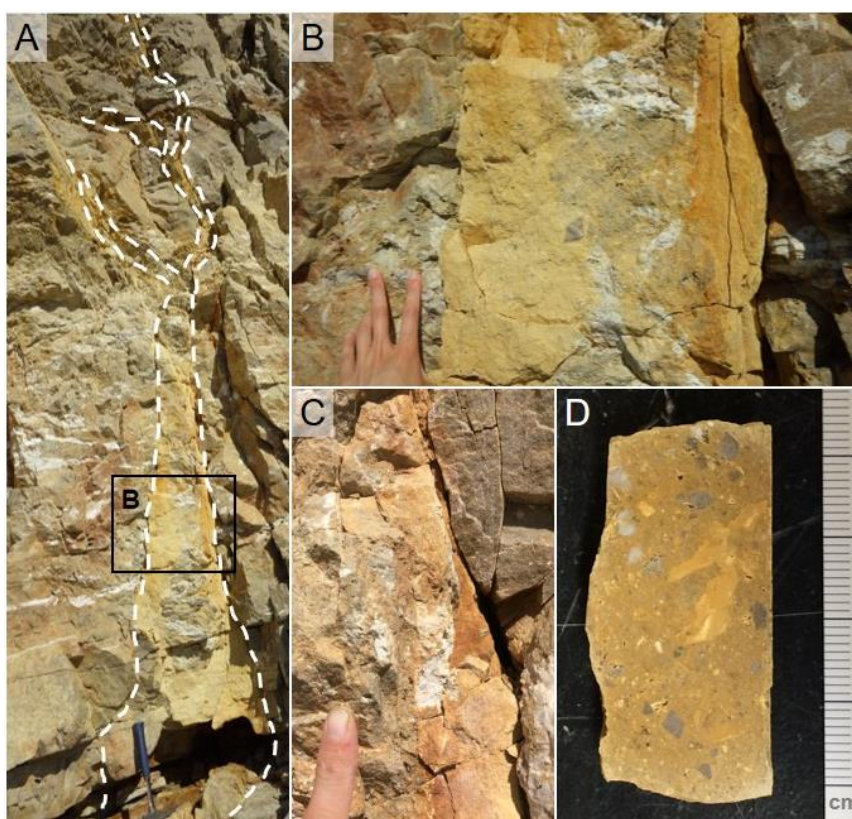


Figure 2-16. Type 4 breccia from Rim Canyon. A) Wedge-shaped dyke with narrow branches extending into the host rock at the top of the dyke; dyke boundaries indicated by white dashed lines. B) Blocks of grey host dolostone with white chert are present within the dyke, surrounded by a very fine yellow matrix. C) Contact between dyke and host rock is sharp. D) Fine-grained yellow matrix contains dolomite and chert clasts.

The outcrop contains white chert nodules several cm thick and up to a metre in length. The Type 4 (T4) breccia dyke is located along a fault and is the only dyke observed in this section of the canyon where other large faults and fractures are present. The top of the dyke has several thin branches of breccia that extend into the host rock (Fig. 2-16A). Clearly visible within this dyke are large dolostone blocks, including white chert, identical to the host rock immediately adjacent to the dyke (Fig. 2-16B). Contrasting with these large blocks are portions of the dyke that are clast-poor and consist primarily of the yellow-orange matrix. The contact between the breccia and host rock is sharp (Figs. 2-16B–C).

2.4.4.2 Petrography and geochemistry

The clasts in the T4 breccia are matrix-supported and the matrix is too fine to be resolved using transmitted light microscopy. Backscattered electrons reveal the T4 matrix texture is quite different from T1 (e.g., compare Fig. 2-17C with Fig. 2-4) where individual grains are difficult to discriminate and are more homogenous in T4 than T1. Irregular shaped pores up to several mm in diameter are present throughout the dolomite-rich matrix.

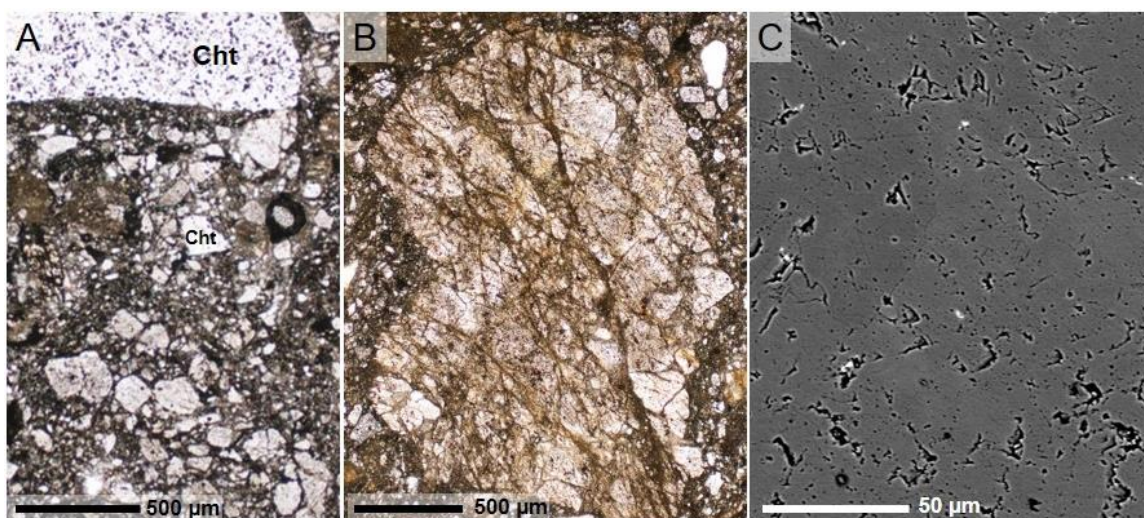


Figure 2-17. A) Matrix and clasts in T4 breccia are composed of dolomite and chert; 2 chert (Cht) clasts are indicated, PPL. B) Large brecciated dolomite clast present within T4 breccia; PPL. C) BSE image shows dolomite matrix is poorly defined and individual clast boundaries are not visible.

Clasts are sub-angular to sub-rounded, poorly sorted, and range from fine to coarse-grained (Fig. 2-17A). The composition of the T4 breccia corresponds to the chert-bearing dolostone host rock where the dyke is found (Fig. 2-16). Some of the largest carbonate clasts are highly brecciated and resemble a crackle breccia (Fig. 2-17B). In BSE, clasts of dolomite, quartz, and chert appear nearly identical but close examination reveals quartz and chert to have smoother surfaces while dolomite has a more porous texture. The silicate fraction of chert clasts and detrital quartz grains comprise less than 5% of the sample. Impact glass fragments are absent from the T4 breccia.

2.5 Discussion

2.5.1 Silicate impact glass

The melting of silicates in the target sequence to form impact glass is a product of shock compression (Osinski et al. 2018; Stöffler 1984). The impact glass identified from Tunnunik in Type 1 breccias is the first discovery of glass at this impact structure. The Tunnunik impact event did not reach the crystalline basement so any impact glass that formed must, therefore, have been generated from silicates within the sedimentary target sequence. Based on the updated classification of impact glass by Osinski et al. (2018), some glass fragments identified in T1 breccias correspond to mineral glasses which have the same composition as the host mineral and may contain flow features and vesicles and others would be considered whole rock impact glass. Whole rock impact glass composition comprises that of the whole rock and may contain flow features, vesicles, lithic clasts, and crystallites (Osinski et al. 2018). The silicate melt generated upon decompression would have rapidly quenched once mixed with colder nonmelted carbonates that comprise T1 breccias thereby preserving the observed flow textures; quenching may be complete within 100 seconds (Kieffer and Simonds 1980).

Impact glass fragments have been identified in T1 breccia samples from Shatter Cone Canyon, Big Lake, and Big Lake south, which are all found within the shatter cone distribution of the central uplift (Osinski and Ferrière 2016). The scarcity of glass fragments among breccia dykes is not unexpected given the low abundance of silicates within the carbonate-rich target sequence and the low proportion of nonmelted silicate

clasts observed in breccia samples. The inter- and intra-dyke compositions of glass fragments are not identical, suggesting that glass fragments did not originate from a single source or they were not distributed evenly throughout a common source.

The flow textures in many fragments show the glass was molten at one point to acquire the patterns observed and rapidly quenched from that liquid melt. The flow banding and schlieren (Fig. 2-8) also have similarities in appearance to type 1 glass clasts from the Ries impact structure (Osinski 2003) but differ in their composition. Unlike glasses from younger impact sites such as Ries and Haughton (Graup 1999; Osinski et al. 2008), most glass fragments from Tunnunik do not appear as fresh and instead show signs of devitrification. The SiO₂-rich glass fragments are likely sourced from sandstone or chert, both of which have been identified in T1 breccia samples. The higher K content in many of the impact glass fragments could be the result of alteration or represent a more K-rich source unit. In addition to K, many of the glass fragments also contain between 2–20 wt% Al₂O₃ (Table 2-2), suggesting K-feldspar, muscovite, illite, and kaolinite as potential sources. The presently exposed rocks and nonmelted silicate breccia clasts contain very little potassium, which suggests these fragments came from a unit higher in the pre-impact target sequence that has since been eroded and are not locally derived. Presumably the eroded unit(s) would have been near the pre-impact surface and contained a higher abundance of K-feldspar than the scarce amount of detrital feldspar grains observed in the exposed units to give the proportions of SiO₂-rich and K₂O-rich compositions detected in the glass fragments. Based on the drill log from the well on the northwest coast of Victoria Island, the bulk chemistry of the glass fragments is most consistent with sandstone, shale, argillaceous dolostone and limestone, mudstone, and/or wackestone, which were present in the overlying units that are now eroded at the impact site. Additional elemental oxides that were analyzed for were Na₂O, MgO, CaO, TiO₂, FeO, MnO, and SO₃ (Table 2-2) were either not detected or present in trace amounts, < 1 wt%. Only the analyses for the Si-Al-K mixture³ from the dark band, and not a silicate glass fragment, in the T1 breccia (Fig. 2-7) returned oxides greater than 1 wt%.

The occurrence of glass fragments may be underestimated in some T1 samples. Some T1 breccia thin section samples contain holes several hundred μm to over 1000 μm in diameter

and these samples typically have few glass fragments. Along the interior edge of several larger holes are small glass remnants. These holes and glass remnants could indicate where larger fragments existed which were more susceptible to weathering or were lost during sample preparation.

2.5.2 Evidence for melting of carbonates

In thin section, very fine-grained areas or clasts too fine to resolve optically were found, though many occurrences were quite subtle and only became apparent in BSE images. Textural evidence that supports fine-grained carbonates were once melted include flow-like bands and distinctive feathery textured clasts. Feathery clasts are interpreted as the product of rapidly quenched carbonate melts (Jones et al. 2000). Feathery clasts are rare in T1 and T3 breccias but are reported to comprise up to ~10 vol% of breccias at Chicxulub (Jones et al. 2000). Feathery carbonate textures are also identified in the polymict breccia associated with the Alamo Event in Nevada (Pinto and Warme 2008). Feathery clasts from Chicxulub and Alamo have calcite compositions while the Tunnunik clasts are dolomite showing that such textures can form in either limestone or dolostone-rich targets. Just as rare as the feathery clasts are those with the irregular radiating texture found in T3 breccia (Figs. 2-13A, C and 2-14). The 1 cm clasts containing the irregular radiating texture (Figs. 2-11B, C) could be a variation of feathery clast that did not quench quite as rapidly or were only partially melted, resulting in the complex pattern of calcite and ferroan dolomite. This texture has similarities to a calcite-carbonate spinifex quench texture in a carbonatite dyke from Rajasthan, India (Wall et al. 1993). While the composition of the carbonatite dyke is different and more complex than the T3 dyke from Tunnunik, it provides another example showing carbonates forming intricate textures under the right conditions. The radiating texture of the T3 quenched melt clasts are not observed in any other breccias examined from this impact structure.

The smooth fine-grained carbonate bands identified in BSE images from T1 and T3 breccias vary in dolomite and calcite abundances. In dolomite-rich T1 breccia, bands of calcite melt are more common (Figs. 2-5 and 2-6) and in calcite-rich T3 breccia the bands are primarily dolomite (Fig. 2-13). In both cases the melt bands are not exclusively

dolomite or calcite, and often contain minor amounts of the other carbonate intermixed along with small non-carbonate grains such as quartz, K-feldspar, or sulfides.

The mottled nature observed in areas of the matrix in the T3 breccia is not simply a mix of different grains where changes in composition do not correspond to discrete grain boundaries. The mottled texture of the matrix (Fig. 2-12A) is not quite the same as the quenched carbonate melt clast textures (Fig. 2-14) but it is possible they formed in a similar manner. The nature of the matrix is difficult to determine as it does not appear completely clastic and its mottled texture, quenched carbonate clasts, and low number of clasts suggests the matrix was partially melted. The scarcity of silicates to help identify immiscible textures with carbonates (Osinski et al. 2008) makes it difficult to establish the presence and extent of carbonate melt.

Macroscopic evidence of impact melt is not visible at hand sample scales so the extent across the impact structure is difficult to determine. The localized occurrences of carbonate melt present in crater floor breccia dykes suggests that more extensive carbonate melt could have been found nearer to the surface before the crater was so deeply eroded. The eroded crater-fill deposits at Tunnunik were likely similar to the impact melt breccia found in the crater-fill deposits at the 23 km diameter Haughton impact structure, which formed in similar target rocks ~800 km northeast from the Tunnunik site (e.g., Osinski et al. 2005).

The discussion regarding the response of carbonates during hypervelocity impacts as being dominated by melting or decomposition continues as evidence for both processes exist (e.g., Graup 1999; Hörz et al. 2015; Kieffer and Simonds 1980; Osinski et al. 2008; Sahoui et al. 2016). We have not found any evidence for carbonate decomposition.

2.5.3 Origin and emplacement of the Tunnunik dykes

Crater formation processes are rapid, taking only seconds to minutes for all but the largest structures (Melosh 1989). The deep erosion of the Tunnunik impact structure does not provide a complete picture for this hypervelocity impact, but the examination of exposed breccia dykes helps understand their formation.

2.5.3.1 Type 2

The simplest dykes are autochthonous Type 2 dykes. Based on their textures, these monomict breccias most closely resemble fault breccia. Under the classification scheme of Woodcock and Mort (2008), T2 breccias from Shatter Cone Canyon and Big Lake (Fig. 2-10) would be considered crackle and mosaic breccias, respectively. Crackle breccias have clasts that show very little rotation and are separated by thin veins of matrix whereas mosaic breccias have slightly more separation and rotation between clasts but can still fit with adjacent clasts (Woodcock and Mort 2008). There is no evidence that material in either occurrence of T2 breccia was transported any significant distance. Minimal material transport supports local brecciation of the host dolostone in situ due to faulting. Type 2 breccia was not found on its own in the field and was only identified by its direct association with T1 breccias. There are likely more occurrences of T2 breccia associated with T1 or independently in the field, but the similarity of T2 to the colour and weathering of the host dolostone make them difficult to detect.

The direct contact between T2 and T1 coupled with the truncation of T2 by T1 dykes demonstrates that T2 breccias were generated first, potentially during the excavation stage. Faulting initiated during the excavation stage relates to the expansion of the transient cavity and the release of pressure following the passage of the shock wave, making this the most probable time for T2 breccia to form (Lambert 1981; Osinski and Spray 2005). The unstable cavity begins to collapse due to gravitational forces, marking the start of the modification stage. As the modification stage progresses, new faults are generated in response to collapse and displacement of the transient cavity and faults initiated during the excavation stage that can contain T2 breccia can be re-activated and serve as a conduit for the injection of T1 breccia (Osinski and Spray 2005). There is no obvious mixing between T2 and T1 breccias, which suggests that there was a brief gap in the timing of their respective emplacement, with the T1 breccias being emplaced after T2 breccias. Evidence of this potentially strong flow is shown in Figure 2-10C where the larger clasts in the grey T1 breccia are aligned and oriented parallel to the T2 contact.

2.5.3.2 Type 1

Allochthonous Type 1 breccia dykes are the most common type and the most visually diverse. Looking beyond the visual differences in colour and clasts, there are similarities among T1 breccias that indicate a similar origin. At the outcrop and hand sample scale, T1 breccias show a preferred orientation of larger clasts, especially if they are elongated (Fig. 2-2). This orientation roughly parallels the orientation of the contact with the host rock, indicating that the direction of material transport followed the length of the dyke and the flow regime was strong enough to maintain a constant movement of material. Type 1 breccias are polymict suggesting considerable transport. Breccias from Shatter Cone Canyon occur within the Mount Phayre Formation and while some dolostone layers are present, there is an abundance of mudstone beds in this unit. The degree to which mudstone is present in the host rocks in Shatter Cone Canyon is not reflected in the composition of T1 breccias. Mudstone clasts are a small fraction of the overall composition to the breccia dyke indicating there is not a significant input of local material.

Silicate impact glass fragments have not been identified in the host rocks of T1 breccia dykes, or in T2 breccias, so they must have been transported from elsewhere. Glass fragments are not found in T3 breccia and the absence of crystalline limestone clasts derived from the lower Shaler Supergroup unit within T1 breccias indicates that the glass fragments and, therefore, breccia originated from a higher stratigraphic level. Incorporation of glass material from the melt zone indicates a considerable transport distance of dyke material, which requires a highly energetic process to generate the intrusion of dyke material (Bischoff and Oskierski 1987; Lambert 1981; Stöffler 1977). Injection of impact melt, including glasses, into the crater floor of complex craters has been observed at the West Clearwater Lake and Ries impact structures (Dence 1971; Stöffler 1977). The presence of glass fragments in polymict breccias from the crater floor of the Tunnunik impact structure not only indicates the depth to which material was injected but is also when these breccias formed and the timing of their injection.

The key evidence to determine this timing are the glass fragments since only the floor of the impact structure remains without any overlying crater morphology, stratigraphy, ejecta, or crater-fill. Temperature and pressure required for silicate glass melt to be generated

occurs upon decompression of the target material (Osinski et al. 2018). The faults generated during the collapse of the transient cavity and re-activated faults that contain T2 breccias create a network that facilitates the injection of T1 breccia, containing the glass fragments. Recalling the relationship observed with T2 breccia, T1 breccia dykes were emplaced after a brief pause following the formation of T2 dykes and suggests that the timing of T1 breccia emplacement was early in the modification stage. Emplacement of T1 breccia dykes during this phase of crater formation is comparable to the proposed timing of the emplacement of impact melt-bearing breccia (suevite) dykes in the floor and walls of the Ries impact structure near the end of transient cavity formation, after 15–20 s (Stöffler et al. 2013). The observation in the field of shatter cone fragments within T1 breccias limits the timing constraint further as shatter cones must have formed before the breccia in order to be incorporated into the breccia; shatter cone formation is associated with the compression stage (Osinski and Ferrière 2016).

2.5.3.3 Type 3

The parautochthonous Shaler type 3 breccia dyke is distinct from T1 and T2 dykes. Located in the centre of the impact structure, it is the only breccia dyke found within a limestone-rich section of the Shaler Supergroup. Clasts in the Shaler T3 breccia include crystalline limestone, calcite-rich grainstone, and mudstone, but compared to T1 breccias, T3 breccia is clast-poor. In addition to the dominant calcite composition of the T3 breccia, other distinct features of this breccia include quenched carbonate melt clasts with a unique radiating texture and matrix with a mottled texture (Fig. 2-14). The Shaler T3 breccia is polymict and is comprised of clasts from several units within the Shaler Supergroup. The polymict nature of the T3 breccia indicates transport and mixing of material has occurred, but the displacement of material is much less extensive than in T1 so has formed more locally within the Shaler Supergroup. Transport of material within the dyke is also evident by the presence of the polymict clast (Figs. 2-12C–G) which appears to be a calcite-rich breccia fragment that formed at a different location in the dyke. This exotic clast contains quartz and quartz-rimmed calcite grains with small veinlets extending outward into the clast. The composition of the mottled T3 matrix is a mix of calcite and ferroan dolomite where the dolomite contains 1 to 5 wt% Fe. The occurrence of ferroan dolomite was not

detected within the overlying dolostone units and is therefore limited in extent to the Shaler Supergroup.

The allochthonous West River T3 breccia is also distinct from T1 and T2 breccias in that it is calcite-rich which makes it most similar to the Shaler T3 breccia compositionally, however, the calcite associated with the West River breccia does not originate from the Shaler Supergroup. The calcite-rich West River breccia dyke is emplaced in Allen Bay dolostone, so the calcite was not locally derived. Based on regional geology, the most likely source of the calcite is from the overlying Silurian-aged Cape Storm Formation which is a transitional dolostone and limestone unit or from Douro Formation limestone (Kerr 1975; Mallamo 1989). The occurrence of pyrite in the West River breccia could originate from either the Douro or Cape Storm Formations. The pyrite source is based on drilling logs from a site ~92 km west-northwest near the coast of Victoria Island at 72.75500° N and 117.18694° W (Batten 1975) as pyrite was not identified locally within the Allen Bay or Victoria Island formations within the impact structure. The Douro and Cape Storm Formations are equivalent to the Read Bay and Cape Phillips Formations, respectively as reported in the drilling log (Batten 1975; Dewing et al. 2015). With the absence of shatter cone clasts or association with T2 breccia, the timing of T3 breccias is more difficult to constrain. However, based on the timing of T1 breccia and the presence of clasts from multiple units, indicating material transport similar to T1, T3 breccias could have also been emplaced during the modification stage.

The existence of the West River breccia dyke creates interesting implications regarding the timing of the impact event more than any other breccia dyke within the impact structure. Both the Cape Storm Formation and Douro Formation occur in the Early Ludlovian Stage approximately 423 to 421 Ma and 421 to 418 Ma, respectively (Kerr 1975; Mallamo 1989; Stewart 1987). The Cape Storm and Douro formations are mapped as an undivided unit along with the Allen Bay Formation west of the Tunnunik impact structure on a recent geologic map of Victoria Island (Dewing et al. 2015). The presence of a calcite-rich breccia dyke within host dolostone indicates regional dolomitization of the Allen Bay and underlying Victoria Island formations occurred before the impact event occurred, otherwise any calcite present within the breccia, and the now exposed Shaler Supergroup

in the centre of the impact structure, would have been dolomitized as well. If dolomitization began 6 to 33 Ma following deposition, based on the estimation for the dolomitization of the younger Blue Fiord Formation limestone (Wendte 2012), the maximum age of the Tunnunik impact structure would be changed to the Middle to Late Devonian approximately 385 to 360 Ma. This age contrasts with the palaeomagnetic age of 430 to 450 Ma determined by Lepaulard et al. (2019). More information is required regarding the source of the West River T3 breccia such as comparisons with the younger Devonian-aged rocks exposed along the west coast of Victoria Island (Dewing et al. 2015).

2.5.3.4 Type 4

For the T4 breccia dyke, the similarity of the clast composition to the host rock with no exotic compositions observed, suggests that the T4 breccia is locally derived. The locally derived parautochthonous T4 breccia differs from the T2 breccia by its contact with the host rock which is sharp rather than gradual and the T4 breccia shows some transport has occurred within the dyke. A sharp contact between dyke and host suggests a more dynamic origin of breccia material (cf., Bischoff and Oskierski 1988) than a monomict breccia with a gradual contact with the host rock (Dressler and Reimold 2004; Lambert 1981). Differences between T4 and T2 breccias are also visible by comparing the poorly defined appearance and more homogenous texture of T4 (Fig. 2-17) with the crackle and mosaic textures of T2 (Fig. 2-10).

The almost featureless matrix of T4 also differs in texture from T1 where clasts are typically well-defined (Fig. 2-4). Displacement of the target walls on either side of the dyke indicates movement has taken place. Enough movement occurred to generate a clast-poor breccia with a fine-grained matrix. Clasts that are present are smaller than ~1 cm with the exception of several blocks of host dolostone up to ~30 cm which were likely incorporated during the late stages of dyke emplacement (Fig. 2-16B). Based on the clasts and matrix present, this fault breccia could be called a cataclasite, which is a non-foliated rock with a cohesive matrix that comprises 50–90% of the rock (Woodcock and Mort 2008). The displacement and local transport of material within the dyke suggests this fault breccia was emplaced late in crater formation. Faulting within the rim of a crater occurs during the

modification stage associated with the collapse of the transient crater (Collins et al. 2008; Spray 1997) and is the most probable timing for T4 dyke emplacement.

2.5.3.5 Summary of breccia dykes

Based on breccia characterization, the generation of dykes in the crater floor of the Tunnunik impact structure was not a simultaneous process and they formed under different conditions during the impact cratering process. Classification, physical properties, and features of the four types of breccia dykes identified at the Tunnunik impact structure are summarized in Table 2-3.

Table 2-3. Breccia dyke summary.

Breccia dyke	Monomict or polymict	Clasts	Matrix	Primary composition	Source	Proposed emplacement
Type 1	polymict	lithic, silicate glass, carbonate melt	clastic, matrix-supported	dolomite	allochthonous	injected from melt sheet
Type 2	monomict	lithic	clastic, clast-supported	dolomite	autochthonous	in situ fault breccia
Type 3	polymict	lithic, carbonate melt	clastic, partial carbonate melt, matrix-supported	calcite	parautochthonous allochthonous	injections and in situ melting
Type 4	monomict	lithic	clastic, matrix-supported	dolomite	parautochthonous	in situ fault breccia

2.6 Conclusions

The carbonate breccias examined in this study detail the complexities of dyke formation in a carbonate-rich target from the micron to cm scale. The discovery of carbonate melt clasts and silicate impact glass fragments are important clues preserved in the impact breccia dykes. These clues provide a means to better understand the response of carbonate-rich target material during a hypervelocity event in the absence of crater-fill or ejecta deposits which would presumably contain these materials in greater abundance, based on younger less eroded impact structures such as Ries or Haughton (Dressler and Reimold 2001; Osinski et al. 2005; Stähle 1972). Additionally, the composition of the West River T3

breccia dyke is the only identified dyke within the impact structure that may have preserved overlying formations that have been eroded due to post-impact glaciation events.

The results of this study warrant continued investigation into carbonate-rich breccias and the response of carbonates during hypervelocity impact events since carbonates account for the target material in approximately one third of impact structures (Osinski et al. 2008).

2.7 References

- Batten W. H. R. 1975. Arctic well history report, Murphy Alminex Victoria Island F-36. National Energy Board Report 063-11-09-024.
- Bischoff L., and Oskierski W. 1987. Fractures, pseudotachylite veins and breccia dikes in the crater floor of the Rochechouart impact structure, SW-France, as indicators of crater forming processes. In *Research in Terrestrial Impact Structures*, edited by Pohl J. pp. 5–29.
- Bischoff L., and Oskierski W. 1988. The surface structure of the Haughton impact crater, Devon Island, Canada. *Meteoritics* 23:209–220.
- Collins G. S., Kenkmann T., Osinski G. R., and Wünnemann K. 2008. Mid-sized complex crater formation in mixed crystalline-sedimentary targets: Insight from modeling and observation. *Meteoritics & Planetary Science* 43:1955–1977.
- Dence M. R. 1971. Impact melts. *Journal of Geophysical Research* 76:5552–5565.
- Dewing K., Pratt B. R., Hadlari T., Brent T., Bédard J., and Rainbird R. H. 2013. Newly identified “Tunnunik” impact structure, Prince Albert Peninsula, northwestern Victoria Island, Arctic Canada. *Meteoritics & Planetary Science* 48:211–223.
- Dewing K., Hadlari T., Rainbird R. H., and Bédard J. H. 2015. Phanerozoic geology, northwestern Victoria Island, Northwest Territories; Geological Survey of Canada, Canadian Geoscience Map 171 (preliminary). scale 1:500 000.
- Dressler B. O., and Sharpton V. L. 1997. Breccia formation at a complex impact crater:

- Slate Islands, Lake Superior, Ontario, Canada. *Tectonophysics* 275:285–311.
- Dressler B. O., and Reimold W. U. 2001. Terrestrial impact melt rocks and glasses. *Earth-Science Reviews* 56:205–284.
- Dressler B. O., and Reimold W. U. 2004. Order or chaos? Origin and mode of emplacement of breccias in floors of large impact structures. *Earth-Science Reviews* 67:1–54.
- Graup G. 1999. Carbonate-silicate liquid immiscibility upon impact melting: Ries Crater, Germany. *Meteoritics & Planetary Science* 34:425–438.
- Hörz F., Archer P. D., Niles P. B., Zolensky M. E., and Evans M. 2015. Devolatilization or melting of carbonates at Meteor Crater, AZ? *Meteoritics & Planetary Science* 50:1050–1070.
- Jones A. P., Claeys P., and Heuschkel S. 2000. Impact melting of carbonates from the Chicxulub Crater. In *Impacts and the Early Earth, Lecture Notes in Earth Sciences*, edited by Gilmour I., and Koeberl C. Springer-Verlag, Berlin-Heidelberg-New York. pp. 343–361.
- Kerr J. W. 1975. Cape Storm Formation - A new Silurian unit in the Canadian Arctic. *Bulletin of Canadian Petroleum Geology* 23:67–83.
- Kieffer S. W., and Simonds C. H. 1980. The role of volatiles and lithology in the impact cratering process. *Reviews of Geophysics and Space Physics* 18:143–181.
- Lambert P. 1981. Breccia Dikes: Geological constraints on the formation of complex craters. In *Multi-ring Basins, Proc. Lunar Planet. Sci.*, edited by Schultz P. H., and Merrill R. B. pp. 59–78.
- Lepaulard C., Gattacceca J., Swanson-Hysell N., Quesnel Y., Demory F., and Osinski G. R. 2019. A Paleozoic age for the Tunnunik impact structure. *Meteoritics & Planetary Science* 1–12.
- Mallamo M. P. Ordovician and Silurian stratigraphy, sedimentology, and paleoecology,

- Central Canadian Arctic Islands. MSc thesis, University of Western Ontario, 1989.
- Mathieu J., Turner E. C., and Rainbird R. H. 2013. Sedimentary architecture of a deeply karsted Precambrian – Cambrian unconformity, Victoria Island, Northwest Territories; Geological Survey of Canada, Current Research 2013-1. p. 15.
- Melosh H. J. 1989. *Impact Cratering: A Geologic Process*, New York: Oxford University Press.
- Newman J. D., and Osinski G. R. 2016. Geological mapping of the Tunnunik impact structure, Victoria Island, Canadian High Arctic. *47th Lunar and Planetary Science Conference* Abstract #1591.
- Osinski G. R. 2003. Impact glasses in fallout suevites from the Ries impact structure, Germany: An analytical SEM study. *Meteoritics & Planetary Science* 38:1641–1667.
- Osinski G. R., Spray J. G., and Lee P. 2005. Impactites of the Haughton impact structure, Devon Island, Canadian High Arctic. *Meteoritics & Planetary Science* 40:1789–1812.
- Osinski G. R., and Spray J. G. 2005. Tectonics of complex crater formation as revealed by the Haughton impact structure, Devon Island, Canadian High Arctic. *Meteoritics & Planetary Science* 40:1813–1834.
- Osinski G. R., Spray J. G., and Grieve R. A. F. 2008. Impact melting in sedimentary target rocks: An assessment. In *The Sedimentary Record of Meteorite Impacts, Special Paper 437*, edited by Evans K. R., Horton W., King Jr. D. K., and Morrow J. R. Geological Society of America, Boulder, CO. pp. 1–18.
- Osinski G. R., Abou-Aly S., Francis R., Hansen J., Marion C. L., Pickersgill A. E., and Tornabene L. L. 2013. The Prince Albert structure, Northwest Territories, Canada: A new 28-km diameter complex impact structure. *44th Lunar and Planetary Science Conference* Abstract #2099.
- Osinski G. R., and Ferrière L. 2016. Shatter cones: (Mis)understood? *Science Advances* 2, e160061:1–10.

- Osinski G. R., Grieve R. A. F., Bleacher J. E., Neish C. D., Pilles E. A., and Tornabene L. L. 2018. Igneous rocks formed by hypervelocity impact. *Journal of Volcanology and Geothermal Research* 353:25–54.
- Pinto J. A., and Warme J. E. 2008. Alamo Event, Nevada: Crater stratigraphy and impact breccia realms. In *The Sedimentary Record of Meteorite Impacts, Special Paper 437*, edited by Evans K. R., Horton W., King Jr. D. K., and Morrow J. R. Geological Society of America, Boulder, CO. pp. 99–137.
- Quesnel Y., Zylberman W., Rochette P., Uehara M., Gattacceca J., Osinski G. R., Dussouillez P., Lepaulard C., and Champollion C. 2020. Geophysical signature of the Tunnunik impact structure, Northwest Territories, Canada. *Meteoritics & Planetary Science* 55:480-495.
- Sahoui R., Belhai D., and Jambon A. 2016. Impact-generated carbonate melts in the Talemzane impact structure (Laghouat, Algeria). *Arabian Journal of Geosciences* 9:641.
- Spray J. G. 1997. Superfaults. *Geology* 25:579–582.
- Stähle V. 1972. Impact glasses from the suevite of the Nördlinger Ries. *Earth and Planetary Science Letters* 17:275–293.
- Stewart W. D. 1987. *Late Proterozoic to Early Tertiary stratigraphy of Somerset Island and Northern Boothia Peninsula, District of Franklin, N.W.T.*, Paper 83-26, Geological Survey of Canada.
- Stöffler D. 1977. Research drilling, Nördlingen 1973: Polymict breccias, crater basement and cratering model of the Ries impact structure. *Geologica Bavarica* 75:443–458.
- Stöffler D. 1984. Glasses formed by hypervelocity impact. *Journal of Non-Crystalline Solids* 67:465–502.
- Stöffler D., and Grieve R. A. F. 2007. Impactites. In *Metamorphic Rocks: A Classification and Glossary of Terms, Recommendations of the International Union of Geological*

- Sciences*, edited by Fettes D., and Desmons J. Cambridge University Press, Cambridge. pp. 82–92.
- Stöffler D., Artemieva N. A., Wünnemann K., Reimold W. U., Jacob J., Hansen B. K., and Summerson I. A. T. 2013. Ries crater and suevite revisited-Observations and modeling Part I: Observations. *Meteoritics & Planetary Science* 48:515–589.
- Stöffler D., Hamann C., and Metzler K. 2018. Shock metamorphism of planetary silicate rocks and sediments: Proposal for an updated classification system. *Meteoritics & Planetary Science* 49:5–49.
- Wall F., Le Bas M. J., and Srivastava R. K. 1993. Calcite and carbocernaite exsolution and cotectic textures in a Sr,REE-rich carbonatite dyke from Rajasthan, India. *Mineralogical Magazine* 57:495–513.
- Wendte J. C. 2012. Core, petrographic, and rock petrophysical evaluation of the Blue Fiord Formation from wells in the Canadian Arctic Islands. *Geological Survey of Canada, Open File* 6984:1–126.
- Woodcock N. H., and Mort K. M. 2008. Classification of fault breccias and related fault rocks. *Geological Magazine* 145:435–440.
- Zylberman W. Geophysical Study of Complex Meteorite Impact Structures. PhD thesis, University of Western Ontario, 2017, Electronic Thesis and Dissertation Repository (5165).

Chapter 3

3 Impact-generated carbonate-rich dykes from the Haughton impact structure, Canada

3.1 Introduction

The Haughton impact structure on Devon Island, Nunavut, is a well-preserved complex impact structure 23 km in diameter (e.g., Osinski et al. 2005a; Robertson and Grieve 1978). The Haughton structure is located in a carbonate-rich sedimentary sequence comprised of limestone, dolostone, sandstone, shale, and sulfates, overlying gneiss and metagranite (Osinski et al. 2008a). The preservation and exposure of this impact structure offers many aspects for study from its geology, shatter cones, impactites, hydrothermal activity, to geomicrobiology (e.g., Osinski and Spray 2001; Osinski et al. 2005a, 2005b; Pontefract et al. 2014; Redeker and Stöffler 1988). The various allochthonous crater-fill impact melt rocks have been studied in detail (Osinski and Spray 2001, 2003; Osinski et al. 2005b; Redeker and Stöffler 1988); however, the one impactite that has not been studied in depth at Haughton are impact-generated dykes. Bischoff and Oskierski (1988) provided the first and only description of the occurrence of monomict and polymict impact breccia dykes with a clastic matrix as part of their review of surface structures at Haughton, but these lithologies were not described in any detail.

Breccia dykes are a prevalent feature in impact structures and their distribution can be underestimated in the field due to erosion or poor exposure (Lambert 1981). The generation of breccia dykes known to occur in carbonate-rich targets is limited to a few terrestrial impact sites (Osinski et al. 2008a). The well-preserved state and exposure of the Haughton impact structure provide an excellent opportunity to examine characteristics of dykes formed within the near-surface portion of a complex impact crater. The diversity observed among lithic breccias and impact melt rocks in this study of a well-preserved impact structure highlight the complexity of dyke formation in the impact cratering process. Many previous detailed studies of impact-generated dykes have been conducted at deeply eroded impact structures such as Rochechouart, Slate Islands, Vredefort, Ile Rouleau, and Tunnunik, which is described in Chapter 2 (Bischoff and Oskierski 1987; Caty et al. 1976;

Dressler and Reimold 2004; Dressler and Sharpton 1997; Lambert 1981). Examining dykes at Haughton will provide insights into the products generated and present in a well-preserved impact structure.

3.2 Geologic setting

The Haughton impact structure on Devon Island, Nunavut is located in a sedimentary target sequence of limestone, dolostone, evaporites, and sandstone of Cambrian to Silurian age, estimated to have been ~1880 m thick at the time of impact (Osinski et al. 2005a). The formations exposed and associated with samples in this study include Eleanor River, Bay Fiord, Thumb Mountain, and Allen Bay formations. These four formations can be heterogenous and most contain multiple members which may consist of limestone, dolostone, and/or anhydrite/gypsum. The Precambrian crystalline basement is not exposed within the impact structure but is found as clasts in the crater-fill impact melt rock deposits (Metzler et al. 1988; Osinski et al. 2005a, 2005b).

The crater-fill impact melt rocks cover the central area of the impact structure and are pale grey in colour, with the groundmass consisting of microcrystalline calcite, silicate impact melt glass, and anhydrite (Osinski and Spray 2001; Osinski et al. 2005b). These impact melt rocks are clast-rich and contain shocked mineral and lithic clasts from all target lithologies (Osinski et al. 2005b). Lithic breccias identified in dykes by Bischoff and Oskierski (1988) were distinguished as monomict and polymict. The monomict breccias consisted of a fine-grained dolomite or calcite matrix with clasts of dolostone or limestone, corresponding to the matrix composition (Bischoff and Oskierski 1988). Polymict breccias consisted primarily of limestone and dolostone clasts with fewer chert clasts and rare gypsum (Bischoff and Oskierski 1988). The Haughton impact structure is ~23.5 Ma as determined by U-Th/He dating of zircons (Young et al. 2013) and also preserves Miocene crater lake deposits that overlies some of the crater-fill impact melt rocks (Hickey et al. 1988; Osinski et al. 2005a).

3.3 Samples and methods

Fieldwork related to this study was conducted over four weeks in July and August 2016 at the Haughton impact structure. The primary field objective was to locate impact-generated

dykes then document and collect samples for further analysis. Rock samples hosting the dykes were also collected from most locations. Twenty dykes were identified in 2016 (Fig. 3-1). Fieldwork focused on the Haughton River valley where outcrops were well-exposed and accessible (Fig. 3-1B). From the 2016 samples collected, a suite of thin sections was prepared for detailed analysis of carbonate-rich dykes and target rock. Multiple samples from the same dyke were collected at several locations, but only one representative sample ID is indicated on the map (Fig. 3-1) for clarity.

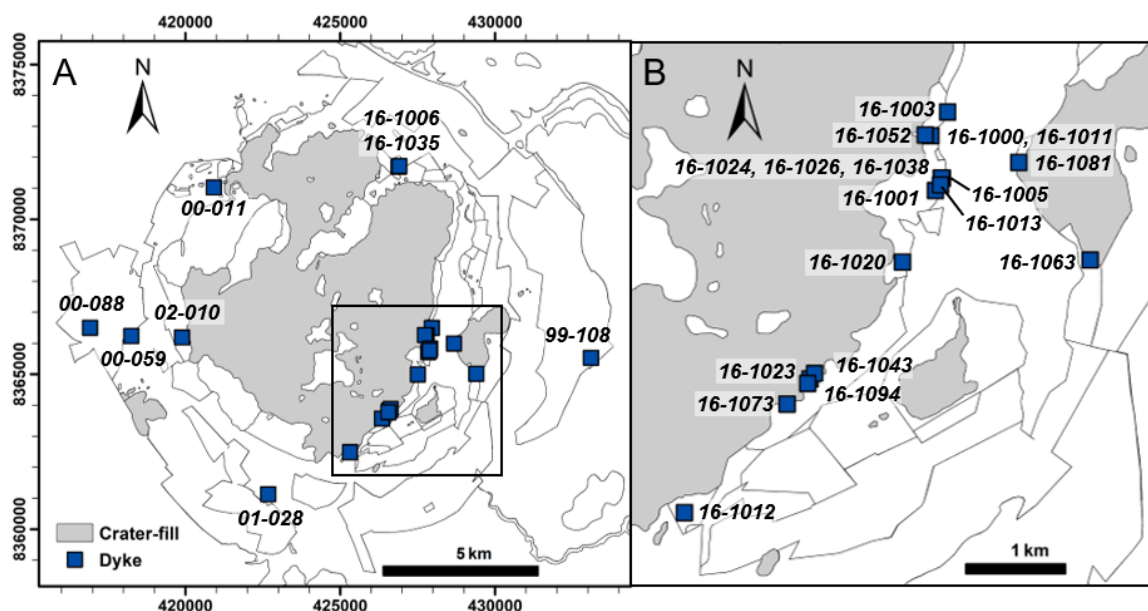


Figure 3-1. Simplified map of the Haughton impact structure with outlines of geological formations shown, see Osinski et al. (2005a) for detailed geologic map. A) Dyke locations in this study and the extent of crater-fill deposits are highlighted. First two numbers in each sample ID indicate the year the sample was collected. B) Dykes located along the Haughton River valley. UTM grid with Easting and Northing at 1000 m intervals for Zone 16.

Six breccia dykes identified in previous field seasons are included in this study. These pre-2016 breccia dykes are located farther from the centre of the impact structure than most of the 2016 samples, providing a wider range of occurrence and host formation association (Fig. 3-1A). Samples from impact-generated dykes examined in this study differ from the deposits of pale grey crater-fill impact melt rocks preserved within the central uplift region and ejecta megablocks of the rim region. Details and descriptions of the crater-fill

impactites can be found in Osinski and Spray (2001), Osinski and Spray (2003), and Osinski et al. (2005b).

Polished thin sections were examined petrographically in transmitted light using Nikon Eclipse LV 100POL microscopes with a NIS-Elements D laboratory image analysis system. The nature, texture, and composition of each dyke were studied. Samples were carbon coated for electron probe microanalysis (EPMA) using a JEOL JXA-8530F field-emission electron microprobe in the Earth and Planetary Materials Analysis Laboratory at the University of Western Ontario. Energy dispersive spectrometry (EDS) was used to obtain semi-quantitative elemental data for mineral identification. Backscattered electron (BSE) images were captured and used to examine microtextures within the samples using a 15 kV accelerating voltage and working distance of 11 mm. Wavelength dispersive spectrometry (WDS) provided quantitative compositions of samples. Analytical conditions for WDS analyses for elements Si, Al, Na, Mg, Ca, Ti, Fe, Ba, Mn, K, and S were an accelerating voltage of 15 kV, beam current of 20 nA, spot size of 5 μm , and working distance of 11 mm. Element maps of Mg, Al, Si, S, Ca, and Fe were acquired for specific targets in sample 00-011 using an accelerating voltage of 15 kV, beam current of 50 nA, and spot size of 1–2 μm .

Micro X-ray diffraction (μXRD) analysis was applied to two whole rock samples of impact melt rock for in situ mineral identification of fragile, heavily weathered clasts composed of unconsolidated grains. Micro XRD is a rapid, non-destructive technique and was performed on cut rock slab surfaces with no additional sample preparation required (Flemming 2007). Samples were analyzed using a Bruker D8 Discover microdiffractometer with a 60mm cobalt Gobel mirror, Co X-ray source (Co $K\alpha = 1.78897 \text{ \AA}$), and a 300 μm beam diameter while operating at 35 kV and 45 mA. Using omega scan mode (Flemming 2007) two frames were collected with frame 1 parameters $\theta_1 = 14.5^\circ$, $\theta_2 = 25.5^\circ$, $\omega = 10^\circ$, and time = 60 minutes and frame 2 parameters $\theta_1 = 40^\circ$, $\theta_2 = 40^\circ$, $\omega = 10^\circ$, and time = 90 minutes where θ_1 is the source angle and θ_2 is the detector angle such that $(\theta_1 + \theta_2) = 2\theta$. Operational parameters were identical for both samples.

3.4 Results

The Houghton impact-generated dykes divided into two main groups based on whether they comprise lithic breccias or clast-rich impact melt rocks. Both groupings show diversity among each other in terms of colour, composition and texture at hand sample scales. The extent of weathering also varies among dykes.

Mechanical twinning is commonly observed in calcite grains within lithic breccias and clast-rich impact melt rocks while similar mechanical twinning is absent in dolomite. Variation and deformation observed in calcite mechanical twinning are provided in Figure 3-2 where calcite twins vary from thin and straight, progressing to thicker twins, curved twins, and thick patchy twins. Since the calcite grains that display mechanical twinning and deformation in Figure 3-2 have been incorporated into impact breccias and melt rocks, their pre-impact location within the target sequence is unknown. Thus, comparisons of mechanical twinning to shock pressure cannot be made with these samples and was not investigated further in this study.

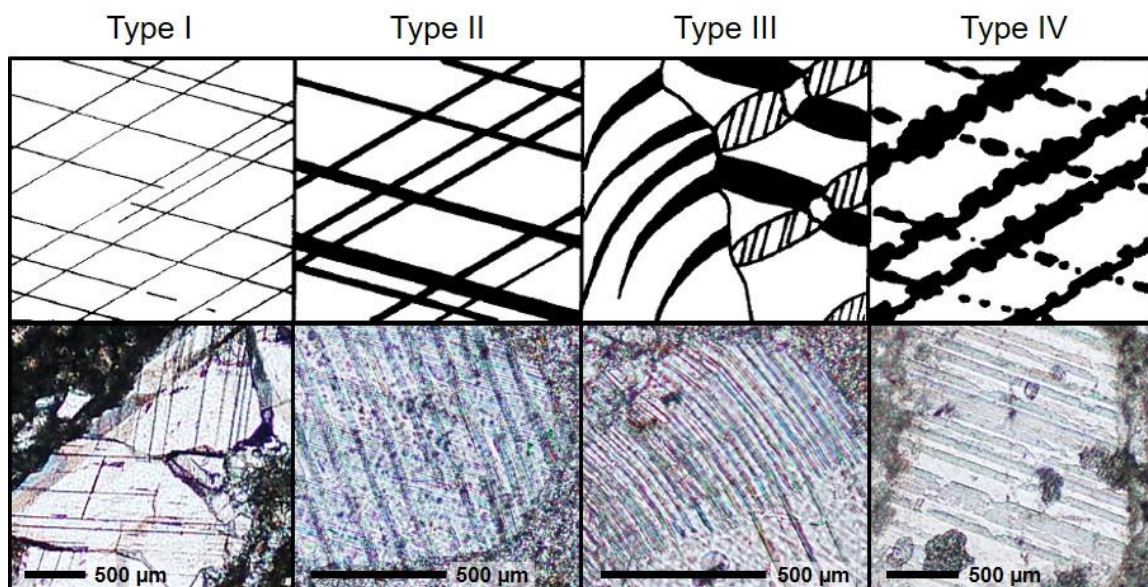


Figure 3-2. Classification of calcite twins in thin sections from the Houghton impact structure. Top row drawings are modified from Burkhard (1993) and bottom row photomicrographs, viewed in plane-polarized light, are calcite grains in lithic breccia samples 16-1035, 16-1006, 16-1012, and 16-1081 respectively.

3.4.1 Lithic breccia dykes

3.4.1.1 Field observations

Dykes with lithic breccia are predominantly located toward the rim of the impact structure and within the Houghton River Valley (Fig. 3-1). Within the group of lithic breccia dykes identified in 2016, 5 are monomict and 3 are polymict while the 6 breccia dyke samples examined from the 1999 and 2000 field seasons are monomict lithic breccias. Monomict lithic breccia dykes are clast-rich and range in colour from grey, brown, or yellow depending on the host rock formation and extent of weathering. The three polymict lithic breccia dykes are located near contacts between units and are described separately and further in the sulfate breccia section. Narrow monomict lithic dykes with widths less than ~20 cm typically have sharp, even contacts and appear confined within the host rock (Fig. 3-3). Several monomict lithic breccias found are more expansive and reach widths close to ~1 m. These larger dykes usually have irregular edges, as opposed to straight contacts, but this is partially due to weathering and erosion as the contacts with host rock are not always preserved.

Lithic dykes are typically straight but may be offset by small faults (Fig. 3-3A). The orientation of lithic dykes within the target rock may follow bedding planes or cut across a unit located along a fault. Several lithic breccia dykes show a resistance to weathering compared to the surrounding target rock (Figs. 3-3B, C). Both dykes show noticeable relief compared to the host rock on either side of the dyke and their breccias are well lithified and as they do not break or crumble easily. The dyke in Figure 3-3B has similar weathering as the adjacent Thumb Mountain Formation and is more difficult to discern than the differential weathering between the dyke shown in Figure 3-3C in the Allen Bay Formation. Clasts in the lithic breccias are typically less than 1 cm (Fig. 3-4) but larger clasts over 5 cm are sometimes present, especially in the wider dykes.

Alignment of elongated clasts to be parallel with the orientation of the dyke is not typically observed at hand-sample scale with clast orientations appearing to be random (Fig. 3-4). There are occurrences where a specific section may demonstrate this alignment, but these are isolated and not widespread through the sample.



Figure 3-3. Monomict lithic breccia dykes. A) Dyke 16-1012 is outlined by white dashed lines and offset by two nearly parallel faults, indicated by solid black lines. Rock hammer at lower left corner for scale. B) Oblique view of dyke in (A) below the bottom fault showing the dyke protruding outward from the weathered host rock surface; black arrow indicates dyke width and white arrow shows depth of dyke. C) Dyke 00-059 protruding from weathered rock surface. Lens cap for scale; photo by G. Osinski. D) Weathering of dyke 16-1012, outlined by white dashed lines, gives it a more yellow hue compared to adjacent host rock; rock hammer for scale.

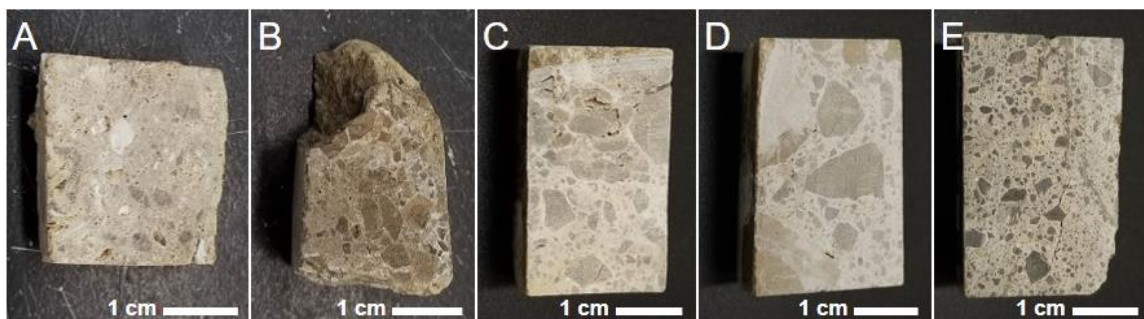


Figure 3-4. Examples of lithic monomict breccias from various formations within the Haughton impact structure. A) Sample 16-1006 from the Eleanor River Formation. B) Sample 16-1063 from the Bay Fiord Formation Member C. C) Sample 00-088 and 01-028 (D) from the Allen Bay Formation Lower Member. E) Sample 02-010 from the Thumb Mountain Formation.

Overall, the monomict dykes are not prominent outcrop features as they are similar in colour to their host rock formation, so their identification requires close proximity and examination of the outcrop in order to be detected.

3.4.1.2 Petrology and geochemistry

Monomict lithic breccias are carbonate-rich, melt-free, clast-rich, poorly sorted, and are generally matrix-supported. Most clasts are several hundred μm in size and clast shapes range from angular to sub-rounded. The fine-grained lithic matrix is too fine to resolve petrographically (Fig. 3-5). Sulfide grains, if present, are sparse, less than $\sim 10 \mu\text{m}$, and are more likely to be found in the matrix than in clasts.

Clast compositions may consist of limestone, dolostone, and chert with some limestones being fossil-bearing. The Thumb Mountain Formation contains both macrofossils and microfossils. Macrofossils such as gastropods, crinoids, corals, and brachiopods can be several cm in size up to 12 cm and are visible to the unaided eye. Microfossils are not visible at hand sample-scale but can be readily observed in thin section and include fragments and cross-sections of conodonts and trilobites (Fig. 3-6).

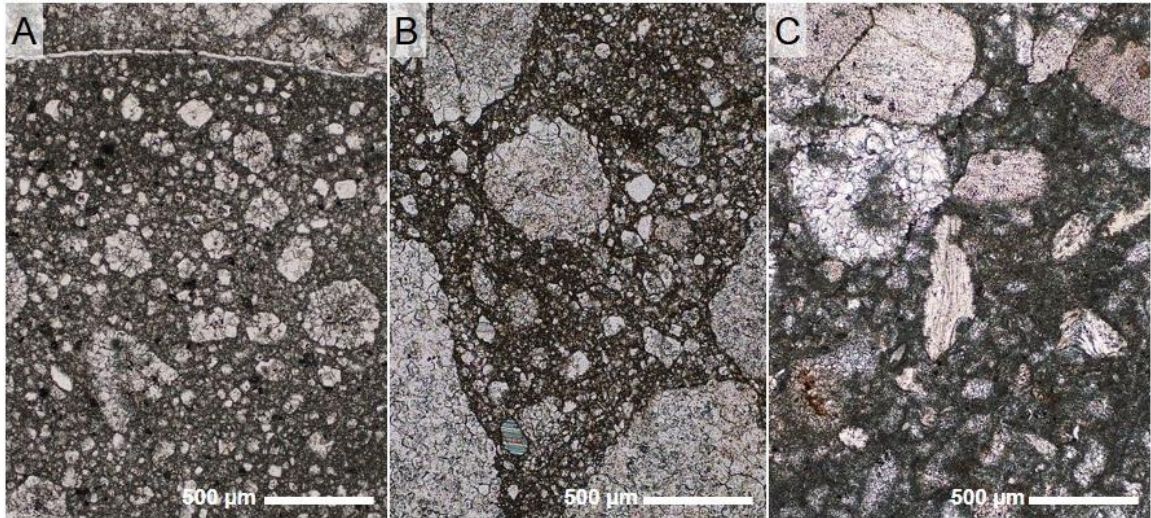


Figure 3-5. Examples of the matrix in lithic breccias from the Haughton impact structure shown at 50x magnification in plane-polarized light. A) Sample 99-108. B) Sample 00-088. C) Sample 16-1006.

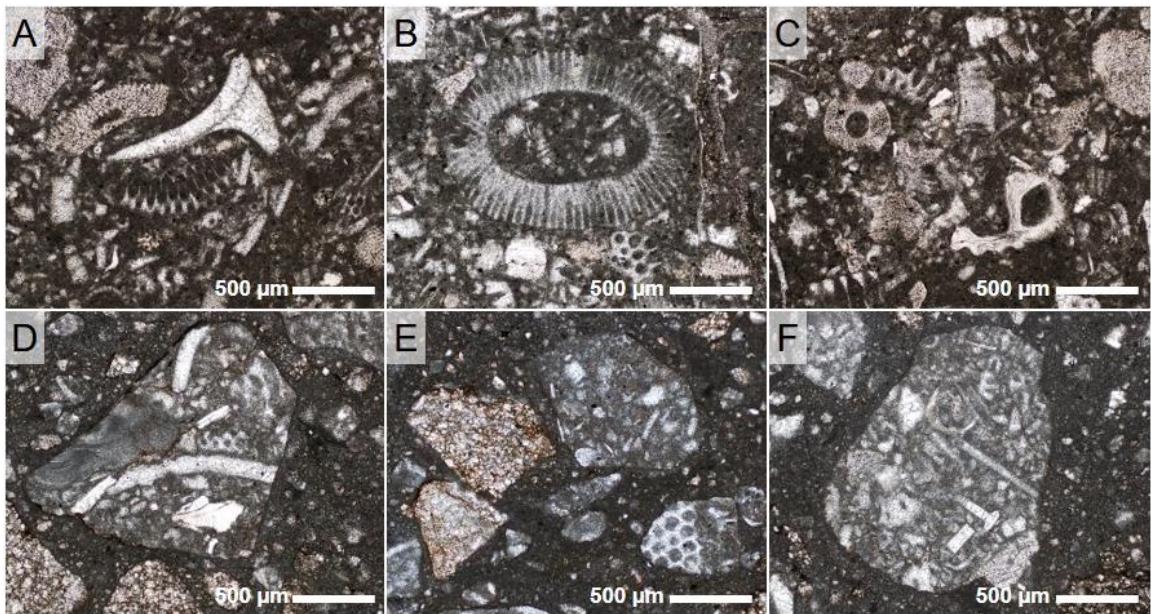


Figure 3-6. Microfossils in lithic breccia samples originating from the Thumb Mountain Formation. (A–C) Microfossil assemblages in large clasts that include fragments of conodonts and trilobites; sample 16-1035. (D–E) Smaller sub-rounded lithic clasts surrounded by a fine-grained matrix from sample 02-010. Samples are shown at 50x magnification in plane-polarized light.

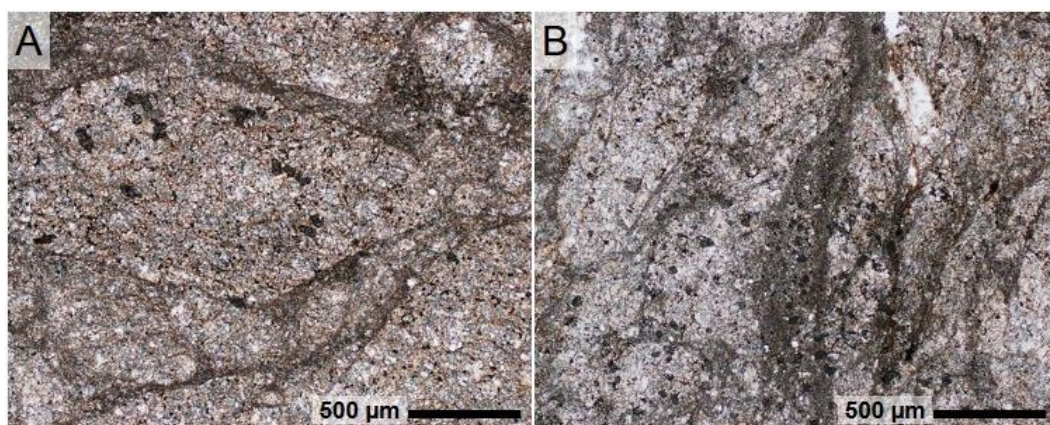


Figure 3-7. Crackle type fault breccia occurrences located adjacent to an impact melt rock dyke. Lithic fragments are separated by thin seams of fine-grained matrix. A) Sample 16-1026. B) Sample 16-1038. Samples are shown at 50x magnification in plane-polarized light.

Within the sample suite, two examples of fault breccia were identified and classified as crackle breccia, according to the revised classification of fault rocks by Woodcock and Mort (2008). Both fault breccias are found adjacent to dykes of impact melt rock. Crackle breccia is recognized as clasts that appear to fit together with minimal rotation but are separated by thin seams of fine-grained matrix (Fig. 3-7). At hand sample scale, these crackle breccias are difficult to identify and discriminate from the host rock. There is a ~1000 µm zone of transition between the fault breccia and impact melt rock contact which may be gradual or sharp. There is no impact melt rock material mixed with the crackle breccia and within the transition zone the lithic fragments grade into the impact melt rock.

3.4.2 Quartz-cemented carbonate breccia dyke

Located ~5 km northwest from the centre of the impact structure, a dyke with an unusual composition compared to the rest of the dykes in the sample suite was identified and examined. Sample 00-011 (Fig. 3-1A) is found in the Allen Bay Formation Lower Member just beyond the extent of the impact melt rock crater-fill. This clast-rich lithic breccia is not distinctive in hand sample with angular to sub-rounded dolomite, rounded to sub-rounded calcite clasts, and sub-angular chert clasts in a matrix too fine to resolve with the unaided eye (Fig. 3-8A).

In thin section, this breccia also appears as an unremarkable lithic breccia as the matrix is still too fine-grained to resolve. The clasts are confirmed as carbonates and chert. There are no microfossils present within the clasts. A sample of host rock collected from the same location as the breccia dyke consists of a microfossil-bearing limestone.

Using backscattered electron imagery is when this sample becomes distinct as the fine-grained matrix is revealed to be a quartz cement (Fig. 3-8B). Within the cement, small rounded calcite globules are present that contain <0.4 wt% SiO_2 and Al_2O_3 . Using wavelength dispersive spectroscopy, electron probe microanalysis reveals the cement composition is close to 100% SiO_2 , with <2, <1, and <0.5 wt% of CaO , MgO , and Al_2O_3 (Table 3-1).

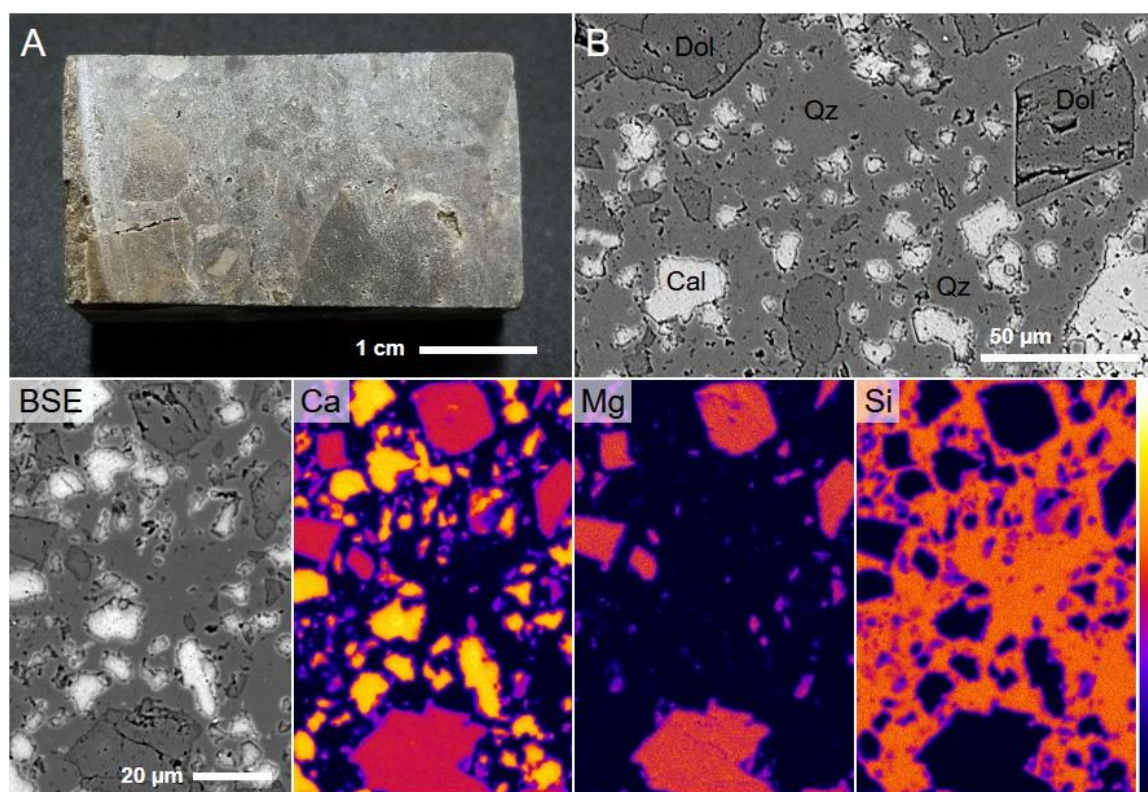


Figure 3-8. Sample 00-011. A) Flat hand sample with angular dark dolomite and pale chert clasts visible. B) Image acquired using backscattered electrons (BSE) showing typical clast and cement association of quartz (Qz), calcite (Cal), and dolomite (Dol). Bottom series of images shows the same location in BSE and element maps to show the distribution of Ca (calcium), Mg (magnesium), and Si (silicon).

Table 3-1. Compositions from the quartz-cemented carbonate breccia dyke.

Sample type	Quartz cement		Calcite clasts		Dolomite clasts	
	<i>n</i>	76	25	24		
	wt%	s.d.	wt%	s.d.	wt%	s.d.
SiO₂	99.42	0.66	0.14	0.11	0.10	0.12
Al₂O₃	0.11	0.12	0.05	0.09	0.06	0.07
MgO	0.11	0.22	0.31	0.14	21.26	0.31
CaO	0.31	0.43	56.22	1.15	31.11	0.23
FeO	0.03	0.03	0.04	0.07	0.02	0.02
Total	100.02	0.01	56.78	1.11	52.61	0.27

n = number of points analyzed.

wt% = average oxide composition in weight %.

s.d. = standard deviation.

Na₂O, TiO₂, MnO, BaO, K₂O, and SO₃ were below detection.

3.4.3 Sulfate-bearing polymict breccia

Within a 350 m section of the Houghton River Valley, three occurrences of sulfate-bearing polymict lithic breccias were identified within the Bay Fiord Formation Member A (see Figure 3-1, samples 16-1023, 16-1073, and 16-1094). This member mainly consists of anhydrite, often laminated, and secondary gypsum. One distinctive property of these breccias is they are weakly lithified and can easily be broken apart by hand. These dykes and the outcrops where they are found are highly weathered which is attributed to their high evaporite content.

Most of the dyke contacts with the host rock are obscured by the heavily weathered evaporite layers in the Bay Fiord Formation, but one contact was visible and is shown in Figure 3-9A. Here, the vertical dyke has a sharp contact with inclined anhydrite layers on the right side of the outlined dyke. To the left of the dyke underneath the rock hammer, is the relatively loose, powdery weathered deposits that blanket much of the sulfate-rich outcrops along the Houghton River valley. The light-toned vein-like structures that cut across the vertical dyke are deposits of secondary gypsum as they fill cracks within the breccia.



Figure 3-9. Sulfate-bearing polymict breccia. A) Vertically oriented dyke (outlined in white dashed lines) cuts through inclined gypsum and anhydrite beds within the Bay Fiord Formation Member A. B) Sample 16-1074 collected from top right area of dyke visible in (A). C) In situ photograph of sample 16-1023, with a light-toned, layered anhydrite clast near centre of image.

Unlike the majority of lithic breccias described above, the sulfate-bearing breccias are clearly polymict at hand sample-scale (Fig. 3-9). Visible clasts of dolomite and layered gypsum and anhydrite from the Bay Fiord Formation are mixed with grey coloured limestone clasts from the Eleanor River Formation. Small clasts of black chert, also from the Eleanor River Formation, are present. The sulfate breccias are clast-rich with most of the visible clasts being at the mm scale, up to ~1 cm. Sulfate-bearing breccias are also matrix-supported and poorly sorted. Despite the contribution of clasts from the Eleanor River Formation, breccias from these three dykes appear to be dominated by sulfate minerals. The main focus of this study was carbonate-rich dykes so the sulfate-bearing breccias were not investigated further.

3.4.4 Impact melt rock dykes

3.4.4.1 Field observations

Dykes of impact melt rock are exposed along the Haughton River valley in the Eleanor River Formation. Impact melt rock dykes are pale grey to beige in colour and reflect the chert-bearing limestone composition of the adjacent Eleanor River Formation. These dykes differ from the widespread crater-fill impact melt rocks as these crater-fill deposits contain clasts from all target lithologies, including the crystalline basement (Osinski et al. 2005b). The extent of crater-fill deposits is shown in Figure 3-1. The dyke morphologies of impact melt rocks are more diverse than the more linear lithic dykes identified at the Haughton impact structure (Fig. 3-3). Examples of impact melt rock dykes are provided in Figure 3-10 and include a branching H-shaped dyke, a dyke over 1 m wide at the base of its exposure, and a more linear dyke but with an irregular contact with host rock. These morphologies distinguish impact melt rock dykes from lithic dykes since the contact between the impact melt rock dykes and host rock tend to be irregular rather than straight. Compared to the crater-fill impact melt rocks, the melt rocks from the dykes are harder and when freshly broken, the edges tend to be fairly straight and sharp (Fig. 3-10F) and do not break apart as easily. In the field, the dyke melt rocks also feel denser compared with lithic breccias of similar size. There was no observed contact between impact melt rock dykes and lithic breccia dykes or one cutting through the other.

Another notable feature that separates the impact melt rock group from the lithic suite of dykes is the presence of small cavities and vesicles within the impact melt rock (Figs. 3-10D–F and 3-11). The cavities and vesicles are visible at hand sample-scales where the cavities tend to be larger (up to several cm in diameter) and more angular than the smaller more rounded vesicles. The shape of the larger cavities resembles clasts giving the impression they have been weathered out of the groundmass, based on clast morphologies observed in other dykes and less weathered clasts within the groundmass.

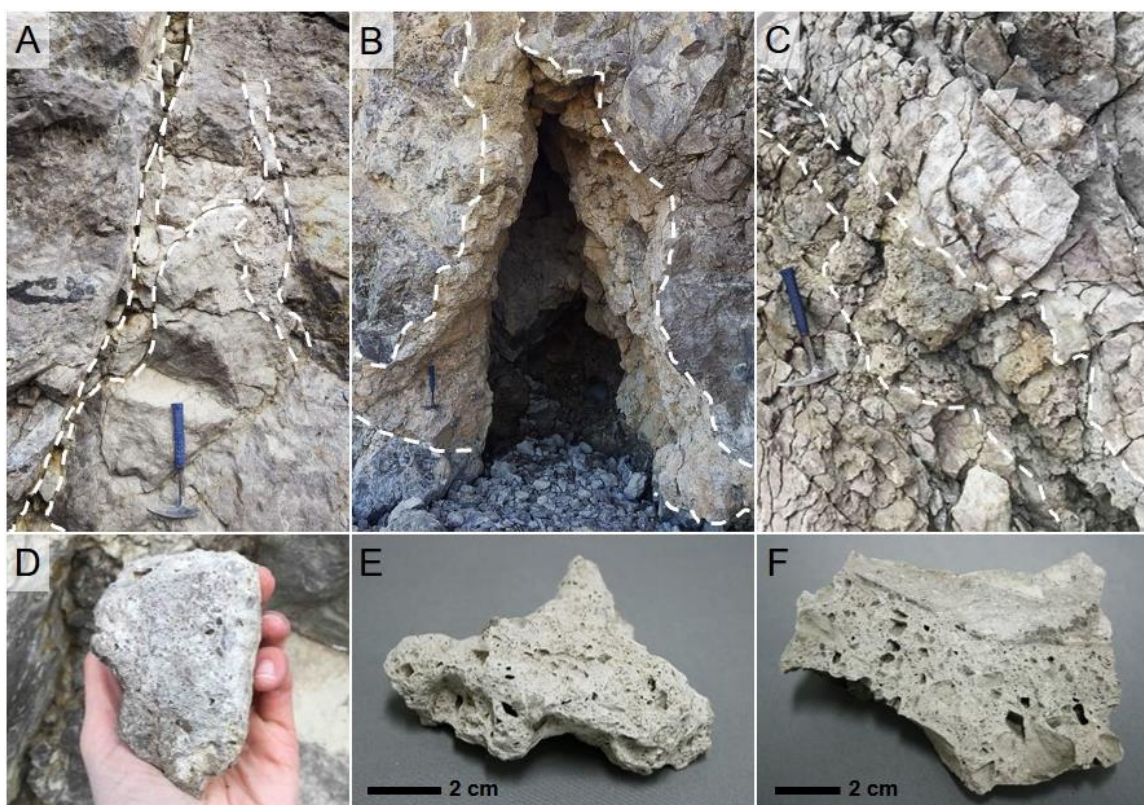


Figure 3-10. Impact melt rock dykes (A–C) show a range of morphologies. Dykes are outlined by white dashed lines for clarity as impact melt rock is very similar in colour to host rock; hammer for scale. A) A narrow H-shaped branching dyke. B) Wide dyke that has eroded in the centre to form a small cave. C) An intermediate width dyke that has irregular contact with host rock and large cavities and vesicles. D) Sample 16-1000 from the dyke shown in (A). E) Sample 16-1003 from the dyke in (B). F) Sample 16-1020 from the dyke in (C).

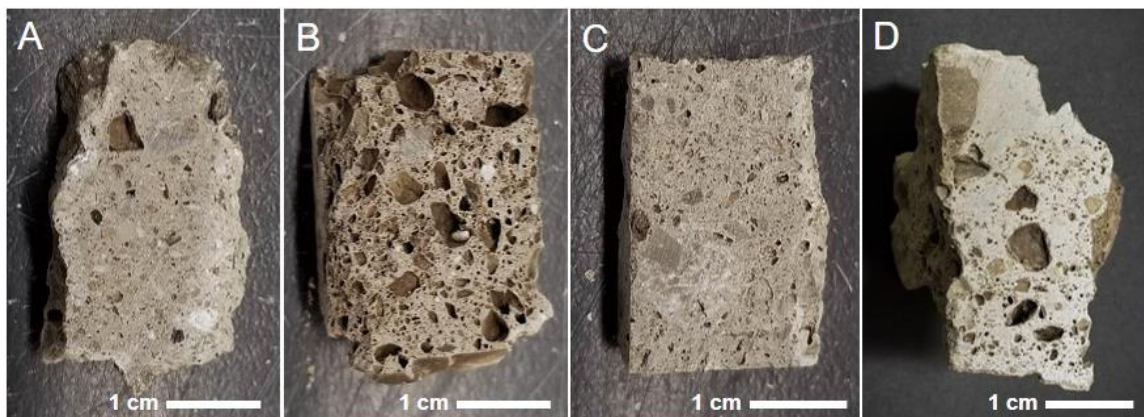


Figure 3-11. Examples of impact melt rock that vary in the proportion of vesicles they contain. A) Sample 16-1001. B) Sample 16-1003. C) Sample 16-1005. D) Sample 16-1020.

The impact melt rock from the H-shaped dyke has smaller mm-sized vesicles and cavities (Fig. 3-10D) compared to the larger and more numerous ones present in the impact melt rock samples in Figures 3-10E and F. Extending this observation to the rest of the impact melt rock dykes, there appears to be a weak correlation between the width of the dyke and size and volume of vesicles and cavities at the outcrop scale. Narrower dykes have fewer and smaller holes compared with wider dykes.

Impact melt rocks collected from dykes are clast-rich even with the presence of cavities and vesicles and these clasts are generally <1 cm. Shatter cone clasts can be found in crater-fill deposits, but shatter cones have not been identified in the dyke impact melt rock samples. The absence of shatter cones could be the result of smaller clasts sizes in the dykes which would make shatter cones more difficult to recognize if they were present.

3.4.4.2 Petrology and geochemistry

The clast-rich impact melt rocks sampled from 12 dykes are monomict and reflect the composition of the chert-bearing limestone of the host Eleanor River Formation. The impact melt rock dykes do not have any clast contributions from the crater-fill impact melt rocks as there are no sandstone, sulfate, shale, mafic, or other crystalline clasts such as gneiss or amphibolite present. Several thin sections in the sample suite could be mistaken as polymict based on the variety of limestone textures among the clasts that range from

coarse to fine-grained, however, assessment and observation of the Eleanor River Formation reveals it is a heterogenous limestone unit with multiple members. Toasted and untoasted chert clasts are present within impact melt rock samples. The aphanitic groundmass of impact melt rocks consists of microcrystalline calcite which is too fine to be resolved using optical microscopy and is generally homogenous in appearance.

Electron probe microanalysis was used to resolve the aphanitic groundmass and determine its composition. Backscattered electron imagery shows the groundmass consists of interlocking grains of equigranular calcite less than 15 μm in size (Fig. 3-12). The more porous groundmass in Figure 3-12A corresponds with the cut sample shown in Figure 3-13B. The finer groundmass in Figure 3-12B corresponds with the cut sample shown in Figure 3-13A. These two examples of groundmass endmembers, based on number of vesicles present, show that impact melt rocks are generally similar but there are slight differences among samples from different dykes.

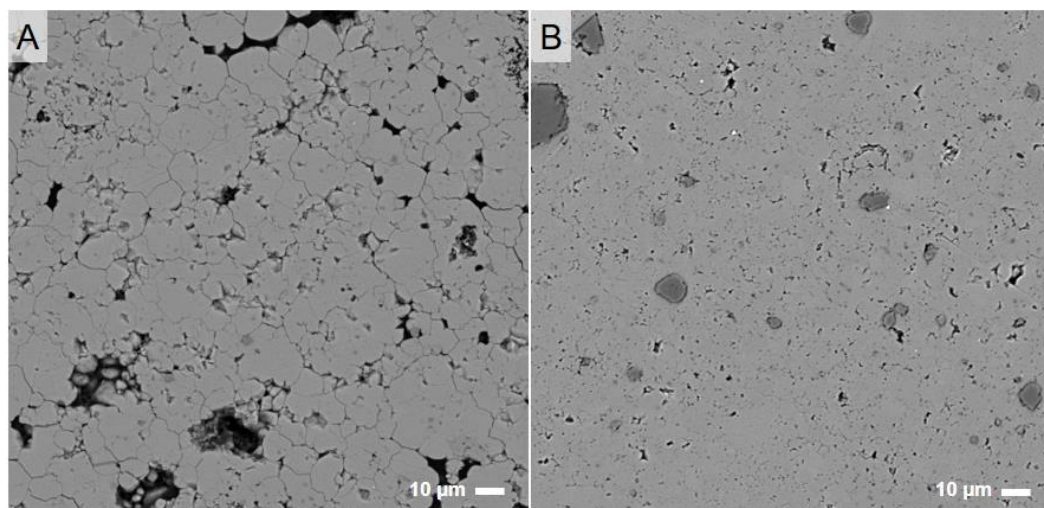


Figure 3-12. Backscattered electron images of impact melt rock groundmass. A) Groundmass consists entirely of microcrystalline calcite and black areas are holes or pore spaces; sample 16-1003. B) Groundmass is microcrystalline calcite with small rounded quartz grains. Small black spots are pore spaces; sample 16-1011. Magnification for both images is 500x.

During sample preparation, two impact melt rock samples revealed heavily weathered clasts in the interior of the hand sample after being cut apart (Figs. 3-11D and 3-13A).

These clasts are coarse-grained and are so weathered that they could easily be plucked out of the groundmass using only a fingernail. To determine the mineral composition of the heavily weathered clasts in situ and avoid loss or damage during thin section production, they were analyzed using micro X-ray diffraction (μ XRD) as no additional sample preparation was required. The aphanitic groundmass was also analyzed using μ XRD.

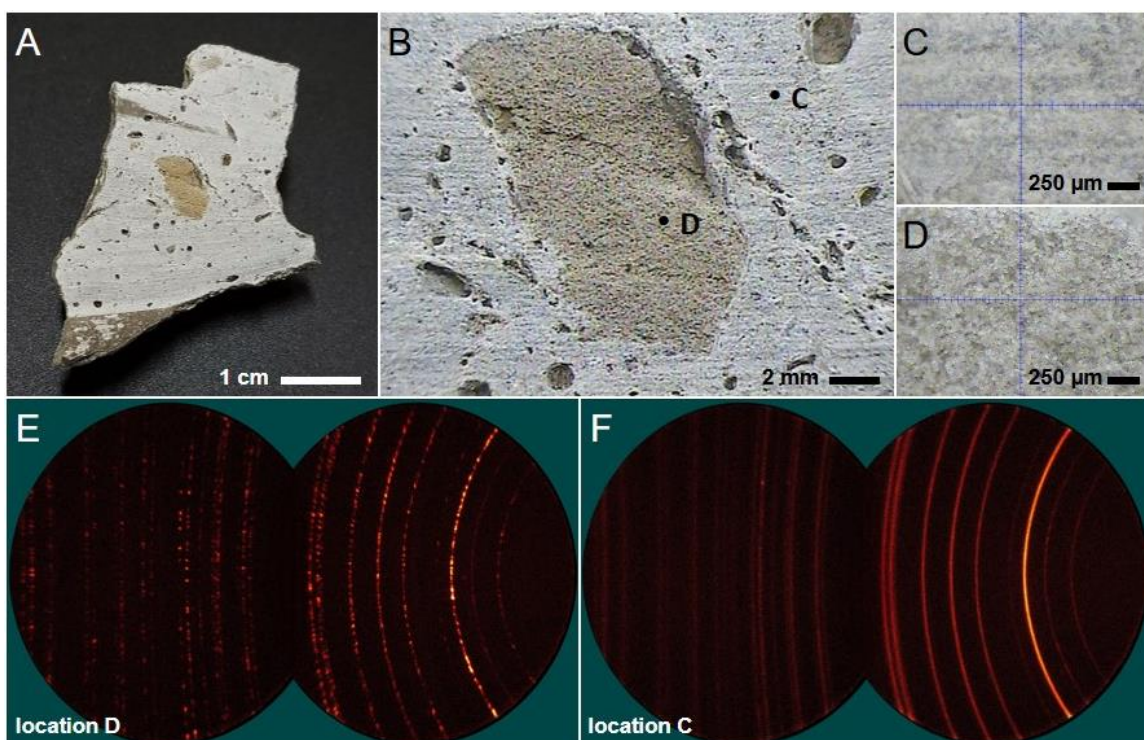


Figure 3-13. Sample 16-1011. A) Flat cut surface of impact melt rock sample with a heavily weathered clast at its centre. B) Weathered clast showing analysis spots on the groundmass (C) and clast (D). C) Magnified (7x) image of impact melt rock groundmass indicated in (B). D) Magnified (7x) image of weathered clast indicated in (B). E) 2-D analysis of weathered clast at location D. F) 2-D analysis of aphanitic groundmass at location C.

The results from both samples were similar where the main phase in both the heavily weathered clasts and groundmass is calcite with a minor quartz phase. Dolomite was detected in the clasts and absent in the groundmass. The bright Debye rings for clast and groundmass (Figs. 3-13E, F) correspond with calcite lattice planes and several of the fainter rings correspond with quartz lattice planes. Details of all 2-D analysis points and diffraction

patterns from both samples are provided in Appendix D. The difference in appearance of the rings between the two analysis spots in Figure 3-13, spotty or smooth and continuous, shows there is a change in grain size. The smooth rings of the groundmass (Fig. 3-13F) indicate the grain size is less than 5 μm , which is supported by the backscattered electron image of the groundmass for the same sample shown in Figure 3-12B. The spotty rings from the calcite grains in the weathered clast are larger, $\sim 15 \mu\text{m}$, and their random orientations contribute to the variation in intensity of the rings.

The composition of the impact melt rock groundmass as determined using electron probe microanalysis is summarized in Table 3-2. EPMA detected several wt% of SiO_2 and Al_2O_3 present in the groundmass calcite with the highest SiO_2 wt% being ~ 5 wt%; 31 SiO_2 analyses were greater than 0.5 wt%. Trace amounts of SiO_2 were also detected in calcite and dolomite clasts but were never above ~ 0.6 wt%.

Table 3-2. Electron probe microanalysis (WDS) of carbonate phases in impact melt rock dykes.

Sample type <i>n</i>	Groundmass <i>156</i>		Calcite clasts <i>118</i>		Dolomite clasts <i>23</i>	
	wt%	s.d.	wt%	s.d.	wt%	s.d.
SiO₂	0.43	0.77	0.12	0.14	0.17	0.14
Al₂O₃	0.09	0.19	0.08	0.19	0.04	0.06
Na₂O	0.02	0.05	b.d.	b.d.	b.d.	b.d.
MgO	0.57	0.63	0.68	1.97	20.73	1.66
CaO	55.60	1.55	55.49	3.21	31.87	1.74
FeO	0.03	0.04	0.04	0.05	0.05	0.06
K₂O	0.04	0.11	0.02	0.03	b.d.	b.d.
SO₃	0.06	0.05	0.07	0.05	0.03	0.02
Total	56.77	1.06	56.46	2.24	52.85	1.30

n = number of points analyzed.

wt% = average oxide composition in weight %.

s.d. = standard deviation.

b.d. = below detection.

TiO₂, MnO, BaO were below detection.

In thin section, some of the cavities have a thin interior rim of orange-brown devitrified silicate glass. Based on this observation, the heavily weathered carbonate clasts analyzed via μXRD (e.g., Fig. 3-13) are not considered to have been the common precursor in terms

of composition for the majority of cavities. The weathered carbonate clasts are less common than the small cavities with glass remnants. Silicate glass remnants are discussed further below.

3.4.4.3 Silicate glass

Small fragments of silicate glass, up to ~600 μm , are found in the calcite groundmass of impact melt rock dykes. Most glass fragments are devitrified and orange-red to brown in colour under plane-polarized light (Fig. 3-14). Intact silicate glass fragments do not make up a large portion within the impact melt rocks and are not found in all melt rock dykes. When present, silicate glass fragments comprise less than ~2% of a thin section. This value does not include any cavities that may contain glass remnants, which may comprise ~5–30% in some impact melt rock samples.

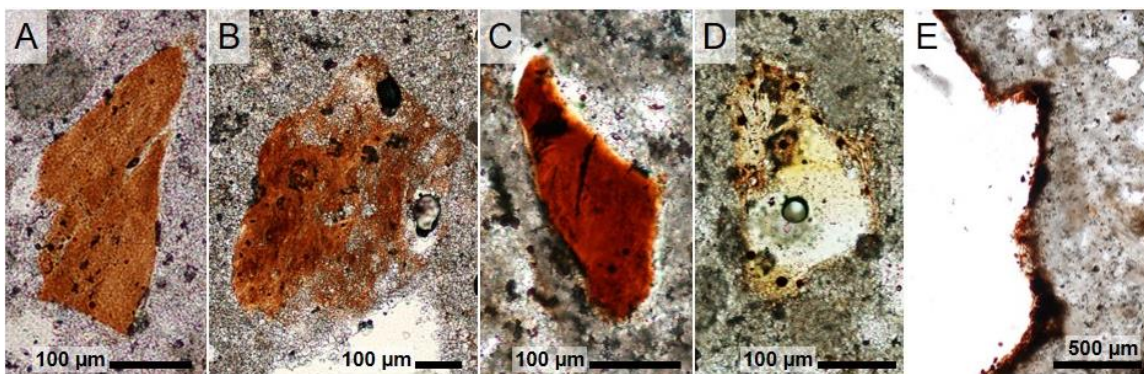


Figure 3-14. A) MgO-rich glass from 16-1020B. B) MgO-rich glass from 16-1003. C) MgO-rich glass from 16-1020A. D) C4-like glass from 16-1020B. E) Cavity (white area) with silicate glass remnants along the interior edge from 16-1020A. Images shown in plane-polarized light with magnification of 200x (A, C, D), 100x (B), and 50x (E).

Two types of silicate glass compositions were identified using EPMA (Table 3-3). Based on WDS results, the one type of silicate glass is MgO-rich with a MgO content from ~21–29 wt%, SiO₂ content ~50 wt%, and no Al₂O₃ or K₂O and the second type has a C4-like composition (Osinski et al. 2005b) with a MgO content up to ~25 wt%, Al₂O₃ ~12 wt%, and FeO ~8 wt%. For a given impact melt rock sample, both types of silicate glass compositions can be found. Based on EDS measurements using elemental totals in MgO-

rich glass and C4-like glass, the average carbon content detected is ~12 wt% and ~20 wt%, respectively. Due to a probable combination of weathering and sample preparation, silicate glass from larger clasts have been eroded or plucked out leaving thin remnants behind in cavities.

Table 3-3. Electron probe microanalysis (WDS) of silicate glass.

Sample type <i>n</i>	MgO-rich glass		C4-like glass	
	31		32	
	wt%	s.d.	wt%	s.d.
SiO₂	49.85	2.71	44.85	7.73
Al₂O₃	0.34	0.25	11.44	2.61
Na₂O	0.17	0.06	0.16	0.06
MgO	24.37	1.50	13.90	5.64
CaO	0.21	0.06	0.97	1.88
TiO₂	0.02	0.02	0.51	0.69
FeO	0.33	0.53	3.64	1.55
K₂O	0.17	0.10	4.69	1.91
SO₃	0.17	0.12	0.44	0.74
Total	75.63	4.06	80.59	6.31

n = number of points analyzed.

wt% = average oxide composition in weight %.

s.d. = standard deviation.

TiO₂, MnO, BaO were below detection.

3.4.5 Chert

The Eleanor River Formation is a chert-bearing limestone unit. In outcrops beyond the rim of the Houghton impact structure, chert nodules are white. Where the Eleanor River Formation is exposed within the impact structure, particularly within the central uplift, some of the chert nodules and fragments are coloured black instead of white. At outcrop scales, the black chert can be found as small cm-sized fragments in brecciated areas of the Eleanor River Formation (Fig. 3-15A) or as larger rounded chert nodules (Fig. 3-15B). The impact melt rock dyke outlined in Figure 3-15B, below the black chert nodules, is the dyke that is adjacent to the fault breccia described in the previous section.

In addition to the central uplift outcrops of the Eleanor River Formation that contain black chert, clasts of black chert are present in lithic breccia and impact melt rock dykes. Due to

its colour, black chert is easily identified at hand sample-scale and is distinct at thin section-scale.

In plane-polarized light, black chert appears orange-brown in colour or “toasted” (Fig. 3-16) compared to white chert that is colourless and therefore “untoasted”. Microcrystalline chert grains tend to be completely toasted or untoasted but in rare occurrences both may be present in the same clast (Fig. 3-16A). When viewed using backscattered electron imagery, the toasted chert areas appear rougher with more pitting, contrasting with the smoother adjacent untoasted chert (Fig. 3-16). There is no detectable difference in composition between the toasted and untoasted areas of chert based on quantitative WDS analyses. The differences between the two areas of chert are visual and textural in nature as they are identical in composition.

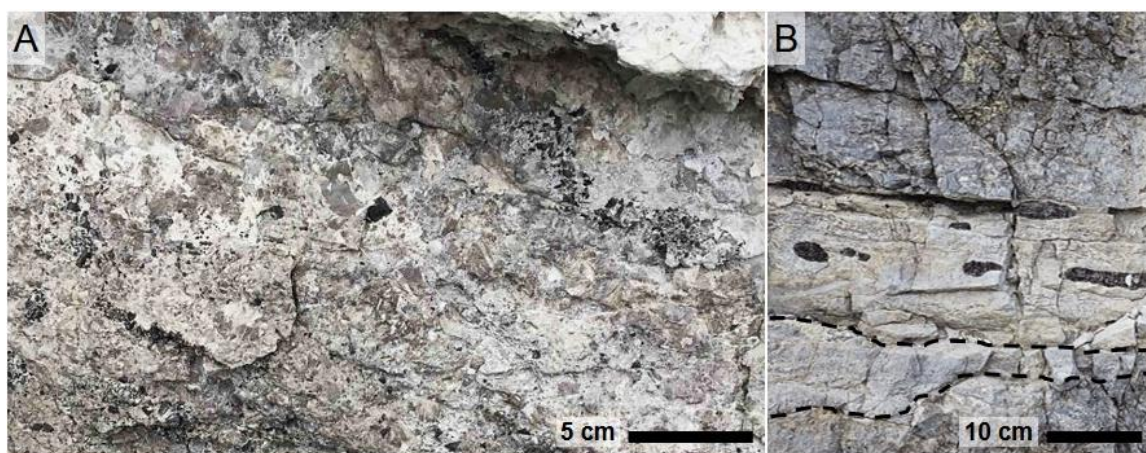


Figure 3-15. Occurrences of black chert in the Eleanor River Formation. A) Brecciated area within the Houghton River valley with abundant black chert. B) Large rounded black chert nodules are prominent within the middle layer. An impact melt rock dyke is directly below this layer, outlined by black dashed lines.

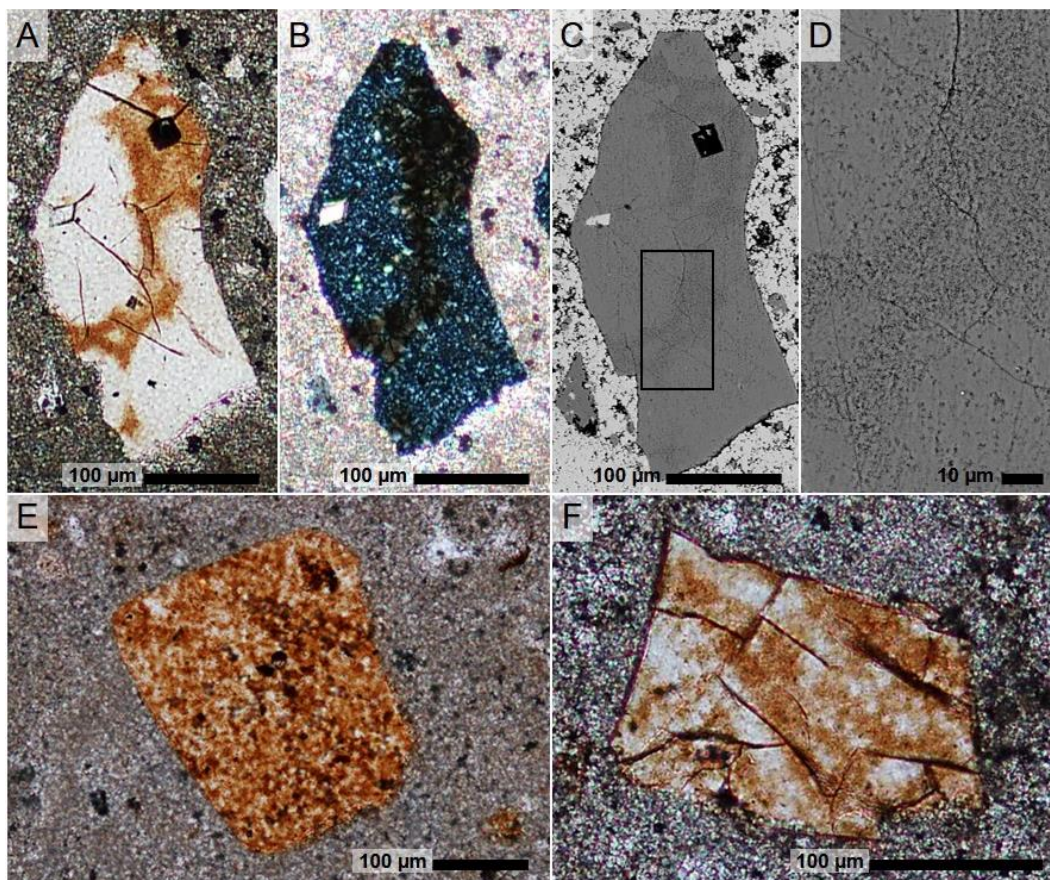


Figure 3-16. Toasted chert has a brown appearance when observed in thin section. A–D) Partially toasted chert clast viewed by different methods to highlight the differences between the colourless untoasted areas and brown toasted areas of the clast as shown in plane-polarized light (A); sample 16-1001. A) Plane-polarized light photomicrograph of chert surrounded by calcite-rich groundmass. B) Cross-polarized light. C) Backscattered electron imagery shows a slight texture change between the two areas of the clast. Box outlines view provided in (D). D) Area corresponding to the toasted area of the clast is more pitted than the untoasted area. E) Chert clast has a fully toasted appearance; sample 16-1038. F) Chert clast is toasted and fractured; sample 16-1026.

3.5 Discussion

3.5.1 Impact-related features

Impact-generated dykes identified at the Houghton impact structure may contain notable features such as variations in mechanical twinning or black chert. Neither of these features

are specific to a certain dyke material i.e., lithic breccia or impact melt rock, as they can be found in both.

Variation in mechanical twinning of calcite has been examined and correlated with changes in temperature (Burkhard 1993) and through experimental work by Lindgren et al. (2013) that investigated the peak shock pressure threshold required to generate calcite twins and found they begin to form ~110 to 480 MPa. As shown in samples from Haughton in Figure 3-2, calcite twins have a range of appearances. Type I calcite twins can form at temperatures <200°C and with increasing temperature and deformation, Type IV calcite twins can form at >250°C (Burkhard 1993). Twin formation can also depend on factors such as grain size, crystallographic orientation, and porosity of the host rock (Burkhard 1993; Lindgren et al. 2013) so it is not a straightforward relationship. While the range in appearance of calcite twins is interesting, mechanical twinning is not a reliable diagnostic feature to identify shocked carbonates as twinning occurs naturally as a deformation mechanism (Burkhard 1993).

The Eleanor River Formation on Devon Island is a limestone unit that can contain abundant white chert nodules (Thorsteinsson and Mayr 1987). White chert nodules may also occur in lower stratigraphic units, e.g., the Cape Clay Formation, or higher stratigraphic units e.g., the Thumb Mountain Formation (Thorsteinsson and Mayr 1987). The abundance of white chert nodules within the sedimentary target sequence of the Haughton impact structure makes the occurrence of black chert within the Eleanor River Formation in the central uplift region of the impact structure a curious observation. Compositional difference was ruled out as the cause for colour change. In thin section under plane-polarized light, the chert clasts that appear orange-brown in colour are described as toasted which correspond with black chert clasts. Comparing the differences between the toasted and untoasted or colourless chert there are parallel observations that can be made with toasted quartz from other terrestrial impact structures.

Toasted quartz was first described in quartz from the Manson impact structure and thought to be the result of fluid inclusions generated along the recrystallized glass of planar deformation features, or PDFs (Short and Gold 1996; Whitehead et al. 2002). The fluid

inclusions enhance the scattering of transmitted light which results in a brown or orange-brown colour to the quartz (Whitehead et al. 2002). The origin of toasted quartz was revisited by Ferrière et al. (2009) and their conclusions suggested that toasted quartz exhibits a higher quantity of vesicles compared with untoasted quartz that scatter transmitted light, which is similar to previous findings. The main difference found by Ferrière et al. (2009) in revisiting the origins of toasted quartz is that the vesicles are unrelated to recrystallized glass associated with PDFs, as was proposed by Whitehead et al. (2002).

In backscattered electron images, toasted chert from Haughton has a more porous texture (Fig. 3-16) than untoasted chert which is consistent with the sponge-like texture observed in toasted quartz (Ferrière et al. 2009). Shock metamorphism conditions required to generate toasted quartz have previously been identified at Haughton as toasted quartz has been reported in classes 2 through 4 of impact metamorphosed sandstones collected from crater-fill impact melt rocks (Osinski 2007). Toasted quartz has been identified from at least 26 terrestrial impact structures (Ferrière et al. 2009; Short and Gold 1996; Whitehead et al. 2002) but this is the first report of toasted chert from an impact structure. In hand samples, toasted quartz takes on a white chalky appearance but is not the same as milky quartz (Short and Gold 1996; Whitehead et al. 2002). The colour change of chert from white to black at Haughton could be an effect of grain size as chert is a microcrystalline form of quartz. Based on the observations and parallels with toasted quartz, the black chert in the central uplift suggests the colour change is a result of increased exposure to shock.

3.5.2 Dyke formation

Impact-generated dykes throughout the Haughton impact structure are diverse and this is reflected in the composition and state (i.e., lithic breccia or impact melt rock) among dykes. Dykes are exposed near the edge of the central uplift and toward the rim of the impact structure (Fig. 3-1). Based on cratering models (e.g., Lambert 1981; Osinski and Spray 2005) and more eroded terrestrial impact structures, such as Tunnunik (Chapter 2), dykes are found throughout the central uplift within the floor of an impact structure. Despite extensive crater-fill deposits that blanket the central area of Haughton, many of the dykes

identified in this study were found within the central uplift (Fig. 3-1). The dykes examined by Bischoff and Oskierski (1988) show a similar distribution as this study.

Several lithic breccia dykes are associated with faults or bedding planes within the target rock. Faults can be initiated during several points during the impact cratering process. The first faults are created during the excavation stage of crater formation which are related to the expanding transient cavity and release of pressure following the shock wave (e.g., Lambert 1981). Subsequent collapse of the unstable transient cavity during the modification stage creates new faults, especially toward the rim region of the crater. The sharp, and generally straight, contact between lithic dykes and host rock indicate a dynamic origin for lithic dykes (Bischoff and Oskierski 1988). The majority of lithic dykes examined in this study are monomict, indicating the lithic material was not transported great distances and were derived from a single unit within the target sequence. Overall, the monomict breccias do not show preferred alignment within the dykes which suggests flow within the dyke was not strong enough to orient clasts with elongated shapes. These autochthonous dykes represent the uppermost portion of the dyke and as they continue deeper into the crater floor, more clasts were likely incorporated into the dyke to change the dyke from monomict to polymict. We suggest several dykes examined, specifically the sulfate-bearing breccias, were determined to be polymict as a result of these dykes being located near contacts between units and had a short transport distance.

From the single thin section from the quartz-cemented dyke, it is not clear if the quartz cement is widespread throughout the dyke or just happened to be more localized where the sample was collected. What can be inferred based on the clasts is there was more transport within this dyke since the dolomite and calcite clasts do not match the microfossil-bearing limestone host rock. The absence of microfossils within the calcite clasts makes this an allochthonous breccia which differs from the autochthonous monomict breccias found within the impact structure. The slight anomaly in calcite composition suggests the rounded calcite clasts are actually melted calcite globules that had limited mixing with the surrounding silicate cement (Osinski et al. 2008a). Quartz-cemented breccias have been reported from other locations in the Haughton impact structure (Osinski et al. 2005c). These occurrences are associated with hydrothermal activity and have a different

appearance in hand sample and thin section compared to sample 00-011, the quartz-cemented carbonate breccia in this study. In hand sample and thin section, the quartz cement is prominent with large interlocking crystals visible in thin section compared to sample 00-011 where the cement is not resolvable even using optical microscopy.

Impact melt rocks are generated following the passage of the rarefaction wave and decompression within the target (Grieve et al. 1977; Osinski et al. 2018). Dykes containing impact melt rocks would then be emplaced during the excavation stage as impact melt is injected downward and outward into fractures in the crater floor and walls (Osinski et al. 2018). At Haughton, the crater floor within the central uplift area is not exposed but the Haughton River valley does expose impact melt rock dykes near the edge of the present-day extent of crater-fill deposits. The contact between melt rock dykes and host rock is not as sharp as the contacts observed with lithic breccia dykes and the edge of the melt rock dykes are more irregular and less straight than the lithic dykes. This observation could be due to the lower viscosity of carbonate-rich melt rocks (Jones et al. 2013) which would allow the melts to fill irregular fractures with less erosion of the host rock. The monomict clast composition within the melt rock dykes indicates the injection of these dykes is not simply an extension of the crater-fill impact melt rock which contains clasts from the entire target sequence. Since the impact melt rock dykes have only been identified within the Eleanor River Formation to date, it remains unclear if the clasts within the dykes always match the host formation. To answer this question, impact melt rock dykes would need to be identified in additional locations around the edge of the crater-fill deposits where the host formations include the Bay Fiord Formation, Thumb Mountain Formation, and Allen Bay Formation (Osinski et al. 2005a).

3.5.3 Clast-rich impact melt rocks

Clast-rich impact melt rocks have been associated with the Haughton impact structure as crater-fill impactite deposits since their re-examination and reclassification in 2001 (Osinski and Spray 2001). Before this time the Haughton crater-fill deposits were described as fragmental or clastic breccia (Redeker and Stöffler 1988). The crater-fill impact melt rocks at Haughton are carbonate-rich, unlike most impact melt rocks from terrestrial impact structures which originate from crystalline target rocks. Deposits of impact melt rocks were

later identified in the crater rim region and interpreted as ejecta deposits by Osinski et al. (2005b). This study has added a third occurrence of impact melt rocks at the Haughton impact structure which are located in dykes exposed near the southeast edge of the crater-fill deposits in the Haughton River valley (Fig. 3-1). Carbonate-rich melt rocks have been reported from a number of impact sites including the Ries and Chicxulub impact structures (e.g., Graup 1999; Jones et al. 2000; Osinski et al. 2008a).

The impact melt rocks described here from impact-generated dykes have similarities and differences with the crater-fill deposits at Haughton. The primary difference is crater-fill impactites contain clasts from all units in the target sequence down to and including the crystalline basement (Osinski and Spray 2001) whereas impact melt rocks in the dykes only contain clasts from the Eleanor River Formation. The crater-fill impactites are currently found up to ~5 km from the centre of the impact structure and have a current maximum thickness of ~125 m (Osinski and Spray 2001). The pale grey impact melt rocks near the southwest rim of the impact structure are ejecta and have a resemblance to the crater-fill impactites but are not identical and differ in groundmass and clast composition. The groundmass of crater rim impactites is up to ~60 vol% calcite, <10 vol% impact melt glass, and no anhydrite whereas the crater-fill impactites are more diverse with <10 to >50 vol% calcite, <0.5 to ~40 vol% silicate impact melt glass, and can have ~30 to 60 vol% anhydrite (Osinski et al. 2005b). As previously noted, crater-fill impactites contain clasts from the entire target sequence while the clasts in the crater rim impactites are mainly limestone and dolostone with sandstone and evaporite clasts rare and crystalline clasts are absent (Osinski et al. 2005b).

Based on these modal compositions, the dyke impact melt rocks more closely resemble the pale grey crater rim impactites than the crater-fill deposits. While the dyke melt rocks are more similar to the pale grey crater rim impactites with a calcite-rich groundmass but without the impact melt glass (Table 3-2), several key differences remain. Clast-wise, the dykes closely resemble the composition of the Eleanor River Formation where dolostone clasts are rare and chert is more common compared to the crater rim impactites (Osinski et al. 2005b). The overall texture and appearance of the impact melt rock dykes is the most obvious difference, especially at hand sample-scale, with the presence of vesicles and

cavities in the groundmass of dyke impact melt rocks. Vesicles and cavities are rare in both the crater rim and crater-fill impact melt rocks. The only mention of vesicles observed in crater-fill or crater rim impactites are specifically within silicate impact melt glass and not within the calcite groundmass (Osinski et al. 2005b).

Additional physical differences between dyke impact melt rocks and impact melt rocks from crater-fill and crater rim deposits include 1) the groundmass in dyke melt rocks is more difficult to break apart than crater-fill deposits, and 2) in thin section, the aphanitic melt rock groundmass is finer in dykes than crater-fill or crater rim samples. These differences could relate to the cooling rate of the melt rock at each location. Since the dyke impact melt rocks are finer grained, it suggests they cooled more rapidly. Heat should conduct more rapidly from the melt rock in the narrow dykes (Osinski et al. 2018). Conversely, the thicker crater-fill impact melt rocks, originally ~200 m thick, would have taken longer to cool to ambient temperatures on the order of several thousand years, based on evidence from post-impact hydrothermal systems present within the Haughton impact structure (Osinski et al. 2005c).

3.5.4 Comparison with other impact structures

The aphanitic texture of the impact melt rock dykes at Haughton is comparable to aphanitic melt rocks described from other impact structures (Osinski et al. 2018). The Haughton impact melt rock dykes also contain lithic and mineral clasts as well as shocked clasts in the form of silicate glass and shocked chert. The main difference between the melt rocks from Haughton and most other impact structures is composition, where the Haughton melt rocks are carbonate-rich with the melt rock dykes being more specifically calcite-rich. While calcite typically does not form igneous textures in impact structures, mantle-derived carbonatites have a significant carbonate fraction and are the most comparable non-impact source of igneous carbonates (Osinski et al. 2018). Textures observed in the impact melt rock dykes are not as varied or complex in composition as can be found in carbonatites (e.g. Chakhmouradian et al. 2016), especially when the bulk of the melt rock dyke groundmass has a calcite composition.

What makes the dyke melt rocks most distinct from the crater-fill and crater rim melt rock

deposits is the presence of vesicles. As described earlier, not all the holes in the dyke melt rocks are vesicles but instead some appear as cavities left behind from weathered out clasts. Focusing here on the more rounded silicate glass remnant-free holes, these vesicles have a probable origin similar to vesicles formed in crystalline impact melts.

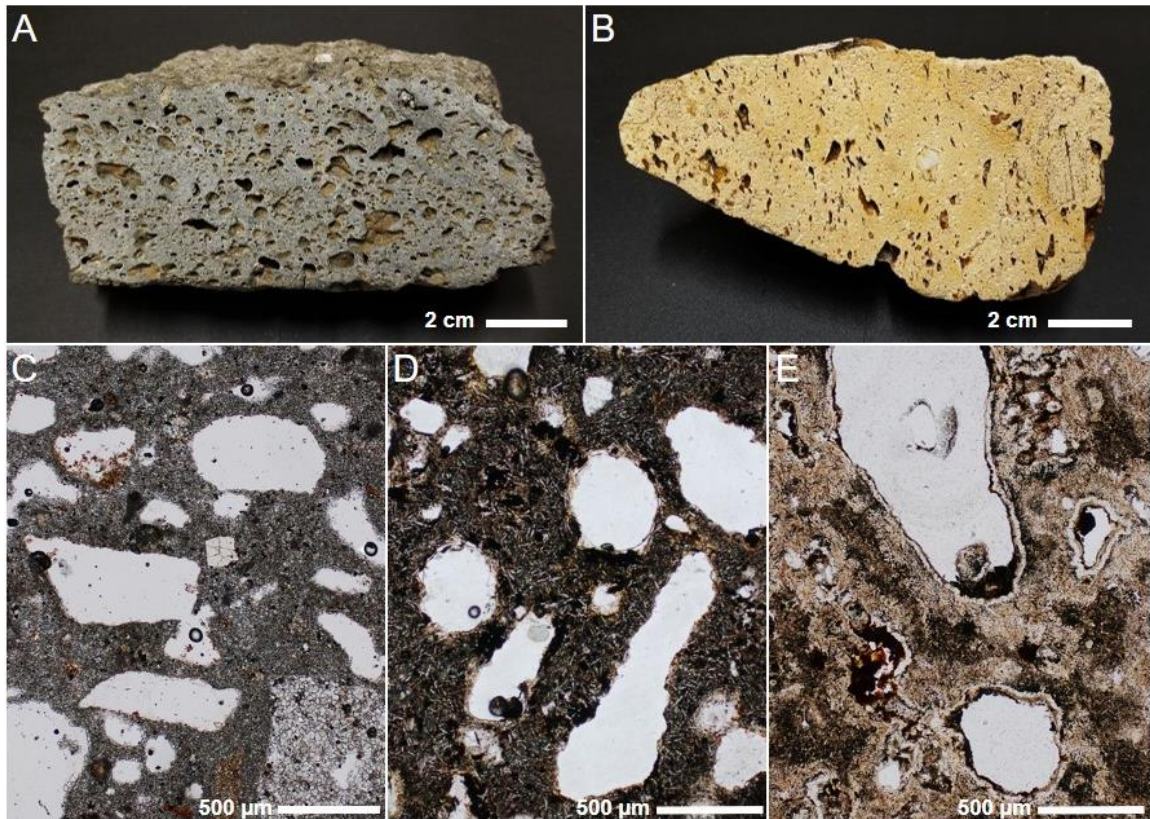


Figure 3-17. Comparison of vesicular impact melt rocks from terrestrial impact structures. A) Hand sample of vesicular melt rock from Côté Creek locality, Mistastin. B) Hand sample of vesicular melt rock from Babaudus locality, Rochechouart. C) Clast-rich impact melt rock from the Haughton impact structure; sample 16-1003, see Figure 3-11B. D) Clast-poor impact melt rock from the Mistastin impact structure; sample MM 11-23A. E) Clast-poor impact melt rock from the Rochechouart impact structure; sample RO-01-043.

The overall textures and morphology of the impact melt rocks found in dykes resemble vesicular melt rocks from the Mistastin and Rochechouart impact structures. Mistastin is a 28 km impact structure in northern Labrador, Canada (Marion and Sylvester 2010) and Rochechouart, located in western France, is slightly larger at 32 km (Osinski and Ferrière

2016). Visually, the features of the clast-poor vesicular impact melt rocks from Mistastin and Rochechouart² (Figs. 3-17A, B) have a resemblance to the melt rock dykes described for Haughton (Figs. 3-10 and 3-11). These impact melt rocks consist of an aphanitic groundmass of interlocking grains or crystallites as well as μm - to mm-sized vesicles (Fig. 3-17). The main difference among the vesicular melt rocks from these three impact structures is their composition. Highly vesicular silicate impact melt rocks from Mistastin are ~53.36 wt% SiO_2 and primarily anorthositic in composition (Grieve 1975; Marion and Sylvester 2010); whereas at Rochechouart the impact melt rocks are ~66.0 wt% SiO_2 and predominantly comprised of K-feldspar (Cohen et al. 2017; Sapers et al. 2014). As shown in the results above (Table 3-2), the impact melt rocks from dykes at Haughton are calcite-rich. The differences among these melt rock compositions reflect the target lithologies of each impact structure, which helps explain the variation in clast volume. Crystalline target lithologies have a different cooling rate than sedimentary lithologies which in turn affects the ability of an impact melt to assimilate clasts (Osinski et al. 2008b). Impact melt generated in a sedimentary target, such as Haughton, will quench faster and assimilate fewer clasts than crystalline targets like Mistastin or Rochechouart (Osinski et al. 2008b). This can be seen in the impact melt rock dykes discussed here, which are typically clast-rich and would likely have quenched more rapidly than the crater-fill deposits in order to preserve vesicles. The confining nature of the dykes could also help preserve any trapped air in the melt rocks as the dykes cooled.

3.6 Conclusions

The diversity within the suite of impact-generated carbonate-rich dykes examined in this study highlights the complexity of dyke formation in the cratering process. Examining new and previously uncharacterized dykes has expanded the knowledge and range of impactites at the Haughton impact structure to include impact melt rock dykes. The melt rocks within these dykes contain vesicles which is the first report of vesicles present in the groundmass of a carbonate-rich impact melt rock from Haughton. New impact related products

² At both the Mistastin and Rochechouart impact structures there is a diverse range of impact melt rocks, impact melt-bearing breccias, and lithic breccias. The comparisons of impact melt rocks between these impact structures and Haughton in this section are specific to the highly vesicular impact melt rocks as noted in the text and comparisons do not necessarily apply to all impactites for a given impact structure.

associated with this impact site were identified and includes toasted chert. These impactites and products provide further insights into the products generated during the impact event and present in a well-preserved impact structure.

3.7 References

- Bischoff L., and Oskierski W. 1987. Fractures, pseudotachylite veins and breccia dikes in the crater floor of the Rochechouart impact structure, SW-France, as indicators of crater forming processes. In *Research in Terrestrial Impact Structures*, edited by Pohl J. Braunschweig: Friedrich Vieweg and Sohn. pp. 5–29.
- Bischoff L., and Oskierski W. 1988. The surface structure of the Haughton impact crater, Devon Island, Canada. *Meteoritics* 23:209–220.
- Burkhard M. 1993. Calcite twins, their geometry, appearance and significance as stress-strain markers and indicators of tectonic regime: a review. *Journal of Structural Geology* 15:351–368.
- Caty J.-L., Chown E. H., and Roy D. W. 1976. A new astrobleme: Ile Rouleau structure, Lake Mistassini, Quebec. *Canadian Journal of Earth Sciences* 13:824–831.
- Chakhmouradian A. R., Reguir E. P., Zaitsev A. N., and Chakhmouradian A. R. 2016. Calcite and dolomite in intrusive carbonatites. I. Textural variations. *Mineralogy and Petrology* 110:333–360.
- Cohen B. E., Mark D. F., Lee M. R., and Simpson S. L. 2017. A new high-precision $^{40}\text{Ar}/^{39}\text{Ar}$ age for the Rochechouart impact structure: At least 5 Ma older than the Triassic–Jurassic boundary. *Meteoritics & Planetary Science* 52:1600–1611.
- Dressler B. O., and Sharpton V. L. 1997. Breccia formation at a complex impact crater: Slate Islands, Lake Superior, Ontario, Canada. *Tectonophysics* 275:285–311.
- Dressler B. O., and Reimold W. U. 2004. Order or chaos? Origin and mode of emplacement of breccias in floors of large impact structures. *Earth-Science Reviews* 67:1–54.

- Ferrière L., Koeberl C., Reimold W. U., Hecht L., and Bartosova K. 2009. The origin of “toasted” quartz in impactites revisited. *40th Lunar and Planetary Science Conference Abstract #1751*.
- Flemming R. L. 2007. Micro X-ray diffraction (μ XRD): a versatile technique for characterization of Earth and planetary materials. *Canadian Journal of Earth Sciences* 44:1333–1346.
- Graup G. 1999. Carbonate-silicate liquid immiscibility upon impact melting: Ries Crater, Germany. *Meteoritics & Planetary Science* 34:425–438.
- Grieve R. A. F. 1975. Petrology and chemistry of the impact melt at Mistastin Lake crater, Labrador. *Geological Society of America Bulletin* 86:1617–1629.
- Grieve R. A. F., Dence M. R., and Robertson P. B. 1977. Cratering processes: As interpreted from the occurrence of impact melts. In *Impact and Explosion Cratering*, edited by Roddy D. J., Pepin R. O., and Merrill R. B. New York: Pergamon Press. pp. 79–814.
- Hickey L. J., Johnson K. R., and Dawson M. R. 1988. The stratigraphy, sedimentology, and fossils of the Haughton Formation: A post-impact crater-fill, Devon Island, N.W.T., Canada. *Meteoritics* 23:221–231.
- Jones A. P., Claeys P., and Heuschkel S. 2000. Impact melting of carbonates from the Chicxulub Crater. In *Impacts and the Early Earth, Lecture Notes in Earth Sciences*, edited by Gilmour I., and Koeberl C. Springer-Verlag, Berlin-Heidelberg-New York. pp. 343–361.
- Jones A. P., Genge M., and Carmody L. 2013. Carbonate melts and carbonatites. *Reviews in Mineralogy and Geochemistry* 75:289–322.
- Lambert P. 1981. Breccia Dikes: Geological constraints on the formation of complex craters. In *Multi-ring Basins, Proc. Lunar Planet. Sci.*, edited by Schultz P. H., and Merrill R. B. pp. 59–78.

- Lindgren P., Price M. C., Lee M. R., and Burchell M. J. 2013. Constraining the pressure threshold of impact induced calcite twinning: Implications for the deformation history of aqueously altered carbonaceous chondrite parent bodies. *Earth and Planetary Science Letters* 384:71–80.
- Marion C. L., and Sylvester P. J. 2010. Composition and heterogeneity of anorthositic impact melt at Mistastin Lake crater, Labrador. *Planetary and Space Science* 58:552–573.
- Metzler A., Ostertag R., Redeker H. J., and Stoffler D. 1988. Composition of the crystalline basement and shock metamorphism of crystalline and sedimentary target rocks at the Haughton impact crater, Devon Island, Canada. *Meteoritics* 23:197–207.
- Osinski G. R., and Spray J. G. 2001. Impact-generated carbonate melts: Evidence from the Haughton structure, Canada. *Earth and Planetary Science Letters* 194:17–29.
- Osinski G. R., and Spray J. G. 2003. Evidence for the shock melting of sulfates from the Haughton impact structure, Arctic Canada. *Earth and Planetary Science Letters* 215:357–370.
- Osinski G. R., Lee P., Spray J. G., Parnell J., Lim D. S. S., Bunch T. E., Cockell C. S., and Glass B. 2005a. Geological overview and cratering model for the Haughton impact structure, Devon Island, Canadian High Arctic. *Meteoritics & Planetary Science* 40:1759–1776.
- Osinski G. R., Spray J. G., and Lee P. 2005b. Impactites of the Haughton impact structure, Devon Island, Canadian High Arctic. *Meteoritics & Planetary Science* 40:1789–1812.
- Osinski G. R., and Spray J. G. 2005. Tectonics of complex crater formation as revealed by the Haughton impact structure, Devon Island, Canadian High Arctic. *Meteoritics & Planetary Science* 40:1813–1834.
- Osinski G. R., Lee P., Parnell J., Spray J. G., and Baron M. 2005c. A case study of impact-induced hydrothermal activity: The Haughton impact structure, Devon Island, Canadian High Arctic. *Meteoritics & Planetary Science* 40:1859–1877.

- Osinski G. R. 2007. Impact metamorphism of CaCO₃-bearing sandstones at the Haughton structure, Canada. *Meteoritics & Planetary Science* 42:1945–1960.
- Osinski G. R., Spray J. G., and Grieve R. A. F. 2008a. Impact melting in sedimentary target rocks: An assessment. In *The Sedimentary Record of Meteorite Impacts, Special Paper 437*, edited by Evans K. R., Horton W., King Jr. D. K., and Morrow J. R. Geological Society of America, Boulder, CO. pp. 1–18.
- Osinski G. R., Grieve R. A. F., Collins G. S., Marion C., and Sylvester P. 2008b. The effect of target lithology on the products of impact melting. *Meteoritics & Planetary Science* 43:1939–1954.
- Osinski G. R., and Ferrière L. 2016. Shatter cones: (Mis)understood? *Science Advances* 2, e160061:1–10.
- Osinski G. R., Grieve R. A. F., Bleacher J. E., Neish C. D., Pilles E. A., and Tornabene L. L. 2018. Igneous rocks formed by hypervelocity impact. *Journal of Volcanology and Geothermal Research* 353:25–54.
- Pontefract A., Osinski G. R., Cockell C. S., Moore C. A., Moores J. E., and Southam G. 2014. Impact-generated endolithic habitat within crystalline rocks of the Haughton impact structure, Devon Island, Canada. *Astrobiology* 14:522–33.
- Redeker H. J., and Stöffler D. 1988. The allochthonous polymict breccia layer of the Haughton impact crater, Devon Island, Canada. *Meteoritics* 23:185–196.
- Robertson P. B., and Grieve R. A. F. 1978. The Haughton impact structure. *Meteoritics* 13:615–619.
- Sapers H. M., Osinski G. R., Banerjee N. R., Ferrière L., Lambert P., and Izawa M. R. M. 2014. Revisiting the Rochechouart impact structure, France. *Meteoritics & Planetary Science* 49:2152–2168.
- Short N. M., and Gold D. P. 1996. Petrography of shocked rocks from the central peak at the Manson impact structure edited by Koeberl C., and Anderson R. R. *Special Paper*

- *Geological Society of America* 302:245–265.

Thorsteinsson R., and Mayr U. 1987. *The Sedimentary Rocks of Devon Island, Canadian Arctic Archipelago*, Memoir 411. Geological Survey of Canada.

Whitehead J., Spray J. G., and Grieve R. A. F. 2002. Origin of “toasted” quartz in terrestrial impact structures. *Geology (Boulder)* 30:431–434.

Woodcock N. H., and Mort K. M. 2008. Classification of fault breccias and related fault rocks. *Geological Magazine* 145:435–440.

Young K. E., Van Soest M. C., Hodges K. V., Watson E. B., Adams B. A., and Lee P. 2013. Impact thermochronology and the age of Haughton impact structure, Canada. *Geophysical Research Letters* 40:3836–3840.

Chapter 4

4 Shock effects in dolomite and calcite from the Haughton impact structure, Canada, using X-ray diffraction and Rietveld refinement

4.1 Introduction

Shock metamorphism is a process that occurs in rocks that have been subjected to shock pressures generated by hypervelocity impacts. Shock effects produced by shock metamorphism are the primary identifiers used to confirm a new impact structure and these effects are typically microscopic. The only macroscopic evidence of shock metamorphism manifested in impact structures are shatter cones and depending on the erosion level or target rock type, may not be well-preserved or exposed for a given impact structure. Shatter cones develop in rocks associated with meteorite impact structures where shock waves generated during the impact event generate striated conical fractures in the target rock (e.g., Baratoux and Reimold 2016; Dietz 1959; Osinski and Ferrière 2016). Microscopic evidence of shock metamorphism is more abundant and includes planar fractures (PFs), planar deformation features (PDFs), diaplectic glasses, and high-pressure mineral phases (French and Koeberl 2010). These microscopic shock features are accepted as diagnostic of the silicate minerals quartz and feldspar and represent shock pressures from ~2 GPa (French 1998) up to ~50 GPa (Stöffler et al. 2018).

A range of shock effects have been identified and proposed for other silicate minerals to identify reliable shock features to provide further proof of impact-induced shock metamorphism (e.g., Cavosie et al. 2018; Černok et al. 2019; Stöffler et al. 2018). Identification of shock is a necessary step to confirm a proposed new impact structure (e.g., French and Koeberl 2010) but not all impacts occur in targets with an abundance of silicate minerals. Impact structures in sedimentary targets that are rich in carbonates are often poor in silicates and, therefore, often do not contain any of the accepted microscopic evidence listed above. Carbonates tend to be fine-grained which is conducive to shatter cone formation from shock pressures in the 2–10 GPa range (French 1998). Fresh carbonate surfaces display well-developed shatter cones in the field, however, identification can

become particularly difficult for carbonates as physical and chemical weathering from dissolution of acidic rain waters and erosion can obscure shatter cones and consequently any macroscopic evidence of shock (French and Koeberl 2010). Relying on shatter cones as confirmation for impacts into carbonate-rich targets can result in an impact origin being suggested but not confirmed for a number of sites where shatter cones have not been observed, such as Jephtha Knob, Kentucky, USA (Cressman 1981). Having an alternative shock effect other than shatter cone presence would be highly beneficial in helping to confirm terrestrial impact structures. Shatter cones have also been identified in crystalline rocks that have been exposed to pressures up to 30 to 45 GPa (Sharpton et al. 1996), so the upper pressure limit for carbonate targets could also fall within this range; although this is unclear at present.

At higher pressures, the relative importance of melting versus decomposition is also part of an ongoing debate (e.g., Graup 1999; Hörz et al. 2015; Jones et al. 2000; O'Keefe and Ahrens 1989; Osinski et al. 2008; Stöffler et al. 2013). Indeed, a recent review on shock metamorphism of silicate rocks and sediments (Stöffler et al. 2018) highlights the lack of consensus regarding shock in carbonates and cannot currently offer a classification scheme for carbonates. It is clear more studies are required to fully understand shock metamorphic and melting processes in carbonates.

A method that may offer a way to quantify shock in carbonates is through X-ray diffraction (XRD). Several studies have shown that using XRD to measure lattice strain and strain-related mosaicity in meteorites can help determine shock pressures experienced by the meteorites using the minerals olivine and pyroxene (Izawa et al. 2011; Jenkins et al. 2019; McCausland et al. 2010). The ability to quantify shock in carbonates without depending on the presence of shatter cones would be a valuable tool as XRD would identify changes to the crystal structure of carbonates as a result of exposure to elevated shock pressures. There have been several previous studies that investigated terrestrial carbonate-rich impact structures using XRD in slightly different manners. For example, early work began at the Steinheim and Kara impact structures show increases in peak broadening in XRD patterns by examining full width at half maximum values versus 2θ (Skála and Jakeš 1999). An investigation at the Ries impact structure then determined peak broadening is the result of

a decrease in crystallite size in shocked calcite (Skála 2002). A study at the Sierra Madera impact structure investigated if XRD patterns of shocked carbonates associated with the impact structure could be distinguished from terrestrial tectonic processes (Huson et al. 2009). Most recently, at the Wells Creek impact structure, carbonates were studied via XRD to determine if a relationship exists between shock and depth of samples recovered from the central uplift (Seeley and Milam 2018).

The Houghton impact structure is located on Devon Island, NU, Canada and is a well-preserved complex crater with a diameter of ~23 km (Osinski et al. 2005a). The age of the Houghton impact structure is ~23.5 Ma based on thermochronology of zircon crystals from impact melt rocks (Young et al. 2013). The sedimentary sequence at Houghton consists of Ordovician to Silurian-aged rocks that include limestone, dolostone, sandstone, and evaporites, with carbonates comprising ~75–80% of the target (Osinski et al. 2005a). Limestone formations within the Houghton impact structure include Eleanor River, Thumb Mountain, and Allen Bay Lower Member. Dolostone formations include Bay Fiord Member C/D and Allen Bay Middle Member. For descriptions of formations and a detailed geologic map of the Houghton impact structure see Thorsteinsson and Mayr (1987) and Osinski et al. (2005). Older rocks down to the Precambrian crystalline basement have been identified as clasts within the impact melt rocks of the crater-fill deposits (Osinski et al. 2005b). Crater-fill deposits cover most of the central uplift of the impact structure with discontinuous deposits of impact melt rock present to a radius of ~7.5 km (Osinski and Spray 2001). The well-preserved state of this impact structure includes the preservation of megablocks and remnants of the continuous ejecta blanket near the rim (Osinski et al. 2005b).

Shatter cones at the Houghton impact structure are found in the target rocks of the central uplift, megablocks in the ballistic ejecta blanket, and as clasts in the crater-fill impact melt rocks (Osinski and Spray 2006). Within the central uplift, shatter cones are found in situ up to approximately 4.5 km from the centre of the impact structure (Osinski and Ferrière 2016). Shatter cones present in ballistic ejecta and crater-fill deposits represent shock pressures and conditions from their original position within the target sequence and not the location where the sample was collected post-impact.

This study investigates the effect of shock metamorphism in carbonate target rocks at pressures that generate shatter cones at this well-preserved and exposed complex impact structure. Whole rock powders of in situ target dolostone and limestone were examined as well as shatter cones collected from the impact melt rock crater-fill and ballistic ejecta deposits in order to identify evidence of shock metamorphism at crystal structure scales.

4.2 Samples and methods

4.2.1 Suite 1: In situ carbonate target rocks

Data were collected from two sample suites. The first suite includes 14 in situ carbonate target rocks collected from limestone and dolostone outcrops inside and outside the shatter cone distribution of Osinski and Ferrière (2016) as well as beyond the rim of the Haughton impact structure (Fig. 4-1). Rocks collected near and beyond the rim represent low to unshocked target samples. One of these samples was collected ~160 km east of the impact structure near the Devon Island ice cap. Shocked target samples from the central uplift were difficult to acquire since most of the central area of the impact structure is comprised of impact melt rock, leaving limited outcrops of exposed target rock. From available outcrops within the central uplift, samples were selected that displayed shatter cones to establish they experienced a certain level of shock prior to analysis when possible (Fig. 4-2). Suite 1 samples form a general northwest to southeast transect across the impact structure collected at roughly 1 km intervals (Fig. 4-1). Samples from similar distances from the centre of structure represent target rock from different units and/or composition to provide the best range shock that could be acquired.

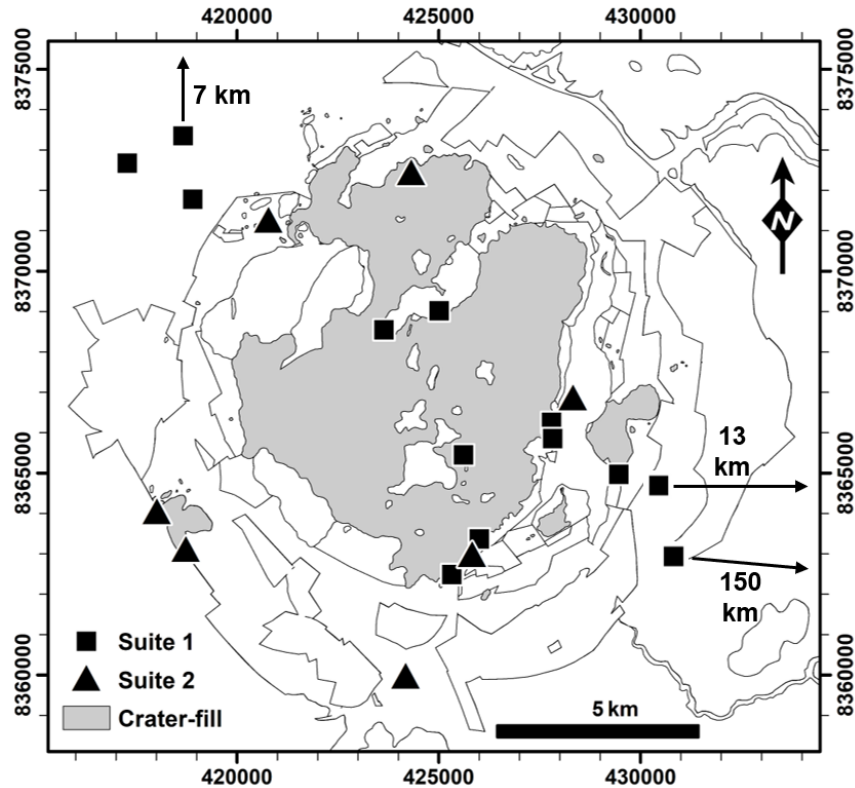


Figure 4-1. Location of samples from the Haughton impact structure with outlines of geological formations shown. Suite 1 consists of in situ samples collected from known outcrop locations while suite 2 consists of shatter cone clasts and fragments from crater-fill and ballistic ejecta deposits. Three suite 2 samples were collected from at the northernmost site. Three suite 1 samples are located beyond the visible extent of the map are indicated by an arrow for direction with approximate distance. UTM grid with Easting and Northing at 1000 m intervals for Zone 16.



Figure 4-2. Example shatter cones from the central uplift of the Haughton impact structure in suite 1. A) Sample 99-063B. B) Sample 02-139. C) Sample 06-093. Scale bars are 2 cm.

Bulk rock samples were powdered wet by hand using a mortar and pestle for 30 minutes under ethanol; ethanol reduces friction and heat that may be generated during grinding to prevent excess strain being introduced to samples (Hill and Madsen 2002). Coarse samples were ground for an additional 15 minutes to ensure grain size of powder was $\sim 5 \mu\text{m}$. Once dry, powders were reverse mounted onto 220 grit sandpaper using a 3.5 by 5.0 cm large volume aluminum sample holder for backpacking samples. This technique involves tightly packing the $\sim 5 \mu\text{m}$ powder dry into a 1.85 by 2.00 cm opening 2 mm deep in an aluminum sample holder backed by the sandpaper. Once there is enough powder to fill and be flush with the upper surface of the metal holder, ~ 0.8 g total, a glass slide is taped to cover the powder surface. The glass slide becomes the back of the sample holder and the sandpaper is carefully removed to expose a flat surface of packed powder. The sandpaper provides a slightly rough surface to reduce preferred orientation within the mounted powder as random orientation of the powder gives all orientations the same probability of diffracting (Hill and Madsen 2002). Preferred orientation can cause deviation of reflection intensities to be enhanced or weakened, thereby affecting the quality of the refinement (Klug and Alexander 1974). The reverse mounting method produced better scans than wet mounting on a recessed glass slide with ethanol. Reverse mounting showed less preferred orientation effects and was the preferred method when enough powder is available. Samples were analyzed using a Rigaku DMAX powder diffractometer with Bragg-Brentano geometry, graphite monochromator, and scintillation counter, with operating parameters of $\text{Co K}\alpha_1$ radiation with a 1.78897 \AA wavelength, 40 kV, 35 mA, $0.02^\circ/\text{step}$, 5 s dwell time per step, and a 2θ range from $5\text{--}120^\circ$.

4.2.2 Suite 2: Shatter cone clasts from crater-fill and ballistic ejecta deposits

The second suite consists of seven shatter cones (Fig. 4-3) and one shocked limestone clast that does not exhibit shatter cone morphology from the impact melt rocks crater-fill and one shatter cone from ballistic ejecta deposits. Shatter cones from suite 2 represent allochthonous samples and so their collection location has no direct bearing on shock level. Suite 2 samples, however, can be compared with the in situ samples from suite 1 to assess their relative shock level. Shatter cones form to a certain radius within the transient crater

during crater formation, based on shock pressures generated, which is where suite 2 samples originate. The exact radius of shatter cone formation within the transient crater is not known, due to crater modification processes. What is known is the final distribution of shatter cones which are found to a radius of ~4.5 km from the centre of the impact structure (Osinski and Ferrière 2016). For comparison, all suite 2 samples were collected beyond the current 4.5 km shatter cone distribution (Fig. 4-1).

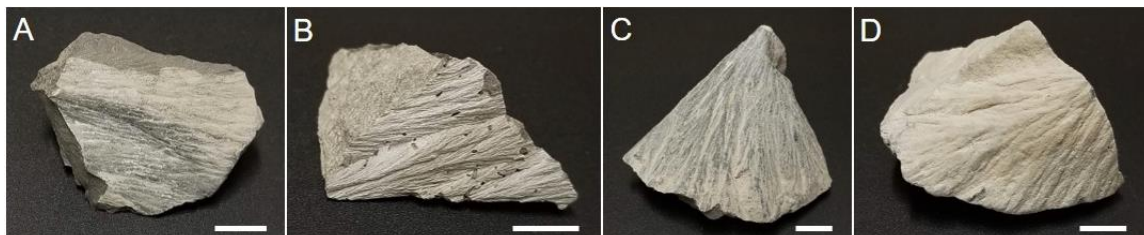


Figure 4-3. Example shatter cone clasts from suite 2. A) Sample 00-019. B) Sample 02-061. C) Sample 02-127. D) Sample 02-128. Scale bars are 1 cm.

Bulk rock samples were powdered wet by hand using a mortar and pestle for 30 minutes under ethanol. Once the powders were dry, powders were wet-mounted with ethanol onto a recessed glass slide using ethanol rather than reverse mounting as done for suite 1 due to limited sample volume. Suite 2 was analyzed using the same equipment and operating parameters as suite 1.

4.2.3 Rietveld refinement

To determine the effects of shock pressures on rocks from both suites, Rietveld refinement of crystal structures to quantify lattice strain were conducted using TOPAS 5 software by Bruker AXS. Refined parameters include background intensity, sample displacement, absorption, scale factor, unit cell dimensions, profile shape PV-TCHZ parameters U, V, W, and X, Beq, Stephen's model trigonal-high for calcite and dolomite, crystal size G (Gaussian), and strain G (Gaussian). Mineral phases present in several wt%, up to ~5 wt%, were not refined on Beq, Stephen's model, crystal size G, or strain G as the errors for these parameters increased significantly as the proportion of the mineral phase declined in the bulk rock sample (e.g., Hill and Howard 1987; Turvey et al. 2018). All refinements were fit from 16°–80° 2 θ with fixed parameters including fifth-order background, and preferred

orientation used spherical harmonics order-8. Refinement sequence of turning on parameters was performed in the same order for all samples. To get the best fit for each mineral phase, starting structural models are noted here for calcite (Markgraf and Reeder 1985; Maslen et al. 1995), dolomite (Althoff 1977; Miser et al. 1987; Reeder and Wenk 1983; Ross and Reeder 1992), quartz (Brill et al. 1939; Glinnemann et al. 1992; Levien et al. 1980), and microcline (Ribbe 1979).

4.3 Results

4.3.1 Powder X-ray diffraction

X-ray diffraction patterns of counts versus 2θ obtained for suite 1 and 2 were divided based on whether the primary mineral phase was calcite or dolomite. Bulk rock samples with a primary calcite or dolomite phase may contain minor quartz and microcline (Fig. 4-4). Patterns for in situ (suite 1) calcite samples (99-063B, 02-139, 06-093, 07-020, 16-1018) collected within the central uplift show more peak broadening than the unshocked sample collected beyond the rim of the impact structure (Fig. 4-5A). Calcite-bearing suite 2 samples also show varying degrees of peak broadening. Peak broadening in dolomite-bearing samples is well-defined between suite 1 and 2 which is attributed to sample location bias as there were no in situ dolomite samples from the central uplift available for analysis (Fig. 4-5B).

Overall, dolomite-bearing samples from the central uplift display more peak broadening than calcite-bearing samples as observed by the merging of the (018) and (116) dolomite peaks at 59° and 60° 2θ compared to the (018) and (116) calcite peaks at 56° and 57° 2θ using Co $K\alpha_1$ radiation (Fig. 4-4). Peaks were selected within this range because there are no overlapping diffraction angles between calcite and dolomite. Once higher angles are compared e.g., between 66° – 81° 2θ , encompassing peaks between (211) and (0,0,12), the specific diffraction angles for these two minerals begin to overlap and become more difficult to recognize. Additionally, peaks begin to broaden naturally as 2θ increases so comparing peak broadening within the 35° – 61° 2θ range or peaks between (104) and (116) is an ideal zone to avoid these issues.

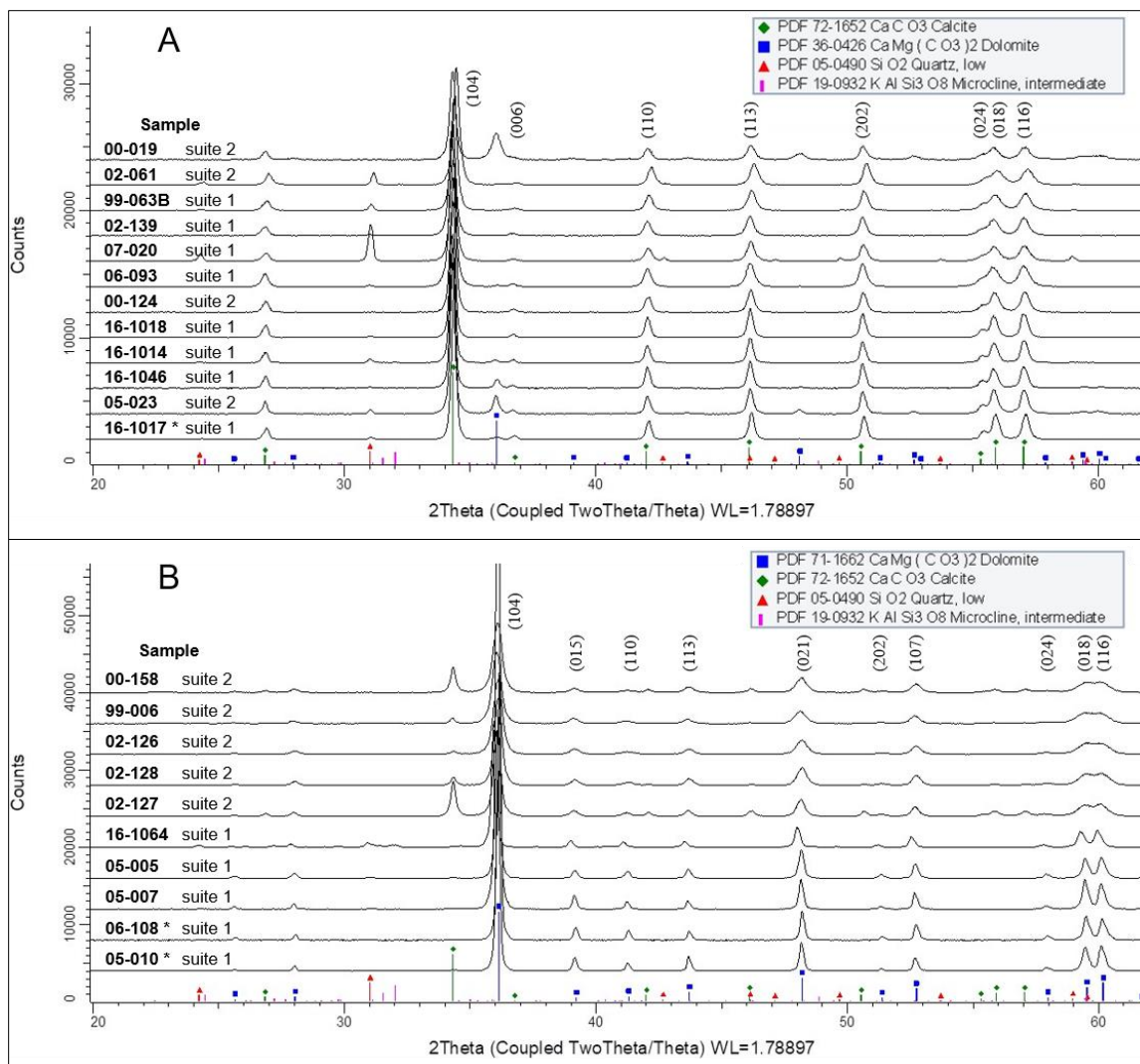


Figure 4-4. X-ray diffraction patterns of powdered samples divided by calcite (A) and dolomite (B) as the primary mineral phase from the Houghton impact structure. Stacked patterns arranged by relative peak broadening. Vertical numbers in brackets above stacks in (A) and (B) indicate Miller Indices (*hkl*) associated with peaks for calcite and dolomite, respectively. Unshocked samples are indicated by (*). A y-offset has been applied to sample patterns for clarity. Analyses were conducted with DIFFRAC.EVA software version 4.2 by Bruker AXS and phases were matched using the ICDD (International Centre for Diffraction Data) database PDF-4+ (2019).

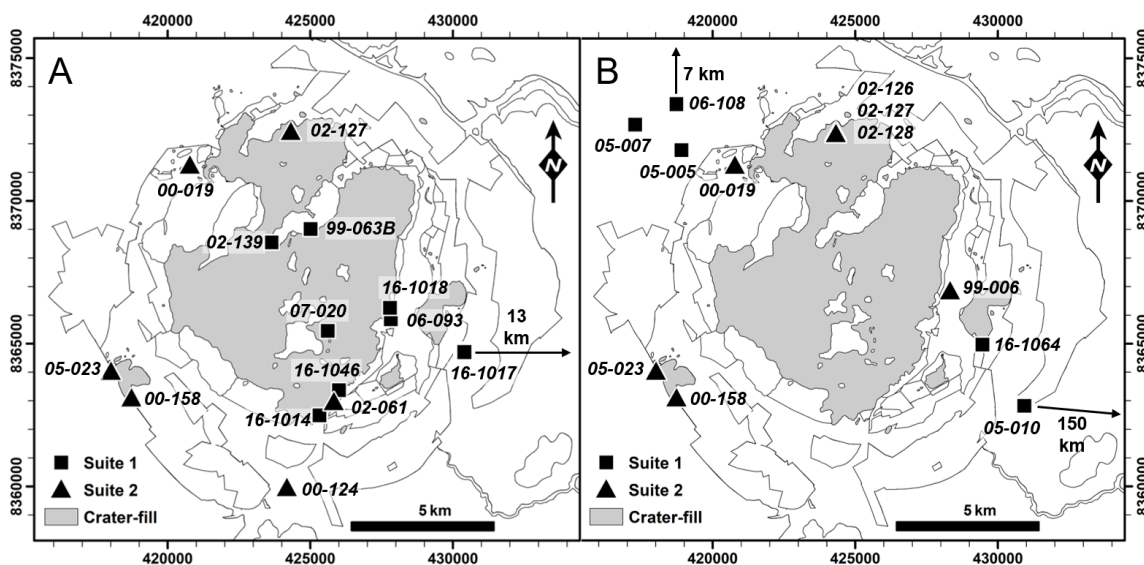


Figure 4-5. Locations of A) calcite-bearing and B) dolomite-bearing samples from the Houghton impact structure. Four samples contain both calcite and dolomite and so appear on both maps (samples 00-019, 00-158, 02-127, and 05-023). UTM grid with Easting and Northing at 1000 m intervals for Zone 16.

4.3.2 Rietveld refinement

Rietveld refinements of powder XRD scans using the software TOPAS 5 were conducted to estimate the modal proportion of each mineral phase within the bulk rock sample suites. Additional outputs of interest from sample refinements include crystallite size and strain as well as d-spacing, 2θ , and intensity values for each Miller Index (hkl).

Based on modal proportions (Table 4-1), the major phase present in suite 1 and 2 samples consist of 80–99 wt% calcite or dolomite. The exceptions to this are samples 00-019 and 07-020 which have nearly equal amounts of calcite and dolomite and up to 31 wt% quartz, respectively. Minor mineral phases occur with ~5 wt% or less if present in a sample. Crystallite size and strain for calcite and dolomite were refined when their weight percent was greater than 10 wt% as weight percent, obtained from Rietveld refinements, is proportional to product of the scale factor with the mass and volume of the unit cell to avoid increased errors when proportions decline below ~10 wt% (Hill and Howard 1987).

Table 4-1. Modal mineral proportions of samples in weight percent with crystal size and lattice strain values for carbonates determined by Rietveld refinement of bulk rock powders from the Houghton impact structure.

Sample	Calcite			Dolomite			Quartz	Microcline
	wt% (error) *	crystal size §, nm (error)	strain % † (error)	wt% (error)	crystal size, nm (error)	strain % (error)	wt% (error)	wt% (error)
99-006 ²	4.7(3)	–	–	91.9(8)	56(8)	0.55(4)	–	3.4(8)
99-063B ¹	96.2(6)	51(7)	0.35(10)	–	–	–	3.8(6)	–
00-019 ²	57.1(15)	52(2)	0.18(8)	42.9(15)	51(10)	0.73(10)	–	–
00-124 ²	99.7(17)	64(6)	0.41(3)	–	–	–	0.3(17)	–
00-158 ²	12.9(10)	85(8)	0.31(3)	87.1(10)	34.8(7)	0.43(3)	–	–
02-061 ²	91.0(10)	71(5)	0.20(5)	–	–	–	4.0(4)	5.0(10)
02-126 ²	1.7(4)	–	–	95(2)	40(4)	0.46(8)	1.7(4)	–
02-127 ²	18.3(7)	72(7)	0.16(8)	81.7(7)	52(3)	0.42(3)	–	–
02-128 ²	4.2(3)	–	–	95.8(3)	52(9)	0.60(6)	–	–
02-139 ¹	99.5(7)	55(6)	0.34(6)	–	–	–	0.5(7)	–
05-005 ¹	1.0(4)	–	–	98.1(18)	71(4)	0.16(3)	1.0(17)	–
05-007 ¹	0.6(5)	–	–	97.7(18)	109(8)	0.19(4)	0.9(17)	0.9(4)
05-010 ¹	0.20(13)	–	–	99.7(4)	81(7)	0.20(3)	0.1(4)	–
05-023 ²	81(2)	80(6)	0.17(7)	13.6(18)	70(7)	0.40(4)	3.901(2)	–
06-093 ¹	99.1(3)	59(5)	0.37(4)	0.52(19)	–	–	0.4(2)	–
06-108 ¹	0.27(10)	–	–	99.5(4)	80(6)	0.11(9)	0.2(4)	–
07-020 ¹	69.0(7)	53.7(15)	0.421(19)	–	–	–	31.0(7)	–
16-1014 ¹	96.6(3)	71(2)	0.282(9)	1.21(11)	–	–	2.2(2)	–
16-1017 ¹	92.6(8)	54.2(10)	0.12(4)	3.2(5)	–	–	2.0(5)	2.2(3)
16-1018 ¹	98.0(11)	70(10)	0.32(4)	–	–	–	1.3(11)	0.7(3)
16-1046 ¹	93.1(8)	60(7)	0.21(9)	5.9(4)	–	–	1.0(7)	–
16-1064 ¹	0.14(13)	–	–	89.8(4)	91(7)	0.251(14)	3.2(4)	6.9(2)

¹ Suite 1; in situ carbonate target rock.

² Suite 2; shatter cone from crater-fill or ballistic ejecta deposit.

* Standard error shown in parentheses corresponds to the last decimal place.

§ Crystal size = Gaussian crystal size.

† Strain = Gaussian lattice strain.

Lattice strain values for shocked calcite samples range from 0.16% to 0.42% with the single unshocked sample at 0.12% (Table 4-1). The range of lattice strain values for shocked dolomite samples is slightly higher from 0.25% to 0.73% and low to unshocked samples range from 0.11% to 0.20% (Table 4-1); low shock samples were collected near the crater rim. The distance from the centre of the impact structure for each sample along with their lattice strain values are provided in Table 4-2 for suite 1 samples and in Table 4-3 for suite

2. Table 4-2 shows a general trend of decreasing lattice strain values with increasing distance from the centre. The same trend is not applicable for suite 2 samples. Even though many of the suite 2 samples were collected at similar distances, the variation in strain emphasizes how random the distribution of rock fragments within crater-fill deposits can be (Table 4-3).

Table 4-2. Lattice strain values sorted by distance from the centre of the Haughton impact structure for suite 1 carbonates.

Sample suite 1	Distance from centre (km)	Calcite strain % (error)	Dolomite strain % (error)
02-139	1.46	0.34(6)	–
99-063B	1.59	0.35(10)	–
07-020	2.26	0.421(19)	–
16-1018	3.41	0.32(4)	–
06-093	4.10	0.37(4)	–
16-1046	4.34	0.21(9)	–
16-1014	5.05	0.282(9)	–
16-1017 *	18.80	0.12(4)	–
16-1064	5.46	–	0.251(14)
05-005	7.15	–	0.16(3)
05-007	8.50	–	0.19(4)
06-108 *	14.04	–	0.11(9)
05-010 *	160.00	–	0.20(3)

* Unshocked bedrock sample.

Table 4-3. Lattice strain values sorted by distance from the centre of the Haughton impact structure for suite 2 carbonates.

Sample suite 2	Distance from centre (km)	Calcite strain % (error)	Dolomite strain % (error)
99-006	4.19	–	0.55(4)
02-127	4.63	0.16(8)	0.42(3)
02-128	4.63	–	0.60(6)
02-126	4.63	–	0.46(8)
00-019	4.89	0.18(8)	0.73(10)
02-061	5.08	0.20(5)	–
00-158	7.25	0.31(3)	0.43(3)
05-023	7.29	0.17(7)	0.40(4)
00-124	7.52	0.41(3)	–

4.3.3 Williamson-Hall plots

Peak broadening evident in XRD patterns (Fig. 4-4) is the first evidence of strained crystal lattices. Output values of interest from Rietveld refinements of shocked and unshocked limestone and dolostone samples include lattice strain values and modal mineral proportions (Table 4-1). To better visualize the effect of impact-induced strain within the two sample suites, the strain values determined from Rietveld refinements were used to create Williamson-Hall plots (Uchizono et al. 1999; Williamson and Hall 1953). Williamson-Hall plots are typically used to derive lattice strain values from XRD data by measuring the peak area for specific range of diffraction angles. Here, since lattice strain (ϵ) has been determined through Rietveld refinement, line broadening is calculated instead of measured in order to generate plots for calcite and dolomite. Williamson-Hall plots were generated using equation 4.1 (Uchizono et al. 1999; Wilson 1962) to calculate the integral breadth or line broadening due to strain (β_s) using Gaussian crystal lattice strain (ϵ) determined from Rietveld refinement and diffracted angles (θ).

$$\beta_s = 4\epsilon \tan\theta \quad (4.1)$$

The strain value (ϵ) is responsible for the vertical spread of plotted samples. Samples that contain more than 10 wt% of calcite and dolomite are found on both of the following Williamson-Hall plots.

The Williamson-Hall plot for calcite (Fig. 4-6) shows a range of strain effects on peak broadening where shocked samples result in slope values up to 1.7 compared to the unshocked sample 16-1017 which has a slope of 0.5. All samples display a linear trend and plot in order from lowest strain value (16-1017) to the highest (07-020). A notable small gap exists in the middle of the plot that separates samples that have a strain value above 0.28% and below 0.21%. Six calcite-bearing samples from suite 1 plot above the gap (Fig. 4-6); all but one of these (16-1014) are located within 3.5 km from the centre of the impact structure with sample 16-1014 being 5 km from the centre. The two suite 1 samples that plot below the gap are 4.3 and 18.4 km from the centre, respectively.

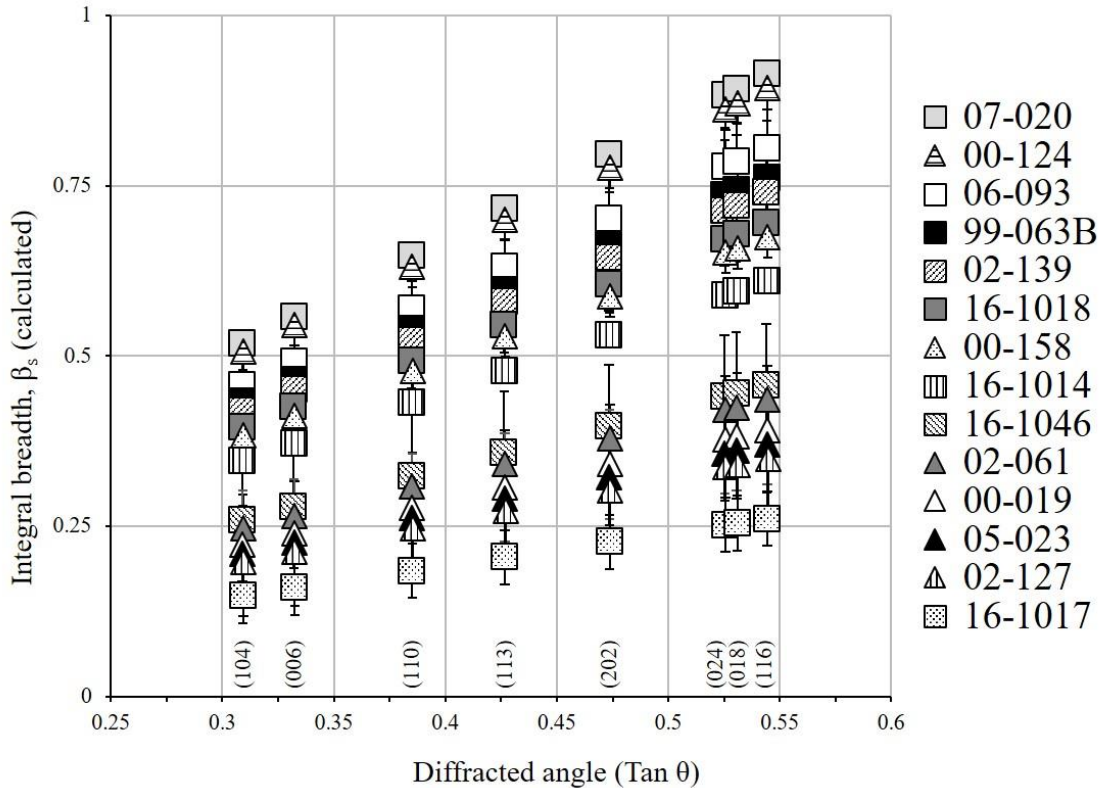


Figure 4-6. Williamson-Hall plot for calculated line broadening due to strain by diffracted angle of shocked to unshocked calcite associated with the Haughton impact structure. Squares represent suite 1 in situ target rock samples and triangles represent suite 2 samples from crater-fill and ballistic ejecta deposits. Numbers in brackets at bottom of chart indicate Miller indices (*hkl*).

The distance from the centre for suite 2 samples has no influence on the reported strain value (Table 4-1). The strain values for suite 2 reflect the effect of shock experienced by the sample at its original location and not where it was collected. It is interesting to note, however, that sample 00-124 is the suite 2 sample collected the farthest from the centre of the structure but has the highest reported strain value. Sample 00-124 is also the only suite 2 sample collected from a ballistic ejecta deposit rather than from crater-fill impact melt rock.

Dolomite has a wider range of strain values (Table 4-1) manifest as a larger vertical spread than calcite in the Williamson-Hall plot for dolomite (Fig. 4-7). Slopes range between 0.5 for unshocked dolomite and 2.9 for shocked dolomite. Similar to the calcite plot, dolomite-

bearing samples plot from lowest to highest strain and have a gap in the distribution corresponding to a slightly larger range in strain values, ϵ , between 0.25% and 0.42%. In contrast with calcite, all dolomite samples from suite 1 plot below the gap and suite 2 samples plot above. It should be noted that no in situ dolomite samples were available from the central uplift (Fig. 4-5) so further comparisons with calcite samples are not possible. The higher strain values for suite 2 dolomite shatter cone samples is consistent with higher pressures that would have been generated within a 4.5 km radius from the centre, which is the extent of in situ shatter cones at Haughton (Osinski and Ferrière 2016).

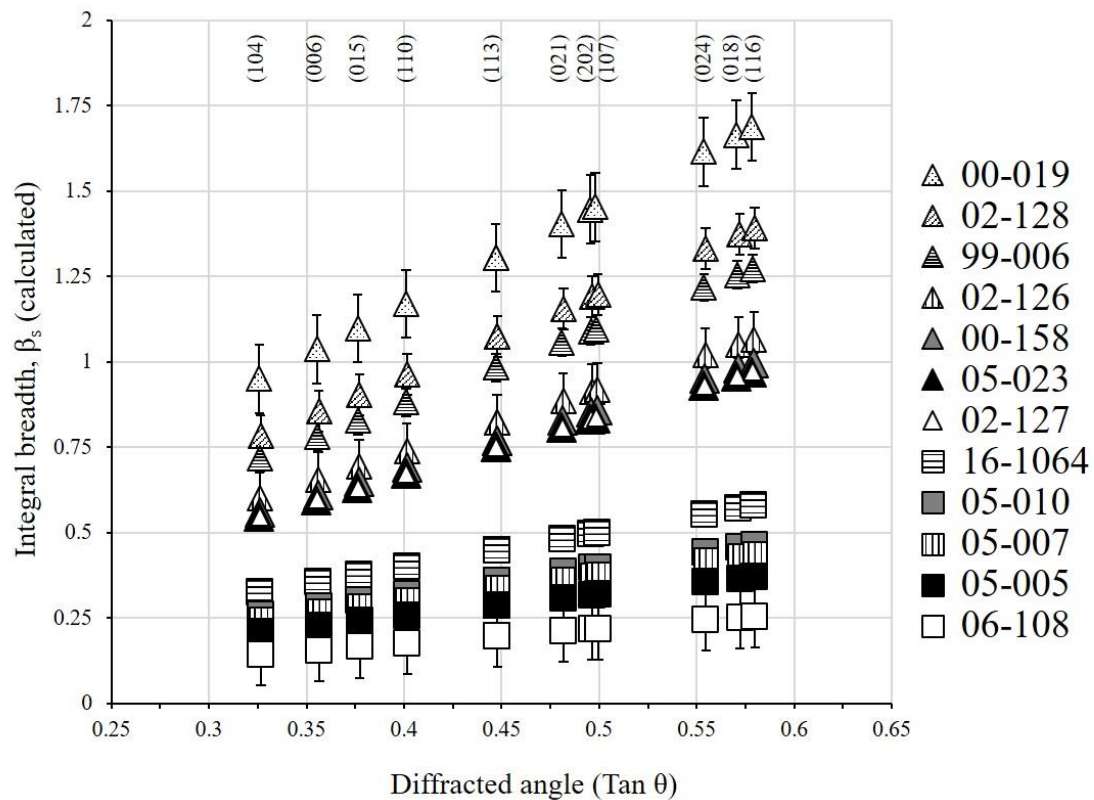


Figure 4-7. Williamson-Hall plot for calculated line broadening due to strain by diffracted angle of shocked to unshocked dolomite associated with the Haughton impact structure. Squares represent suite 1 in situ target rock samples and triangles represent suite 2 samples from crater-fill and ballistic ejecta deposits. Numbers in brackets at top of chart indicate Miller indices (*hkl*).

All dolomite-bearing samples from suite 1 are all located over 5 km from the centre of the impact structure and plot below the gap (Fig. 4-7). The dolomite-bearing suite 2 samples

like the equivalent calcite-bearing samples were displaced from their original location within the target sequence by the impact event.

Samples containing both dolomite and calcite typically do not plot at similar positions on their respective plots. Four bulk rock samples from suite 2 that contain both carbonate phases with modal proportions greater than 10 wt% are 00-019, 00-158, 02-127, and 05-023 (Figs. 4-6 and 4-7). First, 00-158 (81.7 wt% dolomite, 12.9 wt% calcite) sees both carbonate minerals plot in the relatively same position just above the gap. Comparing 00-158 with 02-127 which has nearly the same carbonate composition (81.7 wt% dolomite, 18.3 wt% calcite), dolomite plots at the same location above the gap whereas calcite plots noticeably below the gap. Next, 05-023 has carbonate proportions reversed (81.0 wt% calcite, 13.6 wt% dolomite) with dolomite plotting at the same position as 00-158 and 02-127 and calcite plotting below the gap with 02-127. The final mixed carbonate, 00-019 (57.1 wt% calcite, 42.9 wt% dolomite) shows the widest spread in relative position between the two plots with dolomite at the top while calcite falls below the gap near 05-023 and 02-127.

4.4 Discussion

4.4.1 Shock effects in calcite versus dolomite

The sample suites in this study are all naturally occurring rocks where limestone and dolostone are not necessarily pure and may contain up to several wt% of quartz or microcline (Table 4-1). Dolomite and calcite are similar carbonate minerals with main differences related to crystal symmetry and structure caused by Mg atoms substituting for Ca atoms in alternating cation layers in dolomite (Reeder 1983). Mg has a smaller ionic radius than Ca which leads to less distortion in CaO_6 octahedra in dolomite than calcite and the smaller Mg cation stabilizes the dolomite structure and prevents further octahedral distortion under pressure (Ross and Reeder 1992; Shannon 1976). High pressure experiments using diamond-anvil cells have shown the *c*-axis in carbonates is approximately 3 times more compressible than the *a*-axis (Fiquet et al. 1994; Ross and Reeder 1992). More specifically, compressibility only occurs within the CaO_6 and MgO_6 octahedral cation layers as the CO_3 carbonate groups are rigid units and not affected by

increasing pressure (Ross and Reeder 1992). Compressibility is also controlled by the polarizability of cations, decreasing from Ca to Mg, which supports the observed decrease in compressibility for the calcite (CaCO_3), dolomite ($\text{CaMg}(\text{CO}_3)_2$), and magnesite (MgCO_3) sequence (Fiquet et al. 1994).

Since CaO_6 octahedra are more compressible and able to distort more than MgO_6 octahedra (Ross and Reeder 1992), we suggest calcite is able to accommodate impact-generated shock pressures through distortion better than dolomite, resulting in less lattice strain. When both minerals occur together, dolomite would experience more lattice strain compared to calcite since it cannot distort as much when compressed. This is observed in samples 05-023 and 00-019 where dolomite has the lower modal proportion and as the proportion of dolomite increases from ~14 wt% to ~43 wt%, respectively, the spread between relative strain in dolomite and calcite increases. With a set of only four samples, care should be exercised in making definitive conclusions, but dolomite does appear to be preferentially strained compared to calcite when both minerals are present in the same target rock. Another important observation is that dolomite never has a lower relative strain value compared to calcite in the same sample, further supporting this conclusion.

The sample with the highest strain value for calcite is 07-020 (Table 4-1) and this sample plots at the top of Figure 4-6. Sample 07-020 is the third closest to the centre of the impact structure but the reason for the high strain value may also relate to composition. Sample 07-020 contains 69 wt% calcite and 31 wt% quartz. Sample 07-020 is the only sample in the suite with more than 4 wt% quartz so it is unclear how the proportion of quartz affects strain in calcite. The increased presence of quartz could introduce impedance matching between quartz and calcite, that contributes to increased shock metamorphism and the elevated strain detected in calcite compared to samples collected closer to the centre of the impact structure (e.g., Kenkmann et al. 2000). This observation also supports the above conclusion for mixed carbonate samples in that distance from the centre of the impact structure is not a linear relationship with strain and individual sample properties such as composition are important factors.

Suite 1 samples 06-093 and 16-1014 also plot higher on the calcite Williamson-Hall plot than their distance from the centre would suggest when compared with other suite 1 samples. A common aspect of these two samples is they were collected over 50 to 100 m in elevation above the Haughton River channel. Currently, it is unclear how strain changes vertically through an impact crater but this could be a potential factor. Seeley and Milam (2018) began investigating this idea by analyzing dolostone at varying depths in a drill core from the central uplift of the Wells Creek impact structure and is described further in the following section.

The unshocked suite 1 sample 05-010 was collected ~160 km east of the impact structure and, therefore, was not affected by the hypervelocity impact event. As such, this sample would be expected to have the lowest lattice strain value, but it has the fourth lowest strain value at 0.20% (Table 4-1). This could suggest that the area where sample 05-010 was collected has experienced mild tectonic strain which has been shown to be detectable by XRD (Huson et al. 2009).

4.4.2 Comparison with other craters in carbonate target rocks

There are currently 198 confirmed terrestrial impact structures and of these 82 formed in completely sedimentary targets and 54 in a mixed sedimentary and crystalline target sequence (Impact Earth 2020). From these sedimentary rock-bearing impact structures, carbonates from only five have been investigated for the presence of shock in carbonates using XRD and include the Ries, Kara, Steinheim, Sierra Madera, and Wells Creek impact structures (Huson et al. 2009; Seeley and Milam 2018; Skála 2002; Skála and Jakeš 1999). One common aspect that studies from these five impact structures highlight is the occurrence of peak broadening in XRD patterns as an indicator that there has been a decrease in crystallite size in shocked carbonates (Skála 2002). A main difference among these studies is that each examined a different 2θ range, and within these ranges, reflections or peaks for calcite, dolomite, and quartz often overlap. Identifying peak broadening is a relatively quick qualitative method to visualize if further shock investigation is warranted but becomes more difficult to compare between studies when different 2θ ranges are reported.

In the studies by Skála and Jakeš (1999), Skála (2002) and Huson et al. (2009), peak broadening observations from XRD patterns were further examined using Rietveld refinement to derive full width half maximum (FWHM) values and regression curves, which offer a better comparison than peak broadening alone. Data from Skála and Jakeš (1999) show they were qualitatively able to estimate the level of shock in their samples and state “the results obtained in this research are rather qualitative and require detailed calibration using experimentally shocked calcite samples”. Skála and Jakeš (1999) showed that Rietveld refinement data is more reliable than single-peak profile fitting, however, their regression curves only display relative levels of shock among plotted samples. These three studies provided FWHM values or curves versus 2θ which were stacked with other samples in their respective sample suites. Each set of stacked sample suite curves from Skála and Jakeš (1999), Skála (2002), and Huson et al. (2009) show variation between shocked and unshocked rocks but is similar to the stacking of diffraction patterns to compare peak broadening, where a single curve is more difficult to interpret. If the Rietveld refinements by Skála and Jakeš (1999), Skála (2002), and Huson et al. (2009) had gone one step further and determined strain values for their carbonate samples, the results could be easier to compare among studies.

The preliminary summary by Seeley and Milam (2018) examined how peak broadening changes with depth in a 401 m drill core from the central uplift of the Wells Creek impact structure. From their diffraction patterns they suggest peak broadening does not appear to directly correspond to an expected decrease with depth. Their results from comparing peak broadening in diffraction patterns alone do not show a clear decrease in peak broadening with depth, however, they intend to compare this to more robust data from Rietveld refinements in the future (Seeley and Milam 2018). It is not mentioned if the Rietveld data would then be used to create FWHM curves or if lattice strain values might be determined. Determining lattice strain from a vertical sequence of samples at Wells Creek or any other impact structure could reveal a clearer idea of the relationship between depth and strain.

The difference in 2θ ranges compared for peak broadening in diffraction patterns and the qualitative display of stacked curves from peak fitting reveal a lack of directly comparable parameters among previous studies and indicates that a different approach may be

necessary. To identify a more quantifiable method of identifying shock in carbonates, we determined lattice strain for dolomite and calcite in samples from the Haughton impact structure. Lattice strain values obtained from Rietveld refinement indicate there is a detectable change in lattice strain associated with carbonates subjected to hypervelocity impact at the Haughton impact structure (Table 4-1). Strain values offer a numerical comparison between samples rather than a relative comparison of broadening in diffraction patterns or FWHM curves. Having a consistent set of parameters would help work toward a shock classification scheme for carbonates, which does not currently exist (Stöffler et al. 2018) and will be discussed in the following section.

4.4.3 Carbonates as shock indicators

In this study, specific shock pressures or classes cannot be assigned to individual carbonate samples because they are not directly associated with other quartz-bearing rocks such as sandstone where shock level can be determined through the presence of features such as PDFs. Sandstone clasts from crater-fill deposits at Haughton have been divided into six shock pressure classes ranging from 0 GPa to >30 GPa (Osinski 2007). The only visual sign of shock metamorphism in carbonate samples is the occurrence of shatter cones at hand sample scale.

Sample 07-020 contains the highest modal proportion of silicates, ~31 wt% quartz, and based on the diffraction pattern for this sample, there are no peaks to indicate the presence of stishovite or coesite. The peaks of these high pressure polymorphs of quartz are not observed, however, their positions overlap with the large calcite peaks, so it is possible they are obscured, especially if either are present in low proportions. Stishovite forms at pressures between ~12–45 GPa and coesite forms between ~30–55 GPa (Stöffler 1971).

Strain values in this study cannot be directly quantified since lattice strain values from experimentally shocked dolomite and calcite samples at known pressures have yet to be measured. Such a pressure scale was suggested by Martinez et al. (1995) but has yet to be produced. However, in the study by Martinez et al. (1995) they experimentally shocked dolomitic rocks collected on Devon Island near the Haughton impact structure to 60 GPa. They compared one unshocked sample and two samples from shock recovery experiments

using a multiple reverberation technique to achieve 60 GPa (Martinez et al. 1995). Similar to this study, Martinez et al. (1995) performed Rietveld refinements on the three of their samples to determine strain for dolomite and calcite (Table 4-4).

Table 4-4. Comparison of lattice strain measurements by Rietveld refinement from the Houghton impact structure and experimentally shocked carbonates.

Sample	Shock level	Calcite		Dolomite		Reference
		wt%	strain %	wt%	strain %	
DIG-4	unshocked	21.0	0.065	79.0	0.16	Martinez et al. (1995)
DIG-4S1	~60 GPa	18.5	0.24	81.5	0.54	Martinez et al. (1995)
DIG-4S3 §	~60 GPa	22.0	0.26	78.0	0.58	Martinez et al. (1995)
16-1017 ¹	unshocked	92.6	0.12	–	–	this study
99-063B ¹	shocked	96.2	0.35	–	–	this study
00-124 ²	shocked	99.7	0.41	–	–	this study
06-108 ¹	unshocked	–	–	99.5	0.11	this study
05-010 ¹	unshocked	–	–	99.7	0.20	this study
16-1064 ¹	shocked	–	–	89.8	0.25	this study
00-019 ²	shocked	57.1	0.18	42.9	0.73	this study

§ Shocked under vacuum conditions.

¹ Suite 1; in situ carbonate target rock.

² Suite 2; shatter cone from crater-fill or ballistic ejecta deposit.

The comparison of results from both studies (Table 4-4) show strain values are quite similar for shocked and unshocked dolomite and calcite. The experimentally shocked samples only represent one pressure, 60 GPa, so additional pressures would be required to fully assess any further similarities in lattice strain values. Another aspect that would need to be investigated is to determine how well such reverberation shock experiments scale up to match large impact events as small-scale shock experiments do not always equal large-scale events, similar to scaling related to impact melt production (Grieve and Cintala 1992). If the strain values from the experimentally shocked carbonates are an adequate comparison for hypervelocity impacts, then some carbonates from the central uplift of the Houghton impact structure experienced pressure greater than 60 GPa based on lattice strain values greater than 0.54% and 0.24% for dolomite and calcite, respectively (Table 4-4).

Revisiting Table 4-3, it is conceivable that the strain values for suite 2 samples indicate relative distance from the centre of the impact structure, but without a calibration scale for

strain associated with known pressures, this cannot be determined. What the strain values from the two sample suites here do show is that strain values are higher near the centre of the impact structure for in situ target samples and decrease toward the rim (Table 4-2). The strain variation among the samples in this study indicates that the shatter cone-bearing target rocks did not experience the same sample shock pressure during the impact event and helps to support that lattice strain could be a proxy for shock pressure. If lattice strain was not induced by shock pressure, then strain values for all samples within both sample suites should have similar values. The ability to recognize strain in carbonates using XRD and associate the strain with a shock pressure could be used to help identify and confirm an impact structure in a sedimentary target.

X-ray diffraction data and subsequent strain derived from Williamson-Hall plots has shown success in estimating shock pressure in forsterite (Uchizono et al. 1999). The calibration curve generated by experimentally shocking forsterite up to 82 GPa was used to determine shock pressures experienced by olivine in a LL6 chondrite meteorite (Uchizono et al. 1999). By measuring lattice strain of olivine in Martian meteorites Jenkins et al. (2019) also produced strain values that are comparable to literature values for shock pressures, giving further support to the value of lattice strain measurements.

As shock indicators, carbonates would not be as straightforward as silicates. Results here show that rocks with a mixed carbonate composition result in preferential strain in dolomite over calcite, likely due to crystal structure differences between the two minerals. Future experiments need to consider this aspect of naturally occurring carbonates and not limit experimental samples to pure calcite or dolomite. While pure limestone and dolostone rocks will produce the best calibration scales for quantifying strain in experimentally shocked samples, mixed carbonate rocks of known compositions will also reveal any effects or trends that result from varying carbonate compositions. The effect of porosity and grain size on strain in carbonates should also be explored in controlled experiments to determine if they contribute to lattice strain caused by hypervelocity-generated shock pressures, and if so to what extent do they contribute to strain.

When calcite and dolomite are both available to determine strain, dolomite appears to be the better mineral for several reasons. First, in mixed carbonate samples its strain value has less variation when considering modal abundance. Second, weakly shocked dolostone from an impact event can be distinguished from tectonically strained dolostone whereas mildly shocked calcite cannot make the same distinction (Huson et al. 2009). And third, dolomite does not undergo displacive-type phase transformations at pressures below 5.0 GPa, unlike calcite where this has been shown to occur at pressures around 1.5 GPa and 2.2 GPa (Ross and Reeder 1992). Additional structural transformation in calcite has also been observed between 7 GPa and 18.3 GPa (Fiquet et al. 1994). This study did not investigate the effect of phase transformations so future experiments should determine the effect these transformations have on lattice strain.

4.5 Conclusions

Peak broadening in X-ray diffraction patterns was observed in this study as well as in previous studies of carbonates from impact events (Huson et al. 2009; Seeley and Milam 2018; Skála 2002; Skála and Jakeš 1999). Further assessment of XRD data by Rietveld refinement show lattice strain variation in dolomite and calcite among shocked samples. Both calcite and dolomite show variation in strain values with trends showing highest strain within the central uplift and decreases toward the rim. Higher strain values for dolomite show it is more affected by hypervelocity impact than calcite. This is supported by the results from mixed carbonate samples that show strain is not evenly distributed through calcite and dolomite with dolomite preferentially strained over calcite.

This study has shown promising results to identify shocked carbonates associated with impact structures. Further study of naturally and experimentally shocked limestone and dolostone samples will prove the reliability of using lattice strain measurement to identify shock in dolomite and calcite. In the future, experimentally shocked carbonates could produce a calibration scale where strain values could estimate impact-generated shock pressures in an effort to initiate a reliable shock classification system for carbonates.

4.6 References

- Althoff P. 1977. Structural refinements of dolomite and a magnesian calcite and implications for dolomite formation in the marine environment. *American Mineralogist* 62:772–783.
- Baratoux D., and Reimold W. U. 2016. The current state of knowledge about shatter cones: Introduction to the special issue. *Meteoritics & Planetary Science* 51:1389–1434.
- Brill R., Hermann C., and Peters C. 1939. Studien über chemische Bindung mittels Fourieranalyse III. *Die Naturwissenschaften* 27:677–678.
- Cavosie A. J., Timms N. E., Ferrière L., and Rochette P. 2018. FRIGN zircon - The only terrestrial mineral diagnostic of high-pressure and high-temperature shock deformation. *Geology* 46:891–894.
- Černok A., White L. F., Darling J., Dunlop J., and Anand M. 2019. Shock-induced microtextures in lunar apatite and merrillite. *Meteoritics & Planetary Science* 54:1262–1282.
- Cressman E. R. 1981. *Surface geology of the Jephtha Knob cryptoexplosion structure, Shelby County, Kentucky.*, Professional Paper 1151-B, United States Geological Survey.
- Dietz R. S. 1959. Shatter cones in cryptoexplosion structures (meteorite impact?). *The Journal of Geology* 67:496–505.
- Fiquet G., Guyot F., and Itie J. P. 1994. High-pressure X-ray diffraction study of carbonates: MgCO₃, CaMg(CO₃)₂, and CaCO₃. *American Mineralogist* 79:15–23.
- French B. M. 1998. *Traces of Catastrophe: A Handbook of Shock-Metamorphic Effects in Terrestrial Meteorite Impact Structures*, LPI Contribution No. 954, Lunar and Planetary Science Institute, Houston.
- French B. M., and Koeberl C. 2010. The convincing identification of terrestrial meteorite

- impact structures: What works, what doesn't, and why. *Earth-Science Reviews* 98:123–170.
- Glennemann J., King Jr. H. E., Schulz H., Hahn T., La Placa S. J., and Dacol F. 1992. Crystal structures of the low-temperature quartz-type phases of SiO₂ and GeO₂ at elevated pressure. *Zeitschrift für Kristallographie* 198:177–212.
- Graup G. 1999. Carbonate-silicate liquid immiscibility upon impact melting: Ries Crater, Germany. *Meteoritics & Planetary Science* 34:425–438.
- Grieve R. A. F., and Cintala M. J. 1992. An analysis of differential impact melt-crater scaling and implications for the terrestrial impact record. *Meteoritics* 27:526–538.
- Hill R. J., and Howard C. J. 1987. Quantitative phase analysis from neutron powder diffraction data using the Rietveld method. *Journal of Applied Crystallography* 20:467–474.
- Hill R. J., and Madsen I. C. 2002. Sample preparation, instrument selection and data collection. In *Structure Determination from Powder Diffraction Data*, edited by David W. I. F., Shankland K., McCusker L. B., and Baerlocher C. New York. pp. 98–117.
- Hörz F., Archer P. D., Niles P. B., Zolensky M. E., and Evans M. 2015. Devolatilization or melting of carbonates at Meteor Crater, AZ? *Meteoritics & Planetary Science* 50:1050–1070.
- Huson S. A., Foit F. F., Watkinson A. J., and Pope M. C. 2009. Rietveld analysis of X-ray powder diffraction patterns as a potential tool for the identification of impact-deformed carbonate rocks. *Meteoritics & Planetary Science* 44:1695–1706.
- Impact Earth. Impact Earth Database. 2020. www.impactearth.com (Accessed February 18, 2020).
- Izawa M. R. M., Flemming R. L., Banerjee N. R., and Mccausland P. J. A. 2011. Micro-X-ray diffraction assessment of shock stage in enstatite chondrites. *Meteoritics &*

Planetary Science 46:638–651.

- Jenkins L. E., Flemming R. L., and McCausland P. J. A. 2019. Quantitative in situ XRD measurement of shock metamorphism in Martian meteorites using lattice strain and strain-related mosaicity in olivine. *Meteoritics & Planetary Science* 54:902–918.
- Jones A. P., Claeys P., and Heuschkel S. 2000. Impact melting of carbonates from the Chicxulub Crater. In *Impacts and the Early Earth, Lecture Notes in Earth Sciences*, edited by Gilmour I., and Koeberl C. Springer-Verlag, Berlin-Heidelberg-New York. pp. 343–361.
- Kenkmann T., Hornemann U., and Stöffler D. 2000. Experimental generation of shock-induced pseudotachylites along lithological interfaces. *Meteoritics & Planetary Science* 35:1275–1290.
- Klug H. P., and Alexander L. E. 1974. *X-Ray Diffraction Procedures for Polycrystalline and Amorphous Materials*, New York: John Wiley & Sons, Inc.
- Levien L., Prewitt C. T., and Weidner D. J. 1980. Structure and elastic properties of quartz at pressure. *American Mineralogist* 65:920–930.
- Markgraf S. A., and Reeder R. J. 1985. High-temperature structure refinements of calcite and magnesite. *American Mineralogist* 70:590–600.
- Martinez I., Deutsch A., Scharer U., Ildefonse P., Guyot F., and Agrinier P. 1995. Shock recovery experiments on dolomite and thermodynamical calculation of impact induced decarbonation. *Journal of Geophysical Research* 100:15465–15476.
- Maslen E. N., Streltsov V. A., Streltsova N. R., and Ishizawa N. 1995. Electron density and optical anisotropy in rhombohedral carbonates. III. Synchrotron X-ray studies of CaCO₃, MgCO₃ and MnCO₃. *Acta Crystallographica Section B* 51:929–939.
- McCausland P. J. A., Flemming R. L., and Izawa M. R. M. 2010. Quantitative shock stage assessment in olivine and pyroxene bearing meteorites via in situ micro-XRD. *American Geophysical Union, Fall Meeting 2010, abstract #P14C-03*.

- Miser D. E., Swinnea J. S., and Steinfink H. 1987. TEM observations and X-ray crystal-structure refinement of a twinned dolomite with a modulated microstructure. *American Mineralogist* 72:188–193.
- O’Keefe J. D., and Ahrens T. J. 1989. Impact production of CO₂ by the Cretaceous/Tertiary extinction bolide and the resultant heating of the Earth. *Nature* 338:247–249.
- Osinski G. R., and Spray J. G. 2001. Impact-generated carbonate melts: Evidence from the Houghton structure, Canada. *Earth and Planetary Science Letters* 194:17–29.
- Osinski G. R., Lee P., Spray J. G., Parnell J., Lim D. S. S., Bunch T. E., Cockell C. S., and Glass B. 2005a. Geological overview and cratering model for the Houghton impact structure, Devon Island, Canadian High Arctic. *Meteoritics & Planetary Science* 40:1759–1776.
- Osinski G. R., Spray J. G., and Lee P. 2005b. Impactites of the Houghton impact structure, Devon Island, Canadian High Arctic. *Meteoritics & Planetary Science* 40:1789–1812.
- Osinski G. R., and Spray J. G. 2006. Shatter cones of the Houghton impact structure, Canada. In *Proceedings, 1st International Conference on Impact Cratering in the Solar System, European Space Agency Special Publication SP-612. CD-ROM*. pp. 95–99.
- Osinski G. R. 2007. Impact metamorphism of CaCO₃-bearing sandstones at the Houghton structure, Canada. *Meteoritics & Planetary Science* 42:1945–1960.
- Osinski G. R., Spray J. G., and Grieve R. A. F. 2008. Impact melting in sedimentary target rocks: An assessment. In *The Sedimentary Record of Meteorite Impacts, Special Paper 437*, edited by Evans K. R., Horton W., King Jr. D. K., and Morrow J. R. Geological Society of America, Boulder, CO. pp. 1–18.
- Osinski G. R., and Ferrière L. 2016. Shatter cones: (Mis)understood? *Science Advances* 2, e160061:1–10.

- Reeder R. J., and Wenk H. R. 1983. Structure refinements of some thermally disordered dolomites. *American Mineralogist* 68:769–776.
- Reeder R. J. 1983. Crystal chemistry of the rhombohedral carbonates. In *Reviews in Mineralogy Volume 11 Carbonates: Mineralogy and Chemistry*, edited by Reeder R. J. Mineralogical Society of America. pp. 1–47.
- Ribbe P. H. 1979. The structure of a strained intermediate microcline in cryptoperthitic association with twinned plagioclase. *American Mineralogist* 64:402–408.
- Ross N. L., and Reeder R. J. 1992. High-pressure structural study of dolomite and ankerite. *American Mineralogist* 77:412–421.
- Seeley J. R., and Milam K. A. 2018. Optical and X-ray diffraction analyses of shock metamorphosed dolostone at increasing depths within the central uplift of the Wells Creeks impact structure. *49th Lunar and Planetary Science Conference Abstract #2755*.
- Shannon R. D. 1976. Revised effective ionic radii and systematic studies of interatomic distances in halides and chalcogenides. *Acta Crystallographica* A32:751–767.
- Sharpton V. L., Dressler B. O., Herrick R. R., Schnieders B., and Scott J. 1996. New constraints on the Slate Islands impact structure, Ontario, Canada. *Geology* 24:851–854.
- Skála R., and Jakeš P. 1999. Shock-induced effects in natural calcite-rich targets as revealed by X-ray powder diffraction. In *Large Meteorite Impacts and Planetary Evolution II, Special Paper 339*, edited by Dressler B. O., and Sharpton V. L. Geological Society of America (GSA), Boulder, CO. pp. 205–214.
- Skála R. 2002. Shock-induced phenomena in limestones in the quarry near Ronheim, the Ries Crater, Germany. *Bulletin of the Czech Geological Survey* 77:313–320.
- Stöffler D. 1971. Coesite and stishovite in shocked crystalline rocks. *Journal of Geophysical Research* 76:5474–5488.

- Stöffler D., Artemieva N. A., Wünnemann K., Reimold W. U., Jacob J., Hansen B. K., and Summerson I. A. T. 2013. Ries crater and suevite revisited - Observations and modeling Part I: Observations. *Meteoritics & Planetary Science* 48:515–589.
- Stöffler D., Hamann C., and Metzler K. 2018. Shock metamorphism of planetary silicate rocks and sediments: Proposal for an updated classification system. *Meteoritics & Planetary Science* 49:5–49.
- Thorsteinsson R., and Mayr U. 1987. *The Sedimentary Rocks of Devon Island, Canadian Arctic Archipelago*, Memoir 411. Geological Survey of Canada.
- Turvey C. C., Hamilton J. L., and Wilson S. A. 2018. Comparison of Rietveld-compatible structureless fitting analysis methods for accurate quantification of carbon dioxide fixation in ultramafic mine tailings. *American Mineralogist* 103:1649–1662.
- Uchizono A., Shinno I., Nakamuta Y., Nakamura T., and Sekine T. 1999. Characterization of artificially shocked forsterites: (1) Diffraction profile analysis by Gandolfi camera. *Mineralogical Journal* 21:15–23.
- Williamson G. K., and Hall W. H. 1953. X-ray line broadening from filed aluminium and wolfram. *Acta Metallurgica* 1:22–31.
- Wilson A. J. C. 1962. *X-Ray Optics: The Diffraction of X-rays by Finite and Imperfect Crystals*, London: Methuen & Co Ltd.
- Young K. E., Van Soest M. C., Hodges K. V., Watson E. B., Adams B. A., and Lee P. 2013. Impact thermochronology and the age of Haughton impact structure, Canada. *Geophysical Research Letters* 40:3836–3840.

Chapter 5

5 An X-ray diffraction study of shocked carbonates from the deeply eroded Tunnunik impact structure, Canada

5.1 Introduction

Carbonates are an important component in sedimentary target sequences and sedimentary rocks are present in approximately 70% of terrestrial impact craters (Osinski et al. 2008). Despite the common occurrence of carbonates in hypervelocity impact structures, the response of carbonates to these extreme events is poorly understood. The lack in understanding is due, in part, to the absence of any reliable shock metamorphic features in carbonates compared to silicates, such as planar fractures, planar deformation features, and diaplectic glass – which are common in quartz or feldspar (French and Koeberl 2010).

This study focuses on the Tunnunik impact structure, a 28 km diameter structure located on Victoria Island, Northwest Territories, Canada. The target sequence of the ~430 Ma deeply eroded Tunnunik impact structure is entirely sedimentary and consists of Precambrian limestone and Cambrian to Silurian dolostone units (Dewing et al. 2013; Lepaulard et al. 2019). Much of what remains of the structure is covered by a blanket of glacial till but outcrops across the structure may show impact-related features such as inclined bedding planes, shatter cones, and impact-generated breccia dykes, with shatter cones providing the only visual indicator of shock.

Shatter cones are macroscopic evidence of shock metamorphism in impact structures and are found in all rock types, however, their forms are best developed in fine-grained rocks such as carbonates (French 1998). At the Tunnunik impact structure, shatter cones are found in the central uplift area in an ellipse approximately 10 km by 12 km (Osinski and Ferrière 2016) in both dolostone and limestone target rocks (Fig. 5-1). Shatter cones are typically generated from lower shock pressures of ~2–10 GPa (French 1998), but the complete pressure range for developing shatter cones in all target types is reported as 1–45 GPa (Stöffler et al. 2018).

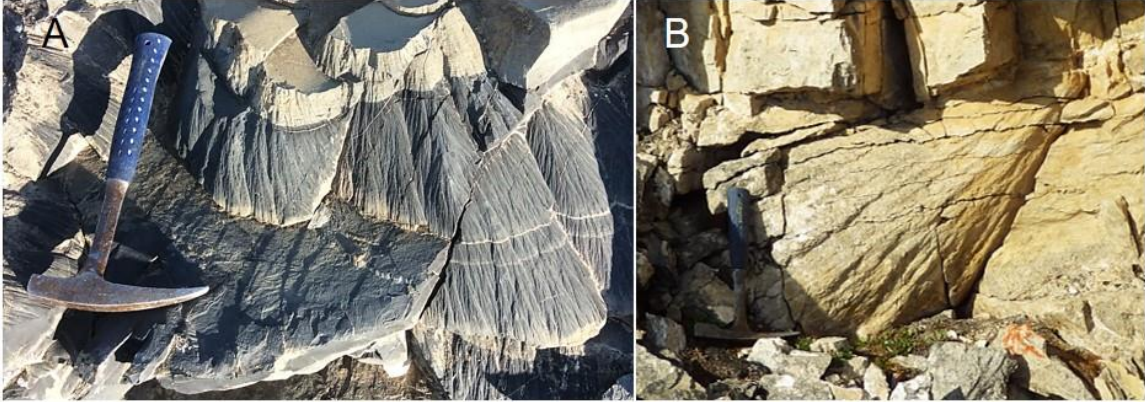


Figure 5-1. Examples of shatter cones from the Tunnunik impact structure in limestone (A) and dolostone (B) target rock. Rock hammer for scale.

The goal of this study is to identify the presence of shock in dolomite and calcite by determining strain in these minerals by analyzing target rocks exposed at the surface of the deeply eroded Tunnunik impact structure, both within the shatter cone distribution and beyond. Identifying strain in dolomite and calcite has been demonstrated from the Haughton impact structure (Chapter 4) using high quality powder X-ray diffraction scans followed by Rietveld refinement. X-ray diffraction (XRD) has also been used to investigate shock at the Steinheim, Kara, Ries, Sierra Madera, and Wells Creek impact structures (Huson et al. 2009; Seeley and Milam 2018; Skála 2002; Skála and Jakeš 1999). Here, the effect of XRD scan quality in determining strain results is investigated and compared with the results obtained from Haughton. If strain is determined to be a quantifiable product of hypervelocity shock that can be detected in deeply eroded or carbonate-rich impact structures, it demonstrates a similar approach could be applied to other impact sites or suspected sites in the absence of traditional silicate shock indicators.

5.2 Samples and methods

Samples selected for this study were collected over five weeks of field work in July and August 2015. A set of 14 samples, eleven dolostone and three limestone, represent target material from the central uplift area out to the rim of the structure and one sample collected from beyond the rim (Fig. 5-2). The sample collected beyond the impact structure is approximately 37 km from the centre represents an unshocked dolostone sample. The 13 samples that span the impact structure were selected at intervals of ~1–2 km, where

possible, to capture a range of shock pressure in a roughly northeast-southwest transect through the middle of the structure.

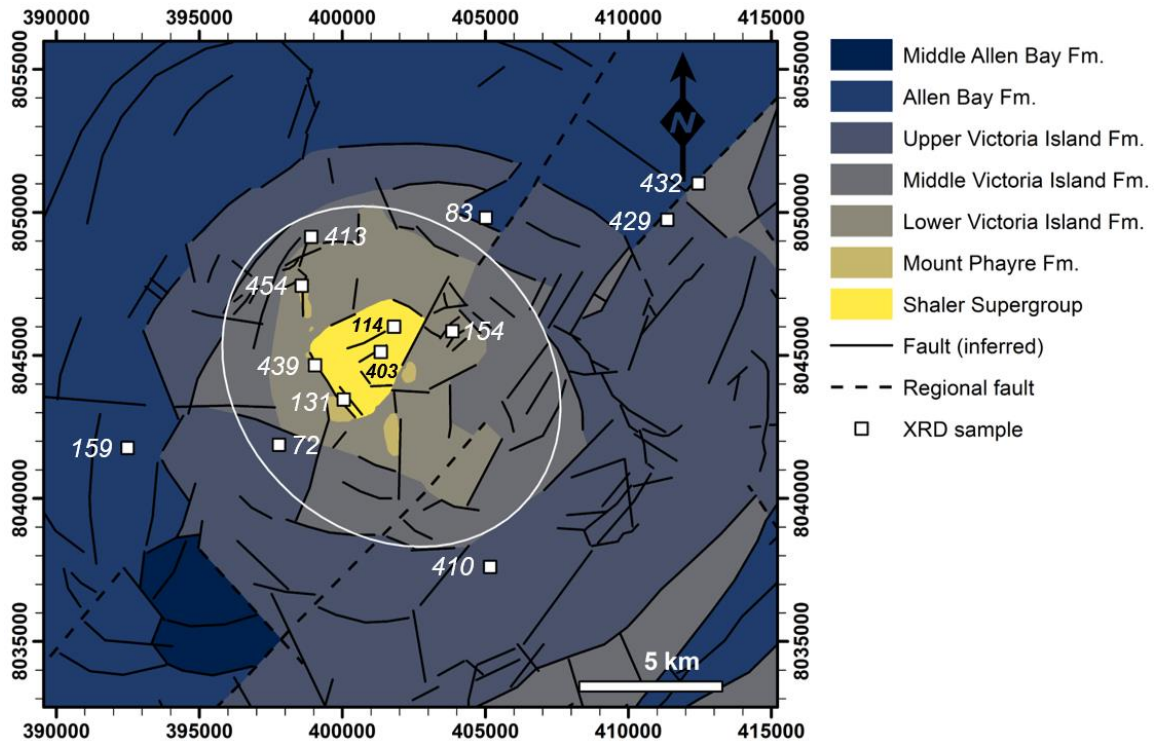


Figure 5-2. X-ray diffraction sample locations within the Tunnunik impact structure. Unshocked dolostone sample 40 (not shown) was collected ~37 km southeast from the centre of the impact structure. White ellipse indicates the extent of the shatter cone distribution. UTM grid with Easting and Northing at 1000 m intervals for Zone 11 and Zone 12.

Samples located off the NE-SW transect line were selected to preserve the spacing interval and distance from the centre when outcrop exposures were not present along the transect. An unshocked limestone sample was not obtainable from Tunnunik since the exposed central uplift of the impact structure is the only exposed limestone of the Shaler Supergroup within the study area. The nearest outcrops from the Shaler Supergroup are in the Shaler Mountains located in central Victoria Island over 60 km east of the Tunnunik study area. For comparison purposes, a limestone sample collected near, but beyond, the rim of the Houghton impact structure on Devon Island, Nunavut, Canada serves as an unshocked limestone sample. The unshocked limestone, sample 16-1017, was prepared and analyzed

during a similar investigation at the Haughton impact structure (see Chapter 4). The unshocked limestone sample from Devon Island is from the late Ordovician Thumb Mountain Formation, which falls within the age of the target sequence at Tunnunik but is absent on Victoria Island due to an Ordovician-aged disconformity (Mallamo 1989; Stewart 1987).

Bulk rock samples free of weathered surfaces were prepared by grinding in a mortar and pestle for 30 minutes. Powders were mounted onto a recessed glass slide using 100% ethanol then analyzed by a Rigaku DMAX powder diffractometer with Bragg-Brentano geometry, graphite monochromator, and scintillation counter. X-ray diffraction patterns were collected using Co $K\alpha_1$ radiation with a 1.78896 Å wavelength and operating parameters of 40 kV, 35 mA, 0.02°/step, 1 s dwell time per step, and a 2θ range from 10–90°.

It should be noted that powder preparation and analysis of the Tunnunik samples varies slightly from Chapter 4. A total of 61 samples from the Tunnunik impact structure were powdered for the purpose of mineral phase identification. There was no concern regarding the potential introduction of excess strain into the samples by powdering them dry, as this would not affect phase identification. The shorter dwell time and 2θ range for Tunnunik samples compared to the high-quality Haughton scans, 1 s versus 5 s and 10–90° versus 5–120°, favoured sample volume over data quality as this allowed a Tunnunik sample to be analyzed in 1 hour compared to 8 hours for one Haughton sample. The shorter analysis time did not affect the ability to detect main mineral phases within the bulk rock powders.

The software used to run the Rigaku diffractometer was MDI Data Scan 3.2. The data files were converted to a raw format by the open source software ConveX. Analysis of raw data files was conducted with DIFFRAC.EVA software version 4.2 by Bruker AXS and phases were identified and matched using the ICDD (International Centre for Diffraction Data) database PDF-4+ (2019).

Rietveld refinement for several samples was attempted by following the same procedure used for Haughton samples in Chapter 4 to quantify lattice strain using TOPAS 5 software by Bruker AXS. Refined parameters include background intensity, sample displacement,

absorption, scale factor, unit cell dimensions, profile shape PV-TCHZ parameters U, V, W, and X, Beq, Stephen's model trigonal-high for calcite and dolomite, crystal size G (Gaussian), and strain G (Gaussian). Mineral phases present in several wt%, up to ~5 wt%, were not refined on Beq, Stephen's model, crystal size G, or strain G as the errors for these parameters increased significantly as the proportion of the mineral phase declined in the bulk rock sample (e.g., Hill and Howard 1987; Turvey et al. 2018). Refinements were fit from 16° – 80° 2θ with fixed parameters including fifth-order background, and preferred orientation used spherical harmonics order-8. Refinement sequence of turning on parameters was performed in the same order for all samples. To get the best fit for each mineral phase, starting structural models are noted here for calcite (Maslen et al. 1995), dolomite (Althoff 1977; Ross and Reeder 1992), microcline (Ribbe 1979) and quartz (Brill et al. 1939).

5.3 Results

5.3.1 Powder X-ray diffraction

X-ray diffraction patterns of counts versus 2θ for the 14 bulk rock samples from Tunnunik were divided based on whether the primary mineral phase was dolomite or calcite. Samples with a primary dolomite phase may contain a minor quartz phase and samples with a primary calcite phase may also contain minor dolomite, quartz, and orthoclase phases (Fig. 5-3).

Dolomite samples (Fig. 5-3A) are ordered by distance from the centre of the impact structure with sample 439 the closest at ~2.6 km to sample 40 collected ~37 km away. The greatest peak broadening is observed in sample 439 with broadening decreasing as distance from the centre increases. Samples 439, 154, 454, 413, and 72 fall within the mapped shatter cone distribution Tunnunik (Osinski and Ferrière 2016). Importantly, these samples also show the greatest peak broadening. All three calcite samples (Fig. 5-3B) were collected within 2 km from the centre of the impact structure and exhibit peak broadening compared with the unshocked sample. Samples that display well-developed shatter cones are 131, 439, 154, and 454.

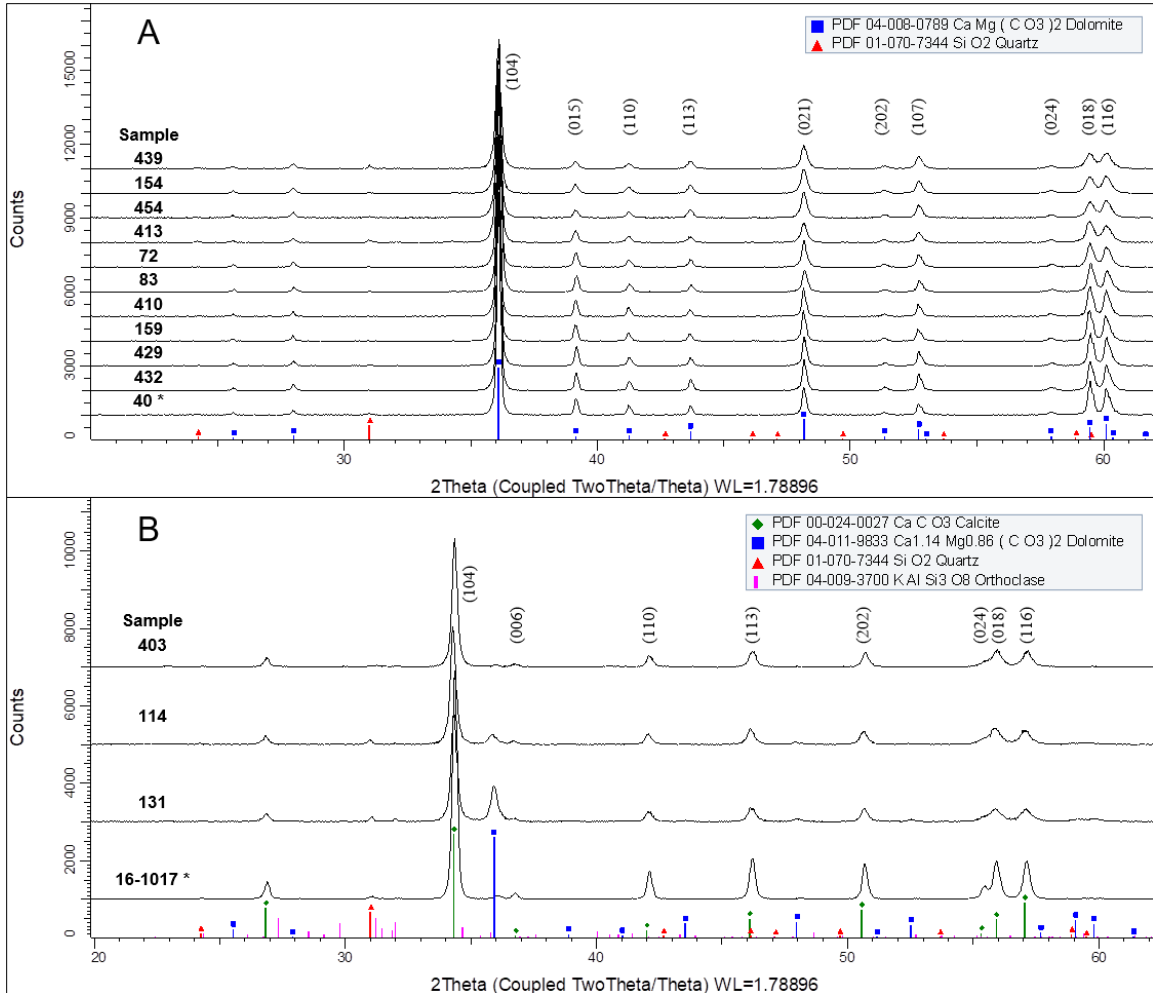


Figure 5-3. X-ray diffraction patterns of powdered samples divided by dolomite (A) and calcite (B) as the primary mineral phase from the Tunnunik impact structure. Vertical numbers in brackets above stacks in (A) and (B) indicate Miller Indices (hkl) associated with peaks for dolomite and calcite, respectively. Unshocked samples are indicated by (*). A y-offset has been applied to sample patterns for clarity. Note: sample 16-1017 is from the Haughton impact structure.

5.3.2 Rietveld refinement

Rietveld refinements of two powder XRD scans using TOPAS 5 were attempted to estimate the modal proportions of each mineral phase for each bulk rock sample. Additional outputs of interest from the refinement include crystallite size and strain as well as d-spacing, 2θ , and intensity values for each Miller Index (hkl). Samples 454 (dolomite) and 131 (calcite) were selected based on their proximity to the centre of the impact structure and the presence

of shatter cones. Refinements were unable to produce consistent values and/or values within acceptable error so modal proportions of mineral phases could not be determined so Rietveld refinements were not used for further analysis of samples from Tunnunik.

5.3.3 Strain estimation

In Chapter 4, strain values were obtained through Rietveld refinements, which were then used to generate Williamson-Hall plots by calculating the integral breadth or line broadening due to strain, β_s . The equation used to calculate line broadening also uses crystal strain, ϵ , as determined from Rietveld refinement, and diffracted angles, θ .

$$\beta_s = 4\epsilon \tan\theta \quad (5.1)$$

Using DIFFRAC.EVA software, it is possible to measure the area of each peak to get an integral breadth value then calculate the crystal strain based on equation (5.1). To see how accurate this method estimates lattice strain, ϵ , the samples from Haughton with the highest and lowest strain values (Chapter 4), as determined through Rietveld refinement, for calcite and dolomite were selected. A second calcite sample (99-063B) with high strain and a high modal proportion of calcite was selected from the Haughton sample suite to assess the effect of mineral proportion on strain estimation, since the highest strained calcite sample (07-020) has a low calcite proportion (Table 5-1). In EVA, the observed maximum 2θ value and integral breadth value for each (hkl) peak area was measured and recorded. Due to peak broadening, some (hkl) peak areas were measured as one peak, resulting in a higher integral breadth value as shown with the (018) and (116) plotted value in Figure 5-4. The 2θ values were converted to $\tan \theta$. To determine the strain value for the sample, $\tan \theta$ values were plotted against their integral breadth values. Example Williamson-Hall plots for dolomite and calcite are shown in Figures 5-4 and 5-5, respectively. Williamson-Hall plots for the rest of the sample suite are provided in Appendix C.

The slope value from the trendline equation, 4ϵ , was divided by 4 to give the final crystal lattice strain value ϵ . Table 5-1 compares the Gaussian strain, strain G, output values determined by Rietveld refinements using TOPAS and the crystal strain, strain ϵ , values derived from the slope of the trendline in Williamson-Hall plots by measuring peak areas

using EVA. These results show the two methods produce similar values, with dolomite generating similar and comparable values.

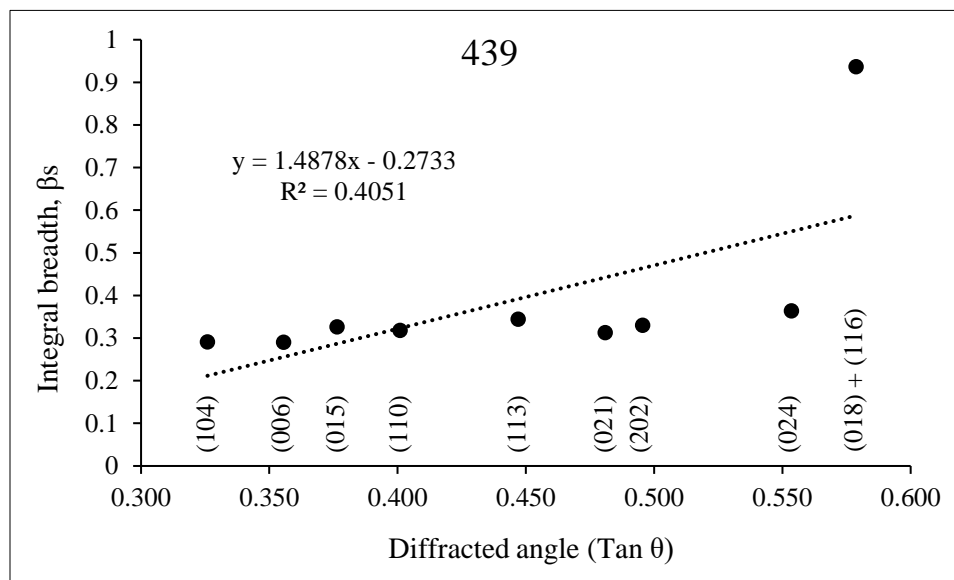


Figure 5-4. Williamson-Hall plot for dolomite sample 439 showing integral breadth values measured from peak area plotted for a given diffracted angle with (hkl) indicated. Linear trendline equation and R^2 value are displayed on chart.

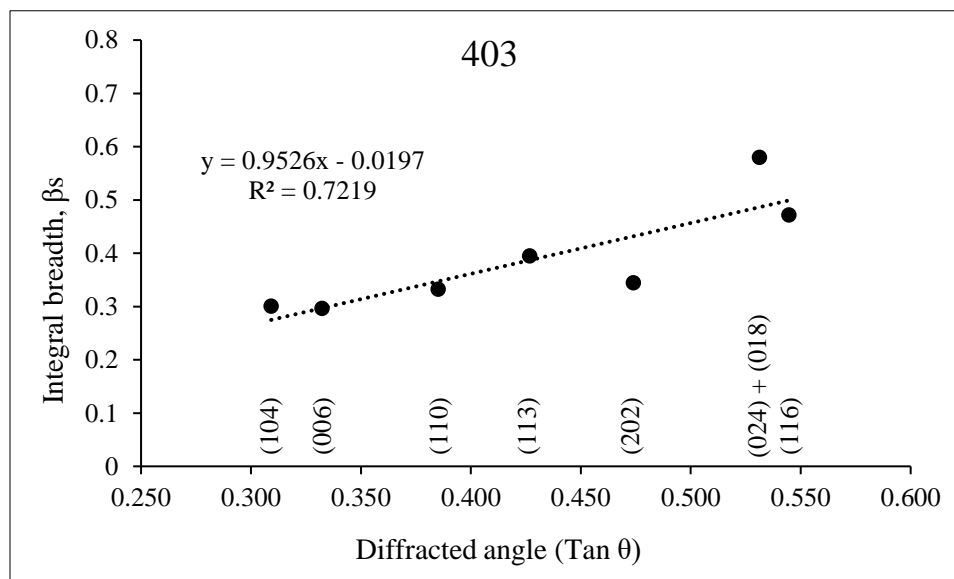


Figure 5-5. Williamson-Hall plot for calcite sample 439 showing integral breadth values measured from peak area plotted for a given diffracted angle with (hkl) indicated. Linear trendline equation and R^2 value are displayed on chart.

Table 5-1. Comparison of lattice strain values determined by two methods for samples from the Houghton impact structure.

Sample	Mineral	Strain % (TOPAS)*	Strain % (EVA) †	Modal proportion (wt%) §
02-128	dolomite	0.60	0.67	95.8
06-108	dolomite	0.11	0.10	99.7
07-020	calcite	0.42	0.30	69.0
99-063B	calcite	0.35	0.31	96.2
16-1017	calcite	0.12	0.17	92.6

* TOPAS = strain value determined from Rietveld refinement of whole rock powder.

† EVA = strain value derived from slope of trendline from Williamson-Hall plot.

§ Modal mineral proportion determined from Rietveld refinement using TOPAS.

Table 5-2. Calculated lattice strain values for carbonate samples from the Tunnunik impact structure sorted by distance from centre.

Sample	Mineral	Strain % (EVA)	Distance from centre (km)
131	dolomite	0.54	2.0
154	dolomite	0.36	2.6
439	dolomite	0.37	3.0
72	dolomite	0.27	4.7
454	dolomite	0.34	4.8
413	dolomite	0.31	5.9
83	dolomite	0.22	6.5
410	dolomite	0.10	7.2
159	dolomite	0.09	7.9
429	dolomite	0.09	11.0
432	dolomite	0.11	12.6
40*	dolomite	0.09	37.0
403	calcite	0.24	1.2
114	calcite	0.30	1.9
131	calcite	0.30	2.0

* Unshocked sample.

Based on the results from the four Houghton samples (Table 5-1), strain values were calculated for the 14 Tunnunik samples selected in this study using the method described above by measuring peak areas from each diffraction pattern (Table 5-2). While there are no Rietveld refinement-derived strain values for the Tunnunik samples, the lattice strain

values derived from their diffraction patterns fall within the range for Haughton samples (Table 5-1). Table 5-2 shows strain values for dolomite are highest for samples collected closest to the centre of the impact structure and decrease toward the rim, approaching the strain value for the unshocked dolomite sample. A similar trend is not as clear among the three calcite-rich Tunnunik samples as they were collected within 1 km of each other (Table 5-2).

5.4 Discussion

5.4.1 Peak broadening in X-ray diffraction patterns

Powder XRD patterns, and specifically broadening of diffraction peaks, provide an initial assessment to determine if a carbonate sample has been exposed to hypervelocity impact. Peak broadening is due to a reduction in crystallite size and unit cell volume when carbonates are shocked (Skála 2002). Mild tectonic deformation can also show peak broadening in carbonates and the broadening with associated FWHM values may appear similar to weakly shocked calcite found near the rim of an impact structure (Huson et al. 2009). Understanding the geologic history of an impact site will help recognize possible sources of peak broadening and further examination of tectonic deformation and shock should help discriminate between these processes in the future.

Exposure to shock resulting from a hypervelocity impact is observed in the samples from Tunnunik by a broadening and merging of peaks for dolomite at (018) and (116) around 59° and 60° 2θ , respectively (Fig. 5-3A) and broadening for calcite at (018) and (116) around 56° and 57° 2θ , respectively (Fig. 5-3B). Similar broadening and merging of peaks for the same range of reflections in experimentally shocked dolomite and calcite were observed by Martinez et al. (1995) when compared to an unshocked reference sample. Other studies have compared reflections of calcite and dolomite within a higher 2θ range and also identified broader peaks for these reflections in samples that had been shocked versus unshocked (Huson et al. 2009; Skála 2002; Skála and Jakeš 1999). A further comparison of shocked and tectonically deformed carbonates show that peak broadening can be detected in samples exposed to mild tectonic deformation where weakly shocked

calcite is more difficult to distinguish from tectonically deformed calcite than more heavily shocked dolomite (Huson et al. 2009).

5.4.2 Strain estimates and trends

When Rietveld quality powder XRD scans are not available to determine lattice strain values, this study has shown that strain values obtained from Williamson-Hall plots are a reasonable approximation. The comparison of strain values from Haughton samples (Table 5-1) demonstrates that relatively “pure” samples are more reliable in producing strain values similar to the refined Rietveld values; pure here means the dominant mineral phase in the sample is >90 wt%. The results from sample 07-020 (Table 5-1), which has the largest difference between strain values, indicate that when the modal proportion of the dominant mineral phase drops to ~70 wt%, this approximation method becomes less effective. Based on this observation, bulk rock samples consisting of one dominant mineral phase, over 90 wt%, are recommended rather than mixed samples, to achieve the best results of strain estimation. It is difficult to compare this variation relating to modal mineral proportions with previous studies as sample compositions in these studies appear to be consistent within their respective sample suites. Composition of sample suites in previous studies were reported as dominantly calcite by Skála and Jakeš (1999), the calcite samples used by Skála (2002) were “more or less uniform” and “contents other than calcite end-members are less than 5 mol%”, the calcite and dolomite samples used by Huson et al. (2009) deviate slightly from stoichiometric values, and the dolomitic rocks used by Martinez et al. (1995) were $79 \pm 1\%$ dolomite, $20 \pm 1\%$ calcite. The dolomitic rocks from Martinez et al. (1995) have the most deviation from an ideal dolomite composition and would have been interesting to see if there was a difference in strain values if they included stoichiometric dolomite and calcite samples in their shock recovery experiments.

Modal proportions for mineral phases in the Tunnunik samples (Table 5-2) were not determined because the quality of the original scans is not suitable for Rietveld refinement. However, based on the XRD patterns for dolomite-rich samples (Fig. 5-3A), peaks associated with calcite were not detected so dolomite is assumed to be the dominant carbonate phase in these samples and, therefore, provide good approximations to Rietveld-determined strain values. Calcite-rich samples 114 and 131 both indicate the presence of

dolomite (Fig. 5-3B) so these mixed carbonate samples may differ slightly in their estimated strain values compared with Rietveld-determined values, depending on their modal mineral proportions.

Other promising results from the Tunnunik strain values (Table 5-2) include both dolomite and calcite strain falling within the range of strain values determined for Haughton samples from Chapter 4 using Rietveld refinement. Several of the strain values for the low shocked and the unshocked dolomite samples from Tunnunik are slightly lower than the Haughton values, but remain comparable at 0.09% versus 0.11%, respectively. Since Tunnunik is deeply eroded, the exposed target rocks within the impact structure would be expected to have experienced lower overall shock pressures compared to the target rocks exposed within the younger and well-preserved Haughton impact structure as the expanding shockwave attenuates with depth (Melosh 1989). The estimated Tunnunik strain values obtained support this expectation.

The highest dolomite strain value occurs within a calcite-rich mixed carbonate sample, 131, collected near the centre of the Tunnunik impact structure. Comparing the distance from the centre to sample 131 and 439, the highest strain from a dolomite-rich sample, they have similar distances and would be expected to have more similar strain values. The difference is explained based on a trend observed for mixed carbonate samples from Haughton (Chapter 4). The trend identified in Haughton mixed carbonate samples is that dolomite is preferentially strained compared to calcite when both occur in bulk rock powders, especially when dolomite is the carbonate present in lower proportion.

In Table 5-2, sample 72 appears to be out of place with respect to decreasing strain value as distance from the centre of the impact structure increases as its value is less than sample 454 or 413 but is closer to the centre. This is explained by the elliptical distribution of shatter cones (Fig. 5-2) where sample 72 is nearer to the edge of the distribution than 454 despite being closer to the centre. The elliptical shatter cone distribution has been suggested to be the result of an oblique impact (Osinski and Ferrière 2016).

5.4.3 Practicality of strain estimation

Based on the results of XRD studies from the Tunnunik and Haughton impact structures, Rietveld refinement of bulk rock powders provides better refined structural information and is a more powerful tool than estimating peak areas from XRD patterns of short scan durations to generate Williamson-Hall plots. This is not meant to diminish the usefulness in generating Williamson-Hall plots for the purpose of measuring lattice strain as these plots have been used successfully for other minerals (e.g., Jenkins et al. 2019; Uchizono et al. 1999). There may be cases where it is more practical to collect a lower quality XRD pattern to look for peak broadening, especially if there is a large sample volume and limited analysis time. One-hour scans versus 8 hours or more could be a preferred option in this case. If peak broadening is observed, Williamson-Hall plots can easily be generated to estimate the lattice strain for that sample. If higher quality strain values are required, then specific samples could be analyzed a second time to produce Rietveld quality data.

5.5 Conclusions

Building from the results and conclusions in Chapter 4, lattice strain in carbonates generated by hypervelocity impact events is a measurable property. This study has shown that good, low quality X-ray diffraction scans can generate lattice strain results that are consistent with and fall within range of the lattice strain values determined when using higher quality XRD data and structural refinement. The strain values from Tunnunik also demonstrate the potential of using lattice strain values to estimate hypervelocity shock pressure and allow for comparisons between carbonate-rich impact structures. Shock pressure estimates could be determined from comparisons to lattice strain values in dolomite and calcite derived from dolostone and limestone experimentally shocked to known pressures with their strain values calculated. This could serve as the first steps in generating a quantifiable shock classification system for carbonates as none currently exist (Stöffler et al. 2018).

5.6 References

- Althoff P. 1977. Structural refinements of dolomite and a magnesian calcite and implications for dolomite formation in the marine environment. *American Mineralogist* 62:772–783.
- Brill R., Hermann C., and Peters C. 1939. Studien über chemische Bindung mittels Fourieranalyse III. *Die Naturwissenschaften* 27:677–678.
- Dewing K., Pratt B. R., Hadlari T., Brent T., Bédard J., and Rainbird R. H. 2013. Newly identified “Tunnunik” impact structure, Prince Albert Peninsula, northwestern Victoria Island, Arctic Canada. *Meteoritics & Planetary Science* 48:211–223.
- French B. M. 1998. *Traces of Catastrophe: A Handbook of Shock-Metamorphic Effects in Terrestrial Meteorite Impact Structures*, LPI Contribution No. 954, Lunar and Planetary Science Institute, Houston.
- French B. M., and Koeberl C. 2010. The convincing identification of terrestrial meteorite impact structures: What works, what doesn't, and why. *Earth-Science Reviews* 98:123–170.
- Hill R. J., and Howard C. J. 1987. Quantitative phase analysis from neutron powder diffraction data using the Rietveld method. *Journal of Applied Crystallography* 20:467–474.
- Huson S. A., Foit F. F., Watkinson A. J., and Pope M. C. 2009. Rietveld analysis of X-ray powder diffraction patterns as a potential tool for the identification of impact-deformed carbonate rocks. *Meteoritics & Planetary Science* 44:1695–1706.
- Jenkins L. E., Flemming R. L., and McCausland P. J. A. 2019. Quantitative in situ XRD measurement of shock metamorphism in Martian meteorites using lattice strain and strain-related mosaicity in olivine. *Meteoritics & Planetary Science* 54:902–918.
- Lepaulard C., Gattacceca J., Swanson-Hysell N., Quesnel Y., Demory F., and Osinski G. R. 2019. A Paleozoic age for the Tunnunik impact structure. *Meteoritics & Planetary*

Science 1–12.

- Mallamo M. P. Ordovician and Silurian stratigraphy, sedimentology, and paleoecology, Central Canadian Arctic Islands. MSc thesis, University of Western Ontario, 1989.
- Martinez I., Deutsch A., Scharer U., Ildefonse P., Guyot F., and Agrinier P. 1995. Shock recovery experiments on dolomite and thermodynamical calculation of impact induced decarbonation. *Journal of Geophysical Research* 100:15465–15476.
- Maslen E. N., Streltsov V. A., Streltsova N. R., and Ishizawa N. 1995. Electron density and optical anisotropy in rhombohedral carbonates. III. Synchrotron X-ray studies of CaCO₃, MgCO₃ and MnCO₃. *Acta Crystallographica Section B* 51:929–939.
- Melosh H. J. 1989. *Impact Cratering: A Geologic Process*, New York: Oxford University Press.
- Osinski G. R., Spray J. G., and Grieve R. A. F. 2008. Impact melting in sedimentary target rocks: An assessment. In *The Sedimentary Record of Meteorite Impacts, Special Paper 437*, edited by Evans K. R., Horton W., King Jr. D. K., and Morrow J. R. Geological Society of America, Boulder, CO. pp. 1–18.
- Osinski G. R., and Ferrière L. 2016. Shatter cones: (Mis)understood? *Science Advances* 2, e160061:1–10.
- Ribbe P. H. 1979. The structure of a strained intermediate microcline in cryptoperthitic association with twinned plagioclase. *American Mineralogist* 64:402–408.
- Ross N. L., and Reeder R. J. 1992. High-pressure structural study of dolomite and ankerite. *American Mineralogist* 77:412–421.
- Seeley J. R., and Milam K. A. 2018. Optical and X-ray diffraction analyses of shock metamorphosed dolostone at increasing depths within the central uplift of the Wells Creeks impact structure. *49th Lunar and Planetary Science Conference Abstract* #2755.

- Skála R., and Jakeš P. 1999. Shock-induced effects in natural calcite-rich targets as revealed by X-ray powder diffraction. In *Large Meteorite Impacts and Planetary Evolution II, Special Paper 339*, edited by Dressler B. O., and Sharpton V. L. Geological Society of America (GSA), Boulder, CO. pp. 205–214.
- Skála R. 2002. Shock-induced phenomena in limestones in the quarry near Ronheim, the Ries Crater, Germany. *Bulletin of the Czech Geological Survey* 77:313–320.
- Stewart W. D. 1987. *Late Proterozoic to Early Tertiary stratigraphy of Somerset Island and Northern Boothia Peninsula, District of Franklin, N.W.T.*, Paper 83-26, Geological Survey of Canada.
- Stöffler D., Hamann C., and Metzler K. 2018. Shock metamorphism of planetary silicate rocks and sediments: Proposal for an updated classification system. *Meteoritics & Planetary Science* 49:5–49.
- Turvey C. C., Hamilton J. L., and Wilson S. A. 2018. Comparison of Rietveld-compatible structureless fitting analysis methods for accurate quantification of carbon dioxide fixation in ultramafic mine tailings. *American Mineralogist* 103:1649–1662.
- Uchizono A., Shinno I., Nakamuta Y., Nakamura T., and Sekine T. 1999. Characterization of artificially shocked forsterites: (1) Diffraction profile analysis by Gandolfi camera. *Mineralogical Journal* 21:15–23.

Chapter 6

6 Impact-generated moissanite (SiC) from the Haughton impact structure, Canada

6.1 Introduction

Moissanite (SiC) is a rare terrestrial mineral typically identified in mantle-derived sources including kimberlites, carbonatites, and ultramafic rocks, as well as from crustal sources such as granitoids, volcanic breccias, and carbonates (e.g., Machev et al. 2018; Shiryaev et al. 2011). Here, we report the first documented in situ occurrence of moissanite crystals from a meteorite impact crater – in clast-rich impact melt rocks from the Haughton impact structure. The Haughton impact structure is a 23-km diameter complex crater located on Devon Island in the Canadian Arctic, consisting of mixed target rocks of Cambrian to Silurian-aged limestone, dolostone, evaporites, and sandstone overlying a Precambrian basement of gneiss and metagranite (Osinski et al. 2005a). Moissanite is associated with impact melt rocks present in 7 dykes within the chert-bearing limestone of the Eleanor River Formation exposed along the Haughton River (Osinski et al. 2005a) within the central uplift of the impact structure (Fig. 6-1).

The physical properties of moissanite include a hardness of 9.5, adamantine lustre, conchoidal fracture, and range from colourless to dark blue or green (e.g., Lyakhovich 1980). Moissanite has a simple crystal structure consisting of stable silicon and carbon tetrahedral layers. Variations in the number of repeated tetrahedral layers along the *c*-axis in the unit cell give rise to the formation of polytypes associated with the hexagonal, rhombohedral, and cubic lattice systems (Ramsdell 1947). The hexagonal polytypes 15R, 6H, and 4H were the first three polytypes identified, as well as the most common, and are known as α -SiC, or true moissanite, while cubic polytypes are classed as β -SiC (Lyakhovich 1980; Verma and Krishna 1966).

Moissanite has been reported in impactites from two other terrestrial impact structures, the Ries impact structure, Germany (Hough et al. 1995) and the Popigai impact structure, Russia (Gromilov et al. 2018). At both sites, moissanite crystals were not observed in situ but were identified in acid-resistant residue from suevite melt rocks at the Otting quarry

(Hough et al. 1995) and in the 250–400 μm fraction of crushed tagamite melt rocks (Gromilov et al. 2018).

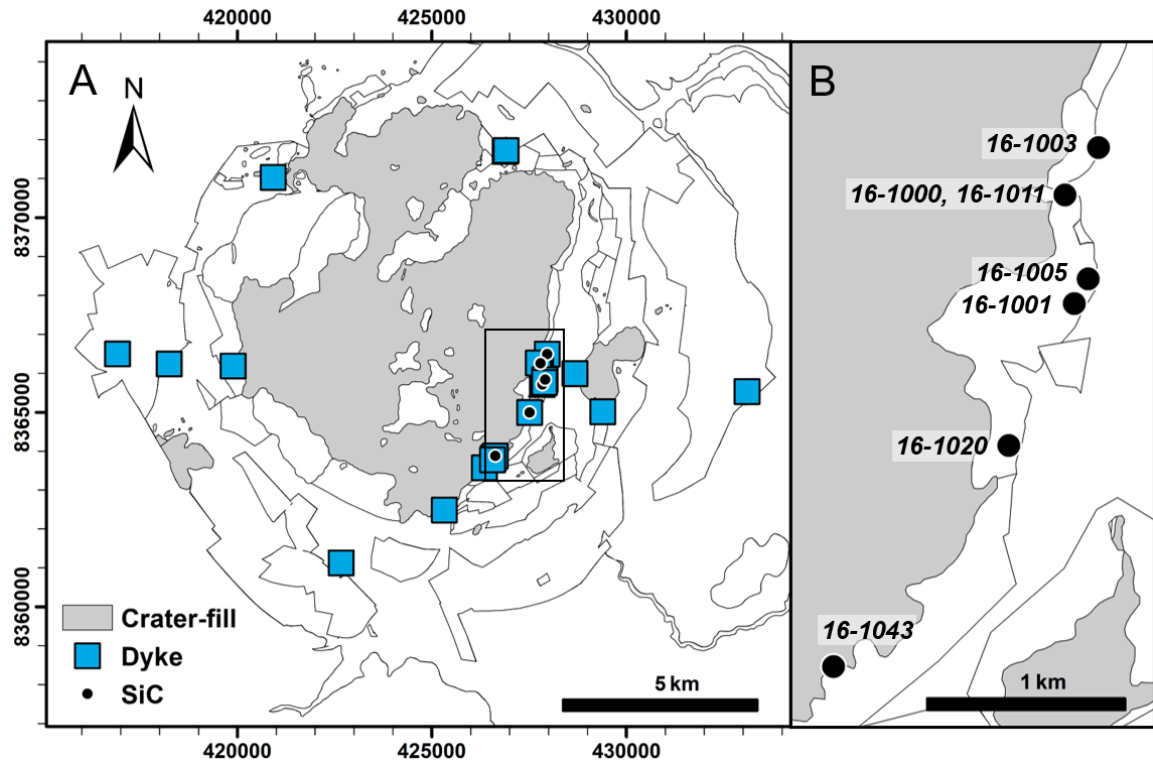


Figure 6-1. A) Overview of the Haughton impact structure with 24 dyke locations containing lithic impact breccia or impact melt rock. Impact melt rock dykes containing lithic impact breccia or impact melt rock. Impact melt rock dykes containing moissanite (SiC) crystals are exposed along the Haughton River Valley, indicated with black rectangle. B) Enlargement of Haughton River Valley showing locations and proximity of moissanite-bearing impact melt rock dykes with sample names indicated. Sample 16-1000 and 16-1011 were collected from dykes only several meters apart at the same outcrop. UTM grid with Easting and Northing at 1000 m intervals for Zone 16.

6.2 Moissanite and polytypism background

The first natural occurrence of moissanite (SiC) was reported from the Canyon Diablo meteorite in 1905 by Henri Moissan and was not identified from a terrestrial source until 1958 in rocks from the Green River Formation in Wyoming (Bauer et al. 1963). The first synthetic silicon carbide (moissanite) was made a few years earlier by (Acheson 1893) and

was later patented as carborundum as typically used as an abrasive. While the names moissanite, silicon carbide, and carborundum all refer to the same mineral, moissanite typically refers to the mineral when it is naturally formed and silicon carbide, carborundum, or simply SiC when the mineral is synthetically derived.

Moissanite belongs primarily to the hexagonal crystal system and its constituent elements of silicon and carbon form a binary tetrahedral structure where each Si atom is surrounded by 4 C and each C atom is surrounded by 4 Si (Verma and Krishna 1966). This is a simple and stable arrangement which gives rise to different packing sequences of the tetrahedral layers and depending how the tetrahedral layers are packed, moissanite can belong to the hexagonal (H), cubic (C), or rhombohedral (R) crystal lattice systems. The H, R, or C designations represent not only symmetry but when paired with a number, i.e., 6H or 15R, indicates the number of tetrahedral layers that repeat to give the unit cell for the given polytype. Cubic forms have a sphalerite-type structure with cubic closest packing and hexagonal forms have a wurtzite-type structure with hexagonal closest packing arrangement (Machev et al. 2018). The rhombohedral system is mentioned separately here from the hexagonal system for historical purposes as moissanite polytypes were designated according to the lattice system divisions at their time of discovery as H, C, or R. The packing differences affect the crystal structure and do not alter the properties of moissanite. These packing variations are referred as polytypes.

Polytypism is a special one-dimensional form of polymorphism where the unit cell is built by stacking identical unit layers of tetrahedra and the resulting polytypes differ only by the stacking sequence of these layers (Verma and Krishna 1966). The Ramsdell notation for designating a given SiC polytype includes the number of layers in the unit cell followed by H, R, or C to indicate the respective lattice type of hexagonal, rhombohedral, or cubic (Ramsdell 1947). Unit cell layers range from 2 to over 400, with most being less than 100 (Verma and Krishna 1966). Other notation systems were developed to identify the increasing number of polytypes including the classical ABC notation, Ott's interval sequence, and Hägg's notation (Verma and Krishna 1966). Each system has pros and cons depending on whether the interest among polytypes is symmetry, lattice type, packing, unit cell size, etc. The Ramsdell notation is simple and is the only notation that is able to define

a polytype with a known lattice but undetermined structure (Verma and Krishna 1966) making it is the most commonly used notation to indicate moissanite polytypes. Over 250 polytypes are now known and most are associated with synthetic silicon carbide while only 10 polytypes have been reported from naturally occurring terrestrial or meteorite sources (Machev et al. 2018; Shiryayev et al. 2011).

6.3 Methods and results

6.3.1 Petrography

Characterization of impact-generated melt rocks at the Haughton impact structure identified the presence of moissanite crystals in 7 dykes associated with limestone in the Eleanor River Formation. In addition to moissanite, the non-calcite fraction of the melt rocks includes clasts of chert, silicate glass, quartz, and dolomite. To rule out the possibility of contamination during sample preparation, several samples were carefully prepared a second time by avoiding synthetic silicon carbide and only using diamond abrasives. Following the second preparation, moissanite crystals were still present.

Initial identification of blue moissanite crystals was by optical examination. Polished thin sections were examined in transmitted and reflected light using a Nikon Eclipse LV 100POL microscope with NIS-Elements D laboratory image analysis system. In thin section, moissanite was easily identified by its blue colour in plane-polarized light. The relatively high reflectance under reflected light compared to the other mineral clasts present in the impact melt rocks (calcite, dolomite, quartz, and chert) also made moissanite crystals easy to identify.

Moissanite (SiC) crystals from the Haughton impact structure range from colourless to a distinctive pale to dark blue and average around 100 μm in size but vary between 20–500 μm (Fig. 6-2). Over 500 moissanite crystals have been observed in clusters or as single crystals which are typically associated with small pores, cavities, or veins that may or may not contain orange to brown-coloured silicate glass (Fig. 6-2). Thin sections that contained moissanite crystals were assessed and the occurrence of crystals within different settings is reported in Table 6-1. Here, the occurrence of moissanite crystals was divided based on whether they were found individually or as a group of 2 or more then based on their

association with clasts, cavities, veins, or matrix.

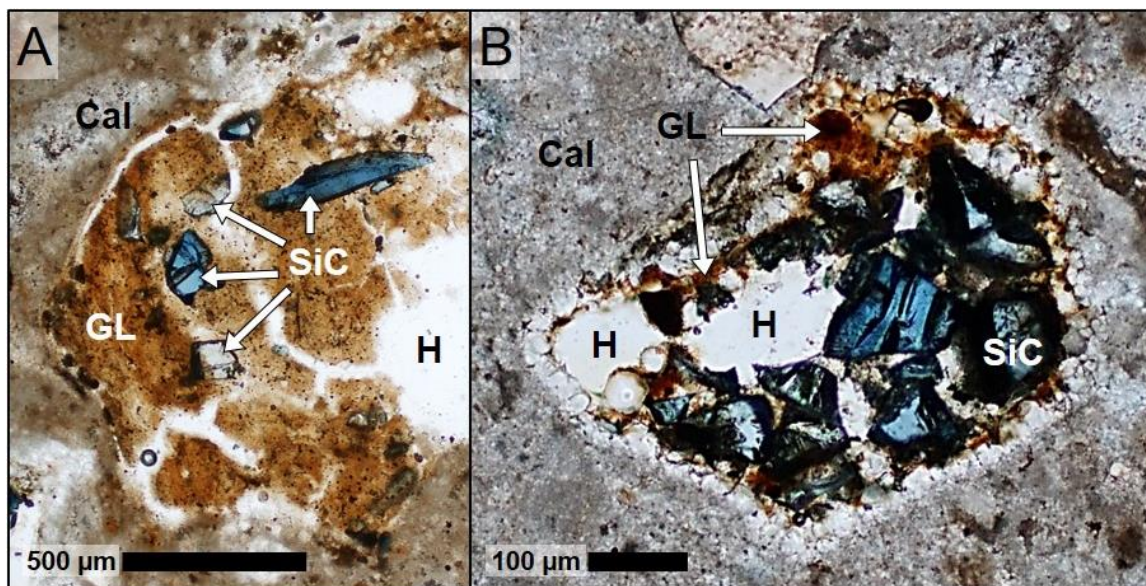


Figure 6-2. In situ colourless to blue moissanite (SiC) crystals in orange-brown silicate glass (GL). Cracks and holes (H) in glass appear white and surrounding fine-grained groundmass is composed of calcite (Cal). Distribution of SiC may be sparse A) or tightly packed B).

Table 6-1. Distribution of moissanite crystals within impact melt rocks from the Haughton impact structure.

Sample	Single crystal				Multiple* crystals					Total
	Ground-mass	Cavity	Partial glass †	Partial clast §	Full glass	Partial glass	Cavity/glass remnant #	Cavity no glass	Vein/crack	
16-1000	7	2	1	–	4	8	20	4	1	47
16-1001	–	2	–	–	–	–	–	–	–	2
16-1003	11	6	3	1	3	6	1	12	–	43
16-1005	32	7	4	–	9	21	12	12	9	106
16-1011	7	2	2	1	5	23	9	6	11	66
16-1020	18	21	1	1	16	38	18	7	2	122
16-1043	2	2	2	–	4	42	20	4	–	76

* Multiple means 2 or more moissanite crystals are found within the same clast, cavity, or vein.

† Partial glass refers to a fractured glass clast that is no longer a fully intact clast.

§ Partial clast refers to a fractured lithic clast.

Only enough glass remains to coat a small portion of the interior rim of a cavity.

6.3.2 Electron probe microanalysis (EPMA)

Back-scattered electron (BSE) images, quantitative wavelength dispersive spectroscopy (WDS), semi-quantitative electron dispersive spectroscopy (EDS), and element mapping data of moissanite crystals and silicate glass were collected using a JEOL JXA-8503F microprobe at the Earth and Planetary Materials Analysis Laboratory at the University of Western Ontario. Operating conditions include an accelerating voltage of 15 kV, beam current of 20 nA, spot size of 5 μm , and a working distance of 11 mm.

Quantitative wavelength dispersive spectroscopy (WDS) analysis for major and minor element abundances of 35 moissanite crystals and silicate impact glasses are provided in Table 6-2. WDS analysis of moissanite crystals yields an average composition of 73.5 (± 1.99) wt% Si and 26.29 (± 1.96) wt% C. Analysis of silicate glass associated with moissanite shows they fall within two groups, MgO-rich and C4-like. C4-like glass gets its name from a glass composition previously described in crater-fill impact melt rocks from the Haughton impact structure (Osinski et al. 2005b). The MgO-rich group has a quantitative WDS composition of major elements of 49.85 (± 2.71) wt% SiO_2 and 24.37 (± 1.50) wt% MgO giving an average analytical total $\sim 76\%$. The low analytical total indicates the presence of undetected volatiles. Based on comparable major elements obtained from parallel EDS analyses, there is up to 12 wt% C detected in these MgO-rich glasses. The quantitative WDS composition of major elements for the C4-like glass group is 44.85 (± 7.73) wt% SiO_2 , 13.90 (± 5.64) wt% MgO, 11.44 (± 2.61) wt% Al_2O_3 , 4.69 (± 1.91) wt% K_2O , and 3.64 (± 1.55) wt% FeO with an average analytical total $\sim 80\%$.

As noted in Table 6-2, the carbon content of moissanite was not directly measured. After the measured SiO_2 was converted from its oxide to Si wt%, that total and any trace elements (i.e., Al) were subtracted from 100 to give the calculated C wt% value. The calculated C wt% for WDS analyses is also comparable to the semi-quantitative EDS totals obtained for moissanite.

Table 6-2. Electron probe microanalysis of silicate glass and moissanite using wavelength dispersive spectrometry.

Sample type	<i>n</i> *	SiO ₂	C	Al ₂ O ₃	Na ₂ O	MgO	CaO
		wt% ± s.d.†	wt% ± s.d.	wt% ± s.d.	wt% ± s.d.	wt% ± s.d.	wt% ± s.d.
MgO-rich glass	31	49.85 ± 2.71	n.a.§	0.34 ± 0.25	0.17 ± 0.06	24.37 ± 1.50	0.21 ± 0.06
C4-like glass	32	44.85 ± 7.73	n.a.	11.44 ± 2.61	0.16 ± 0.06	13.90 ± 5.64	0.97 ± 1.88
moissanite #	35	73.50 ± 1.99	26.29 ± 1.96	0.18 ± 0.25	b.d.**	b.d.	b.d.

Sample type	<i>n</i>	TiO ₂	FeO	K ₂ O	SO ₃	Total
		wt% ± s.d.	wt% ± s.d.	wt% ± s.d.	wt% ± s.d.	wt% ± s.d.
MgO-rich glass	31	0.02 ± 0.02	0.33 ± 0.53	0.17 ± 0.10	0.17 ± 0.12	75.63 ± 4.06
C4-like glass	32	0.51 ± 0.69	3.64 ± 1.55	4.69 ± 1.91	0.44 ± 0.74	80.59 ± 6.31
moissanite	35	b.d.	b.d.	b.d.	b.d.	99.91 ± 0.06

* *n* = number of spots analyzed.

† Mean composition in weight percent and standard deviation.

§ n.a. = not analyzed.

SiO₂ wt% converted to Si wt% and C wt% calculated based on Si content.

** b.d. = below detection.

Inclusions in moissanite crystals are rare in the samples examined as only 14 out of over 500 moissanite crystals contained inclusions. Two types of inclusions were identified. The first type has two occurrences consisting of a single rounded metallic Si (Si⁰) inclusion approximately 20–30 μm in diameter that contains smaller inclusions of Fe or V silicides along the outer edge of the Si⁰ bleb. Element mapping performed by EPMA reveal the distribution of Ti, Ba, Ni, and Al metal substitutions or secondary inclusions within FeSi₂ and VSi₂ (Figs. 6-3 and 6-4).

In plane-polarized light, the second inclusion type appears as black veins within the moissanite crystal with no Si⁰ present (Fig. 6-5). Element mapping performed by EPMA was able to identify the distribution of metals within the dark vein-like inclusions which consist of metal alloys and/or metal silicides of Fe, Ni, Mn, Cr, and Cu (Fig. 6-5). The metals present and their occurrence within moissanite vary by crystal. The vein-like inclusions were found in 12 crystals from 2 different samples.

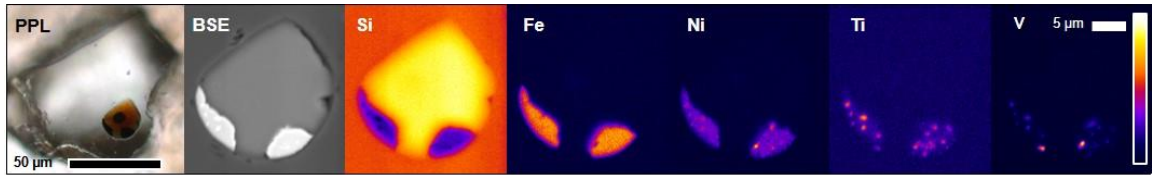


Figure 6-3. Colourless moissanite crystal with rounded orange metallic Si inclusion. Back-scattered electron (BSE) image and element maps of silicon (Si), iron (Fe), nickel (Ni), titanium (Ti), and vanadium (V) show distribution of metals within inclusion. Centre dark inclusion visible in plane-polarized light (PPL) is below the surface so it does not appear in element maps. Colour gradient on right edge indicates number of counts detected for each element from low (dark) to high (bright).

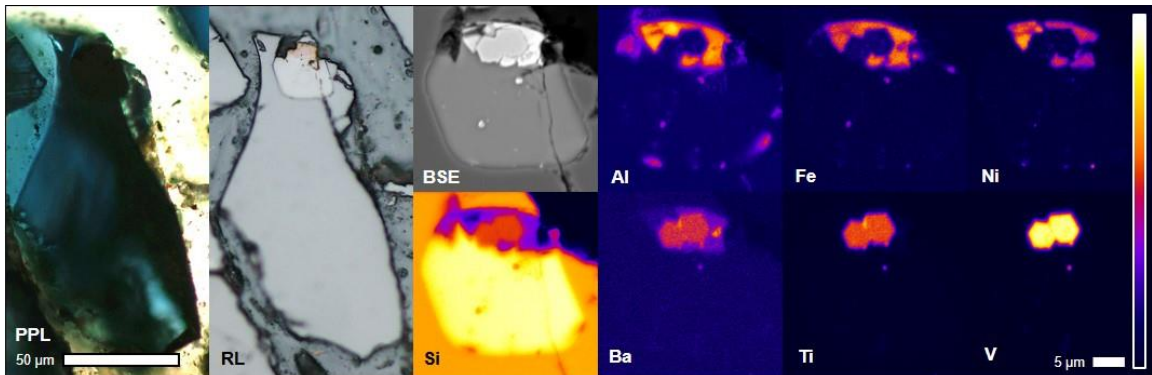


Figure 6-4. In plane-polarized light (PPL) the metallic inclusion in the dark blue moissanite crystal is difficult to identify but is more apparent in reflected light (RL) and with back-scattered electrons (BSE). The rounded metallic Si inclusion contains distinct silicide compositions of 1) aluminum (Al), iron (Fe), and nickel (Ni) and 2) barium (Ba), titanium (Ti), and vanadium (V). The hexagonal crystals are vanadium silicide (VSi_2) with minor Ti and Ba substitutions for V. Colour gradient on right edge indicates number of counts detected for each element from low (dark) to high (bright).

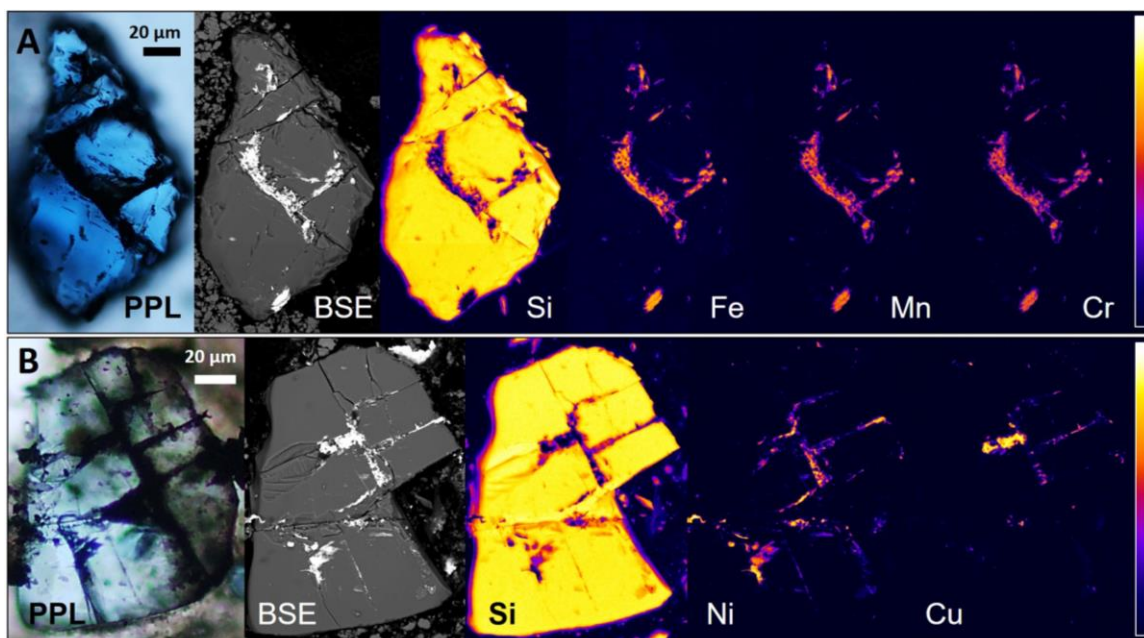


Figure 6-5. Metallic veins within moissanite crystals. A) Dark blue moissanite crystal shown in plane-polarized light (PPL) and back-scattered electron (BSE) image has a relatively even distribution of iron (Fe), manganese (Mn), and chromium (Cr) metal in the absence of silicon (Si). Trace amounts of nickel (Ni) and copper (Cu) were detected but are not shown. B) Pale blue moissanite crystal in PPL image has a more contrasting distribution of Ni and Cu metal within the moissanite crystal compared to the metals more evenly distributed within the crystal shown in (A). Colour gradient on right side of image indicates number of counts detected for each element from low (dark) to high (bright).

6.3.3 Raman Spectroscopy

To determine moissanite polytypes, micro-Raman spectra were collected using a Renishaw InVia Reflex Raman Spectrometer with 1,800 grating at the Surface Science Western facility at the University of Western Ontario. An Ar ion laser with a wavelength of 514 nm and 6 mW of power gave a spot size of 2 μm on the sample surface. The spectrometer was calibrated using a Si film. Sample excitation and Raman scatter collection was performed using a 50x and 100x optical lens on the Raman microscope.

Since micro-Raman spectra depend on crystal orientation, there were slight variations among spectra obtained for each crystal depending if the *c*-axis was oriented parallel (0001), perpendicular ($1\bar{1}00$ or $1\bar{1}20$), or random with respect to the direction of the incoming laser. The orientation of moissanite crystals in the samples examined could not be controlled as crystal orientation is based on their natural occurrence at the time of sample preparation. The orientation of micro-Raman spectra collected were compared with spectra obtained from other studies where the orientation of silicon carbide crystals was known to be parallel or perpendicular to the *c*-axis (Bauer et al. 2009; Dobrzhinetskaya et al. 2018; He et al. 2017; Nakashima and Harima 1997; Qin et al. 2019).

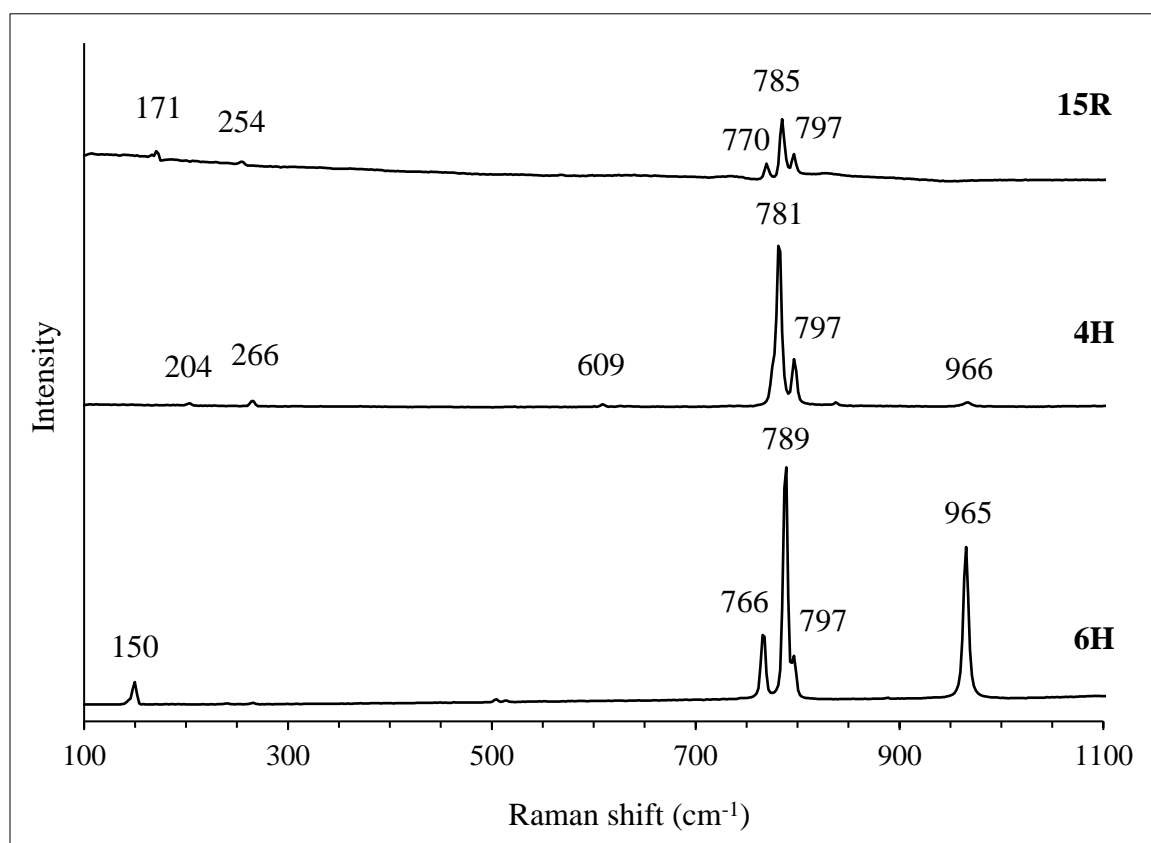


Figure 6-6. Micro-Raman spectra for the three moissanite polytypes identified (6H, 4H, and 15R) which are oriented parallel or close to parallel with respect to the *c*-axis. Major peak values for each polytype are indicated and a Y-offset was applied between spectra for clarity.

One thin section from two different samples was selected for analysis using micro-Raman. In total, 16 moissanite crystals were investigated to determine their polytype. The most

common polytype was 6H which was found in 13 crystals (7 parallel to the *c*-axis and 6 perpendicular) while 2 4H crystals (1 parallel and 1 perpendicular to the *c*-axis) were identified and only one 15R oriented nearly parallel to the *c*-axis was found. For each moissanite crystal, three to five micro-Raman spectra were obtained from different locations on the crystal and each gave the same pattern. A representative spectrum for each of the three polytypes is provided in Figure 6-6. Within a single impact melt rock sample, all three polytypes can be found.

6.4 Discussion

6.4.1 Natural versus synthetic SiC

The strongest evidence supporting the natural origin of moissanite is shown in Figure 6-2 where moissanite crystals are observed in situ with silicate glass in impact melt rocks generated during the impact event. Additionally, (Di Pierro and Gnos 2016) propose six criteria to discriminate between natural moissanite and synthetic contamination which include i) moissanite found as inclusions in other minerals, ii) euhedral and unbroken crystals, iii) melt inclusions, iv) abundant moissanite in freshly broken rocks, v) moissanite intergrown with magmatic minerals, and vi) large crystals greater than 1 cm. In the Haughton impact melt rocks, the best criterion to support the natural origin of moissanite are melt inclusions (Figs. 6-3 and 6-4). The rounded inclusions of Si⁰ and iron silicides suggest they are trapped melt and have been reported in moissanite crystals found in ophiolites (Trumbull et al. 2009), kimberlites (Shiryaev et al. 2011), and volcanic tuff (Dobrzhinetskaya et al. 2018). To address the remaining criteria, moissanite has not been found explicitly as inclusions in other minerals, such as diamonds; however as noted earlier in Haughton melt rocks, the most inclusion-like occurrence of moissanite crystals is within silicate glass formed from the impact event (Fig. 6-2). Moissanite was found as inclusions in diamonds from the Ries impact structure (Hough et al. 1995), but impact diamonds are not known to occur at the Haughton impact site. The majority of moissanite crystals are unbroken and observed conchoidal fractures are likely the result of the cutting and sample preparation process that used diamond tipped saw blades and diamond abrasives. Thin sections were prepared from freshly cut surfaces and not from exposed weathered surfaces, so it is unclear if there is a difference in the abundance of moissanite crystals based on

weathering. Presumably, there would be a difference as moissanite crystals are commonly found in silicate glass which weathers out comparatively easy, thus moissanite would be absent from more weathered surfaces. There are no magmatic minerals in the limestone-derived melt rocks, but moissanite in this case could be considered “intergrown” with silicate glass. Finally, the largest moissanite crystal observed in situ is 500 μm so it is smaller than the proposed 1 cm size, however, this final criterion is the only one that has yet to be fulfilled from any moissanite-bearing source (Di Pierro and Gnos 2016).

6.4.2 Moissanite formation

Moissanite crystallizes under very specific conditions that include extreme reducing conditions and high temperatures (Dobrzhinetskaya et al. 2018; Golubkova et al. 2016; He et al. 2017; Mathez et al. 1995; Schmidt et al. 2014; Trumbull et al. 2009). Based on these conditions, several temperature constraints can be applied to the moissanite-bearing impact melt rock samples based on the polytypes detected and the composition of inclusions. The 6H, 4H, and 15R polytypes (Fig. 6-6) are generated at high temperatures where 6H is stable near 2,500 °C, while 4H and 15R are stable at a slightly lower range between 2,000 °C and 2,450 °C (Verma and Krishna 1966). The rounded inclusion containing vanadium silicide (VSi_2) in Figure 6-4 supports this temperature range as VSi_2 in the trapped melt would be first to crystallize at 1,677 °C (Maex and Van Rossum 1995; Smith 1981). The cooling rate in this inclusion was slow enough that well-developed hexagonal VSi_2 was able to crystallize. Other Fe-silicides representing exsolved immiscible melt have crystallization temperatures in the range of ~1,200–1,400 °C (Maex and Van Rossum 1995). It should also be noted that to generate liquid calcite (CaCO_3) from the Eleanor River limestone, the impact melt rocks would require temperatures between ~1,200–2,500 °C and pressures >1 GPa (Ivanov and Deutsch 2002). Likewise, melting temperatures of the silicate glass associated with moissanite crystals would have experienced temperatures in the range of 1,500–2,000 °C based on immiscible-like textures observed between carbonates and silicate glass (Osinski et al. 2005c). Impact melts are expected to be superheated so the initial temperature of the melt would have exceeded all of these ranges thereby providing a favourable temperature environment for the formation of moissanite (Grieve et al. 1977; Osinski et al. 2005c). The differences in inclusion type could relate to cooling rate where

the rounded inclusions cooled slowly as trapped melt, whereas the vein-like inclusions may result from more rapidly cooled moissanite crystals. Many of the veins are straight within the crystals which suggests the veins are crystallographically controlled. These metallic veins are not merely a filling-in of cracks or post-impact deposition as there are obvious cracks that remain metal-free (Fig. 6-5). There is also no evidence of oxidation in the metals suggesting the veins have remained isolated and are native features within the moissanite crystals.

Reducing conditions are essential in forming moissanite and associated inclusions. The presence of Si^0 inclusions indicates redox conditions during moissanite formation are 4–9 log units below the iron-wüstite (IW) buffer (He et al. 2017; Schmidt et al. 2014; Trumbull et al. 2009). The Mg-Si-C-O system that includes SiC, Fe-Si, and periclase (MgO) corresponds to this low oxygen fugacity (Schmidt et al. 2014). The occurrence of moissanite within the calcite-rich melt rocks indicates the extreme reducing conditions were not widespread within the melt rock dykes. The association of moissanite crystals with small cavities in the melt rocks suggests the reducing conditions are restricted to these cavities. This in situ observation of impact melt rock cavities is similar to the occurrence in carbonatitic xenoliths present in Dalihu basalt where micro-cavities provide a location that buffers the highly reducing environment from surrounding oxidizing phases (He et al. 2017; Schmidt et al. 2014).

Rather than moissanite precipitating in voids from a reduced, highly fractionated fluid within carbonatitic xenoliths in basalt (Schmidt et al. 2014), the process for generating moissanite in cavities in impact melt rocks may be similar to shock processes observed in porous sandstone (Kieffer et al. 1976; Osinski 2007). In porous strongly shocked Coconino Sandstone from Meteor Crater, AZ, coesite crystals nucleate from SiO_2 melt in pores and resembles the Si-Mg-C-O silicate glass and moissanite associations shown in Figure 6-2. As a strong shock wave passed through the sandstone, small jets of molten material were injected into pores and during the subsequent decompression, coesite crystals begin to nucleate and grow while silicate glass was quenched (Kieffer et al. 1976). At Haughton, this process has been observed and reported in sandstones by (Osinski 2007) so extending the process to carbonate impact melt rocks would be consistent with previous observations

of impact processes. In the carbonate-specific process, a strong shock wave generated during the impact event would have created jets of hot reduced Si-Mg-C-O melt that entered pore spaces within the impact melt rock and, in some cases, caused moissanite to nucleate. In the impact melt rocks, not all pores and silicate glass contain moissanite, indicating specific conditions are required but when the conditions are met, several hundred moissanite crystals can be found in a single thin section. Moissanite is not a direct result of shock metamorphism in impacts like coesite, stishovite, or lonsdaleite (Langenhorst 2002); however, generating a strong shock event is required to provide the necessary temperature and reducing conditions in small cavities for moissanite to crystallize.

6.4.3 Occurrence at terrestrial impact sites

Moissanite has been detected from only three terrestrial impact sites, first from the Ries impact structure in Germany (Hough et al. 1995), then the Popigai impact structure in Russia (Gromilov et al. 2018), and now from the Haughton impact structure in Canada. These three sites are not identical and differences among them include the diameter of the impact structure, the nature of the target rocks, and the recovery of impact diamonds. The diameter of Haughton and Ries are similar at 23 km and 24 km, respectively while Popigai is about four times larger at 100 km. Target rocks in all three locations are mixed targets of sedimentary rock overlying crystalline basement (Osinski et al. 2008), however, specific rock composition, abundance, and assemblage vary among impact sites (e.g., Osinski et al. 2005a; Stöffler et al. 2013; Vishnevsky and Montanari 1999). Impact diamonds are found at both the Ries and Popigai impact structures and the diamonds were identified in the same acid-resistant residue and size fraction as moissanite in each case. Impact diamonds have yet to be identified from the Haughton impact structure, indicating the ability to generate diamonds is not a necessary condition to the formation of moissanite. The main similarity between all three locations is the presence of moissanite in impact melt rocks, which could suggest similar formation processes. The current lack of in situ context from Popigai and Ries means that associations and interpretations related to moissanite within melt rocks from Haughton cannot be extended to other impact sites at this time. The discovery of moissanite from a well-studied impact suggests moissanite could have a wider occurrence among terrestrial impact structures and warrants further investigation.

6.5 Conclusions

The discovery of moissanite in clast-rich impact melt rocks from the Haughton impact structure is the first report of moissanite observed in situ and third occurrence from a terrestrial impact structure. The existence of moissanite has provided new information such as temperature constraints involved in generating moissanite-bearing impact melt rocks and the mineral associations of moissanite at the Haughton impact structure. The specific formation conditions of moissanite also offer insights into impact processes at the Earth's surface for a mineral typically associated with mantle sources.

6.6 References

- Acheson E. G. 1893. On carborundum. *Chemical News* 68:179.
- Bauer J., Fiala J., and Hrichova R. 1963. Natural α -silicon carbide. *American Mineralogist* 48:620–634.
- Bauer M., Gigler A. M., Huber A. J., Hillenbrand R., and Stark R. W. 2009. Temperature-depending Raman line-shift of silicon carbide. *Journal of Raman Spectroscopy* 40:1867–1874.
- Dobrzhinetskaya L., Mukhin P., Wang Q., Wirth R., O'Bannon E., Zhao W., Eppelbaum L., and Sokhonchuk T. 2018. Moissanite (SiC) with metal-silicide and silicon inclusions from tuff of Israel: Raman spectroscopy and electron microscope studies. *Lithos* 310–311:355–368.
- Golubkova A., Schmidt M. W., and Connolly J. A. D. 2016. Ultra-reducing conditions in average mantle peridotites and in podiform chromitites: a thermodynamic model for moissanite (SiC) formation. *Contributions to Mineralogy and Petrology* 171.
- Grieve R. A. F., Dence M. R., and Robertson P. B. 1977. Cratering processes: As interpreted from the occurrence of impact melts. In *Impact and Explosion Cratering*, edited by Roddy D. J., Pepin R. O., and Merrill R. B. New York: Pergamon Press. pp. 791–814.

- Gromilov S. A., Afanasiev V. P., and Pokhilenko N. P. 2018. Moissanites of the Popigai astrobleme. *Doklady Earth Sciences* 481:997–999.
- He D., Liu Y., Gao C., Chen C., Hu Z., and Gao S. 2017. SiC-dominated ultra-reduced mineral assemblage in carbonatitic xenoliths from the Dalihu basalt, Inner Mongolia, China. *American Mineralogist* 102:312–320.
- Hough R. M., Gilmour I., Pillinger C. T., Arden J. W., Gilkes K. W. R., Yuan J., and Milledge H. J. 1995. Diamond and silicon carbide in impact melt rock from the Ries impact crater. *Nature* 378:41–44.
- Ivanov B. A., and Deutsch A. 2002. The phase diagram of CaCO₃ in relation to shock compression and decompression. *Physics of the Earth and Planetary Interiors* 129:131–143.
- Kieffer S. W., Phakey P. P., and Christie J. M. 1976. Shock processes in porous quartzite: Transmission electron microscope observations and theory. *Contributions to Mineralogy and Petrology* 59:41–93.
- Langenhorst F. 2002. Shock metamorphism of some minerals: Basic introduction and microstructural observations. *Bulletin of the Czech Geological Survey* 77:265–282.
- Lyakhovich V. V. 1980. Origin of accessory moissanite. *International Geology Review* 22:961–970.
- Machev P., O'Bannon E. F., Bozhilov K. N., Wang Q., and Dobrzhinetskaya L. 2018. Not all moissanites are created equal: New constraints on moissanite from metamorphic rocks of Bulgaria. *Earth and Planetary Science Letters* 498:387–396.
- Maex K., and Van Rossum M., eds. 1995. *Properties of Metal Silicides*, London: INSPEC, the Institution of Electrical Engineers.
- Mathez E. A., Fogel R. A., and Hutcheon I. D. 1995. Carbon isotopic composition and origin of SiC from kimberlites of Yakutia, Russia. *Geochimica et Cosmochimica Acta* 59:781–791.

- Nakashima S., and Harima H. 1997. Raman investigation of SiC polytypes. *Physica Status Solidi (A) Applied Research* 162:39–64.
- Osinski G. R., Lee P., Spray J. G., Parnell J., Lim D. S. S., Bunch T. E., Cockell C. S., and Glass B. 2005a. Geological overview and cratering model for the Houghton impact structure, Devon Island, Canadian High Arctic. *Meteoritics & Planetary Science* 40:1759–1776.
- Osinski G. R., Spray J. G., and Lee P. 2005b. Impactites of the Houghton impact structure, Devon Island, Canadian High Arctic. *Meteoritics & Planetary Science* 40:1789–1812.
- Osinski G. R., Lee P., Parnell J., Spray J. G., and Baron M. 2005c. A case study of impact-induced hydrothermal activity: The Houghton impact structure, Devon Island, Canadian High Arctic. *Meteoritics & Planetary Science* 40:1859–1877.
- Osinski G. R. 2007. Impact metamorphism of CaCO₃-bearing sandstones at the Houghton structure, Canada. *Meteoritics & Planetary Science* 42:1945–1960.
- Osinski G. R., Spray J. G., and Grieve R. A. F. 2008. Impact melting in sedimentary target rocks: An assessment. In *The Sedimentary Record of Meteorite Impacts, Special Paper 437*, edited by Evans K. R., Horton W., King Jr. D. K., and Morrow J. R. Geological Society of America, Boulder, CO. pp. 1–18.
- Di Pierro S., and Gnos E. 2016. Ca-Al-silicate inclusions in natural moissanite (SiC). *American Mineralogist* 101:71–81.
- Qin X., Li X., Chen X., Yang X., Zhang F., Xu X., Hu X., Peng Y., and Yu P. 2019. Raman scattering study on phonon anisotropic properties of SiC. *Journal of Alloys and Compounds* 776:1048–1055.
- Ramsdell L. S. 1947. Studies on silicon carbide. *American Mineralogist* 32:64–82.
- Schmidt M. W., Gao C., Golubkova A., Rohrbach A., and Connolly J. A. 2014. Natural moissanite (SiC) – a low temperature mineral formed from highly fractionated ultra-reducing COH-fluids. *Progress in Earth and Planetary Science* 1:1–14.

- Shiryayev A. A., Griffin W. L., and Stoyanov E. 2011. Moissanite (SiC) from kimberlites: Polytypes, trace elements, inclusions and speculations on origin. *Lithos* 122:152–164.
- Smith J. F. 1981. The Si-V (Silicon-Vanadium) system. *Bulletin of Alloy Phase Diagrams* 2:42–48.
- Stöffler D., Artemieva N. A., Wünnemann K., Reimold W. U., Jacob J., Hansen B. K., and Summerson I. A. T. 2013. Ries crater and suevite revisited-Observations and modeling Part I: Observations. *Meteoritics & Planetary Science* 48:515–589.
- Trumbull R. B., Yang J. S., Robinson P. T., Di Pierro S., Vennemann T., and Wiedenbeck M. 2009. The carbon isotope composition of natural SiC (moissanite) from the Earth's mantle: New discoveries from ophiolites. *Lithos* 113:612–620.
- Verma A. R., and Krishna P. 1966. *Polymorphism and polytypism in crystals*, New York: John Wiley & Sons, Inc.
- Vishnevsky S., and Montanari A. 1999. Popigai impact structure (Arctic Siberia, Russia): Geology, petrology, geochemistry, and geochronology of glass-bearing impactites. In *Large Meteorite Impacts and Planetary Evolution II, Special Paper 339*, edited by Dressler B. O., and Sharpton V. L. Geological Society of America (GSA), Boulder, CO. pp. 19–59.

Chapter 7

7 Summary of results from two terrestrial hypervelocity impacts into carbonate target sequences

The research presented in the preceding chapters cover a range of topics related to carbonates associated with two hypervelocity impact events, located in the Canadian High Arctic. With both the Tunnunik and Haughton impact structures occurring in the sedimentary sequence of the Arctic Platform, comparisons between the similar-scale impacts is inevitable. The erosional state of the two impact structures expose different sections of a complex crater, making the comparisons more informative. A comparison of main features between these impact structures is provided in Table 7-1 below.

Table 7-1. Comparison of physical features and properties at the Tunnunik and Haughton impact structures.

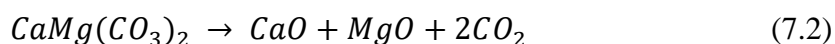
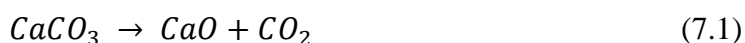
Feature	Tunnunik	Haughton	Reference
Diameter	28 km	23 km	Dewing et al. (2013); Osinski and Spray (2005)
Age	450–430 Ma	23.5 Ma	Lepaulard et al. (2019); Young et al. (2013)
Erosional level	6: crater-fill breccias/ melt rocks eroded	2: ejecta partly preserved; rim partly preserved	Osinski and Ferrière (2016)
Shatter cones	yes; 10 x 12 km distribution	yes; ~4.5 km radial distribution	Osinski and Ferrière (2016)
Crater-fill deposits	no	yes	Chapter 2; Osinski and Spray (2001)
Ejecta deposits	no	yes; proximal	Chapter 2; Osinski et al. (2005a)
Dykes	yes	yes	Chapter 2 & 3
Carbonates	yes; dolostone, limestone	yes; dolostone, limestone	Dewing et al. (2013); Osinski et al. (2005b)
Evaporites	no	yes; gypsum, anhydrite	Chapter 2; Osinski et al. (2005b)
Crystalline basement reached	no	yes	Dewing et al. (2013); Osinski et al. (2005b)
Carbonate melt	very limited	crater-fill and melt rock dykes	Chapter 2 & 3; Osinski et al. (2005a)
Silicate glass	rare	yes	Chapter 2 & 3; Osinski et al. (2005a)

7.1 Carbonate-rich target sequences

The Arctic Platform consists of many sedimentary formations (Daae and Rutgers 1975; Thorsteinsson and Tozer 1970) and the sequences present at both impact sites are dominated by carbonates. Northwest Victoria Island has a thicker sedimentary sequence than on Devon Island and as a result the Tunnunik impact event did not reach the crystalline basement whereas the Haughton impact event did reach the crystalline basement of granitic and metasedimentary rocks (Table 7-1). Presence of crystalline basement material, evaporites, and sandstones leaves a target sequence comprised of ~75–80% carbonates at the Haughton impact structure (Osinski et al. 2005a). Carbonates are even more abundant at the Tunnunik impact structure where dolostone, limestone, and limited mudstone rocks are exposed (Dewing et al. 2013). Limestone and dolostone are present in different amounts at each site with Tunnunik exposing more dolostone than limestone while Haughton exposes more equal portions of carbonate rocks overall.

When it comes to carbonate-rich target rocks, there are still questions to be answered and relate to whether carbonates melt or decompose upon impact. The two carbonate-rich study sites here provided an opportunity to identify if any melting or decomposition of carbonates occurred during these impact events. While this was not a primary goal of this research, evidence to support one or both processes had the potential to be identified through the characterization of impact breccias and impact melt rocks collected from impact-generated dykes.

Recalling the decomposition reactions of calcite (7.1) and dolomite (7.2) (e.g., Agrinier et al. 2001), the main evidence for the decomposition or devolatilization of carbonates would be the presence of CaO or MgO in impactites generated during the impact event (Osinski et al. 2008).



Neither CaO (lime) nor MgO (periclase) were identified in Tunnunik breccias or in Haughton breccias or melt rocks. If either decomposition product had been generated

during the impact, then these impactites would be the most likely location to detect the presence of these products.

As for melting, at Tunnunik there is limited evidence for melt in the form of thin isolated bands of calcite that have a flow-like morphology and as irregular textures in clasts from breccia from the central uplift (Chapter 2). At Haughton, melting has previously been shown to occur in groundmass and associated with impact glass in the crater-fill impact melt rock deposits (Osinski and Spray 2001; Osinski et al. 2005b) and as melt rocks found in some dykes within the central uplift (Chapter 3).

Even within the last several years a consensus has yet to be reached regarding the fate of carbonates associated with hypervelocity impacts. In a recent laboratory experiment a small amount of carbonate melt was generated from a carbonate projectile, to the surprise of the authors, as they were conducting unconfined shock experiments to support CO₂ volatilization dominates in carbonate containing targets (Hörz et al. 2019). The volume of melt generated in the unconfined experiments is not equivalent to what is observed at terrestrial craters i.e., Haughton where the crater-fill impact melt rocks were estimated to be >200 m thick (presently ~125 m thick) and cover an area of ~60 km² (Osinski and Spray 2001). The Hörz et al. (2019) study could be a case where small scale shock experiments do not scale up to simulate large terrestrial impact events (Grieve and Cintala 1992). It has also been suggested that the amount of melt generated in sedimentary target sequences, including carbonates, has been underestimated and the volume of melt generated in sedimentary and crystalline targets is similar (e.g., Kieffer and Simonds 1980; Osinski et al. 2018; Wünnemann et al. 2008).

While the research presented in the preceding chapters does not unequivocally provide evidence that carbonate melting is the dominant process to affect carbonates during hypervelocity impact events, it does contribute support.

The dykes at the Haughton impact structure that contain impact melt rocks also contain the rare mineral moissanite (Chapter 6). Previously, moissanite has only been identified from two terrestrial impact locations, the Ries and Popigai impact structures (Gromilov et al. 2018; Hough et al. 1995). The very specific crystallization setting related to temperature

and reducing conditions for moissanite (e.g., Dobrzhinetskaya et al. 2018; He et al. 2017) provide information regarding temperature constraints that can be applied to the impact melt rocks. The variation of moissanite polytypes detected indicate the crystals formed between 2,000 °C and 2,500 °C (Chapter 6). As impact melts are expected to be superheated (Grieve et al. 1977; Osinski et al. 2005c), the discovery of moissanite further supports the occurrence of high temperatures during crater formation generated carbonate melt in the form of calcite-rich impact melt rock dykes (Chapter 3) and crater-fill deposits (e.g., Osinski and Spray 2001; Osinski et al. 2005a).

7.2 Deeply eroded versus well-preserved impact structures

The difference in the state of preservation between Tunnunik and Haughton is provided in Table 7-1 and shown in Figure 7-1. The post-impact erosion at the Haughton impact structure is estimated at ~150 m which was determined through a combination of the average erosion rate at Haughton of 6.4 m/Ma and the thickness of the units in the target sequence (Osinski et al. 2005a). Post-impact erosion at the Tunnunik impact structure is estimated at ~1.5 km based on gravity and magnetic measurement while using comparable erosion rates from Haughton (Quesnel et al. 2020; Zylberman 2017).

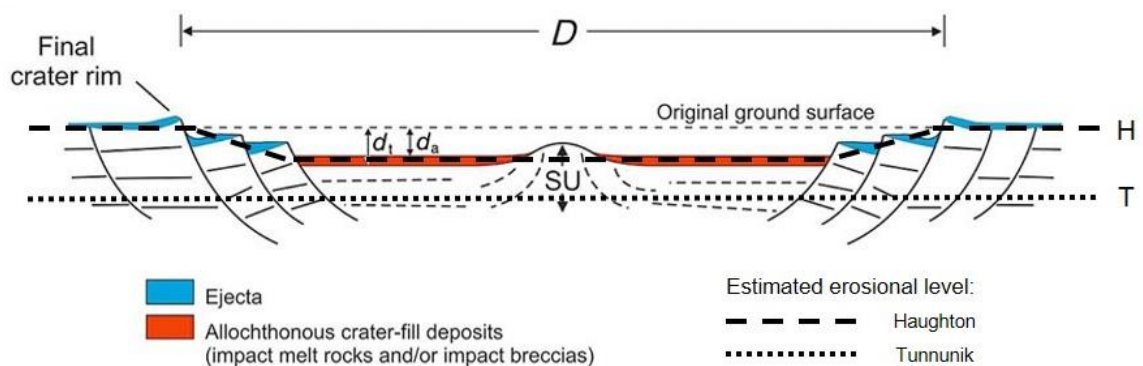


Figure 7-1. Visual estimation of erosion levels at the Haughton (H) and Tunnunik (T) impact structures. Note the actual erosional surfaces of these impact structures are not flat horizontal planes, this is only a representation. Complex crater cross-section image is modified from Osinski and Pierazzo (2013); D = final rim-to-rim crater diameter, d_t = true depth, d_a = apparent depth, SU = structural uplift.

Erosion at Tunnunik has removed all proximal and distal ejecta, crater-fill, and nearly all the surface expression of the impact structure, especially as seen from satellite imagery. This extensive erosion has exposed the crater floor of the Tunnunik impact structure.

Together, these two impact structures could be thought of as two exposures of the same crater based on their size and carbonate-rich target sequence. Since Tunnunik is much older, it is logical that no crater-fill or ejecta deposits remain following the erosion from repeated glaciation events. To get a sense of the appearance and distribution of such deposits, the Haughton impact structure can be examined. While there is no way to verify what a well-preserved Tunnunik impact structure looked like, Haughton would be a good approximation. At Haughton, the crater-fill impact melt rocks cover much of the central portion of the impact structure and obscure the target rocks of the central uplift as well as features such as shatter cones. Where uplifted rocks are exposed within the central uplift at Haughton, shatter cones are easily recognized and well-developed in fine-grained limestone and dolostone (Osinski and Spray 2006). Similarly, the extent of shatter cones was also determined at Tunnunik (Osinski and Ferrière 2016) despite the blanket of Quaternary post-glacial sediments covering most of the flat-lying surfaces. The preservation level of these craters shows differences in dykes based on where they were emplaced during an impact event and is discussed further in the next section.

7.3 Dyke emplacement in the Tunnunik and Haughton impact structures

The distribution of known dykes at the Tunnunik impact structure (Chapter 2) are the result of a comprehensive survey of exposed outcrops conducted during 2012 and 2015. With limited target rock exposure across the impact structure, additional exposed dykes are expected to remain scarce. The distribution of dykes at the Haughton impact structure is more widespread (Chapter 3) than Tunnunik but does remain limited within the central uplift due to the coverage of impact melt rocks in the crater-fill deposits.

In complex craters, dyke distribution is also complex and the spatial distribution of dykes can be difficult to assess or are underestimated in the field due to limited exposure (Lambert 1981; Reimold 1998). Reimold (1998) also notes that “the inherent lack of three-

dimensional geological understanding has generally prevented detailed mapping of distribution and interrelationships of impact breccias”. On their own, the Tunnunik and Haughton impact structures have their own cross-section through an ideal complex crater (Fig. 7-1), but the occurrence of dykes throughout the rest of each structure is unknown. At Tunnunik it is impossible to know the distribution of dykes in the now eroded rocks that once overlaid the current exposure. At Haughton, it could be possible to drill into the target rocks deep into the crater floor but would need to be extremely lucky to encounter any dykes if such a depth was reached. In 2013 three locations in the central uplift were drilled, the depths of these holes were ~4 m, ~5 m, and ~13 m (Zylberman et al. 2017). The material recovered from these cores was limited but consist of several types of polymict impact melt rock (Zylberman et al. 2017). By comparing the distribution of dykes between Haughton and Tunnunik, this problem is addressed to some extent where one crater provides an extended extent toward the other. Combined these impact structures do not generate a complete “three-dimensional geological understanding” but allows for insights and interpretations regarding impact processes that create impact-generated dykes and their contents.

When comparing lithic breccia dykes, Haughton breccias are predominantly monomict compared to Tunnunik which are mostly polymict (Type 1); see Chapters 2 and 3. This suggests that transport distance of dyke contents was a main factor in the type of lithic breccias found relative to their position within the impact structure. Injected Type 1 dykes at Tunnunik were transported greater distances in order to be emplaced in the crater floor and would have entrained clasts from all stratigraphic units the dykes cut across during transport. Impact melt rock dykes are absent from the current exposure at Tunnunik but are common within the central uplift at Haughton. Impact melt rock dykes were only identified within one formation at Haughton, the Eleanor River Formation, and only contain clasts from this formation indicating the impact melt rocks likely experienced little transport. If impact melt rocks were only transported short distances, it corresponds with the lack of melt rocks at the present exposure of Tunnunik. The presence of impact melt rocks at Haughton does suggest, however, that similar melt rocks would have formed at Tunnunik but have since been eroded. Several clasts of possible calcite melt (e.g., Fig. 2-5) could be surviving clasts from Haughton-like impact melt rocks.

7.4 Extent of shock

Using X-ray diffraction (XRD) to identify shock effects in carbonates has not been extensively examined in impact structures around the world. Outside of this study, analysis of shocked carbonates with XRD has been conducted at the Kara and Steinheim (Skála and Jakeš 1999), Ries (Skála 2002), Sierra Madera (Huson et al. 2009), and Wells Creek (Seeley and Milam 2018) impact structures. There are 198 confirmed terrestrial impact structures, 82 of which formed in sedimentary target rocks and 54 in mixed sedimentary and crystalline rocks, so there are many potential candidates that remain to be examined (Impact Earth 2020).

This study has added the Haughton and Tunnunik impact structures to this list as calcite and dolomite from the target sequence at both structures were investigated. Lattice strain values for these minerals were determined and represent varying degrees of shock. As more information is collected about shocked calcite and dolomite, the better our understanding will be about how these minerals respond to shock. An end goal would be to create a classification scheme for carbonates as many already exist for silicate minerals (Stöffler et al. 2018).

7.4.1 Strain versus distance from the centre of impact structures

Investigating lattice strain in shocked carbonates from Haughton (Chapter 4) and Tunnunik (Chapter 5) has shown the highest strain values for dolomite and calcite are associated with samples collected near the centre of the impact structure and decrease toward the rim. This general trend applies to most samples from the two impact structures with several key observations. The first observation is related to strain values from Tunnunik where strain values are not simply correlated with distance from the centre, but also to the distribution of shatter cones. The elliptical shatter cone distribution at Tunnunik is suggested to be caused by an oblique impact (Osinski and Ferrière 2016) and if shock pressures were not evenly distributed in all directions at the time of impact then the strain results appear to support that the well-documented shatter cone distribution is indeed elliptical.

The second observation is that bulk rock sample composition may affect strain values when a mixture of dolomite and calcite are present. The studies at Haughton and Tunnunik

worked with natural samples so compositions cannot be controlled and as a result, the modal proportions of mineral phases from one sample to the next are not consistent. This inconsistency has revealed potential trends associated with carbonate proportions related to strain such as dolomite giving higher strain values and calcite lower values when both are present in proportions >10 wt% in the same sample.

7.4.2 Strain versus depth within impact structures

Variation with depth at the Tunnunik and Haughton impact structures was not specifically investigated in their respective studies. Exact elevation differences between samples was not recorded but could vary up to a couple hundred metres. What can be compared with respect to depth are the overall sample suites from each impact site. Recall that Figure 7-1 shows the relative difference in the exposed surface exposure for each impact structure. Based on this figure alone, it would be expected that the more deeply eroded Tunnunik impact structure would have a lower range of strain values than the Haughton impact structure since shock waves weaken as they propagate downward into target rock (Melosh 1989). As expected, the lattice strain values from both sites appear to agree with this statement. Even though the Tunnunik impact structure has been deeply eroded, it still contains shatter cones. Shock evidence is present at Tunnunik regardless of strain values, the values simply indicate the rocks experienced less shock compared to Haughton. The initial study by Seeley and (Milam 2018) examined how shock changes within a drill core from the central uplift of the Wells Creek impact structure. Peak broadening alone was not able to provide a clear answer but when their study is complete a more definitive result related to shock with depth could be achieved.

7.4.3 Future shock-related research opportunities

The lattice strain studies at Haughton and Tunnunik impact structures provide promising results for identifying shock in carbonate rocks. Parallel investigations of calcite and dolomite from additional carbonate-bearing impact structures are needed to determine if the results from Chapter 4 and Chapter 5 are typical for terrestrial impact structures. Tunnunik and Haughton are similar in diameter so additional lattice strain data from impact structures with a range of diameters would be valuable.

To provide further meaning to lattice strain values obtained from carbonates shocked at terrestrial impact structures, a pressure scale with associated strain values is required. A scale like this was suggested by Martinez et al. (1995) but has yet to be generated. This could be achieved by experimentally shocking limestone and dolostone to increasing levels of known pressure, comparable to hypervelocity shock levels, followed by determining lattice strain. This would allow strain values acquired from impact structures that are without silicates to estimate shock levels or assist in confirming an impact into a carbonate target where shatter cones or other physical crater features are absent.

7.5 Conclusions

This research has produced new information and insights into impact cratering processes associated with carbonate-rich terrestrial environments. A significant contribution of this research comes from the opportunity to study two impact structures of similar diameter, and consequently the ability to compare what would have been similar cratering processes, in different states of preservation.

Characterizing the impact-generated dykes exposed at the Tunnunik and Haughton impact structures has identified the diversity of impact breccias and impact melt rocks present these sites. The range of diversity within these dykes was previously unreported can be used to compare with characteristics of dykes from other carbonate-rich impact structures. The results of the X-ray diffraction studies of lattice strain related to shock is promising and indicates more research is required to better understand how carbonates respond to shock, which could help lead to a shock classification system for carbonates. It would be interesting to determine if the occurrence of moissanite is truly rare where it has only been identified at three impact structures or has been dismissed as contamination and was not fully investigated further at other impact sites.

Based on the results presented in these studies, related future work would continue to investigate and revisit previously studied carbonate-rich impact structures to determine similarities or even variation related to this research conducted at the Tunnunik and Haughton impact structures.

7.6 References

- Agrinier P., Deutsch A., Schärer U., and Martinez I. 2001. Fast back-reactions of shock-released CO₂ from carbonates: An experimental approach. *Geochimica et Cosmochimica Acta* 65:2615–2632.
- Daae H. D., and Rutgers A. T. C. 1975. Geologic history of the Northwest Passage. *Bulletin of Canadian Petroleum Geology* 23:84–108.
- Dewing K., Pratt B. R., Hadlari T., Brent T., Bédard J., and Rainbird R. H. 2013. Newly identified “Tunnunik” impact structure, Prince Albert Peninsula, northwestern Victoria Island, Arctic Canada. *Meteoritics & Planetary Science* 48:211–223.
- Dobrzhinetskaya L., Mukhin P., Wang Q., Wirth R., O’Bannon E., Zhao W., Eppelbaum L., and Sokhonchuk T. 2018. Moissanite (SiC) with metal-silicide and silicon inclusions from tuff of Israel: Raman spectroscopy and electron microscope studies. *Lithos* 310–311:355–368.
- Grieve R. A. F., Dence M. R., and Robertson P. B. 1977. Cratering processes: As interpreted from the occurrence of impact melts. In *Impact and Explosion Cratering*, edited by Roddy D. J., Pepin R. O., and Merrill R. B. New York: Pergamon Press. pp. 791–814.
- Grieve R. A. F., and Cintala M. J. 1992. An analysis of differential impact melt-crater scaling and implications for the terrestrial impact record. *Meteoritics* 27:526–538.
- Gromilov S. A., Afanasiev V. P., and Pokhilenko N. P. 2018. Moissanites of the Popigai astrobleme. *Doklady Earth Sciences* 481:997–999.
- He D., Liu Y., Gao C., Chen C., Hu Z., and Gao S. 2017. SiC-dominated ultra-reduced mineral assemblage in carbonatitic xenoliths from the Dalihu basalt, Inner Mongolia, China. *American Mineralogist* 102:312–320.
- Hörz F., Cintala M. J., Thomas-Keprta K. L., Ross D. K., and Clemett S. J. 2019. Unconfined shock experiments: A pilot study into the shock-induced melting and

- devolatilization of calcite. *Meteoritics & Planetary Science* 28:1–28.
- Hough R. M., Gilmour I., Pillinger C. T., Arden J. W., Gilkes K. W. R., Yuan J., and Milledge H. J. 1995. Diamond and silicon carbide in impact melt rock from the Ries impact crater. *Nature* 378:41–44.
- Huson S. A., Foit F. F., Watkinson A. J., and Pope M. C. 2009. Rietveld analysis of X-ray powder diffraction patterns as a potential tool for the identification of impact-deformed carbonate rocks. *Meteoritics & Planetary Science* 44:1695–1706.
- Impact Earth. Impact Earth Database. 2020. www.impactearth.com (Accessed February 18, 2020).
- Kieffer S. W., and Simonds C. H. 1980. The role of volatiles and lithology in the impact cratering process. *Reviews of Geophysics and Space Physics* 18:143–181.
- Lambert P. 1981. Breccia Dikes: Geological constraints on the formation of complex craters. In *Multi-ring Basins, Proc. Lunar Planet. Sci.*, edited by Schultz P. H., and Merrill R. B. pp. 59–78.
- Lepaulard C., Gattacceca J., Swanson-Hysell N., Quesnel Y., Demory F., and Osinski G. R. 2019. A Paleozoic age for the Tunnunik impact structure. *Meteoritics & Planetary Science* 1–12.
- Martinez I., Deutsch A., Scharer U., Ildefonse P., Guyot F., and Agrinier P. 1995. Shock recovery experiments on dolomite and thermodynamical calculation of impact induced decarbonation. *Journal of Geophysical Research* 100:15465–15476.
- Melosh H. J. 1989. *Impact Cratering: A Geologic Process*, New York: Oxford University Press.
- Osinski G. R., and Spray J. G. 2001. Impact-generated carbonate melts: Evidence from the Houghton structure, Canada. *Earth and Planetary Science Letters* 194:17–29.
- Osinski G. R., and Spray J. G. 2005. Tectonics of complex crater formation as revealed by

- the Haughton impact structure, Devon Island, Canadian High Arctic. *Meteoritics & Planetary Science* 40:1813–1834.
- Osinski G. R., Spray J. G., and Lee P. 2005a. Impactites of the Haughton impact structure, Devon Island, Canadian High Arctic. *Meteoritics & Planetary Science* 40:1789–1812.
- Osinski G. R., Lee P., Spray J. G., Parnell J., Lim D. S. S., Bunch T. E., Cockell C. S., and Glass B. 2005b. Geological overview and cratering model for the Haughton impact structure, Devon Island, Canadian High Arctic. *Meteoritics & Planetary Science* 40:1759–1776.
- Osinski G. R., Lee P., Parnell J., Spray J. G., and Baron M. 2005c. A case study of impact-induced hydrothermal activity: The Haughton impact structure, Devon Island, Canadian High Arctic. *Meteoritics & Planetary Science* 40:1859–1877.
- Osinski G. R., and Spray J. G. 2006. Shatter cones of the Haughton Impact Structure, Canada. In *Proceedings, 1st International Conference on Impact Cratering in the Solar System, European Space Agency Special Publication SP-612. CD-ROM*. pp. 95–99.
- Osinski G. R., Spray J. G., and Grieve R. A. F. 2008. Impact melting in sedimentary target rocks: An assessment. In *The Sedimentary Record of Meteorite Impacts, Special Paper 437*, edited by Evans K. R., Horton W., King Jr. D. K., and Morrow J. R. Geological Society of America, Boulder, CO. pp. 1–18.
- Osinski G. R., and Pierazzo E. 2013. Ch 01 Impact cratering: processes and products. In *Impact Cratering: Processes and Products*. pp. 1–20.
- Osinski G. R., and Ferrière L. 2016. Shatter cones: (Mis)understood? *Science Advances* 2, e160061:1–10.
- Osinski G. R., Grieve R. A. F., Bleacher J. E., Neish C. D., Pilles E. A., and Tornabene L. L. 2018. Igneous rocks formed by hypervelocity impact. *Journal of Volcanology and Geothermal Research* 353:25–54.

- Quesnel Y., Zylberman W., Rochette P., Uehara M., Gattacceca J., Osinski G. R., Dussouillez P., Lepaulard C., and Champollion C. 2020. Geophysical signature of the Tunnunik impact structure, Northwest Territories, Canada. *Meteoritics & Planetary Science* 55:480-495.
- Reimold W. U. 1998. Exogenic and endogenic breccias: a discussion of major problematics. *Earth Science Reviews* 43:25–47.
- Seeley J. R., and Milam K. A. 2018. Optical and X-ray diffraction analyses of shock metamorphosed dolostone at increasing depths within the central uplift of the Wells Creeks impact structure. *49th Lunar and Planetary Science Conference Abstract* #2755.
- Skála R., and Jakeš P. 1999. Shock-induced effects in natural calcite-rich targets as revealed by X-ray powder diffraction. In *Large Meteorite Impacts and Planetary Evolution II, Special Paper 339*, edited by Dressler B. O., and Sharpton V. L. Geological Society of America (GSA), Boulder, CO. pp. 205–214.
- Skála R. 2002. Shock-induced phenomena in limestones in the quarry near Ronheim, the Ries Crater, Germany. *Bulletin of the Czech Geological Survey* 77:313–320.
- Stöffler D., Hamann C., and Metzler K. 2018. Shock metamorphism of planetary silicate rocks and sediments: Proposal for an updated classification system. *Meteoritics & Planetary Science* 49:5–49.
- Thorsteinsson R., and Tozer E. T. 1970. Geology of the Arctic Archipelago. In *Geology and Economic Minerals of Canada*, edited by Douglas R. J. W. Geological Survey of Canada. pp. 547–590.
- Wünnemann K., Collins G. S., and Osinski G. R. 2008. Numerical modelling of impact melt production in porous rocks. *Earth and Planetary Science Letters* 269:529–538.
- Young K. E., Van Soest M. C., Hodges K. V., Watson E. B., Adams B. A., and Lee P. 2013. Impact thermochronology and the age of Haughton impact structure, Canada. *Geophysical Research Letters* 40:3836–3840.

Zylberman W. Geophysical Study of Complex Meteorite Impact Structures. PhD thesis, University of Western Ontario, 2017, Electronic Thesis and Dissertation Repository (5165).

Zylberman W., Quesnel Y., Rochette P., Osinski G. R., Marion C., and Gattacceca J. 2017. Hydrothermally enhanced magnetization at the center of the Haughton impact structure? *Meteoritics & Planetary Science* 52:2147–2165.

Appendix A: List of samples

Table A-1. Sample list from the Tunnunik impact structure.

RFID / sample number	Location (UTM)			Formation*	Sample type (DST = dolostone; LST = limestone)
	Zone	Easting	Northing		
33	12X	403611	8045694	lower Victoria Island	breccia
40	12X	431211	8021394	middle Victoria Island	target; DST
48	12X	403768	8045633	lower Victoria Island	breccia
60	12X	404083	8045523	lower Victoria Island	breccia
72	11X	397779	8041858	upper Victoria Island	target; DST
81	12X	403768	8045633	lower Victoria Island	breccia
83	12X	405018	8049808	Allen Bay	target; DST
94	12X	403765	8045634	lower Victoria Island	breccia
105	12X	403765	8045634	lower Victoria Island	breccia
114	12X	401809	8046005	Shaler Supergroup	target; LST
131	12X	400047	8043468	Shaler Supergroup	target; LST
135	12X	403697	8045772	lower Victoria Island	breccia
154	12X	403844	8045845	lower Victoria Island	target; DST
159	11X	392505	8041774	Allen Bay	target; DST
222	12X	403842	8046069	lower Victoria Island	breccia
223	12X	403819	8045971	lower Victoria Island	breccia
401	12X	401340	8045121	Shaler Supergroup	breccia
403	12X	401342	8045122	Shaler Supergroup	target; LST
410	12X	405241	8037679	upper Victoria Island	target; DST
413	11X	398913	8049139	middle Victoria Island	target; DST
429	12X	411464	8049709	upper Victoria Island	target; DST
432	12X	412449	8051013	middle Victoria Island	target; DST
436	12X	412506	8051044	middle Victoria Island	breccia
439	11X	399046	8044654	upper Mount Phayre	target; DST
441	11X	398677	8047117	Mount Phayre	breccia
448	11X	398635	8047078	Mount Phayre	breccia
449	11X	398613	8047014	Mount Phayre	target; DST
450	11X	398638	8046975	Mount Phayre	breccia
452	11X	398643	8046947	Mount Phayre	breccia
453	11X	398666	8046886	Mount Phayre	breccia
454	11X	398477	8047439	lower Victoria Island	target; DST
CI009	12X	403436	8039651	middle Victoria Island	breccia
CI023	11X	394100	8047050	Allen Bay	breccia
CIAP10	12X	404089	8045509	lower Victoria Island	breccia
CIAP14	12X	404905	8042693	middle Victoria Island	breccia

* A formation listed for a breccia sample refers to the formation adjacent to the breccia.

Table A-2. Sample list from the Haughton impact structure.

Sample number	Location (UTM) Zone 16X		Formation*	Sample type (DST = dolostone; LST = limestone)
	Easting	Northing		
99-006	428330	8366905	n/a; crater-fill	shatter cone clast; DST
99-057	424130	8367390	n/a; crater-fill	impact melt breccia
99-063B	425010	8369055	Eleanor River	shocked target; LST
99-065	424930	8368240	n/a; crater-fill	impact melt breccia
99-108	433100	8365565	Allen Bay Middle Member	breccia
99-115	428070	8364365	Bay Fiord Member A	breccia
00-011	420920	8371065	Allen Bay Lower Member	breccia
00-019	420780	8371305	n/a; crater-fill	shatter cone clast; LST
00-059	418250	8366275	Allen Bay Lower Member	breccia
00-088	416920	8366535	Allen Bay undivided	breccia
00-124	424180	8360015	Allen Bay Lower Member	ballistic ejecta; LST
00-158	418730	8363155	n/a; crater-fill	shatter cone clast; DST
01-028	422670	8361165	Allen Bay Lower Member	breccia
02-010	419890	8366225	Thumb Mountain	breccia
02-061	425830	8363025	n/a; crater-fill	shatter cone clast; LST
02-126	424230	8372485	n/a; crater-fill	shatter cone clast; DST
02-127	424230	8372485	n/a; crater-fill	shatter cone clast; DST
02-128	424230	8372485	n/a; crater-fill	shatter cone clast; DST
02-139	423640	8368585	Eleanor River	shocked target; LST
05-005	418902	8371815	Allen Bay Middle Member	shocked target; DST
05-007	417277	8372712	Allen Bay Middle Member	unshocked target; DST
05-010	582940	8374420	Allen Bay Middle Member	unshocked target; DST
05-023	418011	8364086	n/a; crater-fill	shatter cone clast; LST
06-093	427823	8365859	Eleanor River	shocked target; LST
06-108	418678	8380712	Allen Bay Middle Member	unshocked target; DST
07-020	425612	8365452	Eleanor River	shocked target; LST
16-1000	427793	8366257	Eleanor River	melt rock
16-1001	427841	8365709	Eleanor River	melt rock
16-1003	427964	8366495	Eleanor River	melt rock
16-1005	427911	8365834	Eleanor River	melt rock
16-1006	426885	8371696	Thumb Mountain	breccia
16-1011	427796	8366256	Eleanor River	melt rock
16-1012	425321	8362487	Thumb Mountain	breccia
16-1013	427893	8365765	Eleanor River	melt rock
16-1014	425322	8365765	Thumb Mountain	shocked target; LST
16-1016	427909	8365834	Eleanor River	melt rock
16-1017	443210	8364699	Thumb Mountain	unshocked target; LST
16-1018	427795	8366256	Eleanor River	shocked target; LST

Sample number	Location (UTM) Zone 16X		Formation*	Sample type (DST = dolostone; LST = limestone)
	Easting	Northing		
16-1020	427512	8364994	Eleanor River	melt rock
16-1023	426587	8363821	Bay Fiord Member A	breccia
16-1024	427904	8365837	Eleanor River	melt rock
16-1026	427902	8365836	Eleanor River	breccia
16-1035	426908	8371720	Thumb Mountain	breccia
16-1037	426905	8371725	Thumb Mountain	shocked target; LST
16-1038	427901	8365835	Eleanor River	breccia
16-1043	426629	8363880	Eleanor River	melt rock
16-1044	426001	8363365	Bay Fiord Member C	breccia
16-1046	426005	8363369	Bay Fiord Member C	shocked target; DST
16-1052	427738	8366266	Eleanor River	breccia
16-1063	429393	8365012	Bay Fiord Member C	breccia
16-1064	429460	8364972	Bay Fiord Member C	shocked target; DST
16-1073	426352	8363573	Bay Fiord Member A	breccia
16-1081	428678	8365992	Thumb Mountain	breccia
16-1094	426559	8363779	Bay Fiord Member A	breccia

* A formation listed for a breccia, melt rock, or ballistic ejecta sample refers to the formation adjacent to the given sample type.

Appendix B: EDS electron probe microanalysis data

B.1 Data collection

The energy dispersive spectrometry (EDS) electron probe microanalysis (EPMA) data presented in this appendix were collected using a Jeol JXA-8530F field-emission electron microprobe in the Earth and Planetary Materials Analysis Laboratory at the University of Western Ontario. Energy dispersive spectrometry was used to obtain semi-quantitative elemental data for mineral identification.

B.2 Tunnunik impact structure

Table B-1. Elemental abundances for minerals present in Tunnunik samples as determined by energy dispersive spectroscopy (EDS).

Mineral	Elemental wt%												
	O	F	Na	Mg	Al	Si	P	S	K	Ca	Ti	Fe	Zr
Dolomite	ave [†] 49.49	—	—	16.23	—	—	—	—	—	30.94	—	—	—
<i>n</i> = 295	<i>s.d.*</i> 3.94	—	—	1.43	—	—	—	—	—	3.79	—	—	—
Calcite	ave 46.05	—	—	0.61	—	—	—	—	—	49.54	—	—	—
<i>n</i> = 85	<i>s.d.</i> 2.87	—	—	0.40	—	—	—	—	—	3.17	—	—	—
Ankerite	ave 45.09	—	—	15.80	—	—	—	—	—	34.19	—	2.15	—
<i>n</i> = 40	<i>s.d.</i> 4.64	—	—	1.85	—	—	—	—	—	4.33	—	1.18	—
Quartz	ave 50.69	—	—	—	—	49.31	—	—	—	—	—	—	—
<i>n</i> = 160	<i>s.d.</i> 0.82	—	—	—	—	0.82	—	—	—	—	—	—	—
K-feldspar	ave 43.23	—	—	—	10.00	32.01	—	—	14.54	—	—	—	—
<i>n</i> = 145	<i>s.d.</i> 0.88	—	—	—	0.44	2.50	—	—	0.78	—	—	—	—
Sanidine	ave 43.38	—	0.46	—	10.12	31.99	—	—	14.13	—	—	—	—
<i>n</i> = 134	<i>s.d.</i> 1.48	—	0.24	—	0.29	0.88	—	—	0.92	—	—	—	—
Rutile	ave 36.94	—	—	2.25	1.16	0.98	—	—	0.78	2.23	59.99	1.30	—
<i>n</i> = 15	<i>s.d.</i> 2.84	—	—	1.88	0.67	1.63	—	—	0.84	1.98	6.24	0.44	—
Pyrite	ave —	—	—	—	—	—	—	49.98	—	—	—	49.64	—
<i>n</i> = 11	<i>s.d.</i> —	—	—	—	—	—	—	0.60	—	—	—	0.78	—
Zircon	ave 32.22	—	—	0.71	0.60	14.53	—	—	—	2.54	—	—	51.54
<i>n</i> = 10	<i>s.d.</i> 1.61	—	—	0.28	0.25	1.66	—	—	—	1.34	—	—	2.04
Apatite	ave 33.85	4.64	0.57	—	—	—	17.68	—	—	43.27	—	—	—
<i>n</i> = 3	<i>s.d.</i> 3.67	0.63	0.11	—	—	—	1.29	—	—	3.07	—	—	—
Ilmenite	ave 33.66	—	—	—	—	—	—	—	—	—	42.34	24.00	—
<i>n</i> = 2	<i>s.d.</i> 0.73	—	—	—	—	—	—	—	—	—	2.27	1.53	—

[†] ave = average composition from total number of occurrences (*n*).

* s.d. = standard deviation.

B.3 Haughton impact structure

Table B-2. Elemental abundances for minerals present in Haughton samples as determined by energy dispersive spectroscopy (EDS).

Mineral		Elemental wt%												
		C	O	Na	Mg	Al	Si	S	K	Ca	Ti	Fe	Sr	Ba
Calcite	ave [†]	–	43.02	–	0.43	0.52	0.64	0.70	–	51.35	–	–	–	–
	<i>n</i> - 369	<i>s.d.</i> [*]	4.46	–	0.33	0.91	0.50	0.00	–	5.47	–	–	–	–
Dolomite	ave	–	47.37	–	16.12	1.51	1.04	0.33	–	31.06	–	–	–	–
	<i>n</i> - 122	<i>s.d.</i>	4.24	–	1.60	0.28	0.66	0.00	–	5.57	–	–	–	–
Quartz	ave	–	50.38	0.21	0.61	0.45	49.33	–	0.70	0.64	–	1.50	–	–
	<i>n</i> - 208	<i>s.d.</i>	1.06	0.00	0.37	0.23	1.16	–	0.10	0.52	–	0.47	–	–
K-feldspar	ave	–	42.61	0.59	–	10.23	32.78	–	13.46	–	0.60	–	–	1.50
	<i>n</i> - 19	<i>s.d.</i>	1.15	0.31	–	0.23	0.60	–	0.97	–	0.00	–	–	0.00
Pyrite	ave	–	8.51	0.72	0.38	0.42	1.17	46.04	–	1.12	–	48.82	–	–
	<i>n</i> - 33	<i>s.d.</i>	5.77	0.00	0.10	0.04	0.40	5.88	–	0.69	–	2.87	–	–
Celestine	ave	–	28.38	–	–	–	–	16.16	–	3.01	–	1.65	46.82	2.53
	<i>n</i> - 2	<i>s.d.</i>	0.74	–	–	–	–	1.17	–	0.00	–	0.00	4.03	0.00
Ilmenite	ave	–	29.91	–	–	1.54	1.54	–	–	0.60	27.12	32.90	–	–
	<i>n</i> - 2	<i>s.d.</i>	4.97	–	–	1.16	0.10	–	–	0.00	2.57	1.45	–	–
Moissanite	ave	22.79	–	–	–	–	77.21	–	–	–	–	–	–	–
	<i>n</i> - 40	<i>s.d.</i>	1.76	–	–	–	1.75	–	–	–	–	–	–	–

[†] ave = average composition from total number of occurrences (*n*).

^{*} *s.d.* = standard deviation.

Appendix C: Powder X-ray diffraction (XRD) analysis data from the Tunnunik impact structure

C.1 Tunnunik impact structure

Powder X-ray diffraction (XRD) analysis of samples from the Tunnunik impact structure was conducted to determine the mineral phases present in each sample. A representative total of 61 samples collected within the impact structure and beyond its rim (Fig. C-1) were examined in this study and are listed in Table C-1. Minerals identified using powder XRD were used to construct a geologic map of the Tunnunik impact structure when combined with field observations and satellite imagery. Analyzed samples were collected during the 2015 field season by Jennifer Newman, Racel Sopoco, Jeremy Hansen, and Gordon Osinski.

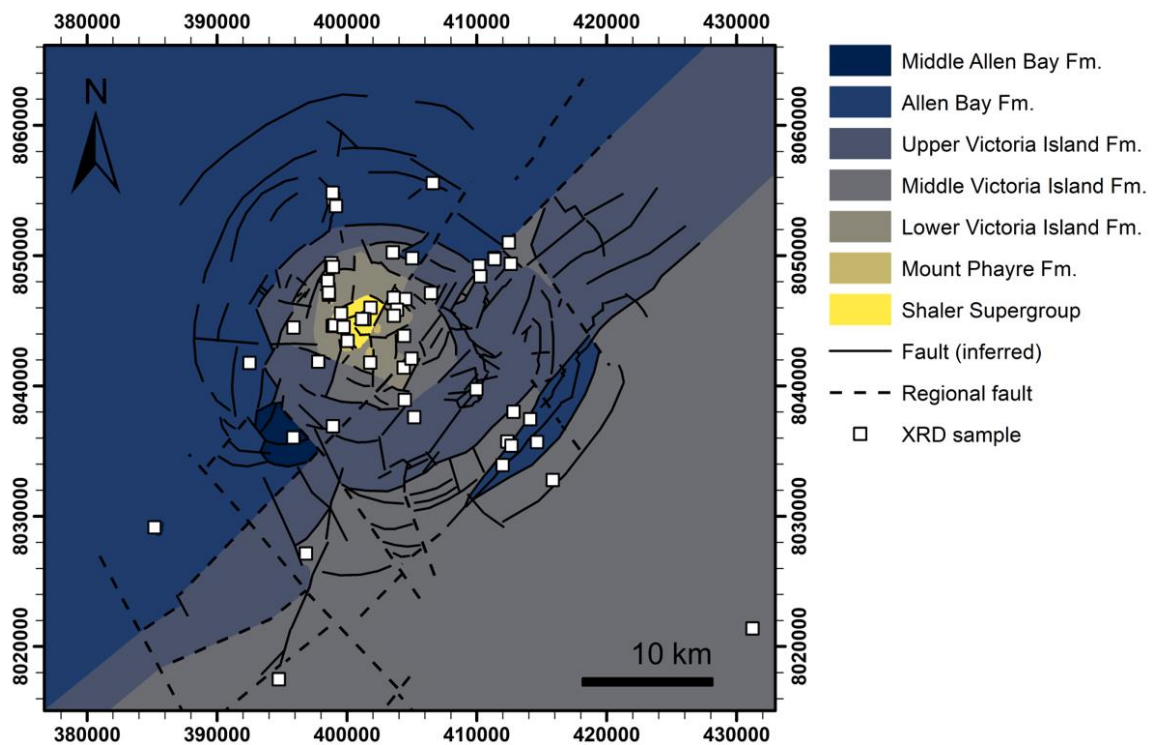


Figure C-1. Simplified geologic map of the Tunnunik impact structure showing locations of samples collected that were analyzed by powder X-ray diffraction. Four additional samples (not shown) were collected 18 to 23 km SE of sample located in lower right corner of map. UTM grid with Easting and Northing at 2000 m intervals for Zone 11 and Zone 12.

Table C-1. Powder X-ray diffraction sample list.

RFID / sample number	Outcrop	Location (UTM)			Collected by
		Zone	Easting	Northing	
18	July 20-3	11X	599036	8017177	Jen
20	24	12X	410225	8046749	Racel
28	50	11X	597476	8044153	Racel
29	12	12X	410271	8048420	Racel
32	July 14 outcrop 3	12X	412812	8038029	Jeremy
40	July 19-2	12X	415939	8032717	Jen
42	4.3	12X	414632	8035691	Oz
53	July 13.03	12X	398920	8036910	Jeremy
56	25	12X	404493	8046679	Racel
57	4.4	12X	411988	8033925	Oz
61	July 19-4	12X	444113	8007916	Jen
64	3.3	11X	598301	8035759	Oz
72	July 13.01	11X	599632	8041744	Jeremy
74	July 20-2	11X	588350	8027832	Jen
75	July 20-4	11X	600158	8026989	Jen
79	23	12X	403598	8046767	Racel
83	7	12X	405017	8049812	Racel
93	10	12X	410169	8049218	Racel
104	27	12X	406472	8047126	Racel
109	July 14 outcrop 5	12X	414101	8037455	Jeremy
111	July 20-3	11X	599032	8017198	Jen
112	July 11-4	12X	403529	8050247	Jen
114	July 16-1	12X	401809	8046000	Jen
116	July 19-7	12X	447899	8006490	Jen
121	July 16-2	12X	403600	8046752	Jen
123	33	12X	404366	8041404	Racel
131	52	12X	400047	8043456	Racel
132	July 19-7	12X	447899	8006490	Jen
138	July 22-1	11X	599746	8047966	Jen
143	July 19-5	12X	448134	8005396	Jen
150	July 19-3	12X	444176	8008071	Jen
152	44	12X	399542	8045575	Racel
154	48	12X	403844	8045845	Jen
159	July 20-1	11X	594375	8041110	Jen
160	July 14 outcrop 2	12X	409967	8039757	Jeremy
162	July 19-1	12X	415835	8032787	Jen
164	30	12X	401783	8041801	Racel
166	46	12X	401158	8045146	Racel

RFID / sample number	Outcrop	Location (UTM)			Collected by
		Zone	Easting	Northing	
171	45	12X	399730	8044528	Racel
177	July 19-7	12X	447899	8006490	Jen
403	July 23-5	12X	401342	8045122	Jen
410	July 24-5	12X	405170	8037608	Jen
413	July 25-1	11X	600029	8049086	Jen
414	July 25-2	11X	599885	8049357	Jen
417	July 25-2	11X	599873	8049347	Jen
419	July 27-1	11X	599800	8053754	Jen
422	July 27-3	11X	599535	8054289	Jen
424	July 27-5	11X	599430	8054750	Jen
426	July 27-8	12X	406607	8055569	Jen
429	July 28-2	12X	411358	8049744	Jen
431	July 28-3	12X	411342	8049811	Jen
432	July 28-5	12X	412449	8051013	Jen
438	July 28-9	12X	412615	8049374	Jen
439	July 29-1	11X	600608	8044637	Jen
444	July 30-4	11X	599898	8047142	Jen
446G	July 30-6	11X	599908	8047085	Jen
446R	July 30-6	11X	599908	8047085	Jen
446T	July 30-6	11X	599908	8047085	Jen
449	July 30-10	11X	599941	8046942	Jen
454	July 31-1	11X	599869	8047362	Jen
473	Aug 1-7	11X	600471	8044586	Jen

C.2 Operational parameters

Bulk rock samples free of weathered surfaces were prepared by grinding in a mortar and pestle for 30 minutes. Powders were mounted onto a recessed glass slide using 100% ethanol then analyzed by a Rigaku DMAX powder diffractometer with Bragg-Brentano geometry, graphite monochromator, and scintillation counter. X-ray diffraction patterns were collected using Co $K\alpha_1$ radiation with a 1.78896 Å wavelength and operating parameters of 40 kV, 35 mA, 0.02°/step, 1 s dwell time per step, and a 2θ range from 10–90°.

C.3 Stacked powder XRD diffraction patterns

Diffraction patterns from powder XRD analyses were grouped based on the similarity of mineral phases within the sample. Analyses were conducted with DIFFRAC.EVA software version 4.2 by Bruker AXS and phases were identified and matched using the ICDD (International Centre for Diffraction Data) database PDF-4+ (2016-2019). A y-offset has been applied to the diffraction patterns for clarity and count values are only valid for the bottom pattern in each stack; the relative scale of each pattern has been preserved.

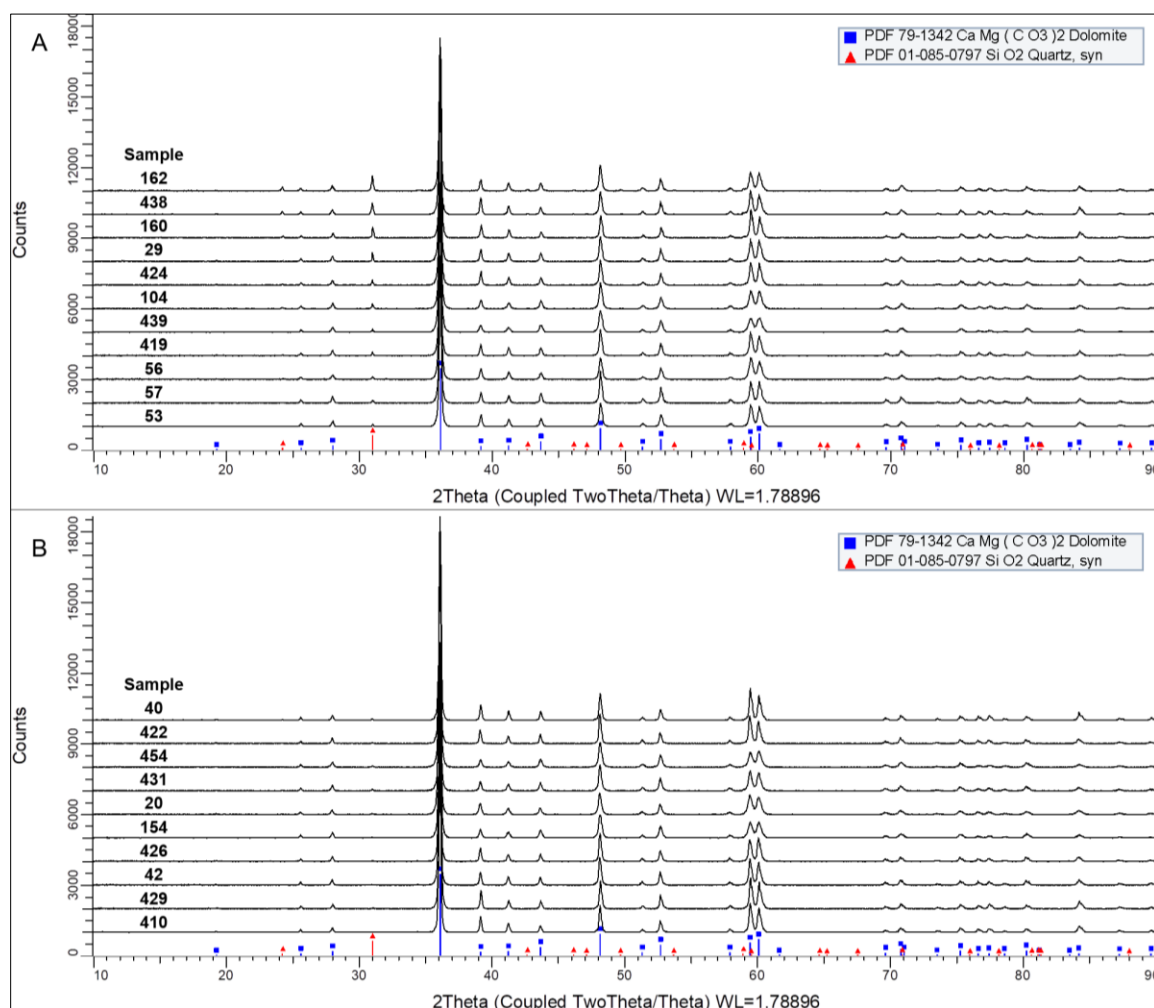


Figure C-2. Dolomite-rich samples with quartz.

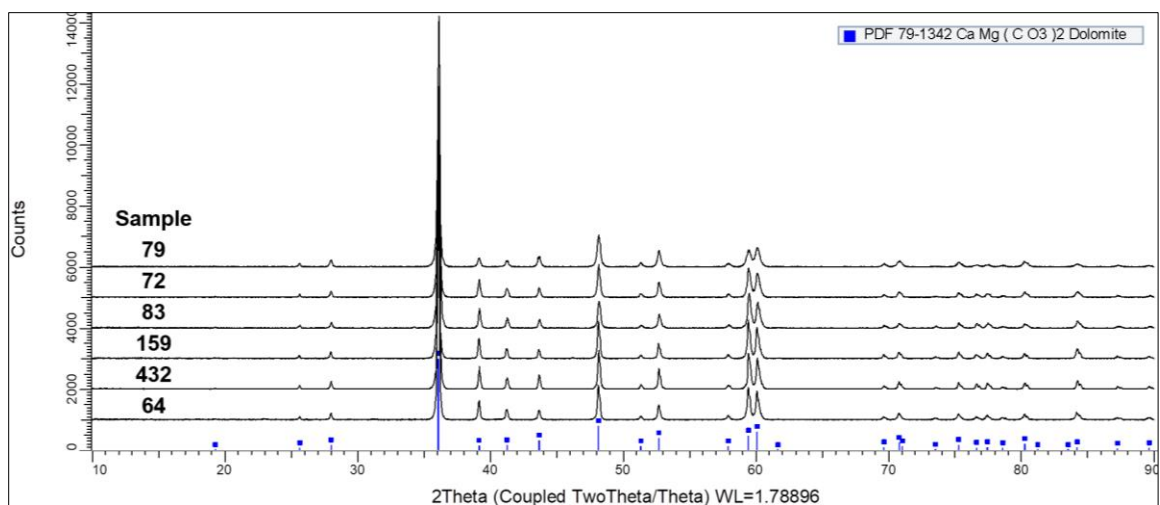


Figure C-3. Dolomite-rich samples.

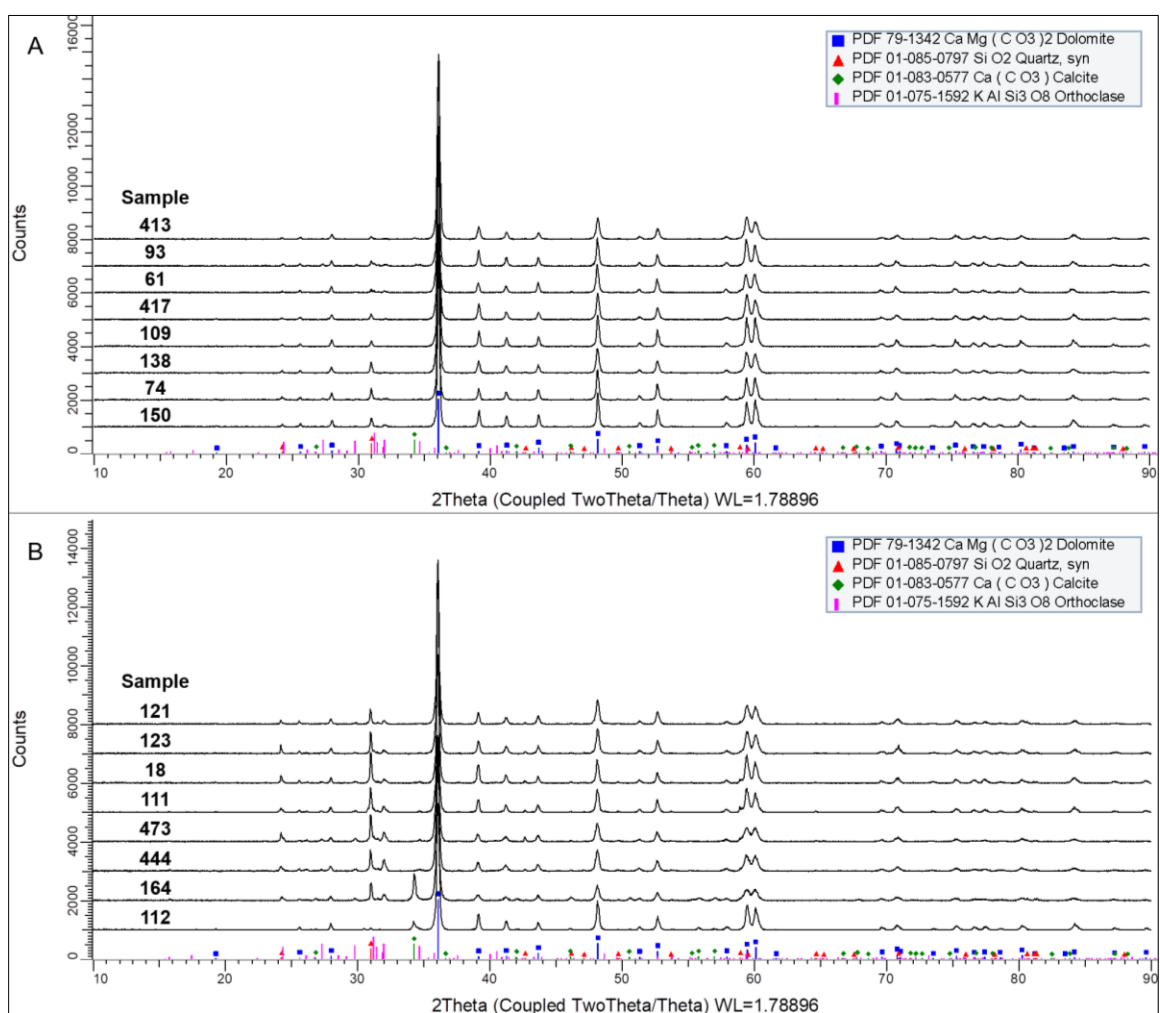


Figure C-4. Dolomite-rich samples with quartz, calcite, and orthoclase.

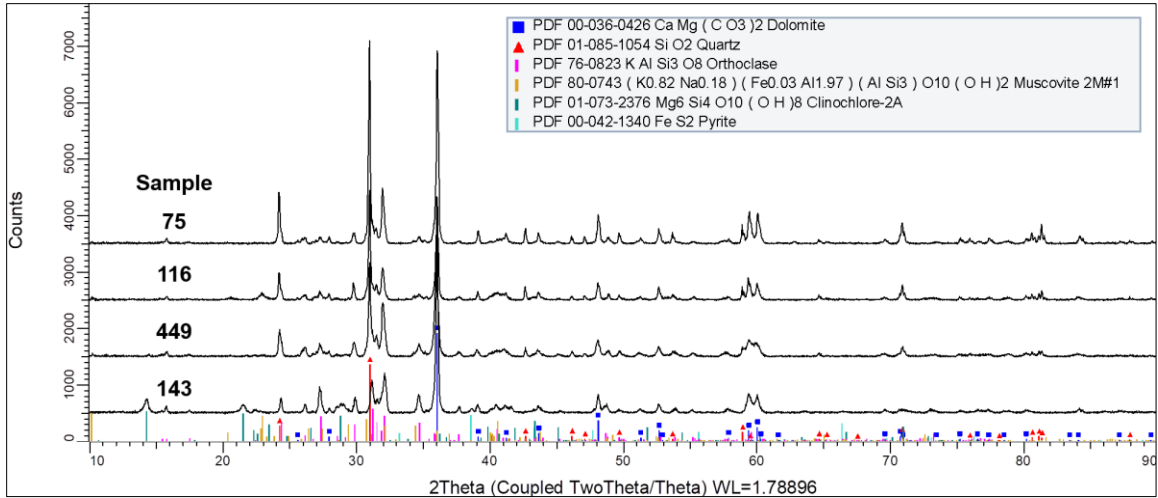


Figure C-5. Dolomite and quartz-bearing samples with orthoclase, muscovite, pyrite, and clinocllore.

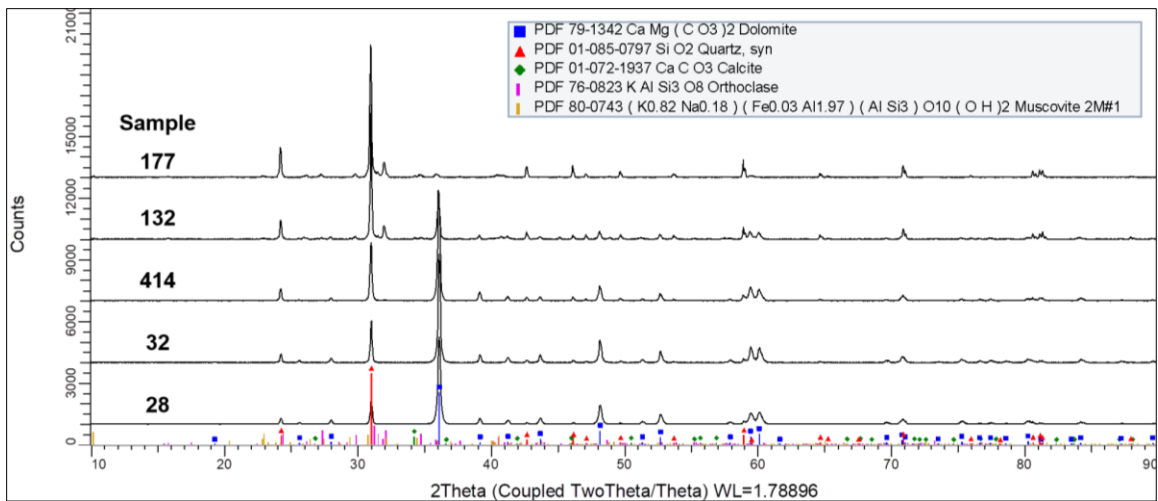


Figure C-6. Quartz-rich samples with dolomite, calcite, orthoclase, and muscovite.

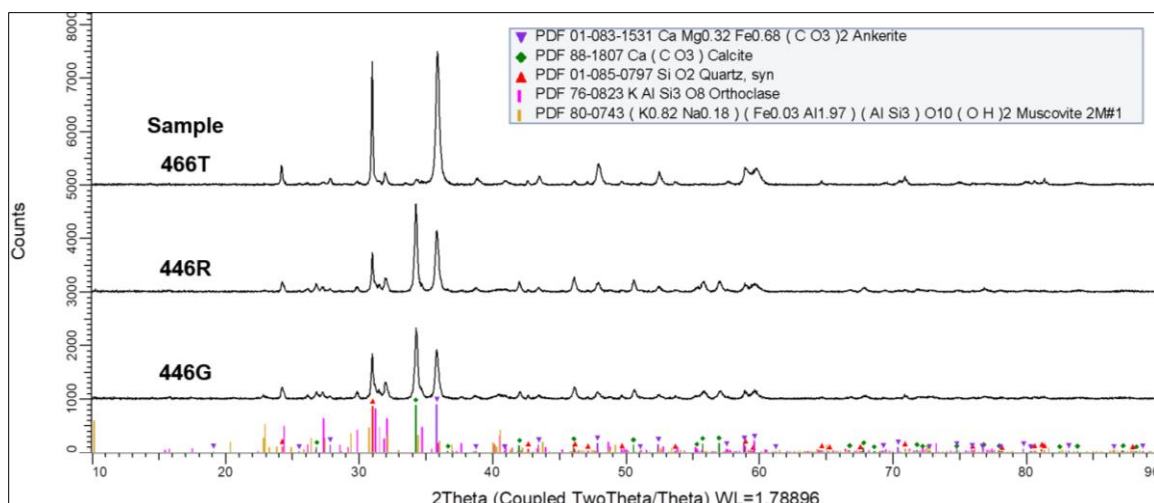


Figure C-7. Ankerite-bearing samples with calcite, quartz, orthoclase, and muscovite.

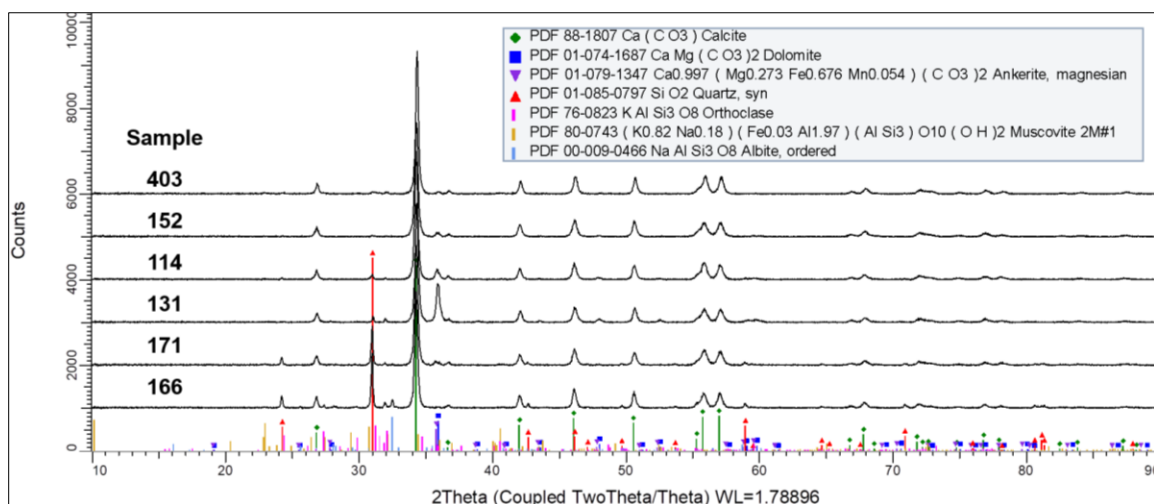


Figure C-8. Calcite-rich samples with dolomite, quartz, ankerite, orthoclase, muscovite, and albite.

C.4 Strain calculations

The 14 representative bulk rock samples selected in Chapter 5 were investigated to measure their crystal strain based on their diffraction patterns. Below are tables with the measured and calculated values from diffraction patterns using DIFFRAC.EVA software to derive crystal strain values, ϵ . Williamson-Hall plots (Uchizono et al. 1999; Williamson and Hall 1953) with trendline equations are also provided for each sample.

Table C-2. Measured 2θ and integral breadth values from diffraction pattern for dolomite sample 439. $\tan \theta$ values derived from 2θ observed maximum value.

hkl	2θ (observed max)	θ (degrees)	θ (radians)	$\tan \theta$	Integral breadth
104	36.100	18.050	0.315	0.326	0.291
006	39.150	19.575	0.342	0.356	0.290
015	41.250	20.625	0.360	0.376	0.326
110	43.695	21.848	0.381	0.401	0.318
113	48.170	24.085	0.420	0.447	0.344
021	51.367	25.684	0.448	0.481	0.313
202	52.714	26.357	0.460	0.495	0.330
024	57.934	28.967	0.506	0.554	0.364
116 *	60.120	30.060	0.525	0.579	0.937

* Area for (018) and (116) peak calculated together due to broadening and merging of peaks.

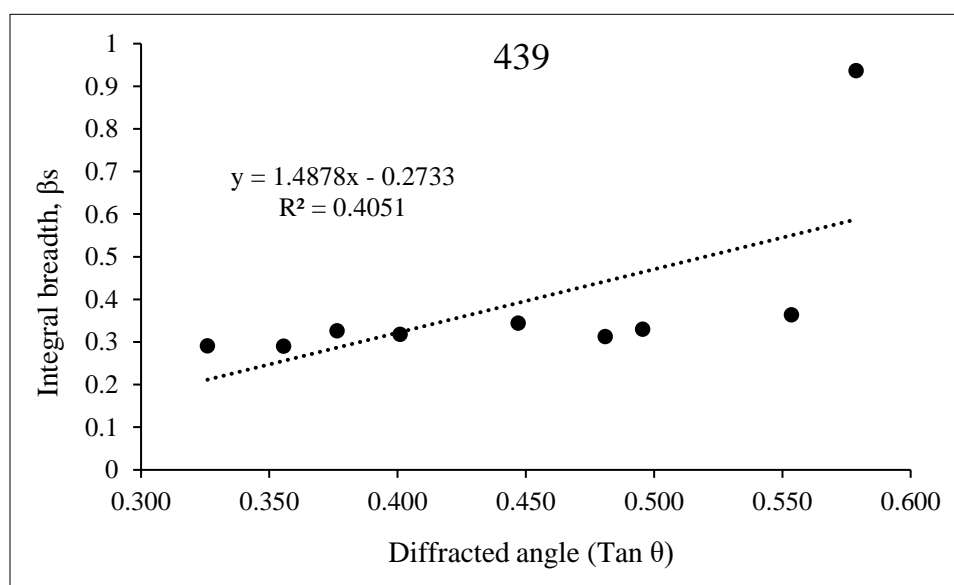


Figure C-9. Williamson-Hall plot for dolomite sample 439 showing integral breadth values measured from peak area plotted for a given diffracted angle. Linear trendline equation and R^2 value are displayed on chart.

Crystal strain ϵ for sample 439 is 0.37%. Strain is derived from the slope of the trendline equation (Fig. C-9) where ϵ equals 1.4878 divided by 4.

Table C-3. Measured 2θ and integral breadth values from diffraction pattern for dolomite sample 154. $\tan \theta$ values derived from 2θ observed maximum value.

hkl	2θ (observed max)	θ (degrees)	θ (radians)	$\tan \theta$	Integral breadth
104	36.098	18.049	0.315	0.326	0.270
006	39.148	19.574	0.342	0.356	0.249
015	41.254	20.627	0.360	0.376	0.312
110	43.687	21.844	0.381	0.401	0.280
113	48.168	24.084	0.420	0.447	0.334
021	51.352	25.676	0.448	0.481	0.287
202	52.721	26.361	0.460	0.496	0.313
024	57.944	28.972	0.506	0.554	0.368
116 *	60.121	30.061	0.525	0.579	0.858

* Area for (018) and (116) peak calculated together due to broadening and merging of peaks.

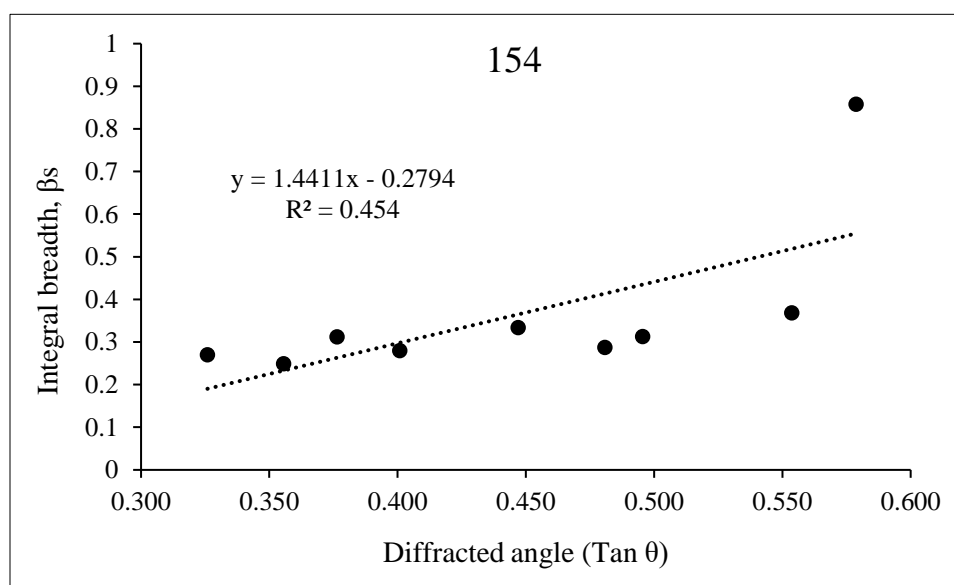


Figure C-10. Williamson-Hall plot for dolomite sample 154 showing integral breadth values measured from peak area plotted for a given diffracted angle. Linear trendline equation and R^2 value are displayed on chart.

Crystal strain ϵ for sample 154 is 0.36%. Strain is derived from the slope of the trendline equation (Fig. C-10) where ϵ equals 1.4411 divided by 4.

Table C-4. Measured 2θ and integral breadth values from diffraction pattern for dolomite sample 454. $\tan \theta$ values derived from 2θ observed maximum value.

hkl	2θ (observed max)	θ (degrees)	θ (radians)	Tan θ	Integral breadth
104	36.101	18.051	0.315	0.326	0.284
006	39.163	19.582	0.342	0.356	0.266
015	41.267	20.634	0.360	0.377	0.307
110	43.684	21.842	0.381	0.401	0.295
113	48.168	24.084	0.420	0.447	0.336
021	51.365	25.683	0.448	0.481	0.340
202	52.717	26.359	0.460	0.496	0.321
024	57.939	28.970	0.506	0.554	0.370
116 *	60.125	30.063	0.525	0.579	0.823

* Area for (018) and (116) peak calculated together due to broadening and merging of peaks.

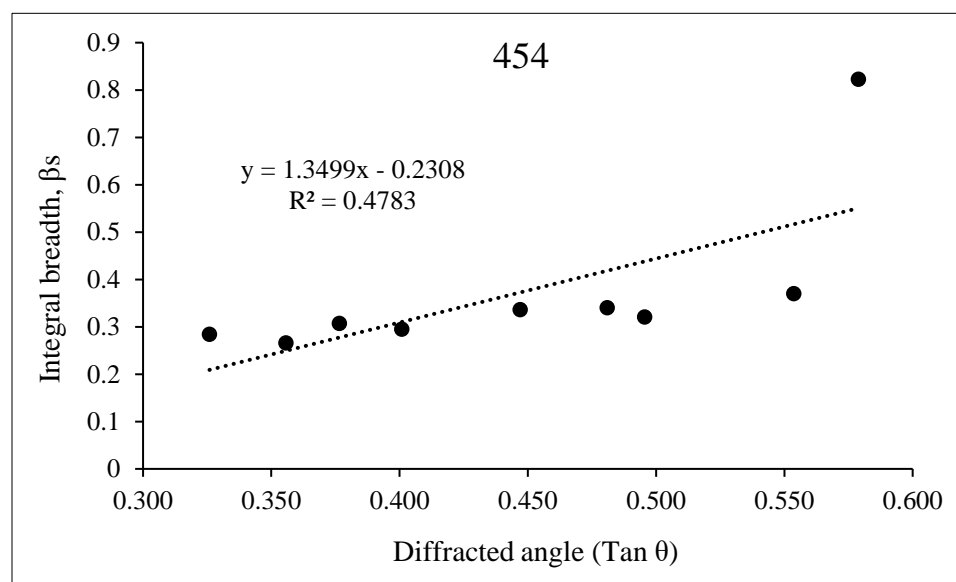


Figure C-11. Williamson-Hall plot for dolomite sample 454 showing integral breadth values measured from peak area plotted for a given diffracted angle. Linear trendline equation and R^2 value are displayed on chart.

Crystal strain ϵ for sample 454 is 0.34%. Strain is derived from the slope of the trendline equation (Fig. C-11) where ϵ equals 1.3499 divided by 4.

Table C-5. Measured 2θ and integral breadth values from diffraction pattern for dolomite sample 413. $\tan \theta$ values derived from 2θ observed maximum value.

hkl	2θ (observed max)	θ (degrees)	θ (radians)	$\tan \theta$	Integral breadth
104	36.101	18.051	0.315	0.326	0.261
006	39.152	19.576	0.342	0.356	0.254
015	41.257	20.629	0.360	0.376	0.278
110	43.677	21.839	0.381	0.401	0.292
113	48.171	24.086	0.420	0.447	0.336
021	51.338	25.669	0.448	0.481	0.308
202	52.707	26.354	0.460	0.495	0.328
024	57.921	28.961	0.505	0.553	0.304
116 *	59.467	29.734	0.519	0.571	0.785

* Area for (018) and (116) peak calculated together due to broadening and merging of peaks.

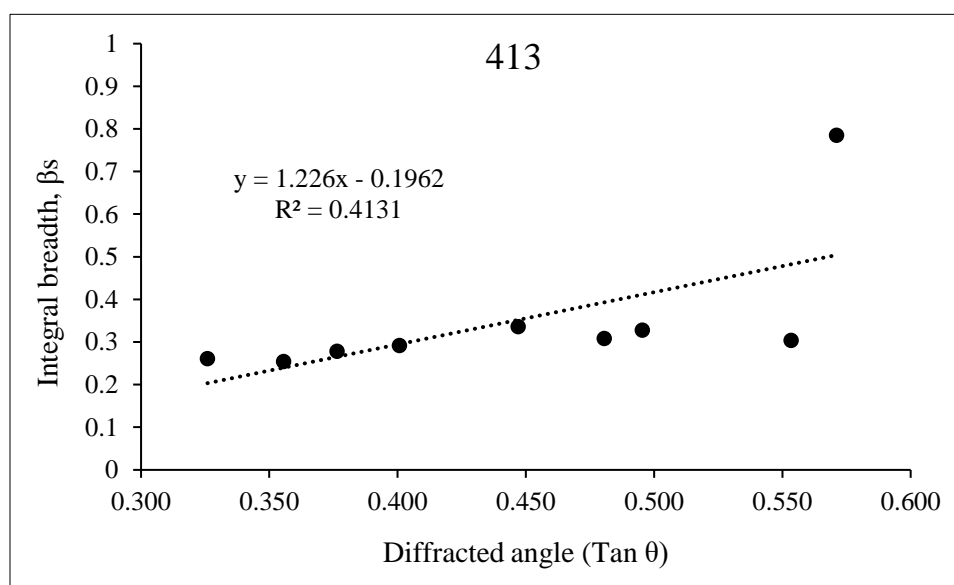


Figure C-12. Williamson-Hall plot for dolomite sample 413 showing integral breadth values measured from peak area plotted for a given diffracted angle. Linear trendline equation and R^2 value are displayed on chart.

Crystal strain ϵ for sample 413 is 0.31%. Strain is derived from the slope of the trendline equation (Fig. C-12) where ϵ equals 1.226 divided by 4.

Table C-6. Measured 2θ and integral breadth values from diffraction pattern for dolomite sample 72. $\tan \theta$ values derived from 2θ observed maximum value.

hkl	2θ (observed max)	θ (degrees)	θ (radians)	$\tan \theta$	Integral breadth
104	36.115	18.058	0.315	0.326	0.241
006	39.175	19.588	0.342	0.356	0.223
015	41.264	20.632	0.360	0.377	0.269
110	43.694	21.847	0.381	0.401	0.245
113	48.174	24.087	0.420	0.447	0.273
021	51.344	25.672	0.448	0.481	0.286
202	52.723	26.362	0.460	0.496	0.303
024	57.921	28.961	0.505	0.553	0.282
116 *	59.480	29.740	0.519	0.571	0.688

* Area for (018) and (116) peak calculated together due to broadening and merging of peaks.

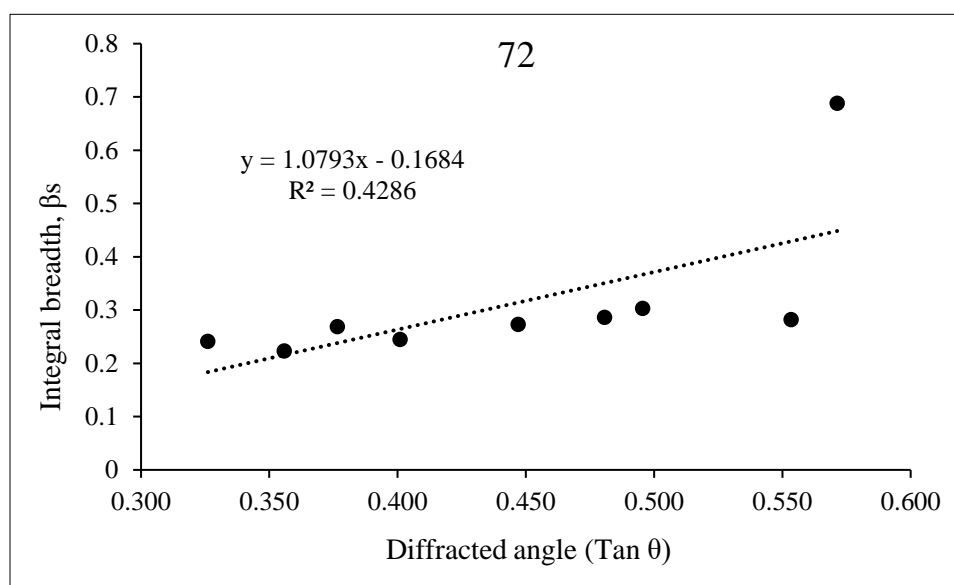


Figure C-13. Williamson-Hall plot for dolomite sample 72 showing integral breadth values measured from peak area plotted for a given diffracted angle. Linear trendline equation and R^2 value are displayed on chart.

Crystal strain ϵ for sample 72 is 0.27%. Strain is derived from the slope of the trendline equation (Fig. C-13) where ϵ equals 1.0793 divided by 4.

Table C-7. Measured 2θ and integral breadth values from diffraction pattern for dolomite sample 83. $\tan \theta$ values derived from 2θ observed maximum value.

hkl	2θ (observed max)	θ (degrees)	θ (radians)	$\tan \theta$	Integral breadth
104	36.139	18.070	0.315	0.326	0.221
006	39.196	19.598	0.342	0.356	0.214
015	41.295	20.648	0.360	0.377	0.229
110	43.717	21.859	0.382	0.401	0.232
113	48.200	24.100	0.421	0.447	0.295
021	51.364	25.682	0.448	0.481	0.254
202	52.740	26.370	0.460	0.496	0.291
024	58.000	29.000	0.506	0.554	0.245
116 *	59.507	29.754	0.519	0.572	0.593

* Area for (018) and (116) peak calculated together due to broadening and merging of peaks.

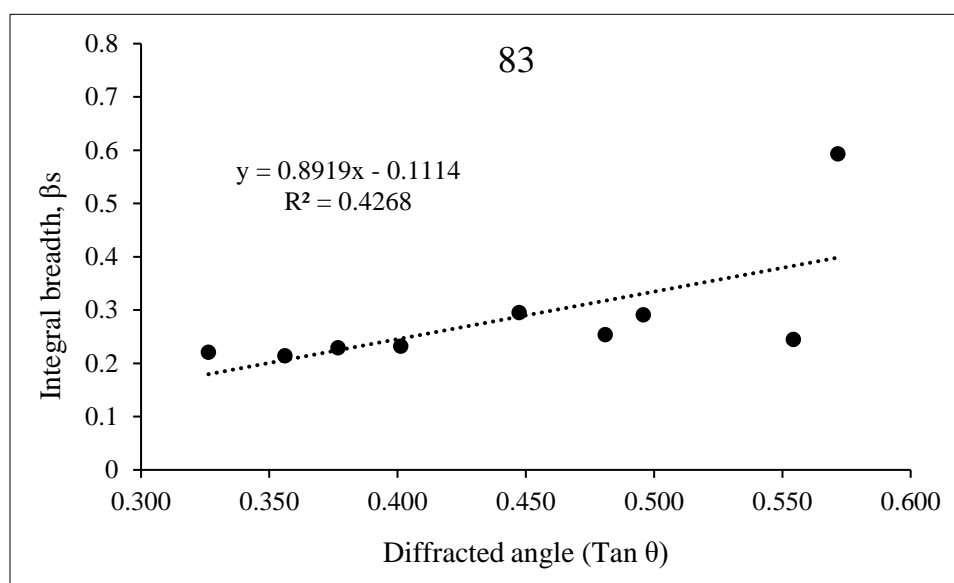


Figure C-14. Williamson-Hall plot for dolomite sample 83 showing integral breadth values measured from peak area plotted for a given diffracted angle. Linear trendline equation and R^2 value are displayed on chart.

Crystal strain ϵ for sample 83 is 0.22%. Strain is derived from the slope of the trendline equation (Fig. C-14) where ϵ equals 0.8919 divided by 4.

Table C-8. Measured 2θ and integral breadth values from diffraction pattern for dolomite sample 410. $\tan \theta$ values derived from 2θ observed maximum value.

hkl	2θ (observed max)	θ (degrees)	θ (radians)	$\tan \theta$	Integral breadth
104	36.096	18.048	0.315	0.326	0.210
006	39.162	19.581	0.342	0.356	0.201
015	41.249	20.625	0.360	0.376	0.220
110	43.669	21.835	0.381	0.401	0.222
113	48.160	24.080	0.420	0.447	0.235
021	51.336	25.668	0.448	0.481	0.228
202	52.694	26.347	0.460	0.495	0.250
024	57.929	28.965	0.506	0.553	0.274
018	59.471	29.736	0.519	0.571	0.306
116	60.117	30.059	0.525	0.579	0.326

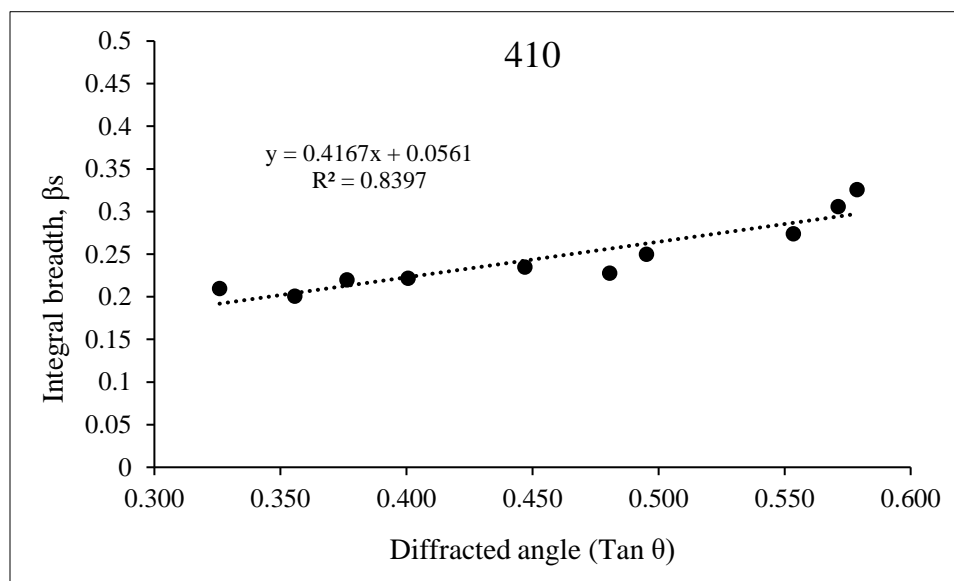


Figure C-15. Williamson-Hall plot for dolomite sample 410 showing integral breadth values measured from peak area plotted for a given diffracted angle. Linear trendline equation and R^2 value are displayed on chart.

Crystal strain ϵ for sample 410 is 0.10%. Strain is derived from the slope of the trendline equation (Fig. C-15) where ϵ equals 0.4167 divided by 4.

Table C-9. Measured 2θ and integral breadth values from diffraction pattern for dolomite sample 159. $\tan \theta$ values derived from 2θ observed maximum value.

hkl	2θ (observed max)	θ (degrees)	θ (radians)	Tan θ	Integral breadth
104	36.091	18.046	0.315	0.326	0.208
006	39.156	19.578	0.342	0.356	0.199
015	41.246	20.623	0.360	0.376	0.224
110	43.668	21.834	0.381	0.401	0.226
113	48.156	24.078	0.420	0.447	0.244
021	51.351	25.676	0.448	0.481	0.248
202	52.686	26.343	0.460	0.495	0.256
024	57.903	28.952	0.505	0.553	0.261
018	59.449	29.725	0.519	0.571	0.296
116	60.106	30.053	0.525	0.579	0.326

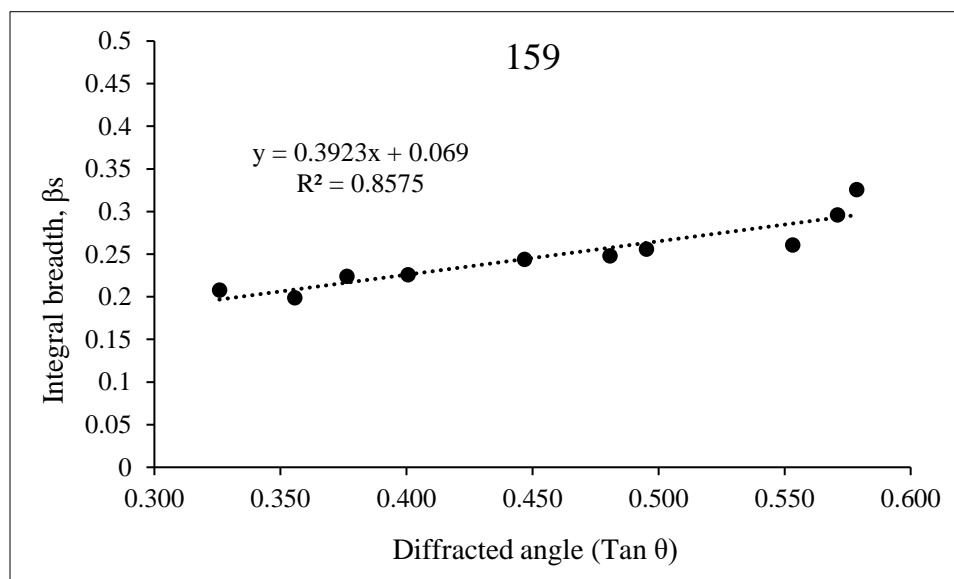


Figure C-16. Williamson-Hall plot for dolomite sample 159 showing integral breadth values measured from peak area plotted for a given diffracted angle. Linear trendline equation and R^2 value are displayed on chart.

Crystal strain ϵ for sample 159 is 0.09%. Strain is derived from the slope of the trendline equation (Fig. C-16) where ϵ equals 0.3923 divided by 4.

Table C-10. Measured 2θ and integral breadth values from diffraction pattern for dolomite sample 429. $\tan \theta$ values derived from 2θ observed maximum value.

hkl	2θ (observed max)	θ (degrees)	θ (radians)	Tan θ	Integral breadth
104	36.128	18.064	0.315	0.326	0.209
006	39.191	19.596	0.342	0.356	0.194
015	41.280	20.640	0.360	0.377	0.227
110	43.702	21.851	0.381	0.401	0.222
113	48.184	24.092	0.420	0.447	0.240
021	51.344	25.672	0.448	0.481	0.242
202	52.716	26.358	0.460	0.495	0.245
024	57.948	28.974	0.506	0.554	0.261
018	59.485	29.743	0.519	0.571	0.295
116	60.133	30.067	0.525	0.579	0.318

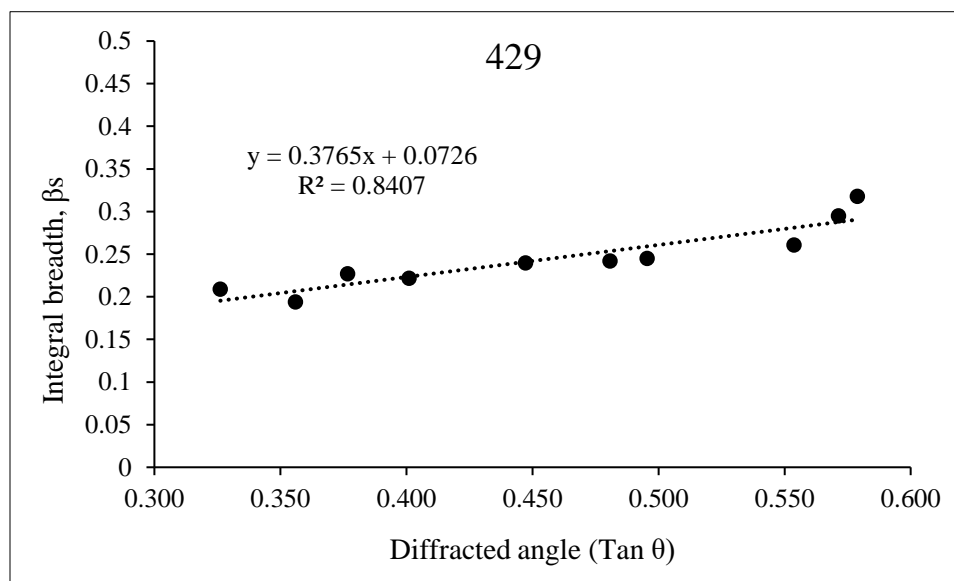


Figure C-17. Williamson-Hall plot for dolomite sample 429 showing integral breadth values measured from peak area plotted for a given diffracted angle. Linear trendline equation and R^2 value are displayed on chart.

Crystal strain ϵ for sample 429 is 0.09%. Strain is derived from the slope of the trendline equation (Fig. C-17) where ϵ equals 0.3765 divided by 4.

Table C-11. Measured 2θ and integral breadth values from diffraction pattern for dolomite sample 432. $\tan \theta$ values derived from 2θ observed maximum value.

hkl	2θ (observed max)	θ (degrees)	θ (radians)	Tan θ	Integral breadth
104	36.120	18.060	0.315	0.326	0.199
006	39.181	19.591	0.342	0.356	0.189
015	41.277	20.639	0.360	0.377	0.226
110	43.697	21.849	0.381	0.401	0.204
113	48.181	24.091	0.420	0.447	0.235
021	51.357	25.679	0.448	0.481	0.221
202	51.714	25.857	0.451	0.485	0.232
024	57.951	28.976	0.506	0.554	0.289
018	59.486	29.743	0.519	0.571	0.300
116	60.131	30.066	0.525	0.579	0.323

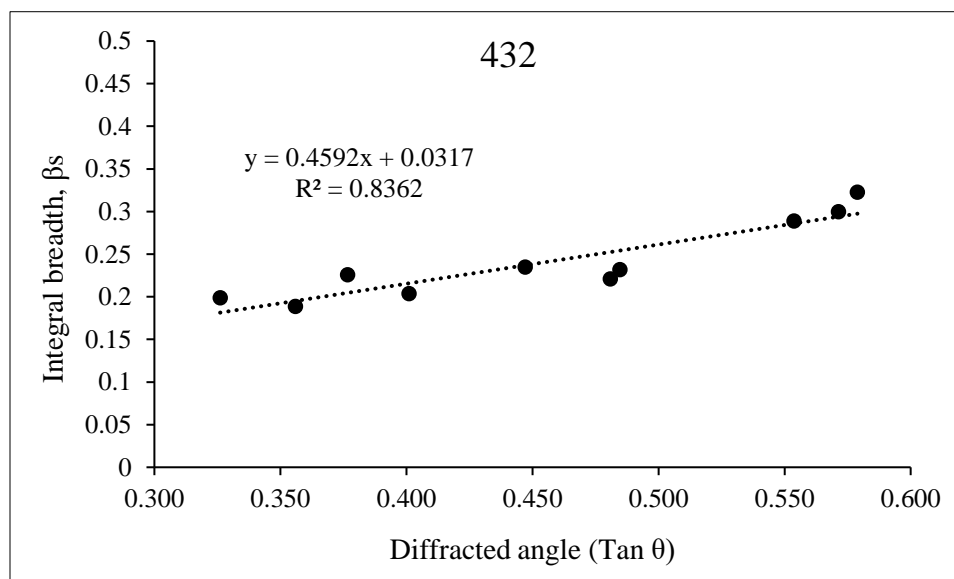


Figure C-18. Williamson-Hall plot for dolomite sample 432 showing integral breadth values measured from peak area plotted for a given diffracted angle. Linear trendline equation and R^2 value are displayed on chart.

Crystal strain ϵ for sample 432 is 0.11%. Strain is derived from the slope of the trendline equation (Fig. C-18) where ϵ equals 0.4592 divided by 4.

Table C-12: Measured 2θ and integral breadth values from diffraction pattern for dolomite sample 40. $\tan \theta$ values derived from 2θ observed maximum value.

hkl	2θ (observed max)	θ (degrees)	θ (radians)	Tan θ	Integral breadth
104	36.112	18.056	0.315	0.326	0.203
006	39.175	19.588	0.342	0.356	0.202
015	41.270	20.635	0.360	0.377	0.211
110	43.693	21.847	0.381	0.401	0.213
113	48.168	24.084	0.420	0.447	0.240
021	51.344	25.672	0.448	0.481	0.242
202	52.709	26.355	0.460	0.495	0.273
024	57.930	28.965	0.506	0.554	0.265
018	59.473	29.737	0.519	0.571	0.275
116	60.124	30.062	0.525	0.579	0.310

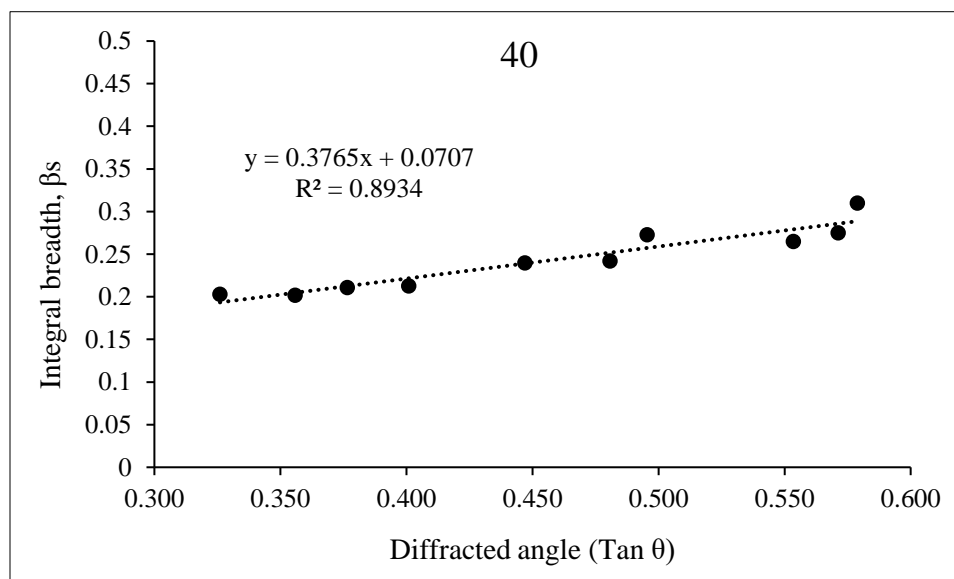


Figure C-19. Williamson-Hall plot for dolomite sample 40 showing integral breadth values measured from peak area plotted for a given diffracted angle. Linear trendline equation and R^2 value are displayed on chart.

Crystal strain ϵ for sample 40 is 0.09%. Strain is derived from the slope of the trendline equation (Fig. C-19) where ϵ equals 0.3765 divided by 4.

Table C-13. Measured 2θ and integral breadth values from diffraction pattern for calcite sample 403. $\tan \theta$ values derived from 2θ observed maximum value.

hkl	2θ (observed max)	θ (degrees)	θ (radians)	Tan θ	Integral breadth
104	34.361	17.181	0.300	0.309	0.301
006	36.769	18.385	0.321	0.332	0.297
110	42.119	21.060	0.368	0.385	0.333
113	46.217	23.109	0.403	0.427	0.395
202	50.708	25.354	0.443	0.474	0.345
018 *	55.951	27.976	0.488	0.531	0.580
116	57.152	28.576	0.499	0.545	0.472

* Area for (024) and (018) peak calculated together due to broadening and merging of peaks.

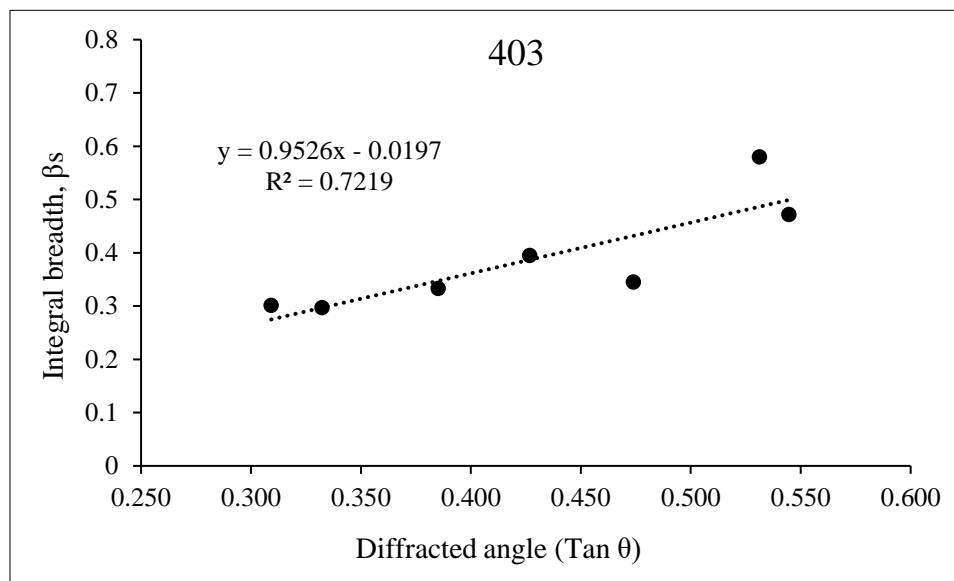


Figure C-20. Williamson-Hall plot for calcite sample 403 showing integral breadth values measured from peak area plotted for a given diffracted angle. Linear trendline equation and R^2 value are displayed on chart.

Crystal strain ϵ for sample 403 is 0.24%. Strain is derived from the slope of the trendline equation (Fig. C-20) where ϵ equals 0.9526 divided by 4.

Table C-14. Measured 2θ and integral breadth values from diffraction pattern for calcite sample 114. $\tan \theta$ values derived from 2θ observed maximum value.

hkl	2θ (observed max)	θ (degrees)	θ (radians)	Tan θ	Integral breadth
104	34.294	17.147	0.299	0.309	0.322
006	36.701	18.351	0.320	0.332	0.262
110	42.059	21.030	0.367	0.384	0.358
113	46.140	23.070	0.403	0.426	0.392
202	50.630	25.315	0.442	0.473	0.391
018 *	55.864	27.932	0.488	0.530	0.644
116	57.065	28.533	0.498	0.544	0.509

* Area for (024) and (018) peak calculated together due to broadening and merging of peaks.

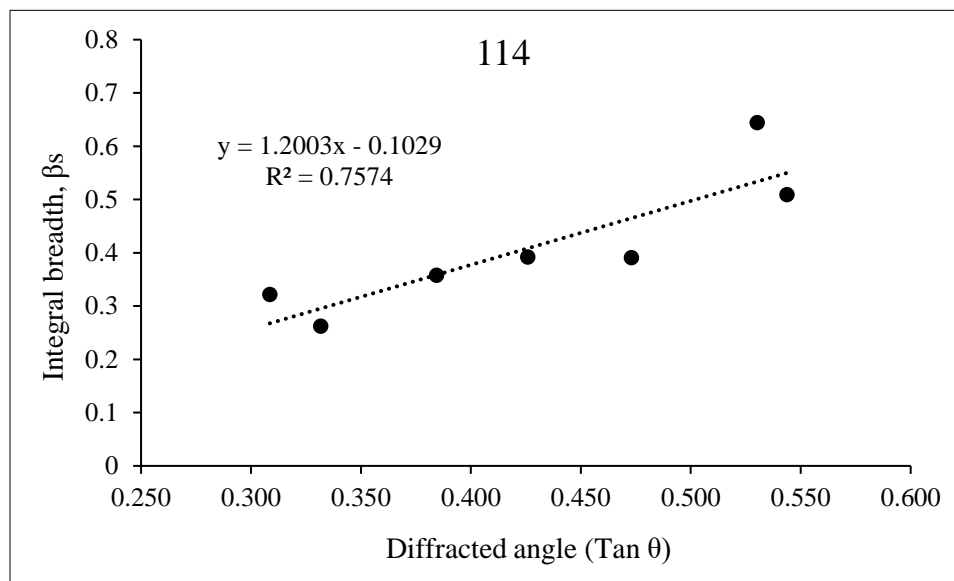


Figure C-21. Williamson-Hall plot for calcite sample 114 showing integral breadth values measured from peak area plotted for a given diffracted angle. Linear trendline equation and R^2 value are displayed on chart.

Crystal strain ϵ for sample 114 is 0.30%. Strain is derived from the slope of the trendline equation (Fig. C-21) where ϵ equals 1.2003 divided by 4.

Table C-15. Measured 2θ and integral breadth values from diffraction pattern for calcite sample 131. $\tan \theta$ values derived from 2θ observed maximum value.

hkl	2θ (observed max)	θ (degrees)	θ (radians)	Tan θ	Integral breadth
104	34.332	17.166	0.300	0.309	0.337
006	36.767	18.384	0.321	0.332	0.267
110	42.099	21.050	0.367	0.385	0.365
113	46.179	23.090	0.403	0.426	0.436
202	50.666	25.333	0.442	0.473	0.375
018 *	55.885	27.943	0.488	0.530	0.643
116	57.094	28.547	0.498	0.544	0.533

* Area for (024) and (018) peak calculated together due to broadening and merging of peaks.

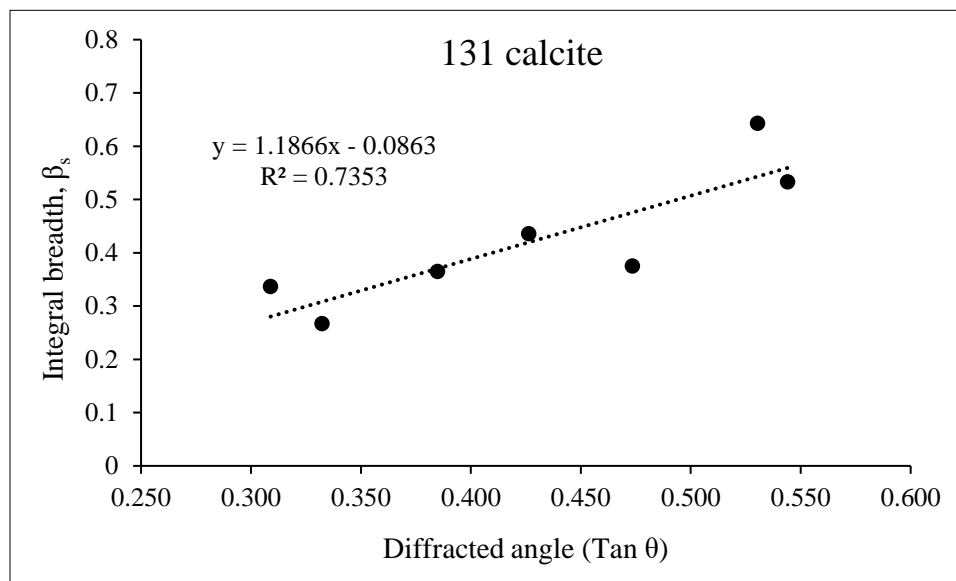


Figure C-22. Williamson-Hall plot for calcite sample 131 showing integral breadth values measured from peak area plotted for a given diffracted angle. Linear trendline equation and R^2 value are displayed on chart.

Crystal strain ϵ for sample 131 is 0.30%. Strain is derived from the slope of the trendline equation (Fig. C-22) where ϵ equals 1.1866 divided by 4.

Table C-16. Measured 2θ and integral breadth values from diffraction pattern for dolomite in calcite-rich sample 131. $\tan \theta$ values derived from 2θ observed maximum value.

hkl	2θ (observed max)	θ (degrees)	θ (radians)	$\tan \theta$	Integral breadth
104	35.928	17.964	0.314	0.324	0.378
006	38.898	19.449	0.339	0.353	0.310
015	41.294	20.647	0.360	0.377	0.422
110	43.545	21.773	0.380	0.399	0.319
113	47.990	23.995	0.419	0.445	0.406
202	52.538	26.269	0.458	0.494	0.302
116 *	59.739	29.870	0.521	0.574	1.035

* Area for (018) and (116) peak calculated together due to broadening and merging of peaks.

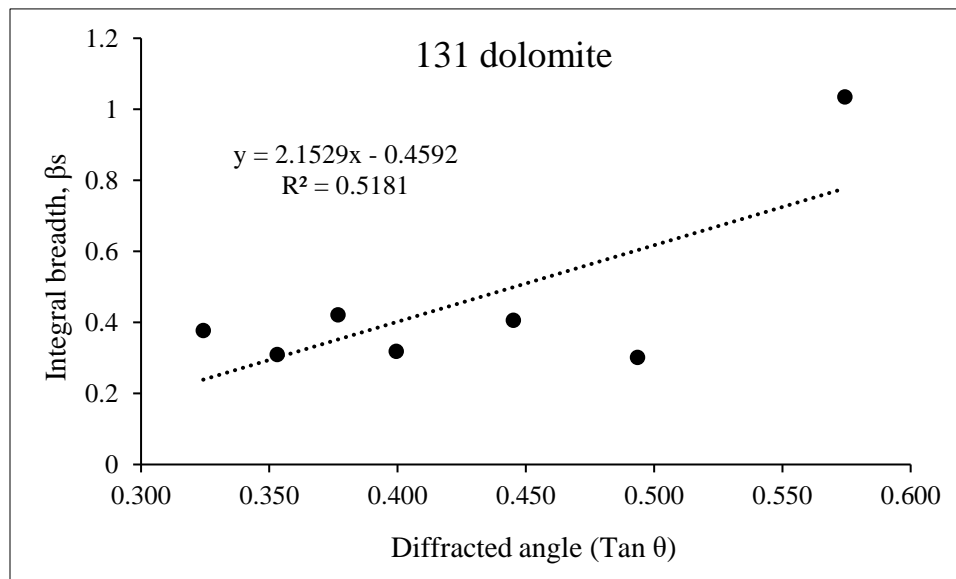


Figure C-23. Williamson-Hall plot for dolomite in calcite-rich sample 131 showing integral breadth values measured from peak area plotted for a given diffracted angle. Linear trendline equation and R^2 value are displayed on chart.

Crystal strain ϵ for sample 131 is 0.54%. Strain is derived from the slope of the trendline equation (Fig. C-23) where ϵ equals 2.1529 divided by 4.

C.5 References

- Uchizono A., Shinno I., Nakamuta Y., Nakamura T., and Sekine T. 1999. Characterization of artificially shocked forsterites: (1) Diffraction profile analysis by Gandolfi camera. *Mineralogical Journal* 21:15–23.
- Williamson G. K., and Hall W. H. 1953. X-ray line broadening from filed aluminium and wolfram. *Acta Metallurgica* 1:22–31.

Appendix D: Micro X-ray diffraction (μ XRD) analysis data

D.1 Data collection and processing

Several breccia dykes from the Haughton impact structure were notable in the field since most of their clasts had been weathered away, leaving behind cavities. Further inspection of these samples after cutting for thin section preparation, revealed some of the clast cavities were lined or partially filled with small sand-sized pale brown grains and several of the more interior clasts within the sample were not completely weathered away (Figs. D-1A and D-6A).

The heavily weathered clasts contained unconsolidated grains that did not survive the thin section process in other samples; these grains could easily be plucked out with a fingernail. To determine clast composition, the cut face from whole rock sample slabs that still contained the partially weathered clasts were analyzed using micro X-ray diffraction (μ XRD). No further sample preparation was required. The μ XRD data was collected using a Bruker D8 Discover microdiffractometer with a 60 mm cobalt Gobel mirror, Co X-ray source (Co $K\alpha_1 = 1.78897 \text{ \AA}$), and a 300 μm beam diameter while operating at 35 kV and 45 mA.

The Bruker diffractometer produces two-dimensional general area detector diffraction system (GADDS) frames. Each analysis generated two GADDS frames (e.g., Fig. D-2B) that ranged in appearance from smooth/full Debye rings to spotty rings, indicating fine-grained or microcrystalline material ($<5 \mu\text{m}$) to coarser grained crystals of $\sim 15 \mu\text{m}$, respectively in all orientations. Large single crystals would generate single discrete spots corresponding to specific lattice planes from a single orientation. Each set of GADDS frames were imported and integrated using DIFFRAC.EVA software version 4.2 by Bruker AXS by choosing the full frame cursor to select all data in both frames to generate a scan pattern of counts versus 2θ for the sample. The background for the scan was subtracted then peak matching was conducted to identify minerals present in the sample. Searching by mineral name within the candidate list produced a list of cards associated with the searched mineral phase using the ICDD (International Centre for Diffraction Data) database PDF-4+ 2018. The best match for each phase was kept (e.g., Fig. D-2C).

D.2 Haughton sample 16-1011

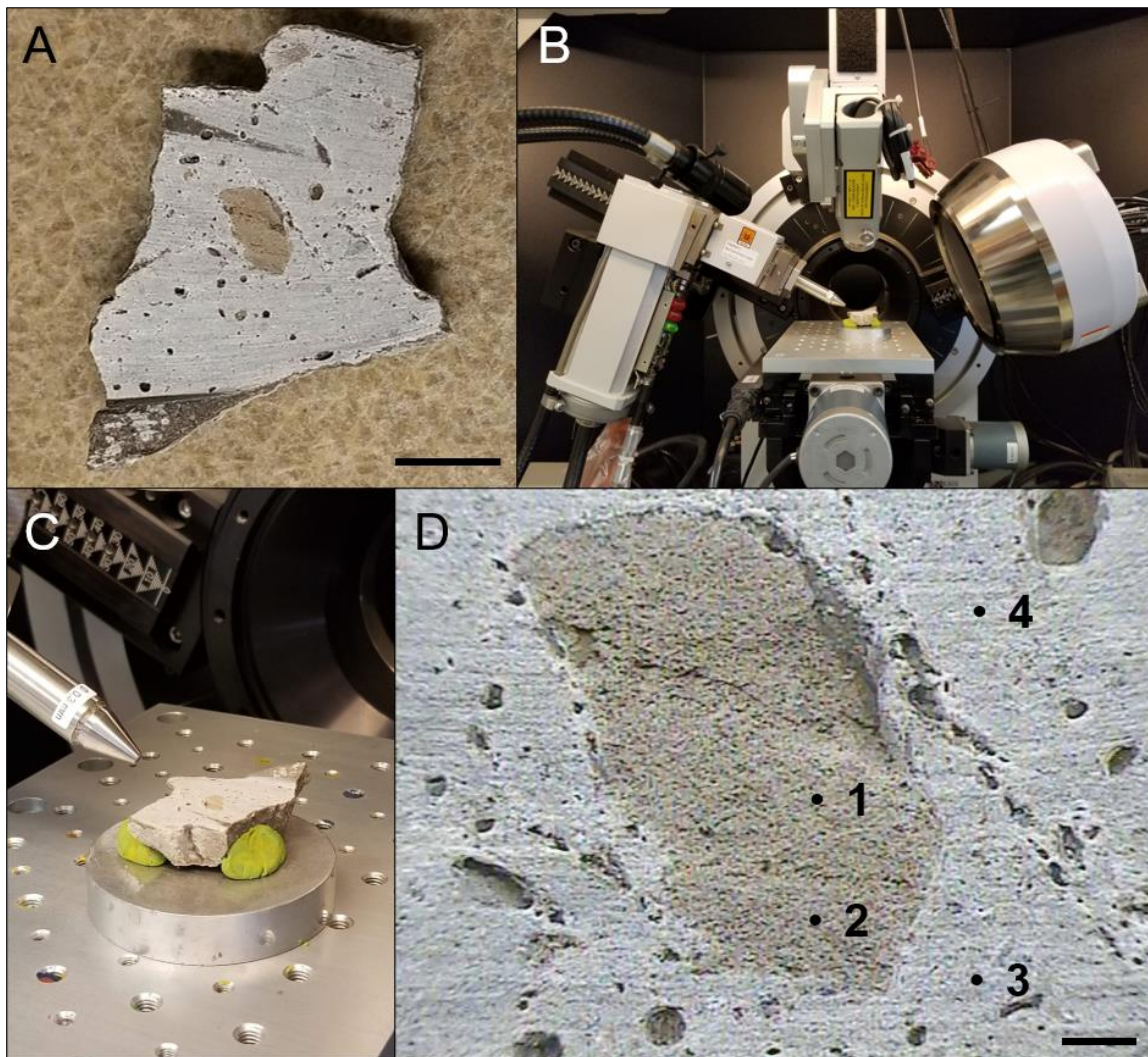


Figure D-1. Sample Hau_16_1011 A) Flat surface after cutting reveals partially weathered pale brown clast in centre of breccia sample. Smaller dark spots are cavities. Scale bar is 1 cm. B) Sample positioned within the Bruker D8 Discover Micro X-ray diffractometer. C) Close-up of sample mounted for analysis. D) Map of clast shown in (A) indicating analysis locations. Spot 1 and 2 are within the weathered clast and spot 3 and 4 are in the surrounding matrix. Scale bar is 2 mm.

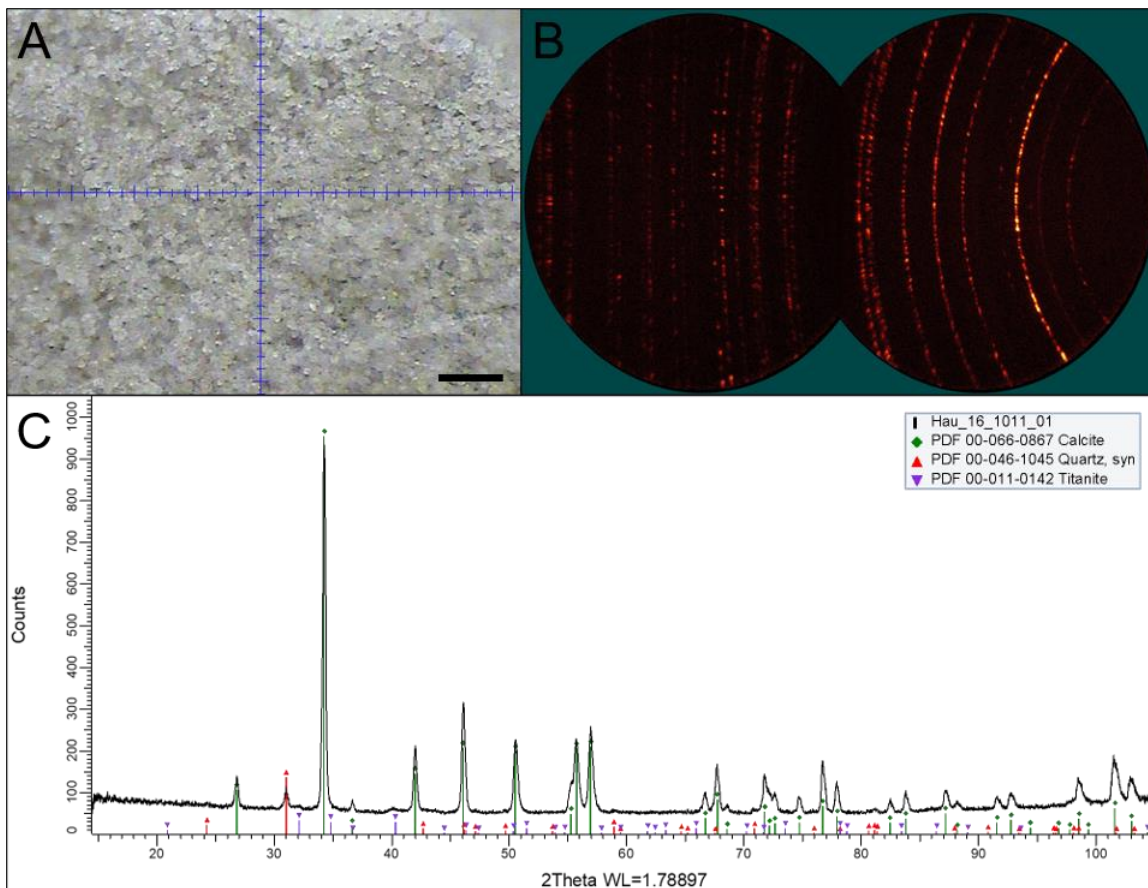


Figure D-2. Sample Hau_16_1011 spot 1 A) Zoom (x7) image of analysis location in weathered pale brown clast. Scale bar is 250 μm . B) Two-dimensional general area detector diffraction system (GADDS) images imported and integrated using DIFFRAC.EVA software. C) Scan pattern of counts versus 2Theta (2θ) derived from the integration of GADDS images. Background subtraction and a Y-offset of 50 counts was applied to scan. Analysis was conducted with DIFFRAC.EVA software and phases were identified and matched using the ICDD (International Centre for Diffraction Data) database PDF-4+ (2018).

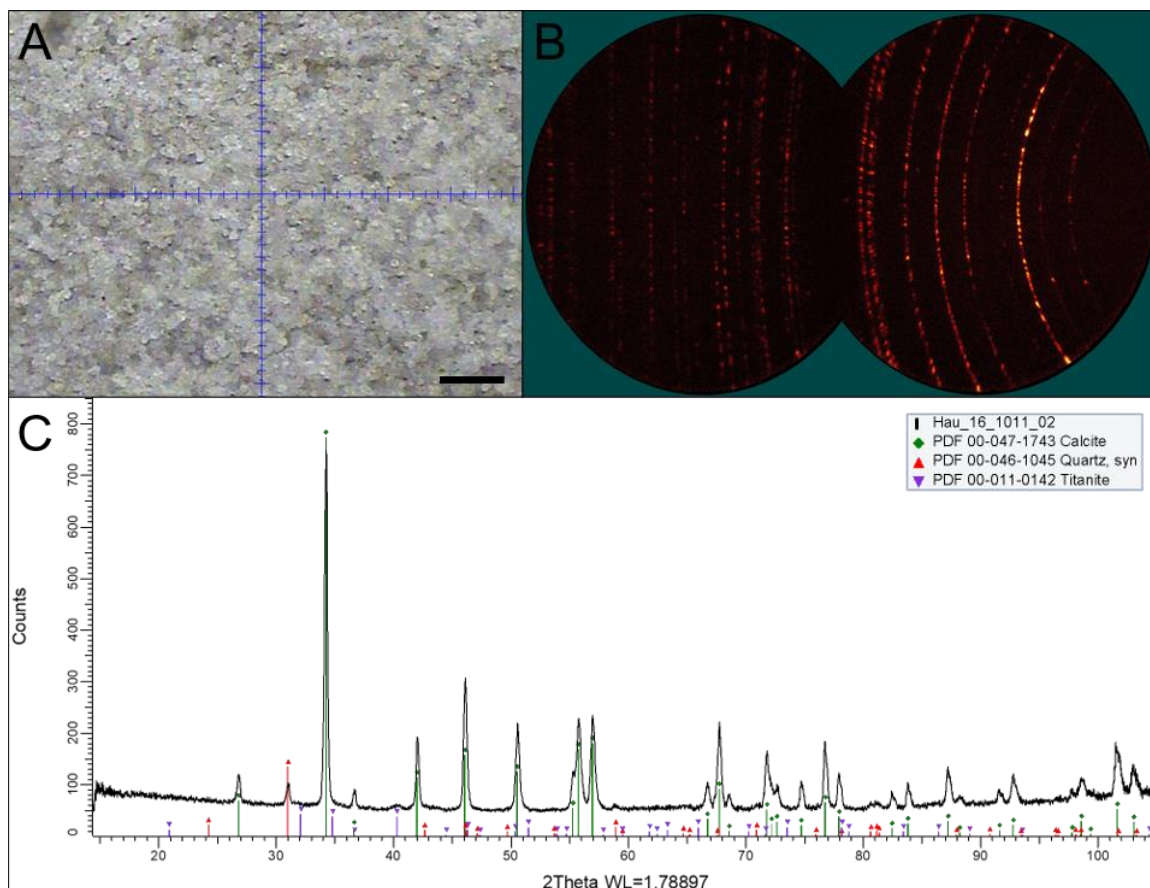


Figure D-3. Sample Hau_16_1011 spot 2 A) Zoom (x7) image of analysis location in weathered pale brown clast. Scale bar is 250 μm . B) Two-dimensional general area detector diffraction system (GADDS) images imported and integrated using DIFFRAC.EVA software. C) Scan pattern of counts versus 2Theta (2θ) derived from the integration of GADDS images. Background subtraction and a Y-offset of 50 counts was applied to scan. Analysis was conducted with DIFFRAC.EVA software and phases were identified and matched using the ICDD (International Centre for Diffraction Data) database PDF-4+ (2018).

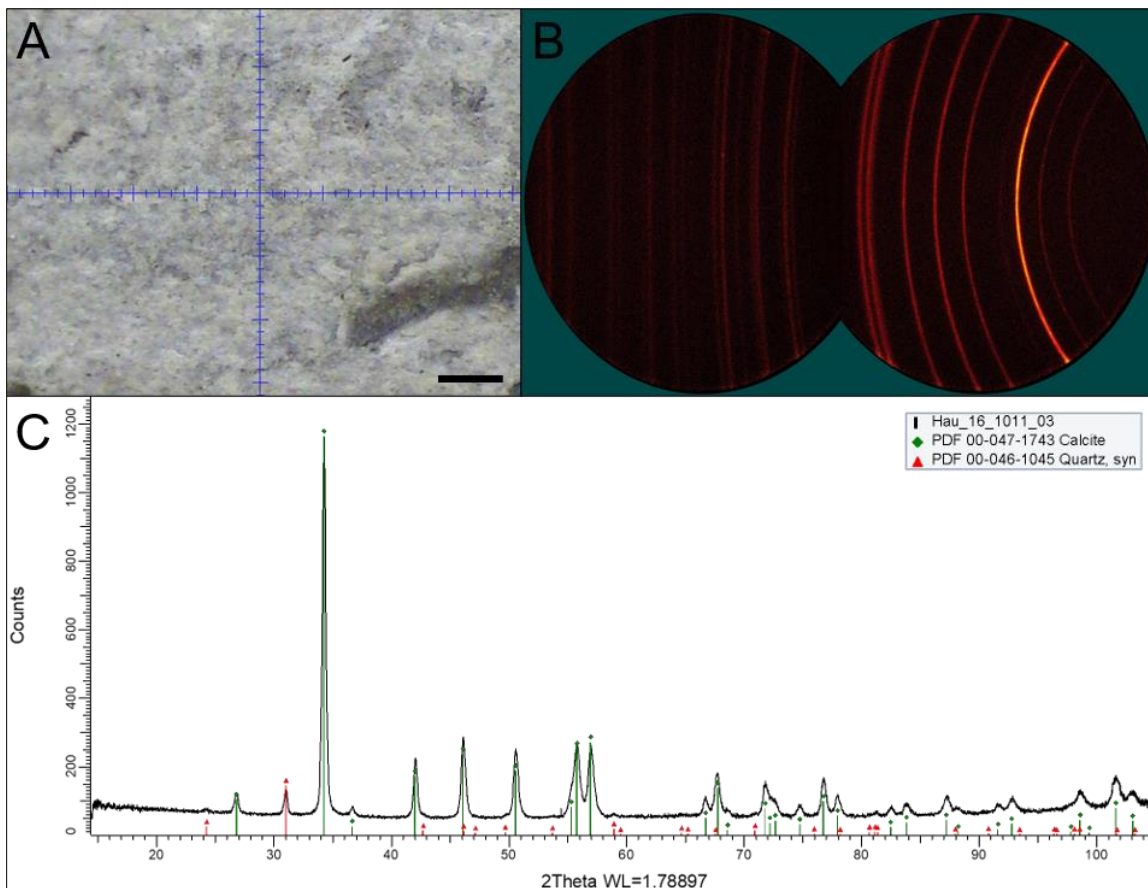


Figure D-4. Sample Hau_16_1011 spot 3 A) Zoom (x7) image of analysis location in weathered pale brown clast. Scale bar is 250 μm . B) Two-dimensional general area detector diffraction system (GADDS) images imported and integrated using DIFFRAC.EVA software. C) Scan pattern of counts versus 2Theta (2θ) derived from the integration of GADDS images. Background subtraction and a Y-offset of 50 counts was applied to scan. Analysis was conducted with DIFFRAC.EVA software and phases were identified and matched using the ICDD (International Centre for Diffraction Data) database PDF-4+ (2018).

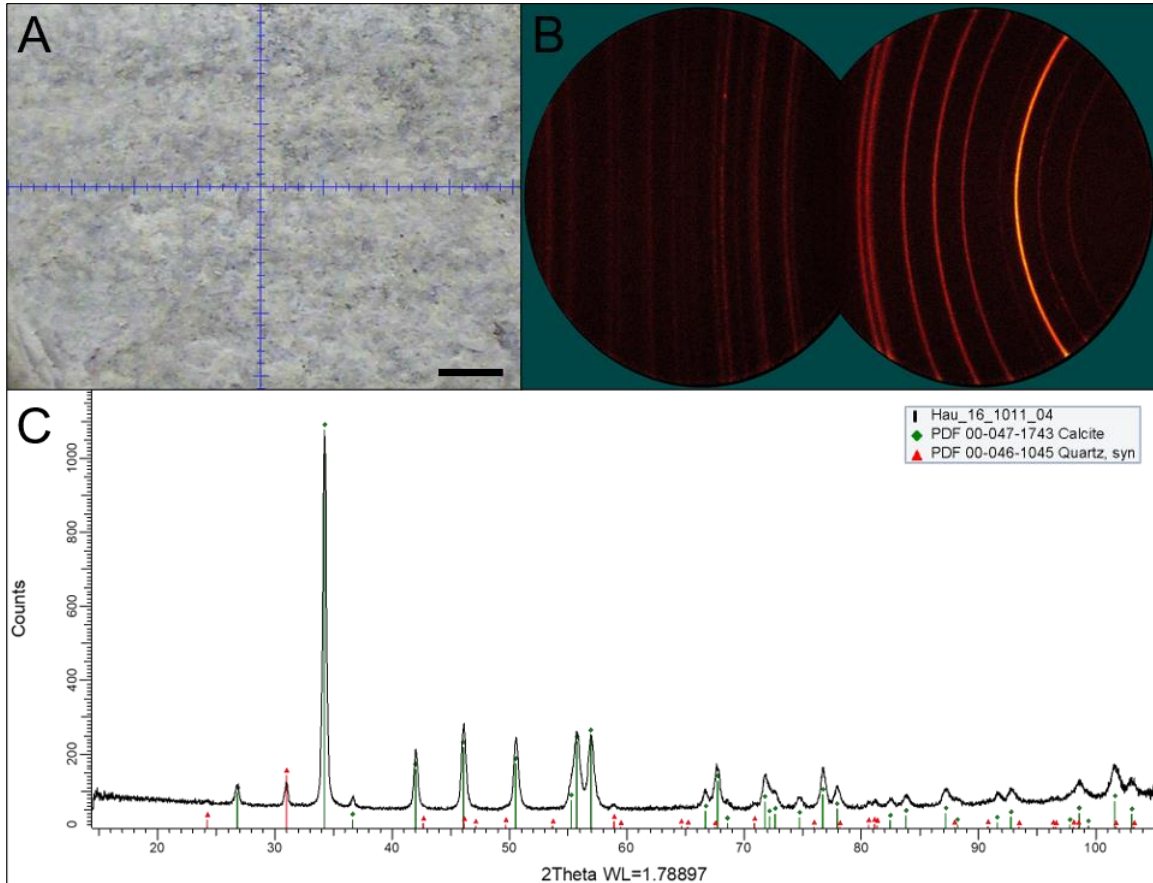


Figure D-5. Sample Hau_16_1011 spot 4 A) Zoom (x7) image of analysis location in weathered pale brown clast. Scale bar is 250 μm . B) Two-dimensional general area detector diffraction system (GADDS) images imported and integrated using DIFFRAC.EVA software. C) Scan pattern of counts versus 2Theta (2θ) derived from the integration of GADDS images. Background subtraction and a Y-offset of 50 counts was applied to scan. Analysis was conducted with DIFFRAC.EVA software and phases were identified and matched using the ICDD (International Centre for Diffraction Data) database PDF-4+ (2018).

D.3 Houghton sample 16-1020

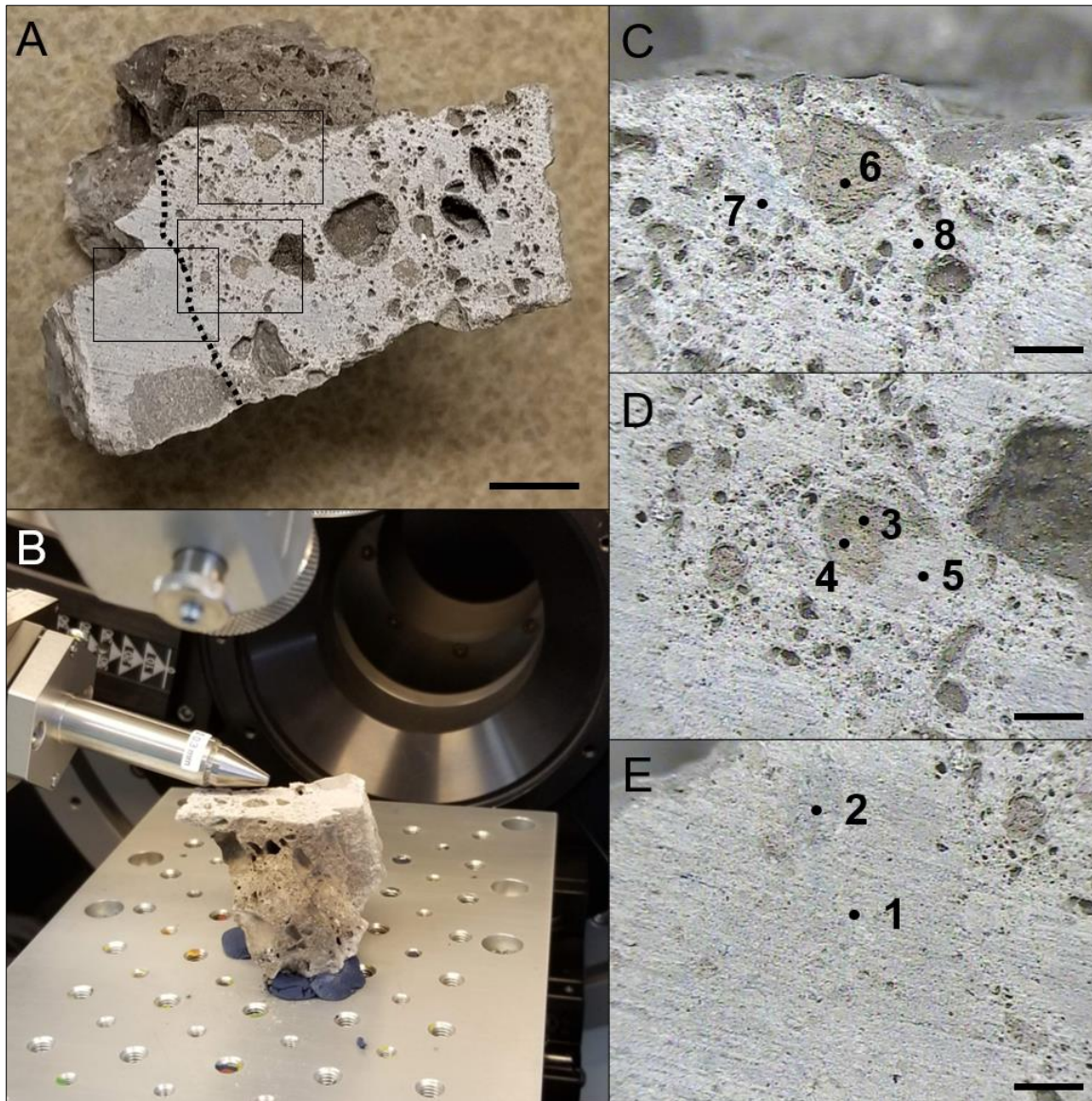


Figure D-6. Sample Hau_16_1020 A) Flat surface after cutting reveals several partially weathered pale brown clasts and two adjacent breccias; contact between breccias is indicated by dashed line. Darker areas in breccia to the right of dashed line are cavities. Boxes indicate sampling locations and correspond from top to bottom with analysis maps shown in (C) (D) and (E), respectively. Scale bar is 1 cm. B) Close-up of sample mounted for analysis in micro X-ray diffractometer. C) Spot 6 is weathered clast, spot 7 is pale grey area in matrix, and spot 8 is white coloured matrix. D) Spot 3 is pale brown portion of weathered clast, spot 4 is colourless grain within clast, and spot 5 is white matrix. E) Spot 1 is pale grey matrix of breccia to the left of dashed line and spot 2 is a slightly darker grey clast. Scale bars in (C – E) are 2 mm.

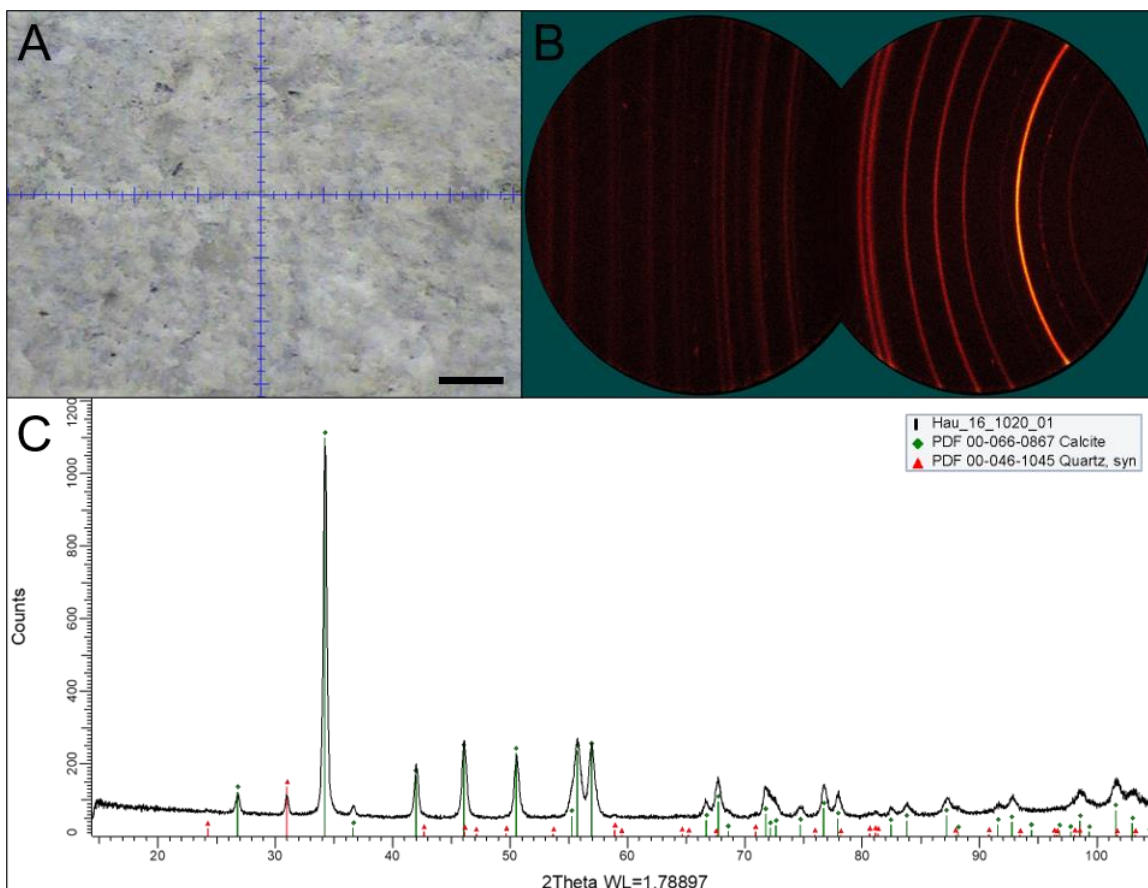


Figure D-7. Sample Hau_16_1020 spot 1 A) Zoom (x7) image of analysis location in weathered pale brown clast. Scale bar is 250 μm . B) Two-dimensional general area detector diffraction system (GADDS) images imported and integrated using DIFFRAC.EVA software. C) Scan pattern of counts versus 2Theta (2θ) derived from the integration of GADDS images. Background subtraction and a Y-offset of 50 counts was applied to scan. Analysis was conducted with DIFFRAC.EVA software and phases were identified and matched using the ICDD (International Centre for Diffraction Data) database PDF-4+ (2018).

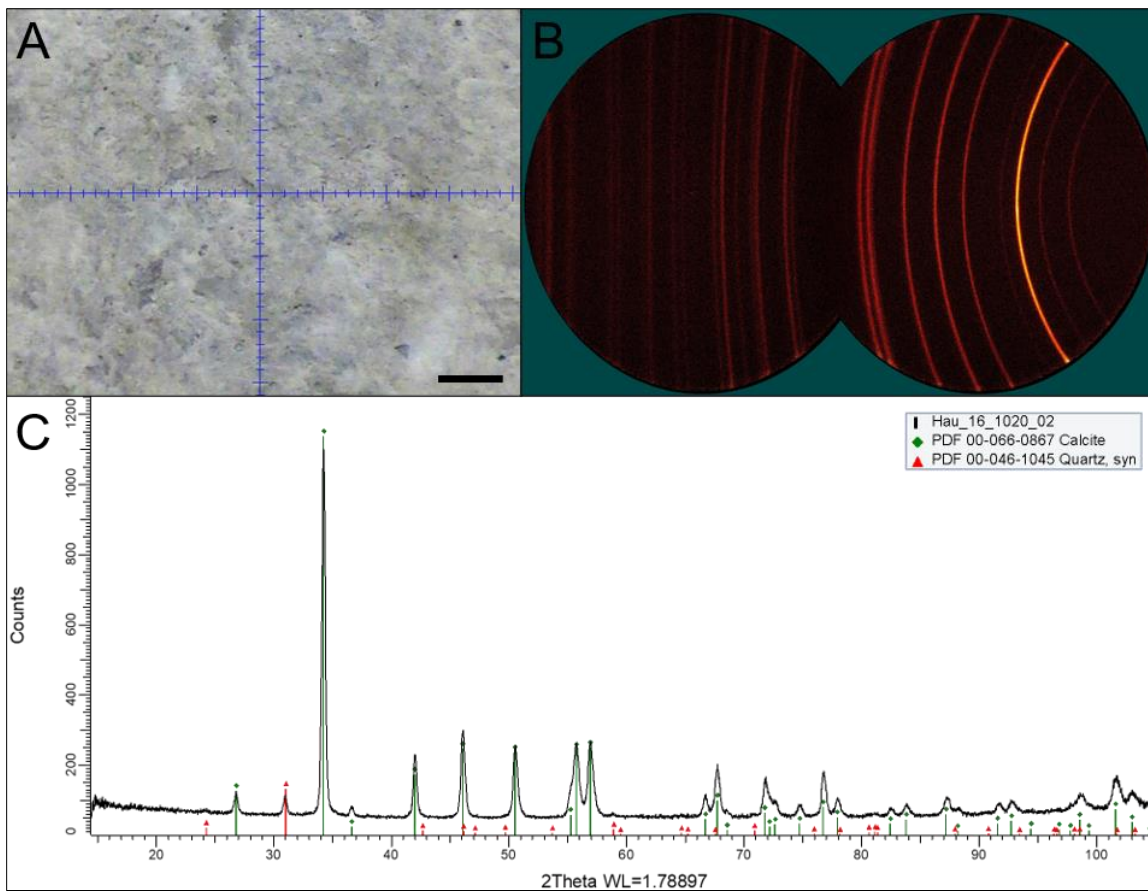


Figure D-8. Sample Hau_16_1020 spot 2 A) Zoom (x7) image of analysis location in weathered pale brown clast. Scale bar is 250 μm . B) Two-dimensional general area detector diffraction system (GADDS) images imported and integrated using DIFFRAC.EVA software. C) Scan pattern of counts versus 2Theta (2θ) derived from the integration of GADDS images. Background subtraction and a Y-offset of 50 counts was applied to scan. Analysis was conducted with DIFFRAC.EVA software and phases were identified and matched using the ICDD (International Centre for Diffraction Data) database PDF-4+ (2018).

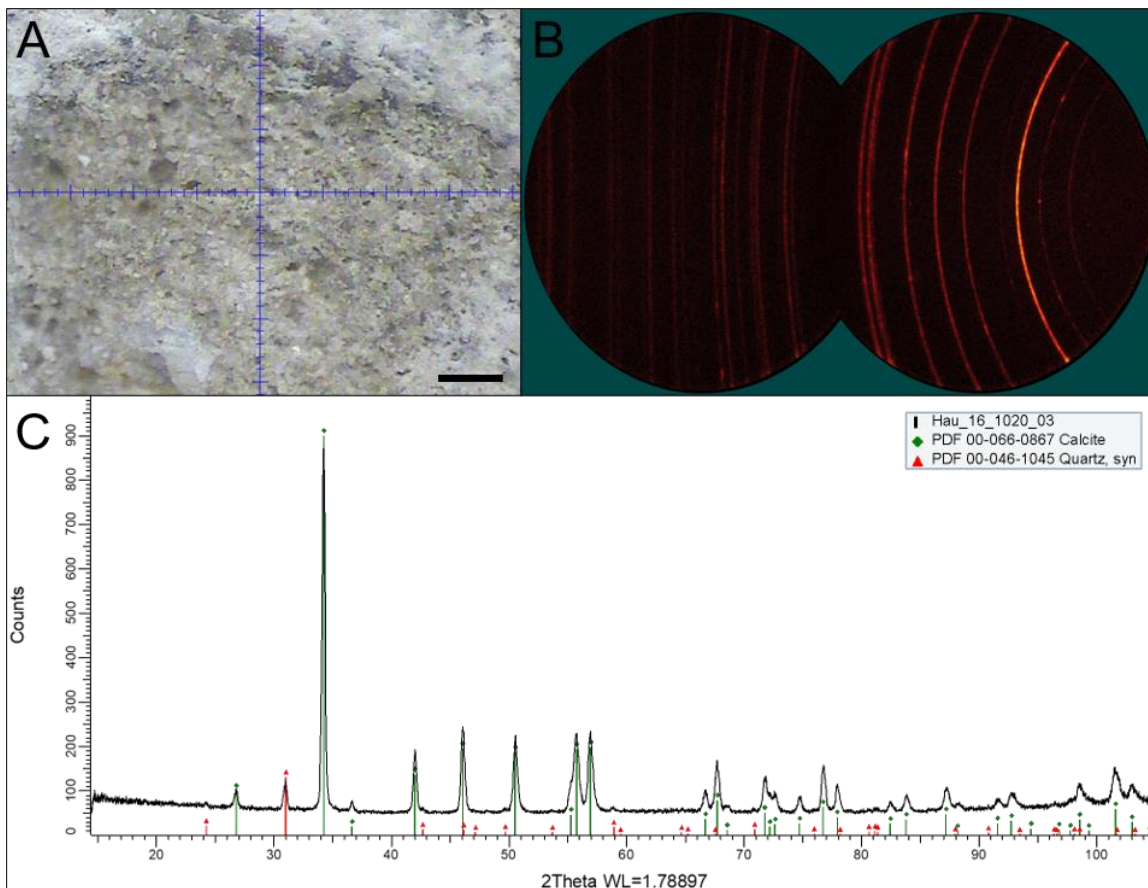


Figure D-9. Sample Hau_16_1020 spot 3 A) Zoom (x7) image of analysis location in weathered pale brown clast. Scale bar is 250 μm . B) Two-dimensional general area detector diffraction system (GADDS) images imported and integrated using DIFFRAC.EVA software. C) Scan pattern of counts versus 2Theta (2θ) derived from the integration of GADDS images. Background subtraction and a Y-offset of 50 counts was applied to scan. Analysis was conducted with DIFFRAC.EVA software and phases were identified and matched using the ICDD (International Centre for Diffraction Data) database PDF-4+ (2018).

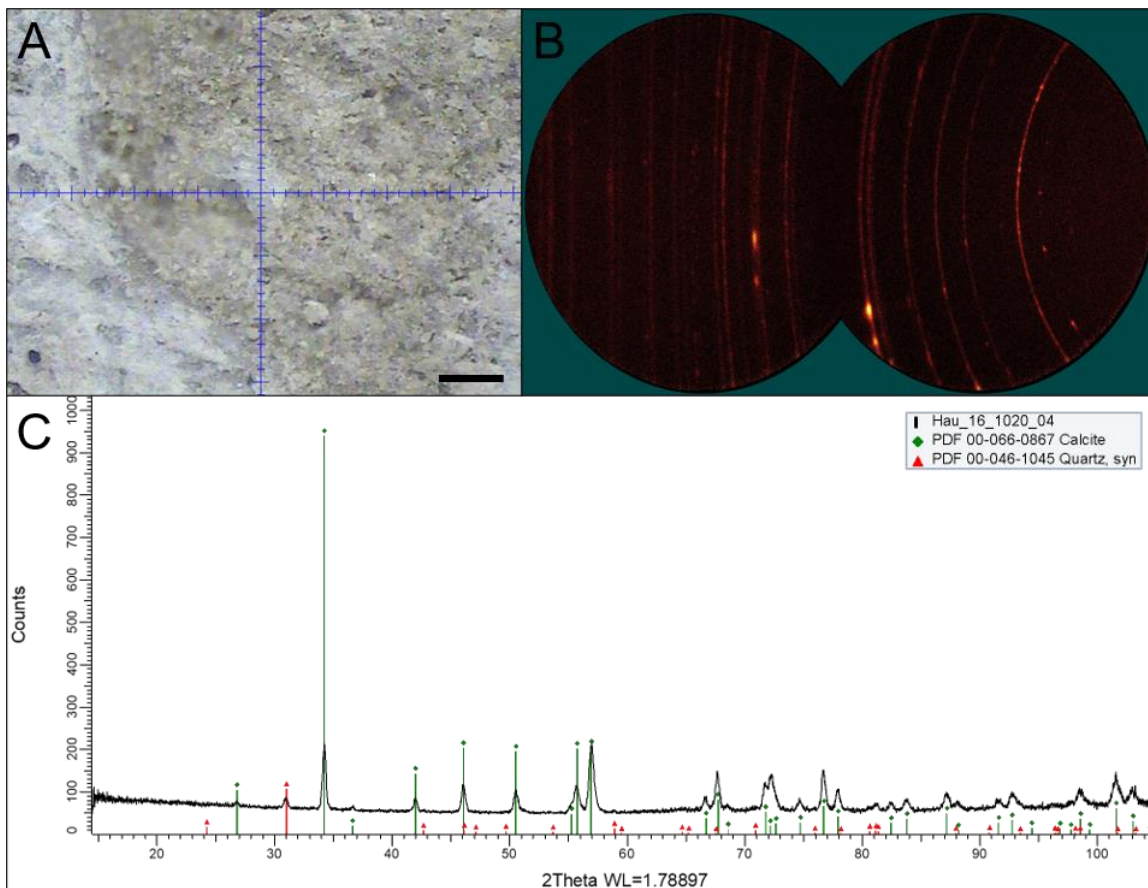


Figure D-10. Sample Hau_16_1020 spot 4 A) Zoom (x7) image of analysis location in weathered pale brown clast. Scale bar is 250 μm . B) Two-dimensional general area detector diffraction system (GADDS) images imported and integrated using DIFFRAC.EVA software. C) Scan pattern of counts versus 2Theta (2θ) derived from the integration of GADDS images. Background subtraction and a Y-offset of 50 counts was applied to scan. Analysis was conducted with DIFFRAC.EVA software and phases were identified and matched using the ICDD (International Centre for Diffraction Data) database PDF-4+ (2018).

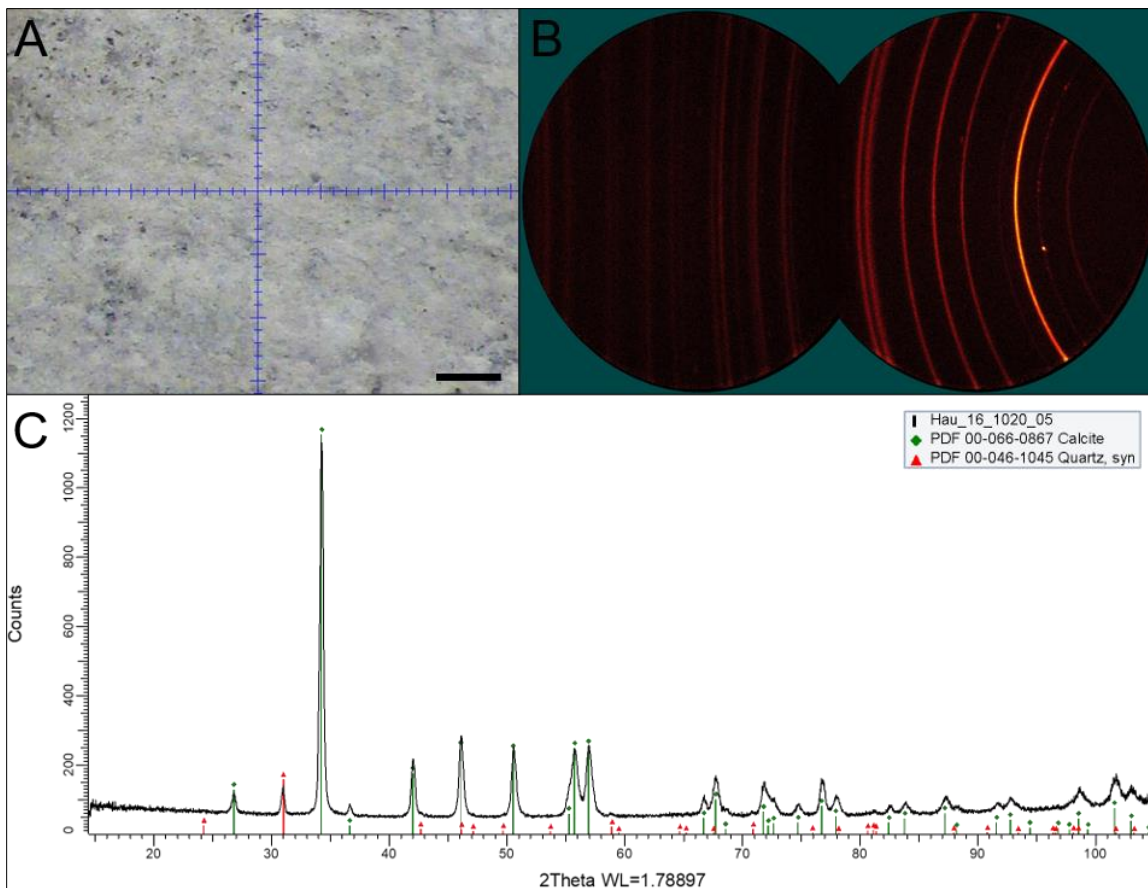


Figure D-11. Sample Hau_16_1020 spot 5 A) Zoom (x7) image of analysis location in weathered pale brown clast. Scale bar is 250 μm . B) Two-dimensional general area detector diffraction system (GADDS) images imported and integrated using DIFFRAC.EVA software. C) Scan pattern of counts versus 2Theta (2θ) derived from the integration of GADDS images. Background subtraction and a Y-offset of 50 counts was applied to scan. Analysis was conducted with DIFFRAC.EVA software and phases were identified and matched using the ICDD (International Centre for Diffraction Data) database PDF-4+ (2018).

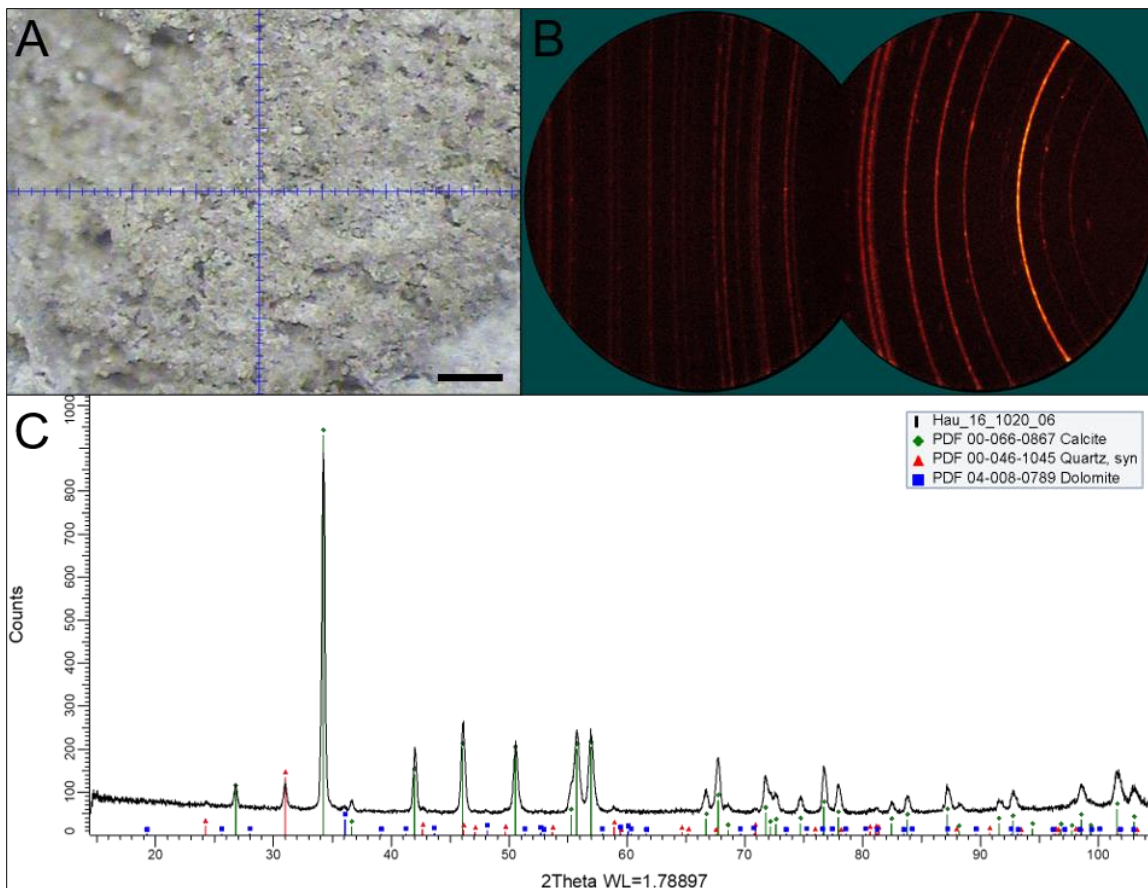


Figure D-12. Sample Hau_16_1020 spot 6 A) Zoom (x7) image of analysis location in weathered pale brown clast. Scale bar is 250 μm . B) Two-dimensional general area detector diffraction system (GADDS) images imported and integrated using DIFFRAC.EVA software. C) Scan pattern of counts versus 2Theta (2θ) derived from the integration of GADDS images. Background subtraction and a Y-offset of 50 counts was applied to scan. Analysis was conducted with DIFFRAC.EVA software and phases were identified and matched using the ICDD (International Centre for Diffraction Data) database PDF-4+ (2018).

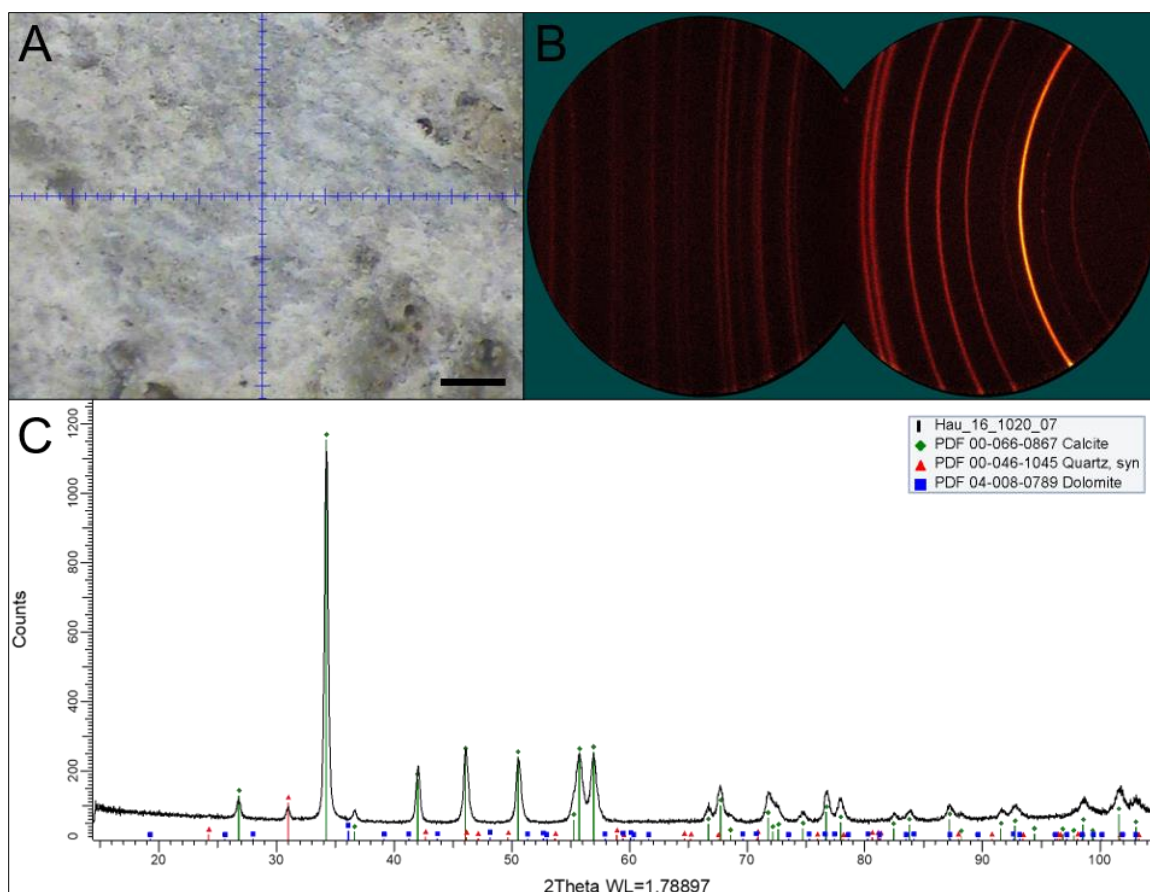


Figure D-13. Sample Hau_16_1020 spot 7 A) Zoom (x7) image of analysis location in weathered pale brown clast. Scale bar is 250 μm . B) Two-dimensional general area detector diffraction system (GADDS) images imported and integrated using DIFFRAC.EVA software. C) Scan pattern of counts versus 2Theta (2θ) derived from the integration of GADDS images. Background subtraction and a Y-offset of 50 counts was applied to scan. Analysis was conducted with DIFFRAC.EVA software and phases were identified and matched using the ICDD (International Centre for Diffraction Data) database PDF-4+ (2018).

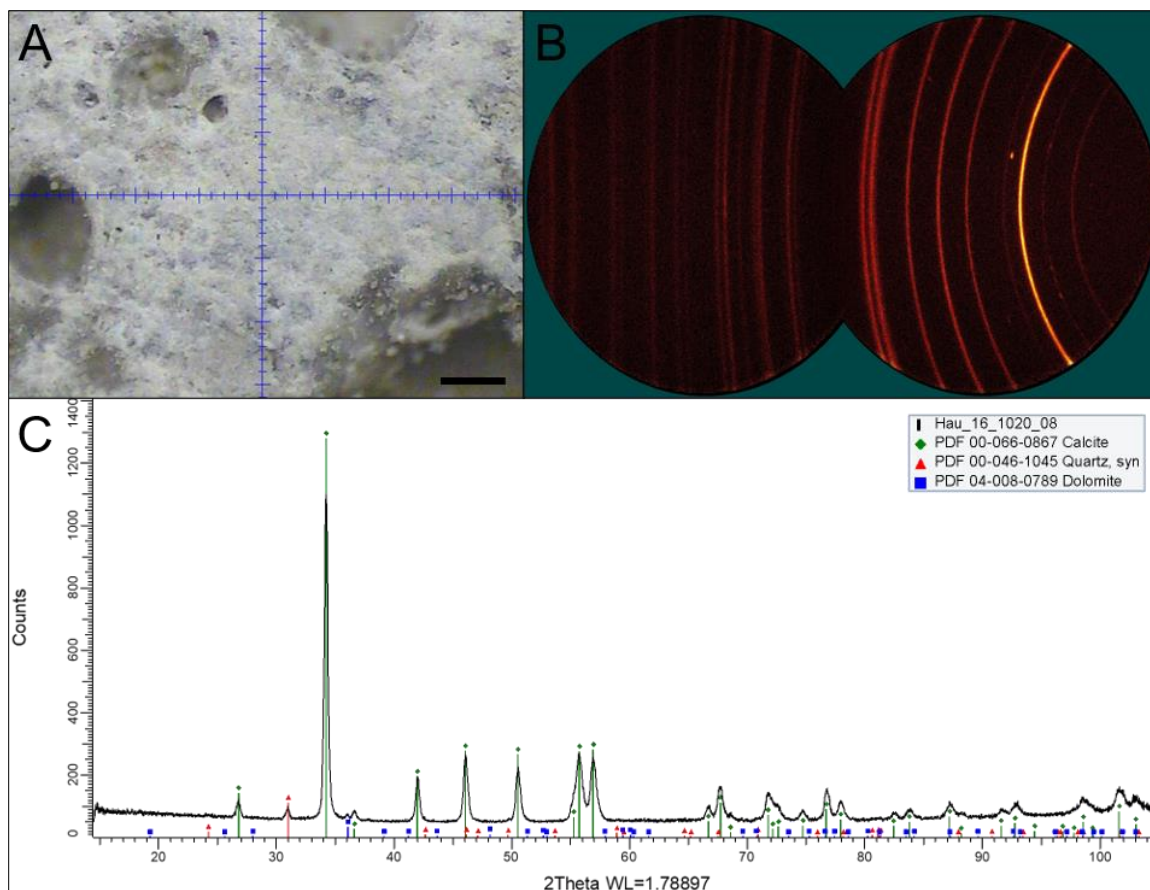


Figure D-14. Sample Hau_16_1020 spot 8 A) Zoom (x7) image of analysis location in weathered pale brown clast. Scale bar is 250 µm. B) Two-dimensional general area detector diffraction system (GADDS) images imported and integrated using DIFFRAC.EVA software. C) Scan pattern of counts versus 2Theta (2θ) derived from the integration of GADDS images. Background subtraction and a Y-offset of 50 counts was applied to scan. Analysis was conducted with DIFFRAC.EVA software and phases were identified and matched using the ICDD (International Centre for Diffraction Data) database PDF-4+ (2018).

Appendix E: Detailed analytical methods and output values for Rietveld refinement of powder X-ray diffraction (pXRD) scans from the Haughton impact structure

E.1 Analytical methods

E.1.1 Powder X-ray diffraction sample preparation

Typically, powder samples for X-ray diffraction are mounted on a recessed glass slide using 100% ethanol, as was done for samples in Chapter 5. This method requires minimal powder volume and provides enough sample for phase identification. Mounting powders with ethanol, however, can introduce preferred orientation effects. Preferred orientation does not affect phase identification but can create issues during Rietveld refinement. To avoid such effects, powders were finely ground then reverse mounted as explained in Chapter 4 and shown in Figure E-1 below. Reverse mounting requires ~1 g of powder.

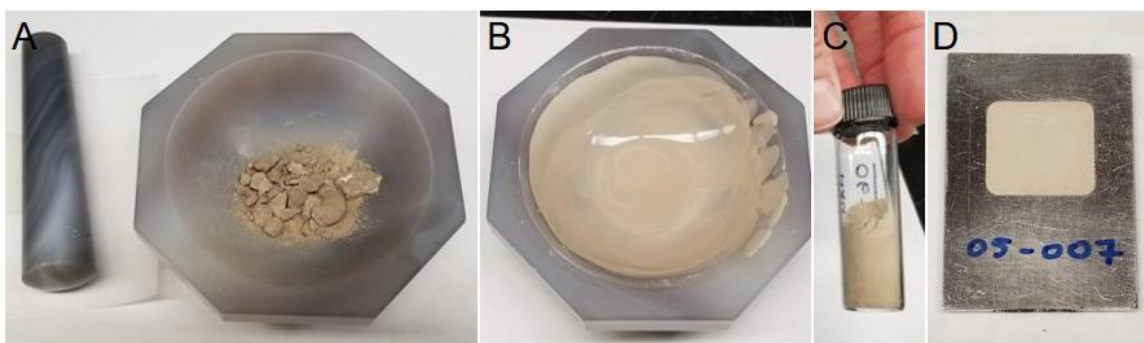


Figure E-1. Sample preparation. A) An agate mortar and pestle were used to grind each sample into a powder. B) Ethanol was added while sample was ground from small fragments into a fine powder. C) Once the ethanol had evaporated from the powder it was transferred to a vial. D) Reverse mounted powder is packed flush with aluminum sample holder and ready for X-ray diffraction analysis.

E.1.2 Powder X-ray diffraction (pXRD) analysis using EVA 4.2

Mineral identification in raw scans of each powdered carbonate sample were done using DIFFRAC.EVA version 4.2 software by Bruker AXS. Each raw scan gives an X-ray diffraction pattern of counts versus 2θ for a sample then minerals were selected to match

with the visible peaks. Mineral phases were identified using the ICDD (International Centre for Diffraction Data) database PDF-4+ 2019.

Steps for Mineral Identification in EVA 4.2

- load .raw file for sample into EVA version 4.2
- remove background
 - move slider down to bottom
 - select background subtracted to view sample pattern without background
 - close window without appending scan
- Search by Name
 - check that the most recent database available (by year) is selected in the left hand column e.g., PDF-4+2019
 - this is found in the Database Filter tab
 - in the Candidate List tab, enter name of a mineral expected to be in sample (e.g., calcite/dolomite/quartz)
 - Candidate List will return a list of cards associated with the searched mineral
 - scroll through list to find card that matches best to sample
 - when a good match is found, select the card by checking the box on the left side of the window
 - repeat search with another mineral if there are still unidentified peaks until all are associated with a mineral phase
- once all mineral cards have been selected, open Selected Candidates tab in the Search by Name window
 - adjust the y-scale (if needed) for each mineral by moving the slider
 - in details, scroll down to find the author(s) associated with the publication in the card

go to the American Mineralogist Crystal Structure Database and locate the entry by searching the mineral and author here:
<http://rruff.geo.arizona.edu/AMS/amcsd.php>
 - if the author is not found, search for all entries associated with the mineral name and find the one that best matches *a/b/c*-axis dimensions
 - download CIF file and include mineral, author name, and year in filename
[this file will be used later for Rietveld refinement]
- diffraction patterns can be stacked in a single plot, which is useful for comparing peak broadening in shocked samples
 - import the samples of interest
 - remove background from each sample
 - duplicate the sample and uncheck the original scan
 - determine the best interval between scans to best display samples with minimal overlap of peaks
 - enter this value in the Y-Offset window
 - click replace *[append will add another scan to plot]*

- the order of samples in the pattern list tree at bottom of screen will be the order of samples displayed in legend, so adjust this order to match the order of stacked scan patterns
- keeping one card of each mineral present is sufficient to display which minerals are present in the stacked samples
 - adjust height, colour, and thickness of sticks for best visibility
 - adding a marker shape also helps discriminate mineral phases
- once complete, use Copy View to copy plot as a metafile and paste into PowerPoint for reference or for generating figures

E.1.3 Rietveld refinement using TOPAS 5

Rietveld refinements were performed on powdered carbonate samples using TOPAS version 5 software by Bruker AXS. The goal of the refinements was to obtain an RWP value around 10 or below while refining the crystal structure to generate Gaussian size and strain values for calcite and dolomite with small error values. The steps to achieve these results are outlined below. Final output reports for each sample are provided in section E.2 and hkl output values used to generate Williamson-Hall plots are provided in section E.3.

Steps for Rietveld Refinement using TOPAS 5:

- load .raw file for sample into TOPAS version 5
- zoom in from 16 to 80, 2theta [*this is the 2theta range of interest for sample suites*]
 - under fit options, ensure Fit Zoomed Region is selected
- Emission Profile
 - check box for Ref
 - Area = 1
 - WL (Angstrom) = 1.788970
 - Lortz. HW = 0.501844 (default)
 - everything else is set to 0 (zero)
- Background
 - check box for Chebychev (default is checked) [refine]
 - check box for 1/X Bkg [refine] → *this is background intensity*
 - change order from 1 to 3
- Instrument
 - Goniometer radii
 - Primary radius (mm) = 185
 - Secondary radius (mm) = 185
 - Point Detector = box checked (default)

- Corrections
 - Zero error = leave box unchecked
 - Sample displacement = check box [refine]
 - LP factor = keep box checked (default)
 - change 0 to 26.4 [fix]
 - Absorption = check box [refine]
- load CIFs
 - recall from EVA which mineral phases were identified
 - download CIF file for each mineral from American Mineralogist Crystal Structure Database if it has not been done at:
<http://rruff.geo.arizona.edu/AMS/amcsd.php>
- (then for each CIF:)
 - append the name of the CIF author (and year if necessary) to the mineral name (otherwise you won't know which one you used in case you need to pick a different one if the first does not work)!
 - Sites
 - add each atom
 - leave Beq [fixed] for now
 - leave Occ. at 1
 - for quartz* >> enter =1/3 for SiO₂ for z code (bottom set of rows); numbers should change to blue from black
 - Preferred Orientation (only select for main phase(s), change minor phases later if needed)
 - under PO spherical harmonics:
 - check box to use
 - change order to 8
 - Mineral structure name (i.e., dolomite, calcite, quartz, etc.)
 - Structure
 - Scale = check box [refine]
 - change code for axes (a, b, and c) from [fix] to [refine]
 - Microstructure
 - leave everything unchecked, for now except for main phase(s)
 - for main phase(s) only, check Cry size G [but keep this fixed for now]
 - Peak Type
 - select PV_TCHZ
 - [refine] U, V, W, X (default)
 - [fix] Z, Y (default)

<RUN>

➔ remember to SAVE often as there is no undo in TOPAS after sample RUNS, and when saving, it helps to change file name each time to reflect what change was made

- resulting RWP should be less than 20, ideally less than 15 and close to 10
- do the following ONLY if a mineral is >10.0 wt%
- Mineral name
 - Microstructure
 - Cry size G = check box [refine]
 - Strain G = check box [refine]

<RUN>

- Background
 - Order = change from 3 to 5

<RUN>

- Mineral name
 - Microstructure
 - Stephen's model = check box
 - Type = Stephens_trigonal_high [refine all, this is the default]
 - use this for calcite or dolomite (i.e., main phase(s) present)

<RUN>

- turn on PO for minor phases
 - Preferred Orientation (for phases not selected earlier)
 - under PO spherical harmonics:
 - check box to use
 - change order to 8

<RUN>

- Mineral name (for main phase(s) only)
 - Sites
 - change Beq from [fix] to [refine]
 - *[these refinements may not be necessary for minor phases in sample, some trial and error may be required here]*
 - *[start this and next step for the dominant mineral phase(s); depending on modal proportions, may need to make changes to one phase at a time and RUN to see if the change made any effect]*

<RUN>

- if there is more than one mineral phase >10 wt%, try setting the lower wt% phase so that U, V, W, X in Peak Type are equal to the dominant phase *[this step may not be necessary if RWP is already low, and may not even change RWP much]*
 - dominant phase

- change code for U, V, W, and X to UU, VV, WW, and XX respectively
- minor phase(s)
 - change code for U, V, W, and X to =UU, =VV, =WW, and =XX respectively

<RUN>

- turn on errors by going to:
 - Fit (top menu bar)
 - select calculate errors
 - will not see any errors until RUN is clicked
 - *[errors can be turned on earlier in refinement process to track the progress of refinement to monitor when a change may cause errors to become too high]*

The final 4 or 5 steps may require slight variation regarding their order of refinement and may not be necessary for all mineral phases if more than one phase is present. Make these adjustments based on the resulting RWP value after selecting RUN.

E.2 TOPAS output reports

99-006

File 1 : "D:\XRD Haughton group_organized\sample files\RAW files\99-006\Rietveld_99006gr.raw"

Range Number : 1

R-Values

Rexp : 6.21 Rwp : 7.78 Rp : 5.26 GOF : 1.25
 Rexp` : 6.12 Rwp` : 7.67 Rp` : 5.19 DW : 1.37

Quantitative Analysis - Rietveld

Phase 1 : Microcline_Ribbe 3.4(8) %
 Phase 2 : "Dolomite_Ross and Reeder 1992" 91.9(8) %
 Phase 3 : "Calcite_Markgraf and Reeder" 4.7(3) %

Background

One on X		2000(4000)
Chebyshev polynomial, Coefficient	0	0(120)
	1	0(90)
	2	0(40)
	3	0(14)
	4	-9(5)
	5	-4(3)

Instrument

Primary radius (mm)	185
Secondary radius (mm)	185

Corrections

Specimen displacement	0.075(13)
LP Factor	26.4
Absorption (1/cm)	0(5000)

Structure 1

Phase name	Microcline_Ribbe
R-Bragg	6.756
Spacegroup	C-1
Scale	0.000016(4)
Cell Mass	1549.447
Cell Volume (Å ³)	740.5(9)
Wt% - Rietveld	3.4(8)
Crystal Linear Absorption Coeff. (1/cm)	261.9(3)
Crystal Density (g/cm ³)	3.475(4)
Preferred Orientation Spherical Harmonics	
Order	8
y00	1
y20	-1.0(8)
y21m	0.2(12)
y21p	-0.4(5)
y22m	-1.4(9)
y22p	-1.3(5)
y40	-0.3(11)
y41m	-7(3)
y41p	0.9(5)
y42m	-8(3)
y42p	1.3(8)
y43m	-10(3)
y43p	-0.0(4)
y44m	-4.2(12)
y44p	1.5(6)
y60	5.6(17)
y61m	-5(3)
y61p	3.0(8)
y62m	-5(2)
y62p	3.8(13)
y63m	2(3)
y63p	2.8(10)
y64m	-6(2)
y64p	3.3(7)
y65m	2.2(15)
y65p	-0.1(4)
y66m	5.0(17)
y66p	0.6(4)
y80	-4.9(17)
y81m	-3(2)
y81p	1.7(18)
y82m	2.0(19)
y82p	1.1(9)
y83m	1.9(12)
y83p	0.1(8)
y84m	0.6(19)
y84p	2.4(8)
y85m	9(2)
y85p	-0.6(6)
y86m	-2.5(12)
y86p	-1.9(7)
y87m	-4.4(16)
y87p	1.2(4)
y88m	-2.9(12)
y88p	0.4(8)

PV_TCHZ peak type						
U					2.0 (17)	
V					1.0 (12)	
W					-0.4 (2)	
Z					0	
X					1.32 (15)	
Y					0	
Lattice parameters						
a (Å)					8.663 (6)	
b (Å)					13.137 (7)	
c (Å)					7.211 (5)	
alpha (°)					91.26 (4)	
beta (°)					115.49 (5)	
gamma (°)					88.56 (5)	
Site	Np	x	y	z	Atom Occ	Beq
K	4	0.28670	0.99850	0.14060	K+1 1	1
Si1o	4	0.00950	0.18440	0.22250	Si+4 1	1
Al1o	4	0.00950	0.18440	0.22250	Al+3 1	1
Si1m	4	0.00910	0.81680	0.22490	Si+4 1	1
Al1m	4	0.00910	0.81680	0.22490	Al+3 1	1
Si2o	4	0.71050	0.11840	0.34130	Si+4 1	1
Al2o	4	0.71050	0.11840	0.34130	Al+3 1	1
Si2m	4	0.70950	0.88260	0.34330	Si+4 1	1
Al2m	4	0.70950	0.88260	0.34330	Al+3 1	1
Oa1	4	0.00050	0.14400	0.99770	O-2 1	1
Oa2	4	0.63820	0.00110	0.28090	O-2 1	1
Obo	4	0.82510	0.14720	0.22280	O-2 1	1
Obm	4	0.82780	0.85340	0.22740	O-2 1	1
Oco	4	0.03670	0.31160	0.25800	O-2 1	1
Ocm	4	0.03780	0.69030	0.26020	O-2 1	1
Odo	4	0.18150	0.12400	0.40750	O-2 1	1
Odm	4	0.17900	0.87490	0.40850	O-2 1	1

Structure 2

Phase name	Dolomite_Ross and Reeder
1992	
R-Bragg	0.645
Spacegroup	R-3
Scale	0.00286 (5)
Cell Mass	553.202
Cell Volume (Å ³)	320.5 (2)
Wt% - Rietveld	91.9 (8)
Double-Voigt Approach	
Cry size Gaussian	56 (8)
k: 1 LVol-IB (nm)	53 (8)
k: 0.89 LVol-FWHM (nm)	50 (7)
Strain	
Strain G	0.55 (4)
e0	0.00120 (9)
Crystal Linear Absorption Coeff. (1/cm)	202.03 (14)
Crystal Density (g/cm ³)	2.8665 (19)
Preferred Orientation Spherical Harmonics	
Order	8
y00	1
y20	0.67 (4)
y40	0.23 (7)

y43m	0.03 (3)
y43p	0.08 (8)
y60	-0.33 (5)
y63m	-0.10 (3)
y63p	0.4 (2)
y66m	-0.24 (8)
y66p	0.126 (18)
y80	-0.26 (6)
y83m	-0.46 (6)
y83p	0.35 (14)
y86m	0.02 (12)
y86p	0.23 (3)
PV_TCHZ peak type	
U	-0.18 (7)
V	-0.01 (4)
W	0.049 (15)
Z	0
X	0.544 (14)
Y	0
Lattice parameters	
a (Å)	4.8064 (15)
c (Å)	16.018 (5)

Site	Np	x	y	z	Atom Occ	Beq
CaA	3	0.00000	0.00000	0.00000	Ca+2 1	1.0 (8)
MgB	3	0.00000	0.00000	0.50000	Mg+2 1	1.0 (3)
C	6	0.00000	0.00000	0.24310	C 1	1.0 (6)
O	18	0.24820	-0.03570	0.24400	O-2 1	1.0 (11)

Structure 3

Phase name	Calcite_Markgraf and
Reeder	
R-Bragg	1.149
Spacegroup	R-3c
Scale	0.000118 (6)
Cell Mass	600.521
Cell Volume (Å ³)	365.7 (3)
Wt% - Rietveld	4.7 (3)
Crystal Linear Absorption Coeff. (1/cm)	295.6 (2)
Crystal Density (g/cm ³)	2.7271 (19)
Preferred Orientation Spherical Harmonics	
Order	8
y00	1
y20	0.2 (2)
y40	-0.1 (3)
y43m	-0.34 (10)
y60	-0.9 (3)
y63m	-0.06 (18)
y66p	-0.25 (8)
y80	-0.81 (19)
y83m	-0.4 (3)
y86p	0.16 (12)
PV_TCHZ peak type	
U	0.0 (3)
V	-0.1 (2)
W	0.02 (4)
Z	0

X					0.63 (5)	
Y					0	
Lattice parameters						
a (Å)					4.9804 (16)	
c (Å)					17.022 (6)	
Site	Np	x	y	z	Atom Occ	Beq
Ca	6	0.00000	0.00000	0.00000	Ca+2 1	1
C	6	0.00000	0.00000	0.25000	C 1	1
O	18	0.25670	0.00000	0.25000	O-2 1	1

99-063B

File 1 : "D:\XRD - May 2019\pXRD sandpaper\RAW files\HAU_99_063B_sp.raw"

Range Number : 1

R-Values

Rexp : 7.36 Rwp : 9.38 Rp : 6.48 GOF : 1.27
Rexp` : 8.70 Rwp` : 11.08 Rp` : 8.18 DW : 1.29

Quantitative Analysis - Rietveld

Phase 1 : "Calcite_Markgraff and Reeder 1985" 96.2 (6) %
Phase 2 : "Quartz_Levian 1980" 3.8 (6) %

Background

Chebyshev polynomial, Coefficient	0	45.0 (3)
	1	-34.3 (5)
	2	17.8 (4)
	3	-9.3 (4)
	4	4.4 (4)
	5	0.9 (3)

Instrument

Primary radius (mm)	185
Secondary radius (mm)	185

Corrections

Specimen displacement	-0.037 (7)
LP Factor	26.4
Absorption (1/cm)	0 (3000)

Structure 1

Phase name	Calcite_Markgraff and Reeder 1985
R-Bragg	1.158
Spacegroup	R-3c
Scale	0.001389 (14)
Cell Mass	600.521
Cell Volume (Å ³)	365.47 (15)
Wt% - Rietveld	96.2 (6)
Double-Voigt Approach	
Cry size Gaussian	51 (7)
k: 1 LVol-IB (nm)	48 (7)
k: 0.89 LVol-FWHM (nm)	46 (6)
Strain	
Strain G	0.35 (10)
e0	0.0008 (2)
Crystal Linear Absorption Coeff. (1/cm)	295.70 (12)
Crystal Density (g/cm ³)	2.7285 (11)

Preferred Orientation Spherical Harmonics

Order	8
y00	1
y20	-0.158 (18)
y40	-0.099 (19)
y43m	-0.071 (8)
y60	0.09 (2)
y63m	0.112 (12)
y66p	-0.049 (7)
y80	0.019 (16)
y83m	0.02 (2)
y86p	-0.063 (10)
PV_TCHZ peak type	
U	0.50 (10)
V	-0.44 (5)
W	0.102 (19)
Z	0
X	0.275 (13)
Y	0
Lattice parameters	
a (Å)	4.9789 (9)
c (Å)	17.024 (3)

Site	Np	x	y	z	Atom	Occ	Beq
Ca	6	0.00000	0.00000	0.00000	Ca+2	1	0.18 (7)
C	6	0.00000	0.00000	0.25000	C	1	1.48 (16)
O	18	0.25670	0.00000	0.25000	O-2	1	0.49 (10)

Structure 2

Phase name	Quartz_Levian 1980
R-Bragg	2.362
Spacegroup	P3221
Scale	0.00041 (7)
Cell Mass	264.509
Cell Volume (Å ³)	112.74 (6)
Wt% - Rietveld	3.8 (6)
Crystal Linear Absorption Coeff. (1/cm)	258.79 (13)
Crystal Density (g/cm ³)	3.896 (2)

Preferred Orientation Spherical Harmonics

Order	8
y00	1
y20	-0.46 (18)
y40	-1.54 (19)
y43m	1.0 (5)
y60	1.0 (2)
y63m	-0.0 (2)
y66p	-0.77 (13)
y80	0.2 (2)
y83m	1.2 (4)
y86p	-1.08 (12)
PV_TCHZ peak type	
U	0.03 (15)
V	-0.07 (14)
W	0.04 (3)
Z	0
X	0.22 (3)
Y	0

Lattice parameters						
	a (Å)				4.9099 (10)	
	c (Å)				5.4003 (15)	

Site	Np	x	y	z	Atom Occ	Beq
Si	6	0.46970	0.00000	0.33333	Si+4 1	1
O	6	0.41350	0.26690	0.11910	O-2 1	1

00-019

File 1 : "C:\Documents and Settings\BrukerAdministrator\Desktop\Jared Geiger\MX00019.raw"

Range Number : 1

R-Values

Rexp : 10.91 Rwp : 12.36 Rp : 8.48 GOF : 1.13
 Rexp` : 9.74 Rwp` : 11.04 Rp` : 7.67 DW : 1.66

Quantitative Analysis - Rietveld

Phase 1 : "Calcite_Markgraf and Reeder" 57.1 (15) %
 Phase 2 : Dolomite_Althoff 42.9 (15) %

Background

One on X 1000 (1400)
 Chebychev polynomial, Coefficient

0	-10 (40)
1	10 (30)
2	-3 (11)
3	2 (4)
4	0.7 (16)
5	0.6 (7)

Instrument

Primary radius (mm) 185
 Secondary radius (mm) 185

Corrections

Specimen displacement 0.052 (6)
 LP Factor 26.4
 Absorption (1/cm) 0 (3000)

Structure 1

Phase name Calcite_Markgraf and
 Reeder
 R-Bragg 1.112
 Spacegroup R-3c
 Scale 0.000326 (5)
 Cell Mass 600.521
 Cell Volume (Å³) 365.27 (18)
 Wt% - Rietveld 57.1 (15)
 Double-Voigt|Approach
 Cry size Gaussian 52 (2)
 k: 1 LVol-IB (nm) 49 (2)
 k: 0.89 LVol-FWHM (nm) 46.1 (19)
 Strain
 Strain G 0.18 (8)
 e0 0.00038 (18)
 Crystal Linear Absorption Coeff. (1/cm) 201.87 (10)
 Crystal Density (g/cm³) 2.7300 (13)
 Preferred Orientation Spherical Harmonics

Order					8	
y00					1	
y20					-0.14 (3)	
y40					-0.17 (3)	
y43m					-0.139 (14)	
y60					-0.01 (3)	
y63m					0.094 (18)	
y66p					-0.037 (15)	
y80					-0.01 (3)	
y83m					-0.07 (3)	
y86p					-0.084 (16)	
PV_TCHZ	peak type					
U					0.19 (4)	
V					-0.11 (2)	
W					0.014 (5)	
Z					0	
X					0.372 (10)	
Y					0	
Lattice parameters						
a	(Å)				4.9775 (11)	
c	(Å)				17.024 (4)	
Site	Np	x	y	z	Atom Occ	Beq
Ca	6	0.00000	0.00000	0.00000	Ca+2 1	0.81 (11)
C	6	0.00000	0.00000	0.25000	C 1	1.7 (3)
O	18	0.25670	0.00000	0.25000	O-2 1	1.02 (16)

Structure 2

Phase name	Dolomite_Althoff
R-Bragg	1.615
Spacegroup	R-3
Scale	0.000302 (17)
Cell Mass	553.202
Cell Volume (Å ³)	320.84 (17)
Wt% - Rietveld	42.9 (15)
Double-Voigt Approach	
Cry size Gaussian	51 (10)
k: 1 LVol-IB (nm)	48 (9)
k: 0.89 LVol-FWHM (nm)	45 (9)
Strain	
Strain G	0.73 (10)
e0	0.0016 (2)
Crystal Linear Absorption Coeff. (1/cm)	139.37 (7)
Crystal Density (g/cm ³)	2.8632 (15)
Preferred Orientation Spherical Harmonics	
Order	8
y00	1
y20	0.17 (6)
y40	0.14 (8)
y43m	-0.41 (5)
y43p	-0.35 (19)
y60	-0.39 (8)
y63m	-0.12 (5)
y63p	-0.5 (2)
y66m	-2.0 (2)
y66p	-0.06 (3)
y80	-0.25 (11)

y83m						-0.29 (9)
y83p						-0.6 (2)
y86m						-2.2 (3)
y86p						0.01 (6)
PV_TCHZ peak type						
U						0.4 (3)
V						-0.5 (3)
W						0.11 (8)
Z						0
X						0.35 (7)
Y						0
Lattice parameters						
a (Å)						4.8072 (11)
c (Å)						16.031 (4)
<hr/>						
Site	Np	x	y	z	Atom Occ	Beq
Ca	3	0.00000	0.00000	0.00000	Ca+2 1	6.3 (5)
Mg	3	0.00000	0.00000	0.50000	Mg+2 1	-0.4 (4)
C	6	0.00000	0.00000	-0.24230	C 1	6.0 (10)
O	18	0.28290	0.03500	-0.24400	O-2 1	1.5 (6)

00-124

File 1 : "D:\XRD - May 2019\pXRD sandpaper\RAW files\HAU_00_124_sp.raw"

Range Number : 1

R-Values

Rexp : 7.43 Rwp : 9.86 Rp : 6.83 GOF : 1.33

Rexp` : 6.10 Rwp` : 8.10 Rp` : 5.77 DW : 1.24

Quantitative Analysis - Rietveld

Phase 1 : "Calcite_Markgraff and Reeder 1995" 99.7(17) %

Phase 2 : "Quartz_Brill 1939" 0.3(17) %

Background

One on X 3000 (2000)

Chebyshev polynomial, Coefficient 0 -40 (60)

1 30 (50)

2 -6 (18)

3 -1 (7)

4 2 (2)

5 1.7 (10)

Instrument

Primary radius (mm) 185

Secondary radius (mm) 185

Corrections

Specimen displacement 0.044 (6)

LP Factor 26.4

Absorption (1/cm) 0 (2000)

Structure 1

Phase name Calcite_Markgraff and
Reeder 1995

R-Bragg 1.264

Spacegroup R-3c

Scale 0.001337 (14)

Cell Mass 600.521

Cell Volume (\AA^3)						365.18 (12)	
Wt% - Rietveld						99.7 (17)	
Double-Voigt Approach							
Cry size Gaussian						64 (6)	
k: 1 LVol-IB (nm)						60 (6)	
k: 0.89 LVol-FWHM (nm)						57 (6)	
Strain							
Strain G						0.41 (3)	
e0						0.00089 (7)	
Crystal Linear Absorption Coeff. (1/cm)						295.94 (10)	
Crystal Density (g/cm ³)						2.7307 (9)	
Preferred Orientation Spherical Harmonics							
Order						8	
y00						1	
y20						-0.007 (17)	
y40						-0.10 (2)	
y43m						-0.066 (8)	
y60						0.06 (2)	
y63m						0.087 (12)	
y66p						-0.051 (7)	
y80						0.004 (16)	
y83m						0.01 (2)	
y86p						-0.059 (11)	
PV_TCHZ peak type							
U						0.06 (13)	
V						-0.15 (12)	
W						0.06 (3)	
Z						0	
X						0.202 (4)	
Y						0	
Lattice parameters							
a (\AA)						4.9780 (7)	
c (\AA)						17.017 (2)	
Site	Np	x	y	z	Atom	Occ	Beq
Ca	6	0.00000	0.00000	0.00000	Ca+2	1	0.19 (7)
C	6	0.00000	0.00000	0.25000	C	1	1.42 (16)
O	18	0.25670	0.00000	0.25000	O-2	1	0.40 (11)

Structure 2

Phase name	Quartz_Brill 1939
R-Bragg	4.673
Spacegroup	P3121
Scale	0.0000 (2)
Cell Mass	180.253
Cell Volume (\AA^3)	114.4 (13)
Wt% - Rietveld	0.3 (17)
Crystal Linear Absorption Coeff. (1/cm)	135.7 (15)
Crystal Density (g/cm ³)	2.62 (3)
Preferred Orientation Spherical Harmonics	
Order	8
y00	1
y20	0 (30)
y40	6 (30)
y43m	-1 (17)
y60	0 (50)
y63m	0 (60)

y66p					-3 (13)	
y80					-10 (50)	
y83m					0 (30)	
y86p					0 (20)	
PV_TCHZ peak type						
U					0 (30)	
V					1 (30)	
W					1 (5)	
Z					0	
X					0 (2)	
Y					0	
Lattice parameters						
a (Å)					4.90 (2)	
c (Å)					5.49 (4)	
Site	Np	x	y	z	Atom Occ	Beq
Si1	3	0.46500	0.00000	0.33333	Si+4 1	1
O1	6	0.41500	0.27200	0.21300	O-2 1	1

00-158

File 1 : "D:\XRD Haughton group_organized\sample files\RAW files\00-158\Rietveld_158_reground Co.raw"

Range Number : 1

R-Values

Rexp : 5.63 Rwp : 9.06 Rp : 6.37 GOF : 1.61

Rexp` : 6.15 Rwp` : 9.91 Rp` : 7.01 DW : 0.82

Quantitative Analysis - Rietveld

Phase 1 : Dolomite_Althoff 87.1(10) %

Phase 2 : "Calcite_Markgraf and Reeder" 12.9(10) %

Background

One on X 2000 (4000)

Chebyshev polynomial, Coefficient 0 30 (120)

1 -10 (90)

2 2 (40)

3 9 (14)

4 -2 (5)

5 2 (3)

Instrument

Primary radius (mm) 185

Secondary radius (mm) 185

Corrections

Specimen displacement 0.065 (11)

LP Factor 26.4

Absorption (1/cm) 0 (5000)

Structure 1

Phase name Dolomite_Althoff

R-Bragg 1.091

Spacegroup R-3

Scale 0.0035 (3)

Cell Mass 553.202

Cell Volume (Å³) 319.8 (2)

Wt% - Rietveld 87.1 (10)

Double-Voigt Approach						
Cry size Gaussian		34.8 (7)				
k: 1 LVol-IB (nm)		32.7 (7)				
k: 0.89 LVol-FWHM (nm)		31.0 (6)				
Strain						
Strain G		0.43 (3)				
e0		0.00095 (7)				
Crystal Linear Absorption Coeff. (1/cm)		202.48 (14)				
Crystal Density (g/cm ³)		2.8728 (19)				
Preferred Orientation Spherical Harmonics						
Order		8				
y00		1				
y20		0.30 (4)				
y40		0.14 (7)				
y43m		-0.21 (3)				
y43p		-0.2 (3)				
y60		-0.14 (6)				
y63m		-0.08 (4)				
y63p		-0.3 (6)				
y66m		-0.5 (5)				
y66p		0.036 (16)				
y80		-0.35 (9)				
y83m		-0.18 (8)				
y83p		-0.3 (10)				
y86m		-0.47 (19)				
y86p		-0.02 (9)				
PV_TCHZ peak type						
U		-0.54 (10)				
V		0.40 (8)				
W		-0.067 (16)				
Z		0				
X		0.459 (8)				
Y		0				
Lattice parameters						
a (Å)		4.8025 (14)				
c (Å)		16.009 (5)				
Site	Np	x	y	z	Atom Occ	Beq
Ca	3	0.00000	0.00000	0.00000	Ca+2 1	2.7 (7)
Mg	3	0.00000	0.00000	0.50000	Mg+2 1	-0.3 (3)
C	6	0.00000	0.00000	-0.24230	C 1	3.6 (5)
O	18	0.28290	0.03500	-0.24400	O-2 1	1.0 (10)

Structure 2

Phase name	Calcite_Markgraf and
Reeder	
R-Bragg	0.890
Spacegroup	R-3c
Scale	0.000419 (16)
Cell Mass	600.521
Cell Volume (Å ³)	364.9 (2)
Wt% - Rietveld	12.9 (10)
Double-Voigt Approach	
Cry size Gaussian	
k: 1 LVol-IB (nm)	
k: 0.89 LVol-FWHM (nm)	
Strain	

Strain G					0.31 (3)	
e0					0.00068 (7)	
Crystal Linear Absorption Coeff. (1/cm)					296.2 (2)	
Crystal Density (g/cm ³)					2.7328 (18)	
Preferred Orientation Spherical Harmonics						
Order					8	
y00					1	
y20					-0.08 (7)	
y40					-0.04 (8)	
y43m					0.05 (3)	
y60					0.03 (8)	
y63m					0.09 (5)	
y66p					0.02 (3)	
y80					-0.05 (7)	
y83m					-0.03 (9)	
y86p					-0.08 (4)	
PV_TCHZ peak type						
U					-0.54 (10)	
V					0.40 (8)	
W					-0.067 (16)	
Z					0	
X					0.459 (8)	
Y					0	
Lattice parameters						
a (Å)					4.9764 (15)	
c (Å)					17.014 (5)	
Site	Np	x	y	z	Atom Occ	Beq
Ca	6	0.00000	0.00000	0.00000	Ca+2 1	0.3 (3)
C	6	0.00000	0.00000	0.25000	C 1	0.2 (5)
O	18	0.25670	0.00000	0.25000	O-2 1	1.2 (4)

02-061

File 1 : "D:\XRD Haughton group_organized\sample files\RAW files\02-061\Rietveld_02061gr_exp.raw"

Range Number : 1

R-Values

Rexp : 6.87 Rwp : 8.54 Rp : 5.76 GOF : 1.24

Rexp` : 6.74 Rwp` : 8.39 Rp` : 5.69 DW : 1.34

Quantitative Analysis - Rietveld

Phase 1 : "Calcite_Markgraf and Reeder" 91.0 (10) %

Phase 2 : Quartz_Brill 4.0 (4) %

Phase 3 : Microcline_Ribbe 5.0 (10) %

Background

One on X 1000 (4000)

Chebyshev polynomial, Coefficient 0 0 (110)

1 -10 (80)

2 8 (30)

3 -17 (12)

4 3 (5)

5 6 (2)

Instrument

Primary radius (mm) 185

Secondary radius (mm)	185					
Corrections						
Specimen displacement	-0.180 (7)					
LP Factor	26.4					
Absorption (1/cm)	0 (3000)					
Structure 1						
Phase name	Calcite_Markgraf and					
Reeder						
R-Bragg	0.645					
Spacegroup	R-3c					
Scale	0.00174 (3)					
Cell Mass	600.521					
Cell Volume (Å ³)	365.14 (14)					
Wt% - Rietveld	91.0 (10)					
Double-Voigt Approach						
Cry size Gaussian	71 (5)					
k: 1 LVol-IB (nm)	66 (4)					
k: 0.89 LVol-FWHM (nm)	63 (4)					
Strain						
Strain G	0.20 (5)					
e0	0.00044 (12)					
Crystal Linear Absorption Coeff. (1/cm)	295.97 (12)					
Crystal Density (g/cm ³)	2.7310 (11)					
Preferred Orientation Spherical Harmonics						
Order	8					
y00	1					
y20	-0.48 (3)					
y40	-0.17 (4)					
y43m	0.006 (16)					
y60	0.18 (4)					
y63m	0.19 (3)					
y66p	-0.075 (14)					
y80	0.11 (4)					
y83m	0.17 (4)					
y86p	-0.12 (2)					
PV_TCHZ peak type						
U	0.26 (10)					
V	-0.25 (9)					
W	0.06 (2)					
Z	0					
X	0.506 (19)					
Y	0					
Lattice parameters						
a (Å)	4.9771 (9)					
c (Å)	17.021 (3)					
Site	Np	x	y	z	Atom Occ	Beq
Ca	6	0.00000	0.00000	0.00000	Ca+2 1	1.00 (13)
C	6	0.00000	0.00000	0.25000	C 1	1.0 (2)
O	18	0.25670	0.00000	0.25000	O-2 1	1.00 (14)

Structure 2

Phase name	Quartz_Brill
R-Bragg	4.029
Spacegroup	P3121
Scale	0.00057 (5)

Cell Mass 264.509
 Cell Volume (Å³) 112.73 (5)
 Wt% - Rietveld 4.0 (4)
 Crystal Linear Absorption Coeff. (1/cm) 258.82 (12)
 Crystal Density (g/cm³) 3.8962 (18)
 Preferred Orientation Spherical Harmonics
 Order 8
 y00 1
 y20 -1.1 (2)
 y40 -1.4 (2)
 y43m -2.5 (5)
 y60 1.0 (2)
 y63m 2.6 (3)
 y66p -0.55 (11)
 y80 0.71 (19)
 y83m -3.5 (4)
 y86p -1.14 (11)
 PV_TCHZ peak type
 U -0.03 (17)
 V 0.05 (13)
 W -0.02 (2)
 Z 0
 X 0.54 (4)
 Y 0
 Lattice parameters
 a (Å) 4.9110 (10)
 c (Å) 5.3974 (14)

Site	Np	x	y	z	Atom	Occ	Beq
Si1	6	0.46500	0.00000	0.33333	Si+4	1	1
O1	6	0.41500	0.27200	0.21300	O-2	1	1

Structure 3

Phase name Microcline_Ribbe
 R-Bragg 26.844
 Spacegroup C-1
 Scale 0.000018 (4)
 Cell Mass 1549.447
 Cell Volume (Å³) 736.6 (8)
 Wt% - Rietveld 5.0 (10)
 Crystal Linear Absorption Coeff. (1/cm) 263.3 (3)
 Crystal Density (g/cm³) 3.493 (4)
 Preferred Orientation Spherical Harmonics
 Order 8
 y00 1
 y20 -0.6 (6)
 y21m 4.4 (13)
 y21p 0.9 (4)
 y22m 6 (2)
 y22p 0.2 (4)
 y40 -0.6 (11)
 y41m -7.8 (15)
 y41p -2.0 (4)
 y42m -3.1 (12)
 y42p 1.7 (7)
 y43m -8 (4)
 y43p 4.3 (6)

y44m							-10 (5)
y44p							-2.2 (7)
y60							-3.0 (9)
y61m							4.1 (18)
y61p							0.4 (11)
y62m							3 (2)
y62p							2.3 (11)
y63m							-6.1 (19)
y63p							1.5 (6)
y64m							3.8 (19)
y64p							1.2 (4)
y65m							-6 (4)
y65p							1.9 (5)
y66m							-1 (3)
y66p							-0.1 (6)
y80							4.3 (12)
y81m							19 (5)
y81p							-7.1 (17)
y82m							1.6 (15)
y82p							-4.6 (8)
y83m							2.5 (13)
y83p							2.4 (12)
y84m							-8.5 (17)
y84p							0.0 (5)
y85m							0.8 (11)
y85p							4.9 (8)
y86m							6.8 (19)
y86p							-4.1 (9)
y87m							-7 (2)
y87p							-4.0 (8)
y88m							-1.9 (14)
y88p							0.0 (5)
PV_TCHZ peak type							
U							-1 (2)
V							-1.0 (14)
W							0.3 (2)
Z							0
X							2.00 (17)
Y							0
Lattice parameters							
a (Å)							8.671 (4)
b (Å)							13.080 (7)
c (Å)							7.286 (4)
alpha (°)							92.15 (5)
beta (°)							116.88 (5)
gamma (°)							89.02 (2)
Site	Np	x	y	z	Atom	Occ	Beq
K	4	0.28670	0.99850	0.14060	K+1	1	1
Si1o	4	0.00950	0.18440	0.22250	Si+4	1	1
Al1o	4	0.00950	0.18440	0.22250	Al+3	1	1
Si1m	4	0.00910	0.81680	0.22490	Si+4	1	1
Al1m	4	0.00910	0.81680	0.22490	Al+3	1	1
Si2o	4	0.71050	0.11840	0.34130	Si+4	1	1
Al2o	4	0.71050	0.11840	0.34130	Al+3	1	1
Si2m	4	0.70950	0.88260	0.34330	Si+4	1	1
Al2m	4	0.70950	0.88260	0.34330	Al+3	1	1

Preferred Orientation Spherical Harmonics

Order	8
y00	1
y20	0.63 (3)
y40	0.40 (5)
y43m	-0.49 (3)
y43p	0.95 (10)
y60	-0.37 (4)
y63m	-0.26 (3)
y63p	-0.6 (2)
y66m	0.5 (3)
y66p	-0.07 (2)
y80	-0.88 (6)
y83m	-0.64 (5)
y83p	-0.2 (4)
y86m	0.2 (3)
y86p	-0.09 (5)
PV_TCHZ peak type	
U	0.4 (3)
V	-0.3 (3)
W	0.03 (7)
Z	0
X	0.479 (11)
Y	0
Lattice parameters	
a (Å)	4.8019 (17)
c (Å)	16.003 (6)

Site	Np	x	y	z	Atom	Occ	Beq
CaA	3	0.00000	0.00000	0.00000	Ca+2	1	4.8 (7)
MgB	3	0.00000	0.00000	0.50000	Mg+2	1	-0.3 (3)
C	6	0.00000	0.00000	0.24310	C	1	0.1 (4)
O	18	0.24820	-0.03570	0.24400	O-2	1	0.8 (7)

Structure 2

Phase name	Calcite_Markgraf and
Reeder	
R-Bragg	1.438
Spacegroup	R-3c
Scale	0.000060 (13)
Cell Mass	600.521
Cell Volume (Å ³)	364.7 (4)
Wt% - Rietveld	1.7 (4)
Crystal Linear Absorption Coeff. (1/cm)	296.3 (3)
Crystal Density (g/cm ³)	2.734 (3)
Preferred Orientation Spherical Harmonics	
Order	8
y00	1
y20	-4.7 (19)
y40	-10 (3)
y43m	-0.1 (3)
y60	1.8 (19)
y63m	5 (2)
y66p	-0.8 (4)
y80	3.7 (18)
y83m	6 (3)
y86p	-1.3 (8)

PV_TCHZ peak type						
	U				1.1 (6)	
	V				-0.1 (2)	
	W				-0.06 (5)	
	Z				0	
	X				1.04 (10)	
	Y				0	
Lattice parameters						
	a (Å)				4.980 (3)	
	c (Å)				16.983 (9)	
Site	Np	x	y	z	Atom Occ	Beq
Ca	6	0.00000	0.00000	0.00000	Ca+2 1	1
C	6	0.00000	0.00000	0.25000	C 1	1
O	18	0.25670	0.00000	0.25000	O-2 1	1

Structure 3

Phase name	Quartz_Brill					
R-Bragg	100.000					
Spacegroup	P3121					
Scale	0.0013 (9)					
Cell Mass	180.253					
Cell Volume (Å ³)	120.1 (4)					
Wt% - Rietveld	4 (3)					
Crystal Linear Absorption Coeff. (1/cm)	129.3 (5)					
Crystal Density (g/cm ³)	2.492 (9)					
Preferred Orientation Spherical Harmonics						
Order	8					
y00	1					
y20	4.8 (11)					
y40	20 (8)					
y43m	1 (2)					
y60	12 (3)					
y63m	-0.6 (16)					
y66p	-0.2 (9)					
y80	3 (3)					
y83m	7 (3)					
y86p	-3 (3)					
PV_TCHZ peak type						
	U				-1 (14)	
	V				-1 (11)	
	W				-1 (2)	
	Z				0	
	X				2.0 (7)	
	Y				0	
Lattice parameters						
	a (Å)				5.053 (6)	
	c (Å)				5.433 (15)	
Site	Np	x	y	z	Atom Occ	Beq
Si1	3	0.46500	0.00000	0.33333	Si+4 1	1
O1	6	0.41500	0.27200	0.21300	O-2 1	1

y83m						-0.24 (4)
y83p						-0.0 (5)
y86m						0.0 (2)
y86p						0.02 (4)
PV_TCHZ peak type						
U						0.01 (7)
V						-0.02 (6)
W						0.009 (14)
Z						0
X						0.428 (9)
Y						0
Lattice parameters						
a (Å)						4.8055 (9)
c (Å)						16.015 (3)
<hr/>						
Site	Np	x	y	z	Atom Occ	Beq
CaA	3	0.00000	0.00000	0.00000	Ca+2 1	2.2 (4)
MgB	3	0.00000	0.00000	0.50000	Mg+2 1	0.2 (2)
C	6	0.00000	0.00000	0.24310	C 1	2.5 (3)
O	18	0.24820	-0.03570	0.24400	O-2 1	0.6 (3)

Structure 2

Phase name	Calcite_Markgraf and
Reeder	
R-Bragg	0.816
Spacegroup	R-3c
Scale	0.000577 (16)
Cell Mass	600.521
Cell Volume (Å ³)	364.73 (16)
Wt% - Rietveld	18.3 (7)
Double-Voigt Approach	
Cry size Gaussian	72 (7)
k: 1 LVol-IB (nm)	68 (7)
k: 0.89 LVol-FWHM (nm)	64 (7)
Strain	
Strain G	0.16 (8)
e0	0.00035 (17)
Crystal Linear Absorption Coeff. (1/cm)	296.31 (13)
Crystal Density (g/cm ³)	2.7341 (12)
Preferred Orientation Spherical Harmonics	
Order	8
y00	1
y20	-0.10 (4)
y40	-0.34 (5)
y43m	-0.07 (2)
y60	0.04 (6)
y63m	0.22 (3)
y66p	-0.04 (2)
y80	0.00 (4)
y83m	0.12 (6)
y86p	-0.13 (3)
PV_TCHZ peak type	
U	0.01 (7)
V	-0.02 (6)
W	0.009 (14)
Z	0
X	0.428 (9)

y20	-2.6 (6)
y40	-3.8 (6)
y43m	0.06 (10)
y60	-2.0 (5)
y63m	1.6 (3)
y66p	0.40 (13)
y80	-1.4 (4)
y83m	1.7 (6)
y86p	-1.1 (2)
PV_TCHZ peak type	
U	0.2 (4)
V	-0.2 (4)
W	0.06 (8)
Z	0
X	0.42 (3)
Y	0
Lattice parameters	
a (Å)	4.9751 (16)
c (Å)	16.999 (5)

Site	Np	x	y	z	Atom	Occ	Beq
Ca	6	0.00000	0.00000	0.00000	Ca+2	1	1
C	6	0.00000	0.00000	0.25000	C	1	1
O	18	0.25700	0.00000	0.25000	O-2	1	1

Structure 2

Phase name	Dolomite_Ross and Reeder
1992	
R-Bragg	1.732
Spacegroup	R-3
Scale	0.00304 (3)
Cell Mass	553.202
Cell Volume (Å ³)	319.2 (2)
Wt% - Rietveld	95.8 (3)
Double-Voigt Approach	
Cry size Gaussian	52 (9)
k: 1 LVol-IB (nm)	49 (9)
k: 0.89 LVol-FWHM (nm)	46 (8)
Strain	
Strain G	0.60 (6)
e0	0.00131 (12)
Crystal Linear Absorption Coeff. (1/cm)	202.86 (14)
Crystal Density (g/cm ³)	2.8782 (19)
Preferred Orientation Spherical Harmonics	
Order	8
y00	1
y20	0.32 (3)
y40	0.10 (2)
y43m	-0.034 (17)
y43p	0.32 (5)
y60	0.06 (4)
y63m	-0.039 (14)
y63p	-0.48 (11)
y66m	-0.26 (6)
y66p	-0.027 (13)
y80	-0.32 (3)
y83m	0.01 (4)

y83p						-0.34 (10)
y86m						-0.71 (9)
y86p						-0.10 (2)
PV_TCHZ	peak type					
U						0.13 (13)
V						-0.15 (10)
W						0.04 (3)
Z						0
X						0.373 (13)
Y						0
Lattice parameters						
a (Å)						4.8005 (14)
c (Å)						15.992 (5)

Site	Np	x	y	z	Atom	Occ	Beq
CaA	3	0.00000	0.00000	0.00000	Ca+2	1	0.7098
MgB	3	0.00000	0.00000	0.50000	Mg+2	1	0.4998
C	6	0.00000	0.00000	0.24310	C	1	0.7304
O	18	0.24820	-0.03570	0.24400	O-2	1	0.8401

02-139

File 1 : "D:\XRD - May 2019\pXRD sandpaper\RAW files\HAU_02_139_sp.raw"

Range Number : 1

R-Values

Rexp : 7.38 Rwp : 9.14 Rp : 6.29 GOF : 1.24

Rexp` : 7.55 Rwp` : 9.35 Rp` : 6.44 DW : 1.36

Quantitative Analysis - Rietveld

Phase 1 : "Calcite_Maslen 1995" 99.5 (7) %

Phase 2 : Quartz_Levian 0.5 (7) %

Background

One on X 1000 (2000)

Chebyshev polynomial, Coefficient 0 7 (50)

1 -10 (40)

2 8 (16)

3 -6 (6)

4 3 (2)

5 1.3 (9)

Instrument

Primary radius (mm) 185

Secondary radius (mm) 185

Corrections

Specimen displacement 0.068 (7)

LP Factor 26.4

Absorption (1/cm) 0 (3000)

Structure 1

Phase name Calcite_Maslen 1995

R-Bragg 0.958

Spacegroup R-3c

Scale 0.001373 (14)

Cell Mass 600.521

Cell Volume (Å³) 365.65 (14)

Wt% - Rietveld 99.5 (7)

Double-Voigt Approach						
Cry size Gaussian						
k: 1 LVol-IB (nm)						
k: 0.89 LVol-FWHM (nm)						
Strain						
Strain G						
e0						
Crystal Linear Absorption Coeff. (1/cm)						
Crystal Density (g/cm ³)						
Preferred Orientation Spherical Harmonics						
Order						
y00						
y20						
y40						
y43m						
y60						
y63m						
y66p						
y80						
y83m						
y86p						
PV_TCHZ peak type						
U						
V						
W						
Z						
X						
Y						
Lattice parameters						
a (Å)						
c (Å)						
<hr/>						
Site	Np	x	y	z	Atom Occ	Beq
Ca	6	0.00000	0.00000	0.00000	Ca+2 1	0.14 (7)
C	6	0.00000	0.00000	0.25000	C 1	1.61 (17)
O	18	0.25700	0.00000	0.25000	O-2 1	0.49 (11)

Structure 2

Phase name	Quartz_Levian
R-Bragg	1.951
Spacegroup	P321
Scale	0.00005 (7)
Cell Mass	264.509
Cell Volume (Å ³)	112.67 (18)
Wt% - Rietveld	0.5 (7)
Crystal Linear Absorption Coeff. (1/cm)	259.0 (4)
Crystal Density (g/cm ³)	3.898 (6)
Preferred Orientation Spherical Harmonics	
Order	
y00	
y20	
y40	
y43m	
y60	
y63m	
y66p	
y80	

	y83m					-3 (6)
	y86p					-0 (2)
	PV_TCHZ	peak type				
	U					-0.0 (8)
	V					0.1 (6)
	W					-0.03 (12)
	Z					0
	X					0.41 (11)
	Y					0
	Lattice parameters					
	a (Å)					4.908 (3)
	c (Å)					5.400 (5)
Site	Np	x	y	z	Atom Occ	Beq
Si	6	0.46970	0.00000	0.33333	Si+4 1	1
O	6	0.41350	0.26690	0.11910	O-2 1	1

05-005

File 1 : "D:\XRD - May 2019\pXRD sandpaper\RAW files\HAU_05_005_sp.raw"

Range Number : 1

R-Values

Rexp : 6.50 Rwp : 10.09 Rp : 6.81 GOF : 1.55

Rexp` : 7.03 Rwp` : 10.92 Rp` : 7.47 DW : 0.93

Quantitative Analysis - Rietveld

Phase 1 : "Dolomite_Ross Reeder 1992" 98.1 (18) %
 Phase 2 : "Quartz_Brill 1939" 1.0 (17) %
 Phase 3 : "Calcite_Markgraff and Reeder 1985" 1.0 (4) %

Background

One on X 0 (3000)
 Chebychev polynomial, Coefficient
 0 30 (80)
 1 -20 (60)
 2 20 (20)
 3 -2 (10)
 4 4 (3)
 5 2.4 (16)

Instrument

Primary radius (mm) 185
 Secondary radius (mm) 185

Corrections

Specimen displacement 0.0274 (18)
 LP Factor 26.4
 Absorption (1/cm) 18.2 (3)

Structure 1

Phase name Dolomite_Ross Reeder 1992
 R-Bragg 1.305
 Spacegroup R-3
 Scale 0.00251 (8)
 Cell Mass 553.202
 Cell Volume (Å³) 319.026 (17)
 Wt% - Rietveld 98.1 (18)
 Double-Voigt|Approach
 Cry size Gaussian 71 (4)

k:	1	LVol-IB (nm)				67(4)	
k:	0.89	LVol-FWHM (nm)				63(4)	
Strain							
		Strain G				0.16(3)	
		e0				0.00035(8)	
		Crystal Linear Absorption Coeff. (1/cm)				202.943(11)	
		Crystal Density (g/cm ³)				2.87943(15)	
Preferred Orientation Spherical Harmonics							
		Order				8	
		y00				1	
		y20				0.26(2)	
		y40				-0.05(2)	
		y43m				0.18(2)	
		y43p				0.24(6)	
		y60				0.26(5)	
		y63m				-0.116(19)	
		y63p				-0.43(10)	
		y66m				0.37(5)	
		y66p				-0.025(15)	
		y80				-0.23(4)	
		y83m				0.26(5)	
		y83p				-0.1(3)	
		y86m				-0.4(3)	
		y86p				-0.24(4)	
PV_TCHZ peak type							
		U				0.123(17)	
		V				-0.12(2)	
		W				0.030(7)	
		Z				0	
		X				0.145(18)	
		Y				0	
Lattice parameters							
		a (Å)				4.80055(11)	
		c (Å)				15.9851(5)	
<u>Site</u>	<u>Np</u>	<u>x</u>	<u>y</u>	<u>z</u>	<u>Atom</u>	<u>Occ</u>	<u>Beq</u>
CaA	3	0.00000	0.00000	0.00000	Ca+2	1	0.0(3)
MgB	3	0.00000	0.00000	0.50000	Mg+2	1	0.58(14)
C	6	0.00000	0.00000	0.24310	C	1	3.5(3)
O	18	0.24820	-0.03570	0.24400	O-2	1	0.3(5)

Structure 2

Phase name	Quartz_Brill 1939
R-Bragg	3.492
Spacegroup	P3121
Scale	0.0002(4)
Cell Mass	180.253
Cell Volume (Å ³)	112.3(4)
Wt% - Rietveld	1.0(17)
Crystal Linear Absorption Coeff. (1/cm)	138.2(5)
Crystal Density (g/cm ³)	2.665(11)
Preferred Orientation Spherical Harmonics	
Order	8
y00	1
y20	2(4)
y40	1(9)
y43m	-1(4)

y60						-3 (18)
y63m						-10 (20)
y66p						-0.2 (12)
y80						-1 (8)
y83m						-3 (10)
y86p						-0.6 (12)
PV_TCHZ peak type						
U						2 (6)
V						1 (4)
W						-0.3 (7)
Z						0
X						0.56 (15)
Y						0
Lattice parameters						
a (Å)						4.896 (7)
c (Å)						5.412 (14)
<hr/>						
Site	Np	x	y	z	Atom Occ	Beq
Si1	3	0.46500	0.00000	0.33333	Si+4 1	1 (50)
O1	6	0.41500	0.27200	0.21300	O-2 1	1 (90)

Structure 3

Phase name	Calcite_Markgraff and					
Reeder 1985						
R-Bragg	10.269					
Spacegroup	R-3c					
Scale	0.000020 (9)					
Cell Mass	600.521					
Cell Volume (Å ³)	365.5 (6)					
Wt% - Rietveld	1.0 (4)					
Crystal Linear Absorption Coeff. (1/cm)	295.7 (4)					
Crystal Density (g/cm ³)	2.729 (4)					
Preferred Orientation Spherical Harmonics						
Order	8					
y00	1					
y20	-3 (3)					
y40	-5 (4)					
y43m	-1.6 (9)					
y60	-9 (4)					
y63m	-0.2 (17)					
y66p	0.1 (11)					
y80	-6.0 (13)					
y83m	-1 (2)					
y86p	0.7 (8)					
PV_TCHZ peak type						
U	1 (3)					
V	0 (2)					
W	-0.1 (5)					
Z	0					
X	1.1 (3)					
Y	0					
Lattice parameters						
a (Å)	4.987 (4)					
c (Å)	16.967 (9)					
<hr/>						
Site	Np	x	y	z	Atom Occ	Beq
Ca	6	0.00000	0.00000	0.00000	Ca+2 1	1

C	6	0.00000	0.00000	0.25000	C	1	1
O	18	0.25670	0.00000	0.25000	O-2	1	1

05-007

File 1 : "D:\XRD - June 2018\Newman_HMP_05_007_BP.raw"

Range Number : 1

R-Values

Rexp	: 4.89	Rwp	: 9.31	Rp	: 6.57	GOF	: 1.91
Rexp`	: 4.92	Rwp`	: 9.36	Rp`	: 6.61	DW	: 0.70

Quantitative Analysis - Rietveld

Phase 1	: "Dolomite_Althoff 1977"	97.7(18) %
Phase 2	: Quartz_Wei	0.9(17) %
Phase 3	: Calcite_Ondrus	0.6(5) %
Phase 4	: Microcline_Ribbe	0.9(4) %

Background

One on X		2000(5000)
Chebyshev polynomial, Coefficient	0	4(140)
	1	-10(110)
	2	4(40)
	3	-3(16)
	4	5(6)
	5	2(3)

Instrument

Primary radius (mm)	185
Secondary radius (mm)	185

Corrections

Specimen displacement	0.0496(17)
LP Factor	26.4
Absorption (1/cm)	31.8(10)

Structure 1

Phase name	Dolomite_Althoff 1977
R-Bragg	1.246
Spacegroup	R-3
Scale	0.00393(10)
Cell Mass	553.202
Cell Volume (Å ³)	319.377(18)
Wt% - Rietveld	97.7(18)
Double-Voigt Approach	
Cry size Gaussian	109(8)
k: 1 LVol-IB (nm)	102(8)
k: 0.89 LVol-FWHM (nm)	97(7)
Strain	
Strain G	0.19(4)
e0	0.00042(8)
Crystal Linear Absorption Coeff. (1/cm)	202.724(12)
Crystal Density (g/cm ³)	2.87627(16)
Preferred Orientation Spherical Harmonics	
Order	8
y00	1
y20	1.06(3)
y40	-0.35(3)
y43m	0.61(3)

y43p	0.42 (9)
y60	-0.34 (6)
y63m	-0.58 (2)
y63p	-0.93 (16)
y66m	0.57 (7)
y66p	-0.045 (17)
y80	-0.23 (4)
y83m	-0.04 (7)
y83p	-0.3 (3)
y86m	0.9 (3)
y86p	-0.13 (3)
PV_TCHZ peak type	
U	0.09 (3)
V	-0.05 (2)
W	0.007 (4)
Z	0
X	0.173 (12)
Y	0
Lattice parameters	
a (Å)	4.80230 (12)
c (Å)	15.9909 (5)

Site	Np	x	y	z	Atom Occ	Beq
Ca	3	0.00000	0.00000	0.00000	Ca+2 1	1.4 (3)
Mg	3	0.00000	0.00000	0.50000	Mg+2 1	1.34 (17)
C	6	0.00000	0.00000	-0.24230	C 1	0.8 (3)
O	18	0.28290	0.03500	-0.24400	O-2 1	0.8 (4)

Structure 2

Phase name	Quartz_Wei
R-Bragg	100.000
Spacegroup	P3121
Scale	0.0003 (6)
Cell Mass	180.253
Cell Volume (Å ³)	112.46 (15)
Wt% - Rietveld	0.9 (17)
Crystal Linear Absorption Coeff. (1/cm)	138.06 (18)
Crystal Density (g/cm ³)	2.662 (4)
Preferred Orientation Spherical Harmonics	
Order	8
y00	1
y20	1 (7)
y40	5 (11)
y43m	-3 (7)
y60	14 (15)
y63m	0 (20)
y66p	-2 (3)
y80	9 (11)
y83m	-10 (20)
y86p	-1 (2)
PV_TCHZ peak type	
U	2 (6)
V	1 (4)
W	-0.2 (5)
Z	0
X	0.6 (3)
Y	0

Lattice parameters

a (Å)	4.907(2)
c (Å)	5.394(5)

Site	Np	x	y	z	Atom Occ	Beq
Si1	3	0.46500	0.00000	0.33333	Si+4 1	1
O1	6	0.41700	0.27800	0.22200	O-2 1	1

Structure 3

Phase name	Calcite_Ondrus
R-Bragg	100.000
Spacegroup	R-3c
Scale	0.000019(17)
Cell Mass	600.521
Cell Volume (Å ³)	363.2(4)
Wt% - Rietveld	0.6(5)
Crystal Linear Absorption Coeff. (1/cm)	297.5(3)
Crystal Density (g/cm ³)	2.745(3)
Preferred Orientation Spherical Harmonics	
Order	8
y00	1
y20	-8(9)
y40	-20(20)
y43m	-5(5)
y60	-60(50)
y63m	-12(8)
y66p	7(6)
y80	-50(40)
y83m	-20(15)
y86p	9(6)
PV_TCHZ peak type	
U	-0.5(18)
V	-0(2)
W	0.7(5)
Z	0
X	0.49(10)
Y	0
Lattice parameters	
a (Å)	4.978(3)
c (Å)	16.926(2)

Site	Np	x	y	z	Atom Occ	Beq
Ca	6	0.00000	0.00000	0.00000	Ca+2 1	2.72
C	6	0.00000	0.00000	0.25000	C 1	2.7
O	18	0.25960	0.00000	0.25000	O-2 1	3.57

Structure 4

Phase name	Microcline_Ribbe
R-Bragg	71.121
Spacegroup	C-1
Scale	0.000006(3)
Cell Mass	1549.447
Cell Volume (Å ³)	705.0(9)
Wt% - Rietveld	0.9(4)
Crystal Linear Absorption Coeff. (1/cm)	275.1(4)
Crystal Density (g/cm ³)	3.649(5)
Preferred Orientation Spherical Harmonics	

Order	8
y00	1
y20	2.0 (13)
y21m	10 (4)
y21p	-1.2 (11)
y22m	-0.0 (8)
y22p	1.9 (14)
y40	2.3 (16)
y41m	-3 (3)
y41p	0.5 (8)
y42m	-1.9 (16)
y42p	0.6 (16)
y43m	-5 (2)
y43p	2.7 (12)
y44m	1.0 (15)
y44p	-0.9 (15)
y60	-3.9 (19)
y61m	-3 (3)
y61p	1.7 (18)
y62m	-0.9 (16)
y62p	-6 (3)
y63m	-1.7 (19)
y63p	-3.6 (17)
y64m	-1 (2)
y64p	0.4 (11)
y65m	8 (3)
y65p	0.3 (6)
y66m	1.9 (15)
y66p	-0.2 (8)
y80	-1.0 (13)
y81m	-14 (7)
y81p	0 (2)
y82m	-2 (3)
y82p	-7 (3)
y83m	0 (2)
y83p	1 (2)
y84m	5 (3)
y84p	1.9 (10)
y85m	-4 (2)
y85p	1.1 (10)
y86m	-3 (2)
y86p	1.1 (13)
y87m	-5 (2)
y87p	0.6 (9)
y88m	1.8 (17)
y88p	-0.8 (10)
PV_TCHZ peak type	
U	-0.8 (6)
V	0.1 (3)
W	-0.04 (6)
Z	0
X	0.4 (2)
Y	0
Lattice parameters	
a (Å)	8.586 (9)
b (Å)	12.752 (6)
c (Å)	7.164 (4)

alpha (°) 89.84(6)
 beta (°) 115.98(4)
 gamma (°) 89.19(6)

Site	Np	x	y	z	Atom	Occ	Beq
K	4	0.28670	0.99850	0.14060	K+1	1	1
Si1o	4	0.00950	0.18440	0.22250	Si+4	1	1
Al1o	4	0.00950	0.18440	0.22250	Al+3	1	1
Si1m	4	0.00910	0.81680	0.22490	Si+4	1	1
Al1m	4	0.00910	0.81680	0.22490	Al+3	1	1
Si2o	4	0.71050	0.11840	0.34130	Si+4	1	1
Al2o	4	0.71050	0.11840	0.34130	Al+3	1	1
Si2m	4	0.70950	0.88260	0.34330	Si+4	1	1
Al2m	4	0.70950	0.88260	0.34330	Al+3	1	1
Oa1	4	0.00050	0.14400	0.99770	O-2	1	1
Oa2	4	0.63820	0.00110	0.28090	O-2	1	1
Obo	4	0.82510	0.14720	0.22280	O-2	1	1
Obm	4	0.82780	0.85340	0.22740	O-2	1	1
Oco	4	0.03670	0.31160	0.25800	O-2	1	1
Ocm	4	0.03780	0.69030	0.26020	O-2	1	1
Odo	4	0.18150	0.12400	0.40750	O-2	1	1
Odm	4	0.17900	0.87490	0.40850	O-2	1	1

05-010sp

File 1 : "D:\XRD - Nov 2019\HMP_05_010.raw"

Range Number : 1

R-Values

Rexp : 7.15 Rwp : 10.53 Rp : 6.87 GOF : 1.47
 Rexp` : 5.46 Rwp` : 8.04 Rp` : 5.52 DW : 1.00

Quantitative Analysis - Rietveld

Phase 1 : "Dolomite_Ross Reeder 1992" 99.7(4) %
 Phase 2 : "Quartz_Brill 1939" 0.1(4) %
 Phase 3 : "Calcite_Maslen 1995" 0.20(13) %

Background

One on X 3000(2000)
 Chebychev polynomial, Coefficient 0 -50(60)
 1 40(50)
 2 -12(18)
 3 2(7)
 4 -0(2)
 5 0.8(10)

Instrument

Primary radius (mm) 185
 Secondary radius (mm) 185

Corrections

Specimen displacement 0.094(2)
 LP Factor 26.4
 Absorption (1/cm) 17.1(3)

Structure 1

Phase name Dolomite_Ross Reeder 1992
 R-Bragg 1.165
 Spacegroup R-3

Scale						0.00195 (6)
Cell Mass						553.202
Cell Volume (Å ³)						319.281 (18)
Wt% - Rietveld						99.7 (4)
Double-Voigt Approach						
Cry size Gaussian						81 (7)
k: 1 LVol-IB (nm)						76 (6)
k: 0.89 LVol-FWHM (nm)						72 (6)
Strain						
Strain G						0.20 (3)
e0						0.00045 (7)
Crystal Linear Absorption Coeff. (1/cm)						202.785 (12)
Crystal Density (g/cm ³)						2.87714 (16)
Preferred Orientation Spherical Harmonics						
Order						8
y00						1
y20						0.71 (2)
y40						-0.02 (2)
y43m						0.19 (2)
y43p						0.07 (12)
y60						-0.19 (5)
y63m						-0.19 (2)
y63p						-0.18 (19)
y66m						-0.05 (11)
y66p						-0.049 (16)
y80						-0.27 (4)
y83m						-0.12 (5)
y83p						0.1 (5)
y86m						-0.2 (3)
y86p						-0.03 (3)
PV_TCHZ peak type						
U						0.14 (3)
V						-0.16 (2)
W						0.042 (6)
Z						0
X						0.158 (6)
Y						0
Lattice parameters						
a (Å)						4.80145 (11)
c (Å)						15.9918 (5)
Site	Np	x	y	z	Atom Occ	Beq
CaA	3	0.00000	0.00000	0.00000	Ca+2 1	0.4 (3)
MgB	3	0.00000	0.00000	0.50000	Mg+2 1	-0.27 (14)
C	6	0.00000	0.00000	0.24310	C 1	1.0 (3)
O	18	0.24820	-0.03570	0.24400	O-2 1	0.1 (5)

Structure 2

Phase name	Quartz_Brill 1939
R-Bragg	3.895
Spacegroup	P3121
Scale	0.00001 (6)
Cell Mass	180.253
Cell Volume (Å ³)	112.8 (2)
Wt% - Rietveld	0.1 (4)
Crystal Linear Absorption Coeff. (1/cm)	137.6 (3)
Crystal Density (g/cm ³)	2.653 (5)

Preferred Orientation Spherical Harmonics

Order	8
y00	1
y20	5 (20)
y40	0 (70)
y43m	0 (30)
y60	-20 (150)
y63m	0 (50)
y66p	-1 (8)
y80	4 (30)
y83m	0 (40)
y86p	-1 (10)
PV_TCHZ peak type	
U	0.14 (3)
V	-0.16 (2)
W	0.042 (6)
Z	0
X	0.158 (6)
Y	0
Lattice parameters	
a (Å)	4.914 (4)
c (Å)	5.394 (6)

Site	Np	x	y	z	Atom	Occ	Beq
Si1	3	0.46500	0.00000	0.33333	Si+4	1	1
O1	6	0.41500	0.27200	0.21300	O-2	1	1

Structure 3

Phase name	Calcite_Maslen 1995
R-Bragg	10.749
Spacegroup	R-3c
Scale	0.000003 (2)
Cell Mass	600.521
Cell Volume (Å ³)	363.6 (2)
Wt% - Rietveld	0.20 (13)
Crystal Linear Absorption Coeff. (1/cm)	297.22 (17)
Crystal Density (g/cm ³)	2.7425 (16)
Preferred Orientation Spherical Harmonics	
Order	8
y00	1
y20	-6 (7)
y40	-13 (11)
y43m	-2.6 (19)
y60	-17 (11)
y63m	1 (3)
y66p	-1 (2)
y80	-8 (3)
y83m	-0 (4)
y86p	-0.1 (16)
PV_TCHZ peak type	
U	0.14 (3)
V	-0.16 (2)
W	0.042 (6)
Z	0
X	0.158 (6)
Y	0
Lattice parameters	

a (Å) 4.9791 (14)
c (Å) 16.936 (3)

Site	Np	x	y	z	Atom	Occ	Beq
Ca	6	0.00000	0.00000	0.00000	Ca+2	1	1
C	6	0.00000	0.00000	0.25000	C	1	1
O	18	0.25700	0.00000	0.25000	O-2	1	1

05-023

File 1 : "D:\XRD Haughton group_organized\sample files\RAW files\05-023
V\reground Co 05-023\Rietveld_5023.raw"

Range Number : 1

R-Values

Rexp : 6.63 Rwp : 9.14 Rp : 6.41 GOF : 1.38
Rexp` : 7.03 Rwp` : 9.70 Rp` : 6.83 DW : 1.08

Quantitative Analysis - Rietveld

Phase 1 : "Calcite_Markgraf and Reeder" 81(2) %
Phase 2 : "Dolomite_Ross and Reeder" 13.6(18) %
Phase 3 : Quartz_Levian 5.0(14) %

Background

One on X 2000(3000)
Chebychev polynomial, Coefficient 0 20(80)
1 -10(60)
2 10(20)
3 -6(9)
4 4(3)
5 2.1(14)

Instrument

Primary radius (mm) 185
Secondary radius (mm) 185

Corrections

Specimen displacement 0.060(6)
LP Factor 26.4
Absorption (1/cm) 0(2000)

Structure 1

Phase name Calcite_Markgraf and
Reeder
R-Bragg 1.094
Spacegroup R-3c
Scale 0.001291(14)
Cell Mass 600.521
Cell Volume (Å³) 365.52(13)
Wt% - Rietveld 81(2)
Double-Voigt|Approach
Cry size Gaussian 80(6)
k: 1 LVol-IB (nm) 75(6)
k: 0.89 LVol-FWHM (nm) 71(6)
Strain
Strain G 0.17(7)
e0 0.00036(15)
Crystal Linear Absorption Coeff. (1/cm) 295.66(10)
Crystal Density (g/cm³) 2.7281(10)

Preferred Orientation Spherical Harmonics

Order	8
y00	1
y20	0.089 (17)
y40	-0.06 (2)
y43m	-0.045 (9)
y60	0.02 (2)
y63m	0.100 (13)
y66p	-0.018 (8)
y80	-0.038 (17)
y83m	-0.05 (2)
y86p	-0.049 (11)
PV_TCHZ peak type	
U	0.01 (8)
V	-0.02 (7)
W	0.006 (14)
Z	0
X	0.358 (9)
Y	0
Lattice parameters	
a (Å)	4.9791 (8)
c (Å)	17.025 (3)

Site	Np	x	y	z	Atom	Occ	Beq
Ca	6	0.00000	0.00000	0.00000	Ca+2	1	-0.74 (8)
C	6	0.00000	0.00000	0.25000	C	1	0.30 (18)
O	18	0.25670	0.00000	0.25000	O-2	1	-0.54 (11)

Structure 2

Phase name	Dolomite_Ross and Reeder
R-Bragg	1.029
Spacegroup	R-3
Scale	0.00027 (4)
Cell Mass	553.202
Cell Volume (Å ³)	320.98 (13)
Wt% - Rietveld	13.6 (18)
Double-Voigt Approach	
Cry size Gaussian	70 (7)
k: 1 LVol-IB (nm)	66 (6)
k: 0.89 LVol-FWHM (nm)	62 (6)
Strain	
Strain G	0.40 (4)
e0	0.00087 (9)
Crystal Linear Absorption Coeff. (1/cm)	201.71 (8)
Crystal Density (g/cm ³)	2.8619 (11)
Preferred Orientation Spherical Harmonics	
Order	8
y00	1
y20	-0.19 (16)
y40	-0.24 (12)
y43m	0.06 (16)
y43p	0.8 (9)
y60	0.3 (3)
y63m	0.08 (9)
y63p	-0.6 (15)
y66m	1.6 (15)
y66p	-0.04 (11)

y80	0.2 (3)
y83m	0.2 (3)
y83p	-2 (4)
y86m	-1 (3)
y86p	-0.17 (16)
PV_TCHZ peak type	
U	0.01 (8)
V	-0.02 (7)
W	0.006 (14)
Z	0
X	0.358 (9)
Y	0
Lattice parameters	
a (Å)	4.8075 (8)
c (Å)	16.036 (3)

Site	Np	x	y	z	Atom	Occ	Beq
CaA	3	0.00000	0.00000	0.00000	Ca+2	1	0.8 (11)
MgB	3	0.00000	0.00000	0.50000	Mg+2	1	-0.5 (11)
C	6	0.00000	0.00000	0.24310	C	1	4 (2)
O	18	0.24820	-0.03570	0.24400	O-2	1	-0.3 (14)

Structure 3

Phase name	Quartz_Levian
R-Bragg	1.554
Spacegroup	P3221
Scale	0.00058 (17)
Cell Mass	264.509
Cell Volume (Å ³)	112.60 (7)
Wt% - Rietveld	5.0 (14)
Crystal Linear Absorption Coeff. (1/cm)	259.11 (16)
Crystal Density (g/cm ³)	3.901 (2)
Preferred Orientation Spherical Harmonics	
Order	8
y00	1
y20	0.7 (4)
y40	-0.1 (5)
y43m	1.8 (6)
y60	2.4 (4)
y63m	-0.8 (4)
y66p	-0.74 (19)
y80	1.3 (6)
y83m	0.3 (5)
y86p	-1.0 (2)
PV_TCHZ peak type	
U	-0.2 (5)
V	0.2 (4)
W	-0.04 (7)
Z	0
X	0.51 (5)
Y	0
Lattice parameters	
a (Å)	4.9066 (13)
c (Å)	5.4007 (18)

Site	Np	x	y	z	Atom	Occ	Beq
Si	6	0.46970	0.00000	0.33333	Si+4	1	1
O	6	0.41350	0.26690	0.11910	O-2	1	1

06-093

File 1 : "D:\Haughton Rietveld 2017 - unorg\group sample files\RAW files\06-093\MX06093.raw"

Range Number : 1

R-Values

Rexp : 6.95 Rwp : 9.63 Rp : 6.76 GOF : 1.39
Rexp` : 6.27 Rwp` : 8.68 Rp` : 6.17 DW : 1.10

Quantitative Analysis - Rietveld

Phase 1 : "Calcite_Markgraff and Reeder 1985" 99.1(3) %
Phase 2 : "Quartz_Brill 1939" 0.4(2) %
Phase 3 : "Dolomite_Ross and Reeder 1992" 0.51(19) %

Background

One on X		2000(3000)
Chebyshev polynomial, Coefficient	0	-20(70)
	1	30(50)
	2	-10(20)
	3	0(8)
	4	3(3)
	5	0.0(11)

Instrument

Primary radius (mm)	185
Secondary radius (mm)	185

Corrections

Specimen displacement	0.063(6)
LP Factor	26.4
Absorption (1/cm)	0(3000)

Structure 1

Phase name	Calcite_Markgraff and
Reeder 1985	
R-Bragg	1.331
Spacegroup	R-3c
Scale	0.001223(13)
Cell Mass	600.521
Cell Volume (Å ³)	365.46(19)
Wt% - Rietveld	99.1(3)
Double-Voigt Approach	
Cry size Gaussian	58(6)
k: 1 LVol-IB (nm)	55(6)
k: 0.89 LVol-FWHM (nm)	52(6)
Strain	
Strain G	0.37(4)
e0	0.00081(9)
Crystal Linear Absorption Coeff. (1/cm)	201.75(10)
Crystal Density (g/cm ³)	2.7286(14)
Preferred Orientation Spherical Harmonics	
Order	8
y00	1
y20	-0.052(18)
y40	-0.032(16)
y43m	-0.114(8)
y60	-0.015(19)
y63m	0.063(10)
y66p	-0.049(8)
y80	-0.021(15)
y83m	-0.087(19)

y86p						-0.002 (9)
PV_TCHZ peak type						
U						0.17 (3)
V						-0.16 (4)
W						0.036 (13)
Z						0
X						0.389 (6)
Y						0
Lattice parameters						
a (Å)						4.9786 (12)
c (Å)						17.025 (4)

Site	Np	x	y	z	Atom	Occ	Beq
Ca	6	0.00000	0.00000	0.00000	Ca+2	1	1.22 (7)
C	6	0.00000	0.00000	0.25000	C	1	2.13 (15)
O	18	0.25670	0.00000	0.25000	O-2	1	1.81 (11)

Structure 2

Phase name						Quartz_Brill 1939
R-Bragg						1.792
Spacegroup						P3121
Scale						0.00006 (3)
Cell Mass						180.253
Cell Volume (Å ³)						112.7 (2)
Wt% - Rietveld						0.4 (2)
Crystal Linear Absorption Coeff. (1/cm)						95.15 (19)
Crystal Density (g/cm ³)						2.657 (5)
Preferred Orientation Spherical Harmonics						
Order						8
y00						1
y20						0.1 (18)
y40						0 (3)
y43m						0.5 (17)
y60						1 (4)
y63m						1.6 (18)
y66p						-0.3 (5)
y80						2 (3)
y83m						-1 (2)
y86p						-0.3 (4)
PV_TCHZ peak type						
U						0.0 (8)
V						0.0 (6)
W						-0.01 (9)
Z						0
X						0.46 (12)
Y						0
Lattice parameters						
a (Å)						4.906 (4)
c (Å)						5.405 (7)

Site	Np	x	y	z	Atom	Occ	Beq
Si1	3	0.46500	0.00000	0.33333	Si+4	1	1
O1	6	0.41500	0.27200	0.21300	O-2	1	1

Structure 3

Phase name						Dolomite_Ross and Reeder
1992						

R-Bragg					2.502	
Spacegroup					R-3	
Scale					0.000008 (3)	
Cell Mass					553.202	
Cell Volume (Å ³)					319.6 (4)	
Wt% - Rietveld					0.51 (19)	
Crystal Linear Absorption Coeff. (1/cm)					139.91 (17)	
Crystal Density (g/cm ³)					2.875 (4)	
Preferred Orientation Spherical Harmonics						
Order					8	
y00					1	
y20					1.0 (12)	
y40					-0.5 (10)	
y43m					0.1 (8)	
y43p					-0.5 (18)	
y60					0.2 (17)	
y63m					0.2 (7)	
y63p					-1 (4)	
y66m					-4 (4)	
y66p					-0.2 (7)	
y80					-0.1 (11)	
y83m					-0.5 (19)	
y83p					-0 (5)	
y86m					-1 (3)	
y86p					0.2 (8)	
PV_TCHZ peak type						
U					-0.1 (14)	
V					-0.1 (11)	
W					-0.01 (19)	
Z					0	
X					0.0 (2)	
Y					0	
Lattice parameters						
a (Å)					4.805 (3)	
c (Å)					15.980 (10)	
Site	Np	x	y	z	Atom Occ	Beq
CaA	3	0.00000	0.00000	0.00000	Ca+2 1	0.7098
MgB	3	0.00000	0.00000	0.50000	Mg+2 1	0.4998
C	6	0.00000	0.00000	0.24310	C 1	0.7304
O	18	0.24820	-0.03570	0.24400	O-2 1	0.8401

06-108**File 1** : "D:\XRD - Nov 2019\HMP_06_108.raw"

Range Number : 1

R-Values

Rexp : 6.90 Rwp : 10.93 Rp : 7.36 GOF : 1.58

Rexp` : 6.72 Rwp` : 10.64 Rp` : 7.17 DW : 0.88

Quantitative Analysis - Rietveld

Phase 1 : "Dolomite_Althoff 1977" 99.5 (4) %

Phase 2 : "Quartz_Brill 1939" 0.2 (4) %

Phase 3 : "Calcite_Markgraf Reeder 1985" 0.27 (10) %

Background

One on X		2000 (2000)
Chebyshev polynomial, Coefficient	0	-10 (60)
	1	8 (50)
	2	0 (18)
	3	-0 (7)
	4	2 (2)
	5	2.0 (11)
Instrument		
Primary radius (mm)		185
Secondary radius (mm)		185
Corrections		
Specimen displacement		-0.0344 (19)
LP Factor		26.4
Absorption (1/cm)		16.3 (2)
Structure 1		
Phase name		Dolomite_Althoff 1977
R-Bragg		1.485
Spacegroup		R-3
Scale		0.00185 (5)
Cell Mass		553.202
Cell Volume (Å ³)		318.935 (18)
Wt% - Rietveld		99.5 (4)
Double-Voigt Approach		
Cry size Gaussian		80 (6)
k: 1 LVol-IB (nm)		75 (5)
k: 0.89 LVol-FWHM (nm)		71 (5)
Strain		
Strain G		0.11 (9)
e0		0.00024 (19)
Crystal Linear Absorption Coeff. (1/cm)		203.005 (11)
Crystal Density (g/cm ³)		2.88026 (16)
Preferred Orientation Spherical Harmonics		
Order		8
y00		1
y20		0.48 (2)
y40		-0.021 (19)
y43m		0.33 (2)
y43p		-0.14 (5)
y60		0.35 (5)
y63m		-0.198 (18)
y63p		0.41 (9)
y66m		-0.45 (4)
y66p		0.001 (13)
y80		-0.21 (4)
y83m		0.34 (5)
y83p		-0.73 (16)
y86m		-0.14 (13)
y86p		-0.36 (3)
PV_TCHZ peak type		
U		-0.08 (6)
V		-0.00 (5)
W		0.015 (12)
Z		0
X		0.126 (12)
Y		0
Lattice parameters		
a (Å)		4.79975 (11)

c (Å) 15.9858 (5)

Site	Np	x	y	z	Atom	Occ	Beq
Ca	3	0.00000	0.00000	0.00000	Ca+2	1	-1.3 (3)
Mg	3	0.00000	0.00000	0.50000	Mg+2	1	0.42 (15)
C	6	0.00000	0.00000	-0.24230	C	1	4.0 (4)
O	18	0.28290	0.03500	-0.24400	O-2	1	-1.3 (4)

Structure 2

Phase name	Quartz_Brill 1939
R-Bragg	3.860
Spacegroup	P3121
Scale	0.00004 (6)
Cell Mass	180.253
Cell Volume (Å ³)	112.5 (2)
Wt% - Rietveld	0.2 (4)
Crystal Linear Absorption Coeff. (1/cm)	138.0 (2)
Crystal Density (g/cm ³)	2.661 (5)
Preferred Orientation Spherical Harmonics	
Order	8
y00	1
y20	5 (7)
y40	5 (12)
y43m	3 (11)
y60	1 (16)
y63m	0 (13)
y66p	1 (2)
y80	5 (9)
y83m	1 (12)
y86p	1 (2)
PV_TCHZ peak type	
U	-0.08 (6)
V	-0.00 (5)
W	0.015 (12)
Z	0
X	0.126 (12)
Y	0
Lattice parameters	
a (Å)	4.908 (3)
c (Å)	5.391 (6)

Site	Np	x	y	z	Atom	Occ	Beq
Si1	3	0.46500	0.00000	0.33333	Si+4	1	1
O1	6	0.41500	0.27200	0.21300	O-2	1	1

Structure 3

Phase name	Calcite_Markgraf Reeder
1985	
R-Bragg	15.026
Spacegroup	R-3c
Scale	0.0000040 (15)
Cell Mass	600.521
Cell Volume (Å ³)	365.3 (2)
Wt% - Rietveld	0.27 (10)
Crystal Linear Absorption Coeff. (1/cm)	295.85 (17)
Crystal Density (g/cm ³)	2.7298 (16)
Preferred Orientation Spherical Harmonics	

Order					8	
y00					1	
y20					-5 (4)	
y40					-9 (5)	
y43m					-1.6 (5)	
y60					-9 (3)	
y63m					0.3 (17)	
y66p					-1.2 (9)	
y80					-5 (2)	
y83m					1 (3)	
y86p					-0.2 (11)	
PV_TCHZ	peak type					
U					-0.08 (6)	
V					-0.00 (5)	
W					0.015 (12)	
Z					0	
X					0.126 (12)	
Y					0	
Lattice parameters						
a	(Å)				4.9865 (14)	
c	(Å)				16.964 (4)	
Site	Np	x	y	z	Atom Occ	Beq
Ca	6	0.00000	0.00000	0.00000	Ca+2 1	1
C	6	0.00000	0.00000	0.25000	C 1	1

07-020

File 1 : "D:\XRD - May 2019\pXRD sandpaper\RAW files\HAU_07_020_sp.raw"

Range Number : 1

R-Values

Rexp : 7.15 Rwp : 10.40 Rp : 7.43 GOF : 1.45

Rexp` : 5.99 Rwp` : 8.72 Rp` : 6.36 DW : 1.03

Quantitative Analysis - Rietveld

Phase 1 : "Calcite_Markgraf and Reeder" 69.0 (7) %

Phase 2 : Quartz_Levian 31.0 (7) %

Background

One on X 3000 (2000)

Chebyshev polynomial, Coefficient 0 -30 (70)

1 30 (50)

2 -5 (19)

3 0 (7)

4 2 (3)

5 2.5 (11)

Instrument

Primary radius (mm) 185

Secondary radius (mm) 185

Corrections

Specimen displacement 0.021 (6)

LP Factor 26.4

Absorption (1/cm) 0 (2000)

Structure 1

Phase name Calcite_Markgraf and
 Reeder
 R-Bragg 1.040
 Spacegroup R-3c
 Scale 0.001321(16)
 Cell Mass 600.521
 Cell Volume (Å³) 365.45(13)
 Wt% - Rietveld 69.0(7)
 Double-Voigt|Approach
 Cry size Gaussian 53.7(15)
 k: 1 LVol-IB (nm) 50.4(14)
 k: 0.89 LVol-FWHM (nm) 47.8(13)
 Strain
 Strain G 0.421(19)
 e0 0.00092(4)
 Crystal Linear Absorption Coeff. (1/cm) 295.72(11)
 Crystal Density (g/cm³) 2.7286(10)
 Preferred Orientation Spherical Harmonics
 Order 8
 y00 1
 y20 -0.06(2)
 y40 -0.08(2)
 y43m -0.093(10)
 y60 0.02(2)
 y63m 0.077(15)
 y66p -0.031(9)
 y80 -0.00(2)
 y83m -0.03(3)
 y86p -0.018(12)
 PV_TCHZ peak type
 U 0.28(5)
 V -0.29(4)
 W 0.073(10)
 Z 0
 X 0.242(8)
 Y 0
 Lattice parameters
 a (Å) 4.9786(8)
 c (Å) 17.025(3)

Site	Np	x	y	z	Atom Occ	Beq
Ca	6	0.00000	0.00000	0.00000	Ca+2 1	0.51(9)
C	6	0.00000	0.00000	0.25000	C 1	1.5(2)
O	18	0.25670	0.00000	0.25000	O-2 1	0.82(12)

Structure 2

Phase name Quartz_Levian
 R-Bragg 4.014
 Spacegroup P3221
 Scale 0.00437(14)
 Cell Mass 264.509
 Cell Volume (Å³) 112.72(4)
 Wt% - Rietveld 31.0(7)
 Double-Voigt|Approach
 Cry size Gaussian 85(4)
 k: 1 LVol-IB (nm) 80(4)
 k: 0.89 LVol-FWHM (nm) 76(4)

Crystal Linear Absorption Coeff. (1/cm)	258.84 (9)						
Crystal Density (g/cm ³)	3.8966 (14)						
Preferred Orientation Spherical Harmonics							
Order	8						
y00	1						
y20	-0.47 (3)						
y40	-1.70 (3)						
y43m	2.27 (6)						
y60	1.13 (3)						
y63m	0.12 (4)						
y66p	-0.969 (17)						
y80	0.08 (3)						
y83m	0.83 (6)						
y86p	-1.244 (17)						
PV_TCHZ peak type							
U	0.28 (5)						
V	-0.29 (4)						
W	0.073 (10)						
Z	0						
X	0.242 (8)						
Y	0						
Lattice parameters							
a (Å)	4.9089 (8)						
c (Å)	5.4013 (9)						
<u>Site</u>	<u>Np</u>	<u>x</u>	<u>y</u>	<u>z</u>	<u>Atom</u>	<u>Occ</u>	<u>Beq</u>
Si	6	0.46970	0.00000	0.33333	Si+4	1	1
O	6	0.41350	0.26690	0.11910	O-2	1	1

16-1014

File 1 : "D:\XRD - May 2019\pXRD sandpaper\RAW files\HAU_16_1014_sp.raw"

Range Number : 1

R-Values

Rexp : 8.20 Rwp : 10.54 Rp : 7.41 GOF : 1.28
Rexp` : 6.81 Rwp` : 8.75 Rp` : 6.26 DW : 1.24

Quantitative Analysis - Rietveld

Phase 1 : "Dolomite_Reeder and Wenk 1983" 1.21 (11) %
Phase 2 : "Calcite_Maslen 1985" 96.6 (3) %
Phase 3 : "Quartz_Brill 1939" 2.2 (2) %

Background

One on X 3040 (30)
Chebychev polynomial, Coefficient 0 -31.9 (9)
1 47.3 (12)
2 -15.4 (6)
3 8.8 (5)

Instrument

Primary radius (mm) 185
Secondary radius (mm) 185

Corrections

Specimen displacement 0.073 (3)
LP Factor 26.4
Absorption (1/cm) 500 (800)

Structure 1

Phase name	Dolomite_Reeder and Wenk					
1983						
R-Bragg	6.667					
Spacegroup	R-3					
Scale	0.0000146(14)					
Cell Mass	746.351					
Cell Volume (Å ³)	321.8(3)					
Wt% - Rietveld	1.21(11)					
Crystal Linear Absorption Coeff. (1/cm)	382.3(3)					
Crystal Density (g/cm ³)	3.851(3)					
Preferred Orientation Spherical Harmonics						
Order	8					
y00	1					
y20	-0.8(4)					
y40	-3.0(5)					
y43m	-0.10(14)					
y43p	-7.2(16)					
y60	-2.4(6)					
y63m	0.7(2)					
y63p	1(2)					
y66m	1.6(19)					
y66p	0.13(13)					
y80	-0.6(5)					
y83m	0.6(5)					
y83p	-6(2)					
y86m	-9(3)					
y86p	0.70(13)					
PV_TCHZ peak type						
U	2.0(8)					
V	-0.7(7)					
W	0.15(15)					
Z	0					
X	0.00(12)					
Y	0					
Lattice parameters						
a (Å)	4.8104(18)					
c (Å)	16.059(7)					

Site	Np	x	y	z	Atom Occ	Beq
Ca1	3	0.00000	0.00000	0.00000	Ca+2 1	1
Mg1	3	0.00000	0.00000	0.00000	Mg+2 1	1
Ca2	3	0.00000	0.00000	0.50000	Ca+2 1	1
Mg2	3	0.00000	0.00000	0.50000	Mg+2 1	1
C	6	0.00000	0.00000	0.24420	C 1	1
O	18	0.25160	-0.02770	0.24514	O-2 1	1

Structure 2

Phase name	Calcite_Maslen 1985					
R-Bragg	1.720					
Spacegroup	R-3c					
Scale	0.001282(6)					
Cell Mass	600.521					
Cell Volume (Å ³)	365.43(3)					
Wt% - Rietveld	96.6(3)					
Double-Voigt Approach						

Cry size Gaussian	71(2)						
k: 1 LVol-IB (nm)	67(2)						
k: 0.89 LVol-FWHM (nm)	64(2)						
Strain							
Strain G	0.282(9)						
e0	0.000616(19)						
Crystal Linear Absorption Coeff. (1/cm)	295.73(3)						
Crystal Density (g/cm ³)	2.7288(2)						
Preferred Orientation Spherical Harmonics							
Order	8						
y00	1						
y20	0.016(10)						
y40	-0.059(11)						
y43m	-0.076(7)						
y60	-0.041(12)						
y63m	0.078(7)						
y66p	-0.027(6)						
y80	-0.020(11)						
y83m	-0.102(12)						
y86p	-0.008(6)						
PV_TCHZ peak type							
U	0.113(11)						
V	-0.178(14)						
W	0.061(4)						
Z	0						
X	0.235(4)						
Y	0						
Lattice parameters							
a (Å)	4.9789(2)						
c (Å)	17.0220(7)						
Site	Np	x	y	z	Atom	Occ	Beq
Ca	6	0.00000	0.00000	0.00000	Ca+2	1	0.36(3)
C	6	0.00000	0.00000	0.25000	C	1	0.69(9)
O	18	0.25700	0.00000	0.25000	O-2	1	0.62(5)

Structure 3

Phase name	Quartz_Brill 1939
R-Bragg	1.993
Spacegroup	P3121
Scale	0.00032(4)
Cell Mass	180.253
Cell Volume (Å ³)	112.62(7)
Wt% - Rietveld	2.2(2)
Crystal Linear Absorption Coeff. (1/cm)	137.85(9)
Crystal Density (g/cm ³)	2.6577(17)
Preferred Orientation Spherical Harmonics	
Order	8
y00	1
y20	-0.1(4)
y40	0.4(5)
y43m	-1.5(3)
y60	1.4(7)
y63m	0.2(3)
y66p	-0.14(10)
y80	1.2(5)
y83m	0.0(5)

Double-Voigt Approach						
Cry size Gaussian		54.2(10)				
k: 1 LVol-IB (nm)		50.9(10)				
k: 0.89 LVol-FWHM (nm)		48.2(9)				
Strain						
Strain G		0.12(4)				
e0		0.00025(10)				
Crystal Linear Absorption Coeff. (1/cm)		295.96(9)				
Crystal Density (g/cm ³)		2.7309(8)				
Preferred Orientation Spherical Harmonics						
Order		8				
y00		1				
y20		0.084(18)				
y40		-0.07(3)				
y43m		-0.060(10)				
y60		-0.02(2)				
y63m		0.10(2)				
y66p		-0.011(10)				
y80		-0.12(3)				
y83m		-0.06(2)				
y86p		-0.03(2)				
PV_TCHZ peak type						
U		0.24(3)				
V		-0.21(3)				
W		0.041(6)				
Z		0				
X		0.174(6)				
Y		0				
Lattice parameters						
a (Å)		4.9782(7)				
c (Å)		17.014(2)				
Site	Np	x	y	z	Atom Occ	Beq
Ca	6	0.00000	0.00000	0.00000	Ca+2 1	0.43(15)
C	6	0.00000	0.00000	0.25000	C 1	1.77(18)
O	18	0.25670	0.00000	0.25000	O-2 1	0.59(14)

Structure 2

Phase name	Quartz_Brill 1939
R-Bragg	100.000
Spacegroup	P3121
Scale	0.00021(6)
Cell Mass	264.509
Cell Volume (Å ³)	112.61(9)
Wt% - Rietveld	2.0(5)
Crystal Linear Absorption Coeff. (1/cm)	259.1(2)
Crystal Density (g/cm ³)	3.901(3)
Preferred Orientation Spherical Harmonics	
Order 8	
y00 1	
y20 -3.1(12)	
y40 -5.9(17)	
y43m -9.7(14)	
y60 0.4(11)	
y63m 4.7(7)	
y66p -2.9(5)	
y80 0.5(8)	

y83m					-10 (2)	
y86p					-3.6 (6)	
PV_TCHZ	peak type					
U					1.2 (6)	
V					-1.0 (5)	
W					0.15 (8)	
Z					0	
X					0.49 (13)	
Y					0	
Lattice parameters						
a (Å)					4.9069 (16)	
c (Å)					5.400 (3)	
Site	Np	x	y	z	Atom Occ	Beq
Si1	6	0.46500	0.00000	0.33333	Si+4 1	1
O1	6	0.41500	0.27200	0.21300	O-2 1	1

Structure 3

Phase name	Dolomite_Reeder and Wenk					
1983						
R-Bragg	43.978					
Spacegroup	R-3					
Scale	0.000041 (7)					
Cell Mass	746.351					
Cell Volume (Å ³)	321.6 (3)					
Wt% - Rietveld	3.2 (5)					
Crystal Linear Absorption Coeff. (1/cm)	382.5 (3)					
Crystal Density (g/cm ³)	3.853 (3)					
Preferred Orientation Spherical Harmonics						
Order	8					
y00	1					
y20	0.8 (5)					
y40	-3.5 (7)					
y43m	-1.0 (3)					
y43p	-16 (3)					
y60	-1.8 (6)					
y63m	1.9 (5)					
y63p	33 (4)					
y66m	-10 (4)					
y66p	0.8 (2)					
y80	2.7 (7)					
y83m	-1.2 (6)					
y83p	12 (10)					
y86m	-33 (10)					
y86p	1.22 (14)					
PV_TCHZ	peak type					
U					0.6 (8)	
V					-0.4 (6)	
W					0.05 (12)	
Z					0	
X					0.70 (9)	
Y					0	
Lattice parameters						
a (Å)					4.8103 (17)	
c (Å)					16.051 (8)	
Site	Np	x	y	z	Atom Occ	Beq

Ca1	3	0.00000	0.00000	0.00000	Ca+2	1	1
Mg1	3	0.00000	0.00000	0.00000	Mg+2	1	1
Ca2	3	0.00000	0.00000	0.50000	Ca+2	1	1
Mg2	3	0.00000	0.00000	0.50000	Mg+2	1	1
C	6	0.00000	0.00000	0.24420	C	1	1
O	18	0.25160	-0.02770	0.24514	O-2	1	1

Structure 4

Phase name	Microcline_Ribbe
R-Bragg	4.011
Spacegroup	C-1
Scale	0.0000061(9)
Cell Mass	1549.447
Cell Volume (Å ³)	727.5(6)
Wt% - Rietveld	2.2(3)
Crystal Linear Absorption Coeff. (1/cm)	266.6(2)
Crystal Density (g/cm ³)	3.537(3)
Preferred Orientation Spherical Harmonics	
Order	8
y00	1
y20	1.3(3)
y21m	1.0(3)
y21p	0.64(18)
y22m	0.60(19)
y22p	-0.31(19)
y40	-1.3(5)
y41m	-2.9(5)
y41p	0.5(2)
y42m	0.0(2)
y42p	-1.9(4)
y43m	-0.6(2)
y43p	-0.9(2)
y44m	-1.1(3)
y44p	-0.4(3)
y60	-0.4(5)
y61m	3.0(7)
y61p	0.5(5)
y62m	1.0(3)
y62p	1.2(4)
y63m	-0.1(3)
y63p	-0.1(3)
y64m	-3.8(5)
y64p	1.6(3)
y65m	-0.9(2)
y65p	1.9(3)
y66m	1.3(3)
y66p	0.3(2)
y80	0.4(4)
y81m	0.3(5)
y81p	1.5(6)
y82m	1.3(5)
y82p	1.5(4)
y83m	-2.4(4)
y83p	-0.7(4)
y84m	-1.5(4)
y84p	1.6(3)
y85m	2.4(5)

y85p	-1.7(3)
y86m	0.5(4)
y86p	1.5(4)
y87m	0.8(2)
y87p	-1.2(4)
y88m	-0.5(3)
y88p	-0.6(3)
PV_TCHZ peak type	
U	-0.3(3)
V	0.2(3)
W	-0.13(7)
Z	0
X	0.00(10)
Y	0
Lattice parameters	
a (Å)	8.619(5)
b (Å)	13.007(4)
c (Å)	7.197(3)
alpha (°)	89.68(3)
beta (°)	115.59(3)
gamma (°)	88.74(3)

Site	Np	x	y	z	Atom	Occ	Beq
K	4	0.28670	0.99850	0.14060	K+1	1	1
Si1o	4	0.00950	0.18440	0.22250	Si+4	1	1
Al1o	4	0.00950	0.18440	0.22250	Al+3	1	1
Si1m	4	0.00910	0.81680	0.22490	Si+4	1	1
Al1m	4	0.00910	0.81680	0.22490	Al+3	1	1
Si2o	4	0.71050	0.11840	0.34130	Si+4	1	1
Al2o	4	0.71050	0.11840	0.34130	Al+3	1	1
Si2m	4	0.70950	0.88260	0.34330	Si+4	1	1
Al2m	4	0.70950	0.88260	0.34330	Al+3	1	1
Oa1	4	0.00050	0.14400	0.99770	O-2	1	1
Oa2	4	0.63820	0.00110	0.28090	O-2	1	1
Obo	4	0.82510	0.14720	0.22280	O-2	1	1
Obm	4	0.82780	0.85340	0.22740	O-2	1	1
Oco	4	0.03670	0.31160	0.25800	O-2	1	1
Ocm	4	0.03780	0.69030	0.26020	O-2	1	1
Odo	4	0.18150	0.12400	0.40750	O-2	1	1
Odm	4	0.17900	0.87490	0.40850	O-2	1	1

16-1018

File 1 : "D:\XRD - May 2019\pXRD sandpaper\RAW files\HAU_16_1018_sp.raw"

Range Number : 1

R-Values

Rexp : 7.43 Rwp : 10.21 Rp : 7.03 GOF : 1.37
Rexp` : 7.52 Rwp` : 10.33 Rp` : 7.13 DW : 1.21

Quantitative Analysis - Rietveld

Phase 1 : "Calcite_Maslen 1995" 98.0(11) %
Phase 2 : "Quartz_Levian 1980" 1.3(11) %
Phase 3 : "Microcline_Ribbe 1979" 0.7(3) %

Background

One on X		1000 (3000)				
Chebyshev polynomial, Coefficient	0	6 (70)				
	1	-10 (50)				
	2	9 (20)				
	3	-7 (8)				
	4	4 (3)				
	5	0.9 (12)				
Instrument						
Primary radius (mm)		185				
Secondary radius (mm)		185				
Corrections						
Specimen displacement		0.035 (5)				
LP Factor		26.4				
Absorption (1/cm)		0 (2000)				
Structure 1						
Phase name		Calcite_Maslen 1995				
R-Bragg		1.286				
Spacegroup		R-3c				
Scale		0.001352 (16)				
Cell Mass		600.521				
Cell Volume (Å ³)		365.84 (10)				
Wt% - Rietveld		98.0 (11)				
Double-Voigt Approach						
Cry size Gaussian		70 (10)				
k: 1 LVol-IB (nm)		66 (10)				
k: 0.89 LVol-FWHM (nm)		63 (9)				
Strain						
Strain G		0.32 (4)				
e0		0.00069 (9)				
Crystal Linear Absorption Coeff. (1/cm)		295.40 (8)				
Crystal Density (g/cm ³)		2.7257 (7)				
Preferred Orientation Spherical Harmonics						
Order		8				
y00		1				
y20		-0.194 (17)				
y40		-0.073 (19)				
y43m		-0.068 (9)				
y60		0.098 (19)				
y63m		0.107 (13)				
y66p		-0.044 (8)				
y80		0.018 (15)				
y83m		0.05 (2)				
y86p		-0.051 (11)				
PV_TCHZ peak type						
U		0.14 (4)				
V		-0.17 (3)				
W		0.053 (10)				
Z		0				
X		0.195 (5)				
Y		0				
Lattice parameters						
a (Å)		4.9806 (6)				
c (Å)		17.029 (2)				
Site	Np	x	y	z	Atom Occ	Beq
Ca	6	0.00000	0.00000	0.00000	Ca+2 1	0.15 (9)

C	6	0.00000	0.00000	0.25000	C	1	1.40 (17)
O	18	0.25700	0.00000	0.25000	O-2	1	0.52 (11)

Structure 2

Phase name	Quartz_Levian 1980
R-Bragg	2.404
Spacegroup	P3221
Scale	0.00013 (11)
Cell Mass	264.509
Cell Volume (Å ³)	112.63 (16)
Wt% - Rietveld	1.3 (11)
Crystal Linear Absorption Coeff. (1/cm)	259.0 (4)
Crystal Density (g/cm ³)	3.900 (6)
Preferred Orientation Spherical Harmonics	
Order	8
y00	1
y20	-0.3 (12)
y40	-2.2 (16)
y43m	-0 (4)
y60	2.4 (16)
y63m	-0.1 (14)
y66p	-1.3 (5)
y80	1.3 (18)
y83m	3 (4)
y86p	-1.2 (6)
PV_TCHZ peak type	
U	0.1 (12)
V	-0.2 (10)
W	0.1 (2)
Z	0
X	0.47 (17)
Y	0
Lattice parameters	
a (Å)	4.909 (3)
c (Å)	5.398 (4)

Site	Np	x	y	z	Atom Occ	Beq
Si	6	0.46970	0.00000	0.33333	Si+4 1	1
O	6	0.41350	0.26690	0.11910	O-2 1	1

Structure 3

Phase name	Microcline_Ribbe 1979
R-Bragg	53.313
Spacegroup	C-1
Scale	0.0000019 (7)
Cell Mass	1549.447
Cell Volume (Å ³)	719 (3)
Wt% - Rietveld	0.7 (3)
Crystal Linear Absorption Coeff. (1/cm)	269.6 (11)
Crystal Density (g/cm ³)	3.578 (14)
Preferred Orientation Spherical Harmonics	
Order	8
y00	1
y20	-1.2 (13)
y21m	-2 (3)
y21p	-1.2 (8)
y22m	2 (3)

y22p	-0.5 (8)						
y40	0.9 (16)						
y41m	1 (5)						
y41p	0.4 (11)						
y42m	3 (5)						
y42p	-1.9 (10)						
y43m	4 (4)						
y43p	1.5 (7)						
y44m	-0 (3)						
y44p	-0.6 (13)						
y60	-1.2 (14)						
y61m	4 (6)						
y61p	5 (2)						
y62m	-1 (5)						
y62p	-0.3 (17)						
y63m	-2 (6)						
y63p	-1.3 (9)						
y64m	-5 (5)						
y64p	0.0 (8)						
y65m	2 (3)						
y65p	0.3 (7)						
y66m	7 (4)						
y66p	-1.2 (8)						
y80	0.6 (16)						
y81m	1 (6)						
y81p	0 (2)						
y82m	-4 (8)						
y82p	-2.5 (13)						
y83m	-1 (4)						
y83p	-2.0 (14)						
y84m	-3 (5)						
y84p	-0.4 (12)						
y85m	-0 (5)						
y85p	2.4 (11)						
y86m	2 (4)						
y86p	0.5 (9)						
y87m	2 (3)						
y87p	-1.2 (11)						
y88m	2 (3)						
y88p	-0.7 (10)						
PV_TCHZ peak type							
U	1 (2)						
V	0.2 (13)						
W	0.0 (2)						
Z	0						
X	0.3 (6)						
Y	0						
Lattice parameters							
a (Å)	8.600 (15)						
b (Å)	12.91 (3)						
c (Å)	7.195 (17)						
alpha (°)	89.94 (11)						
beta (°)	115.80 (19)						
gamma (°)	89.55 (16)						
Site	Np	x	y	z	Atom	Occ	Beq
K	4	0.28670	0.99850	0.14060	K+1	1	1

Si1o	4	0.00950	0.18440	0.22250	Si+4	1	1
Al1o	4	0.00950	0.18440	0.22250	Al+3	1	1
Si1m	4	0.00910	0.81680	0.22490	Si+4	1	1
Al1m	4	0.00910	0.81680	0.22490	Al+3	1	1
Si2o	4	0.71050	0.11840	0.34130	Si+4	1	1
Al2o	4	0.71050	0.11840	0.34130	Al+3	1	1
Si2m	4	0.70950	0.88260	0.34330	Si+4	1	1
Al2m	4	0.70950	0.88260	0.34330	Al+3	1	1
Oa1	4	0.00050	0.14400	0.99770	O-2	1	1
Oa2	4	0.63820	0.00110	0.28090	O-2	1	1
Obo	4	0.82510	0.14720	0.22280	O-2	1	1
Obm	4	0.82780	0.85340	0.22740	O-2	1	1
Oco	4	0.03670	0.31160	0.25800	O-2	1	1
Ocm	4	0.03780	0.69030	0.26020	O-2	1	1
Odo	4	0.18150	0.12400	0.40750	O-2	1	1
Odm	4	0.17900	0.87490	0.40850	O-2	1	1

16-1046

File 1 : "D:\XRD - May 2019\pXRD sandpaper\RAW files\HAU_16_1046_sp.raw"

Range Number : 1

R-Values

Rexp : 7.33 Rwp : 10.26 Rp : 7.15 GOF : 1.40
Rexp` : 6.88 Rwp` : 9.64 Rp` : 6.74 DW : 1.08

Quantitative Analysis - Rietveld

Phase 1 : "Calcite_Markgraff and Reeder 1985" 93.1(8) %
Phase 2 : "Dolomite_Ross and Reeder 1992" 5.9(4) %
Phase 3 : "Quartz_Brill 1939" 1.0(7) %

Background

One on X 2000(2000)
Chebychev polynomial, Coefficient 0 -10(60)
1 8(50)
2 1(18)
3 -4(7)
4 2(2)
5 0.8(10)

Instrument

Primary radius (mm) 185
Secondary radius (mm) 185

Corrections

Specimen displacement 0.047(6)
LP Factor 26.4
Absorption (1/cm) 0(2000)

Structure 1

Phase name Calcite_Markgraff and
Reeder 1985
R-Bragg 1.347
Spacegroup R-3c
Scale 0.001343(18)
Cell Mass 600.521
Cell Volume (Å³) 365.79(11)
Wt% - Rietveld 93.1(8)

Double-Voigt Approach						
Cry size Gaussian						
k: 1 LVol-IB (nm)						
k: 0.89 LVol-FWHM (nm)						
Strain						
Strain G						
e0						
Crystal Linear Absorption Coeff. (1/cm)						
Crystal Density (g/cm ³)						
Preferred Orientation Spherical Harmonics						
Order						
y00						
y20						
y40						
y43m						
y60						
y63m						
y66p						
y80						
y83m						
y86p						
PV_TCHZ peak type						
U						
V						
W						
Z						
X						
Y						
Lattice parameters						
a (Å)						
c (Å)						
Site	Np	x	y	z	Atom Occ	Beq
Ca	6	0.00000	0.00000	0.00000	Ca+2 1	0.30 (10)
C	6	0.00000	0.00000	0.25000	C 1	1.34 (16)
O	18	0.25670	0.00000	0.25000	O-2 1	0.56 (11)

Structure 2

Phase name		Dolomite_Ross and Reeder				
1992						
R-Bragg		1.684				
Spacegroup		R-3				
Scale		0.000105 (8)				
Cell Mass		553.202				
Cell Volume (Å ³)		320.19 (13)				
Wt% - Rietveld		5.9 (4)				
Crystal Linear Absorption Coeff. (1/cm)		202.21 (8)				
Crystal Density (g/cm ³)		2.8689 (12)				
Preferred Orientation Spherical Harmonics						
Order						
y00						
y20						
y40						
y43m						
y43p						
y60						
y63m						

y63p	-2.0 (10)
y66m	-0.6 (5)
y66p	-0.11 (12)
y80	-0.18 (18)
y83m	0.1 (4)
y83p	-1.4 (9)
y86m	-1.3 (7)
y86p	-0.14 (18)
PV_TCHZ peak type	
U	-0.0 (3)
V	0.2 (3)
W	-0.01 (6)
Z	0
X	0.25 (3)
Y	0
Lattice parameters	
a (Å)	4.8054 (9)
c (Å)	16.011 (3)

Site	Np	x	y	z	Atom	Occ	Beq
CaA	3	0.00000	0.00000	0.00000	Ca+2	1	0.7098
MgB	3	0.00000	0.00000	0.50000	Mg+2	1	0.4998
C	6	0.00000	0.00000	0.24310	C	1	0.7304
O	18	0.24820	-0.03570	0.24400	O-2	1	0.8401

Structure 3

Phase name	Quartz_Brill 1939
R-Bragg	2.145
Spacegroup	P3121
Scale	0.00016 (11)
Cell Mass	180.253
Cell Volume (Å ³)	112.77 (12)
Wt% - Rietveld	1.0 (7)
Crystal Linear Absorption Coeff. (1/cm)	137.67 (14)
Crystal Density (g/cm ³)	2.654 (3)
Preferred Orientation Spherical Harmonics	
Order	8
y00	1
y20	0 (3)
y40	0 (4)
y43m	-1 (2)
y60	-0 (4)
y63m	-1 (5)
y66p	-0.4 (5)
y80	-0 (3)
y83m	-0 (4)
y86p	-0.1 (6)
PV_TCHZ peak type	
U	-0.2 (5)
V	0.2 (4)
W	-0.04 (6)
Z	0
X	0.42 (9)
Y	0
Lattice parameters	
a (Å)	4.9142 (18)
c (Å)	5.392 (4)

y20	0.599 (13)					
y40	-0.051 (15)					
y43m	0.088 (9)					
y43p	0.007 (19)					
y60	-0.045 (17)					
y63m	-0.116 (8)					
y63p	0.22 (3)					
y66m	0.09 (3)					
y66p	0.005 (7)					
y80	-0.145 (15)					
y83m	-0.136 (16)					
y83p	0.10 (4)					
y86m	-0.10 (3)					
y86p	0.015 (8)					
PV_TCHZ peak type						
U	0.116 (10)					
V	-0.128 (16)					
W	0.035 (6)					
Z	0					
X	0.214 (4)					
Y	0					
Lattice parameters						
a (Å)	4.80350 (10)					
c (Å)	16.0031 (4)					
<hr/>						
Site	Np	x	y	z	Atom Occ	Beq
Ca	3	0.00000	0.00000	0.00000	Ca+2 1	0.34 (6)
Mg	3	0.00000	0.00000	0.50000	Mg+2 1	-0.00 (7)
C	6	0.00000	0.00000	0.24300	C 1	0.69 (15)
O	18	0.24760	0.96500	0.24410	O-2 1	0.28 (7)

Structure 2

Phase name	Quartz_Glinnemann 1992
R-Bragg	2.814
Spacegroup	P3121
Scale	0.00063 (8)
Cell Mass	180.253
Cell Volume (Å ³)	112.42 (7)
Wt% - Rietveld	3.2 (4)
Crystal Linear Absorption Coeff. (1/cm)	138.10 (8)
Crystal Density (g/cm ³)	2.6625 (15)
Preferred Orientation Spherical Harmonics	
Order	8
y00	1
y20	0.7 (4)
y40	-0.7 (5)
y43m	0.4 (5)
y60	-0.0 (6)
y63m	-2.0 (4)
y66p	-0.44 (16)
y80	1.9 (6)
y83m	0.3 (3)
y86p	-0.34 (19)
PV_TCHZ peak type	
U	0.12 (13)
V	-0.26 (13)
W	0.09 (3)

Z					0	
X					0.37 (6)	
Y					0	
Lattice parameters						
a (Å)					4.9011 (10)	
c (Å)					5.404 (2)	
<u>Site</u>	<u>Np</u>	<u>x</u>	<u>y</u>	<u>z</u>	<u>Atom</u>	<u>Occ</u>
Si	3	0.46980	0.00000	0.33333	Si+4	1
O	6	0.41510	0.26750	-0.11940	O-2	1

Structure 3

Phase name	Microcline_Ribbe 1979
R-Bragg	4.011
Spacegroup	C-1
Scale	0.0000243 (8)
Cell Mass	1549.447
Cell Volume (Å ³)	720.3 (3)
Wt% - Rietveld	6.9 (2)
Crystal Linear Absorption Coeff. (1/cm)	269.23 (12)
Crystal Density (g/cm ³)	3.5719 (16)
Preferred Orientation Spherical Harmonics	
Order	8
y00	1
y20	0.17 (6)
y21m	1.5 (5)
y21p	0.08 (4)
y22m	0.14 (17)
y22p	-0.13 (6)
y40	0.13 (9)
y41m	2.0 (8)
y41p	-0.23 (5)
y42m	-0.4 (2)
y42p	-0.06 (7)
y43m	-1.3 (3)
y43p	-0.01 (4)
y44m	-0.1 (2)
y44p	0.03 (5)
y60	0.20 (9)
y61m	-2.2 (9)
y61p	0.35 (9)
y62m	0.6 (3)
y62p	0.21 (9)
y63m	1.0 (4)
y63p	-0.11 (6)
y64m	-0.5 (3)
y64p	0.44 (6)
y65m	0.6 (3)
y65p	-0.01 (4)
y66m	0.1 (2)
y66p	-0.32 (5)
y80	-0.36 (9)
y81m	-0.9 (6)
y81p	0.06 (12)
y82m	0.6 (5)
y82p	-0.49 (8)
y83m	2.0 (5)

Order	8
y00	1
y20	-17 (17)
y40	-50 (40)
y43m	-16 (13)
y60	-40 (40)
y63m	2 (4)
y66p	-8 (7)
y80	-30 (20)
y83m	-4 (4)
y86p	-3 (4)
PV_TCHZ peak type	
U	0.1 (9)
V	0.2 (10)
W	-0.3 (2)
Z	0
X	0.39 (12)
Y	0
Lattice parameters	
a (Å)	4.955 (4)
c (Å)	16.936 (4)

Site	Np	x	y	z	Atom	Occ	Beq
Ca	6	0.00000	0.00000	0.00000	Ca+2	1	1
C	6	0.00000	0.00000	0.25000	C	1	1
O	18	0.25670	0.00000	0.25000	O-2	1	1

E.3 TOPAS *hkl* output values

99-006 dolomite

h	k	l	m	d	th2	F ²
0	0	3	2	5.33942	19.28788	0.104
1	0	1	6	4.02865	25.65668	2.674
0	1	2	6	3.69343	28.03082	4.794
1	0	4	6	2.88586	36.11301	272.360
0	0	6	2	2.66971	39.15112	19.455
0	1	5	6	2.53877	41.25981	21.056
1	1	0	6	2.40319	43.70361	39.759
1	1	3	6	2.19145	48.17986	10.589
1	-2	-3	6	2.19145	48.17986	37.713
0	2	1	6	2.06388	51.36710	26.511
2	0	2	6	2.01433	52.72664	87.156
1	0	7	6	2.00527	52.98320	1.970
0	2	4	6	1.84671	57.94185	34.440
0	1	8	6	1.80437	59.43600	133.526
1	1	6	6	1.78613	60.10534	60.353
1	-2	-6	6	1.78613	60.10534	115.894
0	0	9	2	1.77981	60.34096	10.489
2	0	5	6	1.74528	61.66341	1.817
1	2	-1	6	1.56572	69.68068	25.110
2	1	1	6	1.56572	69.68068	15.663

1	-3	-2	6	1.54376	70.81969	73.973
1	2	2	6	1.54376	70.81969	27.414
0	2	7	6	1.53967	71.03608	0.627
1	0	10	6	1.49495	73.50188	9.110
1	2	-4	6	1.46431	75.30324	50.032
2	1	4	6	1.46431	75.30324	33.288
2	0	8	6	1.44293	76.61907	36.610
1	-2	-9	6	1.43027	77.42243	32.946
1	1	9	6	1.43027	77.42243	14.592
1	-3	-5	6	1.41217	78.60487	32.396
1	2	5	6	1.41217	78.60487	2.243
0	3	0	6	1.38748	80.28364	114.525

99-063B calcite

h	k	l	m	d	th2	F ²
0	1	2	6	3.84648	26.89406	7.943
1	0	4	6	3.02898	34.35209	199.988
0	0	6	2	2.83730	36.75289	6.582
1	1	0	6	2.48945	42.11571	41.129
1	1	3	12	2.27972	46.20359	77.412
2	0	2	6	2.08993	50.68108	74.184
0	2	4	6	1.92324	55.43244	36.488
0	1	8	6	1.90824	55.90612	116.311
1	1	6	12	1.87127	57.11084	137.265
2	1	1	12	1.62231	66.92142	31.948
1	2	2	12	1.60065	67.94920	100.810
1	0	10	6	1.58344	68.79081	11.416
2	1	4	12	1.52196	71.99081	60.106
2	0	8	6	1.51449	72.40165	28.222
1	1	9	12	1.50610	72.86973	31.894
1	2	5	12	1.47000	74.96106	25.212
0	3	0	6	1.43728	76.97501	84.318
0	0	12	2	1.41865	78.17667	49.461

00-019 calcite

h	k	l	m	d	th2	F ²
0	1	2	6	3.84563	23.10959	1.785
1	0	4	6	3.02857	29.46943	45.656
0	0	6	2	2.83731	31.50578	1.456
1	1	0	6	2.48875	36.05962	9.276
1	1	3	12	2.27919	39.50656	17.155
2	0	2	6	2.08938	43.26758	16.159
0	2	4	6	1.92281	47.23264	7.964
0	1	8	6	1.90814	47.61816	25.343
1	1	6	12	1.87098	48.62440	29.352
2	1	1	12	1.62186	56.71185	6.722
1	2	2	12	1.60022	57.54985	20.788
1	0	10	6	1.58338	58.22022	2.271

2	1	4	12	1.52159	60.82832	12.495
2	0	8	6	1.51428	61.15294	5.859
1	1	9	12	1.50595	61.52816	6.602
1	2	5	12	1.46967	63.21942	5.186
0	3	0	6	1.43688	64.83575	17.289
0	0	12	2	1.41865	65.77318	10.110
2	1	7	12	1.35359	69.37194	4.131
0	2	10	6	1.33593	70.42377	7.827
1	2	8	12	1.29364	73.08947	9.668
3	0	6	6	1.28188	73.87092	1.303
0	3	6	6	1.28188	73.87092	1.303
2	2	0	6	1.24438	76.48973	4.265
1	1	12	12	1.23248	77.36409	8.005
2	2	3	12	1.21549	78.65206	0.094
1	3	1	12	1.19262	80.46443	0.020

00-019 dolomite

h	k	l	m	d	th2	F ²
0	0	3	2	5.34379	16.57590	0.008
1	0	1	6	4.02949	22.04157	0.133
0	1	2	6	3.69456	24.06838	0.410
1	0	4	6	2.88732	30.94631	24.884
0	0	6	2	2.67190	33.51196	2.082
0	1	5	6	2.54023	35.30450	1.148
1	1	0	6	2.40359	37.38365	2.658
1	-2	-3	6	2.19206	41.14642	8.296
1	1	3	6	2.19206	41.14642	5.644
0	2	1	6	2.06424	43.82156	1.228
2	0	2	6	2.01475	44.95619	8.039
1	0	7	6	2.00661	45.14843	0.013
0	2	4	6	1.84728	49.28949	1.858
0	1	8	6	1.80563	50.50505	9.907
1	1	6	6	1.78695	51.07089	10.464
1	-2	-6	6	1.78695	51.07089	5.284
0	0	9	2	1.78126	51.24557	0.418
2	0	5	6	1.74590	52.36131	0.989
1	2	-1	6	1.56600	58.92982	3.534
2	1	1	6	1.56600	58.92982	0.811
1	-3	-2	6	1.54405	59.85202	2.263
1	2	2	6	1.54405	59.85202	6.380
0	2	7	6	1.54038	60.00924	0.621
1	0	10	6	1.49605	61.97993	0.603
1	2	-4	6	1.46468	63.45982	1.558
2	1	4	6	1.46468	63.45982	2.644
2	0	8	6	1.44366	64.49448	1.773
1	-2	-9	6	1.43111	65.12932	3.662
1	1	9	6	1.43111	65.12932	0.982
1	-3	-5	6	1.41258	66.09208	1.407
1	2	5	6	1.41258	66.09208	1.011
0	3	0	6	1.38771	67.43299	7.428
0	1	11	6	1.37555	68.11076	0.675
0	3	3	6	1.34316	69.98865	0.584

3	0	3	6	1.34316	69.98865	0.039
0	0	12	2	1.33595	70.42246	3.972
1	2	-7	6	1.29691	72.87554	0.937
2	1	7	6	1.29691	72.87554	1.448
0	2	10	6	1.27012	74.67056	3.850
1	-3	-8	6	1.23759	76.98618	2.589
1	2	8	6	1.23759	76.98618	0.228
3	0	6	6	1.23152	77.43575	0.102
0	3	6	6	1.23152	77.43575	0.185
2	2	0	6	1.20180	79.72624	1.171
2	0	11	6	1.19387	80.36323	0.025

00-124 calcite

h	k	l	m	d	th2	F ²
0	1	2	6	3.84557	26.90056	7.592
1	0	4	6	3.02805	34.36298	192.682
0	0	6	2	2.83611	36.76894	6.431
1	1	0	6	2.48898	42.12409	39.440
1	1	3	12	2.27920	46.21471	75.108
2	0	2	6	2.08950	50.69214	71.422
0	2	4	6	1.92278	55.44672	34.941
0	1	8	6	1.90752	55.92901	112.176
1	1	6	12	1.87073	57.12897	132.179
2	1	1	12	1.62200	66.93597	31.251
1	2	2	12	1.60034	67.96451	97.013
1	0	10	6	1.58282	68.82145	10.784
2	1	4	12	1.52162	72.00908	57.466
2	0	8	6	1.51403	72.42743	26.958
1	1	9	12	1.50559	72.89823	31.270
1	2	5	12	1.46966	74.98154	24.748
0	3	0	6	1.43701	76.99232	81.531
0	0	12	2	1.41805	78.21593	48.012

00-158 calcite

h	k	l	m	d	th2	F ²
0	1	2	6	3.84449	26.90825	2.346
1	0	4	6	3.02736	34.37107	60.029
0	0	6	2	2.83570	36.77441	1.883
1	1	0	6	2.48819	42.13802	12.951
1	1	3	12	2.27855	46.22878	21.746
2	0	2	6	2.08887	50.70871	20.847
0	2	4	6	1.92225	55.46361	11.605
0	1	8	6	1.90719	55.93979	34.619
1	1	6	12	1.87028	57.14399	37.992
2	1	1	12	1.62149	66.95976	8.378
1	2	2	12	1.59984	67.98841	27.216
1	0	10	6	1.58256	68.83453	3.196
2	1	4	12	1.52118	72.03353	19.306

2	0	8	6	1.51368	72.44659	9.122
1	1	9	12	1.50528	72.91571	8.178
1	2	5	12	1.46924	75.00646	6.414
0	3	0	6	1.43656	77.02108	24.609
0	0	12	2	1.41785	78.22930	13.899

00-158 dolomite

h	k	l	m	d	th2	F ²
0	0	3	2	5.33631	19.29923	0.129
1	0	1	6	4.02548	25.67723	2.553
0	1	2	6	3.69064	28.05241	5.862
1	0	4	6	2.88387	36.13871	318.781
0	0	6	2	2.66815	39.17487	23.199
0	1	5	6	2.53708	41.28846	19.904
1	1	0	6	2.40127	43.74042	41.789
1	1	3	6	2.18978	48.21902	56.241
1	-2	-3	6	2.18978	48.21902	118.148
0	2	1	6	2.06223	51.41105	23.122
2	0	2	6	2.01274	52.77135	108.569
1	0	7	6	2.00400	53.01938	0.629
0	2	4	6	1.84532	57.98973	33.703
0	1	8	6	1.80325	59.47680	146.584
1	1	6	6	1.78487	60.15197	143.345
1	-2	-6	6	1.78487	60.15197	75.100
0	0	9	2	1.77877	60.37978	8.774
2	0	5	6	1.74399	61.71377	5.878
1	2	-1	6	1.56447	69.74442	30.804
2	1	1	6	1.56447	69.74442	19.571
1	-3	-2	6	1.54253	70.88430	35.576
1	2	2	6	1.54253	70.88430	92.502
0	2	7	6	1.53859	71.09352	3.116
1	0	10	6	1.49404	73.55417	11.620
1	2	-4	6	1.46318	75.37150	31.162
2	1	4	6	1.46318	75.37150	48.173
2	0	8	6	1.44194	76.68134	34.531
1	-2	-9	6	1.42933	77.48306	31.025
1	1	9	6	1.42933	77.48306	24.428
1	-3	-5	6	1.41110	78.67604	8.995
1	2	5	6	1.41110	78.67604	24.645
0	3	0	6	1.38637	80.36107	120.273

02-061 calcite

h	k	l	m	d	th2	F ²
0	1	2	6	3.84521	26.90309	9.204
1	0	4	6	3.02816	34.36167	243.277
0	0	6	2	2.83681	36.75952	8.504
1	1	0	6	2.48853	42.13200	49.033
1	1	3	12	2.27895	46.22011	92.390

2	0	2	6	2.08918	50.70048	83.294
0	2	4	6	1.92261	55.45227	41.921
0	1	8	6	1.90784	55.91904	134.590
1	1	6	12	1.87074	57.12857	150.380
2	1	1	12	1.62171	66.94926	36.357
1	2	2	12	1.60007	67.97720	104.796
1	0	10	6	1.58312	68.80654	10.708
2	1	4	12	1.52143	72.01947	65.347
2	0	8	6	1.51408	72.42433	30.610
1	1	9	12	1.50573	72.89051	35.752
1	2	5	12	1.46951	74.99031	28.100
0	3	0	6	1.43675	77.00866	91.497
0	0	12	2	1.41840	78.19289	53.789

02-126 dolomite

h	k	l	m	d	th2	F ²
0	0	3	2	5.33428	19.30662	0.163
1	0	1	6	4.02488	25.68111	2.144
0	1	2	6	3.68996	28.05772	4.701
1	0	4	6	2.88312	36.14847	381.861
0	0	6	2	2.66714	39.19035	34.466
0	1	5	6	2.53635	41.30089	19.867
1	1	0	6	2.40095	43.74655	48.016
1	1	3	6	2.18940	48.22798	131.061
1	-2	-3	6	2.18940	48.22798	80.500
0	2	1	6	2.06195	51.41862	22.764
2	0	2	6	2.01244	52.77981	105.702
1	0	7	6	2.00336	53.03781	0.235
0	2	4	6	1.84498	58.00152	38.030
0	1	8	6	1.80265	59.49862	173.364
1	1	6	6	1.78444	60.16813	67.951
1	-2	-6	6	1.78444	60.16813	142.669
0	0	9	2	1.77809	60.40509	8.725
2	0	5	6	1.74363	61.72789	11.740
1	2	-1	6	1.56426	69.75525	16.898
2	1	1	6	1.56426	69.75525	48.675
1	-3	-2	6	1.54231	70.89591	84.034
1	2	2	6	1.54231	70.89591	24.839
0	2	7	6	1.53821	71.11356	8.769
1	0	10	6	1.49352	73.58396	4.922
1	2	-4	6	1.46294	75.38621	56.962
2	1	4	6	1.46294	75.38621	35.062
2	0	8	6	1.44156	76.70501	39.212
1	-2	-9	6	1.42891	77.50994	24.321
1	1	9	6	1.42891	77.50994	48.195
1	-3	-5	6	1.41084	78.69305	23.304
1	2	5	6	1.41084	78.69305	16.319
0	3	0	6	1.38619	80.37396	145.987

02-127 calcite

h	k	l	m	d	th2	F ²
0	1	2	6	3.84387	26.91271	3.241
1	0	4	6	3.02691	34.37633	82.521
0	0	6	2	2.83535	36.77917	2.732
1	1	0	6	2.48776	42.14562	17.010
1	1	3	12	2.27817	46.23683	31.565
2	0	2	6	2.08851	50.71791	29.896
0	2	4	6	1.92193	55.47341	15.002
0	1	8	6	1.90693	55.94797	47.485
1	1	6	12	1.87000	57.15346	54.959
2	1	1	12	1.62121	66.97278	12.805
1	2	2	12	1.59957	68.00159	39.846
1	0	10	6	1.58235	68.84486	4.447
2	1	4	12	1.52092	72.04738	24.482
2	0	8	6	1.51346	72.45905	11.499
1	1	9	12	1.50507	72.92776	12.714
1	2	5	12	1.46900	75.02084	10.030
0	3	0	6	1.43631	77.03679	33.921
0	0	12	2	1.41767	78.24097	19.814

02-127 dolomite

h	k	l	m	d	th2	F ²
0	0	3	2	5.33840	19.29160	0.113
1	0	1	6	4.02792	25.66146	2.381
0	1	2	6	3.69275	28.03609	5.229
1	0	4	6	2.88532	36.12000	296.785
0	0	6	2	2.66920	39.15891	22.908
0	1	5	6	2.53829	41.26792	19.797
1	1	0	6	2.40275	43.71200	38.679
1	1	3	6	2.19105	48.18929	117.728
1	-2	-3	6	2.19105	48.18929	50.913
0	2	1	6	2.06350	51.37717	24.757
2	0	2	6	2.01396	52.73703	99.107
1	0	7	6	2.00489	52.99400	1.033
0	2	4	6	1.84637	57.95355	31.635
0	1	8	6	1.80403	59.44839	140.042
1	1	6	6	1.78579	60.11769	68.328
1	-2	-6	6	1.78579	60.11769	133.167
0	0	9	2	1.77947	60.35369	9.350
2	0	5	6	1.74495	61.67606	4.895
1	2	-1	6	1.56544	69.69525	21.866
2	1	1	6	1.56544	69.69525	26.967
1	-3	-2	6	1.54347	70.83459	85.357
1	2	2	6	1.54347	70.83459	30.477
0	2	7	6	1.53938	71.05132	2.223
1	0	10	6	1.49467	73.51814	9.217
1	2	-4	6	1.46404	75.31948	47.329
2	1	4	6	1.46404	75.31948	29.518
2	0	8	6	1.44266	76.63599	33.148
1	-2	-9	6	1.43000	77.43970	28.371

1	1	9	6	1.43000	77.43970	27.884
1	-3	-5	6	1.41191	78.62214	28.378
1	2	5	6	1.41191	78.62214	6.842
0	3	0	6	1.38723	80.30128	119.222

02-128 dolomite

h	k	l	m	d	th2	F ²
0	0	3	2	5.33060	19.32009	0.111
1	0	1	6	4.02364	25.68922	2.842
0	1	2	6	3.68859	28.06834	5.295
1	0	4	6	2.88169	36.16700	295.109
0	0	6	2	2.66530	39.21852	20.573
0	1	5	6	2.53499	41.32420	22.532
1	1	0	6	2.40026	43.75965	44.211
1	1	3	6	2.18862	48.24609	118.989
1	-2	-3	6	2.18862	48.24609	41.076
0	2	1	6	2.06135	51.43470	28.453
2	0	2	6	2.01182	52.79745	96.426
1	0	7	6	2.00216	53.07191	2.055
0	2	4	6	1.84429	58.02509	39.287
0	1	8	6	1.80154	59.53886	149.018
1	1	6	6	1.78361	60.19910	67.687
1	-2	-6	6	1.78361	60.19910	128.927
0	0	9	2	1.77687	60.45116	11.323
2	0	5	6	1.74293	61.75564	2.066
1	2	-1	6	1.56381	69.77830	27.154
2	1	1	6	1.56381	69.77830	17.521
1	-3	-2	6	1.54185	70.92036	83.852
1	2	2	6	1.54185	70.92036	31.701
0	2	7	6	1.53749	71.15194	0.759
1	0	10	6	1.49257	73.63867	10.996
1	2	-4	6	1.46244	75.41622	58.094
2	1	4	6	1.46244	75.41622	39.100
2	0	8	6	1.44085	76.74994	42.945
1	-2	-9	6	1.42813	77.56026	35.934
1	1	9	6	1.42813	77.56026	16.409
1	-3	-5	6	1.41033	78.72721	35.326
1	2	5	6	1.41033	78.72721	2.611
0	3	0	6	1.38579	80.40152	131.502

02-139 calcite

h	k	l	m	d	th2	F ²
0	1	2	6	3.84710	26.88964	7.994
1	0	4	6	3.02946	34.34649	197.253
0	0	6	2	2.83774	36.74708	6.452
1	1	0	6	2.48986	42.10848	40.535
1	1	3	12	2.28009	46.19567	76.745
2	0	2	6	2.09027	50.67222	73.734

0	2	4	6	1.92355	55.42271	36.141
0	1	8	6	1.90854	55.89671	114.833
1	1	6	12	1.87157	57.10092	136.924
2	1	1	12	1.62258	66.90902	31.401
1	2	2	12	1.60091	67.93658	100.418
1	0	10	6	1.58368	68.77871	11.585
2	1	4	12	1.52220	71.97728	59.770
2	0	8	6	1.51473	72.38838	28.002
1	1	9	12	1.50634	72.85647	31.603
1	2	5	12	1.47024	74.94684	24.776
0	3	0	6	1.43752	76.96008	83.852
0	0	12	2	1.41887	78.16246	48.938

05-005 dolomite

h	k	l	m	d	th2	F ²
0	0	3	2	5.32837	19.32815	0.095
1	0	1	6	4.02354	25.68971	2.509
0	1	2	6	3.68827	28.07069	5.179
1	0	4	6	2.88107	36.17490	241.226
0	0	6	2	2.66418	39.23540	16.461
0	1	5	6	2.53432	41.33529	19.794
1	1	0	6	2.40027	43.75928	33.277
1	1	3	6	2.18847	48.24933	108.173
1	-2	-3	6	2.18847	48.24933	33.631
0	2	1	6	2.06134	51.43465	26.554
2	0	2	6	2.01177	52.79853	91.361
1	0	7	6	2.00152	53.08998	2.646
0	2	4	6	1.84413	58.03029	29.026
0	1	8	6	1.80093	59.56078	121.830
1	1	6	6	1.78327	60.21111	66.353
1	-2	-6	6	1.78327	60.21111	123.568
0	0	9	2	1.77612	60.47876	10.314
2	0	5	6	1.74271	61.76368	1.620
1	2	-1	6	1.56381	69.77799	27.455
2	1	1	6	1.56381	69.77799	14.536
1	-3	-2	6	1.54183	70.92101	84.758
1	2	2	6	1.54183	70.92101	33.675
0	2	7	6	1.53720	71.16694	0.343
1	0	10	6	1.49202	73.66948	12.524
1	2	-4	6	1.46236	75.42052	45.205
2	1	4	6	1.46236	75.42052	29.112
2	0	8	6	1.44053	76.76910	32.653
1	-2	-9	6	1.42774	77.58459	34.892
1	1	9	6	1.42774	77.58459	15.058
1	-3	-5	6	1.41021	78.73418	35.556
1	2	5	6	1.41021	78.73418	2.047
0	3	0	6	1.38580	80.40076	110.319

05-007 dolomite

h	k	l	m	d	th2	F ²
0	0	3	2	5.33031	19.32113	0.141
1	0	1	6	4.02501	25.68027	3.795
0	1	2	6	3.68962	28.06035	5.747
1	0	4	6	2.88212	36.16141	372.015
0	0	6	2	2.66516	39.22071	28.054
0	1	5	6	2.53525	41.31973	29.091
1	1	0	6	2.40115	43.74267	52.340
1	1	3	6	2.18927	48.23082	54.310
1	-2	-3	6	2.18927	48.23082	150.488
0	2	1	6	2.06209	51.41473	35.216
2	0	2	6	2.01251	52.77799	114.981
1	0	7	6	2.00225	53.06938	2.090
0	2	4	6	1.84481	58.00736	43.623
0	1	8	6	1.80159	59.53718	177.936
1	1	6	6	1.78393	60.18716	152.906
1	-2	-6	6	1.78393	60.18716	77.788
0	0	9	2	1.77677	60.45475	14.660
2	0	5	6	1.74335	61.73896	2.516
1	2	-1	6	1.56438	69.74914	23.678
2	1	1	6	1.56438	69.74914	34.785
1	-3	-2	6	1.54240	70.89154	34.193
1	2	2	6	1.54240	70.89154	95.673
0	2	7	6	1.53776	71.13739	1.092
1	0	10	6	1.49257	73.63860	9.866
1	2	-4	6	1.46290	75.38855	41.177
2	1	4	6	1.46290	75.38855	62.151
2	0	8	6	1.44106	76.73639	44.976
1	-2	-9	6	1.42827	77.55142	21.083
1	1	9	6	1.42827	77.55142	45.994
1	-3	-5	6	1.41073	78.70026	3.709
1	2	5	6	1.41073	78.70026	45.373
0	3	0	6	1.38630	80.36580	150.450

05-010 dolomite

h	k	l	m	d	th2	F ²
0	0	3	2	5.33059	19.32013	0.071
1	0	1	6	4.02436	25.68451	1.762
0	1	2	6	3.68915	28.06402	3.534
1	0	4	6	2.88196	36.16358	194.093
0	0	6	2	2.66529	39.21861	13.849
0	1	5	6	2.53516	41.32116	14.514
1	1	0	6	2.40073	43.75079	28.291
1	1	3	6	2.18897	48.23790	80.848
1	-2	-3	6	2.18897	48.23790	29.459
0	2	1	6	2.06174	51.42426	18.859
2	0	2	6	2.01218	52.78721	67.932
1	0	7	6	2.00225	53.06946	1.251
0	2	4	6	1.84457	58.01549	25.503
0	1	8	6	1.80160	59.53661	101.990

1	1	6	6	1.78379	60.19210	48.768
1	-2	-6	6	1.78379	60.19210	92.920
0	0	9	2	1.77686	60.45131	7.537
2	0	5	6	1.74316	61.74642	1.915
1	2	-1	6	1.56411	69.76306	18.708
2	1	1	6	1.56411	69.76306	14.376
1	-3	-2	6	1.54214	70.90524	62.814
1	2	2	6	1.54214	70.90524	23.712
0	2	7	6	1.53765	71.14339	0.718
1	0	10	6	1.49260	73.63670	8.191
1	2	-4	6	1.46268	75.40147	40.038
2	1	4	6	1.46268	75.40147	26.332
2	0	8	6	1.44098	76.74165	29.268
1	-2	-9	6	1.42822	77.55412	25.017
1	1	9	6	1.42822	77.55412	14.477
1	-3	-5	6	1.41054	78.71268	24.939
1	2	5	6	1.41054	78.71268	2.674
0	3	0	6	1.38606	80.38288	95.331

05-023 calcite

h	k	l	m	d	th2	F ²
0	1	2	6	3.84665	26.89283	7.516
1	0	4	6	3.02913	34.35036	196.099
0	0	6	2	2.83746	36.75079	6.636
1	1	0	6	2.48955	42.11384	41.199
1	1	3	12	2.27982	46.20142	79.451
2	0	2	6	2.09002	50.67874	76.455
0	2	4	6	1.92333	55.42973	38.454
0	1	8	6	1.90834	55.90292	123.588
1	1	6	12	1.87136	57.10785	145.220
2	1	1	12	1.62238	66.91821	36.121
1	2	2	12	1.60072	67.94590	111.727
1	0	10	6	1.58352	68.78661	12.354
2	1	4	12	1.52202	71.98714	68.296
2	0	8	6	1.51457	72.39755	32.110
1	1	9	12	1.50617	72.86546	37.211
1	2	5	12	1.47007	74.95712	29.749
0	3	0	6	1.43734	76.97115	99.193
0	0	12	2	1.41873	78.17154	58.765

05-023 dolomite

h	k	l	m	d	th2	F ²
0	0	3	2	5.34544	19.26594	0.010
1	0	1	6	4.02984	25.64900	0.221
0	1	2	6	3.69501	28.01861	0.520
1	0	4	6	2.88788	36.08688	26.001
0	0	6	2	2.67272	39.10521	1.928
0	1	5	6	2.54079	41.22547	1.867

1	1	0	6	2.40376	43.69267	3.384
1	1	3	6	2.19230	48.15999	11.283
1	-2	-3	6	2.19230	48.15999	4.431
0	2	1	6	2.06440	51.35316	2.487
2	0	2	6	2.01492	52.70992	9.967
1	0	7	6	2.00712	52.93063	0.151
0	2	4	6	1.84750	57.91476	2.907
0	1	8	6	1.80611	59.37323	13.281
1	1	6	6	1.78726	60.06318	7.230
1	-2	-6	6	1.78726	60.06318	13.748
0	0	9	2	1.78181	60.26590	0.956
2	0	5	6	1.74615	61.62909	0.405
1	2	-1	6	1.56611	69.66101	2.464
2	1	1	6	1.56611	69.66101	2.466
1	-3	-2	6	1.54417	70.79760	9.477
1	2	2	6	1.54417	70.79760	3.583
0	2	7	6	1.54066	70.98370	0.139
1	0	10	6	1.49646	73.41528	1.213
1	2	-4	6	1.46483	75.27169	4.745
2	1	4	6	1.46483	75.27169	2.932
2	0	8	6	1.44394	76.55575	3.339
1	-2	-9	6	1.43143	77.34787	3.199
1	1	9	6	1.43143	77.34787	2.726
1	-3	-5	6	1.41275	78.56634	3.273
1	2	5	6	1.41275	78.56634	0.601
0	3	0	6	1.38781	80.26063	12.397

06-093 calcite

h	k	l	m	d	th2	F ²
0	1	2	6	3.84637	23.10448	6.730
1	0	4	6	3.02904	29.46401	166.834
0	0	6	2	2.83758	31.50196	5.035
1	1	0	6	2.48930	36.05053	34.239
1	1	3	12	2.27964	39.49736	59.745
2	0	2	6	2.08983	43.25685	57.166
0	2	4	6	1.92319	47.22172	28.874
0	1	8	6	1.90837	47.61095	88.972
1	1	6	12	1.87129	48.61461	102.285
2	1	1	12	1.62222	56.69685	21.745
1	2	2	12	1.60057	57.53480	70.773
1	0	10	6	1.58356	58.21162	8.203
2	1	4	12	1.52190	60.81301	44.030
2	0	8	6	1.51452	61.14076	20.691
1	1	9	12	1.50616	61.51698	20.848
1	2	5	12	1.46996	63.20389	16.237
0	3	0	6	1.43720	64.81802	57.499
0	0	12	2	1.41879	65.76444	32.922
2	1	7	12	1.35383	69.35571	12.521
0	2	10	6	1.33612	70.41033	25.544
1	2	8	12	1.29386	73.07272	33.128
3	0	6	6	1.28212	73.85214	4.698
0	3	6	6	1.28212	73.85214	4.698

2	2	0	6	1.24465	76.46773	14.559
1	1	12	12	1.23264	77.35044	27.365
2	2	3	12	1.21575	78.62973	0.271
1	3	1	12	1.19288	80.44087	0.058

06-108 dolomite

h	k	l	m	d	th2	F ²
0	0	3	2	5.32860	19.32742	0.071
1	0	1	6	4.02293	25.69380	2.176
0	1	2	6	3.68782	28.07428	3.854
1	0	4	6	2.88091	36.17722	188.305
0	0	6	2	2.66430	39.23388	13.698
0	1	5	6	2.53424	41.33701	17.381
1	1	0	6	2.39988	43.76709	24.428
1	1	3	6	2.18819	48.25625	27.725
1	-2	-3	6	2.18819	48.25625	96.535
0	2	1	6	2.06101	51.44382	24.551
2	0	2	6	2.01147	52.80743	80.022
1	0	7	6	2.00151	53.09060	2.808
0	2	4	6	1.84391	58.03827	21.632
0	1	8	6	1.80094	59.56088	103.427
1	1	6	6	1.78315	60.21622	113.037
1	-2	-6	6	1.78315	60.21622	60.001
0	0	9	2	1.77620	60.47628	10.394
2	0	5	6	1.74253	61.77109	1.073
1	2	-1	6	1.56355	69.79139	13.399
2	1	1	6	1.56355	69.79139	31.024
1	-3	-2	6	1.54159	70.93422	32.621
1	2	2	6	1.54159	70.93422	82.886
0	2	7	6	1.53709	71.17316	0.279
1	0	10	6	1.49205	73.66857	11.226
1	2	-4	6	1.46216	75.43309	23.523
2	1	4	6	1.46216	75.43309	37.752
2	0	8	6	1.44045	76.77473	26.874
1	-2	-9	6	1.42770	77.58791	14.618
1	1	9	6	1.42770	77.58791	40.628
1	-3	-5	6	1.41004	78.74634	1.763
1	2	5	6	1.41004	78.74634	42.600
0	3	0	6	1.38557	80.41718	105.640

07-020 calcite

h	k	l	m	d	th2	F ²
0	1	2	6	3.84635	26.89503	7.396
1	0	4	6	3.02901	34.35181	187.262
0	0	6	2	2.83753	36.74990	6.200
1	1	0	6	2.48929	42.11855	38.321
1	1	3	12	2.27963	46.20561	71.357
2	0	2	6	2.08981	50.68410	67.453

0	2	4	6	1.92317	55.43456	33.464
0	1	8	6	1.90834	55.90305	106.267
1	1	6	12	1.87127	57.11097	123.520
2	1	1	12	1.62221	66.92620	28.565
1	2	2	12	1.60056	67.95379	88.893
1	0	10	6	1.58353	68.78616	9.922
2	1	4	12	1.52189	71.99464	53.819
2	0	8	6	1.51450	72.40098	25.263
1	1	9	12	1.50614	72.86751	28.244
1	2	5	12	1.46995	74.96437	22.244
0	3	0	6	1.43719	76.98088	74.585
0	0	12	2	1.41876	78.16936	43.612

16-1014 calcite

h	k	l	m	d	th2	F ²
0	1	2	6	3.84604	26.89703	7.219
1	0	4	6	3.02850	34.35757	178.720
0	0	6	2	2.83663	36.76167	5.931
1	1	0	6	2.48924	42.11909	36.365
1	1	3	12	2.27948	46.20856	70.043
2	0	2	6	2.08974	50.68575	66.771
0	2	4	6	1.92302	55.43895	32.214
0	1	8	6	1.90785	55.91832	103.486
1	1	6	12	1.87099	57.11980	123.867
2	1	1	12	1.62217	66.92735	28.775
1	2	2	12	1.60051	67.95556	90.556
1	0	10	6	1.58310	68.80727	10.260
2	1	4	12	1.52180	71.99883	52.810
2	0	8	6	1.51425	72.41462	24.706
1	1	9	12	1.50583	72.88448	28.994
1	2	5	12	1.46984	74.97032	22.744
0	3	0	6	1.43717	76.98201	75.189
0	0	12	2	1.41832	78.19814	44.133

16-1017 calcite

h	k	l	m	d	th2	F ²
0	1	2	6	3.84558	26.90046	7.459
1	0	4	6	3.02789	34.36493	188.232
0	0	6	2	2.83568	36.77470	6.304
1	1	0	6	2.48908	42.12216	38.094
1	1	3	12	2.27923	46.21411	73.070
2	0	2	6	2.08957	50.69041	69.089
0	2	4	6	1.92279	55.44649	33.245
0	1	8	6	1.90731	55.93589	107.374
1	1	6	12	1.87065	57.13153	127.087
2	1	1	12	1.62207	66.93279	29.887
1	2	2	12	1.60039	67.96166	92.220
1	0	10	6	1.58262	68.83125	10.180

2	1	4	12	1.52165	72.00752	53.505
2	0	8	6	1.51394	72.43204	25.066
1	1	9	12	1.50547	72.90499	29.730
1	2	5	12	1.46967	74.98090	23.488
0	3	0	6	1.43707	76.98833	76.165
0	0	12	2	1.41784	78.23002	44.929

16-1018 calcite

h	k	l	m	d	th2	F ²
0	1	2	6	3.84779	26.88475	7.830
1	0	4	6	3.03000	34.34017	194.605
0	0	6	2	2.83824	36.74027	6.381
1	1	0	6	2.49030	42.10062	40.151
1	1	3	12	2.28050	46.18696	75.457
2	0	2	6	2.09064	50.66256	72.225
0	2	4	6	1.92389	55.41198	35.862
0	1	8	6	1.90888	55.88585	113.446
1	1	6	12	1.87191	57.08979	133.988
2	1	1	12	1.62286	66.89554	30.806
1	2	2	12	1.60120	67.92283	98.054
1	0	10	6	1.58396	68.76469	11.259
2	1	4	12	1.52248	71.96246	59.428
2	0	8	6	1.51500	72.37341	27.855
1	1	9	12	1.50660	72.84137	30.982
1	2	5	12	1.47050	74.93118	24.283
0	3	0	6	1.43778	76.94386	82.894
0	0	12	2	1.41912	78.14582	48.271

16-1046 calcite

h	k	l	m	d	th2	F ²
0	1	2	6	3.84779	26.88475	7.830
1	0	4	6	3.03000	34.34017	194.605
0	0	6	2	2.83824	36.74027	6.381
1	1	0	6	2.49030	42.10062	40.151
1	1	3	12	2.28050	46.18696	75.457
2	0	2	6	2.09064	50.66256	72.225
0	2	4	6	1.92389	55.41198	35.862
0	1	8	6	1.90888	55.88585	113.446
1	1	6	12	1.87191	57.08979	133.988
2	1	1	12	1.62286	66.89554	30.806
1	2	2	12	1.60120	67.92283	98.054
1	0	10	6	1.58396	68.76469	11.259
2	1	4	12	1.52248	71.96246	59.428
2	0	8	6	1.51500	72.37341	27.855
1	1	9	12	1.50660	72.84137	30.982
1	2	5	12	1.47050	74.93118	24.283
0	3	0	6	1.43778	76.94386	82.894
0	0	12	2	1.41912	78.14582	48.271

16-1064 dolomite

h	k	l	m	d	th2	F ²
0	0	3	2	5.33437	19.30630	0.074
1	0	1	6	4.02614	25.67293	1.950
0	1	2	6	3.69094	28.05011	3.332
1	0	4	6	2.88361	36.14216	200.103
0	0	6	2	2.66719	39.18967	14.111
0	1	5	6	2.53670	41.29509	15.059
1	1	0	6	2.40175	43.73123	29.812
1	1	3	6	2.19001	48.21363	81.897
1	-2	-3	6	2.19001	48.21363	28.923
0	2	1	6	2.06263	51.40054	19.215
2	0	2	6	2.01307	52.76201	68.284
1	0	7	6	2.00354	53.03266	1.340
0	2	4	6	1.84547	57.98464	26.679
0	1	8	6	1.80279	59.49364	105.013
1	1	6	6	1.78478	60.15543	48.668
1	-2	-6	6	1.78478	60.15543	91.726
0	0	9	2	1.77812	60.40398	7.781
2	0	5	6	1.74405	61.71152	1.514
1	2	-1	6	1.56478	69.72889	19.965
2	1	1	6	1.56478	69.72889	13.742
1	-3	-2	6	1.54281	70.86970	62.121
1	2	2	6	1.54281	70.86970	24.150
0	2	7	6	1.53850	71.09802	0.573
1	0	10	6	1.49360	73.57904	7.990
1	2	-4	6	1.46336	75.36046	40.314
2	1	4	6	1.46336	75.36046	27.265
2	0	8	6	1.44180	76.68971	30.009
1	-2	-9	6	1.42909	77.49811	26.363
1	1	9	6	1.42909	77.49811	12.863
1	-3	-5	6	1.41122	78.66754	26.509
1	2	5	6	1.41122	78.66754	2.366
0	3	0	6	1.38665	80.34173	95.412

E.4 References

Four mineral phases were identified among samples in both sample suites analyzed in Chapter 4. The four mineral phases used in Rietveld refinements are calcite (Markgraf and Reeder 1985; Maslen et al. 1995), dolomite (Althoff 1977; Miser et al. 1987; Reeder and Wenk 1983; Ross and Reeder 1992), quartz (Brill et al. 1939; Glinnemann et al. 1992; Levien et al. 1980), and microcline (Ribbe 1979). Author names indicated for mineral phases can be found next to the phase name for a given structure in a sample located in the TOPAS output reports.

- Althoff P. 1977. Structural refinements of dolomite and a magnesian calcite and implications for dolomite formation in the marine environment. *American Mineralogist* 62:772–783.
- Brill R., Hermann C., and Peters C. 1939. Studien über chemische Bindung mittels Fourieranalyse III. *Die Naturwissenschaften* 27:677–678.
- Glinnemann J., King Jr. H. E., Schulz H., Hahn T., La Placa S. J., and Dacol F. 1992. Crystal structures of the low-temperature quartz-type phases of SiO₂ and GeO₂ at elevated pressure. *Zeitschrift für Kristallographie* 198:177–212.
- Levien L., Prewitt C. T., and Weidner D. J. 1980. Structure and elastic properties of quartz at pressure. *American Mineralogist* 65:920–930.
- Markgraf S. A., and Reeder R. J. 1985. High-temperature structure refinements of calcite and magnesite. *American Mineralogist* 70:590–600.
- Maslen E. N., Streltsov V. A., Streltsova N. R., and Ishizawa N. 1995. Electron density and optical anisotropy in rhombohedral carbonates. III. Synchrotron X-ray studies of CaCO₃, MgCO₃ and MnCO₃. *Acta Crystallographica Section B* 51:929–939.
- Miser D. E., Swinnea J. S., and Steinfink H. 1987. TEM observations and X-ray crystal-structure refinement of a twinned dolomite with a modulated microstructure. *American Mineralogist* 72:188–193.
- Reeder R. J., and Wenk H. R. 1983. Structure refinements of some thermally disordered dolomites. *American Mineralogist* 68:769–776.
- Ribbe P. H. 1979. The structure of a strained intermediate microcline in cryptoperthitic association with twinned plagioclase. *American Mineralogist* 64:402–408.
- Ross N. L., and Reeder R. J. 1992. High-pressure structural study of dolomite and ankerite. *American Mineralogist* 77:412–421.

Appendix F: Raman spectroscopy analysis data

F.1 Data collection and processing

A subset of the suite of impact dykes consisting of carbonate melt rocks characterized from the Haughton impact structure contain blue crystals of moissanite (SiC). Moissanite is a rare terrestrial mineral and the composition of the crystals was identified by electron probe microanalysis using wavelength dispersive spectroscopy (WDS). Naturally occurring and synthetic moissanite crystals have a range of polytypes that belong to the cubic, hexagonal, and rhombohedral crystal classes where the resulting polytype depends on factors present during crystal growth including temperature and pressure.

To determine the polytypes of moissanite crystals in thin sections prepared from Haughton clast-bearing impact melt rocks, micro-Raman spectra were collected using a Renishaw InVia Reflex Raman Spectrometer with 1800 grating at the Surface Science Western facility at the University of Western Ontario. An argon-ion laser with a wavelength of 514 nm was used as the exciting source and the spectrometer was calibrated using a Si film. The sample excitation and Raman scatter collection were performed using a 50x and 100x optical lens on the Raman microscope. An energy of 6 mW was transferred to the sample surface with a spot size of 2 μm . The spectra were analyzed by WiRE software developed by Renishaw.

To confirm moissanite crystals were not the result of contamination during thin section preparation, two thin sections were re-made by avoiding the use of any silicon carbide-containing abrasives; only diamond abrasives were used during grinding and polishing. After this careful preparation, moissanite crystals were still observed within the melt rock samples, thus confirming the in situ identification of moissanite.

The orientation of moissanite crystals within the thin sections examined are random. Based on individual crystal spectral patterns, a parallel or perpendicular orientation relative to the *c*-axis for one of the three identified polytypes (6H, 4H, and 15R) are indicated in Figures F-1 to F-4 and stacked vertically for comparison when needed.

F.2 Moissanite polytype identification

Identification of moissanite polytypes and their orientation with respect to the c -axis were determined using results from various Raman studies (Bauer et al. 2009; Dobrzhinetskaya et al. 2018; He et al. 2017; Nakashima and Harima 1997; Qin et al. 2019).

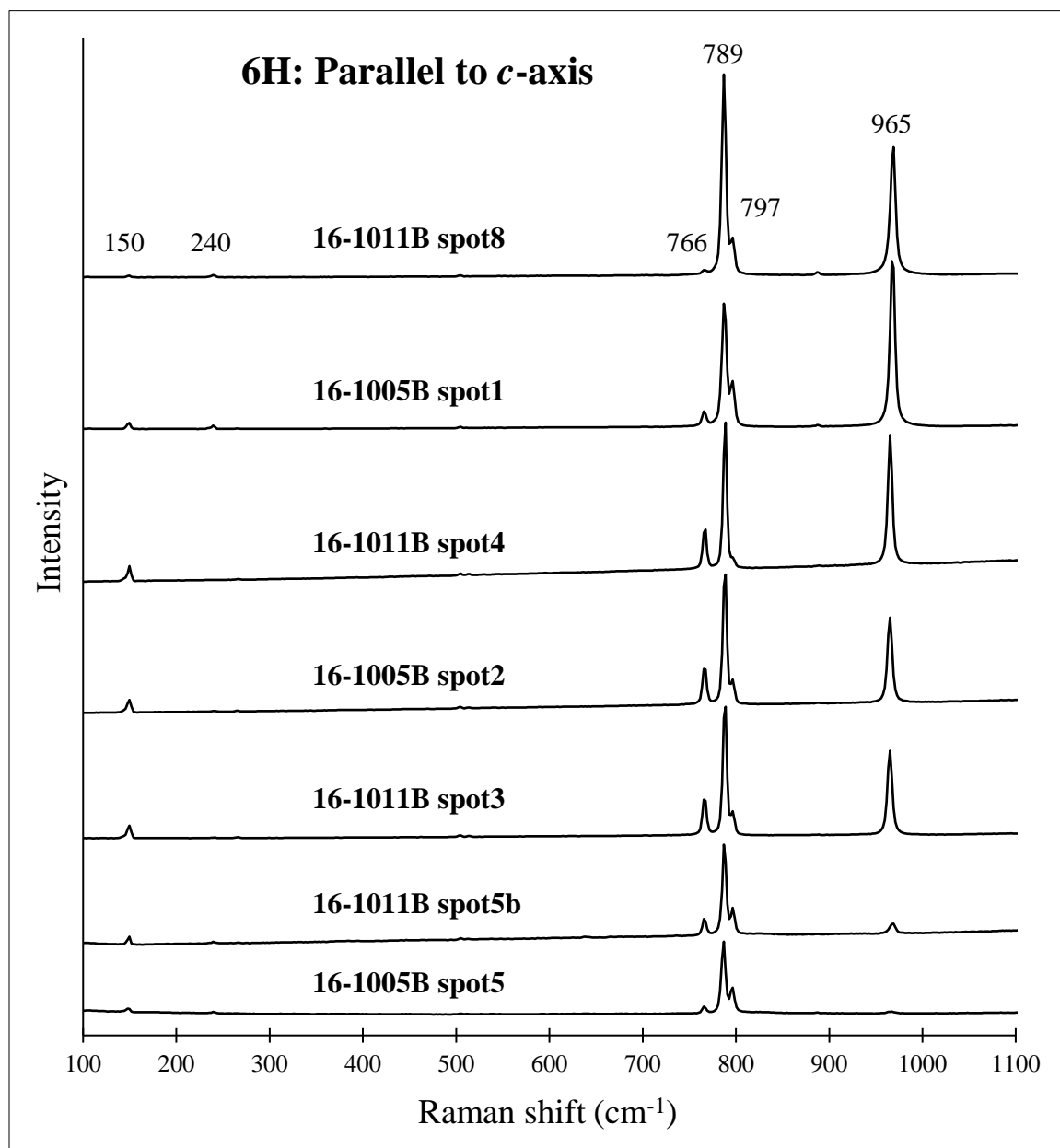


Figure F-1. Raman spectra of moissanite crystals of the 6H polytype oriented relatively parallel to the c -axis with respect to the Ar-ion laser. Values of major peaks are indicated on the top spectrum. Raman spectra have been vertically offset for clarity. Full individual spectra for a given moissanite crystal are available in Figures F-6 to F-22.

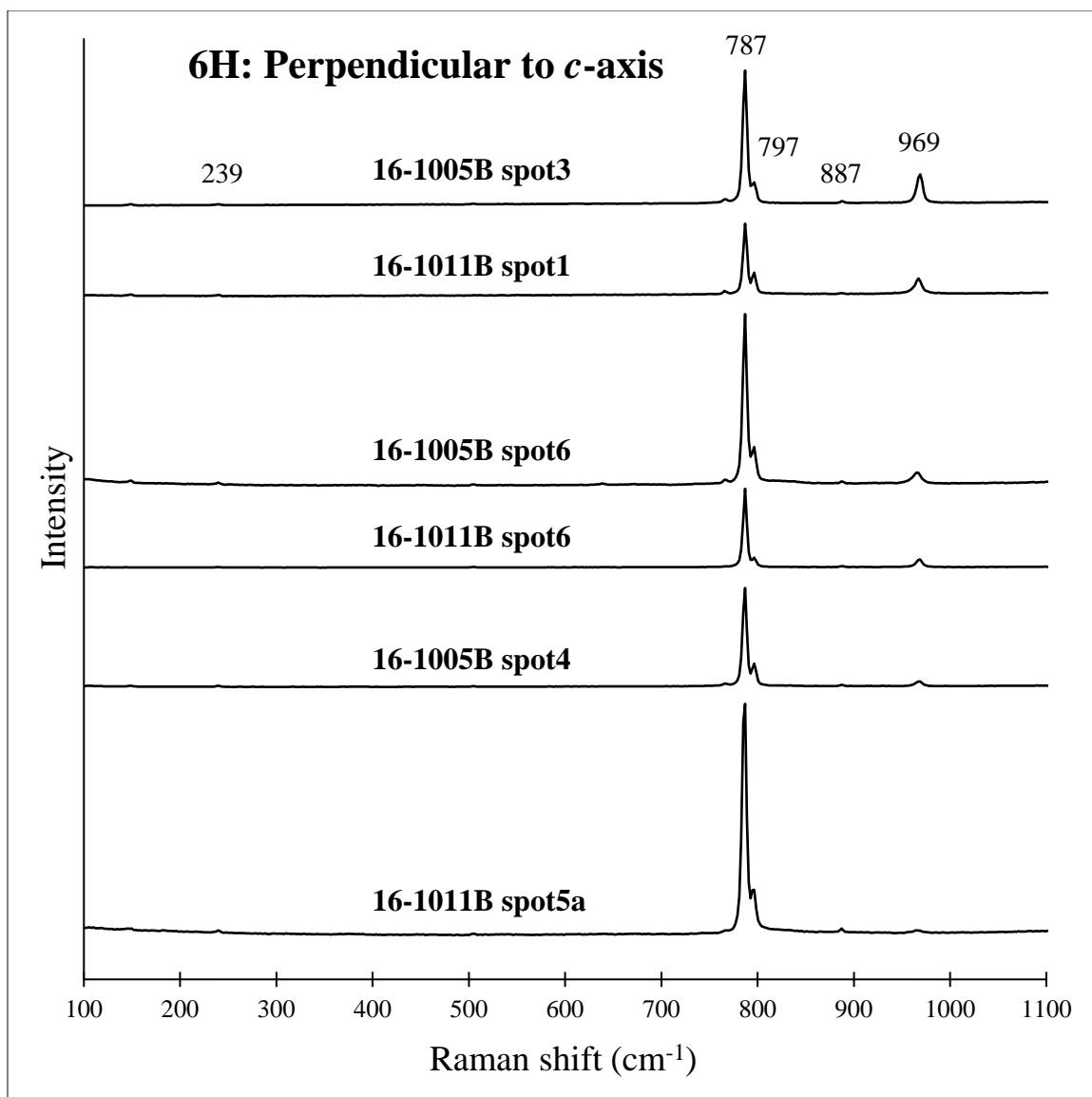


Figure F-2. Raman spectra of moissanite crystals of the 6H polytype oriented relatively perpendicular to the *c*-axis with respect to the Ar-ion laser. Values of major peaks are indicated on the top spectrum. Raman spectra have been vertically offset for clarity. Full individual spectra for a given moissanite crystal are available in Figures F-6 to F-22.

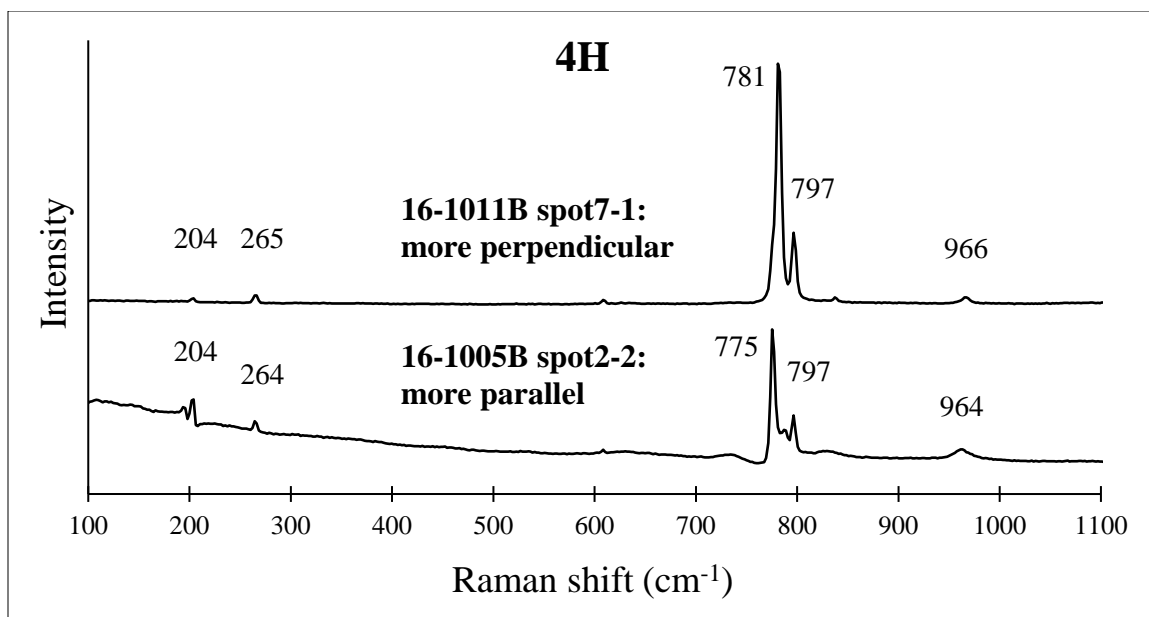


Figure F-3. Raman spectra of 4H polytypes oriented close to parallel and perpendicular to the *c*-axis with respect to the Ar-ion laser, based on peak values. Values of major peaks are indicated. Raman spectra have been vertically offset for clarity. Full individual spectra are available in Figures F-7 and F-20.

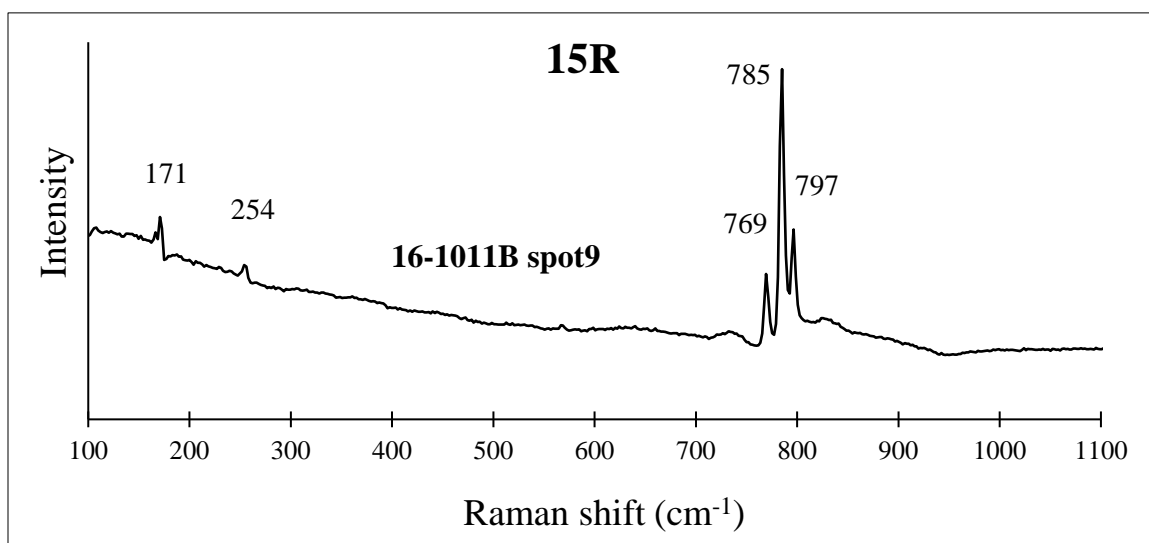


Figure F-4. Raman spectra of 15R polytype oriented nearly parallel to the *c*-axis with respect to the Ar-ion laser. Values of major peaks are indicated. Raman spectra have been vertically offset for clarity. Full spectrum available in Figure F-22.

F.3 Sample 16-1005B

The following figures show the locations of examined moissanite crystals in sample 16-1005B, beginning with an annotated thin section image. This “B” sample is a remade thin section from the original thin section slab cut and was prepared without the use of silicon carbide abrasives. Additionally, the thin section is not carbon coated so there was no carbon that would interfere with gathering the Raman spectra. Moissanite crystals present in the sample are designated as spots from number 1 to 5, as indicated spot in Figure F-5. Each spot was analyzed in up to five locations on the crystal surface, so a spot may have an additional number designation, i.e., spot1-2 if it was the second spectrum acquired at spot 1. Only one representative spectrum is provided for each moissanite crystal.

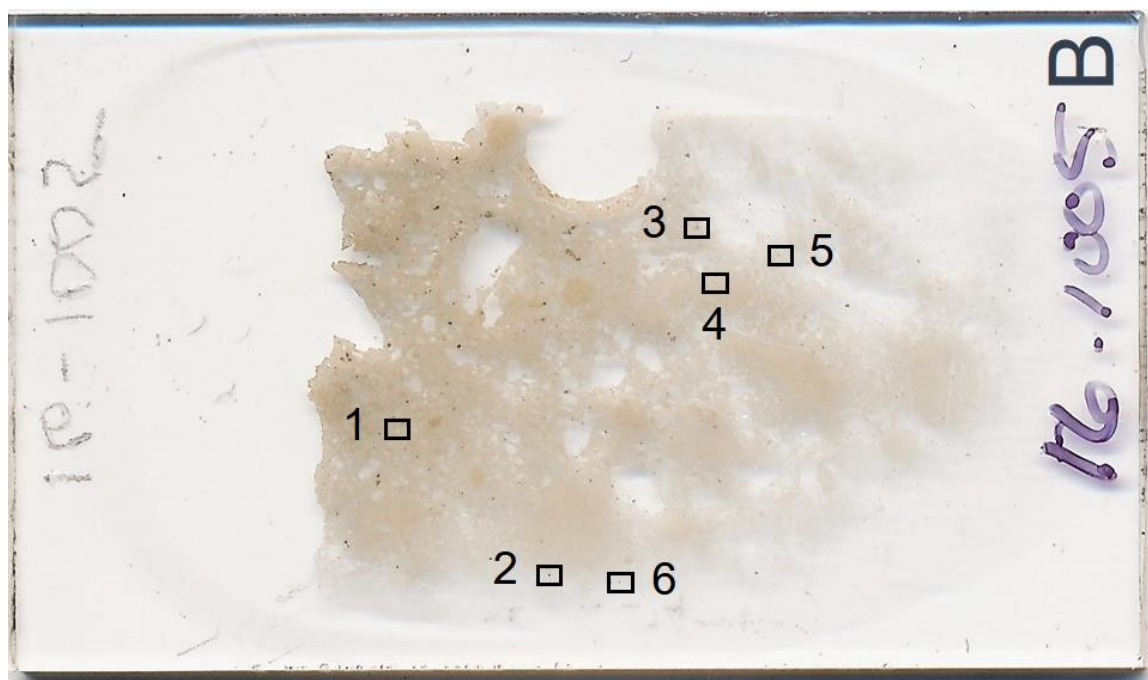


Figure F-5. Scanned image for thin section 16-1005B. Small black boxes indicate the location of moissanite crystals. Spot numbers were assigned to each crystal and are associated with a representative spectrum shown in the following figures.

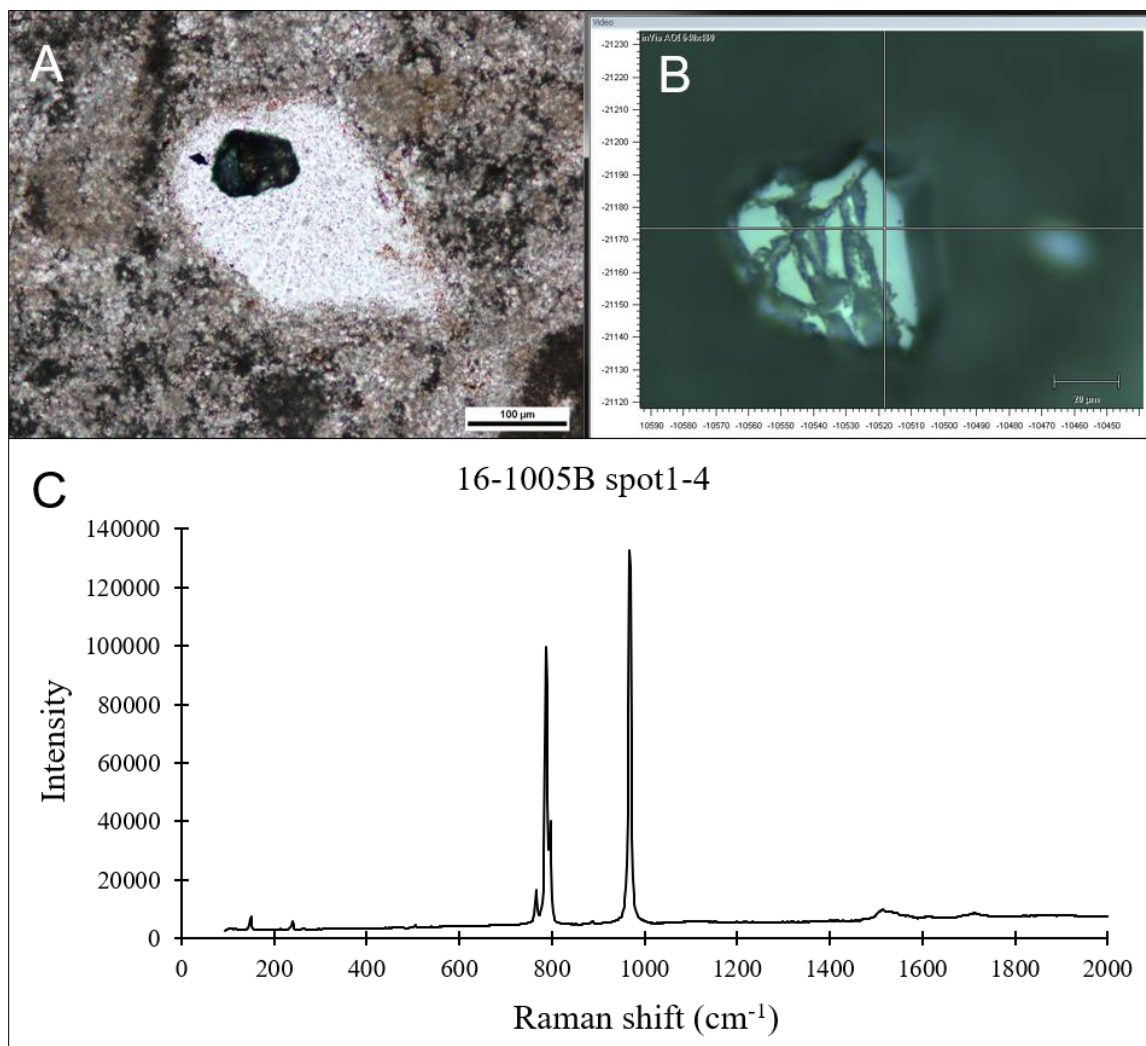


Figure F-6. Sample 16-1005B spot 1. A) In situ photomicrograph of moissanite crystal in plane polarized light (PPL) at 200x magnification. Scale bar is 100 μm . B) Reflected light image of moissanite crystal taken with Raman microscope at 500x magnification. Image is flipped vertically with respect to PPL image. Scale bar is 20 μm . C) Raman spectra obtained for moissanite crystal located at spot 1 in sample 16-1005B.

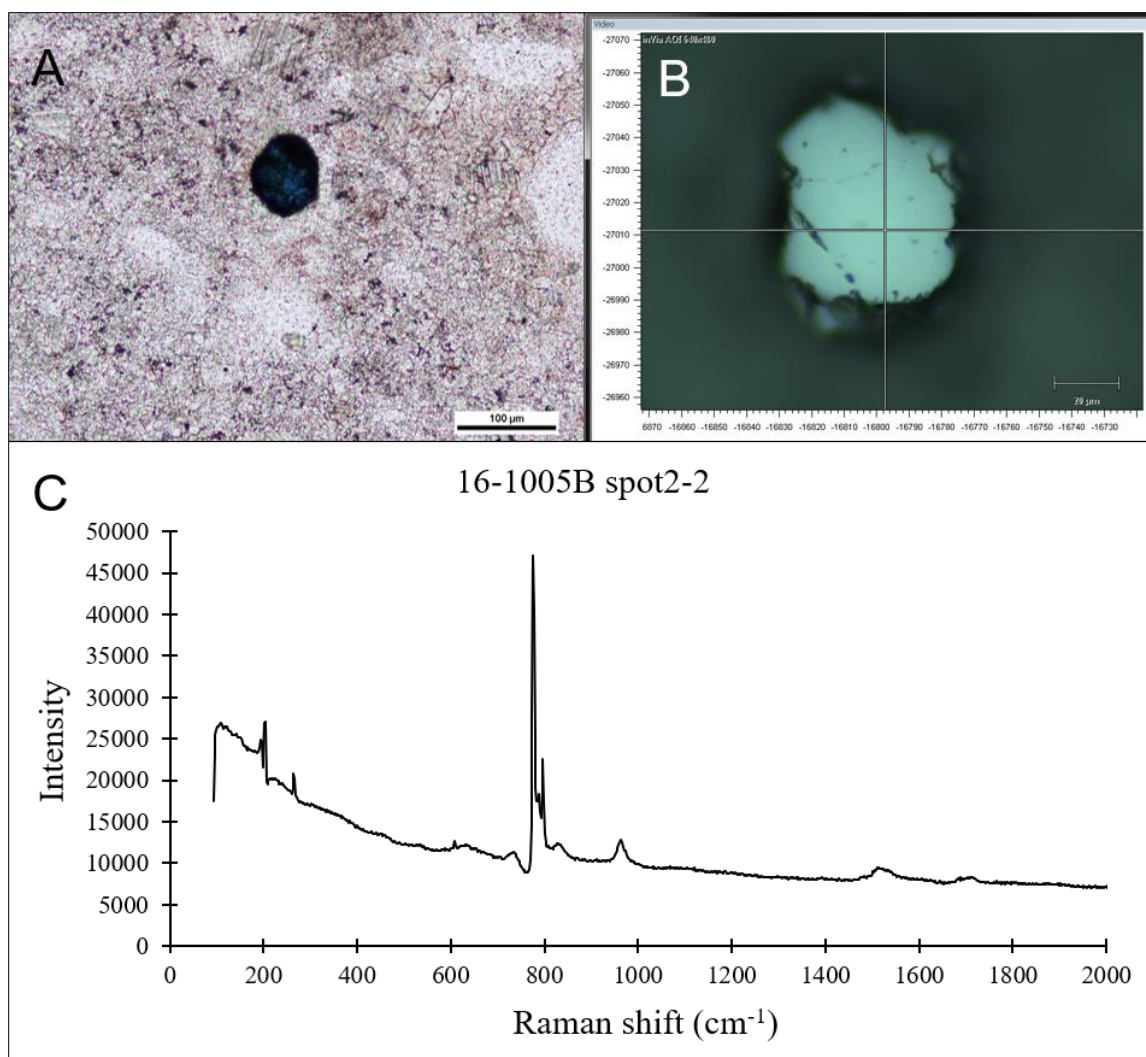


Figure F-7. Sample 16-1005B spot 2. A) In situ photomicrograph of moissanite crystal in plane polarized light (PPL) at 200x magnification. Scale bar is 100 μm . B) Reflected light image of moissanite crystal taken with Raman microscope at 500x magnification. Image is flipped vertically with respect to PPL image. Scale bar is 20 μm . C) Raman spectra obtained for moissanite crystal located at spot 2 in sample 16-1005B.

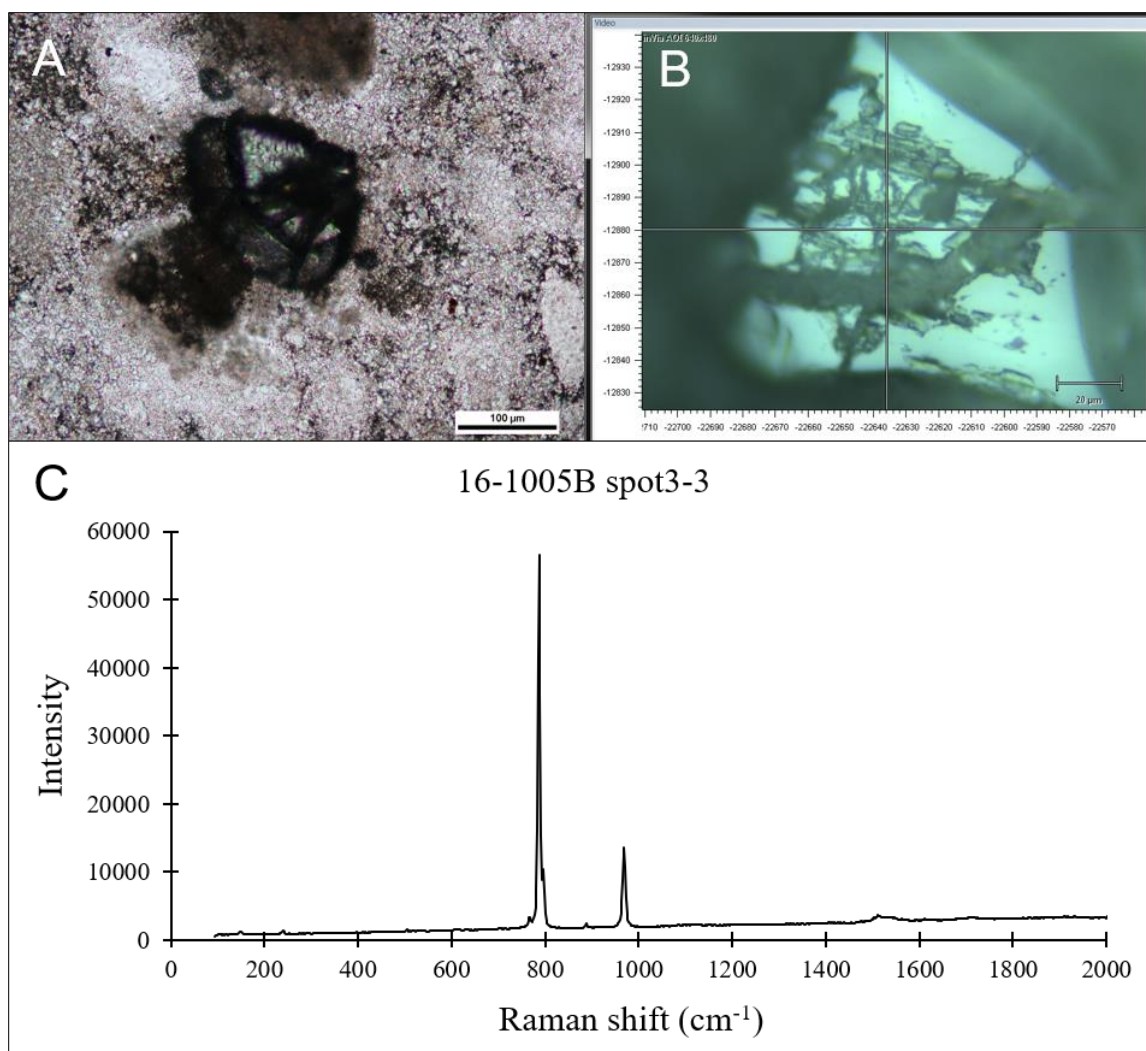


Figure F-8. Sample 16-1005B spot 3. A) In situ photomicrograph of moissanite crystal in plane polarized light (PPL) at 200x magnification. Scale bar is 100 μm . B) Reflected light image of moissanite crystal taken with Raman microscope at 500x magnification. Image is flipped vertically with respect to PPL image. Scale bar is 20 μm . C) Raman spectra obtained for moissanite crystal located at spot 3 in sample 16-1005B.

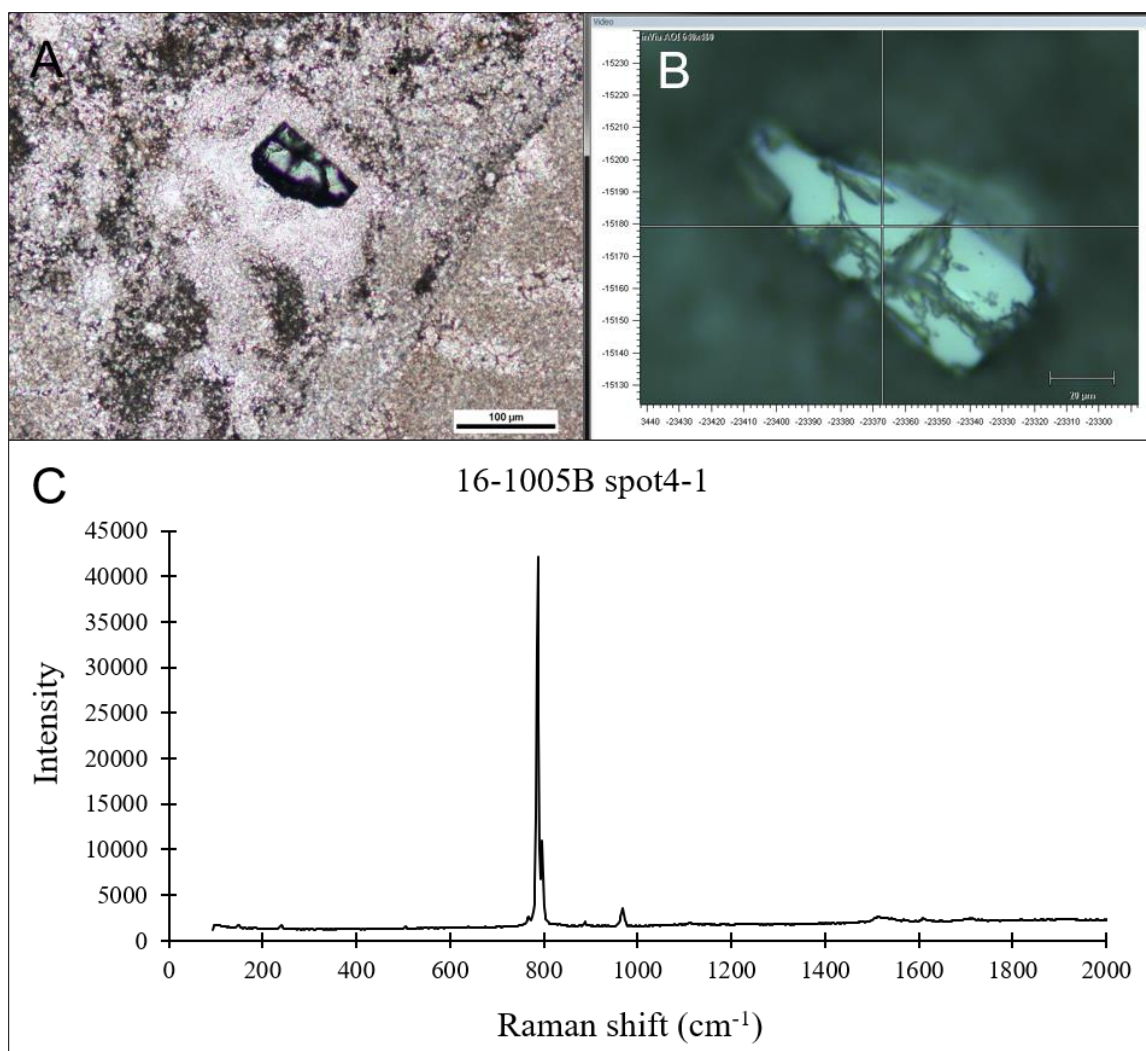


Figure F-9. Sample 16-1005B spot 4. A) In situ photomicrograph of moissanite crystal in plane polarized light (PPL) at 200x magnification. Scale bar is 100 μm . B) Reflected light image of moissanite crystal taken with Raman microscope at 500x magnification. Image is flipped vertically with respect to PPL image. Scale bar is 20 μm . C) Raman spectra obtained for moissanite crystal located at spot 4 in sample 16-1005B.

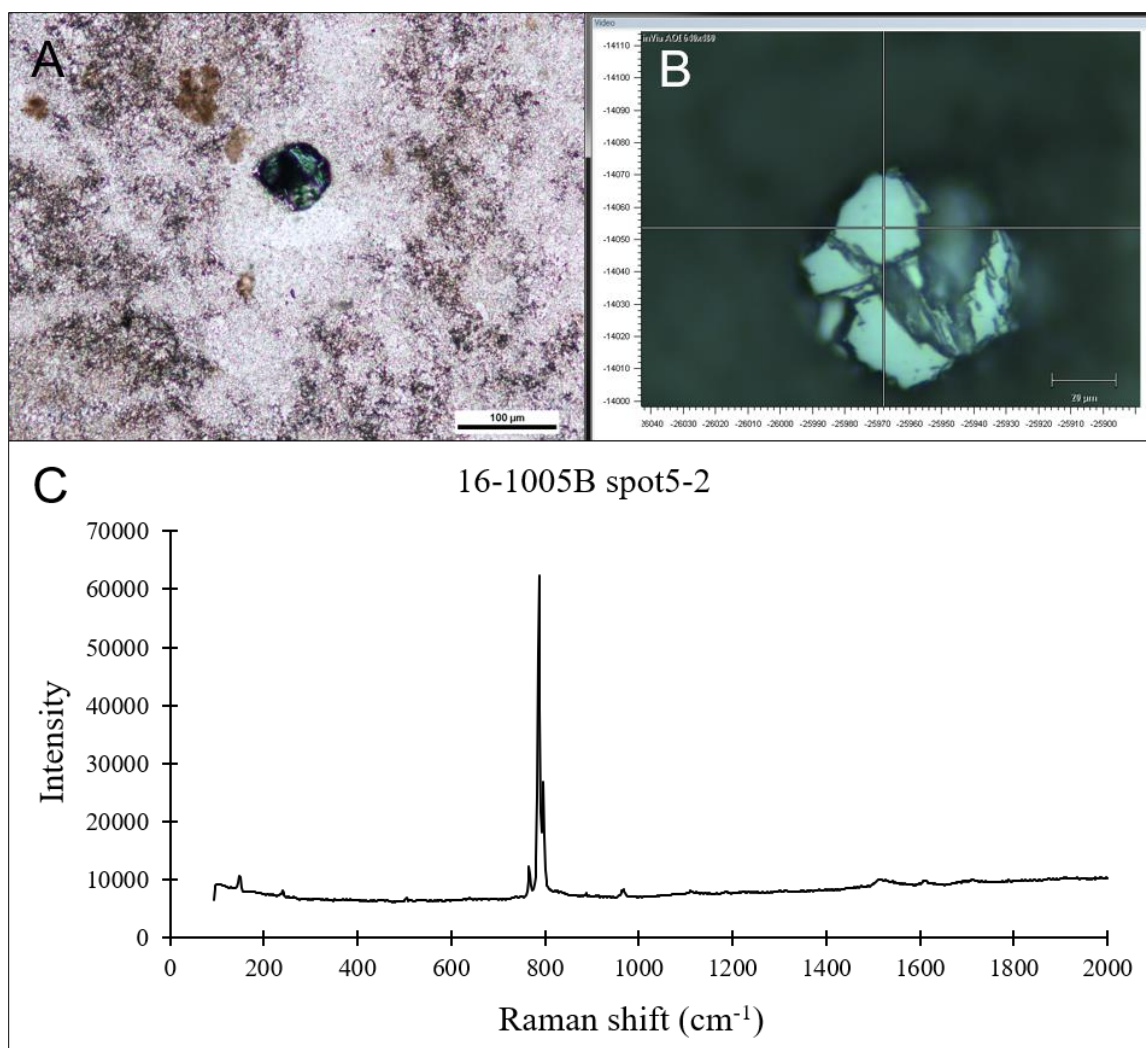


Figure F-10. Sample 16-1005B spot 5. A) In situ photomicrograph of moissanite crystal in plane polarized light (PPL) at 200x magnification. Scale bar is 100 μm . B) Reflected light image of moissanite crystal taken with Raman microscope at 500x magnification. Image is flipped vertically with respect to PPL image. Scale bar is 20 μm . C) Raman spectra obtained for moissanite crystal located at spot 5 in sample 16-1005B.

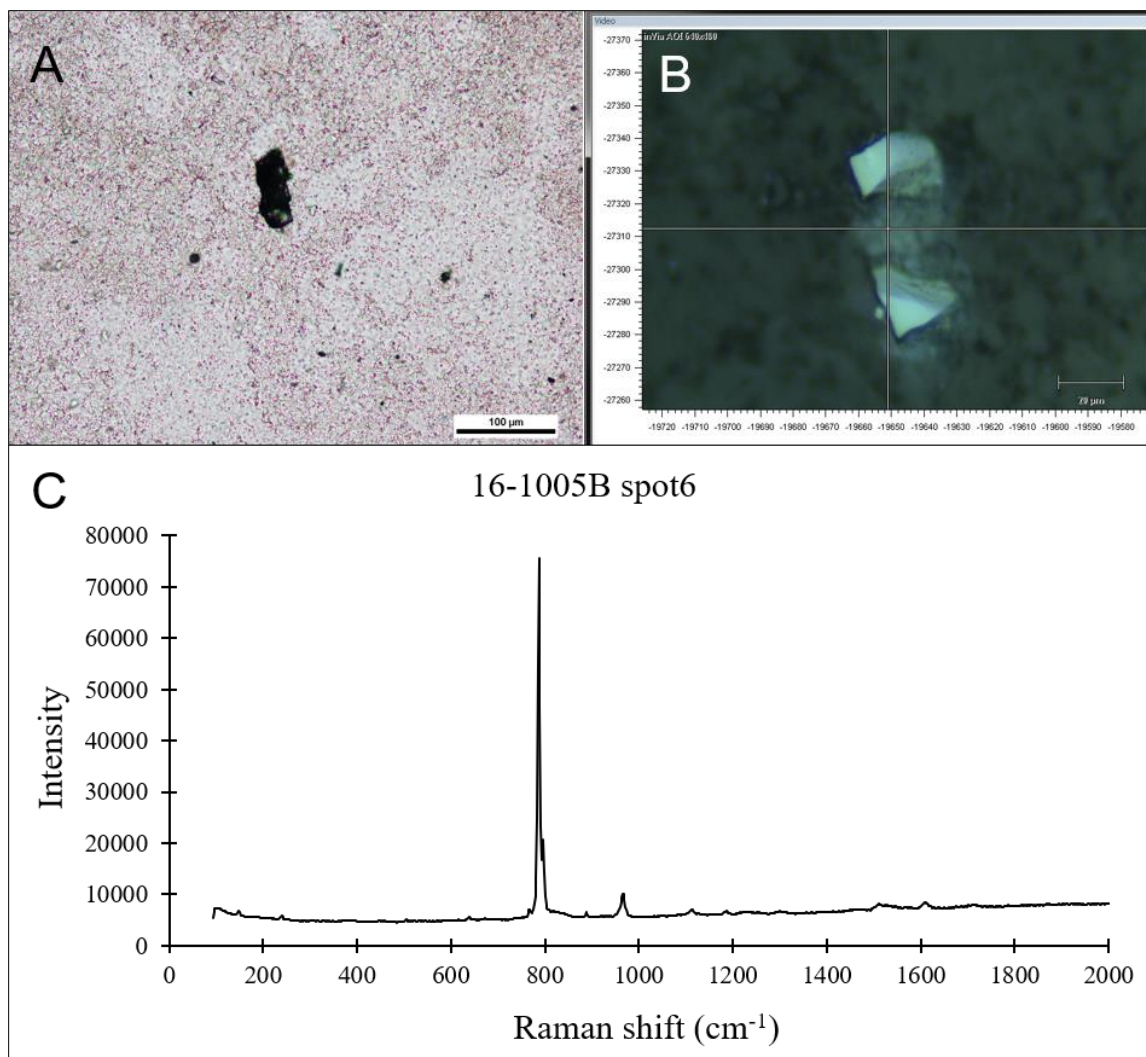


Figure F-11. Sample 16-1005B spot 6. A) In situ photomicrograph of moissanite crystal in plane polarized light (PPL) at 200x magnification. Scale bar is 100 μm . B) Reflected light image of moissanite crystal taken with Raman microscope at 500x magnification. Image is flipped vertically with respect to PPL image. Scale bar is 20 μm . C) Raman spectra obtained for moissanite crystal located at spot 6 in sample 16-1005B.

F.4 Sample 16-1011B

The following figures show the locations of examined moissanite crystals in sample 16-1011B, beginning with an annotated thin section image. This “B” sample is a remade thin section from the original thin section slab cut and was prepared without the use of silicon carbide abrasives. Additionally, the thin section is not carbon coated so there was no carbon that would interfere with gathering the Raman spectra. Moissanite crystals present in the sample are designated as spots from number 1 to 9, as indicated spot in Figure F-12. Each spot was analyzed in up to five locations on the crystal surface, so a spot may have an additional number designation, i.e., spot1-2 if it was the second spectrum acquired at spot 1. Only one representative spectrum is provided for each moissanite crystal.

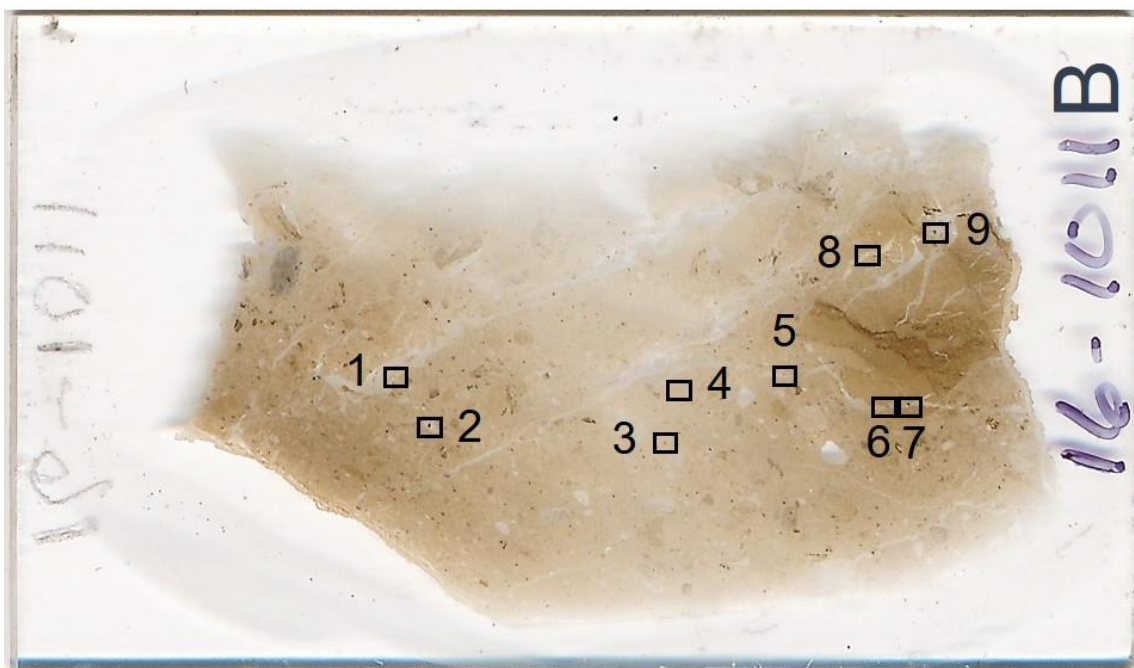


Figure F-12. Scanned image for thin section 16-1011B. Small black boxes indicate the location of moissanite crystals. Spot numbers were assigned to each crystal and are associated with a representative spectrum shown in the following figures.

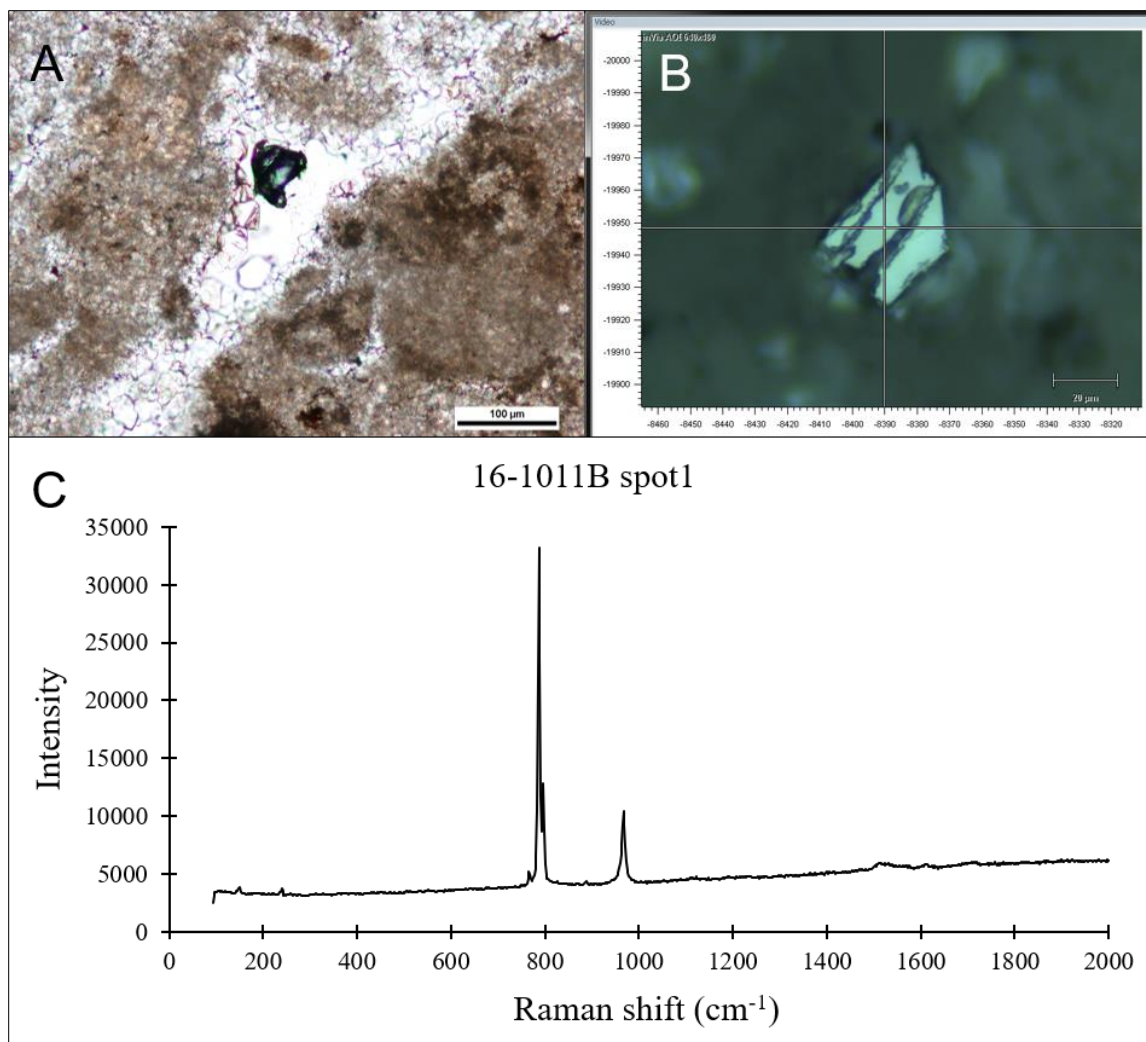


Figure F-13. Sample 16-1011B spot 1. A) In situ photomicrograph of moissanite crystal in plane polarized light (PPL) at 200x magnification. Scale bar is 100 μm . B) Reflected light image of moissanite crystal taken with Raman microscope at 500x magnification. Image is flipped vertically with respect to PPL image. Scale bar is 20 μm . C) Raman spectra obtained for moissanite crystal located at spot 1 in sample 16-1011B.

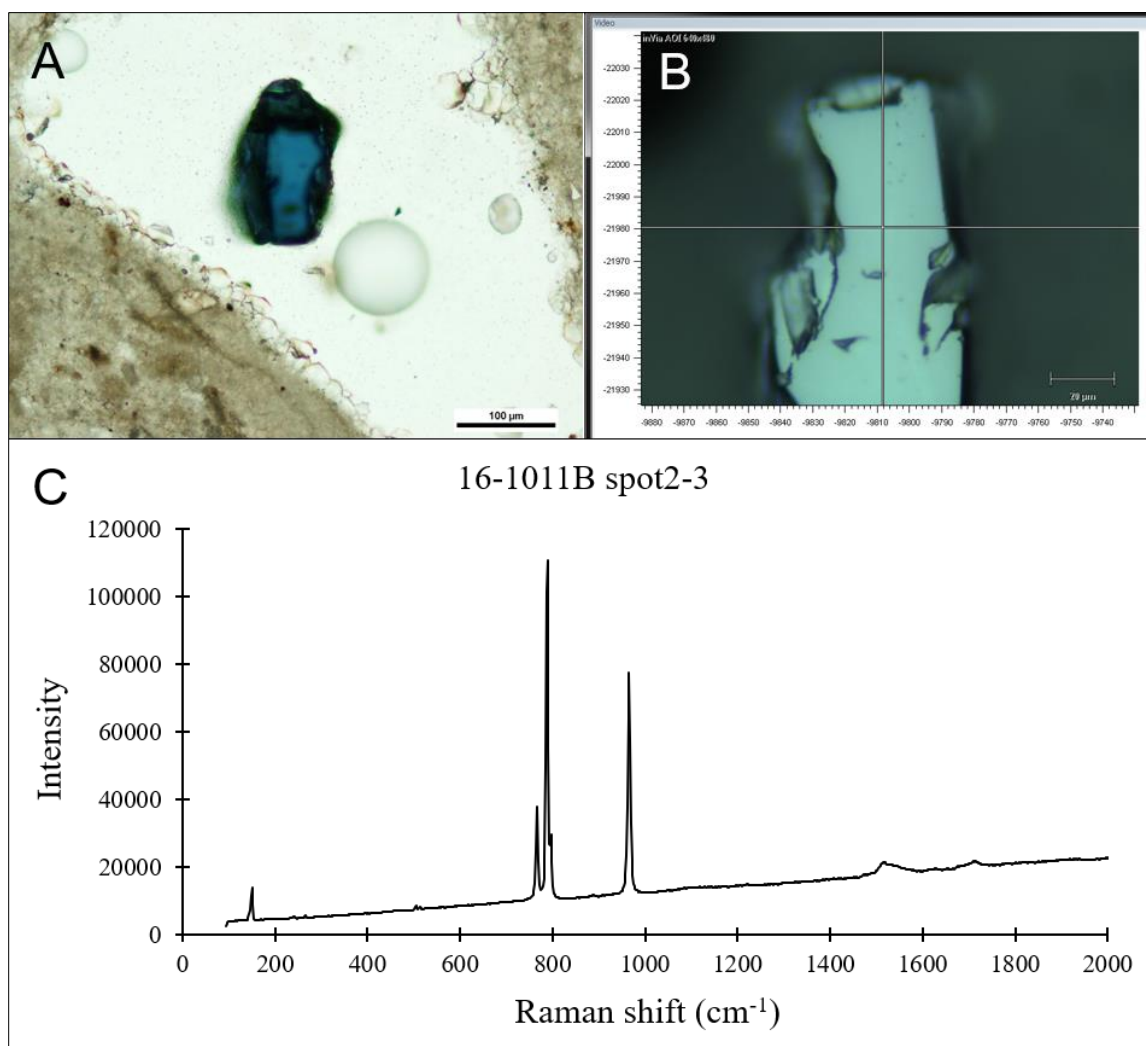


Figure F-14. Sample 16-1011B spot 2. A) In situ photomicrograph of moissanite crystal in plane polarized light (PPL) at 200x magnification. Scale bar is 100 μm . B) Reflected light image of moissanite crystal taken with Raman microscope at 500x magnification. Image is flipped vertically with respect to PPL image. Scale bar is 20 μm . C) Raman spectra obtained for moissanite crystal located at spot 2 in sample 16-1011B.

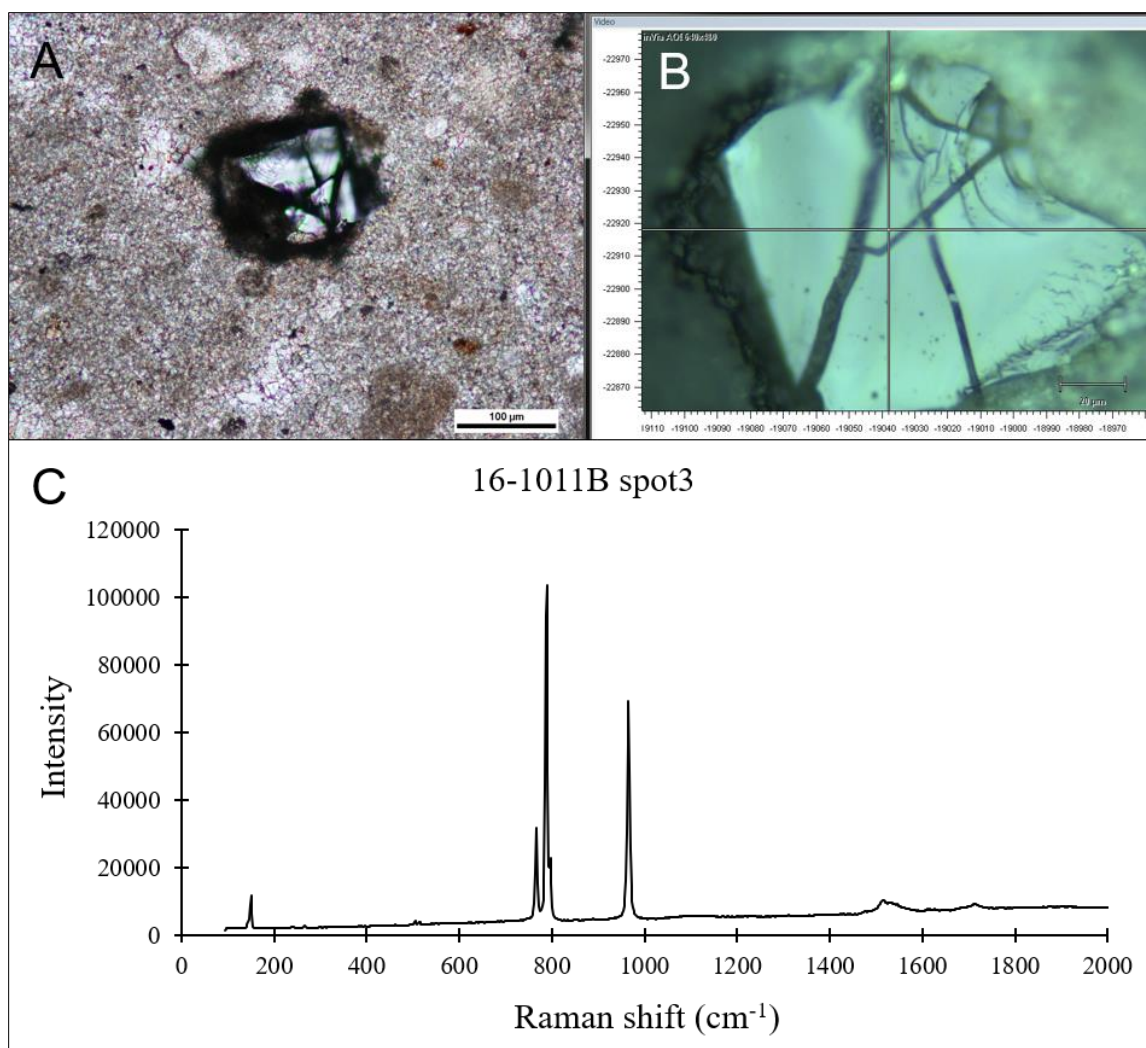


Figure F-15. Sample 16-1011B spot 3. A) In situ photomicrograph of moissanite crystal in plane polarized light (PPL) at 200x magnification. Scale bar is 100 μm . B) Reflected light image of moissanite crystal taken with Raman microscope at 500x magnification. Image is flipped vertically with respect to PPL image. Scale bar is 20 μm . C) Raman spectra obtained for moissanite crystal located at spot 3 in sample 16-1011B.

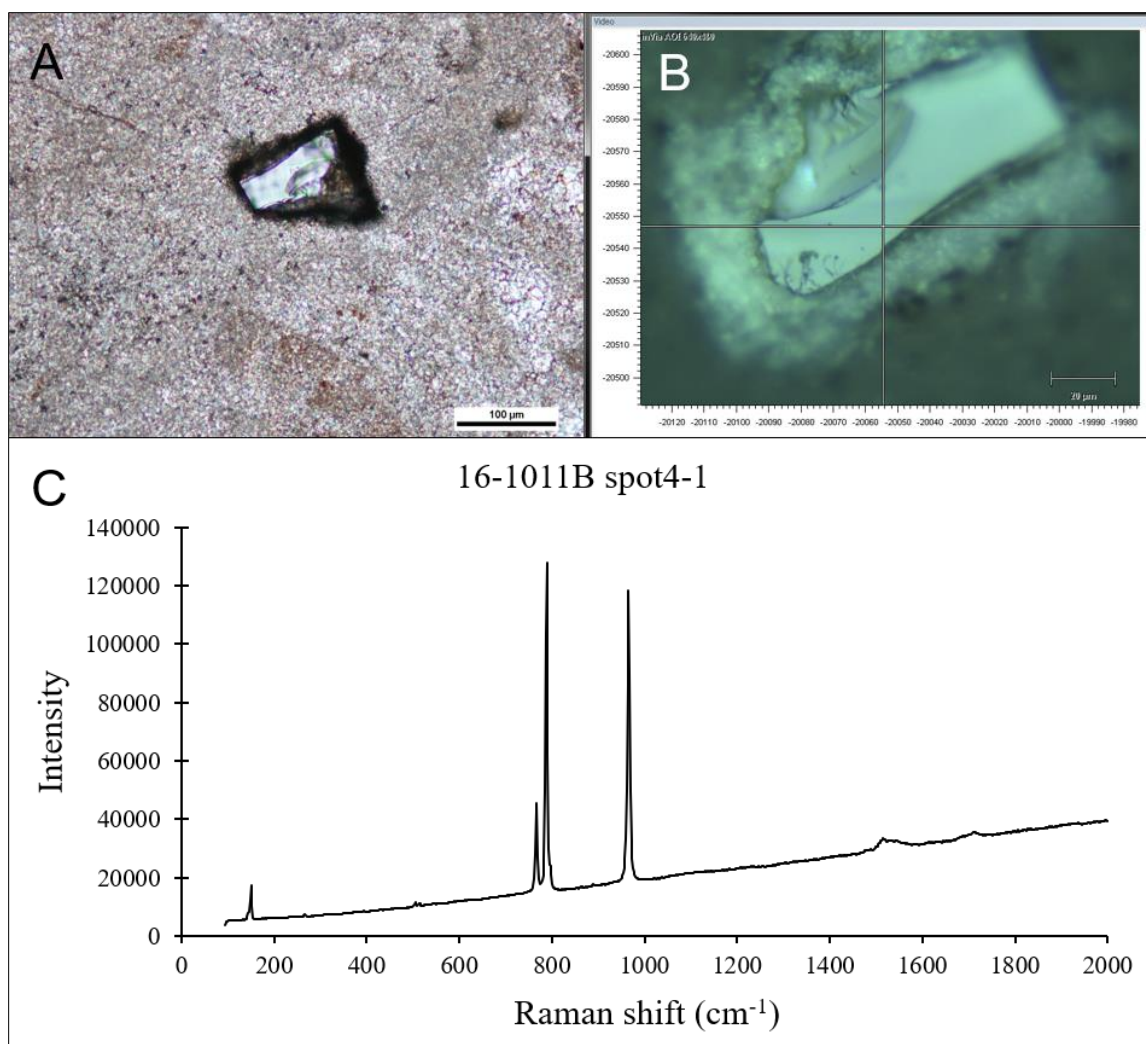


Figure F-16. Sample 16-1011B spot 4. A) In situ photomicrograph of moissanite crystal in plane polarized light (PPL) at 200x magnification. Scale bar is 100 μm . B) Reflected light image of moissanite crystal taken with Raman microscope at 500x magnification. Image is flipped vertically with respect to PPL image. Scale bar is 20 μm . C) Raman spectra obtained for moissanite crystal located at spot 4 in sample 16-1011B.

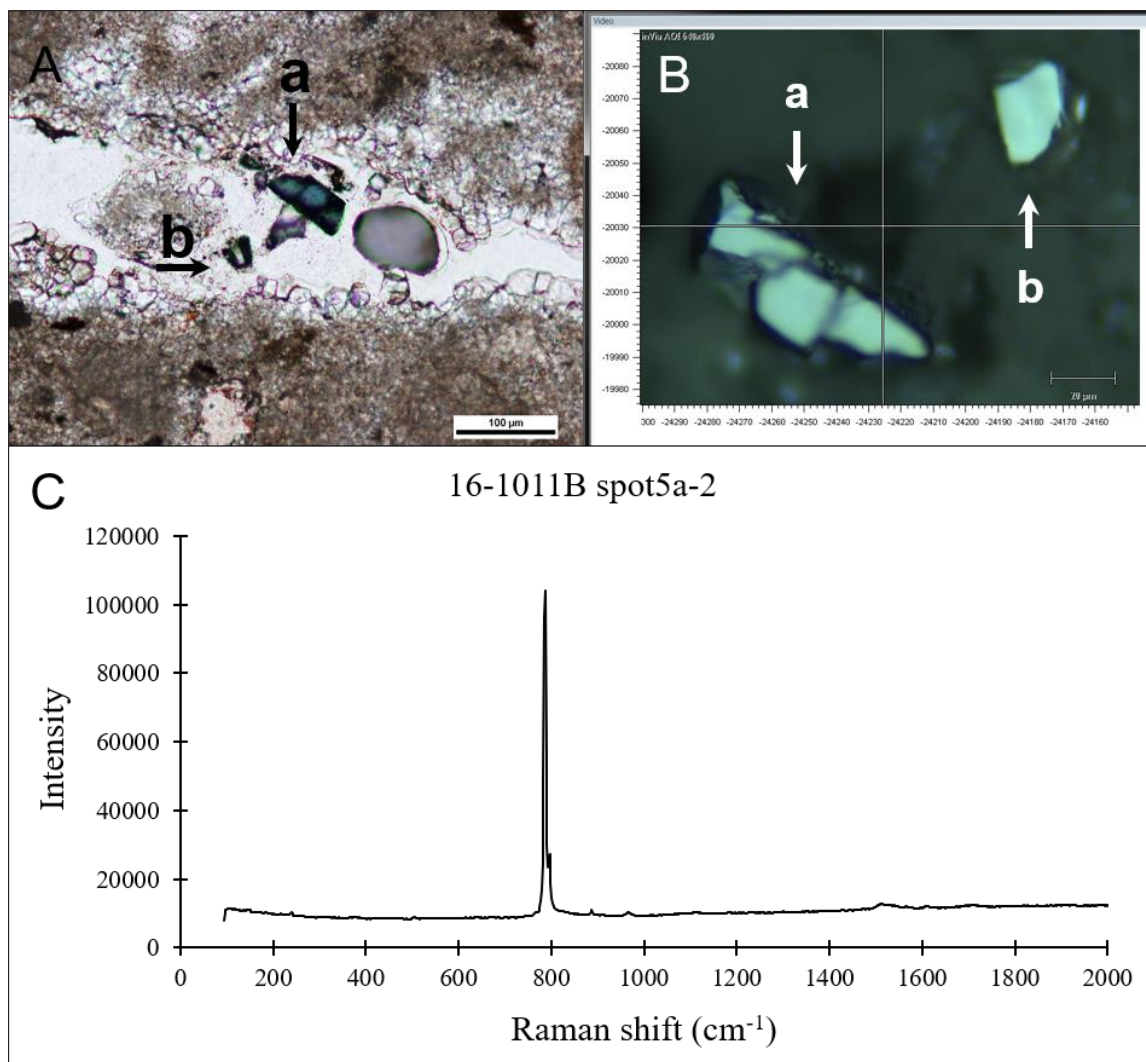


Figure F-17. Sample 16-1011B spot 5a. A) In situ photomicrograph of moissanite crystal in plane polarized light (PPL) at 200x magnification. Scale bar is 100 μm . B) Reflected light image of moissanite crystal taken with Raman microscope at 500x magnification. Image is flipped vertically with respect to PPL image. Scale bar is 20 μm . C) Raman spectra obtained for moissanite crystal located at spot 5a in sample 16-1011B.

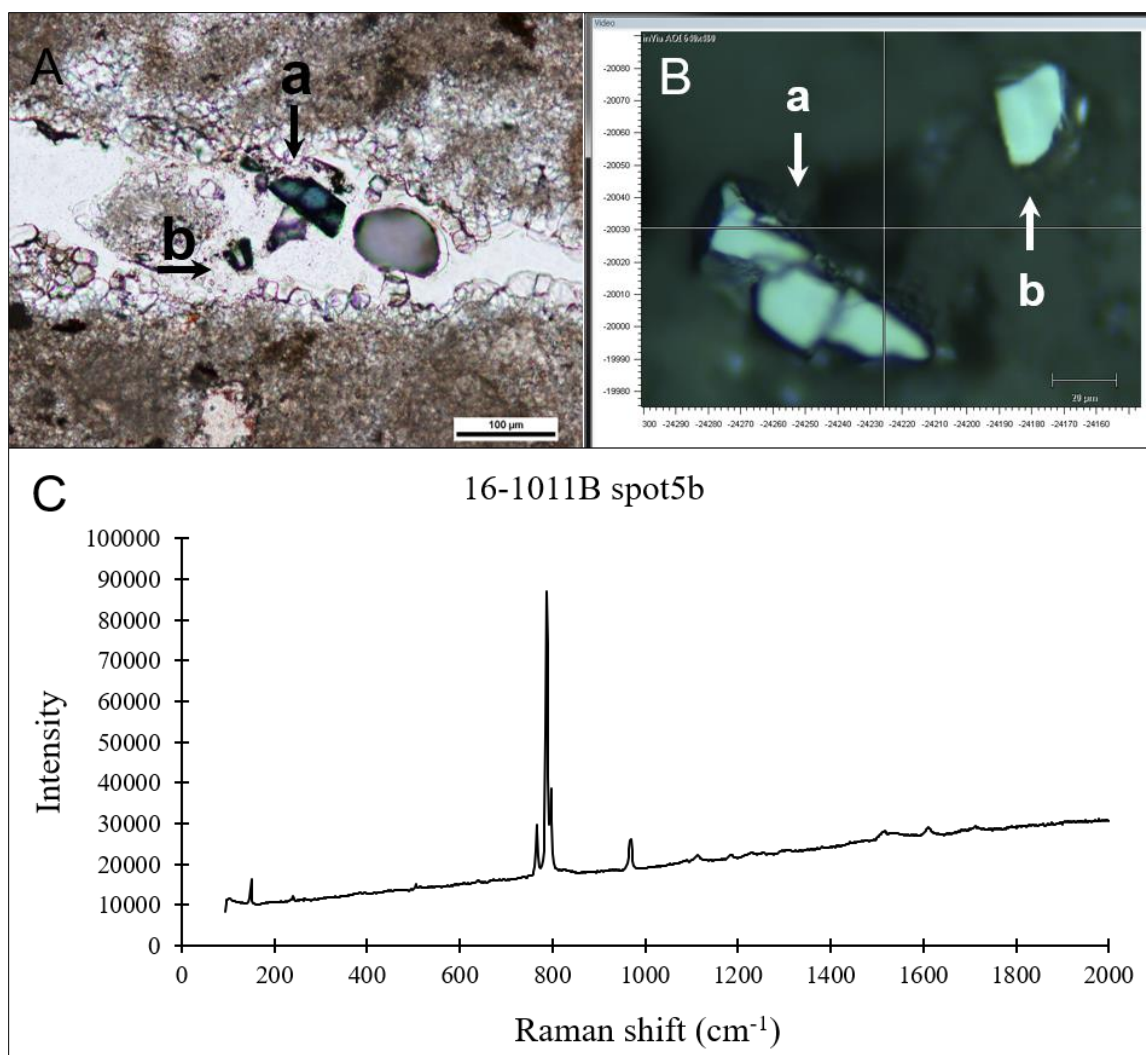


Figure F-18. Sample 16-1011B spot 5b. A) In situ photomicrograph of moissanite crystal in plane polarized light (PPL) at 200x magnification. Scale bar is 100 μm . **B)** Reflected light image of moissanite crystal taken with Raman microscope at 500x magnification. Image is flipped vertically with respect to PPL image. Scale bar is 20 μm . **C)** Raman spectra obtained for moissanite crystal located at spot 5b in sample 16-1011B.

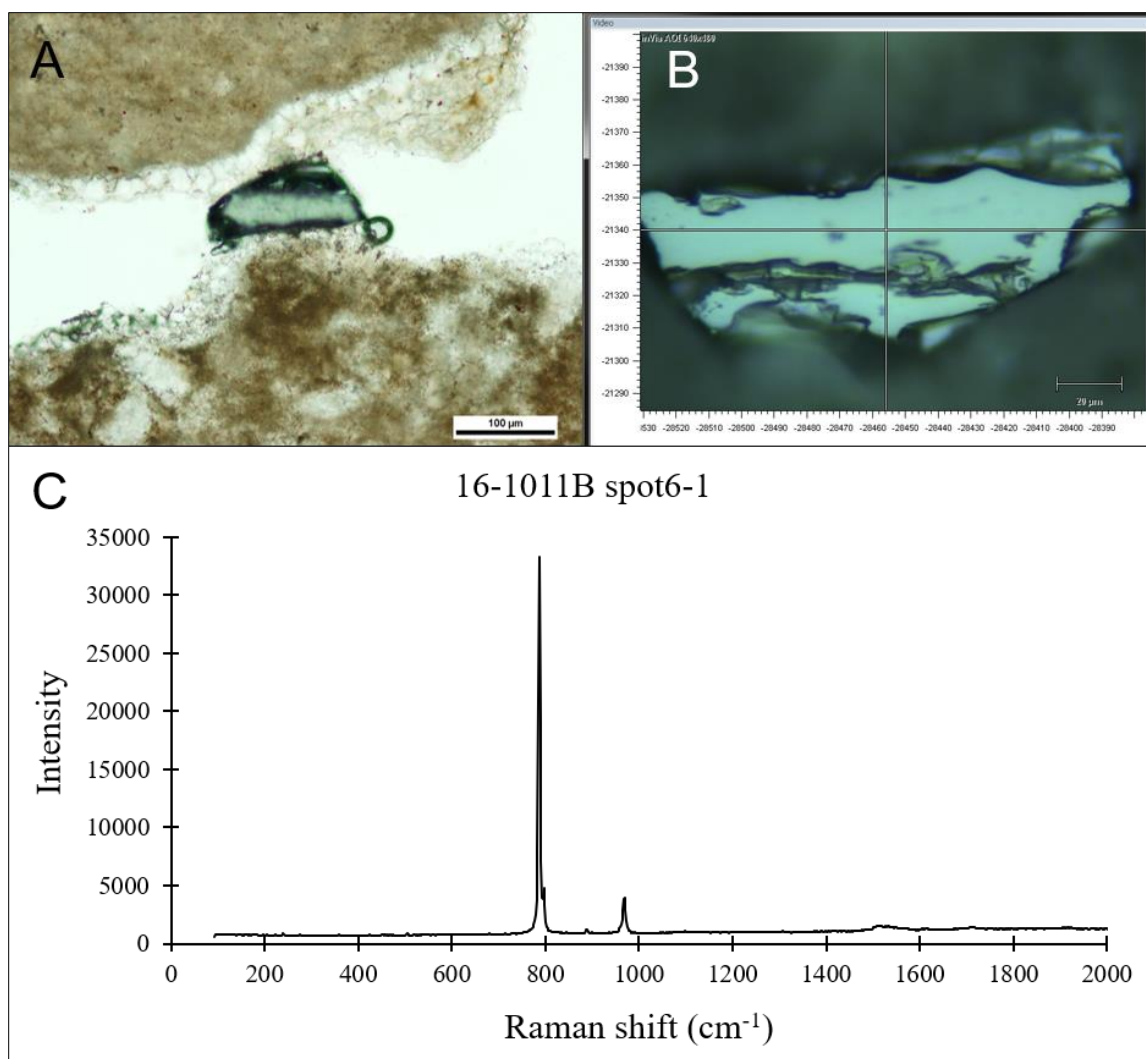


Figure F-19. Sample 16-1011B spot 6. A) In situ photomicrograph of moissanite crystal in plane polarized light (PPL) at 200x magnification. Scale bar is 100 μm . B) Reflected light image of moissanite crystal taken with Raman microscope at 500x magnification. Image is flipped vertically with respect to PPL image. Scale bar is 20 μm . C) Raman spectra obtained for moissanite crystal located at spot 6 in sample 16-1011B.

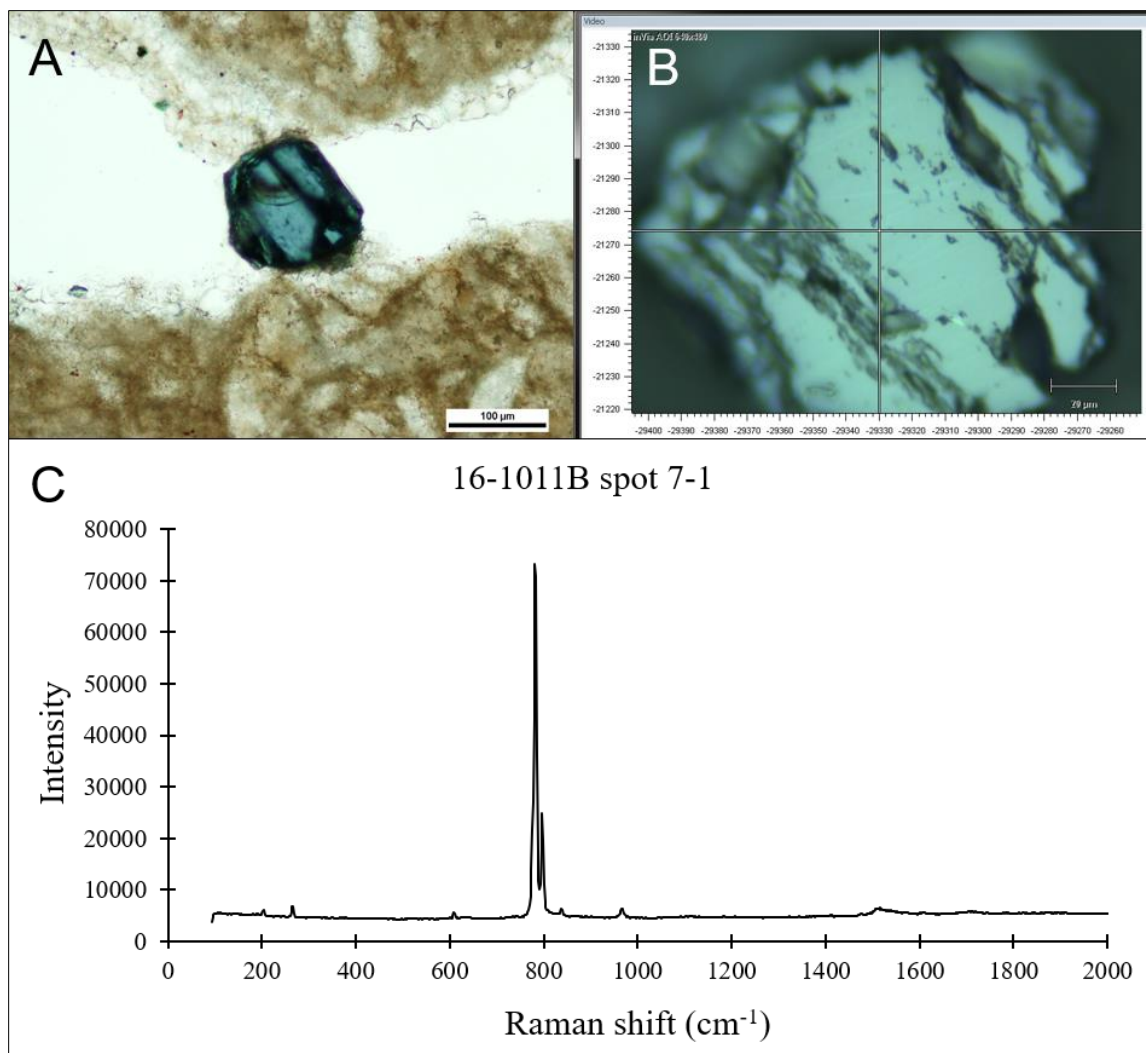


Figure F-20. Sample 16-1011B spot 7. A) In situ photomicrograph of moissanite crystal in plane polarized light (PPL) at 200x magnification. Scale bar is 100 μm . B) Reflected light image of moissanite crystal taken with Raman microscope at 500x magnification. Image is flipped vertically with respect to PPL image. Scale bar is 20 μm . C) Raman spectra obtained for moissanite crystal located at spot 7 in sample 16-1011B.

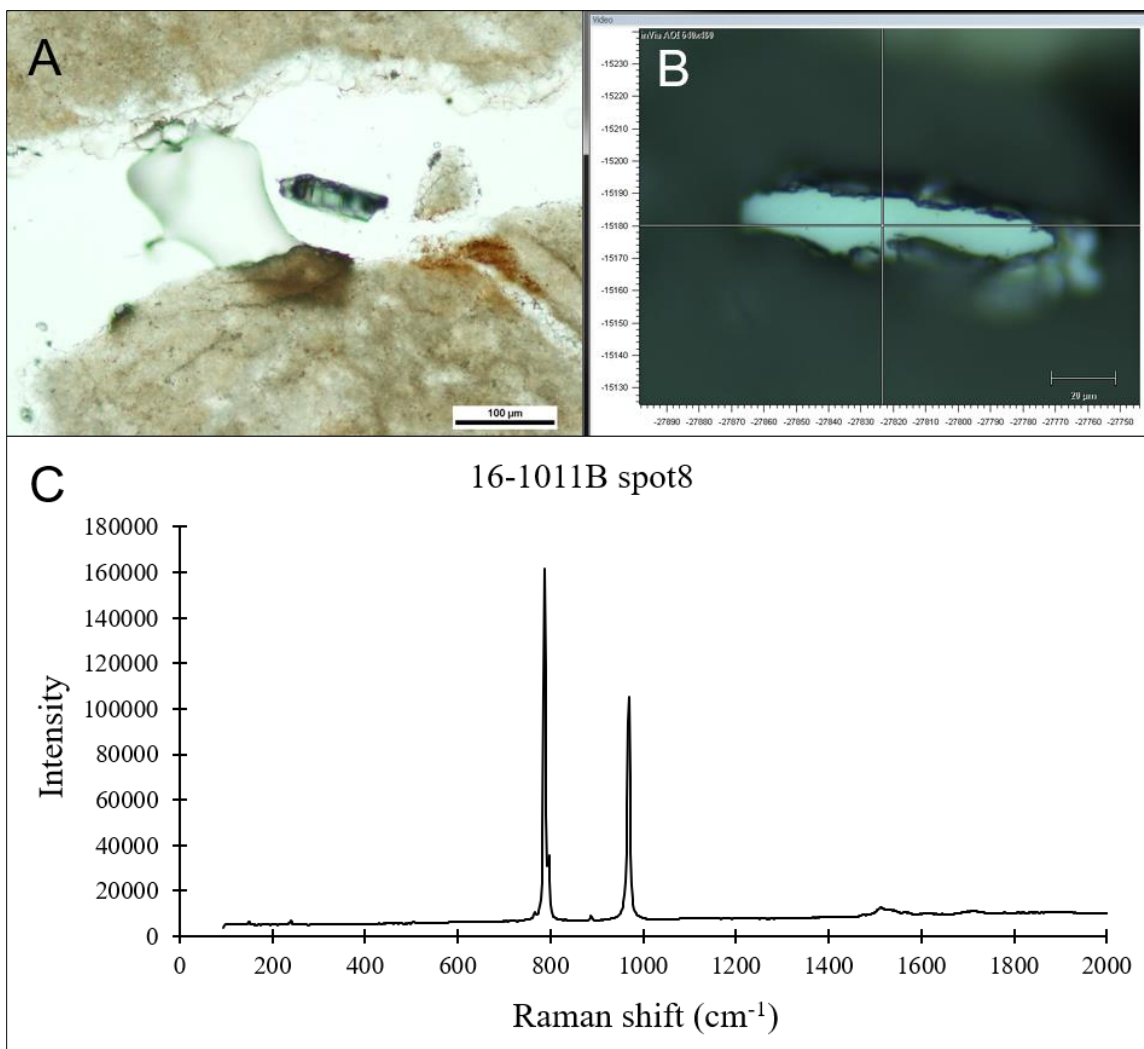


Figure F-21. Sample 16-1011B spot 8. A) In situ photomicrograph of moissanite crystal in plane polarized light (PPL) at 200x magnification. Scale bar is 100 μm . B) Reflected light image of moissanite crystal taken with Raman microscope at 500x magnification. Image is flipped vertically with respect to PPL image. Scale bar is 20 μm . C) Raman spectra obtained for moissanite crystal located at spot 8 in sample 16-1011B.

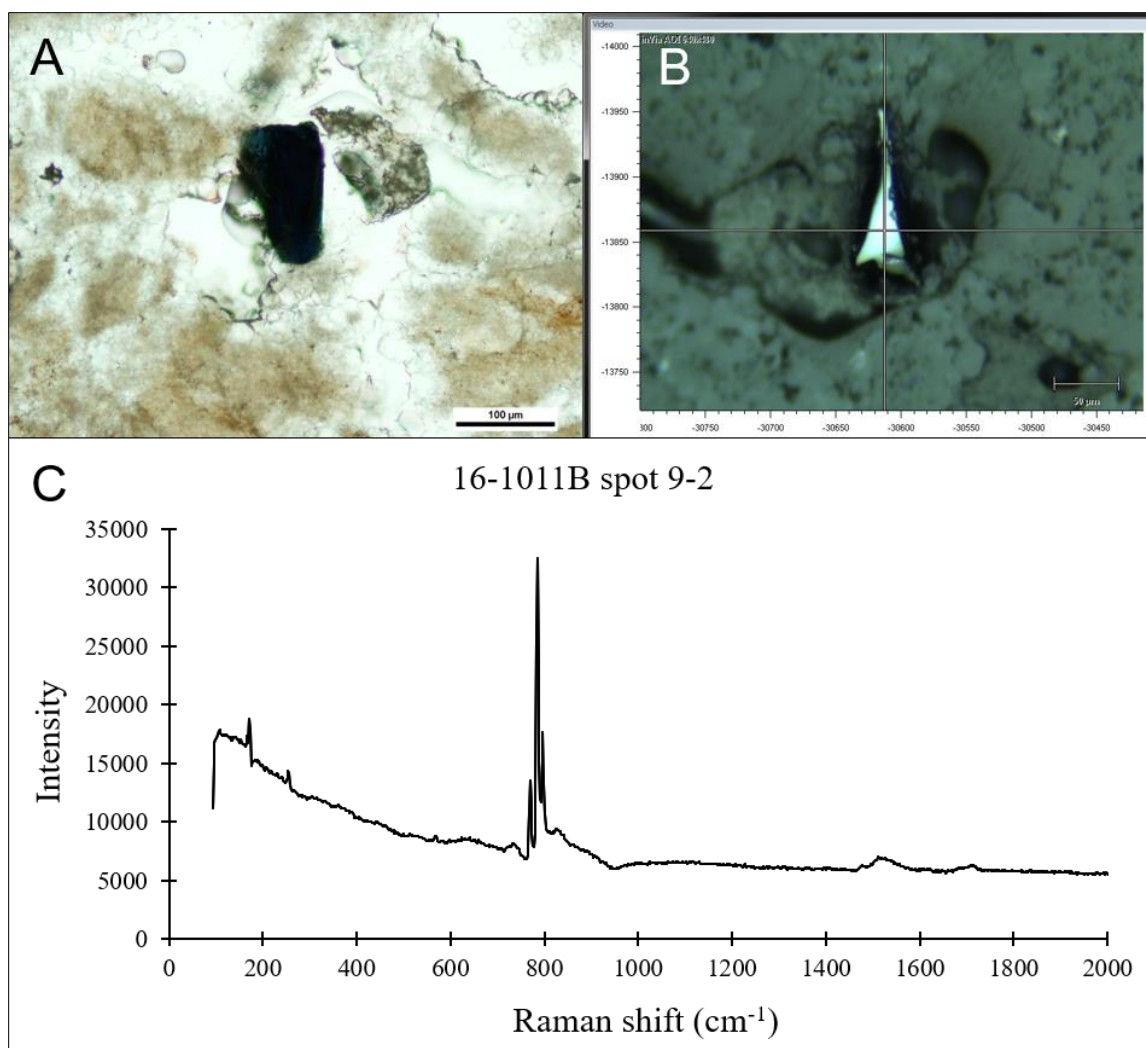


Figure F-22. Sample 16-1011B spot 9. A) In situ photomicrograph of moissanite crystal in plane polarized light (PPL) at 200x magnification. Scale bar is 100 μm . B) Reflected light image of moissanite crystal taken with Raman microscope at 200x magnification. Image is flipped vertically with respect to PPL image. Scale bar is 50 μm . C) Raman spectra obtained for moissanite crystal located at spot 9 in sample 16-1011B.

F.5 References

- Bauer M., Gigler A. M., Huber A. J., Hillenbrand R., and Stark R. W. 2009. Temperature-dependent Raman line-shift of silicon carbide. *Journal of Raman Spectroscopy* 40:1867–1874.
- Dobrzhinetskaya L., Mukhin P., Wang Q., Wirth R., O'Bannon E., Zhao W., Eppelbaum L., and Sokhonchuk T. 2018. Moissanite (SiC) with metal-silicide and silicon inclusions from tuff of Israel: Raman spectroscopy and electron microscope studies. *Lithos* 310–311:355–368.
- He D., Liu Y., Gao C., Chen C., Hu Z., and Gao S. 2017. SiC-dominated ultra-reduced mineral assemblage in carbonatitic xenoliths from the Dalihu basalt, Inner Mongolia, China. *American Mineralogist* 102:312–320.
- Nakashima S., and Harima H. 1997. Raman investigation of SiC polytypes. *Physica Status Solidi (A) Applied Research* 162:39–64.
- Qin X., Li X., Chen X., Yang X., Zhang F., Xu X., Hu X., Peng Y., and Yu P. 2019. Raman scattering study on phonon anisotropic properties of SiC. *Journal of Alloys and Compounds* 776:1048–1055.

Curriculum Vitae

Name: Jennifer Diane Newman

Post-secondary Education and Degrees:

University of Western Ontario
London, Ontario, Canada
2015-2020 Ph.D. Geology & Planetary Science and Exploration

University of Alberta
Edmonton, Alberta, Canada
2011-2014 M.Sc. Earth and Atmospheric Sciences

University of Alberta
Edmonton, Alberta, Canada
2005-2007 B.Sc. Specialization in Environmental Earth Science

University of Alberta
Edmonton, Alberta, Canada
2000-2004 B.Sc. Biological Sciences major Earth Sciences minor

Honours and Awards:

Natural Sciences and Engineering Research Council of Canada
Alexander Graham Bell Canada Graduate Scholarship-Doctoral (NSERC CGS-D)
University of Western Ontario
2017-2019

Doctoral Excellence Research Award
University of Western Ontario
2016-2019

Centre for Planetary Science and Exploration (CPSX)
Certificate of Appreciation for outstanding contributions towards the CPSX Outreach Program
2016-2017

Queen Elizabeth II Graduate Scholarship in Science and Technology (QEII-GSST)
University of Western Ontario
2016-2017 (declined – could not hold concurrently with NSERC)

Natural Sciences and Engineering Research Council of Canada
Postgraduate Scholarship-Doctoral (NSERC PGS-D)
University of Western Ontario
2016-2017

Western Graduate Research Scholarship
University of Western Ontario
2016

Polar Knowledge Canada (POLAR) Northern Scientific Training
Program Award
University of Western Ontario
2016

Queen Elizabeth II Graduate Scholarship in Science and
Technology (QEII-GSST)
University of Western Ontario
2015-2016

PhD Fellowship: NSERC CREATE “Technologies and Techniques
for Earth and Space Exploration”
University of Western Ontario
2015-2017

Graduate Students’ Association Professional Development Grant
University of Alberta
2013

ASTRO/CPSX Graduate Student Travel Award
University of Alberta
2013

Graduate Student Scholarship
University of Alberta
2013

**Related Work
Experience**

Teaching Assistant
University of Western Ontario
2015-2020

Research Assistant
University of Western Ontario
2015-2019

Lab Assistant
University of Alberta
2014

Teaching Assistant
University of Alberta
2011-2013

Planetary Mission Involvement	High Resolution Imaging Science Experiment (HiRISE) on the 2005 Mars Reconnaissance Orbiter (MRO) [PI: Dr. Alfred McEwen]: Science and operations planning for Cycle 301 (under Science Team Member Dr. Livio L. Tornabene), University of Western Ontario 23 April to 30 May 2018
Certificate of Operation	Canadian Space Agency Lunar Exploration Analogue Deployment (LEAD) Science Support in the HOPE-2 CSA/ESA Joint Experiment 13-19 June 2019
Analogue Mission Involvement	CanMoon 2019 Lunar Sample Return Analogue Mission Planning Lead, Planning Team, University of Western Ontario 2019 CanMars 2016 Mars Sample Return Analogue Mission Sequencing Integrator, Planning Team, University of Western Ontario 2016 CanMars 2015 Mars Sample Return Analogue Mission Localization Lead, Science Team, University of Western Ontario 2015
Concept Study Involvement	Canadian Space Agency Contract 9F050-170252/A: Space Exploration Concept Studies for Planetary Exploration and Space Astronomy Science Priorities – “Miniaturized in situ X-ray diffractometer for mineralogical characterization of planetary surfaces”. Student Collaborator, University of Western Ontario 2018-2020

Publications

Morse Z. R., Harrington E., Hill P. J. A., Christoffersen P., **Newman J.**, Choe B-H., Tornabene L. L., Caudill C., Osinski G. R. 2019. The use of GIS, mapping, and immersive technologies in the CanMars Mars Sample Return analogue mission: Advantages for science interpretation and operational decision-making. *Planetary and Space Science* 168: 15-26.

Osinski G. R., Battler M., Caudill C. M., Francis R., Haltigin T., Hipkin V. J., Kerrigan M., Pillis E. A., Pontefract A., Tornabene L. L., ... **Newman J.**, et al. 2019. The CanMars Mars Sample Return Analogue Mission. *Planetary and Space Science* 166: 110-130.

Pilles E. A., Cross M., Caudill C. M., Francis R., Osinski G. R., **Newman J.**, Battler M., Bourassa M., Haltigin T., Hipkin V., Kerrigan M., McLennan S., Silber E. A., Williford K. 2019. Exploring new models for improving planetary rover operations efficiency through the 2016 CanMars Mars Sample Return (MSR) analogue deployment. *Planetary and Space Science* 165: 250-259.

Choe B-H., Tornabene L. L., Osinski G. R., and **Newman J. D.** 2019. Remote predictive mapping of the Tunnunik impact structure in the Canadian Arctic using multispectral and polarimetric SAR data fusion. *Canadian Journal of Remote Sensing* 44: 513-531.

Newman, J. D. and Herd, C. D. K. 2015. Mineralogy, petrology and distribution of meteorites at the Whitecourt Crater, Alberta, Canada. *Meteoritics & Planetary Science* 50: 305-317.

Conference Abstracts

Newman J. D., Flemming R. L., and Osinski G. R. 2020. Shock Effects in Carbonates from the Haughton Impact Structure using X-Ray Diffraction. *51st Lunar and Planetary Science Conference*, Woodlands, TX, abstract #2284.

Newman J. D., Pilles E. A., Morse Z. R., Marion C. L., Christoffersen P. A., Hill P. J. A., Osinski G. R., Cloutis E. A., Andres C. N., Bourassa M., Caudill C. M., Cross M., Dicecca A., Doerksen K., Hibbard S., Hopkins R., Kolleywyn J., Pascual A., Ratcliffe K., Roberts A., Rodriguez Sanchez-Vahamonde C. D., Ryan C., Shah J., Tolometti G., Tornabene L. L., and Vlachopoulos O. 2020. Planning Team Operations for the CanMoon Lunar Sample Return Analogue Mission. *51st Lunar and Planetary Science Conference*, Woodlands, TX, abstract #2196.

Andres C. N., Ratcliffe K., **Newman J. D.**, Osinski G. R., Cloutis E. A., Marion C. L., and Pilles E. A. 2020. Rover Command Sequencing and Instrument Utilization during the CanMoon Analogue Mission. *51st Lunar and Planetary Science Conference*, Woodlands, TX, abstract #2584.

Osinski G. R., Grieve R. A. F., Hill P. J. A., **Newman J. D.**, Patel P., and Tolometti G. D. 2020. Impact Earth – A Resource for Public Outreach and Teaching at the K-12, Undergraduate, and Graduate Level. *51st Lunar and Planetary Science Conference*, Woodlands, TX, abstract #2111.

Flemming R. L., Rupert A. N., Field J., Pilles E. A., Sabarinathan J., Veinberg S. L., Leftwich K., Shaw A., Dickinson C., Berger J. A., Bourassa M., Gellert R., Hiemstra D. M., McCausland P. J. A., McIsaac K. A., Osinski G. R., Schmidt M. E., Tornabene L. L., Vukotic V. N., Bakhtazad A., Cao F., Li Y., Jenkins L. E., McCraig M. A., **Newman J. D.**, Pentesco J. T., Posnov N. M., Simpson S. L., Svenson M. J. O. 2020. In Situ X-ray Diffraction (ISXRD) for Exploring Mars Mineralogy and Geology. *51st Lunar and Planetary Science Conference*, Woodlands, TX, abstract #2965.

Shah J., Andres C. N., Pilles E. A., Roberts A., Rodriguez Sanchez-Vahamonde C. D., Vlachopoulos O., Yingling W., Marion C. L., Osinski G. R., Cloutis E. A., Morse Z. R., **Newman J. D.**, Caudill C. 2020. CanMoon Analogue Mission Operations: GIS, Localization, and Rover Traverse Planning and Monitoring. *51st Lunar and Planetary Science Conference*, Woodlands, TX, abstract #2222.

Marion C. L., Morse Z. R., **Newman J. D.**, Pilles E. A., Hill P. J. A., Osinski G. R., Cloutis E. A., Caudill C. M., Simpson S. L., Xie T. and the 2019 CanMoon Team. 2020. Shift Handovers for Real-Time Lunar Operations: Methods from the CanMoon Analogue Mission. *51st Lunar and Planetary Science Conference*, Woodlands, TX, abstract #2400.

Marion C. L., Osinski G. R., Bourassa M., Caudill C. M., Cloutis E. A., Christoffersen P., Hill P. J. A., Morse Z. R., **Newman J. D.**, Pilles E. A., Simpson S. L., Tornabene L. L., and Xie T. 2020. Overview of the CanMoon Lunar Sample Return Analogue Mission. *51st Lunar and Planetary Science Conference*, Woodlands, TX, abstract #2349.

Morse Z. R., Hill P. J. A., Osinski G. R., Cloutis E. A., Marion C. L., **Newman J. D.**, Caudill C. M., Christoffersen P., Pilles E. A., Simpson S. L., Tornabene L. L., and Xie T. 2020. CanMoon Analogue Mission Tactical Science Team: Scientific Instrumentation and Decision Making during a High Fidelity Realtime Lunar Analogue Mission. *51st Lunar and Planetary Science Conference*, Woodlands, TX, abstract #1253.

Hill P. J. A., Simpson S. L., Xie T., Morse Z. R., Sacks L. E., Osinski G. R., Cloutis E. A., Caudill C. M., Christoffersen P., Marion C. L., **Newman J. D.**, Pilles E. A., Tornabene L. L. 2020. CanMoon Science Interpretation Team: Insights into Volcanic Flows in Lanzarote Spain. *51st Lunar and Planetary Science Conference*, Woodlands, TX, abstract #2152.

Newman J. D., Pilles E. A., Morse Z. R., Marion C. L., Osinski G. R., Cloutis E. A., Caudill C. M., Hill P. J. A., Simpson S. L., Tornabene L. L., and Xie T. Planning Team Operational Structure for the 2019 CanMoon Lunar Sample Return Analogue Mission. 2019 Annual Meeting of the Lunar Exploration Analysis Group, Washington, D. C., abstract #5041.

Osinski G. R., Marion C., Cloutis E., Morse Z., **Newman J.**, Caudill C., Christoffersen P., Cross M., Hill P., Pilles E., Simpson S., Tornabene L. L., and Xie T. 2019. The Role of Analogue Missions in Preparing to Return to the Moon: Lessons and Recommendations from CanMoon. 2019 Annual Meeting of the Lunar Exploration Analysis Group, Washington, D. C., abstract #5018.

Morse Z. R., Hill P. J. A., Osinski G. R., Cloutis E. A., Caudill C. M., Christoffersen P., Marion C. L., **Newman J. D.**, Pilles E. A., Simpson S. L., Tornabene L. L., and Xie T. 2019. 2019 CanMoon Tactical Science Team: Real-Time Instrument Use and Coordination During a Lunar Sample Return Analogue Mission. 2019 Annual Meeting of the Lunar Exploration Analysis Group, Washington, D. C., abstract #5047.

Hill P. J. A., Simpson S. L., Xie T., Osinski G. R., Cloutis E. A., Caudill C. M., Christoffersen P., Marion C. L., Morse Z. R., **Newman J. D.**, Pilles E. A., and Tornabene L. L. 2019. 2019 CanMoon Science Interpretation Team: Insights into Volcanic Flows in Lanzarote, Spain. 2019 Annual Meeting of the Lunar Exploration Analysis Group, Washington, D. C., abstract #5048.

Newman J. D. and Osinski G. R. 2019. Impact-Generated Dykes from the Haughton Impact Structure, Canada. 50th Lunar and Planetary Science Conference, Woodlands, TX, abstract #1558.

Osinski G. R., Grieve R. A. F., Hill P., **Newman J.**, Patel P., and Tolometti G. 2019. Impact Earth – New Insights into the Terrestrial Impact Record and Cratering Processes. 50th Lunar and Planetary Science Conference, Woodlands, TX, abstract #2472.

Tornabene L. L., Block K., Pilles E., Baugh N., McEwen A. S., Hansen C., Espinoza A., Osinski G. R., Bina A., Bourassa M., Capitan R., Caudill C., Hansen K., Harrington E., Hibbard S., Hopkins R., Kissi-Ameyaw J., Morse Z., **Newman J.**, Pritchard I., Silber E., Simpson S., Tolometti G., and Werynski A. 2019. Mission Science/Operations Support and Training for Spacecraft Payloads: Building the Next Generation of Planetary Mission Professionals. 50th Lunar and Planetary Science Conference, Woodlands, TX, abstract #2962.

Newman J. D. and Osinski G. R. 2018. Investigation of Carbonate-rich Breccias and their Emplacement in the Central Uplift of the Decaturville Impact Structure, Missouri. 49th Lunar and Planetary Science Conference, Woodlands, TX, abstract #2880.

Flemming R. L., **Newman J. D.**, Botor R. J., Cao F., Caudill C. M., Galarneau M. R., Geiger J., Houde V. L., Jenkins L. E., Li Y., Maris J. M., Tolometti G. D., Rupert A. N., McCraig M. A., and Osinski G. R. 2018. Preliminary Investigation of Shocked Carbonates from the Haughton Impact Structure, Devon Island, NU using X-Ray Diffraction and Rietveld Refinement. 49th Lunar and Planetary Science Conference, Woodlands, TX, abstract #3000.

Newman J. D. and Osinski G. R. 2017. Characterization of breccia dykes in the deeply eroded Tunnunik impact structure, Canada. 80th Annual Meeting of the Meteoritical Society, Santa Fe, NM, abstract #6248.

Newman J. D., Cross M. D. G., Pilles E. A., Francis R., and Osinski G. R. 2017. Resource Utilization and Efficiency for the CanMars 2016 Mars Sample Return Analogue Mission. 48th Lunar and Planetary Science Conference, Woodlands, TX, abstract #2521.

Pilles E. A., Francis R. **Newman J.**, Cross M., Battler M., and Osinski G. R. 2017. To Hel and Back – Strategic Planning for the CanMars 2016 Mars Sample Return Analogue Mission. 48th Lunar and Planetary Science Conference, Woodlands, TX, abstract #2022.

Newman, J. D. and Osinski, G. R. (2016) Geological mapping of the Tunnunik impact structure, Victoria Island, Canadian High Arctic. 47th Lunar and Planetary Science Conference, Woodlands, TX, abstract #1591.

Christoffersen, P. A., **Newman, J. D.**, Morse, Z. R., Tornabene, L. L., and Osinski, G. R. (2016) Geologic map and stratigraphy of the Yggdrasil quadrangle from the 2015 CanMars MSR Analogue Mission. 47th Lunar and Planetary Science Conference, Woodlands, TX, abstract #2225.

Newman, J. D. and Herd, C. D. K. (2013) Possible impact origin of amorphous carbon spherules found in the soil surrounding the Whitecourt Meteorite Impact Crater. 76th Annual Meteoritical Society Meeting, Edmonton, AB, abstract #5332.

Newman, J. D. and Herd, C. D. K. (2013) Whitecourt Meteorite Impact Crater: Distribution, texture, and mineralogy of meteorites and the discovery of carbon spherules possibly associated with the impact event. 44th Lunar and Planetary Science Conference, Woodlands, TX, abstract #2316.